Solid-State Control and Analysis of Active Pharmaceutical Ingredients

A thesis presented in fulfilment of the requirements for the degree of Doctor of Philosophy in the Faculty of Science of the University of Strathclyde

by

Hector Polyzois

Strathclyde Institute of Pharmacy and Biomedical Sciences

November 2020

This thesis is dedicated to my beloved parents, Mary and Greg, for their encouraging and motivating words that kept me going strong and for their unconditional support throughout the full duration of my PhD journey. The work described herein would have never been possible without you!

Declaration of Author's Rights

This thesis is the result of the author's original research. It has been composed by the author and has not been previously submitted for examination which has led to the award of a degree.

Signed: Hector Polyzois **Date: 2/11/2020**

Acknowledgements

First and foremost, I would like to acknowledge and express my deepest gratitude to my primary supervisor, Professor Alastair Florence, for providing me with the opportunity to conduct my PhD research in his group and for his invaluable guidance and support over the course of the last few years. I also wish to acknowledge the NPL Scottish Hub for funding my PhD studentship and my NPL supervisor, Dr Alex Shard, for our insightful discussions and for hosting me during my various visits to NPL throughout my project. I am extremely grateful to Professor Sally Price from University College London who allowed me to collaborate with her and her group as part of the activities of the EPSRC-funded CPOSS project (EP/K039229/1). I would like to thank Dr Rui Guo from University College London for the discussions that we have shared and conducting the CSP study of OXCBZ (Figures 4.4b and 4.25a) which assisted significantly in the experimental screening work performed for this compound. Dr Guo additionally performed modelling investigations and calculations with DMACRYS, which yielded greater insight into the twisted OXCBZ III crystals that were studied, and kindly provided the material presented in Figures 5.25 – 5.27 and Table 5.4. My sincere gratitude also goes to Dr Susan Reutzel-Edens from the Small Molecule Design & Development team at Lilly Research Laboratories in Indianapolis, USA with whom I collaborated closely during the final stages of my doctoral studies; the work described in Chapter 6 of this thesis is the direct outcome of our collaboration and for that I am extremely grateful.

Many thanks also need to go a number of people from CMAC, Strathclyde and NPL for their contributions to the work described herein: Dr Vijay Srirambhatla and Dr Monika Warzecha, for their vital input and suggestions and for many fruitful discussions that we have shared over the years. Dr Warzecha additionally assisted with the AFM and SEM studies presented. Dr Alan Martin and Dr Deborah Bowering, for providing excellent training and input on the use of XRD, DSC/TGA and DVS. Dr Fraser Mabbott, for training and assistance with CAG analysis. Dr Kenneth Smith, for assistance with SCF experiments. Dr Alice Turner, Eleonora Paladino, and Patricia Keating, for contributing to data collection and processing in GI dissolution, ToF-SIMS and HPLC-MS studies respectively. Last but not least, Magdalena Wywijas and Steve Spencer, for assistance with QBox studies performed at NPL, and Dr Naresh Kumar, for fabricating the metal-coated glass substrates that were used in those studies and some of the work at Strathclyde.

Abstract

The research described herein entails solid-state screening investigations and characterisation of a number of active pharmaceutical ingredients to improve understanding of the range of structural diversity possible and specific factors that impact on specific systems. The pharmaceuticals investigated are the anticonvulsant oxcarbazepine (OXCBZ), the developmental cholesterylester transfer protein inhibitor evacetrapib (EVC) and a novel tetrazole analogue of EVC (TAEVC) that has been custom synthesised by Eli Lilly and Company. All three compounds were subjected to both solvent-based and solvent-free crystallisation protocols to target factors promoting the formation of novel crystal structures, characterise any novel crystal packing arrangements formed and explore how non-classical nucleation and growth mechanisms impact crystal morphology.

Experimental screening studies of OXCBZ enabled form III to be obtained via solution crystallisation and from physical vapour deposition onto various substrates. The *R*-3 crystal structure of this polymorph was determined for the first time using X-ray powder diffraction. OXCBZ form III was also found to crystallise with a striking twisted morphology. Detailed analysis using scanning electron and atomic force microscopy allowed tracking of the formation and evolution of the twisted crystals. Twisting from the vapour phase is proposed to result from surface energy-driven effects owing to aggregation of fibrous crystals. Theoretical models capable of describing twisting in solution-grown crystals are additionally presented.

Solid-state experiments conducted for EVC and TAEVC revealed the propensity of both compounds to crystallise in isostructural solvated forms. Over a dozen novel solvated salt cocrystals of EVC were isolated and characterised and an initial solid-form landscape was established for TAEVC which had never been subjected to solid-state screening and characterisation previously. The propensity of TAEVC to form a highly robust three-dimensional network of hydrogen bonds in the solid state was noted, likely an indication of TAEVC molecules' preference to self-associate during nucleation and growth.

Table of Contents

List of Figures

List of Tables

List of Abbreviations

1D	**One-Dimensional**
2D	**Two-Dimensional**
3D-ED	**Three-Dimensional Electron Diffraction**
AFM	**Atomic Force Microscopy**
BCS	**Biopharmaceutics Classification System**
BFDH	**Bravais–Friedel–Donnay–Harker**
CAG	**Contact Angle Goniometry**
CBZ	**Carbamazepine**
CCD	**Charge-Coupled Detector**
CCDC	**Cambridge Crystallographic Data Centre**
CNT	**Classical Nucleation Theory**
CSD	**Cambridge Structural Database**
CSP	**Crystal Structure Prediction**
CYH	**Cyheptamide**
CYT	**Cytenamide**
DBZ	**Dibenzazepinodione**
DFT-D	**Density Functional Theory**
DSC	**Differential Scanning Calorimetry**
DMA	***N,N*-Dimethylacetamide**
DMF	***N,N*-Dimethylformamide**
DMSO	**Dimethyl Sulfoxide**
DVS	**Dynamic Vapour Sorption**
EVC	**Evacetrapib**
FBRM	**Focused Beam Reflectance Measurement**
FDA	**US Food and Drug Administration**
GI	**Gastrointestinal**
GoF	**Goodness-of-Fit**
HPLC-MS	**High Performance Liquid Chromatography-Mass Spectrometry**
ICH	**International Conference on Harmonization**
IUCr	**International Union of Crystallography**
MAC	**Molar Absorption Coefficient**
MDB	**Mogul Distribution Bias**
MOFS	**Metal-Organic Frameworks**
OXCBZ	**Oxcarbazepine**

PIDD	**Primary Ion Dose Density**
PIHn	**Polymer-Induced Heteronucleation**
PVM	**Particle Vision Measurement**
QCM	**Quartz Crystal Microbalance**
RH	**Relative Humidity**
RMS	**Root Mean Square**
RMSD	**Root Mean Square Deviation**
RT	**Room Temperature**
SC-XRD	**Single-Crystal X-ray Diffraction**
SCF	**Supercritical Fluid**
SDPD	**Structure Determination from Powder Diffraction**
SEM	**Scanning Electron Microscopy**
SURMOFS	**Surface Metal-Organic Frameworks**
TAEVC	**Tetrazole Analogue of Evacetrapib**
TBA	***tert*-Butylamine**
TFE	**2,2,2-Trifluoroethanol**
TGA	**Thermogravimetric Analysis**
THF	**Tetrahydrofuran**
ToF-SIMS	**Time-of-Flight Secondary Ion Mass Spectrometry**
UV-vis	**UV-visible**
VH-XRPD	**Variable Humidity X-ray Powder Diffraction**
VT-XRPD	**Variable Temperature X-ray Powder Diffraction**
XRD	**X-ray Diffraction**
XRPD	**X-ray Powder Diffraction**

List of Appendices

Chapter 1: Introduction

1.1 Introduction to Crystallisation

Crystallisation is a ubiquitous unit operation implemented across a wide range of industries including the pharmaceutical, chemical, and food manufacturing sectors. Its primary role is for isolating and purifying chemicals which can then be used as raw materials to manufacture formulated products and it is common practice in industry for crystallisation to be used in order to facilitate the separation of solid-liquid intermediates (Chen et al., 2011). Hence, a diverse range of molecular types undergo crystallisation, including but not limited to, medicinal drugs (Brown et al., 2018), food additives (Brun et al., 2012), dyes (Taden et al., 2004), pigments (Xiang et al., 2004) and agrochemicals (Poornachary et al., 2011). Crystallisation fundamentally describes the transformation of atoms or molecules from a vapour, liquid or dissolved state to a solid, crystalline form in which the molecular packing extends periodically in three dimensions (Hook and Hall, 1991).

In the context of the pharmaceuticals, crystallisation is employed for the isolation of intermediate products, the purification of crude process stream, as well as the final purification step in the manufacturing process of active pharmaceutical ingredients (APIs). Over 90% of APIs are small organic molecules exhibiting a molecular weight of less than 900 Da (Alvarez and Myerson, 2010; Chen et al., 2011; Macielag, 2012). Key requirements, in particular, for final crystallisation steps are to deliver purity control over the crystal form in addition to control over crystal size and shape to enable ease of subsequent process steps such as filtration. Pharmaceutical crystallisation has been traditionally carried out by means of batch processes (Byrn et al., 2015) in which materials are added to a vessel and the reaction conditions change over time to drive the process to completion. In recent years, however, continuous crystallisation processes have been explored as an alternative approach to batch processes (Mascia et al., 2013; Ferguson et al., 2014; Baxendale et al., 2015; Burcham et al., 2018, Brown et al., 2018). Many stated benefits of continuous crystallisation have been reported, including allowing for safer, more efficient, and less costly use of reagent materials, solvents, energy and manufacturing space, and the enhanced control possible may contribute towards reduced production of waste material and environmental emissions (Plumb, 2005; Swichtenberg, 2008; Baxendale et al., 2015; Burcham et al., 2018). Regulatory authorities such as the U.S. Food and Drug Administration (FDA) have encouraged the adoption of continuous processes by the pharmaceutical industry in order to optimise the robustness of medicines manufacture (Lee et al., 2015).

Before a process can be developed and delivered it is essential to understand the potential crystal forms or structures that a given molecule can adopt. Once these are identified and the most suitable form is selected, the production process can be developed and scaled up as required to meet expected demand (Brown et al., 2018). The focus of the work presented here is at an earlier stage of the development of an API and is concerned with understanding the fundamental stages in crystallisation and the factors that can control polymorphism in particular.

1.2 Overview of Steps and Phenomena Comprising a Crystallisation Process

The crystallisation process is known to consist of multiple individual steps, each one comprising its own mechanisms. These steps are outlined in the following sections.

1.2.1 Nucleation

Crystallisation is initiated through nucleation, a probabilistic phenomenon characterised by randomness in the behaviour of solute molecules present in solution (Toschev et al., 1972; Nordström et al., 2013). There are multiple factors capable of affecting the occurrence of nucleation in a crystallisation process, including supersaturation, solvent type, shear, temperature and the physical chemistry of the compound under investigation (Beck et al., 2009). Supersaturation, or supersolubility, is the thermodynamic driving force behind crystallisation and nucleation (Alatalo et al., 2010). It is defined as the state wherein the concentration of a solute in solution is greater than that of the corresponding equilibrium concentration under fixed temperature and atmospheric pressure. In order for nucleation to occur, a difference in chemical potential must exist between both the supersaturated and saturated state of a solute in solution (Rodríguez-Hornedo and Murphy, 1999). Equations 1.1 and 1.2 (Rodríguez-Hornedo and Murphy, 1999) describe chemical potential difference and supersaturation respectively.

$$\Delta\mu = (\mu_1 - \mu_{eq}) \qquad \textbf{(Equation 1.1)}$$

In Equation 1.1, ∆μ is defined as the difference in chemical potential, μ_1 corresponds to the chemical potential of solute in a supersaturated solution and μ_{eq} is the chemical potential of solute in a saturated solution.

$$\sigma = (c - c^*)/c^* \qquad \textbf{(Equation 1.2)}$$

In Equation 1.2, the relative supersaturation (σ) is dependent on the concentration (c) of solute in a supersaturated solution and the solubility (c^*) of solute. There are multiple methodologies that can be utilised for inducing supersaturation in a solution, including solvent removal by means of evaporation or by cooling and/or changing pH, and by the addition of an anti-solvent that reduces the solubility of a solute (Rodríguez-Hornedo and Murphy, 1999). Crystal nucleation has a direct impact on the morphology, packing density, particle size distribution and polymorphic form of the final product that arises from crystallisation and is categorised into two forms, primary or secondary nucleation (Vekilov, 2010a & 2010b; Beckmann, 2013; Wang et al., 2014).

1.2.1.1 Primary Nucleation

In the context of solution-based crystallisation, which is most often applied in pharmaceuticals, two distinct types of primary nucleation have been described: heterogeneous and homogeneous nucleation (Mullin, 2001). Heterogeneous nucleation is the more commonly encountered and practically relevant of the two mechanisms and is typically instigated when a solution comes in direct contact with solid surfaces, dust particles or impurities in the solution (Beckmann, 2013). On the contrary, homogeneous nucleation occurs in the absence of foreign interfaces in solution. It has been established that heterogeneous nucleation is thermodynamically favoured over homogeneous nucleation because of the lower free energy component required to induce nucleation, for example when a solute becomes adsorbed onto a foreign surface present in solution (Erdemir et al., 2009). Aspects of surface-induced heterogeneous nucleation are described in greater detail in section 1.6.

Two theoretical models have been described to account for homogeneous nucleation (Figure 1.1), namely classical nucleation theory (Davey et al., 2013) and non-classical, two-step nucleation theory (Vekilov, 2010a & 2010b). The classical nucleation theory (CNT) model describes the formation of critical nuclei, which are

capable of undergoing sustained growth, through the arrangement of individual solute molecules in clusters. In order for critical nuclei formation to occur according to CNT, a free energy barrier must be overcome (Figure 1.2). The change in free energy of a given system during the homogeneous nucleation process is defined through Equation 1.3 (Mullin, 2001) and the free energy change required for formation of a critical nucleus is described using Equation 1.4 (Mullin, 2001). CNT can account for the nucleation rate of a given system through Equation 1.5 (Mullin, 2001).

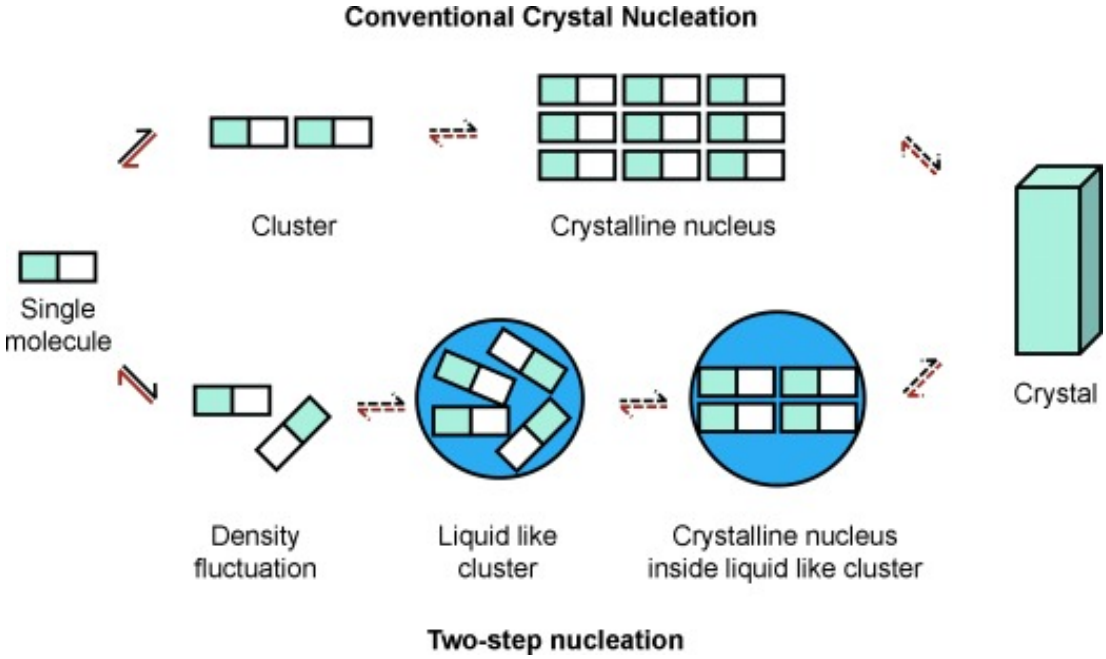

Figure 1.1: Schematic depiction of classical (conventional) nucleation theory and two-step nucleation theory (reproduced from Davey et al., 2013).

$$\Delta G_{crys} = -\frac{4}{3}\pi r^3 \Delta G_v + 4\pi r^2 \gamma \qquad \textbf{(Equation 1.3)}$$

In Equation 1.3, ΔG_{crys} is the free energy change corresponding to a nucleus of spherical shape in solution, r represents the radius of the spherical nucleus, γ is the surface free energy of an emerging nucleus and ΔG_v is indicative of the volume free energy for the growing nucleus.

$$\Delta G_{crit} = \frac{16\pi\gamma^3}{3(\Delta G_v)^2} = \frac{4\pi\gamma {r_c}^2}{3} \qquad \textbf{(Equation 1.4)}$$

In Equation 1.4, ΔG_{crit} represents the free energy change required for the formation of a critical nucleus and r_c is the radius of the critical nucleus. Once r_c has been reached, a constant decrease in the total free energy is observed and growth is favoured energetically over dissolution, which results in the formation of the critical nucleus and subsequent growth.

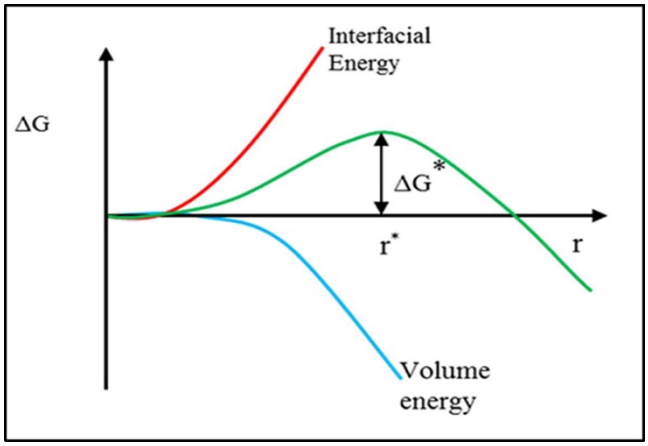

Figure 1.2: Free energy diagram showing the dependence of free energy change required for the formation of a critical nucleus, denoted by ΔG*, on the radius of the critical nucleus denoted by r* (reproduced from Karthika et al., 2016).

$$J = A_{\mathrm{j}} \exp\left[-\frac{16\pi {v_m}^2 \gamma^3}{3{k_{\mathrm{B}}}^3 T^3 \ln^2 S}\right] \qquad \textbf{(Equation 1.5)}$$

In Equation 1.5, J describes the overall rate of nucleation, A_{j} corresponds to the nucleation pre-exponential factor, v_{m} is indicative of the molecular volume, γ is the interfacial energy, k_{B} is the Boltzmann constant and S is the supersaturation ratio, described by the concentration c and equilibrium solubility c^* of a solute ($S = c/c^*$).

The two-step nucleation theory (Figure 1.3) describes the occurrence of nucleation through the formation of critical nuclei in two distinct steps: 1) formation of a dense, liquid-like cluster exhibiting structural disorder from the solution and 2) formation of an ordered crystalline nucleus within the liquid-like cluster. In Figure 1.3, $\Delta G^0_{\mathrm{L-L}}$ represents the free energy of formation of a dense, liquid-like phase, ΔG^*_1 corresponds to the free energy barrier for formation of a dense liquid cluster and ΔG^*_2 is the free energy barrier representing a structure fluctuation that results in the formation of an ordered, crystalline cluster. In instances wherein the liquid phase is unstable and $\Delta G^0_{\mathrm{L-L}}$ is > 0 the liquid phase materialises in the form of mesoscopic

clusters and ΔG^0_{L-L} transforms to ΔG^0 (curve at the top). The curve at the bottom of the diagram reflects occasions wherein the dense liquid phase is stable and ΔG^0_{L-L} is < 0 (reproduced from Vekilov, 2010a & 2010b).

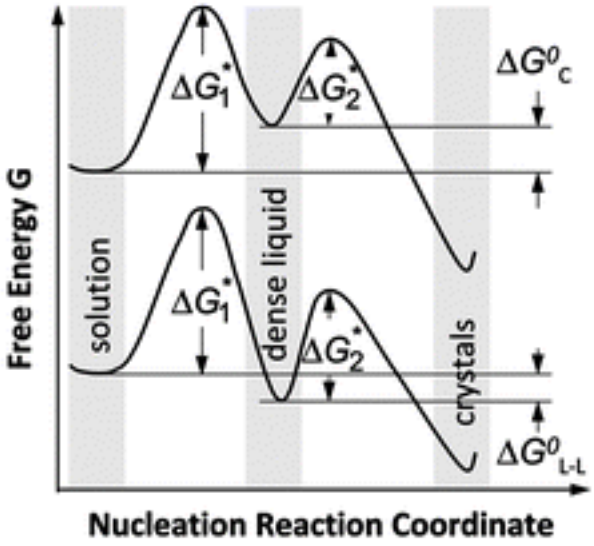

Figure 1.3: Free energy diagram representative of two-step nucleation (reproduced from Vekilov, 2010a & 2010b).

Two-step nucleation has been particularly prevalent in studies investigating the crystallisation behaviour of proteins (Vekilov, 2004; Sleutel and Van Driessche, 2014; Vorontsova et al., 2015) and has additionally been applied to small inorganic compounds (Lee and Maa, 1991; Wolf et al., 2017; Li et al., 2018), biominerals (Veis and Dorvee, 2013), colloids (Zhang and Liu, 2007) and various organic compounds (Shahar et al., 2016; Jiang et al., 2017; Tsarfati et al., 2018), including pharmaceuticals (Warzecha et al., 2017).

1.2.1.2 Secondary Nucleation

Secondary nucleation describes the formation of new crystals in supersaturated solution that occurs in the presence of crystals of the material under investigation (Botsaris, 1976; Kobari et al., 2010; Agrawal and Paterson, 2015). This type of nucleation is most frequently brought about through collisions of existing large crystals with smaller crystalline particles or foreign surfaces (including the vessel or agitator) present in solution which facilitate the formation of secondary nuclei (Beckmann, 2013). Alternative mechanisms of secondary nucleation include production of secondary nuclei via shear forces acting on crystals present in supersaturated solutions (Garabedian and Strickland-Constable, 1972; Yousuf and Frawley, 2018)

and initial breeding wherein fines on the surface of cystals become secondary nuclei through dislodgment (Steendam and Frawley, 2019).

1.2.2 Crystal Growth

Once crystalline particles have formed via nucleation in a supersaturated solution the particles can then grow into larger, observable crystals. The growth of nucleated particles features an expansion of the crystal lattice initially formed during the nucleation event, via the addition of atoms, ions or molecules to the newly formed crystal surface (Bernardo and Giulietti, 2010). There are multiple factors known to affect crystal growth in solution, including crystal structure and structural defects, supersaturation, temperature, solvent type and impurity presence (Rodríguez-Hornedo and Murphy, 1999).

The growth of crystals can occur via classical or non-classical crystal growth. Classical crystal growth mechanisms in solution typically involve the addition of solute monomer units to different sites of a crystal's surface (Figure 1.4a), occurring through gradual generation and accumulation of layers (Burton et al., 1951). There are three types of crystal surface sites that can accommodate monomers in solution-based, classical crystal growth: kinks, steps and terraces (Figure 1.4a). Kink sites favour the formation of up to three intermolecular bonds with monomers, in contrast with step sites that can accommodate the formation of two bonds and terrace sites which can only form one bond (Burton et al., 1951). In instances where solute molecules adsorb onto the surface of a crystal, monomers can become incorporated into the crystal surface through direct incorporation (Gratz et al., 1993) onto one of the kinks (Figure 1.4b) or surface diffusion (Olafson et al., 2015) following adsorption onto a terrace (Figure 1.4c). Figure 1.4d provides a depiction of the free energy profile exhibited by a molecule as it becomes directly incorporated into a step, wherein *i* and *ii* represent kinetic barriers corresponding to the molecule's incorporation and detachment from a growth site. In Figure 1.4e, the free energy profile of a molecule undergoing surface diffusion toward a step is presented, where *i*, *ii*, *iii*, and *iv* indicate kinetic barriers corresponding to adsorption, desorption, surface diffusion, and step incorporation from the surface. It has been established that classical crystal growth usually manifests through two-dimensional, layered growth across terrace sites or step sites arising due to presence of screw dislocations on the crystal surface (Burton et al., 1951).

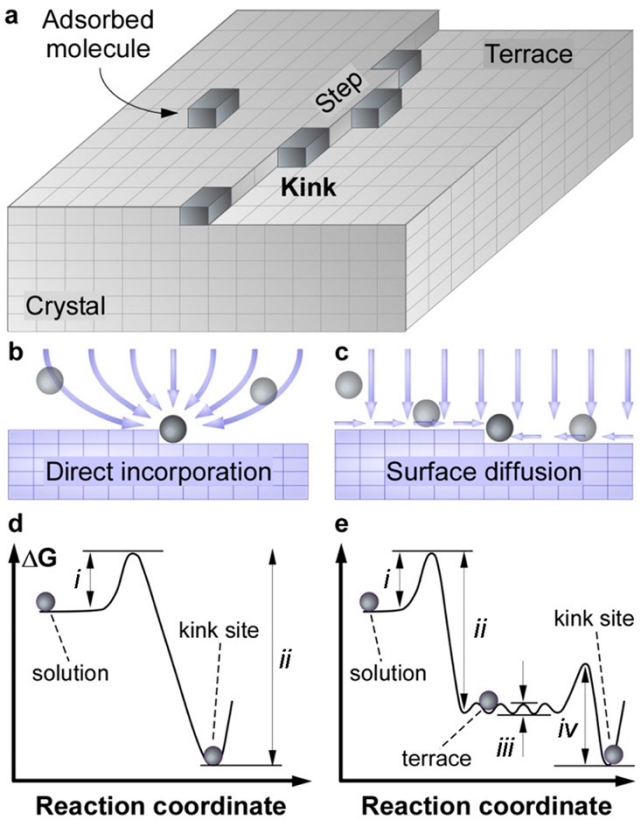

Figure 1.4: Schematic representation of classical crystal growth pathways (reproduced from Olafson et al., 2015).

Contrary to classical growth mechanisms, non-classical growth mechanisms (Figure 1.5) involve the addition of non-monomer growth units such as dimers, trimers, molecular clusters and nanocrystals to the surface of a crystal (De Yoreo et al., 2015). Directly related to the two-step nucleation theory, non-classical crystal growth features the incorporation of different types of precursor layers into the surface of a crystal which precede the formation of fully crystalline layers. Precursor layers in non-classical crystal growth include oligomers (Jiang et al., 2017), liquid-like droplet structures (Jiang et al., 2017) and amorphous or crystalline nanoparticles (Gong et al., 2012; Li et al., 2012)

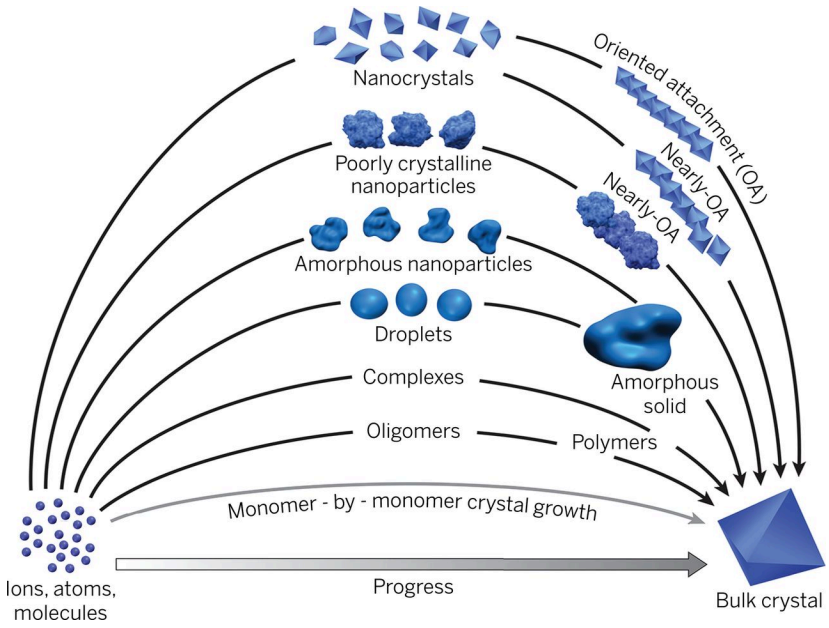

Figure 1.5: Schematic depiction of the multiple and complex pathways of non-classical nucleation and crystal growth relative to classical, monomer-by-monomer crystal growth (reproduced from De Yoreo et al., 2015).

1.2.3 Attrition

One phenomenon that is occasionally encountered in crystallisation processes is that of attrition. Attrition refers to the unwanted breakdown of crystals that have formed in the preliminary stages of crystallisation and it is typically brought about when crystals from the same crystallisation process end up colliding with one another or the crystallisation reactor itself (Mazzarotta et al., 1996). Attrition can result in the formation of secondary nuclei (Bosetti and Mazzotti, 2020) and is described by two distinct phases; the first one is known as abrasion and involves the elimination of parts of a crystal which are significantly smaller than the whole crystal, such as corners or sharp edges; the second phase is known as fragmentation and refers to the splitting of large crystals into smaller ones (Chianese et al., 1993; Madras and McCoy, 2007).

1.2.4 Agglomeration

Agglomeration can often occur during crystallisation and involves the adherence and subsequent growth of crystals that are small in size, resulting in the formation of larger crystalline particles (Brunsteiner et al., 2005). There are typically three stages to consider in an agglomeration process. Stage one involves small crystals colliding with one another in solution. Stage two features aggregation of the colliding crystals,

brought about by crystal attraction forces coming into effect. In the final stage, crystal agglomerates arise due to the formation of crystal bridges between aggregates (Alander and Rasmuson, 2007). Agglomeration is often problematic in the context of medicines manufacture as it may broaden the particle size distribution of APIs and result in the entrapment of solvent and/or impurities within their crystals (Mullin, 2001; Miki et al., 2005).

1.2.5 Ostwald Ripening

The phenomenon of Ostwald ripening (Ostwald, 1900; Vetter et al., 2013) pertains to the ability of large crystalline particles to undergo growth at the expense of smaller ones. The driving force behind the occurrence of Ostwald ripening is the difference in solubility between small and large particles, with small particles dissolving more readily and depositing themselves on the surface of their larger counterparts which consequently results in an increase in their size (Myerson and Ginde, 2002).

1.3 Crystal Structure, Isostructurality, Chirality, Polymorphism and Multi-Component Crystals

1.3.1 Crystal Structure

Thanks to the advent of X-ray crystallography, one of the most thoroughly studied aspects of solid matter is the packing arrangement of individual atoms and molecules in crystalline solids. The main building unit of a crystal structure is the unit cell, a repeating pattern of molecules which arrange themselves in three dimensions and extend periodically in all directions to give rise to the macroscopic crystal (Hook and Hall, 1991). Periodicity and structural order are the deciding factors in terms of distinguishing between crystalline and amorphous (non-crystalline) materials which do not exhibit structural periodicity in three dimensions and therefore cannot be defined in the context of a unit cell (Elliott, 2001).

The geometry of a unit cell is defined by six lattice parameters comprising cell lengths *a*, *b*, and *c* and the angles α, β, and γ between the aforementioned lengths. Depending on the values of the cell lengths and the angles between them, crystal structures can be categorised in seven distinct families which are characteristic of the overall shape of the unit cell (Table 1.1). A space group notation describes the symmetry of a crystal (Hiller, 1986; Glusker et al., 1994). There are 230 possible symmetries in a three-

dimensional crystal structure and these correspond to the 230 space groups that crystallographers use to determine the exact symmetry of a crystal (Hahn, 2002a). The seven crystal families are known to combine with four distinct centring types in three dimensions to give rise to the 14 Bravais lattices (Figure 1.6) which represent 14 out of the 230 space groups that are known to exist. The centring types describe the precise positions of lattice points within a unit cell and are defined in Table 1.2.

Table 1.1: Overview of crystal systems and corresponding unit cell parameters.

Crystal System	Unit Cell Parameters
Cubic	$a = b = c, \alpha = \beta = \gamma = 90°$
Trigonal	$a = b = c, \alpha = \beta = \gamma < 120°$ and $\neq 90$
Hexagonal	$a = b \neq c, \alpha = \beta = 90°$ and $\gamma = 120°$
Tetragonal	$a = b \neq c, \alpha = \beta = \gamma = 90°$
Orthorhombic	$a \neq b \neq c, \alpha = \beta = \gamma = 90°$
Monoclinic	$a \neq b \neq c, \alpha = \gamma = 90° \neq \beta$
Triclinic	$a \neq b \neq c, \alpha \neq \beta \neq \gamma$

Table 1.2: Overview of crystal centring types and corresponding location of lattice points in the unit cell.

Centring Type	Location of Lattice Points in the Unit Cell
Primitive (*P*)	Lattice points found on the corners of the unit cell only
Base-centred (*A*, *B* or *C*)	Lattice points mainly found on the corners of the unit cell with one extra point located at the centre of each face of one pair of parallel faces of the cell
Body-centred (*I*)	Lattice points mainly found on the corners of the unit cell with an extra point located at the centre of the cell
Face-centred (*F*)	Lattice points mainly found on the corners of the unit cell with an extra point located at the centre of each of the faces of the cell

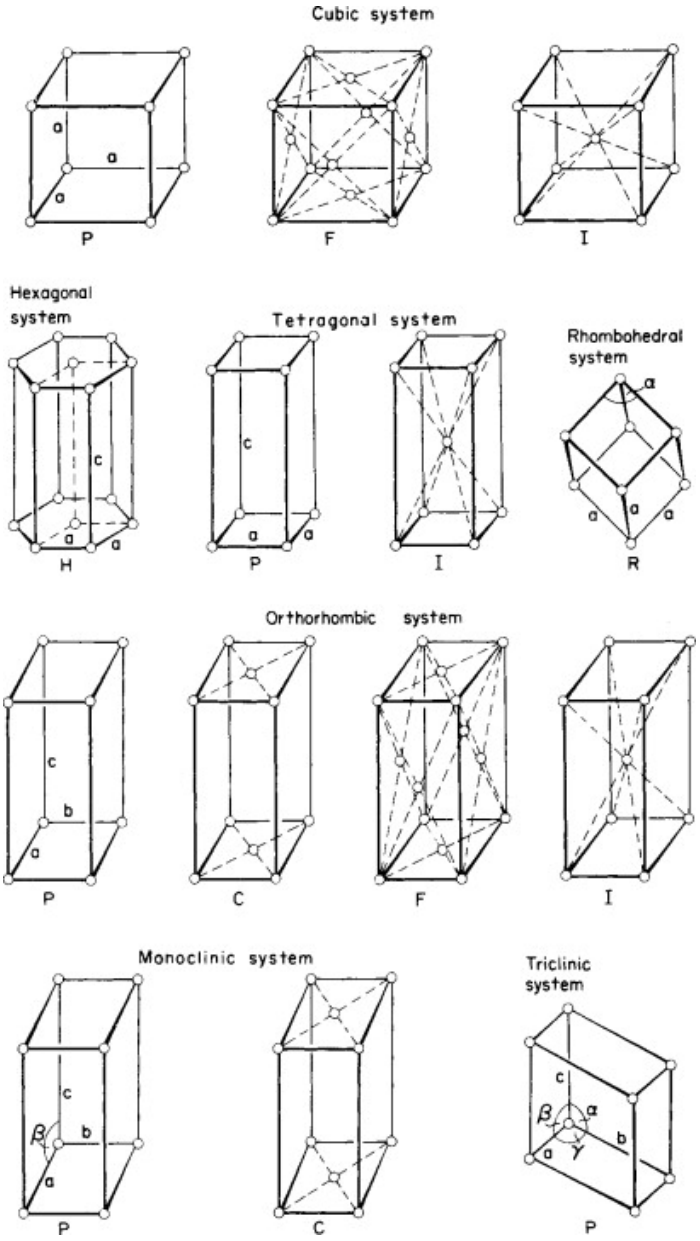

Figure 1.6: Overview of the 14 Bravais lattice systems (reproduced from Landau et al., 1967).

The unit cell of a crystal contains a basic structural motif referred to as the asymmetric unit (denoted *Z')* which consists of part of a molecule or a single molecule or multiple molecules which are not related by crystallographic symmetry. The application of both translational and non-translational symmetry to the asymmetric unit results in generation of the crystal in three dimensions (Ooi, 2010). Two types of translational symmetry operations exist within a unit cell: Screw axis, defined by translation of the unit cell along an axis followed by rotation about the same axis, and glide plane, corresponding to translation followed by reflection of the unit cell. On the contrary,

non-translational symmetry operations involve four distinct forms of rotation of the unit cell which are rotation, rotation-inversion, reflection and inversion centre. Based on the presence of an inversion centre element in the unit cell, space groups can be split into two distinct categories, centrosymmetric and non-centrosymmetric (Tilley, 2006). Centrosymmetric groups are defined by the presence of an inversion centre as one of the symmetry operations in the unit cell whereas non-centrosymmetric ones are completely devoid of inversion centres.

1.3.2 Isostructurality

Crystals may exhibit similarities with respect to their structure, lattice parameters, space group notation and chemical composition. One category of crystals exhibiting such similarities is that of isostructural crystals. The International Union of Crystallography (IUCr) defines isostructural crystals as crystals that "have the same structure, but not necessarily the same lattice parameters or chemical composition, and show 'comparable' variability in the atomic coordinates to that of the lattice parameters and chemical composition" (IUCr Online Dictionary of Crystallography).

1.3.3 Chirality

Chirality is a geometric property of some molecules or ions. A chiral molecule/ion is non-superimposable on its mirror image (Brooks et al., 2011; Viedma et al., 2015) whereas an achiral (non-chiral) molecule/ion can be superimposed on its mirror image (Eliel et al., 1994; Moss, 1996; Flack and Bernardinelli, 1999). The presence of one or more asymmetric (chiral) centers is an attribute characteristic of chiral molecules, as depicted in Figures 1.7a and 1.7b which illustrate the concept of chirality using two enantiomers of the same molecule as an example.

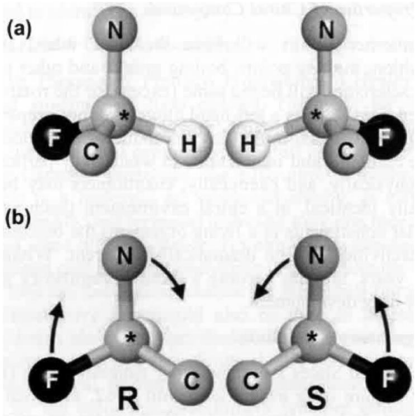

Figure 1.7: Schematic depictions of the concept of chirality (adapted from Brooks et al., 2011).

Enantiomers represent pairs of molecular entities that are non-superimposable mirror images of each other (Moss, 1996; Flack and Bernardinelli, 1999) and exhibit the same physicochemical properties whilst rotating plane polarised light in opposite directions. In Figure 1.7a, the chiral centre of each enantiomer is indicated by the central atom marked * which is surrounded by 4 chemically distinct substituents. Figure 1.7b highlights the *R* (rectus, right-handed) and *S* (sinister, left-handed) conformations of the two enantiomers which are determined based on the Cahn-Ingold-Prelog convention (Cahn et al., 1956) and involve prioritising the substituent atoms to the chiral centre with respect to their atomic number, with higher atomic number corresponding to higher priority. Upon rotation of the molecule, the substituent with the lowest priority (H) moves behind the chiral centre while the remaining substituents rotate in clockwise direction from highest to lowest priority for the *R* conformation and in counterclockwise direction from highest to lowest priority for the *S* conformation.

Chirality is a property that can additionally be utilised to describe crystal structures and a number of distinct categories of crystalline chiral materials have been identified: enantiopure materials, racemic compounds, racemic conglomerates and solid solutions. In enantiopure (or enantiomerically pure) materials, all crystals contain molecules that comprise the same chirality sense, i.e. only a single enantiomer within the corresponding detection limits (Moss, 1996). Racemic compounds, on the contrary, comprise homogeneous crystals wherein two enantiomers are present in equimolar amounts and have a well-defined arrangement (Moss, 1996). Racemic conglomerates represent equimolar mechanical mixtures of crystals wherein each crystal comprises one of the two enantiomers for a given compound (Moss, 1996; Viedma et al., 2015). Solid solutions are crystalline architectures characterised by a random distribution of the enantiomers within the unit cell (Jacques et al., 1981; Brandel et al., 2016). The occurrence of solid solutions is rare as less than 1% of chiral compounds are susceptible to their formation (Jacques et al., 1981).

Chiral crystal structures that are enantiopure can only crystallise in one of the 65 non-centrosymmetric Söhncke space groups that solely comprise rotations and translations, which are both symmetry operations of the first kind (Jacques et al., 1981; Flack, 2003). Chiral structures crystallising in groups $P2_12_12_1$, $P2_1$, $P1$ and $C2$ have been identified as the most commonly occurring ones (Sakamoto, 2004). A variety of techniques have been utilised experimentally over the years to investigate the chiral properties of crystals. These include polarised light microscopy (Lowry,

1964), optical polarimetry (Matsuura and Koshima, 2005) and circular dichroism spectroscopy (Kuroda, 2008). Whilst these methods have proven successful in characterising chiral crystals comprising microscopic to macroscopic sizes, single-crystal X-ray diffraction is the only analytical tool that can be utilised to determine the absolute nature of chirality in a chiral crystal (Flack and Bernardinelli, 1999).

The absolute nature of chirality in crystals is denoted by their absolute structure, a term defined by Flack and Bernardinelli as "the spatial arrangement of the atoms of a physically identified non-centrosymmetric crystal and its description by way of unit cell dimensions, space group and representative coordinates of all atoms" (Flack and Bernardinelli, 1999). Absolute structure is not meant to describe the absolute nature of chirality in a molecule. Instead, the term "absolute configuration" is utilised for that purpose and was defined by Flack and Bernardinelli as "the spatial arrangement of the atoms of a physically identified chiral molecular entity (or group) and its stereochemical description (e.g. *R* or *S*)". The absolute configuration of a molecule can be derived only when the absolute structure has been determined. Determination of a crystal's absolute structure requires knowledge of the Flack parameter (Flack, 1983) which arises because of anomalous scattering of X-rays by the atoms comprising the unit cell and is discussed in greater detail in section 1.7.1.3.3. Absolute configuration can additionally be established experimentally through the use of other analytical techniques such as nuclear magnetic resonance (Uccello-Barretta and Balzano, 2013), vibrational circular dichroism (He et al., 2011) and enantioselective chromatography (Roussel et al., 2004).

Chirality plays a largely important role in the pharmaceutical industry as ≥ 50% of all commercially available pharmaceuticals are chiral in nature (Nikolai et al., 2006; Ribeiro et al., 2012) and > 80% have been marketed in racemic form (Nguyen et al., 2006). Whilst racemates used to be the most readily marketed form of chiral pharmaceuticals, the development of novel methodologies for the mass preparation of highly enantiopure materials encouraged legal authorities such as the FDA to adopt the commercialisation of pure enantiomers more readily, as illustrated by Figure 1.8 (Breuer et al., 2004; Agranat et al., 2012; Viedma et al., 2015).

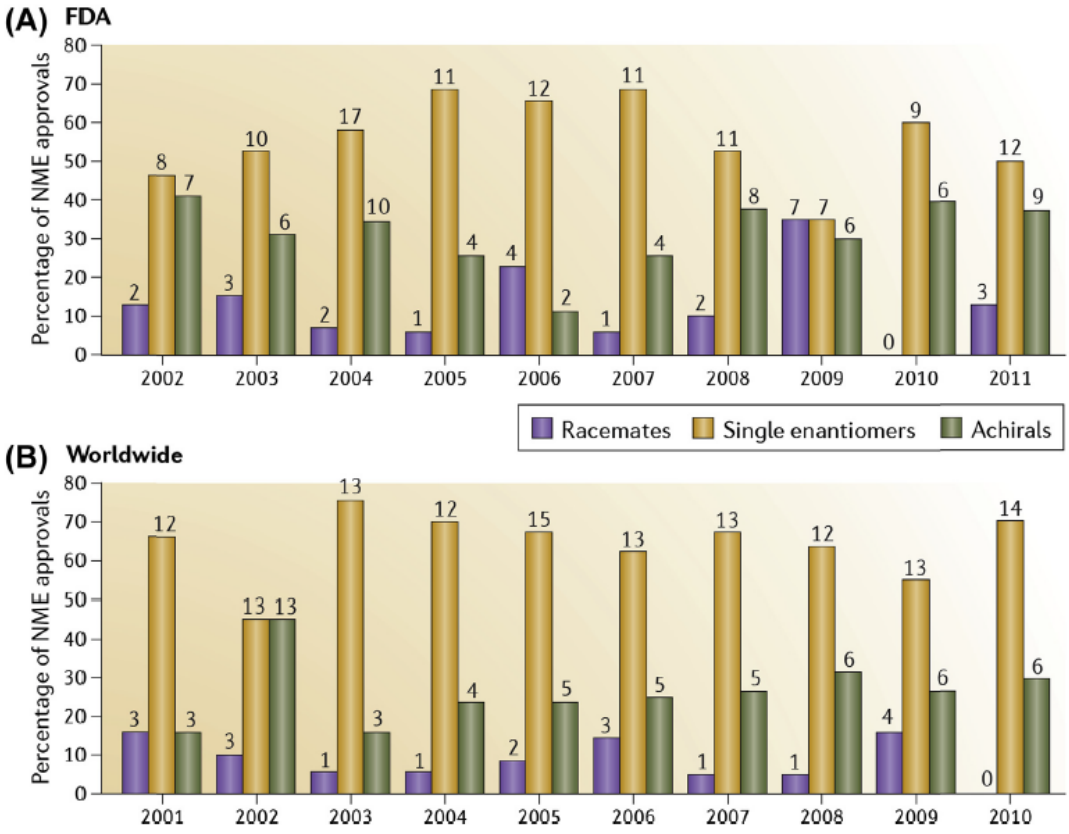

Figure 1.8: Percentages (shown on the *y*-axis) and number (above the bars) of new molecular entity (NME) approvals based on their chiral nature (reproduced from Agranat et al., 2012). NMEs approved by (A) the U.S. Food and Drug Administration (FDA) and (B) worldwide are presented for the period between 2002 and 2011.

The driving force behind the greater adoption of enantiomers over racemates in recent years has been the fact that different enantiomers of the same molecule tend to exhibit differences in properties such as absorption and potency upon administration to patients (Blaser, 2013). On occasion, differences between the properties of two enantiomers in the human body may be so significant that administration of one of the enantiomers could result in highly unwanted, toxic effects capable of compromising patients' health. The most notable example is the case of thalidomide, a sedative agent originally marketed as a racemic mixture, which ended up causing severe deformities in children born in the late 1950s (Muller, 1997). The occurrence of the thalidomide-induced deformities was attributed to the fact that the (*S)* enantiomer of the compound was prone to exhibiting severe teratogenic effects.

1.3.4 Polymorphism

The arrangement of molecules in a crystal structure has a direct effect on the physicochemical properties exhibited by a crystalline solid (Vippagunta et al., 2001; Brittain, 2012; Roy et al., 2012; Perumalla et al., 2012; Wang et al., 2013; Zhang et al., 2013), including thermal and chemical stability, morphology, mechanical properties, solubility, dissolution rate and bioavailability. All of the aforementioned properties are known to play an important part in drug delivery and in ensuring that the desired pharmaceutical outcome is achieved once administration of a medicine has occurred. Chemical compounds can often exist in one of multiple solid crystalline structures that differ in their packing arrangement and/or molecular conformation (Haleblian and McCrone, 1969). Chemically identical molecular solids with different crystal packing are known as polymorphs and their properties have attracted significant interest over the years. It has been estimated that almost half of all organic compounds in existence may be susceptible to having multiple polymorphic forms (Stahly, 2007) and more than 50% of all APIs utilised in industry are estimated to be polymorphic (Cruz-Cabeza and Bernstein, 2014).

Two distinct types of polymorphism have been commonly reported in the literature: conformational and packing/configurational. In the case of conformational polymorphism, molecular compounds possess flexible bond components, prone to rotation, which enable them to adopt different conformations and crystallise in a variety of polymorphic forms; polymorphs of ritonavir (Bauer et al., 2001), tolfenamic acid (López-Mejías et al., 2009), metaxalone (Aitipamula et al., 2011) and mefenamic acid (SeethaLekshmi and Guru Row, 2012) all represent examples of conformational polymorphism in the context of pharmaceutical materials. Differences in the packing arrangement of rigid molecules between different polymorphs of the same material result in packing/configurational polymorphism, with polymorphs of carbamazepine (CBZ) being examples that illustrate the occurrence of this phenomenon in compounds of pharmaceutical relevance (Grzesiak et al., 2003; Rodríguez-Spong et al., 2004; Arlin et al., 2011).

The impact of polymorphism on the physicochemical properties of a compound is well-documented. Chloramphenicol palmitate is a classic example. It is an antibiotic agent known to crystallise in polymorphic forms A, B, and C (Kaneniwa and Otsuka, 1985). Form B has been shown to dissolve quicker than form A as it is significantly more soluble (Aguiar and Zelmer, 1969). Rifaximin, an antibacterial agent, has five known polymorphs (α, β, γ, δ, and ε). A series of in vivo studies involving oral administration

of each rifaximin polymorph, in the form of gelatine capsules, to dog subjects determined that all forms have distinct pharmacokinetic profiles (Viscomi et al., 2008). These studies also showed that forms δ and γ are the ones exhibiting the highest bioavailability profiles.

Thermodynamic stability is an additional property that varies between polymorphs of the same compound and is of paramount importance to the drug manufacturing process and stability (Lee et al., 2011). It is therefore most common to select the most thermodynamically stable polymorph at ambient conditions for development into marketed products. This avoids unwanted transformations occurring during manufacture, storage and use. Metastable (unstable) polymorphic forms of drugs are commonly reported in the literature and due to their higher free energy show a greater aqueous solubility than more stable forms. Whilst this can make them attractive for drug development and commercial use (Singhal and Curatolo, 2004; Hilfiker et al., 2006), care must be taken to prevent conversion to their more thermodynamically stable counterparts over time (Murdande et al., 2011; Censi and Di Martino, 2015). In the case of ritonavir, the emergence of a previously unreported and more stable polymorph during the development process, which was later found to possess enhanced thermal stability compared to the commercially available form of ritonavir, caused withdrawal of the drug from the market (Bauer et al., 2001). This additionally highlights the importance of finding all practically relevant forms as early as possible in the drug development process.

The transition from a metastable form to a stable one may be facilitated by processes such as heating and grinding or the presence of seeds of one polymorph in another (Lutker and Matzger, 2010; Censi and Di Martino, 2015; Censi et al., 2015). Differences in the intermolecular interactions between polymorphs of the same compound can potentially affect the chemical stability of a drug product, with certain polymorphic forms being more likely to undergo degradation. Form II of furosemide represents one such example as it has been found to degrade more readily than form I following direct exposure to sunlight (De Villiers et al., 1992).

Because of the significance of polymorphism in the drug development process, regulatory authorities such as the FDA and the International Conference on Harmonization (ICH) impose strict regulations regarding the study of drug candidate polymorphism during the pharmaceutical manufacturing process and developing a clear picture with respect to the suitability of each polymorph for commercial application (Byrn et al., 1995).

1.3.5 Multi-Component Crystals

Multi-component crystals are quite prevalent for many molecular systems. They are defined by the presence of multiple molecular and/or ionic species within the crystal structure. Whilst the terminology on what constitutes a multi-component crystal has been a subject of debate, crystals containing more than one molecular component can be broadly divided into four distinct categories, namely solvates, hydrates, salts and cocrystals. In addition to the aforementioned categories, more complex systems of multi-component crystals have been reported (Aitipamula et al., 2012; Grothe et al., 2016). These include hydrated/solvated salts, hydrated/solvated cocrystals, anhydrous salt cocrystals and hydrated/solvated salt cocrystals (Figure 1.9). Similar to crystals comprising a single molecular component, multi-component crystals can exhibit polymorphism (Porter III et al., 2008; Ruscica et al., 2010; Beloborodova et al., 2017; Hiendrawan et al., 2017).

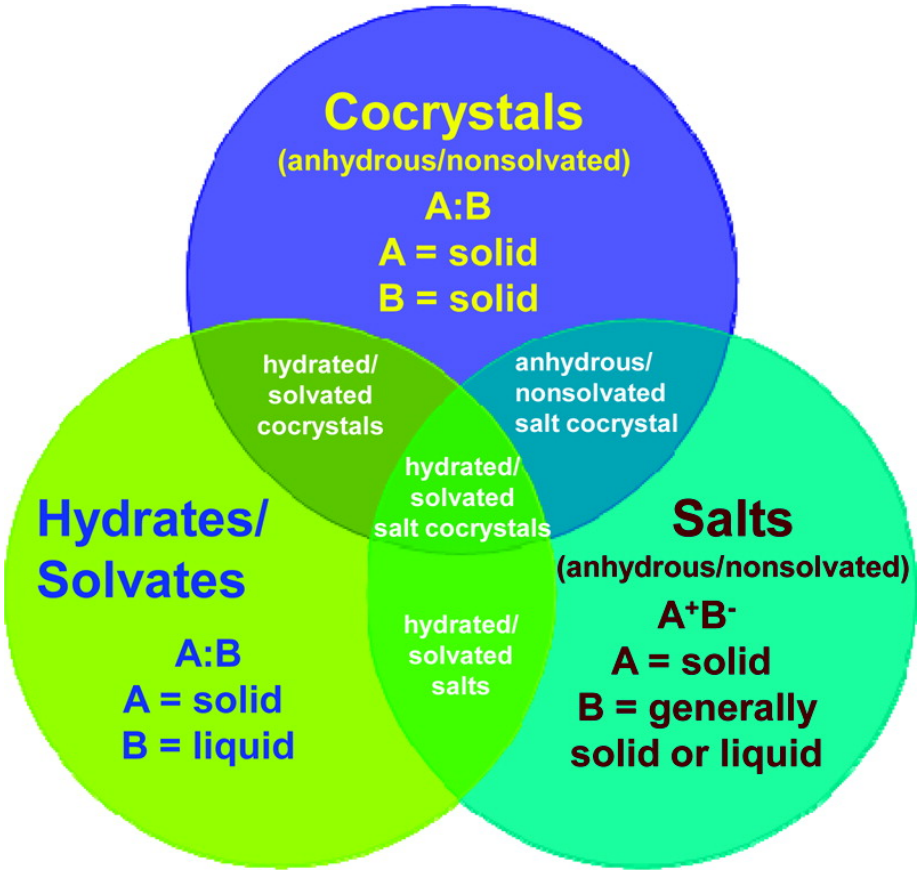

Figure 1.9: Overview schematic showing different types of multi-component crystals (adapted from Aitipamula et al., 2012).

1.3.5.1 Solvates and Hydrates

Solvates are solid forms arising when solvent molecules incorporate themselves into the crystal structure of a solute (Griesser, 2006; Healy et al., 2017). In instances where the solvent incorporated into the crystal structure is water, the resulting solid form is referred to as a hydrate (Griesser, 2006; Healy et al., 2017). Solvates/hydrates comprising a stoichiometric ratio of one solvent molecule per two molecules of solute are hemisolvates/hemihydrates (Braun et al., 2011 & 2019).

Solvates and hydrates are generally categorised as stoichiometric or non-stoichiometric (Griesser, 2006). In stoichiometric solvates and hydrates, the solvent included in the crystal structure typically plays an important role in stabilising the structure and its removal results in either 1) a complete change in crystal structure manifesting in the form of a phase transformation to a different solid form 2) the occurrence of disorder within the original structure of the solvate/hydrate or 3) a loss in crystallinity resulting in the emergence of an amorphous state (Griesser, 2006).

Non-stoichiometric solvates and hydrates represent inclusion compounds, wherein solvent molecules occupy structural voids within the crystallographic unit cell, and are commonly occurring for large and awkwardly-shaped solutes incapable of packing effectively upon crystallisation (Griesser, 2006). A defining characteristic of non-stoichiometric solvates and hydrates is their ability to maintain the same crystal structure under variable amounts of solvent content and the amount of solvent incorporated structurally is dependent on the partial pressure and temperature conditions employed during crystallisation of the solute (Griesser, 2006). The removal of solvent content from the structure of a non-stoichiometric solvate can result in either 1) the emergence of an anhydrous (solvent-free), isostructural, and usually metastable form defined by the same structural features as the solvated/hydrated form or 2) a loss in crystallinity leading to amorphisation (Stephenson et al., 1998; Mimura et al., 2002; Griesser, 2006).

The formation of non-stoichiometric solvates and hydrates is generally undesirable in medicines manufacturing due to challenges in maintaining control over the type and amount of solvent comprising these structures during processing and storage (Braun et al., 2015b; Braun and Griesser, 2018). Hydrates can be further categorised into isolated-site hydrates, which comprise water molecules in segregated void sites within the crystal structure, and channel hydrates which contain water molecules in tunnels or connected void sites (Morris and Rodriguez-Hornedo, 1993). The removal of water molecules from the crystal structure of an isolated-site hydrate typically

requires a significant driving force whereas moderate changes in temperature and relative humidity are sufficient to facilitate the removal of water from the structure of a channel hydrate.

Depending on the experimental conditions employed, solvated/hydrated structures may undergo desolvation/dehydration into an anhydrous form (Braun et al., 2008; Braun et al., 2014a), occasionally giving rise to previously unreported polymorphs for various compounds. The monohydrate of rimonabant, comprising one mole of water per one mole of rimonabant, represents one such example as its desolvation was found to result in the formation of a new metastable polymorph identified as form A_H (Fours et al., 2015). Conversely, it is also possible for an anhydrous polymorph to transform into a solvate or hydrate if appropriate conditions are met; a relevant example is form I of galunisertib (Bhardwaj et al., 2019) which converts to a monohydrate upon exposure to relative humidity greater than 5% at room temperature (Figure 1.10).

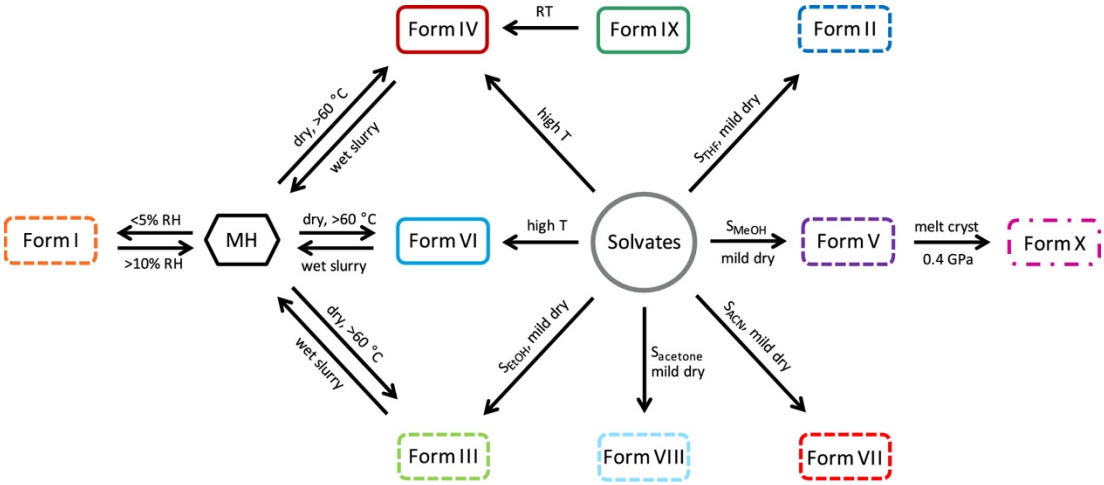

Figure 1.10: Solid forms of galunisertib and corresponding interconversion pathways (reproduced from Bhardwaj et al., 2019). Dotted boxes correspond to forms obtained via desolvation and MH represents the monohydrate structure.

Solvates and hydrates occasionally do exhibit physicochemical properties that make them attractive for commercial application, with the ethanol solvate of indinavir (Zhang et al., 2018a) and monohydrate of bosutinib (Withbroe et al., 2013) both being examples of solvated and hydrated forms of pharmaceuticals that have successfully reached the market. Consequently, characterisation of solvated and hydrated forms and development of an understanding of the properties of these solid forms is also critical in the context of the drug manufacturing process. The selection of solvents

with suitable toxicity profiles for solvate formation and subsequent pharmaceutical application is regulated by initiatives such as the ICH which provide appropriate guidelines for their inclusion in drug products (Connelly et al., 1997).

1.3.5.2 Salts

In the context of pharmaceuticals, preparation of a salt form of an API occurs via an acid-base reaction between an ionisable API and a suitable counterion. This involves either the transfer of a proton or neutralisation of the acid and base components, resulting in API ionisation (Berge et al., 1977). In order for APIs to be susceptible to salt formation, they need to comprise at least one ionisable functional group such as -COOH or an amine. Generally, API – counterion reactions will lead to salt formation if the difference in the respective p*K*a values of the acid and base components (Δp*K*a = p*K*a of base – p*K*a of acid) of the API and counterion is larger than 3 (Bhogala et al., 2005).

The formation of salts can optimise the physicochemical properties of APIs (Serajuddin, 2007; Elder et al., 2013) and is particularly known to result in significant enhancement of their aqueous solubility properties; one such example is the mesylate salt of delveridine which exhibits solubility over 2000 times higher than that of the unionised form (Stephenson et al., 2011). The commercial use of pharmaceutical salts is well documented as approximately 50% of all APIs approved by the FDA have been formulated in salt form (Paulekuhn et al., 2007), with the hydrochloride salt form being the most common for basic APIs and the sodium salt being predominant for acidic APIs (Serajuddin, 2007; Prohotsky and Zhao, 2012; Saal and Becker, 2013).

1.3.5.3 Cocrystals

A cocrystal can be defined as a solid-state crystalline form comprising two or more molecular compounds, referred to as coformers, which coexist in the same crystal structure under a specific stoichiometry and are not solvates or salts (Aitipamula et al., 2012; Karimi-Jafari et al., 2018). The study of pharmaceutical cocrystals has gained significant traction in recent years because the development of cocrystal systems comprising APIs has the potential to enhance the solid-state properties of the APIs and result in optimal pharmaceutical performance (Elder et al., 2013; Sun, 2013; Dai et al., 2018).

1.4 Solid-State Screening and Crystal Structure Prediction (CSP)

1.4.1 Solid-State Screening

Early-stage drug development depends heavily on the process of readily accessing all possible solid forms of a compound so that the form with the optimal physicochemical profile can ultimately be selected for commercial use (Yamano, 2011). For this purpose, solid-state screening studies are implemented and an overview of a typical solid-state screen and form selection process is presented in Figure 1.11.

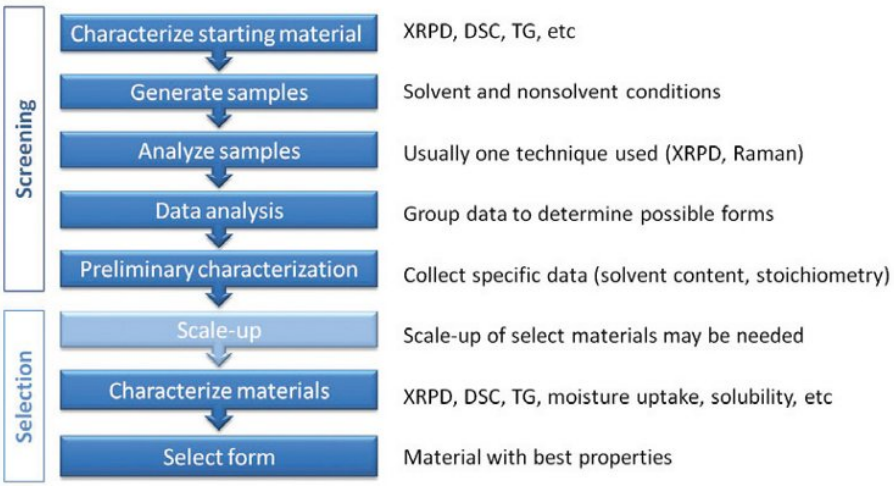

Figure 1.11: Overview of the solid-state screening and form selection process (reproduced from Newman, 2011).

The most thorough screening studies normally involve the assessment of multiple crystallisation methods (Figure 1.12) on the solid-form outcome for a given system, with resulting materials becoming subjected to various solid-state characterisation tools to identify the corresponding forms that have been prepared and obtain a thorough understanding of their physicochemical properties. Cooling crystallisation, solvent evaporation, anti-solvent addition, vapour diffusion and slurry equilibration are experimental protocols that have been utilised regularly in both industrial and academic screening (Morissette et al., 2004; Newman, 2013). A number of non-solution based approaches such as physical vapour deposition (Srirambhatla et al., 2016), crystallisation from the melt (Zhang et al., 2016), crystallisation under high pressure (Neumann et al., 2015), *in-situ* heating (Florence et al., 2008) and exposure

to variable humidity conditions (Stieger et al., 2010) have additionally been explored although solution screening is consistently the most utilised approach in industry (Anderton, 2007; Newman, 2013).

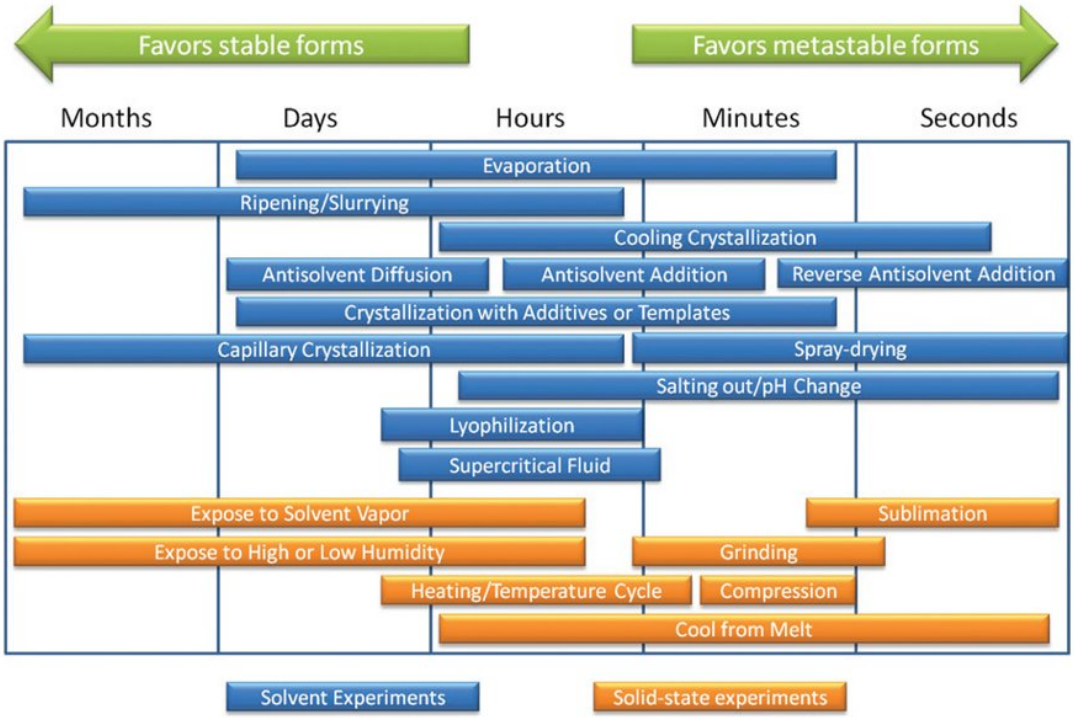

Figure 1.12: Overview of common solid-state screening experimental approaches and corresponding timescales (reproduced from Anderton, 2007).

Solid-state screening from solution traditionally comprises a large library of solvents and/or solvent mixtures which cover a broad spectrum of properties (Allesø et al., 2008). Some of the solvent properties that are typically explored in the context of screening include hydrogen-bonding propensity, polarity, dipole moment interactions, and viscosity (Gu et al., 2004; Mirmehrabi and Rohani, 2005). As a general rule, increasing the diversity in solvent properties will enhance the likelihood of new solid-form discovery (Carlson et al., 2003; Mangin et al., 2009). The use of solvents that are capable of promoting the formation of specific packing motifs in crystals through interactions with the solute of choice is another strategy that has been employed for targeting novel solid forms and particularly anhydrous polymorphs (Blagden and Davey, 2003). In more recent years, the classification of solvents based on molecular descriptors characteristic of their physicochemical properties has gained greater prominence, with approaches such as that of the Strathclyde24 map (Johnston et al.,

2017; Figure 1.13) being used to assist in the efficient selection of solvents for solid-state screening and maximise the possibility of isolating all possible forms of a given compound.

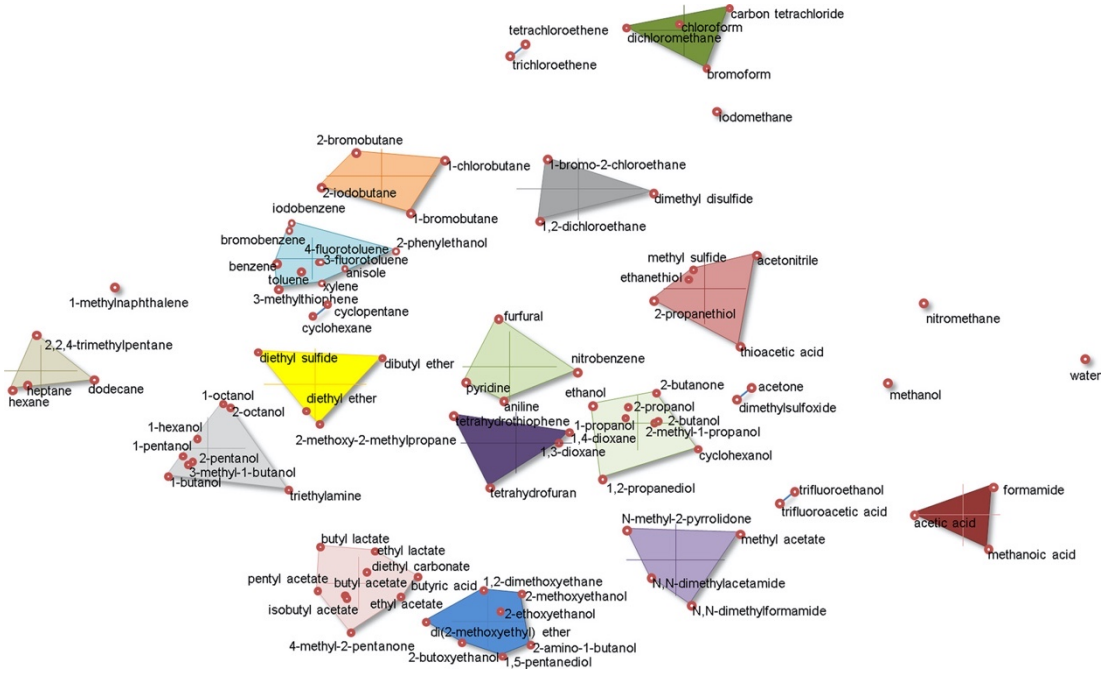

Figure 1.13: The Strathclyde24 solvent selection model for solid-state screening studies (reproduced from Johnston et al., 2017). Solvents are grouped into 24 clusters based on the similarity of their physicochemical properties.

In a screening study, the effect of multiple process conditions on the solid-form outcome is assessed. Temperature, supersaturation, agitation speed, cooling profile, solvent type and rate of solvent addition are some of the conditions that can be readily manipulated in order to target the nucleation of different solid forms (Florence et al., 2006; Newman, 2013). High-throughput methods using automated parallel screens can be conducted to increase the number of possible experiments and maximise the robustness of the screening process (Morissette et al., 2004; Campeta et al., 2010; Pfund and Matzger, 2014; Selekman et al., 2016; Braun et al., 2017). Even though important advances have been made over the years with respect to automating solid-state screening methodologies and enhancing their reliability and robustness, identification of the right set of conditions capable of giving rise to novel crystal structures still relies significantly on trial-and-error approaches (Cross et al., 2002).

1.4.2 Crystal Structure Prediction (CSP)

CSP capabilities (Price, 2004; Price, 2008; Price, 2014; Price et al., 2016; Price and Reutzel-Edens, 2016) are commonly employed as a complementary tool to experimental solid-state screening for the purpose of establishing the most thermodynamically stable form, suggesting potential target forms to crystallise (Arlin et al., 2011; Neumann et al., 2015; Braun et al., 2016a; Srirambhatla et al., 2016; Case et al., 2018) aiding in the identification of unreported crystal structures (Neumann and Perrin, 2009; Kendrick et al., 2013; Braun et al., 2014b; Askin et al., 2019) and providing insights when structural disorder occurs (Braun et al., 2014a).

Computational CSP software can be used to generate hypothetical packing arrangements and molecular conformations for a given compound and identify novel structures (Gavezzotti, 2005). Based on the assumption that crystal structure formation is driven predominantly by thermodynamics (Price, 2009; Day, 2011), CSP-generated crystal structures are ranked according to their geometry-optimised, static lattice energies and the predicted structure exhibiting the lowest lattice energy is anticipated to be the most thermodynamically stable one. An example of a CSP-generated lattice energy landscape is provided in Figure 1.14. Anisotropic, multipole-based atom-atom force fields (Price et al., 2010) and dispersion-corrected, periodic density functional theory (DFT-D) approaches (Neumann and Perrin, 2005) are the most commonly utilised methods for generating and ranking predicted crystal structures, with DFT-D methods generally yielding greater accuracy (Nyman et al., 2016). The inclusion of reliable kinetic and thermodynamic information for the molecules under investigation is critical in the context of CSP studies as the absence of such information may cause the thermodynamic feasibility of certain crystal structures to be overestimated (Price, 2008).

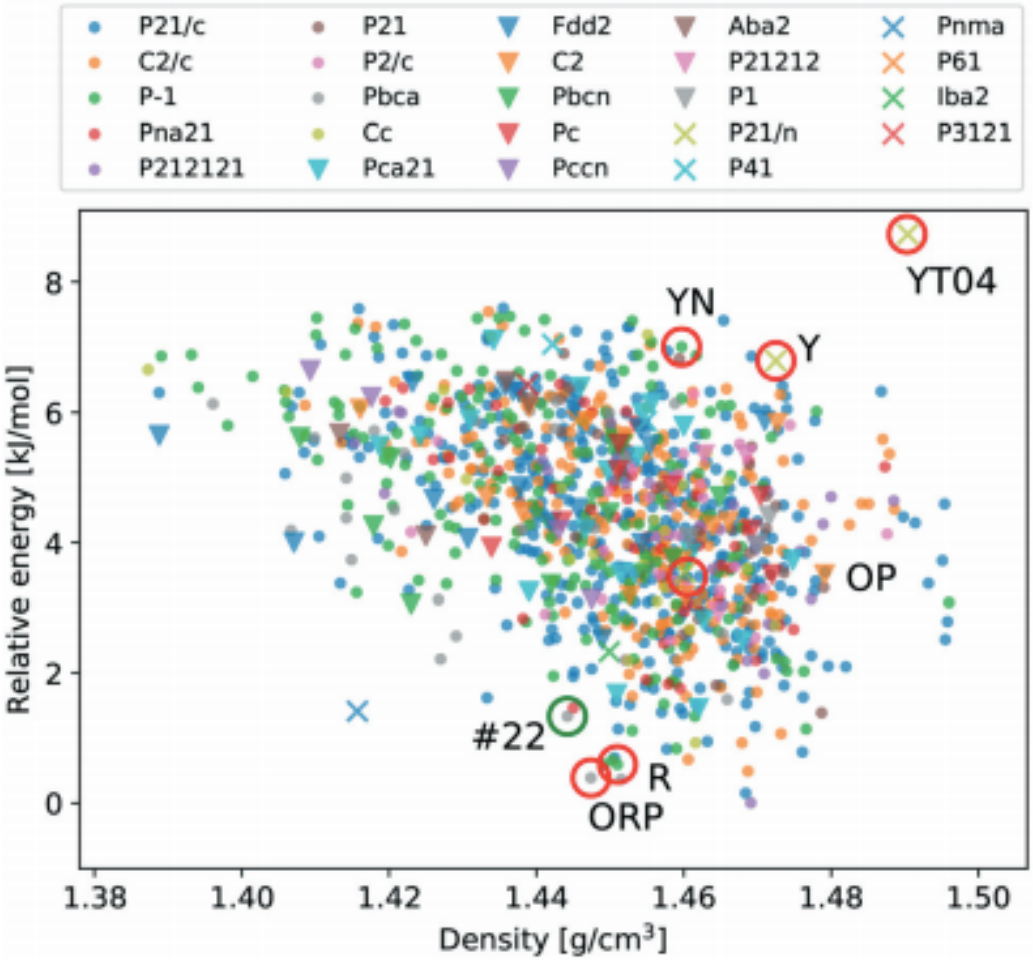

Figure 1.14: Crystal lattice energy landscape of ROY. Each point represents a predicted crystal structure. Structures circled in red correspond to experimentally observed polymorphs (reproduced from Nyman et al., 2019).

The ability of CSP approaches to successfully contribute towards the crystallisation of novel solid forms is evident in the literature. CBZ form V, cyheptamide (CYH) form III and tolfenamic acid forms VI and VII were novel polymorphs identified computationally, then realised experimentally through physical vapour deposition studies (Arlin et al., 2011; Srirambhatla et al., 2016; Case et al., 2018). CSP methods have additionally proven fruitful in targeting the crystallisation of unreported structures in screening studies conducted under high pressure and in experiments involving the presence of impurities (Neumann et al., 2015; Braun et al., 2016a).

1.5 Experimental Factors Influencing Polymorphism

As described in section 1.4, experimental factors utilised in solid-state screening are varied in an attempt to determine the optimal parameters that will promote the nucleation and growth of specific solid forms. This section will consider some of the most prominent of these parameters more closely and explore their impact on the polymorphism of various compounds.

1.5.1 Supersaturation

As discussed previously, supersaturation is the driving force responsible for the commencement of crystallisation. Unless a supersaturated state is reached in solution, crystal nuclei will not nucleate and undergo subsequent growth. The effect of the rate of supersaturation generation on polymorphic outcome has been studied for *m*-hydroxybenzoic acid and *o*-aminobenzoic acid (He et al., 2011). The supersaturation generation was manipulated by altering the cooling and evaporative crystallisation rate in the experiments performed and results showed a positive correlation between high supersaturation generation and metastable polymorph formation for both compounds. The crystallisation of metastable forms at high supersaturation generation was also linked with kinetics playing a more decisive role in the process, whereas thermodynamics appeared to be driving the formation of the more stable polymorphs at low supersaturation generation rates.

The fact that supersaturation generation rate is capable of influencing the polymorphic outcome of crystallisation can be explained in terms of two parameters associated with the nucleation process, the induction time and the metastable zone width (MSZW). The concept of induction time refers to the lag period existing between the time a supersaturated state is achieved in solution and the time crystals are initially detected (Kulkarni et al., 2013). The MSZW is typically utilised to identify the optimal operating window for crystallisation processes and can be defined as the difference between the saturation temperature of a solution and the temperature of detection of the first crystals that appear in said solution upon cooling under a constant profile (Mullin, 2001; Kadam, et al. 2012). Experimental investigations of the MSZW can be carried out using a variety of techniques, including a combination of focused beam reflectance measurement (FBRM) and particle vision and measurement (PVM) as well as turbidity measurements (Barrett and Glennon, 2002; Chew et al., 2007).

MSZW data are normally presented within solubility curve graphs (Figure 1.15) for different solvents and assist significantly in the design and implementation of both small scale and large-scale crystallisation processes. Within the MSZW, which is a reproducible kinetic property under identical process conditions, spontaneous nucleation events are unlikely to occur and only pre-existing crystals present in solution can undergo growth (Kubota, 2008; Lawton et al., 2009; Beckmann, 2013). Outside of the MSZW two separate regions exist, the under-saturated region, wherein nucleation cannot occur, and the supersaturated (labile) region whereby spontaneous nucleation is likely to occur.

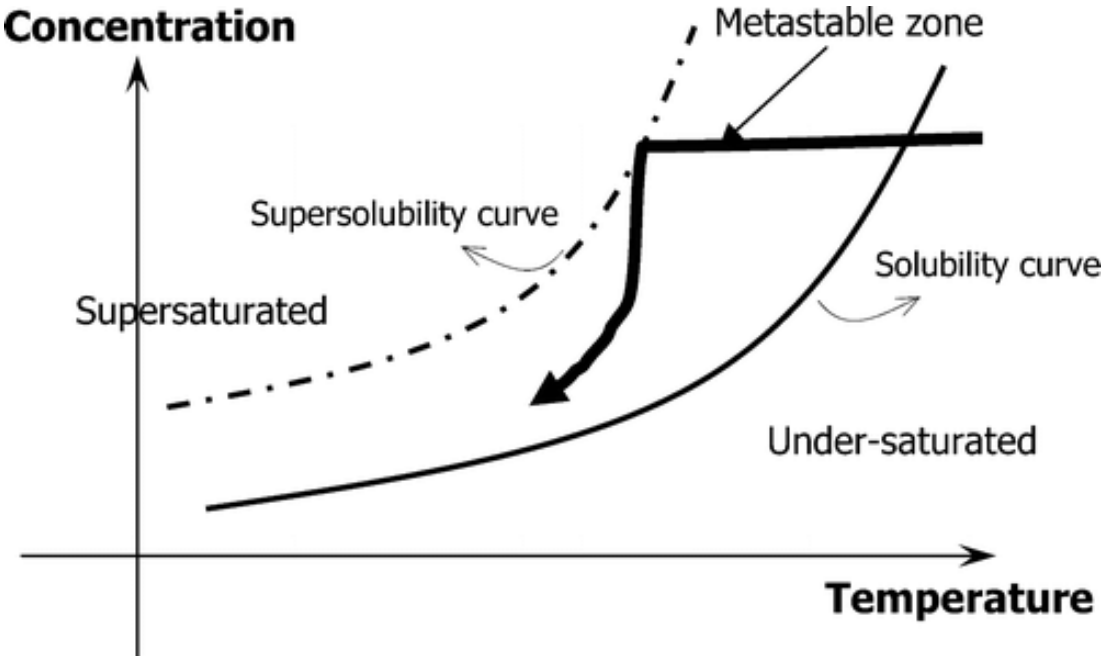

Figure 1.15: Schematic diagram depicting the key regions that pertain to the solubility curve for a given crystallisation system (reproduced from Lawton et al., 2009).

1.5.2 Thermodynamics and Temperature

Thermodynamics play a critical role in understanding the stability of polymorphic forms and gaining greater insight into the relationships between polymorphs of the same compound (Bernstein, 2002). The thermodynamic stability of polymorphs is indicative of their Gibbs free energy and the polymorphic form of a compound exhibiting the lowest free energy, under well-defined conditions, is the most stable one whereas the polymorphs with higher free energy are metastable entities. Metastable forms have a tendency to crystallise ahead of their more stable counterparts and later convert to them through thermodynamic effects facilitating the

occurrence of a polymorphic transformation, as suggested by Ostwald's rule of stages (Ostwald, 1897). The thermodynamic relationship between a pair of polymorphic forms can be described as either enantiotropic or monotropic (Burger and Ramberger, 1979a & 1979b) and knowledge of this relationship is pivotal in the design of crystallisation processes (Hilfiker, 2013a). Diagrams illustrating the behaviours exhibited by enantiotropically and monotropically related polymorphs are presented in Figure 1.16, wherein *G* refers to the Gibbs free energy of a polymorph, A is the polymorph with the lower melting point, B the polymorph with the higher melting point, L the liquid phase, $T_{m,A}$ the melting temperature of polymorph A and $T_{m,B}$ the melting temperature of polymorph B. In the case of enantiotropically related polymorphs, G_A and G_B cross at a transition point T_t, above and below which the stability order of polymorphs A and B is reversed. In monotropically related polymorphic pairs, T_t does not exist below the melting temperature and polymorph B is always more stable than polymorph A. However, extrapolation of G_A and G_B above $T_{m,A}$ and $T_{m,B}$ could result in them crossing at T_{tv}, the virtual transition point.

Temperature is capable of affecting both the thermodynamics and kinetics of polymorph formation and growth. The effect of temperature on the solubility of organic compounds has been well-studied and higher temperature values tend to correlate with an exponential increase in a system's solubility (Black and Muller, 2010). This correlation is particularly important to consider because it is known to bring about solvent-mediated phase transitions for polymorphs. One such example is that of L-glutamic acid. The metastable form α of L-glutamic acid has been shown to crystallise readily from aqueous solutions at 25°C, whereas at 45°C water facilitates the transformation of form α to the stable form β (Kitamura, 1989). In the case of the thiazole-derivative BPT, form C was found to be stable and form A metastable at all temperatures explored experimentally, whereas the stability profiles of forms D and BH were found to change considerably under different temperature profiles (Kitamura and Nakamura, 2002). Consequently, it is crucial that drug manufacturing processes are conducted in a manner that minimises the chances of temperature-induced transitions affecting the crystallinity of the product.

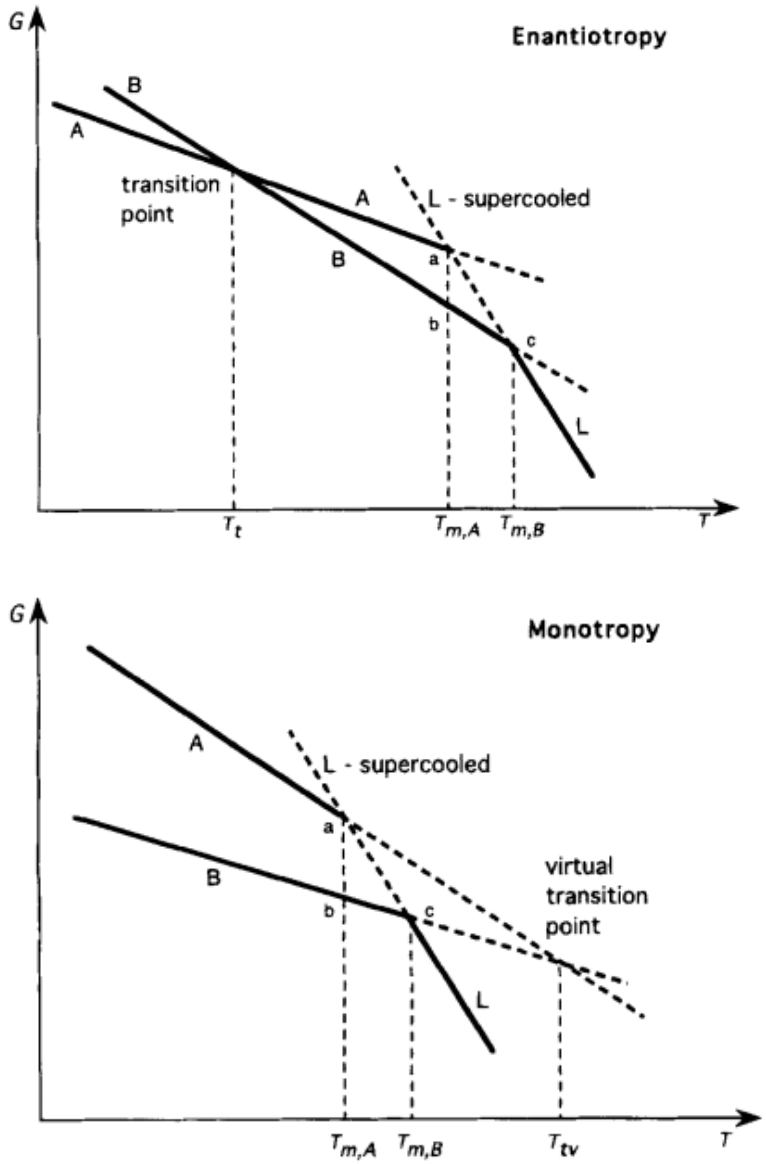

Figure 1.16: Thermodynamic plots depicting the relationship between Gibbs free energy and temperature in enantiotropic (top) and monotropic (bottom) polymorphic pairs (adapted from Yu, 1995).

1.5.3 Solvent Properties

Regarding the role of solvents in impacting polymorphism, there are several factors that need to be considered. The ability of solvents to affect molecular aggregation for different systems has been demonstrated for a number of systems. In the case of dimer-based prenucleation aggregates of CBZ variability in solvent polarity can induce changes in the driving forces facilitating dimerisation of the aggregates, with polar CD_3OH promoting dimerisation through non-polar aromatic interactions

between CBZ molecules and non-polar $CDCl_3$ driving dimer formation through strong hydrogen bonding (Hunter et al., 2012). The crystallisation of acridine via rapid cooling from acetone has been found to result in the formation of metastable form VII whilst chloroform, methanol and carbon tetrachloride solutions all yielded the metastable form III of the compound under identical experimental conditions (Musumeci et al., 2010); this observation was attributed to the distribution of dimer structures present in concentrated solutions of acridine in acetone being different to that of the other solvents that were investigated. The mechanism of solvent effects directing polymorphism of BPT(2-(3-cyano-4-isobutyloxyphenyl)-4-methyl-5-thiazolecarboxylic acid) in rapid cooling experiments was examined and results showed that solute conformation and the interplay between solute and experimental solvents were the driving factors behind the different polymorphic outcomes observed and not the crystallisation kinetics of the polymorphs that were obtained (Kitamura et al., 2012). In the context of sulfathiazole polymorphism, it has been proposed that different solvents mediate the selective growth of polymorphs by adsorbing onto specific faces of a crystalline form and inhibiting its nucleation and subsequent growth (Khoshkhoo and Anwar, 1993). Dielectric constants of solvents have also been found to affect polymorphic outcome, with high constants promoting the growth of 1-nitro-4-(4-nitrophenylmethylthio)benzene form I and low constants resulting in the formation of form III crystals (Wan et al., 2014). Multiple polymorphic forms have been reported for certain cocrystal systems and the interplay between process conditions and the type of solvent employed has been shown to direct the formation of specific polymorphs. In one such example, the use of water and cyclohexane in liquid-assisted grinding experiments resulted in the crystallisation of form I of the agomelatine:hydroquinone cocrystal system, whereas acetonitrile and ethyl acetate promoted the nucleation of form II (Prohens et al., 2016).

1.5.4 Agitation

Agitation can be readily achieved within crystallisation vessels such as stirred tank reactors through the use of impellers (Liu et al., 2015). Alternative means of achieving agitation include the use of experimental setups such as airlift, draft tube, fluidised bed, oscillatory baffled and Taylor-Couette crystallisers (Andereck et al., 1986; Liu and Rasmuson, 2013). Agitation has been found to be the decisive factor in controlling preliminary polymorphic outcome in the cooling crystallisation of CBZ from anhydrous ethanolic solutions and was shown to promote the growth of the thermodynamically

stable form III over the metastable form II (Sypek et al., 2012). The subjection of 1-propanol solutions to various agitation profiles has been shown to impact the polymorphism of *m*-hydroxybenzoic acid, with moderate profiles (200 and 400 rpm) favouring the growth of metastable form II and reducing the proportion of stable form I (Liu et al., 2014). In the case of L-glutamic acid, agitation has been found to promote the growth of different polymorphs by influencing the kinetics of crystallisation (Roelands et al., 2007).

1.5.5 pH

Solvent pH has been shown to affect the polymorphism of glycine in spray-drying studies, with a pH of 6.2 promoting the growth of the α form and higher/lower pH values favouring the crystallisation of γ-glycine by inhibiting formation of the cyclic dimer which is the elemental growth unit of α-glycine (Yu and Ng, 2002). Polymorphism in calcium carbonate has also been found to be influenced by pH, with different pH profiles facilitating the selective nucleation of a specific polymorph (Tai and Chen, 1998; Hu et al., 2015; Choi et al., 2017). Other instances of pH-directed polymorphism are that of ethylenediammonium 3,5-dinitrobenzoate (Jones and Davey, 2005) and the dimorphic dysprosium phosphonate system (Zeng et al., 2015).

1.5.6 Additives and Impurities

The presence of additives and/or impurities in solution and the interplay between the additives/impurities and the solvent may also have an effect on the polymorphic outcome in a crystallisation process. One example is that of bentazon, with the presence of Na_2HPO_4 and alkaline or alkaline earth metal additives in solution promoting the crystallisation of forms II and III but not form I (Braga et al., 2014). The presence of trace amounts of amino acid impurities in solution has been shown to promote the growth of the thermodynamically stable form γ of glycine over the metastable α polymorph (Poornachary et al., 2008). Additives and impurities can exert their effect on polymorphism by influencing the rate of solvent-mediated phase transformations (Mukuta et al., 2005), inhibiting crystal growth through adsorption on crystal surfaces (Weissbuch et al., 2003) and incorporation into the crystal lattice (Vartak and Myerson, 2017), affecting nucleation kinetics (Pons Siepermann et al., 2017; Black et al., 2018), stabilising metastable polymorphs (Lancaster et al., 2001) and facilitating the emergence of atypical crystal morphologies (Zhu et al., 2016).

1.6 Surface-Induced Crystallisation and the Influence of Templates on Polymorphism

Crystallisation is initiated by nucleation and the polymorphic form of a crystal is determined during the early stages of the nucleation process (Tóth et al., 2010). Because of this reason, establishing control over nucleation can ultimately contribute towards controlling polymorphism in the crystallisation of a given compound. In most practical circumstances, crystallisation is initiated by means of heterogeneous nucleation occurring on a surface (Price et al., 2005; Wijethunga et al., 2017; Artusio and Pisano, 2018). There are practically no limitations with respect to the type of surface that can initiate heterogeneous nucleation and surface-induced crystallisation refers to the ability of heterogeneous surfaces to act as templates that can direct nucleation and crystal growth using their physicochemical properties. Such properties (Figure 1.17) typically comprise surface chemistry, topography, and crystal lattice matching (epitaxial matching) and play a role in governing the molecular interactions between the templates and the molecules that interact with them (Chadwick et al., 2011; Diao et al., 2011a; Delmas et al., 2013; Shah et al., 2015; Parambil et al., 2019).

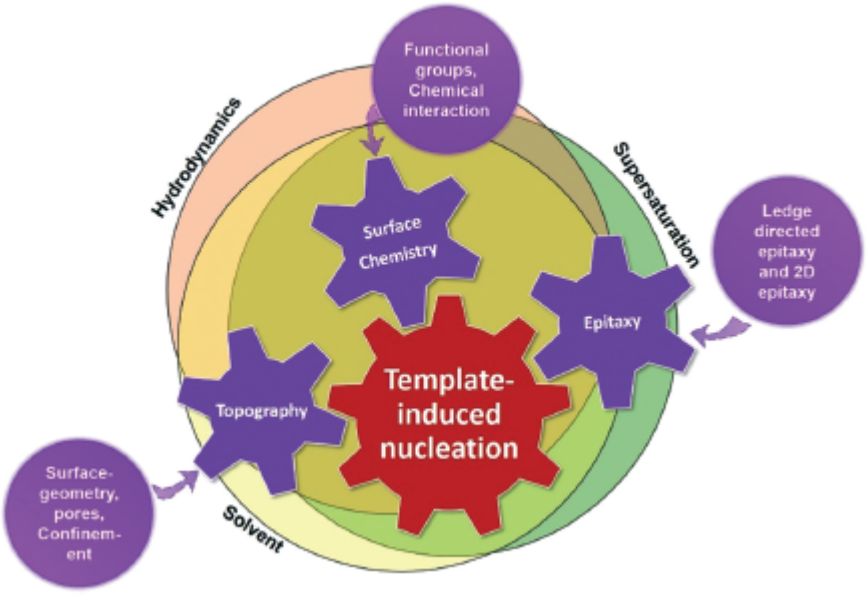

Figure 1.17: Overview of factors affecting template-induced nucleation in solution crystallisation processes (reproduced from Parambil et al., 2019).

Over the years, various types of surfaces have been utilised as templates for the purpose of dictating the polymorphic outcome in different organic and inorganic systems, targeting the crystallisation of previously unreported forms that are only attainable by crystallising on a specific type of template, and stabilising metastable forms (Ehmann and Werzer, 2014; Reischl et al., 2015; Jones et al., 2016; Artusio and Pisano, 2018; Simões et al., 2018). This section will introduce the various types of templates that have been studied with respect to achieving polymorphic selectivity.

1.6.1 Single-Crystal and Polycrystalline Templates

Single-crystal substrates and polycrystalline substrates consisting of multiple single crystals have been studied over the years for achieving templated growth of organic crystals in semiconductor and pharmaceutical systems.

Single crystals of β-alanine have been employed to grow crystals of the metastable polymorphs of semiconductors quaterthiophene and hexathiophene (Trabattoni et al., 2013). In the context of pharmaceutical materials, crystalline templates have been gaining greater traction in recent years with respect to their ability to induce polymorphic selectivity and crystallise novel polymorphs. Epitaxy-based intermolecular interactions between forms II and IV of sulfathiazole have been found to promote the templated growth of form II on crystals of form IV through growth unit mismatching between the two crystal structures (Munroe et al., 2011). An epitaxial methodology involving the assessment of crystalline substrates as templates has been utilised for selectively nucleating the α and γ polymorphs of indomethacin from ethanol with template crystals of L-glutamic acid solely crystallising γ-indomethacin and L-histidine crystals favouring nucleation of α-indomethacin (Wijethunga et al., 2019); these findings were attributed to functional group matching at the interface between indomethacin and the experimental substrates. A single crystal of 10,11-dihydrocarbamazepine (DHC) form II was originally used as a template for the growth of CBZ form V, a structure that had never been accessed previously using solution-based screening methods (Arlin et al., 2011). A CSP approach assisted in identifying the thermodynamically feasible form V and its growth was achieved by physical vapour deposition of CBZ onto the surface of the DHC II crystal. The CSP study that was carried out initially identified an isostructural relationship between CBZ V and DHC II, with both structures crystallising in the orthorhombic space group *Pbca* and sharing similar unit cell parameters (cell length value difference: ± ≈ 0.3 Å). It was this expected isostructural relationship that resulted in the selection of DHC II as the

best candidate for the templated growth of CBZ form V and the experimental cell parameters for this polymorph were in good agreement with those of the predicted structure.

The results obtained by Arlin et al. suggested that both functional group matching and lattice matching in terms of cell parameters are requirements for a crystal substrate to promote the growth of an isostructural crystal structure. The use of a single-crystal template for the crystallisation of CBZ V proved to be a non-reliable approach and a follow-up study a few years later revisited the growth of CBZ V on DHC II (Srirambhatla et al., 2016). The work by Srirambhatla et al. showed the ability of a polycrystalline template of multiple DHC II crystals to produce CBZ V more readily than the single-crystal template originally employed by Arlin et al. The polycrystalline template proved to be a more robust method for obtaining form V due to its larger surface area and broader range of orientations with respect to the facets of the DHC II crystals. In addition to reproducing the growth of CBZ form V, the polycrystalline DHC II template was also used to successfully induce the crystallisation of a new polymorph of cyheptamide (CYH form III), which was shown to be isostructural to both DHC II and CBZ V (Figure 1.18). The results by Srirambhatla et al. provided more evidence to support the hypothesis that functional group and epitaxial matching are both required when designing a template for pursuing the templated growth of crystals that are structurally similar to the crystalline template employed.

Crystalline templates have been commonly employed in physical vapour deposition studies of materials of pharmaceutical relevance and the combination of crystalline template use and crystallisation from the vapour has been found to be an effective solvent-free approach for isolating specific polymorphic forms (Karpinska et al., 2011; Karpinska et al., 2013; Kamali et al., 2016; Kamali et al., 2018). Crystalline templates have also been successfully utilised to seed the growth of novel polymorphs from solution, including ones of pharmaceutical relevance (Bučar et al., 2013; Park et al., 2016).

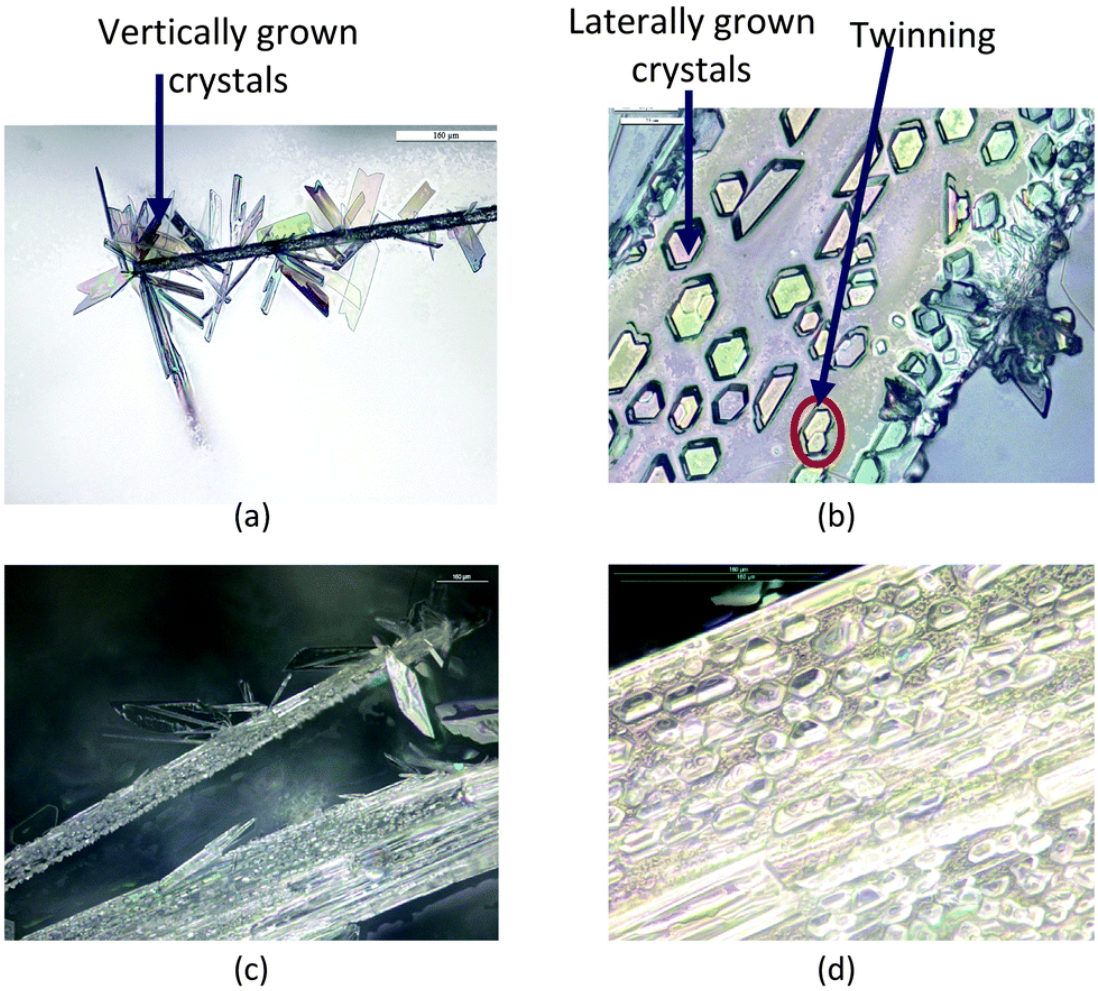

Figure 1.18: Template-induced crystallisation of CBZ form V (a, b) and CYH form III (c, d) on the surface of DHC form II crystals (reproduced from Srirambhatla et al., 2016).

1.6.2 Self-Assembled Monolayer Templates

Self-assembled monolayers (SAMs) are templates formed when molecular entities readily adsorb, from the liquid or the vapour phase, onto a surface and become spontaneously organised in ordered crystals or semicrystalline domains (Love et al., 2005). Molecular entities forming SAMs traditionally possess a headgroup indicative of their functionality. Different headgroups show affinities for different substrates and this facilitates the adsorption of the molecules and the formation of SAM templates. Pure metallic surfaces, metal oxide surfaces, and semiconductors are all known to form SAMs with different molecules. The most commonly studied SAM templates in the context of crystallisation are those obtained through the interactions of alkanethiols with gold substrates. Thiols are particularly attractive for SAM studies

due to their ability to readily adsorb onto noble metal surfaces and form ordered templates with functionalities that can be readily modified (Laibinis and Whitesides, 1992).

There is significant evidence in the literature to suggest that SAM substrates can be employed for achieving polymorphic selectivity. A SAM substrate of L-AAPP, a phenylalanine derivative, successfully crystallised and stabilised the metastable α form of L-glutamic acid (Dressler and Mastai, 2007). Preferential orientation of the α-form crystals was also reported, with crystals growing in the <111> direction. Selective crystallisation of tolbutamide form IV was reported using phenyl-terminated SAMs (Zhang et al., 2011). In the same study, the use of methyl- and trifluoromethyl-terminated SAMs promoted the growth of form II. SAM substrates exhibiting strong interactions with the carboxyl group of mefenamic acid molecules can selectively crystallise form II (Yang et al., 2012). Experiments involving the utilisation of gold-thiol SAMs as templates resulted in the selective nucleation of forms α, β, and γ of 1,3-bis(*m*-nitrophenyl) urea from solution (Hiremath et al., 2005), whereas the use of siloxane SAMs was found to promote the growth of forms β, γ, δ, and ε and suppress the nucleation of form α which is the most thermodynamically stable one (Capacci-Daniel et al., 2010). The results reported by Hiremath et al. in 2005 suggested that a combination of factors can contribute to SAMs promoting preferential polymorphism, with two-dimensional crystal lattice matching and complementary chemical interactions between SAMs and compound molecules both playing a role.

Two-dimensional lattice matching is an important property to consider in the context of template-induced crystallisation as it enables epitaxial growth of one crystal structure on another. If the unit cell parameters of a crystalline template match closely with those of the molecule that interacts with the template, the growth of well-ordered crystals will be promoted in three dimensions (Bonafede and Ward, 1995; Ward, 2001; Olmsted and Ward, 2011). Epitaxial growth was particularly prevalent in templating studies of malonic and succinic acid on gold-based SAMs, where they facilitated the nucleation and subsequent growth of ordered crystals with a highly specific orientation (Pokroy et al., 2009). Pokroy et al. additionally showed that functional interactions between the carboxyl groups in the two molecules and the SAM substrates also played a part in the crystallisation outcome. The significance of functional group interactions between molecules and templates in oriented crystal growth was also highlighted in an earlier study by Hiremath et al. which featured highly oriented growth

of 4-iodo-4‘-nitrobiphenyl crystals on SAM substrates bearing nitro- or iodoaryl substituents (Hiremath et al., 2004).

Self-assembled monolayers can be combined with metal-organic frameworks (MOFS, Figure 1.19) and give rise to surface metal-organic frameworks (SURMOFS, Hermes et al., 2005; Shekhah et al., 2007; Liu and Wöll, 2017), a novel type of template that has recently been found to affect polymorphic outcome in polymorph screening studies of paracetamol (Bolla and Myerson, 2018a & 2018b).

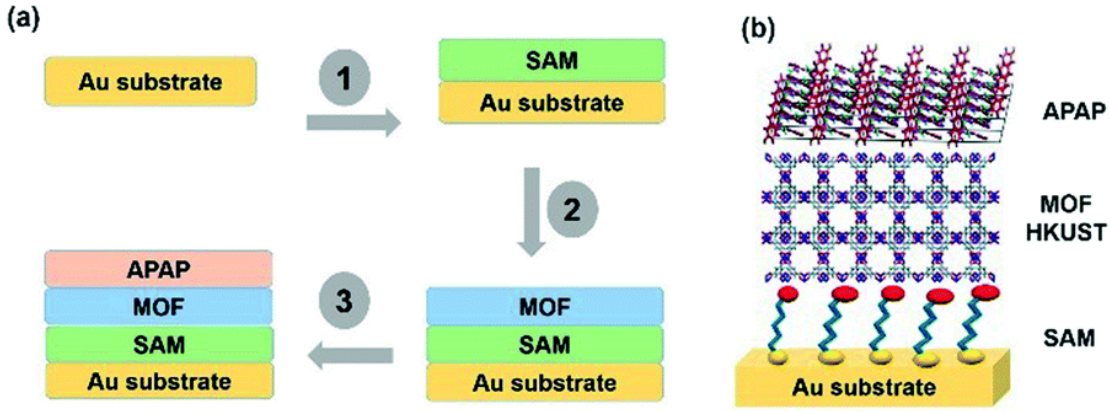

Figure 1.19: Schematic representation of the steps involved in SURMOF-induced crystallisation of paracetamol, herein denoted APAP (reproduced from Bolla and Myerson, 2018a).

1.6.3 Polymeric Templates

Contrary to SAMs and crystal templates, polymer-based templates rarely feature a fully crystalline structure. Instead, they are typically defined by an amorphous or semicrystalline nature (Guo, 2016). Most polymers are largely amorphous and their structures lack the long-range atomic order that is the signature trait of crystalline materials. Factors that make them attractive for templated crystal growth are their diversity in terms of chemical properties and the ability to readily modify their surface properties. Polymeric materials promote crystallisation by polymer-induced heteronucleation (PIHn, Figure 1.20), a solution based-approach wherein compounds are screened against a diverse library of non-soluble polymers that can act as sites of heterogeneous growth for crystals provided that a suitable combination of solvent and temperature conditions is employed (Lang et al., 2002a; Price et al., 2005; López-Mejías et al., 2009; López-Mejías et al., 2012). Price et al. were successful in employing PIHn to isolate and elucidate the crystal structure of a novel polymorph of

CBZ (form IV) and two novels polymorphs of sulfamethoxazole (forms III and IV) while López-Mejías et al. utilised extensive libraries of polymeric materials to access several new metastable phases of tolfenamic acid and flufenamic acid by crystallising from ethanol solutions. The use of a modified polystyrene substrate in melt crystallisation studies resulted in the emergence of a new form of phenobarbital (form XV) and additionally yielded suitable single crystals of the elusive form V which enabled the structure of this polymorph to be elucidated over 60 years after its existence was originally reported (Roy et al., 2016).

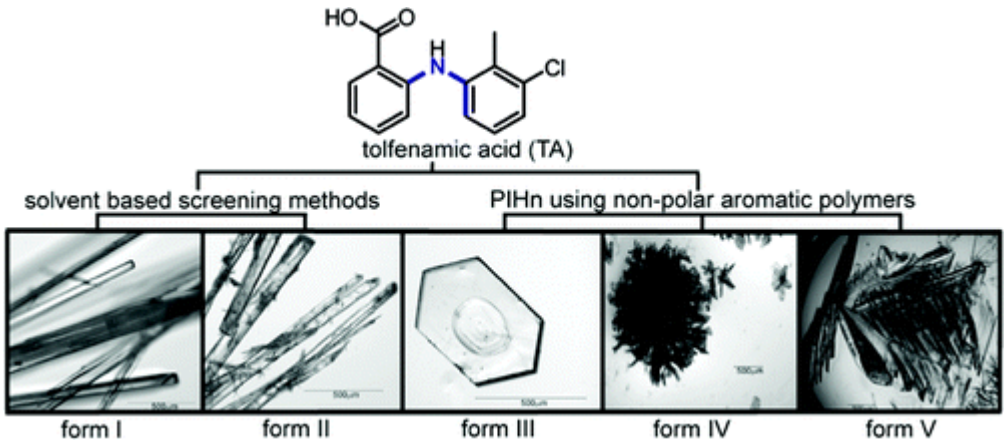

Figure 1.20: Influence of polymer-induced heteronucleation (PIHn) on the polymorphism of tolfenamic acid (reproduced from López-Mejías et al., 2009).

Apart from inducing the formation of previously undiscovered polymorphs, polymers can also be used for achieving polymorphic selectivity. In the case of indomethacin, the use of polymer templates results in preferential crystallisation of the α polymorph (McKellar et al., 2012). The potency of polymers to promote the crystallisation of specific polymorphs over others stems mainly from solvent effects and functional group interactions that occur at the interface between the polymers and the molecules interacting with them; these two factors are primarily responsible for directing the PIHn process (López-Mejías et al., 2011; Frank and Matzger, 2017).

A study investigating the effect of polymer substrates on the crystallisation of paracetamol, glycine and aspirin showed that the surface topography of polymers must be correlated with their wettability in order to develop a thorough understanding of how the surface structure dictates heterogeneous nucleation (Di Profio et al., 2012). The effect of polymer templates with nanoscale level topographical features has been explored for aspirin and it was shown that the presence of nanoscale pores can

enhance nucleation rates for aspirin crystallisation (Diao et al., 2011b). The nucleation rates of pharmaceutical materials can also be enhanced through the incorporation of tailor-made additives into insoluble polymers (Pfund et al., 2015).

1.6.4 Glass Templates

Glass capillaries have been successfully utilised to promote the selective nucleation of metastable CBZ form II over the thermodynamically stable form III in cooling experiments performed using ethanol solutions (Yang et al., 2017). At solute concentrations greater than 60 mg/mL, control glass vials and functionalised glass vials were found to facilitate the preferential crystallisation of CBZ form II over form III in cooled ethanol solutions (Figure 1.21), as well as promote enhanced stability for form II (Parambil et al., 2014). Glass vials functionalised with cyano silane have effectively favoured the nucleation of CBZ form II over form III, whereas glass vials functionalised with mercapto silane and fluoro silane were found to favour the growth of form III (Parambil et al., 2015).

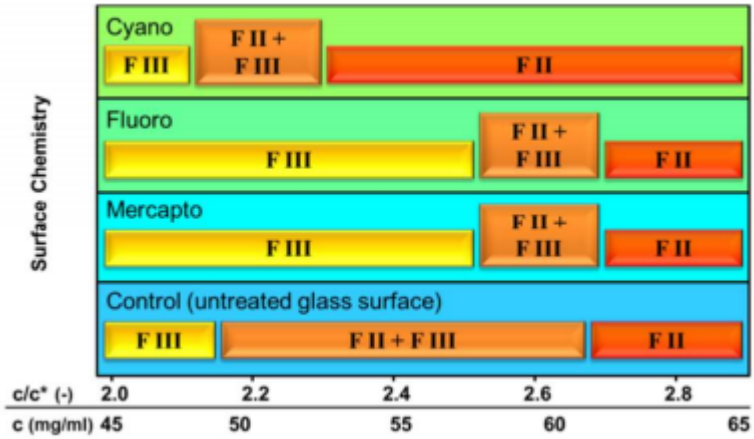

Figure 1.21: Effect of functionalised glass substrates and initial supersaturation (c/c*) on the polymorphism of CBZ crystallised by cooling from ethanol solutions at 20°C (reproduced from Parambil et al., 2014).

1.6.5 Electrochemically Modifiable Templates

Templates that have recently been noted for their ability to impact polymorphism are those with electrochemical potential that is subject to modification. This was demonstrated in a study of entacapone which explored gold substrates with tuneable electrochemistry (Kwokal and Roberts, 2014). The application of negative polarisation

to the gold templates that were utilised resulted in crystallisation of the metastable α form of entacapone at the edges of the substrates. In instances where there was no polarisation applied to the gold templates, nucleation of the thermodynamically stable form A was observed. The authors concluded that controlling the electrochemistry of a template is a promising novel approach for directing polymorphism.

1.6.6 Emulsion Droplet and Gel-Based Templates

The use of emulsion droplets and gels for the templated crystallisation of different polymorphs has additionally been noted in the literature. A study of the crystallisation behaviour of even-numbered *n*-alkanes in water-in-oil droplets reported that previously unreported polymorphic forms were obtainable when surface additives became incorporated into the droplets (Ueno et al., 2003). The presence of additives facilitated the nucleation of novel pseudohexagonal and orthorhombic crystals for *n*-alkanes, whereas the absence of the additives resulted in the crystallisation of known triclinic crystals (Figure 1.22). The results by Ueno et al. hinted at the ability of additives to influence polymorphism by modifying the interface structure of the droplet templates. Polymeric microgels comprising polyethylene glycol diacrylate have been found to selectively crystallise CBZ form II and ROY form R through alteration of the microgel mesh size (Figure 1.23) in solution-based experiments (Diao et al., 2012). Furthermore, the polymorphism of CBZ, caffeine and piroxicam has been found to be regulated via direct crystallisation in metal-phenolic gel systems of specific composition which contained additives (Rahim et al., 2018). Lastly, supramolecular gels containing a gelator mimicking the chemistry of ROY has been shown to promote the preferential nucleation of form R (Foster et al., 2017).

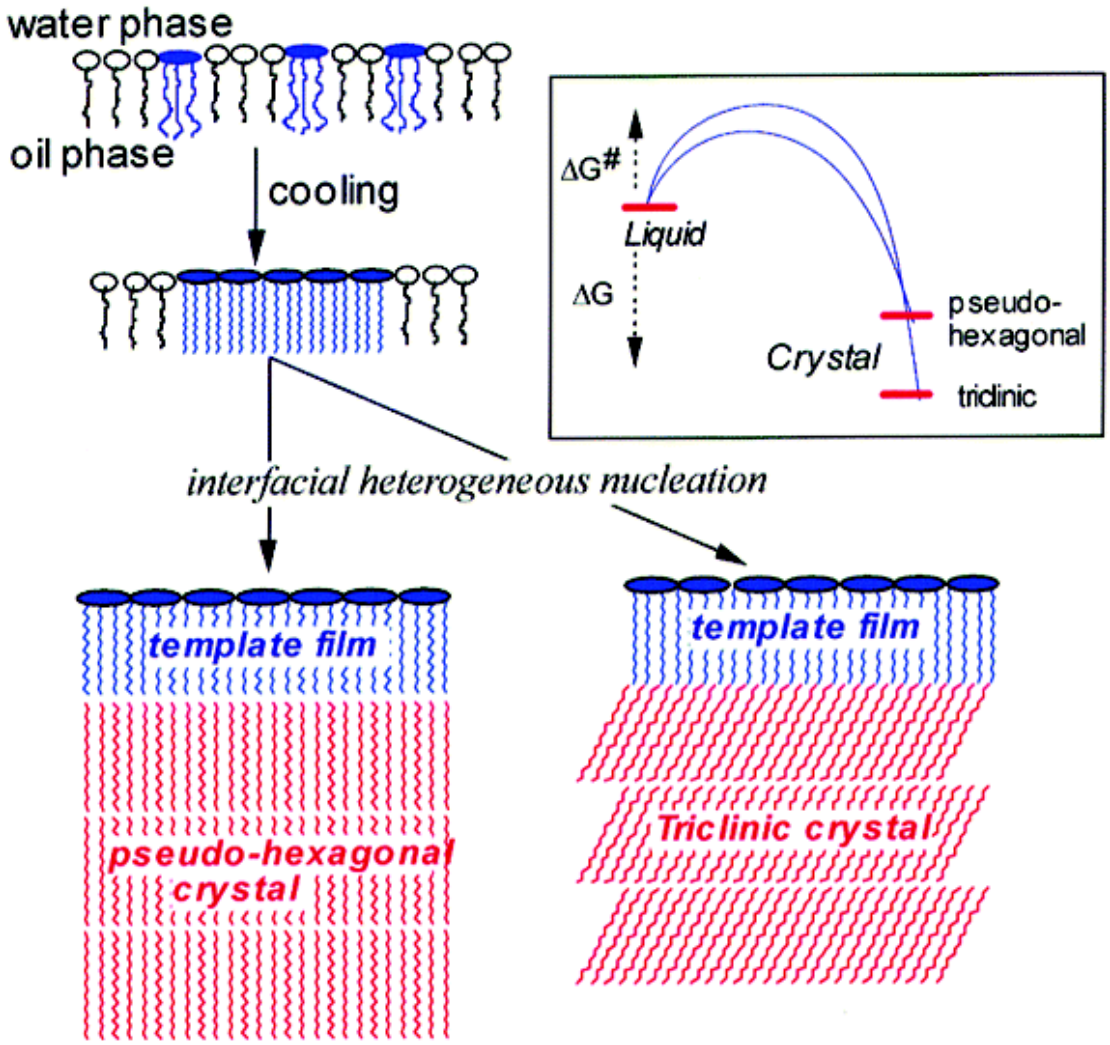

Figure 1.22: Illustration of the interfacial heterogeneous nucleation mechanism of pseudohexagonal and triclinic forms of even-numbered *n*-alkanes with high melting point surfactant additive (reproduced from Ueno et al., 2003). Dark ovals at the oil/water boundary represent polar headgroups of the additive molecule, whereas and zigzag lines correspond to aliphatic chains of the additive and *n*-alkane.

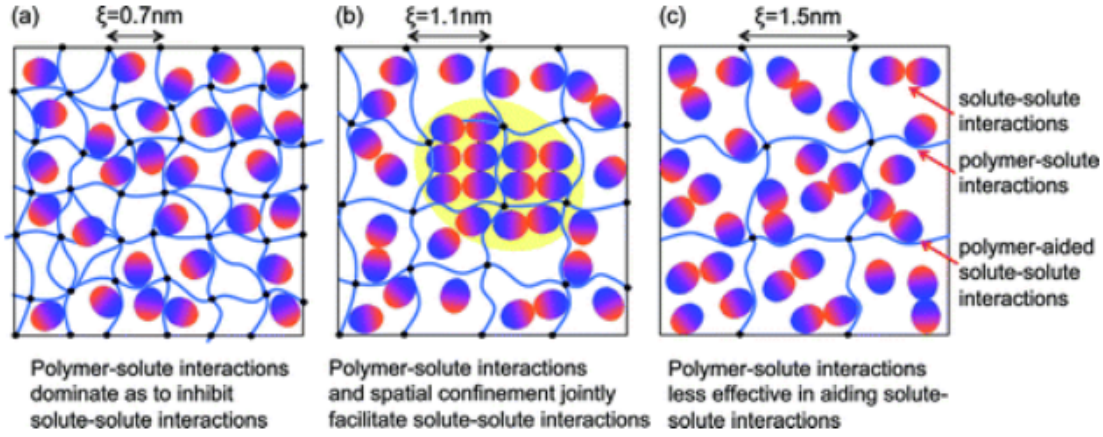

Figure 1.23: Schematic representation illustrating how average polymeric gel mesh size (ξ) directs nucleation and polymorph formation (reproduced from Diao et al., 2012). Blue lines are indicative of the polymer mesh and black-coloured features correspond to cross-linking points.

1.6.7 Nano-Confined and Micro-Confined Templating

Templates featuring nanoscale and microscale features have been explored over the years in an attempt to determine the effect of confined regions in crystallisation processes. Nanoscale pores of various shapes were investigated in nucleation studies of paracetamol and results showed that the morphology of the pores resulted in the appearance of a different polymorph (Graubner et al., 2013). The templates explored in this study were aluminium oxide and porous glass and the findings hinted towards the potential of nano-confined features to be utilised for polymorphic selectivity. The confinement of pharmaceuticals in nano-sized pores has additionally been employed to stabilise polymorphic forms which are normally unstable in the bulk, with form III of paracetamol and form β of glycine being prime examples, as well as enhance the stability of pharmaceuticals in their amorphous form (Beiner et al., 2007; Rengarajan et al., 2008; Rengarajan et al., 2009; Hamilton et al., 2008; Hamilton et al., 2012). Nucleation studies of aspirin in nanoscale pores of polymer films which were fabricated using nanolithography yielded interesting findings (Diao et al., 2011a). The crystallisation of aspirin in spherical pores of identical size was found to result in longer induction times, whereas crystallisation in hexagonal pores resulted in shorter induction times and enhanced nucleation kinetics (Figure 1.24).

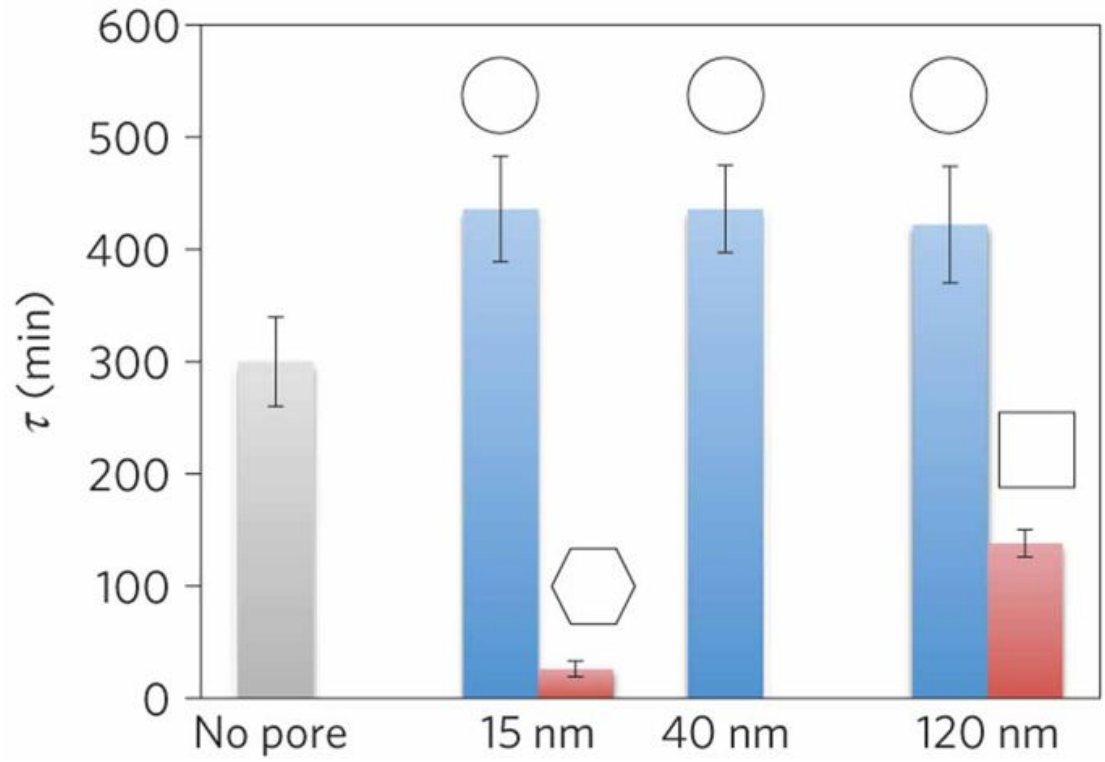

Figure 1.24: Effect of nanopores exhibiting identical size but different shape (spherical, hexagonal, square) in AA-co-DVB polymer films on the nucleation kinetics of aspirin (reproduced from Diao et al., 2011a).

Diao et al. also showed in their work that favourable interactions between a surface and a solute are a prerequisite for achieving enhanced nucleation rates in angular nanopores. A similar effect has been noted for angular nanopatterns that were imprinted on biocompatible polymer films for the purpose of controlling the nucleation of mefenamic acid, indomethacin and paracetamol crystals (López-Mejías et al., 2013; Tan et al., 2015; Stojaković et al., 2017). In addition to nanoscale pore shape, nanoscale pore size has also been found to influence polymorphism (Ha et al., 2004). Crystallisation of anthranilic acid on porous glass beads with a size smaller than 23 nm resulted in the preferential crystallisation of metastable form II, while nucleation in larger pores promoted the growth of form III. Nucleation studies of glycine crystals confined in micro-sized metallic islands of gold showed that the size of the islands directly affected the polymorphism of glycine, with small islands (25 μm) promoting the growth of the β-form and large islands (725 μm) crystallising the α form (Singh et al., 2011). In the same study, island sizes between 25 and 725 microns promoted the concomitant crystallisation of both metastable α and β glycine and the thermodynamically stable form γ.

1.6.8 Challenges Associated with Template-Induced Crystallisation

The field of template-induced crystallisation presents a number of challenges that have yet to be addressed in the literature. One such challenge pertains to developing thorough understanding of the interactions occurring between template surfaces and nucleating crystals (Parambil et al., 2019); the tendency of small organic molecules to form pre-nucleation clusters that could be less than a few nanometers in size poses difficulties with respect to characterising the clusters and gaining insight into how their interactions with a given template may govern nucleation and the corresponding polymorphic outcome.

Computational modelling investigations have attempted to shed light on the interplay between templates and nucleating crystal structures but these studies have mostly neglected the impact that solvent effects may exhibit in crystallisation processes that are facilitated by the presence of a given template (Parambil et al., 2019). A common limitation encountered across the existing literature on template-induced, solution-based crystallisation is the assumption that the chemistry and morphology of a template do not undergo any changes upon introduction of the template into the solution of interest. There have been a few instances where the chemical and morphological properties of a given template were found to change in solution. Crystal templates of 1,5-diaminonaphthalene exhibited a change in morphology depending on the temperature of the solution that they were inserted in (Patel et al., 2016); at a temperature of 10°C, “micro-pyramid’ crystals were observed and found to promote the nucleation of a novel hydrate of 3-aminobenzensulfonic acid whereas at a solution temperature of 50°C “micro-needle” crystals of 1,5-diaminonaphthalene were present and facilitated the crystallisation of form I of 3-aminobenzensulfonic acid. In the case of solution-based calcium carbonate crystallisation, the adsorption of a polyelectrolyte onto a SAM template affected the polymorphic outcome for calcium carbonate (Balz et al., 2005).

Additional challenges associated with template-induced crystallisation include understanding the effect of the relative surface area of a template in scaling-up the template-induced crystallisation and obtaining the desired crystallisation outcome, gaining insight into how the morphology of crystal templates influences intermolecular interactions between nucleating crystals and templates, and obtaining quantitative information on the functional moieties of a template (Parambil et al., 2019).

1.7 Analytical Techniques for Materials Characterisation in the Solid State

A wide range of analytical techniques can be utilised for characterising materials in the solid state, including those of pharmaceutical relevance, and gaining insight into their physicochemical properties. The theoretical background behind some of the most commonly employed of these techniques is provided in this section, in addition to some examples showing how each technique has been used in the context of pharmaceutical solid-form characterisation. A summary of key sample information derived using each technique is provided in Table 1.3 at the end of the section.

1.7.1 X-ray Diffraction (XRD)

1.7.1.1 X-ray Powder Diffraction (XRPD)

XRPD has emerged over the years as a very powerful tool for the structural characterisation of materials in the solid state and is particularly useful for identifying the presence of specific crystalline phases in a specimen of interest, elucidating the complete crystal structure of various types of solid materials (including pharmaceuticals) and obtaining quantitative information with respect to the presence of multiple crystalline phases within a sample (Shankland, 2016). The technique can be utilised to investigate materials under both ambient and non-ambient conditions which additionally makes it ideal for understanding solid-state phenomena such as polymorphic transformations (Florence et al., 2008) and dehydration/desolvation (Braun et al., 2015).

The premise behind XRD experiments lies in the fact that electrons present in the atoms comprising a material are capable of diffracting X-rays in all directions and producing periodic patterns which can yield structural information for a crystal at the atomic level. X-ray beams utilised for diffraction measurements in a typical laboratory setting exhibit wavelengths in the order of 0.8 – 3.0 Å, a range comparable to that corresponding to interatomic bond distances (Ooi, 2010). XRPD measurements are obtained using polycrystalline powder samples which are made up of numerous, small crystalline particles (crystallites) lying in random orientations and the measurements manifest in the form of powder diffraction patterns comprising several peaks which are direct products of the diffraction of X-rays by the atoms comprising the crystal structure of the investigated material (Figure 1.25).

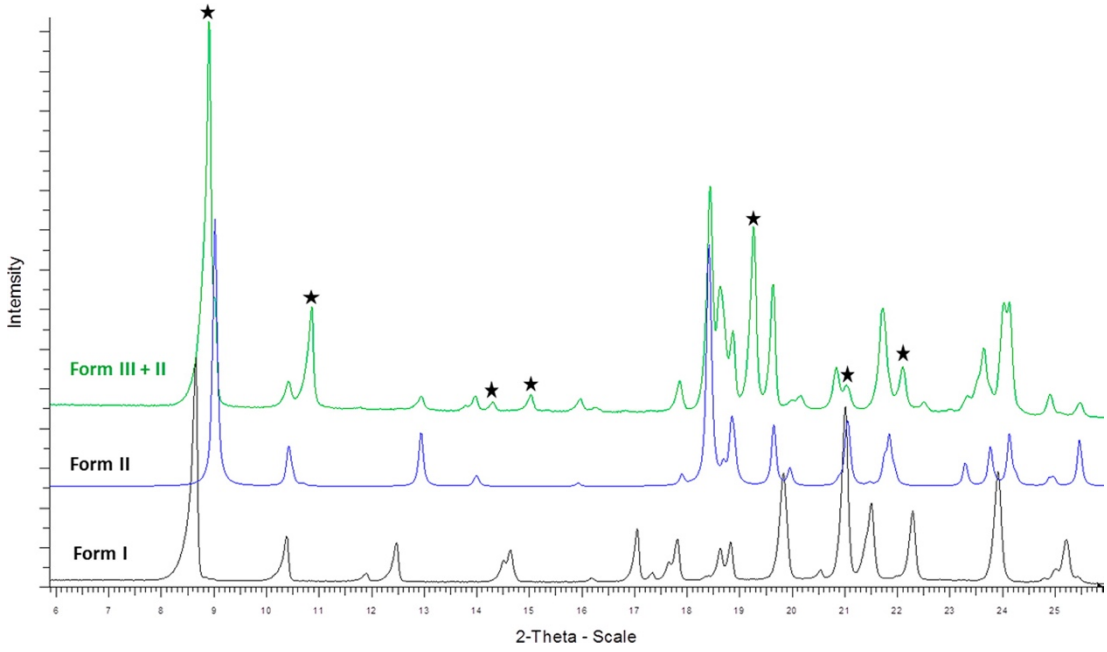

Figure 1.25: Representative XRPD patterns corresponding to different polymorphs of olanzapine (reproduced from Bhardwaj et al., 2013). Asterisks indicate diffraction peaks characteristic of form III.

The diffraction peaks comprising a powder diffraction pattern represent X-ray reflections from individual lattice planes found within the crystallographic unit cell which can only manifest upon satisfaction of Bragg's law which is presented in Equation 1.6 (Bragg, 1934) and Figure 1.26.

$$n\lambda = 2d\sin\theta \qquad \textbf{(Equation 1.6)}$$

In Bragg's law, *n* corresponds to an integer number, *λ* is the characteristic wavelength of the incident X-ray beam, *d* corresponds to the spacing between crystal lattice planes (Miller planes) of atoms that give rise to diffraction peaks and *θ* is the angle between the incident X-ray beam and a given Miller plane. Diffraction manifests when X-rays interact with atomic-scale, parallel crystal lattice planes of atoms separated by *d*-spacing. These planes are commonly referred to as Miller planes and are individually defined by a set of three integers (*hkl*) known as the Miller indices (Ooi, 2010). In order for Bragg's law to be satisfied and X-ray reflections to be obtained in a diffraction pattern, constructive interference between incident and diffracted X-rays must occur and that is only possible when the distance between paths ABC and A'B'C'

of the incident and diffracted X-rays is equal to an integer multiple (n) of the wavelength (λ) of the incident X-ray beam (Figure 1.26).

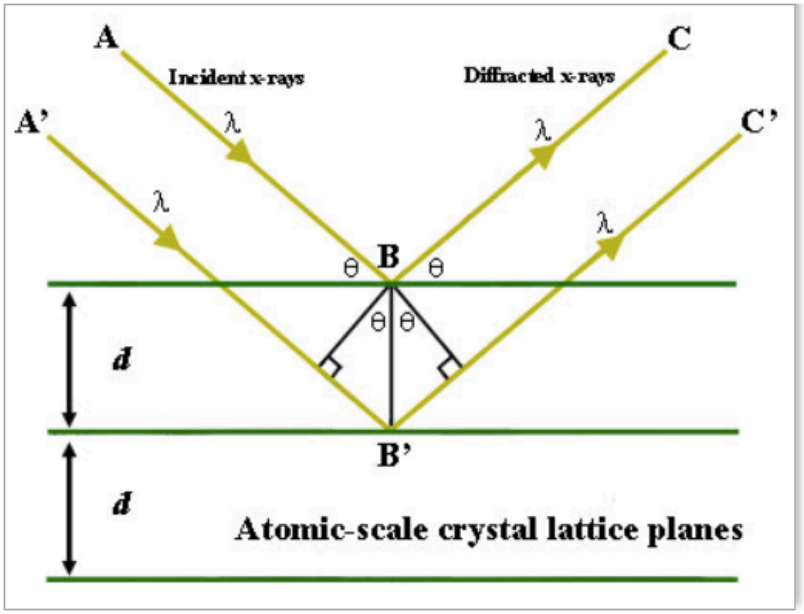

Figure 1.26: Schematic representation of Bragg's law (adapted from Henry et al., 2016).

Laboratory-based XRPD diffractometers generally comprise an X-ray generator source which produces the X-rays interacting with the sample of interest and a detector capable of detecting X-rays diffracting off the sample. The generator source typically consists of a tube comprising a water-cooled copper target (anode) and tungsten filament (cathode) which interact with one another to produce X-rays (Zink, 1997). More specifically, the tungsten cathode emits electrons which are accelerated to the copper anode by applying a suitable voltage and electric current, resulting in the occurrence of interactions between the accelerated electrons and the inner shell orbital electrons within the anode which ultimately bring about the generation of X-rays. XRPD diffractometers generally operate in two distinct geometries, Bragg-Brentano reflection geometry and Debye-Scherrer transmission geometry (refer to sections 3.2.7.1.1 and 3.2.7.1.2 for further details) and measurements are traditionally obtained using Cu Kα radiation which comprises two distinct wavelength components, Cu $K\alpha_1$ (λ = 1.54056 Å) and Cu $K\alpha_2$ (λ = 1.54439 Å). A primary monochromator is often incorporated into the diffraction setup to filter out the weaker Cu $K\alpha_2$ wavelength and ensure that all measured reflections in the experimental pattern manifest in the form of single peaks, minimising the likelihood of data misinterpretation (Shankland, 2016).

1.7.1.2 Single-Crystal X-ray Diffraction (SC-XRD)

SC-XRD is widely regarded as the most prominent technique for the purpose of elucidating the complete structure of pharmaceutical molecules in the solid state, yielding fully three-dimensional information on the structural features comprising an ordered crystal (Bond, 2016). The ability of SC-XRD analysis to produce structural information in three dimensions makes it advantageous over sample characterisation with XRPD in which all structural information is condensed into one-dimensional diffraction patterns. SC-XRD is suitable for structural analysis of crystals comprising 50 – 250 μm in all dimensions (Pindelska et al., 2017) and has additionally proven to be a valuable tool for assessing the chirality of enantiopure compounds and determining their absolute structure (Thompson and Watkin, 2009; Bond, 2016). A schematic illustrating a typical SC-XRD setup is presented in Figure 1.27.

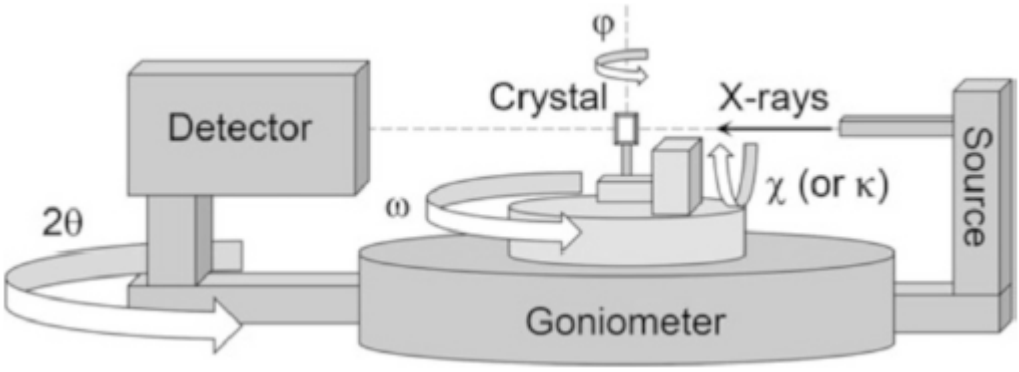

Figure 1.27: Schematic representation of a typical single-crystal diffractometer setup (reproduced from Bond, 2016).

The X-ray source in SC-XRD instruments comprises Cu or Mo radiation of characteristic wavelength ≈ 1.54 and 0.71 Å respectively. The goniometer component allows single crystals to be mounted on the instrument and oriented relative to the incident X-rays. Overall, there are three axes of movement for the purpose of orienting a crystal and ensuring that diffracted X-rays will be detected by the detector component. Along the ω axis, movement of the crystal occurs in the horizontal plane. Along the χ axis, the crystal is elevated in the vertical plane. Lastly, movement along the φ axis involves rotation of the crystal around the corresponding local mount axis. The detector of the experimental setup usually takes the form of a charge-coupled device (CCD) capable of converting diffracted X-rays to visible light and moves along

the 2θ axis, indicative of the angle of diffraction between incident and diffracted X-rays.

XRD patterns obtained from SC-XRD analysis are defined in terms of pattern geometry and the intensity of individual diffracted X-rays. Pattern geometry yields information on the translational periodicity of the crystallographic unit cell and a reciprocal relationship links the unit cell with the diffraction pattern obtained from a SC-XRD measurement. Generally, compact cells will yield diffraction patterns that are more spread out whilst larger unit cells will produce more compact patterns (Bond, 2016).

1.7.1.3 Crystal Structure Determination from XRD Data

In order for the crystal structure of a material to be determined from XRD data, a structural model needs to be derived that is truly representative of the size, shape and symmetry of the corresponding unit cell. Unfortunately, the "phase problem" arising during XRD measurements prevents a truly three-dimensional projection of the crystal structure of a sample to be obtained. The phase problem in X-ray crystallography refers to the fact that X-ray detectors are only capable of recording information on the intensity of diffracted X-rays but not the phase representative of each of these X-rays. This phenomenon is particularly problematic for structure determination because X-ray phases contain pivotal information for determining the distribution of electron density, which is indicative of the precise location of atoms within the unit cell (Clegg, 1998).

For the purpose of overcoming the phase problem and achieving crystal structure determination, a variety of approaches have been developed over the years, including Patterson methods (Patterson, 1934), direct methods (Altomare et al., 1994; Ooi, 2010), global optimisation (David et al., 2006; Fernandes et al., 2007; David and Shankland, 2008) and charge flipping (Oszlányi and Süto, 2004; Šišak Jung et al., 2014). In the context of small organic molecules comprising light atoms only (e.g. carbon, hydrogen, oxygen and nitrogen) in the unit cell, direct methods and global optimisation are generally the most commonly utilised approaches (David et al., 2006; David and Shankland, 2008; Bond, 2016).

Direct methods are capable of overcoming the phase problem by correlating the phase relationships exhibited by the intensities of peaks observed in a diffraction pattern (Massa, 2004). The application of this approach makes it possible for estimates of the phases corresponding to the most intense peaks to be obtained,

typically using a parallel solution method wherein sets of trial phases are assigned to the intense peaks and possible relationships between the phases of the peaks are established. The most probable set of phases then undergoes a Fourier transform to obtain an electron density map which can be employed to assign preliminary atomic positions depending on recognisable molecular features. Preliminary atomic positions can then be used to obtain a more complete set of estimated phases and assign atomic positions to the rest of the atoms found in the unit cell.

In the case of structure determination using the global optimisation approach, one of the most commonly employed methods is simulated annealing (Kirkpatrick et al., 1983; Smith et al., 1983; David et al., 2006), which was initially applied to elucidate the structure of zeolite systems (Deem and Newsam, 1989). The simulated annealing method involves simulating the melting of a well-defined, three-dimensional crystal structure model, enabling the type of molecule contained within the unit cell to adopt all possible conformations, orientations and positions. Simulation of a gradual decrease in the temperature of the system under study occurs following the "melting" stage, allowing the system to reach a global minimum wherein the best possible agreement between calculated and experimentally observed diffraction data can be observed. Once the global minimum has been reached, the crystal structure of the system of interest is considered to be solved.

1.7.1.3.1 Structure Determination from Powder Diffraction (SDPD)

SDPD involves the use of XRPD data as input for structure solution and has been established as the definitive method for elucidating the structure of materials that fail to crystallise as single crystals suitable for characterisation with SC-XRD (Shankland and David, 2002). The application of global optimisation for SDPD has become prominent over the past two decades and enabled organic structures of variable chemical and crystallographic complexity to be solved successfully, including those of pharmaceutically relevant compounds such as CBZ, chlorothiazide and naloxone (Florence et al., 2005; Fernandes et al., 2007; Sugimoto et al., 2007). SDPD is often one of many tools utilised in solid-state screening investigations in order to gain greater insight into the structural properties of pharmaceuticals, with prasterone (Stahly et al., 2006) and galunisertib (Bhardwaj et al., 2019) representing relevant examples. The SDPD process typically comprises several distinct steps that need to

be implemented to ensure success (Figure 1.28), namely powder pattern indexing, space group determination, Pawley refinement (Pawley, 1981), structure solution and Rietveld refinement (Rietveld, 1967 & 1969). Further details of the individual steps comprising SDPD and their implementation in the research described herein are provided in sections 3.2.7.1.5.2 and 3.2.7.1.6 in Chapter 3.

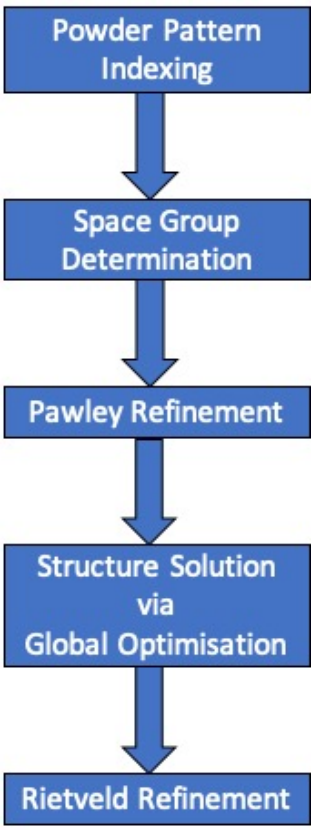

Figure 1.28: Schematic workflow depicting the different stages, in sequential order from top to bottom, involved in a typical SDPD process.

1.7.1.3.2 Structure Determination from SC-XRD

SC-XRD is recognised as the most prominent technique for structure determination of small pharmaceutical molecules in the solid-state and can provide a true three-dimensional representation of crystal structures (Bond, 2016). Structure determination using SC-XRD data is most commonly carried out using direct methods, or variants thereof such as intrinsic phasing (Sheldrick, 2015a), and a flow diagram illustrating the various steps involved in the process is presented in Figure 1.29.

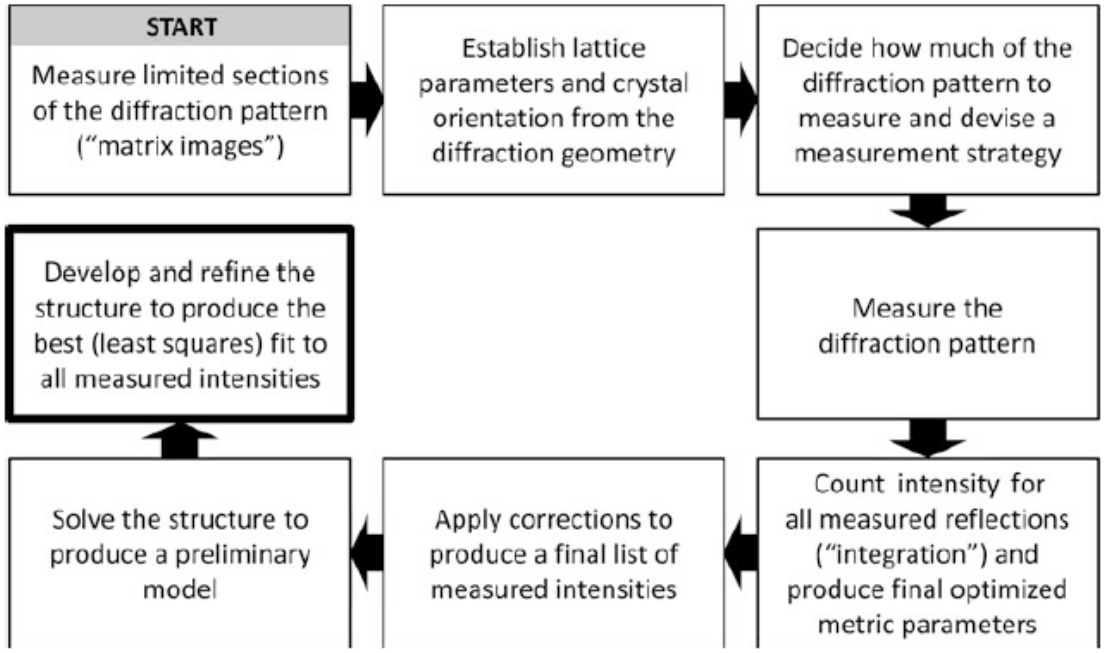

Figure 1.29: Flow diagram illustrating a typical workflow for crystal structure determination using SC-XRD (reproduced from Bond, 2016).

In the first step of the structure determination process from SC-XRD, measurement of limited sections of a crystal's diffraction pattern enables the translational periodicity of the crystal's internal structure to be obtained. Angles of diffraction measured in this step are backconverted to provide information on the cell parameters and relative orientation of the unit cell producing the diffraction pattern. At this stage of the process, the pattern is indexed and each diffracted X-ray is assigned Miller indices characteristic of the corresponding unit cell. With knowledge of this information, a strategy can be devised, through use of appropriate software, to measure a sufficient amount of the complete diffraction pattern for a high-quality final model of the structure to be derived. In the data "integration" stage of the workflow, raw diffraction images derived from the measured pattern are processed to determine the intensity of each diffracted X-ray and produce a final set of optimised unit cell parameters. The next step involves applying corrections and further optimisations to the measured intensities, including absorption corrections, scaling of distinct runs of data, and corrections accounting for systematic errors arising due to factors such as poor centring of the crystal during data collection. Once the measured intensities have been optimised, structure solution can take place using a suitable approach (e.g. direct methods) to produce an initial estimation of the final structure for the sample of interest. This preliminary model can then be developed further using Fourier

syntheses and subjected to a least-squares refinement so that the best possible fit to all of the experimentally measured intensities can be determined. During the refinement stage, the only parameters capable of undergoing refinement are the types and respective positions of atoms in the unit cell, the displacement parameters of atoms, indicative of their deviation from their expected positions within the unit cell, and the site occupancy factors which describe possible variations in the sites that the atoms occupy within the unit cell.

1.7.1.3.3 Absolute Structure and Absolute Configuration Determination

Absolute structure and absolute configuration determination for chiral crystalline materials can be readily carried out from SC-XRD data and has successfully been applied to systems of pharmaceutical relevance (Bredikhin et al., 2017). XRPD has also been employed for absolute structure and configuration determination in pharmaceutical systems (Schlesinger et al., 2018) but its use is significantly less prevalent than SC-XRD.

The determination of absolute structure and configuration generally requires information to be extracted from Friedel pairs (Thompson and Watkin, 2009; Bond, 2016). Friedel pairs can be defined as diffracted X-rays with characteristic Miller indices *hkl* and *-h-k-l*. Differences observed between the intensities of Friedel pairs provide crucial information in the context of absolute structure determination. The intensities of Friedel pairs corresponding to structures crystallising in centrosymmetric space groups are identical. On the contrary, Friedel pair intensities representative of structures crystallising in non-centrosymmetric space groups will differ from one another due to anomalous scattering of X-rays taking place. In instances where anomalous scattering occurs, X-rays are absorbed and re-emitted by the sample which causes them to undergo a phase change of 90°. The distinction of Friedel pair intensities due to the occurrence of anomalous X-ray scattering is made possible through determination of the Flack parameter (x) which is typically derived towards the end of the crystal structure refinement stage (Flack, 1983; Flack and Bernardinelli, 1999; Flack and Bernardinelli, 2000; Flack and Bernardinelli, 2008).

The physical model underpinning the Flack parameter is that of a crystal structure which is treated as an inversion twin containing a reference domain, corresponding to the absolute structure of the crystal, and a second domain wherein the absolute structure is inverted (Flack, 1983). The Flack parameter can only adopt physically

meaningful values in the range of 0 to 1 and is indicative of the proportion of the second domain, i.e. the inverted absolute structure, in the inversion twin model. A Flack parameter value of 0 indicates that the reference domain is the only domain present and the crystal under investigation has the correct absolute structure. In instances where the Flack parameter is equal to 1, the second domain is solely present and the absolute structure of the crystal of interest is completely inverted. Values of the Flack parameter that are greater than 0 but smaller than 1 suggest that both domains are present in different proportions and may signify that the crystal is a racemic twin where one of the domains contains one enantiomer and the other domain comprises the enantiomer's inverse. The Flack parameter is associated with a standard uncertainty *u* which can be used as an indicator of whether the absolute structure of a crystal under investigation using SC-XRD has been elucidated without ambiguity. As a general rule, in instances where the Flack parameter value is near zero, *u* is < 0.04 (or < 0.10 if the measured sample has been found to be enantiopure through other methods of analysis) and the absolute value of the Flack parameter divided by *u* is < 3.0 then the absolute structure of the crystal can be determined unambiguously, followed by determination of the absolute configuration of the chiral molecule or molecules comprising the crystal (Flack and Bernardinelli, 2008).

Absolute structure and configuration determination efforts through SC-XRD are hindered by the fact that the anomalous scattering effect of X-rays is weak, making it challenging to distinguish between the intensities of Friedel pairs. Utilising Cu radiation in SC-XRD measurements will generally enhance the potency of anomalous scattering, however the use of this type of radiation over others will still not enhance differences in intensities between Friedel pairs in a significant manner, particularly for unit cells comprising elements with very low atomic numbers such as carbon, hydrogen, oxygen and nitrogen (Bond, 2016).

1.7.2 Raman Spectroscopy

Raman spectroscopy is an analytical technique wherein scattered light detected by a suitable detector provides information on the composition of a sample irradiated using a monochromatic laser source. Integral to this technique is the occurrence of a phenomenon known as Raman scattering which takes place upon interaction of photons (particles representing light) with a sample (Gordon and Fraser-Miller, 2016). When photons interact with the molecules comprising the sample, the majority of them are subjected to a form of elastic scattering known as Rayleigh scattering, in which

no transfer of energy occurs between the photons and the sample, and the scattered photons exhibit the exact same energy in terms of frequency and wavelength as the incident photons. However, a small minority of the photons interacting with the sample of interest are subjected to an energy transfer which results in Raman scattering, a form of inelastic scattering. This transfer causes the scattered photons to exhibit either higher or lower energy compared to incident photons. In instances where the energy of scattered photons exceeds that of incident photons, Stokes Raman scattering is observed. On the contrary, instances where the energy of scattered photons is lower than that of the incident photons result in anti-Stokes Raman scattering. The Raman spectra obtained from experimental measurements depict the intensity of the Raman scattered photons for a given sample against the corresponding energy of the scattered photons, presented as wavenumbers or Raman shift (both in cm^{-1}).

Raman spectroscopy is a useful tool for distinguishing between different solid-state forms of the same compound, which often exhibit subtle differences between their respective Raman spectra (Figure 1.30). However, the technique cannot be utilised to derive the crystallographic data required for elucidation of the complete structure of crystalline materials.

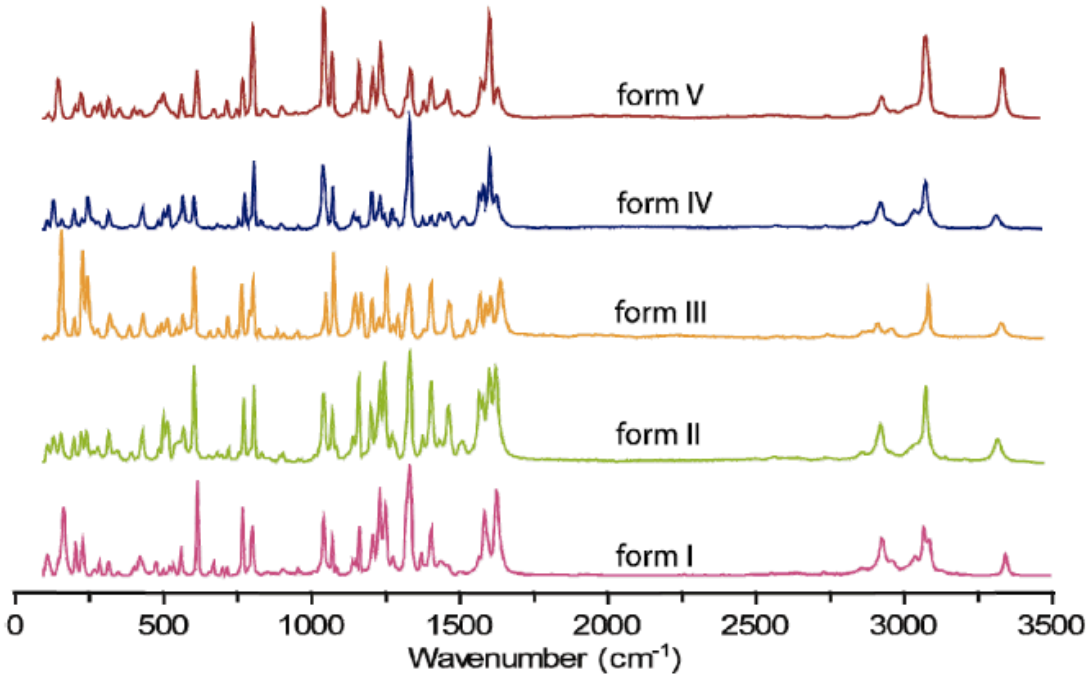

Figure 1.30: Representative Raman spectra of different polymorphs of tolfenamic acid (reproduced from López-Mejías et al., 2009).

1.7.3 Differential Scanning Calorimetry (DSC) & Thermogravimetric Analysis (TGA)

DSC is a thermal analysis technique in which the difference in the amount of heat needed to increase the temperature of both an experimental sample and a reference sample is measured directly as a function of temperature (Craig, 2006; Qi, 2016). During a DSC measurement, identical heating or cooling profiles are applied to the experimental sample and the reference, both of which are situated within a furnace, and the difference in heat flow between the two is recorded. In instances where a change in temperature facilitates a phase transition (e.g. melting, sublimation) or solid-state transition from one solid form to another for the experimental sample, DSC captures these occurrences in the form of exothermic or endothermic events. For exothermic events, the amount of heat released from the sample is captured whereas for endothermic events the amount of heat absorbed is measured. Transition events measured by DSC include sample melting, sublimation, crystallisation, polymorphic transformations, desolvation/dehydration and glass transition of amorphous materials. Typical DSC traces showcasing the manifestation of several of those events in a system of pharmaceutical relevance (paracetamol) are provided in Figure 1.31.

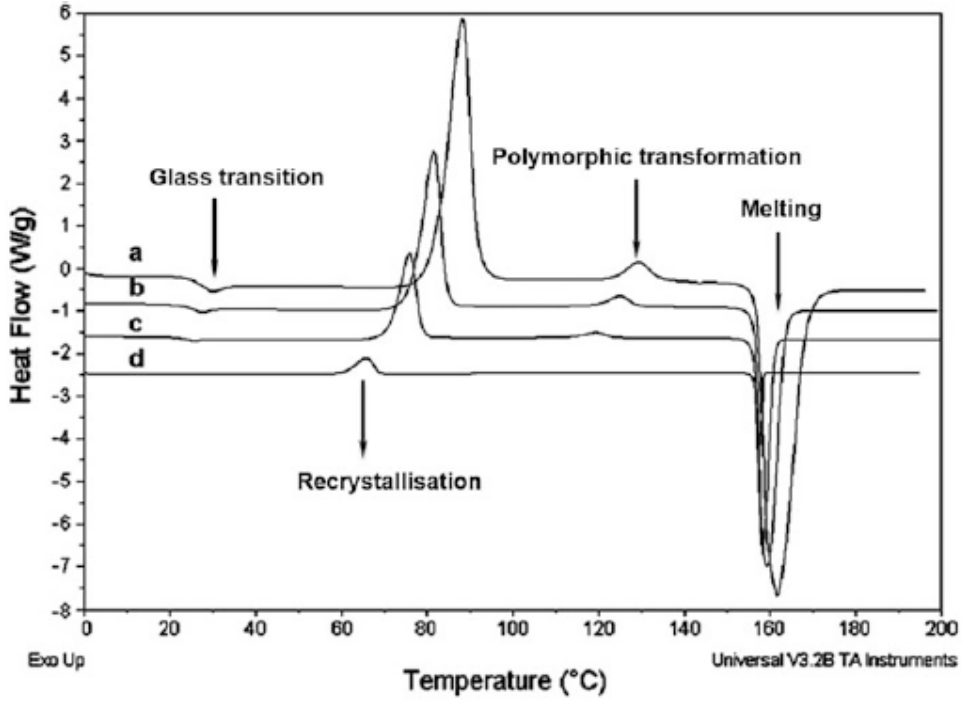

Figure 1.31: Representative DSC traces of the thermal behaviour and corresponding transition events occurring for a sample of amorphous paracetamol subjected to different heating rates (adapted from Qi et al., 2008).

DSC is often combined with TGA, a thermal analysis technique which monitors the amount of change in weight of a sample as a function of temperature and provides information on the degradation properties (mainly thermal) of a sample as well as solvent inclusion and stoichiometry in hydrated/solvated materials (Craig, 2006; Qi, 2016). Simultaneous thermal analysers enable DSC and TGA measurements to be captured in parallel and maximise the information that can be obtained with regards to the thermal behaviour and corresponding properties of the sample under investigation. Simultaneous DSC/TGA is typically conducted under a gaseous flow (typically nitrogen or helium) for the purpose of maintaining an inert atmosphere during measurements (Hilfiker, 2013b).

1.7.4 Optical Microscopy

Optical microscopy is a commonly utilised technique in pharmaceutical analysis for the purpose of investigating the morphological properties of materials and gaining greater insight into the polymorphic behaviour that is frequently exhibited by them. Developing an understanding of sample morphology is crucial in the context of pharmaceuticals as it dictates properties such as solubility and dissolution rate which have a direct impact on the performance of a drug upon administration (Chow et al., 2008). Optical micrographs can be readily used to identify differences in morphology and distinguish between polymorphic forms of the same material (Figure 1.32). Moreover, optical microscopes can be equipped with hot-stage sample holders, enabling the morphology of a sample of interest to be investigated under variable temperature conditions and allowing for potential solid-state transformations to be identified (Grooff et al., 2007).

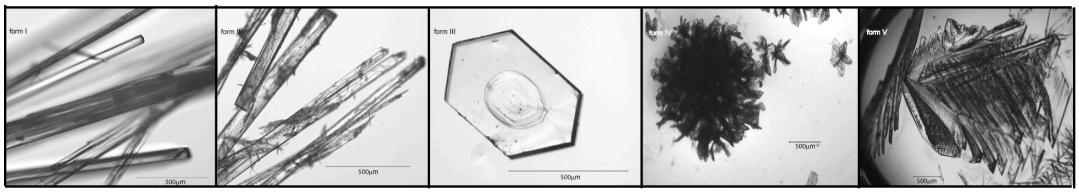

Figure 1.32: Optical micrographs of tolfenamic acid forms I-V, presented from left to right (reproduced from López-Mejías et al., 2009).

1.7.5 Atomic Force Microscopy (AFM)

AFM is a form of scanning probe microscopy, an experimental methodology involving the use of a cantilever probe to scan the surface of a material and identify features of interest using high-resolution imaging at both the nanoscale and microscale level. AFM can be utilised to generate both two-dimensional and three-dimensional images of a sample under investigation and yield direct information on its topography as well as data on the size and height of protrusion of both micron-sized and nano-sized features present on the sample's surface. A schematic diagram highlighting the typical components of an AFM setup is provided in Figure 1.33.

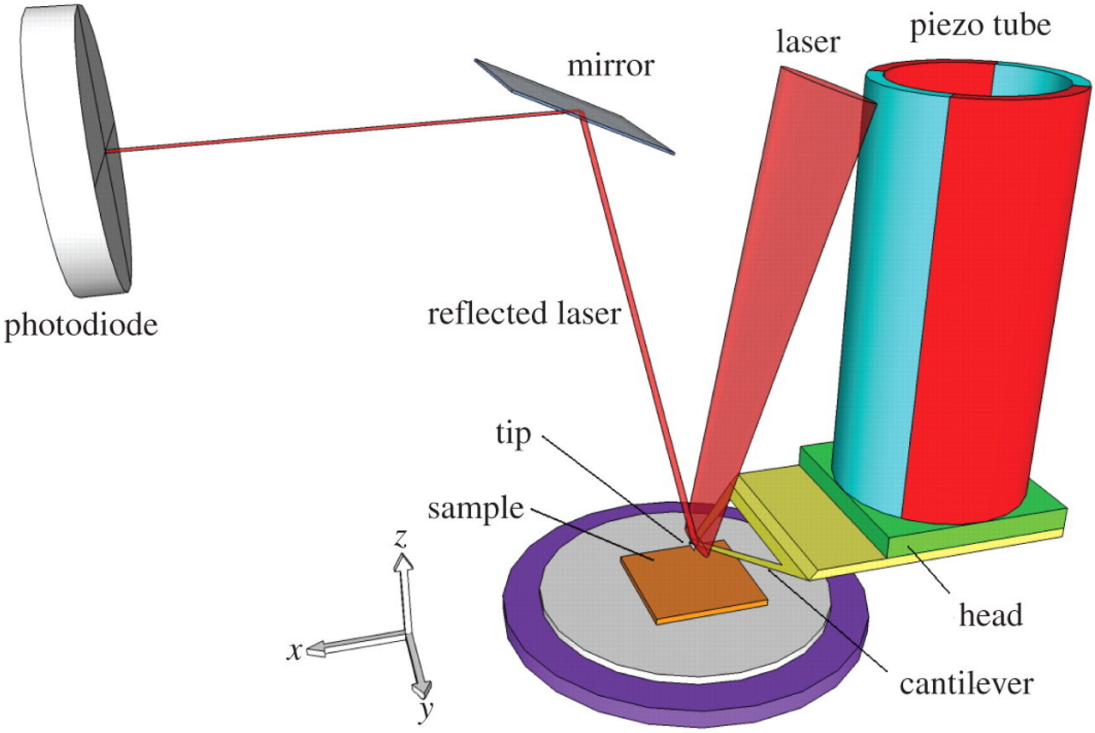

Figure 1.33: Schematic diagram illustrating a typical AFM experimental setup and the corresponding components (reproduced from Payton et al., 2011).

In an AFM setup, a piezoelectric tube is utilised to facilitate rastering of the AFM cantilever probe across the surface of the sample under investigation. This occurs by applying changes to the voltages corresponding to the piezoelectric elements that make up the tube. The movement of the probe occurs along the *x* and *y* directions and facilitates interaction with the sample and its structural features of interest. A laser beam and photodiode detector are constantly in place to monitor for the occurrence of cantilever bending which takes place due to interactions of the cantilever with atomic forces such as van der Waals and electrostatic forces (Chow et al., 2012). The

photodiode detector works by tracing the displacement of the laser beam brought about because of the bending motion of the cantilever upon its interaction with the atomic forces. The displacement of the beam creates an electrical signal which is ultimately picked up by the detector.

There are two main modes of operation for AFM imaging studies: contact and tapping. Contact mode is the most commonly employed of the two and features the use of a cantilever that scans the sample surface under a constant force or height (Payton et al., 2011). Tapping mode involves oscillation of the cantilever at a value at or close to its resonance frequency during surface rastering and generally offers shorter scan times and less likelihood of inducing damage to the sample compared to contact mode.

AFM can be applied to the study of molecular crystals (Chow et al., 2012) and has been used in the past to distinguish between polymorphs of the same material by identifying differences in their respective surface properties, as illustrated by the case of forms A and B of the API cimetidine (Danesh et al., 2000). Moreover, AFM has been employed in different types of crystal growth studies. In one such example, the technique was successfully used to identify the kinetics of the solid-state transformation between caffeine forms I and II (Kishi and Matsuoka, 2010). In another relevant example, AFM was used to assess the role of olanzapine form I single crystals in the templated growth of olanzapine dihydrate D (Warzecha et al., 2017).

1.7.6 Scanning Electron Microscopy (SEM)

SEM is utilised to obtain high-resolution images depicting the morphology and topographic features of various materials, such as pharmaceuticals, at the nanoscale (Bunjes and Kuntsche, 2016). An example of SEM imaging is provided in Figure 1.34 which depicts differences in the morphology of two distinct polymorphs of theophylline (Zhu et al., 2019). The enhanced imaging capabilities that SEM offers compared to traditional optical microscopy make it an ideal tool for obtaining morphological and topographical information that cannot be elucidated using an optical microscope.

The premise behind SEM analysis lies in the interaction of a sample with a fine electron beam generated by the SEM setup which scans the sample periodically and penetrates it to reach the atoms within. The interaction of the electron beam with the atoms comprising the sample results in the generation of electrons from the sample surface. The generated electrons are then detected by a specialised detector and used to yield the high-resolution images that are characteristic of the technique.

SEM analysis is generally carried out under high-vacuum conditions and can accommodate a broad range of sample specimen including powders, tablets and granules, with sample preparation largely depending on the nature of the specimen to be imaged. Data collection generally takes place under ambient temperature but certain SEM setups can be integrated with heating stages in order to pursue variable temperature analysis and assess the behaviour of the sample under different temperature profiles. Samples that are non-conductive generally need to be coated with a thin (nm-sized) continuous layer of material (usually gold or carbon) prior to analysis to optimise the quality of the images obtained and minimise the likelihood of artefacts appearing. Sample coating is carried out using a sputter coater and is usually not required if imaging is conducted under low accelerating voltages or low-vacuum conditions.

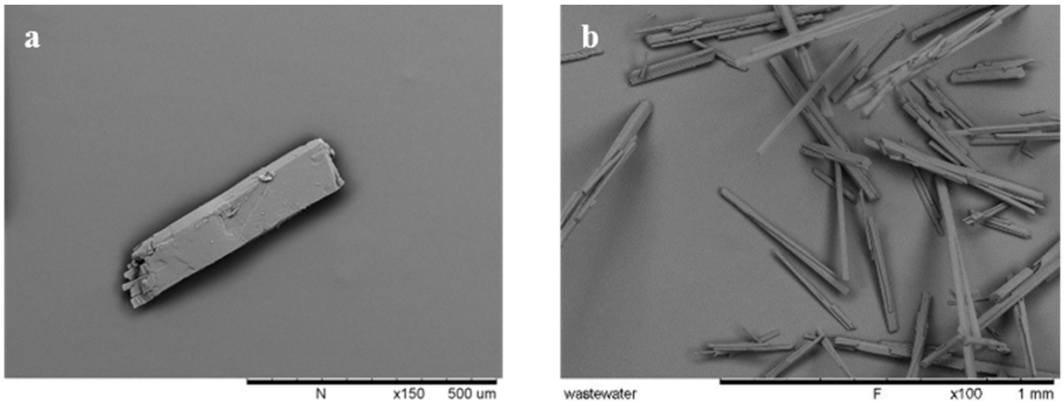

Figure 1.34: SEM micrographs depicting plate-like (a) and needle-like (b) crystals corresponding to form I and II of theophylline respectively (reproduced from Zhu et al., 2019).

1.7.7 Dynamic Vapour Sorption (DVS)

DVS is a gravimetric analytical method that monitors changes in a sample's mass upon prolonged exposure to controlled humidity and temperature conditions. It has gained significant traction in the context of pharmaceutical research as it enables insight to be obtained into the uptake of solvent vapours by APIs and the effect that it has on some critical properties of pharmaceuticals such as their physical stability and processability (Zografi and Kontny, 1995). Moreover, DVS is commonly utilised for developing better understanding of the conditions leading to solvate and hydrate formation of APIs (Giron et al., 2002; Burnett et al., 2007) and quantifying the presence of small amounts of amorphous content in pharmaceutical samples (Hogan

et al., 2001; Young et al., 2007). DVS measurements comprise sorption cycles, in which solvent vapours are taken up by the sample, and desorption wherein solvent vapours are released from the sample (Figure 1.35). The measurements are typically conducted isothermally whilst varying the relative humidity conditions in a stepwise manner and offer remarkable accuracy with respect to monitoring the mass of samples. A variety of organic solvents can be utilised in DVS experiments although water is the most commonly used one.

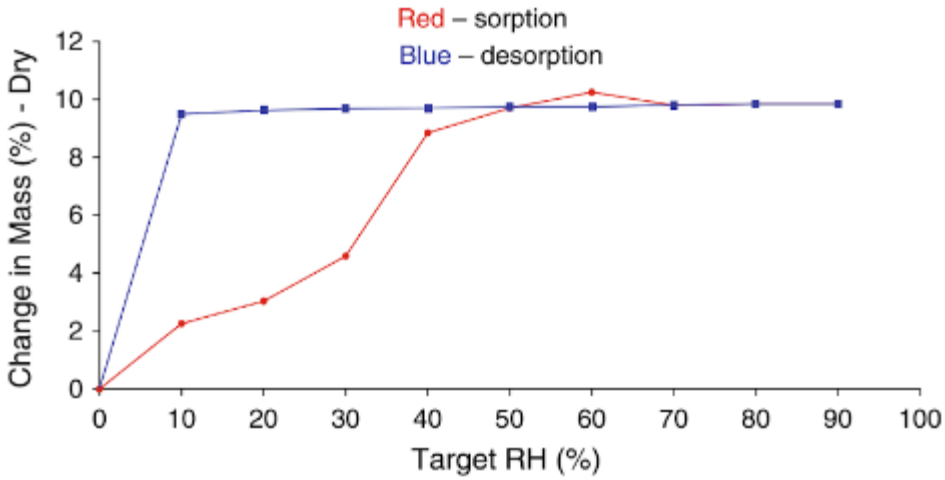

Figure 1.35: DVS isotherm plot depicting the sorption and desorption behaviour of naloxone hydrochloride at 25°C (reproduced from Turner et al., 2017).

Table 1.3: Overview of analytical techniques commonly utilised for materials characterisation in the solid state.

Technique	Key Information Provided
XRPD	Solid-form identification, crystal structure determination, absolute structure/configuration, phase transformations
SC-XRD	Solid-form identification, crystal structure determination, absolute structure/configuration, phase transformations
Raman Spectroscopy	Solid-form identification
DSC/TGA	Thermal stability, phase transformations, melting point, stoichiometry
Optical Microscopy	Morphology
AFM	Morphology, surface analysis at the nanoscale
SEM	Morphology, surface analysis at the nanoscale
DVS	Hydration/dehydration, hygroscopicity

Chapter 2: Aims and Objectives

2.1 Aims

The purpose of the research described herein is to obtain greater insight into the role of crystallisation process conditions and surfaces in directing solid-form selection and/or templating effects for organic molecules of pharmaceutical relevance in small-scale crystallisation processes. The work that was performed focused on utilising a variety of solid-state screening approaches, both solvent-based and solvent-free, whilst varying the thermodynamic and kinetic conditions employed experimentally in an effort to explore and establish solid-form diversity in three compounds of pharmaceutical relevance: oxcarbazepine (OXCBZ), evacetrapib (EVC) and a tetrazole analogue of EVC (TAEVC) which was provided for experimental use in amorphous (TAEVC1), crystalline (TAEVC2) and racemic (TAEVC3) forms. A broad range of crystallisation methods, characterisation techniques and visualisation tools were employed for gaining insight into the solid-state properties of these materials. An additional aim of the work was to assess the effect of metallic surfaces on directing the polymorphism of OXCBZ in solution crystallisation and physical vapour deposition experiments.

2.2 Objectives

For the purposes of achieving the intended research aims, the following objectives were pursued:

I. Perform solid-state screening studies to explore solid-state diversity in OXCBZ.
   - Utilise solvent-based crystallisation methods for screening and employ a diverse library of solvents with respect to physicochemical properties in an attempt to maximise the likelihood of crystallising and characterising all possible solid forms of OXCBZ.
   - Investigate the effect of metallic substrate incorporation in the polymorphic outcome of solution-based screening experiments conducted for OXCBZ.
   - Explore physical vapour deposition onto metallic substrates as a route towards polymorph selectivity and the preparation of novel anhydrous polymorphs for OXCBZ.
   - Prepare samples of OXCBZ form III suitable for crystal structure determination using X-ray diffraction (XRD) methods and employ predicted crystal structure data as a guide towards solving the structure of form III.

II. Investigate the serendipitous emergence of twisted morphology in crystals of OXCBZ form III prepared from solution and the vapour phase.

- Utilise scanning electron microscopy (SEM) to obtain high resolution images of the twisted crystals and extract analytical data with respect to their cross-section size, length, twist period (pitch) and handedness.
- Use SEM, atomic force microscopy (AFM) and time-of-flight secondary ion mass spectrometry (ToF-SIMS) to develop mechanistic understanding of the growth and structural evolution of the vapour-grown, twisted OXCBZ III crystals by performing imaging studies at different time intervals along the physical vapour deposition process.
- Employ ToF-SIMS, XRD, differential scanning calorimetry (DSC) and high performance liquid chromatography-mass spectrometry (HPLC-MS) analyses to investigate the presence of impurities in twisted OXCBZ III crystals.
- Establish whether crystal twisting can occur for two of OXCBZ's structural analogues, carbamazepine (CBZ) and cytenamide (CYT), which both exhibit polymorphic forms isostructural to OXCBZ III.

III. Perform solid-state screening studies to explore solid-state diversity in EVC and TAEVC.

- Utilise solvent-based screening methods and a diverse library of solvents whilst changing the thermodynamic and kinetic conditions explored in order to enhance the likelihood of crystallising and characterising all possible forms for the two compounds.
- Explore solvent-free approaches such as physical vapour deposition, crystallisation from the melt, supercritical fluid extraction and thermal annealing to obtain anhydrous polymorphs of the two materials.
- Use single-crystal X-ray diffraction (SC-XRD) to determine the absolute structure and configuration of crystals obtained from the experimental screen.
- Establish similarities and differences in the structural properties of the solid forms obtained in the experimental screen.
- Pursue cocrystallisation experiments to assess the possibility of EVC and TAEVC forming solid solutions for CSP-inspired templating experiments.

Chapter 3: Materials and Methods

3.1 Materials

The following substrates were utilised in the experimental work described herein and were not modified in any manner prior to experimental use:

- Commercial aluminium foil, Caterwrap®, exact purity and thickness unknown, Stephensons
- Copper foil, Puratronic®, purity 99.999%, 0.025 mm thick, Alfa Aesar
- Silver foil, purity 99.95%, 0.075 mm thick, Alfa Aesar

Before any experiments commenced, all foil substrates were thoroughly rinsed with deionised water (Milli-Q® laboratory grade, Merck Millipore) and 2-propanol (AnalaR NORMAPUR® ACS, Reag. Ph. Eur., purity ≥ 99.7%, VWR Chemicals) and dried under a stream of nitrogen gas in order to remove dust particles and organic contaminants. Copper-coated and silver-coated glass substrates were additionally employed for experimental purposes. The substrates were fabricated by depositing 200 nm of copper or silver (purity 99.99%, Advent Research Materials Ltd.) on 0.17 mm thick glass coverslips sourced from Fisher Scientific UK. Prior to deposition commencing, the glass substrates and metals were cleaned by sonicating in 2-propanol for 30 minutes and drying under a stream of argon gas. The thermal evaporation of the metals was carried out in a MBRAUN MB 200B vacuum evaporator (MBRAUN, Germany) at 10^{-6} mbar pressure with a slow deposition rate of 0.05 nm/s. For solid-state screening studies (solvent-based and solvent-free), the following chemicals were employed as starting materials in powder form and without further purification:

- Oxcarbazepine (OXCBZ) form I, pharmaceutical secondary standard/certified reference material, purity 99.6%, Sigma-Aldrich UK
- OXCBZ form I, purity 99.4%, Molekula Ltd., UK
- Carbamazepine (CBZ) form III, purity ≥ 98%, Sigma-Aldrich UK
- Cytenamide (CYT) form II, exact purity unknown, synthesised using a modification of the method reported by Davis et al., 1964
- Evacetrapib (EVC), exact purity unknown, Lilly Research Laboratories, USA
- Tetrazole analogue of EVC – 1 (TAEVC1), purity 99.5%, Lilly Research Laboratories, USA
- Tetrazole analogue of EVC – 2 (TAEVC2), purity 99.7%, Lilly Research Laboratories, USA
- Tetrazole analogue of EVC – 3 (TAEVC3), purity 97.7%, Lilly Research Laboratories, USA

For solution-based screening studies, over 30 analytical/reagent grade pure solvents sourced from Sigma-Aldrich UK, VWR Chemicals and Acros Organics were used experimentally. 30 binary solvent mixtures were additionally utilised, several of which comprised Milli-Q® laboratory grade deionised water (Merck Millipore) as one of the solvent components.

3.2 Methods

3.2.1 Visualisation and Analysis of Crystal Structures

Crystal structures corresponding to the compounds investigated were visualised using the *Mercury* software (Macrae et al., 2006; Macrae et al., 2008; Macrae et al., 2020) by the Cambridge Crystallographic Data Centre (CCDC). *Mercury* (v.4.3.0) was utilised to visualise the unit cell packing arrangement and hydrogen-bonding interactions for each structure, calculate XRPD patterns from single-crystal data deposited in the Cambridge Structural Database (CSD) and derived from experimentally determined structures in this work, perform packing and conformational analysis, and calculate the dimensions of void space present in structures where appropriate. Void space was calculated in the form of contact surfaces using a probe of radius 1.2 Å and grid spacing of 0.7 Å using the 'Voids' tool in *Mercury*. For solvated structures, the void volume occupied by solvent molecules was calculated as a contact surface using the 'solvate analyser' tool with a probe of radius 1.2 Å and grid spacing of 0.3 Å. *Mercury's* 'packing similarity' tool was employed to quantify similarity in the packing arrangements of the different structures using a 15-molecule cluster, 20% distance tolerance, and 20° angle tolerance. CSD reference codes for reported polymorphic forms visualised in this work are provided below:

- OXCBZ: CANDUR01 (Form I), CANDUR02 (Form II)
- CBZ: CBMZPN13 (Form I), CBMZPN03 (Form II), CBMZPN27 (Form III), CBMZPN12 (Form IV), CBMZPN16 (Form V)
- CYT: SOGLEG (Form I), SODNOP (Form II)
- EVC: GIXHUS (Form I)

3.2.2 Visualisation and Analysis of Predicted Candidates for the Structure of OXCBZ Form III

Unit cell packing arrangements, predicted Bravais-Friedel-Donnay-Harker (BFDH) morphologies (Docherty et al., 1991) and simulated XRPD patterns for predicted candidate structures of OXCBZ form III were visualised using the *Mercury* software (v.4.3.0). *Mercury* was additionally utilised to calculate the dimensions of void space in each candidate structure. Void space was calculated in the form of contact surfaces using a probe of radius 1.2 Å and grid spacing of 0.7 Å using the 'Voids' tool. *Mercury's* 'packing similarity' tool was employed to quantify similarity in the packing arrangements of the candidates using a 30-molecule cluster, 20% distance tolerance, and 20° angle tolerance.

3.2.3 Characterisation of Experimental Substrates

3.2.3.1 Atomic Force Microscopy (AFM)

The topography and average nanoscale roughness (R_a), of the experimental substrates were assessed by collecting peak force error and height sensor images using a Dimension FastScan™ AFM instrument by Bruker. At least 3 images were collected for each substrate under ambient conditions in PeakForce Tapping® mode using Bruker ScanAsyst Air probes with nominal spring constant k = 0.4 N/m and nominal tip radius of 2 nm. The *NanoScope Analysis* software package (v.1.9, Bruker) was utilised to apply first order flattening to all of the height sensor images and calculate substrate R_a values. Calculation of R_a, a parameter representing the average of the absolute values of the height deviations measured from the mean height of a substrate, was based on Equation 3.1 wherein N represents the number of data points measured across the substrate and Z is the height deviation.

$$\mathrm{R}_a = \frac{1}{\mathrm{N}}\sum_{\mathrm{j}=1}^{\mathrm{N}}\left|\mathrm{Z}_\mathrm{j}\right| \qquad \textbf{(Equation 3.1)}$$

3.2.3.2 Contact Angle Goniometry (CAG) and Surface Free Energy Determination

CAG is utilised to determine the contact angle (θ) formed between a liquid-vapour interface and a solid surface and can yield insight into the surface-induced, heterogeneous nucleation of materials by providing information on the wettability of

surfaces and the surface free energy component of a solid substrate. In CAG measurements, a liquid surface, usually in the form of a droplet corresponding to a probe solvent, comes into direct contact with a solid substrate (Figure 3.1) and results in wetting of the aforementioned substrate (Schuster et al., 2015). The placement of the droplet with respect to the substrate and the surrounding atmosphere results in the formation of three interfaces, namely sv (solid-vapour interface), sl (solid-liquid interface) and lv (liquid-vapour interface).

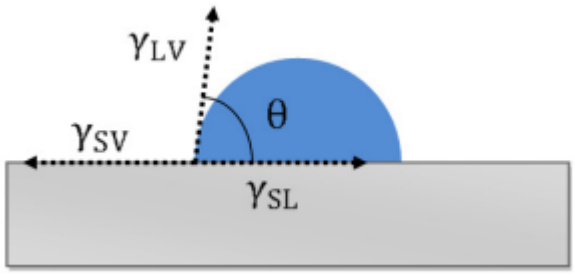

Figure 3.1: Schematic diagram depicting the contact angle formed following placement of a liquid droplet on a solid surface (reproduced from Schuster et al., 2015).

The wettability of a solid substrate of interest can be quantified directly by applying Young's equation which assumes that the substrate is perfectly flat, rigid and chemically homogeneous (Equation 3.2; Yuan and Lee, 2013). In Equation 3.2, the solid-vapour interfacial energy (γ_{sv}) is dependent on the solid-liquid interfacial energy (γ_{sl}), the liquid-vapour interfacial energy (γ_{lv}) and the contact angle (θ) between a liquid droplet and a solid substrate.

$$\gamma_{sv} = \gamma_{sl} + \gamma_{lv}\cos\theta \qquad \textbf{(Equation 3.2)}$$

In instances where water is employed as the probe liquid in CAG studies, the contact angles obtained indicate whether the solid substrate exhibits hydrophilicity (high degree of wettability) or hydrophobicity (low degree of wettability) with regards to its wetting properties (Figure 3.2). Contact angle values < 90° indicate hydrophilicity of the solid substrate whereas values > 90° are indicative of substrate hydrophobicity. Solid substrates exhibiting high degree of wettability generally possess higher surface

free energy compared to substrates exhibiting low degree of wettability (de Gennes, 1985) and will promote heterogeneous nucleation more readily.

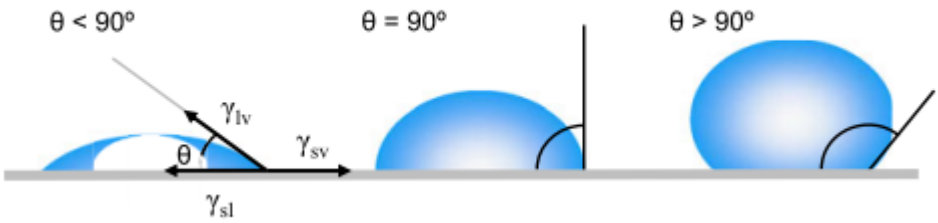

Figure 3.2: Schematic diagram illustrating the different wetting behaviours of a liquid droplet upon contact with a smooth and homogeneous solid substrate (reproduced from Yuan and Lee, 2013).

The wettability of the experimental substrates in this work was assessed by obtaining contact angle measurements using a KRÜSS DSA30 goniometer (KRÜSS, Germany). The static sessile drop method (Schuster et al., 2015) was employed to determine contact angles at room temperature using 3 distinct probing liquids with variable polarity profiles. The probing liquids utilised were water (HPLC grade, Sigma-Aldrich UK), diiodomethane (*ReagentPlus*®, purity 99%, containing copper as stabiliser, Sigma-Aldrich UK) and ethylene glycol (purity 99.8%, Sigma-Aldrich UK). The drop shape analyser ADVANCE software (KRÜSS, Germany) was used for recording data. For each contact angle measurement, manual operation of the goniometer enabled the preparation of a 10 µL probing liquid droplet which was left lying on the substrate for a period of 10 seconds prior to data collection. For each combination of probing liquid and experimental substrate, at least 10 measurements were recorded and average values and standard deviations calculated accordingly. The contact angle values obtained were then utilised to determine the surface free energy of each substrate using the Good and van Oss three-liquid formula (Good and van Oss, 1992) described in Equation 3.3. The Good and Van Oss approach enables the surface free energy of a given substrate to be calculated and experimental contact angle values are obtained with at least three probe liquids, two of which need to be polar and one of them apolar and devoid of the characteristics of a typical Lewis acid or base. In Equation 3.3, γ^{LW} corresponds to the interfacial energy of the dispersive component of a given probe liquid, γ^{+} indicates the interfacial energy of the electron acceptor component of a polar probe liquid and γ^{-} is the interfacial energy of the electron donor component of a polar probe liquid. In the studies described herein, water and ethylene glycol represent polar probe liquids whilst diiodomethane is apolar

(Rudawska and Jacniacka, 2018). The surface energy components of water, diidomethane and ethylene glycol are shown in Table 3.1 and were used as input values for surface energy calculations performed with the in-house Visual Basic program *'Surface Energy Calculator'* (Lamprou et al., 2010).

$$\gamma_{sl} = \gamma_{sv} + \gamma_{lv} - 2\left(\sqrt{\gamma_{sv}^{LW}\gamma_{lv}^{LW}} + \sqrt{\gamma_{sv}^{+}\gamma_{lv}^{-}} + \sqrt{\gamma_{sv}^{-}\gamma_{lv}^{+}}\right) \quad \textbf{(Equation 3.3)}$$

Table 3.1: Probing liquids for CAG measurements and their corresponding surface energy components.

Probing Liquids	Surface energy components (mJ/m^2)			
	γ_l	γ_l^{LW}	γ_l^{+}	γ_l^{-}
Water	72.8	21.8	25.5	25.5
Diidomethane	50.8	50.8	0	0
Ethylene glycol	48	29	1.92	47

3.2.4 Physical Vapour Deposition Studies

3.2.4.1 Physical Vapour Deposition under Atmospheric Conditions

For each experiment, ≈ 20 mg of starting OXCBZ, CBZ, CYT, EVC and TAEVC materials in powder form were weighed using an analytical balance and placed on a glass petri dish which was then positioned on an IKA® RH digital heating plate situated in a fume hood (Figure 3.3). In instances where the influence of a metallic substrate on the solid-form outcome of OXCBZ, CBZ and CYT was to be investigated, the substrate was cut into a 1 cm x 1 cm tile, attached to a glass slide using a double-sided carbon tab and placed on top of the petri dish with a distance of approximately 1 cm separating the substrate from the starting powder. The heating plate was set to heat at a temperature range of 125 - 145°C and maintained at these temperatures to induce sublimation of the starting powder. Resulting vapours emerging from successful sublimation of the starting materials proceeded to deposit themselves on each substrate and form solid crystals. The duration of the deposition process varied from 1 hour to 48 hours. An RS1327 infrared thermometer (RS Components) was used to obtain an estimate of the temperature of experimental substrates whilst each experiment was performed. For EVC and TAEVC experiments, metallic substrates

were not utilised and vapour deposition onto bare glass slides (1 – 1.2 mm thick) was solely attempted for a period of up to 1 week using temperatures of 50 - 100°C .

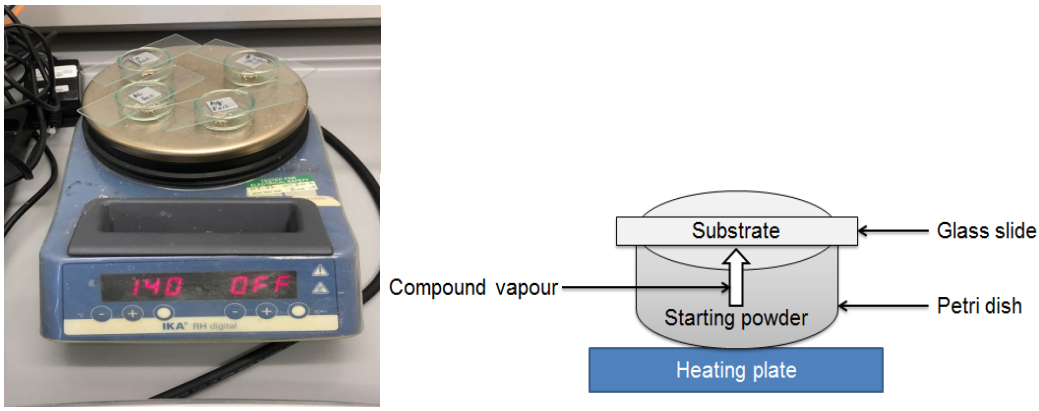

Figure 3.3: Experimental setup for physical vapour deposition studies under atmospheric conditions, presented herein using OXCBZ samples.

3.2.4.2 Physical Vapour Deposition under High Vacuum

Crystalline OXCBZ films of various thicknesses were prepared on experimental substrates by controlled physical vapour deposition studies performed using a custom-made QBox 450 system (Shard et al., 2015) by Mantis Deposition Ltd., U.K (Figure 3.4). An alumina coated crucible was used for subliming the starting material (OXCBZ form I) in powder form and a quartz crystal microbalance (QCM) sensor was positioned close to the crucible to enable the rate of vapour deposition and thickness of the sublimed material on experimental substrates to be monitored in real time. The substrates were cut into 1 cm x 1 cm tiles and placed face down in an appropriate multi-position sample holder (Figure 3.5) positioned 14 cm above the powder-filled crucible. During the vapour deposition process, the holder was constantly rotated at 20 rpm to ensure equal distribution of the deposited material. The TITANIUM software by Mantis Deposition Ltd was utilised to monitor the deposition rate and sample thickness for each experiment. Before any experiments were performed, the QBox was vented to atmospheric pressure and then pumped down to a high vacuum (pressure ≤ 9.99 x 10^{-7} Torr). In order for vapour deposition of the starting material to commence, an electric current of 0.35 V was applied to the crucible in the first instance and the TITANIUM software was used to manipulate the voltage in small increments until the rate of deposition began to increase. The temperature of the powder in the crucible was monitored at all times by using a thermocouple. At the end of each experimental run, a shutter positioned between the crucible and the sample holder was closed to prevent further deposition of OXCBZ on the substrates.

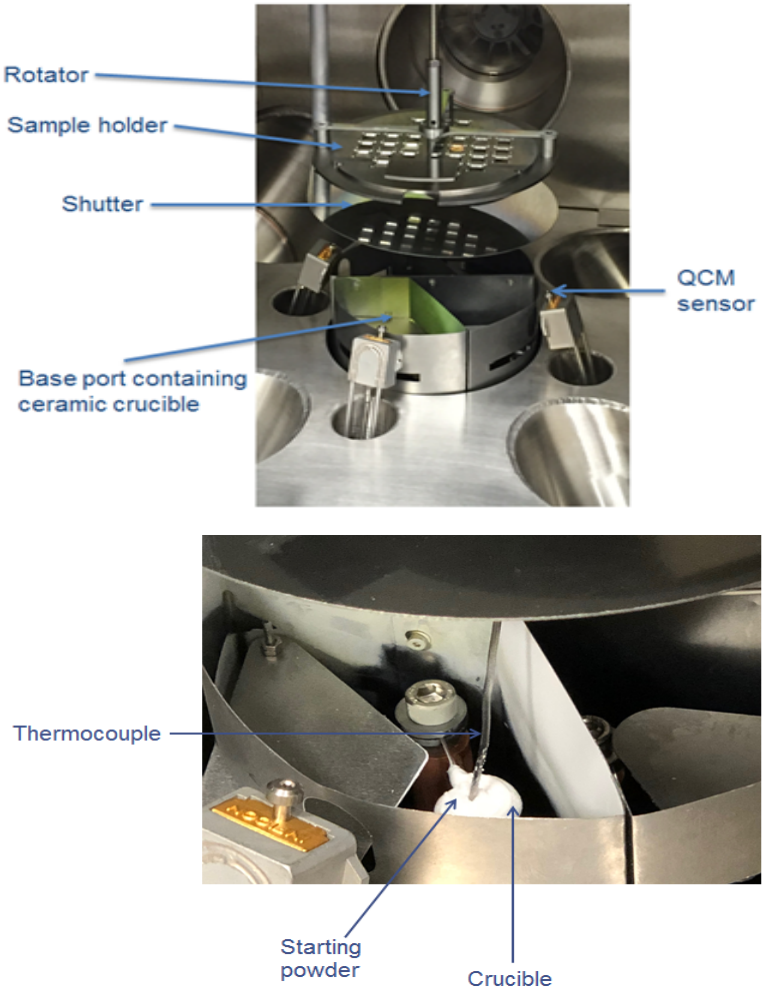

Figure 3.4: Experimental setup for physical vapour deposition studies performed under high-vacuum conditions with the QBox 450 system.

Figure 3.5: 37 position sample holder utilised for physical vapour deposition studies with the QBox 450 system.

3.2.4.3 Comparison of Experimental Setups Employed in Physical Vapour Deposition Studies

Table 3.2 summarises the differences between the physical vapour deposition setups described in sections 3.2.4.1 and 3.2.4.2.

Table 3.2: Overview of differences between the experimental setups used for physical vapour deposition studies performed under atmospheric conditions and high vacuum.

Heating Plate Setup	QBox 450 Deposition System
Vapour deposition was carried out in a fume hood cupboard	Vapour deposition was carried out in a high-vacuum chamber with pressure ≤ 9.9×10^{-7} Torr
Temperature of experimental substrates during deposition was non-ambient	Temperature of experimental substrates during deposition was ambient
Distance between the substrates and the starting powder was ≈ 1 cm	Distance between the substrates and the starting powder was ≈ 14 cm
Rate of deposition and thickness of deposited materials could not be monitored	Rate of deposition and thickness of deposited materials could be monitored in real time using a QCM sensor

3.2.5 Crystallisation from the Melt

Small amounts (5 - 20 mg) of TAEVC2 and TAEVC3 powders were placed between two glass coverslips and melted using an IKA® RH digital heating plate maintained at an appropriate temperature to induce melting. The coverslips were then either quenched in liquid nitrogen or allowed to cool slowly at room temperature conditions.

3.2.6 Parallel Solid-State Screening Studies in Solution

3.2.6.1 Solvent Selection and Solubility Determination

Solvents for screening were generally selected using the Strathclyde24 model (refer to Figure 1.13, section 1.4.1) which classifies solvents into 24 clusters using 250 electronic, feature-count, spatial, thermodynamic and topological molecular descriptors. The premise behind utilising Strathclyde24 for solvent selection in a solid-state screen lies in maximising the possibility of obtaining all possible solid forms of the compound under investigation by selecting at least one solvent for experimental use from each of the 24 clusters comprising the model. The Strathclyde24 approach has been found to enhance the likelihood of successfully deriving all crystalline forms in an experimental screen when compared to solvent selection involving random

sampling of solvents and solvent selection based on a single physicochemical property such as polarity.

Solvents known to be readily miscible in one another were picked for the preparation of the binary mixtures that were investigated in the screening studies. Experimental determination of OXCBZ, EVC, TAEVC1, TAEVC2 and TAEVC3's solubility in the solvent systems of interest was carried out using a solvent addition method. Small aliquots of each pure solvent or solvent mixture were manually dispensed (typically in steps of 100 µL) into glass vials (either 1.5 mL HPLC or 20 mL scintillation) and agitated at 2800 rpm under room temperature conditions using a Lab Dancer vortex mixer (IKA®) until clear solutions were visually observed.

3.2.6.2 Crissy® Screening Platform

Solution-based screening experiments of OXCBZ were performed using a Crissy® platform by Zinsser Analytic (Figures 3.6 and 3.7). Saturated/nearly-saturated solutions were prepared manually in glass scintillation vials with a working volume of 20 mL by dissolving suitable amounts of up to 30 mg of OXCBZ form I in 3 - 6 mL of each solvent (either single component or binary mixture). The IKA® RH digital heating plate and Lab Dancer vortex mixer were used to facilitate solution heating/vortexing and ensure dissolution of starting OXCBZ powders. Crystallisation screening experiments were carried out at fixed temperatures via fast evaporation under a light stream of nitrogen gas. Prior to experiments commencing, all solutions were filtered into clean glass vials using 0.2 µm PTFE syringe filters in order to ensure that no undissolved powder particles were present. Fast evaporation was chosen as the crystallisation method as it tends to favour the formation of metastable forms compared to slow evaporation (refer to Figure 1.12, section 1.4.1), as well as allow for the rapid generation of a large number of samples for analysis within a brief timeframe.

In the majority of crystallisations that were carried out, the solutions prepared were agitated at a constant rate and typically evaporated completely within 20 - 30 minutes. The temperature of evaporation for each experiment was controlled using a heating bath circulator by Huber (Peter Huber Kältemaschinenbau AG, Germany) which was filled with silicone oil. In experiments involving the addition of a substrate to investigate the effect on solid-form outcome, a 1 cm x 1 cm tile of aluminium foil was manually added to each crystallisation vial after solution filtration had been carried out. The evaporation temperature and agitation speed profiles used in each experiment were

all programmed using the Zinsser Method Runner software. A step-by-step overview of the experimental workflow implemented using Crissy® is provided in Figure 3.8 and each experiment was typically performed in triplicate.

Figure 3.6: The Crissy® platform by Zinsser Analytic.

(a) 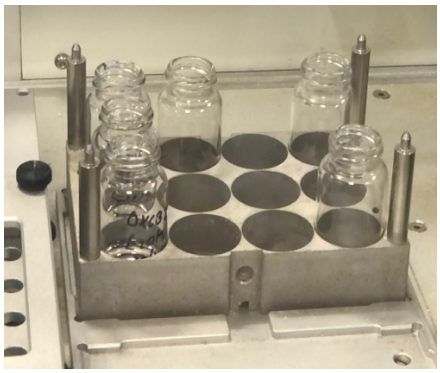 (b) 

Figure 3.7: Glass scintillation vials (a) and evaporation manifold (b) utilised in solution crystallisation screening studies performed using the Crissy® platform.

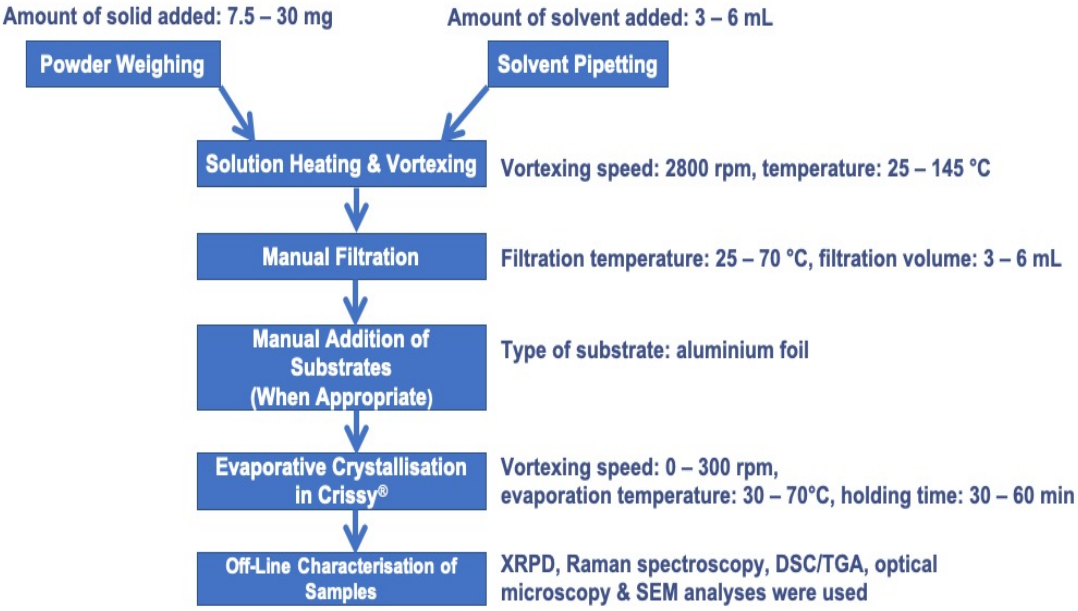

Figure 3.8: Workflow for evaporative crystallisation experiments pursued using the Crissy® platform.

3.2.6.3 Manual Crystallisations and Desolvation Studies

3.2.6.3.1 Evaporation

Evaporative crystallisation experiments were performed at both room temperature and 50°C. 15 - 16 mg of EVC, TAEVC1, TAEVC2 and TAEVC3 powders were weighed into clean glass vials (either 1.5 mL HPLC or 20 mL scintillation) and dissolved in variable amounts of solvent using experimental solubility values derived through the method outlined in section 3.2.6.1 as a guide. For evaporation studies at room temperature, saturated or nearly-saturated solutions of the starting materials were prepared, filtered and left to evaporate in a fume hood until complete solvent evaporation was observed. Evaporative crystallisation at non-ambient temperature was performed by maintaining all solutions at 50°C using an IKA® RH digital heating plate until complete evaporation was noted. Dry products were retrieved for analysis.

3.2.6.3.2 Cooling

Warm saturated solutions of EVC, TAEVC1 and TAEVC2 were prepared by dissolving suitable amounts of powder in glass vials. The solutions were filtered into clean vials which were then immersed in a bath of dry ice to induce crystallisation via cooling. Precipitates emerging from the cooling experiments were isolated by filtration and air-dried prior to analysis.

3.2.6.3.3 Solvent Vapour Diffusion

Selected anti-solvents were diffused through the vapour state into saturated, filtered solutions of EVC, TAEVC1, TAEVC2 and TAEVC3 which were prepared in glass vials using solvents that were found to readily dissolve each compound. The vials containing the filtered solutions were placed in sealed glass beakers which contained a suitable amount of each anti-solvent to allow vapor diffusion to occur at room temperature conditions. In instances where crystallisation was successfully induced, solid products were recovered from each vial by filtration and air-dried before subsequent characterisation was carried out.

3.2.6.3.4 Cocrystallisation Screen for Solid-Solution Formation

Cocrystallisation experiments were carried out by dissolving equimolar amounts of EVC and TAEVC1/TAEVC2 in select solvents using glass vials. The solutions prepared were filtered into clean vials and allowed to evaporate in a fume hood under room temperature conditions until complete evaporation was noted. Dry products were retrieved from the vials for subsequent analysis.

3.2.6.3.5 Supercritical Fluid (SCF) Extraction

SCF extraction experiments using EVC and TAEVC2 as the starting materials were carried out with a custom-made, in-house setup. An extraction basket containing several mg of EVC or TAEVC2 powder was incorporated into a pressure vessel. Liquid CO_2 was pumped from a tank into the pressure vessel through a cooling heat exchanger using a flow rate of 30 g/min and temperature of -4°C. Once CO_2 was introduced into the pressure vessel, the starting powders within the extraction basket were subjected to a critical temperature of 50°C and critical pressure of 200 bar for approximately one hour, followed by a gradual depressurisation and powder retrieval.

3.2.6.3.6 Desolvation Screen

For the purpose of desolvating solvated solid forms of OXCBZ, EVC and TAEVC, freshly-prepared samples were placed in a drying oven maintained at 65°C and kept in storage for a period of 1 - 6 days before being analysed with X-ray powder diffraction to check whether a phase transformation had occurred. For a select number of solvated samples, desolvation was pursued through variable temperature X-ray powder diffraction experiments in the temperature range 7 - 147°C.

3.2.7 Sample Characterisation

3.2.7.1 X-ray Powder Diffraction (XRPD)

3.2.7.1.1 Ambient Analysis of Samples Prepared via Physical Vapour Deposition

Polycrystalline samples of OXCBZ, CBZ and CYT obtained from physical vapour deposition experiments were analysed under room temperature conditions using the instrumentation and data collection parameters depicted in Table 3.3. All samples were analysed using diffractometers operating in Bragg-Brentano reflection geometry and a schematic depicting XRPD analysis using a standard Bragg-Brentano setup is shown in Figure 3.9. The incident X-ray beam focuses on point F of the diffraction circle and divergence occurs before any of the X-rays reach the powder specimen (indicated by dark grey) which is laying on a suitable sample holder (indicated by light grey). Once the incident beam contacts the specimen, it diffracts from it and focuses on the diffraction circle once again. The detector moves along the diffraction circle to detect all X-rays diffracted from the sample. The θ value is indicative of the angle of incidence whereas 2θ corresponds to the angle of diffraction of the incident beam path to the detector.

Table 3.3: Overview of diffractometers and data collection parameters utilised for analysis of samples prepared via physical vapour deposition experiments.

Instrument	**Bruker D8 Discover**	**Bruker D2 Phaser**
Operating Geometry	Bragg-Brentano Reflection	Bragg-Brentano Reflection
Operating Voltage & Current	40 kV, 40 mA	30 kV, 10 mA
X-ray Radiation Type	Cu $K\alpha_{1,2}$ (λ = 1.54060 Å)	Cu $K\alpha_{1,2}$ (λ = 1.54060 Å)
Detector	LynxEye 1D (PSD)	LynxEye 1D (PSD)
Size of Anti-Divergence Slit	0.6 mm	0.2 mm
Sample Holder Type	Silicon crystal low background ring	Silicon crystal low background ring
Scan Range	3 – 35° 2θ	3 – 45° 2θ
Step Size	0.01° 2θ	0.01° 2θ
Count Time	1 – 30 s/step	1 – 10 s/step

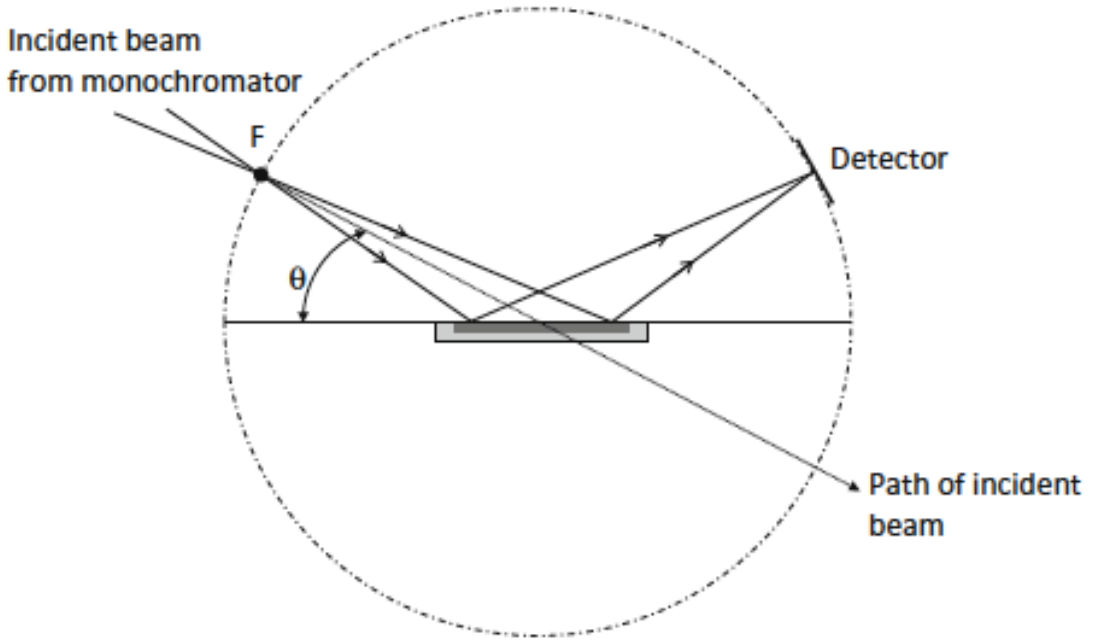

Figure 3.9: Schematic representation of a typical Bragg-Brentano reflection geometry experimental setup for XRPD analysis (reproduced from Shankland, 2016).

3.2.7.1.2 Ambient Analysis of Samples Prepared via Solution-Based Screening Experiments

XRPD analysis of polycrystalline samples prepared through solution-based crystallisation experiments of OXCBZ, CBZ, CYT, EVC, TAEVC1, TAEVC2 and TAEVC3 was carried out at room temperature using the instrumentation and data collection parameters outlined in Table 3.4 after samples had been lightly ground using an agate mortar and pestle set to randomise the orientation of crystallites and minimise preferred orientation effects (Shankland, 2016). Samples were analysed using diffractometers operating in both Bragg-Brentano reflection and Debye-Scherrer transmission geometry. A schematic diagram of a typical Debye-Scherrer transmission setup for analysis of capillary powder specimen is provided in Figure 3.10. High instrumental resolution is obtained upon the incident X-ray beam focusing on the far side of the circle of diffraction. This occurs following the beam's transmission through the capillary specimen in the centre of the circle. The detector component moves along the full circle to detect all the X-rays diffracted from the specimen.

Table 3.4: Overview of diffractometers and data collection parameters utilised for analysis of samples prepared via solution-based screening experiments.

Instrument	Bruker D8 Advance	Bruker D8 Advance II	Bruker D8 Discover	Bruker D2 Phaser
Operating Geometry	Debye-Scherrer transmission (capillary)	Debye-Scherrer transmission (foil)	Bragg-Brentano reflection	Bragg-Brentano reflection
Operating Voltage & Current	40 kV, 50 mA	40 kV, 50 mA	40 kV, 40 mA	30 kV, 10 mA
X-ray Radiation Source	Cu $K\alpha_1$ (λ = 1.54060 Å)	Cu $K\alpha_1$ (λ = 1.54060 Å)	Cu $K\alpha_{1,2}$ (λ = 1.54060 Å)	Cu $K\alpha_{1,2}$ (λ = 1.54060 Å)
Detector	LynxEye 1D (PSD)	Vantec 1D (PSD)	LynxEye 1D (PSD)	LynxEye 1D (PSD)
Size of Anti-Divergence Slit	1 mm	1 mm	0.6 mm	0.2 mm
Sample Holder Type	0.7 mm borosilicate glass capillaries	28 position sample plate supported on Kapton® film (7.5 µm thickness)	Silicon crystal low background ring	Silicon crystal low background ring
Scan Range	3 – 50° 2θ	4 - 35° 2θ	3 - 45° 2θ	3 - 25, 3 - 45° 2θ
Step Size	0.017° 2θ	0.017° 2θ	0.01, 0.017° 2θ	0.01° 2θ
Count Time	1 – 10 s/step	1 – 8 s/step	1 – 10 s/step	0.1 – 10 s/step

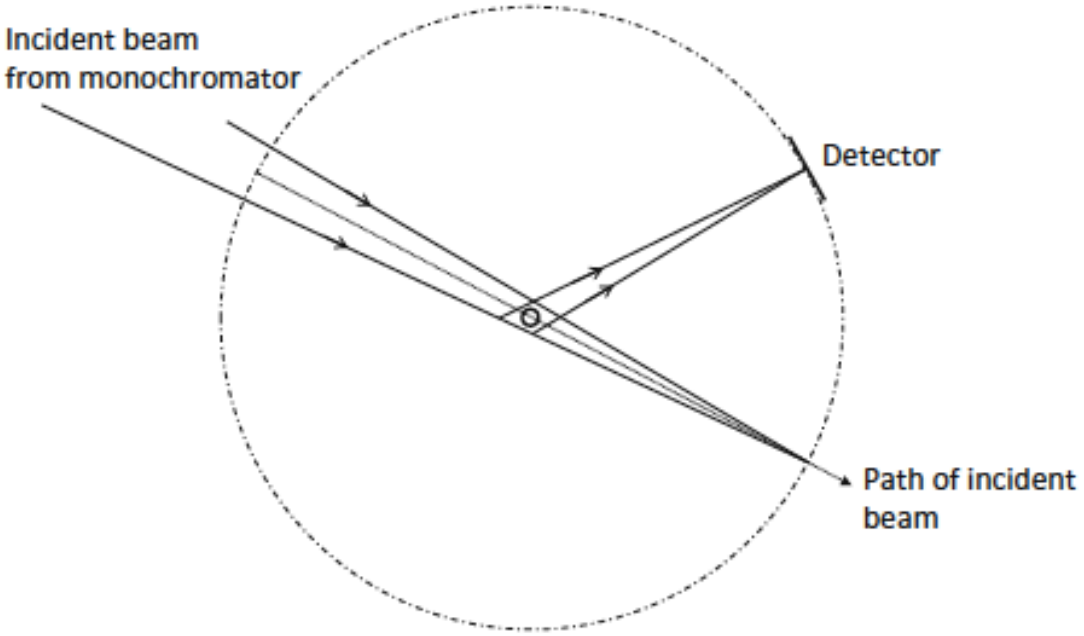

Figure 3.10: Schematic representation of a typical Debye-Scherrer transmission geometry experimental setup for capillary XRPD analysis (reproduced from Shankland, 2016).

3.2.7.1.3 Variable Temperature XRPD (VT-XRPD) Studies

VT-XRPD studies of OXCBZ form III were conducted using the Bruker D8 Discover diffractometer, operating using conditions outlined in Tables 3.3 and 3.4 and additionally equipped with an Anton Paar CHC plus^{+} Cryo and Humidity chamber. Data were collected from 20 to 190°C in increments of 10°C using a scan range of 3 - 40° *2θ,* step size of 0.017° *2θ* and count time of 1 s/step. VT-XRPD data were additionally obtained for the TAEVC2/TAEVC3 starting materials and TAEVC1/TAEVC2 samples obtained from solution crystalliation experiments using the conditions outlined in Table 3.4. Powder samples were finely ground using an agate mortar and pestle and loaded onto 0.7 mm borosilicate glass capillaries (Hilgenberg, Germany) for data collection in the 3 - 50° *2θ* range with a 0.017° 2*θ* step size and 1 s/step count time. An Oxford Cryosystems cryostream was used to regulate the temperature of all capillary specimen. Diffraction data were generally collected in the 7 – 197°C range. All samples subjected to VT-XRPD were held at each of the temperatures investigated for 5 minutes prior to data collection commencing.

3.2.7.1.4 Variable Humidity XRPD (VH-XRPD) Studies

VH-XRPD studies of OXCBZ form III and TAEVC1/TAEVC2 starting materials were conducted using the Bruker D8 Discover diffractometer, operating using conditions outlined in Tables 3.3 and 3.4 and additionally equipped with Anton Paar CHC plus^{+} Cryo and Humidity chamber and modular humidity generator MHG (ProUmid, Germany). Data were collected from 5 to 95% relative humidity (RH) in increments of 5% RH using a scan range of 3 - 40° *2θ,* step size of 0.017° *2θ* and count time of 1 s/step. All measurements were obtained at a temperature of either 20 or 50°C and samples were held at each of the humidity profiles investigated for 15 - 25 minutes prior to data collection commencing.

3.2.7.1.5 Phase Identification of XRPD Samples

3.2.7.1.5.1 Visual Comparison of Experimental XRPD Data with Reference XRPD Data

Reference diffraction patterns, calculated from single-crystal data, for the known polymorphs of OXCBZ, CBZ, CYT and EVC and simulated XRPD patterns for OXCBZ form III candidate structures were obtained using the Cambridge Structural Database's Mercury software (v.4.3.0). The EVA software by Bruker (v.4.1) was utilised to perform a visual comparison between the reference patterns and the measured patterns that were collected for samples prepared from physical vapour deposition studies and polymorph screening experiments conducted in solution for phase identification purposes and to check for the presence of novel solid forms.

3.2.7.1.5.2 Pawley Refinement

Pawley refinement is a potent tool for identifying the purity of crystalline phases present in samples analysed based on the observed diffraction peak positions in the XRPD data. The Pawley refinement approach involves performing a least-squares fit of the profile parameters describing a calculated XRPD pattern to an experimentally observed pattern (Pawley, 1981). The profile parameters that can be included are generally the unit cell parameters, background profile, peak shape profile, the reflection intensities and a zero-point offset.

In instances where the sample under investigation is phase pure (comprising a single crystalline phase), all peaks in the experimental pattern will be accounted for through

the input crystallographic parameters utilised for the refinement. In cases where the difference curve between the experimental and calculated patterns reveals significant misfits and regions where specific peaks cannot be fitted at all using the input crystallographic parameters, there is a strong likelihood of impurity presence in the sample. Alternatively, the presence of major misfits may indicate that the input crystallographic parameters used for the refinement may not be representative of the contents of the sample.

In this work, phase identification of XRPD samples using Pawley refinement was performed by employing both the *TOPAS* software package (v.5; Coelho, 2018) by Bruker and *DASH* (v.3.4.3; David et al., 2006). The background for each refinement in *TOPAS* was modelled using Chebyshev polynomials in the order of 5 – 10.

3.2.7.1.6 Structure Determination from Powder Diffraction (SDPD)

3.2.7.1.6.1 Powder Pattern Indexing

Powder pattern indexing refers to the process of elucidating the size and shape of a unit cell corresponding to a crystalline phase contained in a polycrystalline powder sample by assigning Miller indices to the first ≈ 20 peaks observed in an XRPD pattern (Werner, 2002; Florence, 2009). The assignment of Miler indices to individual peaks in an XRPD pattern is performed using appropriate software such as *DICVOL* (Boultif and Louër, 1991 & 2004) and *TOPAS* which determine the exact position of the observed diffraction peaks using appropriate peak fitting protocols. Once sufficient peaks have been selected, the indexing software will provide a list of suitable unit cell parameters and a corresponding Bravais lattice type for each set of suggested parameters in order to describe the sample of interest. The cell parameters suggested by the indexing software are always ranked based on a figure-of-merit value which is indicative of the similarity of the theoretical unit cell proposed by the software to the experimental unit cell described by the input reflections used to initiate the indexing process.

By performing a visual comparison between the theoretical peaks expected to be present in an experimental pattern and the peaks that are actually observed in said pattern it is possible to confirm whether the cell parameters recommended by the indexing software are truly representative of the crystalline phase present in the measured sample. The observation of experimental peaks that do not match with

theoretical ones derived from the indexing process may indicate that the cell parameters suggested by the indexing software are not representative of the actual sample unit cell or that the sample contains crystalline impurities which manifest in the form of additional reflections in the XRPD pattern.

3.2.7.1.6.2 Space Group Determination

Whilst XRPD pattern indexing enables the unit cell parameters and type of Bravais lattice to be deduced for sufficiently phase-pure samples of interest, the indexing process does not provide information on the space group symmetry of the sample (Shankland, 2016). The space group can only be determined once systematic absences in an XRPD pattern have been identified and a suitable extinction symbol selected. Systematic absences refer to diffraction peaks expected to appear in an XRPD pattern that fail to do so because of the underlying symmetry of the space group corresponding to the sample of interest and the extinction symbol is representative of the translational symmetry operations in a sample's unit cell that are in line with the systematic absences observed. Suitable software such as *ExtSym* (Markvardsen et al., 2008) are employed in order to assess systematic absences in XRPD patterns and facilitate the process of space group determination.

3.2.7.1.6.3 Structure Solution via Global Optimisation and Rietveld Refinement

Details of crystal structure solution via global optimisation have previously been provided in section 1.7.1.3. Once structure solution via global optimisation has been achieved, refinement of the structural model obtained can be pursued. The Rietveld refinement method (Rietveld, 1967 & 1969) is the most commonly employed one and comprises refinement of a solved structural model against experimentally obtained XRPD data. Similarly to Pawley refinement, the Rietveld method involves performing a least-squares fit of a calculated XRPD pattern to an experimentally observed pattern and trying to minimise the differences observed between the two. Unlike Pawley refinement, however, the intensity of diffraction peaks in Rietveld refinement is a function of atomic type and position within the unit cell in the Rietveld method and not a variable that can be freely refined. Apart from peak intensities, the Rietveld method also involves refinement of a residual value, denoted R_p, which relates calculated intensities to experimentally observed intensities. The R_p value can be derived using

Equation 3.4, wherein y_o is the observed intensity and y_c is the calculated intensity at at a given 2θ angle. A decreasing R_p value is indicative of the structure refinement converging so that the best possible fit between the calculated and experimentally observed XRPD data can be obtained.

$$R_{\mathrm{p}} = \frac{\sum[y_{\mathrm{o}}(2\theta) - y_{\mathrm{c}}(2\theta)]}{\sum[y_{\mathrm{o}}(2\theta)]} \quad \textbf{(Equation 3.4)}$$

In addition to the R_p value, the R_{wp} value represents an additional value that is commonly used as a figure-of-merit representative of the quality of a Rietveld refinement and is defined using Equation 3.5, where w is the weight. Similar to the R_p value, a decrease in R_{wp} represents convergence of the structure refinement so that the best possible agreement between the calculated and experimental XRPD data can be reached.

$$R_{\mathrm{wp}} = \sqrt{\frac{\sum w(2\theta)[y_o(2\theta) - y_{\mathrm{c}}(2\theta)]^2}{\sum w(2\theta)[y_{\mathrm{o}}(2\theta)]^2}} \quad \textbf{(Equation 3.5)}$$

The final R_{wp} in the refinement process should approach the statistically expected R value, $R_{exp,}$ which is defined through Equation 3.6 and is indicative of the quality of data used in the refinement. In Equation 3.6, n is the number of observations, p the number of parameters and r the number of restraints imposed on the diffraction data.

$$R_{\mathrm{exp}} = \sqrt{\frac{n-p+r}{\sum w(2\theta)[y_{\mathrm{o}}(2\theta)]^2}} \quad \textbf{(Equation 3.6)}$$

The ratio between R_{wp} and R_{exp} yields a value known as the goodness-of-fit (GoF), described in Equation 3.7 and denoted χ^2. This value needs to approach 1 for the refined structure to be deemed acceptable.

$$\chi^2 = R_{\mathrm{wp}}/R_{\mathrm{exp}} \quad \textbf{(Equation 3.7)}$$

3.2.7.1.6.4 Methodology

For structure determination purposes, capillary XRPD measurements of samples corresponding to OXCBZ form III and the EVC/TAEVC2/TAEVC3 starting materials were obtained at room temperature using Bruker D8 Advance diffractometers operating with the conditions outlined in Table 3.4. Samples of OXCBZ III, EVC and TAEVC2/TAEVC3, all obtained from solution-based screening experiments, were finely ground using a mortar and pestle and then loaded into 0.7 mm borosilicate glass capillaries (Hilgenberg, Germany) which were mounted vertically on the instruments. For OXCBZ samples, data collection occurred in the 3 - 55° *2θ* range with a 0.017° *2θ* step size and 20 s/step count time. In the case of EVC and TAEVC, powder data were collected in the 3 - 50° *2θ* range with a 0.017° *2θ* step size and 1 - 10 s/step count time. For structure determination purposes, the TAEVC3 material was additionally measured at a low temperature of -123°C. The amorphous TAEVC1 starting material was analysed in reflection-geometry using the Bruker D8 Discover diffractometer with the operating conditions described in Table 3.4 and data were collected the 3 - 40° *2θ* range with a 0.017° *2θ* step size and 1 s/step count time.

Powder pattern indexing was carried out using both *DICVOL91/DICVOL04* (Boultif and Louër, 1991 & 2004) as implemented in the *DASH* software (v.3.4.3) and a singular value decomposition algorithm (Coelho, 2003) in *TOPAS*. Pawley fitting of capillary XRPD measurements was performed using *DASH* and *TOPAS*. Space groups were assigned based on an assessment of systematic absences in the XRPD patterns, aided through use of the *ExtSym* software (Markvardsen et al., 2008) as implemented in *DASH*. The crystal structures of OXCBZ III and TAEVC3 were successfully solved by performing simulated annealing in *DASH* and refined further in *TOPAS* using the Rietveld method; both structures were refined against experimentally measured capillary data collected in the 3 – 50° *2θ* range (resolution of 1.82 Å). Input Z-matrix files were used to derive the initial geometry of each molecule and initiate the annealing process which typically comprised 50 runs, each consisting of either 5 x 10^6 or 1 x 10^7 moves and utilising the starting temperature, cooling rate and number of moves at each temperature recommended by Kabova et al. (Kabova et al., 2017a). The Mogul Distribution Bias (MDB) was additionally applied to the torsion angles of OXCBZ and TAEVC prior to annealing in order to reduce the conformational search space and enhance the likelihood of successful structure elucidation (Kabova et al., 2017b).

3.2.7.2 Single-Crystal X-ray Diffraction (SC-XRD)

SC-XRD data of EVC, TAEVC1, TAEVC2 and TAEVC3 samples were obtained using both a Bruker Kappa Apex II Duo diffractometer equipped with an Incoatec IμS microfocussed Mo $K\alpha_1$ X-ray source (λ = 0.71073 Å) and a Bruker D8 Venture equipped with Photon 100 detector and Incoatec IμS microfocussed Cu $K\alpha_1$ X-ray source (λ = 1.54060 Å). Single crystals were mounted on the diffractometers using suitable microloops and the corresponding unit cell parameters were initially determined using fast ω scan runs programmed with the *APEX3* software (v.2016.9-0) by Bruker. Based on the unit cell parameters obtained from the initial ω scans, full collection strategies were calculated and used to obtain single-crystal data at both room and low temperature conditions. An Oxford Cryosystems cryostream was used to control the temperature of the crystals during analysis. Data integration and scaling were both carried out using the *SAINT* software (version 8.34A) as implemented in *APEX3*. Absorption corrections were applied using *SADABS (*v.2014/2, Bruker) as implemented in *APEX3*. Crystal structure solution was carried out using an intrinsic phasing algorithm implemented in the *SHELXT* software (Sheldrick, 2015a) and subsequent Fourier calculations and full matrix least-squares refinements were performed on F^2 with *SHELXL* (Sheldrick, 2015b). All non-hydrogen atoms were refined with anisotropic displacement parameters. Hydrogen atoms were generally placed geometrically and allowed to ride on their parent atoms using isotropic displacement parameters which were appropriate multiples of U_{eq} of the parent atoms. Missing hydrogen atoms were located via inspection of difference Fourier maps and refined isotropically. The SQUEEZE approach implemented within PLATON (Spek, 2015) was used to handle any disordered solvents present in the crystal structures. For Flack parameter determination, the intensity quotients method by Parsons et al. was utilised (Parsons et al., 2013).

3.2.7.3 Differential Scanning Calorimetry/Thermogravimetric Analysis (DSC/TGA)

Simultaneous DSC/TGA analysis of OXCBZ, EVC, TAEVC1/TAEVC2/TAEVC3 samples was performed using a NETZSCH STA 449 F1 Jupiter® thermal analyser (NETZSCH, Germany), calibrated for both temperature and sensitivity over the temperature range -200°C to 675°C, at a heating rate of 20°C/min, using the following set of reference materials supplied by NETZSCH: In, Sn, Bi, Zn, CsCl.

Approximately 2 – 10 mg of each sample were weighed into aluminium pans with pierced lids which were consequently sealed with a presser. An empty aluminium pan was used as a reference standard. Samples were heated from 20 to 300°C using a scan rate of 10°C/min and helium was utilised as the purge gas at a flow rate of 60 mL/min. Measurements were typically conducted in triplicate and data processing was carried out using the *NETZSCH Proteus*® software (v.6.1).

Standalone DSC analysis of OXCBZ powders used in physical vapour deposition studies was performed using a NETZSCH DSC 214 Polyma instrument calibrated for both temperature and sensitivity over the temperature range −93°C to 605°C, at a heating rate of 20°C/min, using thermal standards (In, Sn, Bi and Zn) supplied by NETZSCH. Helium was used as the purge gas at a flow rate of 60 mL/min for all measurements, samples were scanned in triplicate at various heating rates and data were processed with *NETZSCH Proteus*® (v.7.1).

3.2.7.4 Raman Spectroscopy

Raman spectra of OXCBZ, EVC, TAEVC1/TAEVC2/TAEVC3 samples were obtained under ambient conditions using an XploRA™ PLUS Raman microscope by HORIBA Scientific, calibrated with a silicon standard and equipped with a motorised stage, CCD detector, 50x objective lens and either 532 or 785 nm excitation laser source with 1200 grooves/mm grating. All samples were measured on a glass microscope slide and spectra were acquired within the 10 - 4000 cm^{-1} shift region using 2 accumulations, exposure time of 10 - 60 seconds and resolution > 1.4 cm^{-1} FWHM. A variety of slit, hole, and filter settings were utilised in order to minimise fluorescence effects and optimise the quality of the spectra during data collection. The *LabSpec 6 Spectroscopy Suite* (HORIBA Scientific) was employed for performing background subtraction of the obtained spectra where applicable. The XploRA™ PLUS system was additionally utilised to capture optical images of the crystals selected for spectrum collection purposes.

3.2.7.5 Optical Microscopy

Optical microscopy images of OXCBZ, EVC, TAEVC1/TAEVC2/TAEVC3 samples were collected using Leica DM6000 M and M165 CX microscopes (Leica Microsystems) equipped with Leica DFC495 and MC170 HD cameras respectively. The Leica DM6000 M was additionally equipped with a motorised stage. Samples

were imaged under various magnifications and the *Leica LAS* software (v.4.9) was utilised for capturing all images.

3.2.7.6 AFM

AFM studies of vapour deposited OXCBZ samples were conducted using a Dimension FastScan™ AFM instrument by Bruker. Image collection occurred under ambient conditions in PeakForce Tapping® mode using Bruker ScanAsyst Air probes with nominal spring constant k = 0.4 N/m and nominal tip radius of 2 nm. The *NanoScope Analysis* software package (v.1.9, Bruker) was utilised to apply first order flattening to all of the height sensor images that were obtained and measure the diameter of sample features that were of interest.

3.2.7.7 Scanning Electron Microscopy (SEM)

3.2.7.7.1 Data Acquisition

SEM micrographs of experimental substrates and the crystals grown on them via physical vapour deposition under atmospheric conditions were obtained using Keysight 8500B field-emission (Keysight Technologies) and JSM-IT100 InTouchScope™ (JEOL USA, Inc.) SEM instruments. Backscattered electron and secondary electron detectors were both utilised for data collection. OXCBZ, CBZ and CYT samples were adhered to aluminium SEM pin stubs using double-sided conductive carbon tabs and image collection occurred with an acceleration voltage of 0.8 - 20 kV. OXCBZ samples prepared by physical vapour deposition under high-vacuum conditions were analysed using a ZEISS SUPRA® 40 field-emission SEM instrument (ZEISS, Germany) and the acceleration voltage employed for image collection was 2.7 - 5 kV. OXCBZ, CBZ and CYT samples from solution-based experiments and EVC, TAEVC1/TAEVC2/TAEVC3 starting materials were sputter-coated with either 10 or 20 nm of gold using a Leica EM ACE200 coater (Leica Microsystems) and analysed in a manner similar to the vapour-grown crystals.

3.2.7.7.2 Data Processing

The cross-section size, length, angle of twist and pitch of several OXCBZ crystals captured in the SEM micrographs were measured using version 1.51k of the freeware *ImageJ* by the National Institutes of Health (Abràmoff et al., 2004). For pitch measurements, the method described by Fang et al. was used (Fang et al., 2015).

3.2.7.8 Time-of-Flight Secondary Ion Mass Spectrometry (ToF-SIMS)

3.2.7.8.1 Theoretical Background

ToF-SIMS is a mass spectrometry imaging technique that has gained greater traction in recent years with respect to the analysis of pharmaceutical materials (Iuraş et al., 2016; Ottoboni et al., 2018). The technique operates by focusing and rastering a beam of primary ions on the surface of a specimen (Kempson and Prestidge, 2016). Primary ion beams utilised in ToF-SIMS analysis typically comprise a bismuth, gallium or gold source. Upon contact of an ion beam with the surface of the specimen of interest, charged elemental species and molecular fragments (both whole and partial) comprising the sample will be emitted from the upper monolayer of the surface. The species and fragments extracted from the specimen's surface are referred to as secondary ions and will then be accelerated and transported into a mass detector through the use of ion optics. The time of flight of the secondary ion species to the detector from the exact time of their emission is measured and this enables a mass-to-charge ratio for each charged species and a full mass spectrum for the sample of interest to be obtained. Equation 3.8 (Leurs et al., 2016) is used to derive the exact time of flight (*t*) needed for a secondary ion to reach the mass detector, which is dependent on the length (*L*) of the flight tube and the velocity (*v*) that the secondary ion requires to reach the mass detector.

$$t = L/v \qquad \textbf{(Equation 3.8)}$$

The velocity (*v*) that a secondary ion requires to reach the mass detector can be derived using Equation 3.9 (Leurs et al., 2016), wherein q is the charge of the secondary ion, U denotes the electric potential applied to accelerate the secondary ion and m corresponds to the nominal mass of the secondary ion.

$$v = (2\mathrm{qU}/\mathrm{m})^{1/2} \qquad \textbf{(Equation 3.9)}$$

Upon detection of secondary ions, the mass detector is capable of retaining information on their spatial arrangement in the sample surface, allowing for high resolution chemical imaging to be performed. ToF-SIMS analysis can yield images of nanoscale resolution through the use of liquid metal ion gun sources for emitting the

primary ion beam. A schematic workflow of ToF-SIMS analysis is provided in Figure 3.11.

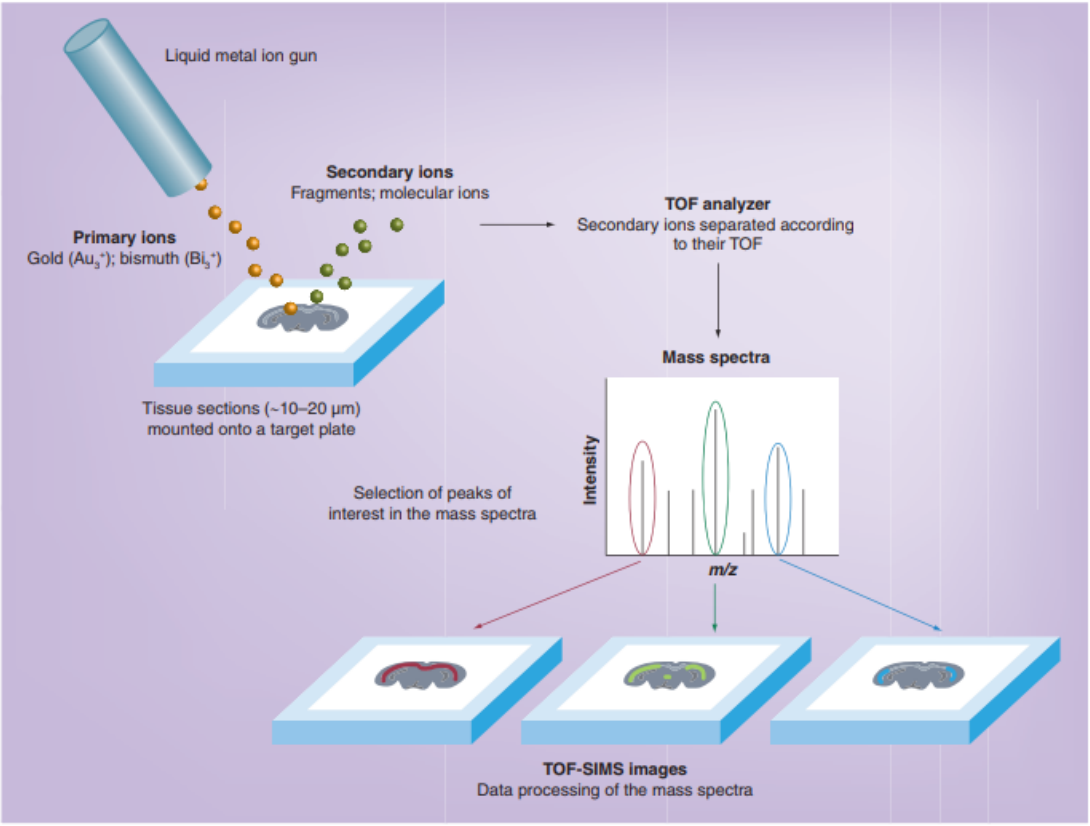

Figure 3.11: Schematic diagram depicting a typical workflow for ToF-SIMS analysis (adapted from Aycıriex et al., 2011). Note that *m/z* corresponds to mass-to-charge ratio and TOF corresponds to time-of-flight.

3.2.7.8.2 Methodology

ToF-SIMS analysis was carried out with a ToF-SIMS V instrument (ION-TOF GmbH, Münster, Germany), equipped with a bismuth liquid metal ion gun and a gridless reflectron time-of-flight mass analyser. Reference spectra were acquired on reference samples of OXCBZ form I powder received from Sigma-Aldrich, samples of OXCBZ powder maintained between 16 and 48 hours at experimental conditions used for physical vapour deposition (refer to section 3.2.4.1) and on each metallic substrate used in the vapour deposition studies. Spectra were collected by employing a pulsed 30 keV Bi_3^+ primary ion beam, in the positive and in the negative secondary ion polarities, in three replicates each, from 100 µm × 100 µm areas in various points of the samples' surface. The total primary ion dose density (PIDD) for each

measurement was approximately 1 × 10^{12} (primary ions/cm^2). The reference spectra were used to select non-overlapping, characteristic mass peaks for each compound. A 60 keV Bi_3^{++} primary ion beam was operated in an un-bunched mode to generate high lateral resolution secondary ion images of selected regions on the samples' surface. The analyser extraction delay was set to 0.055 µs to improve mass-resolving power. The field of view was chosen for each acquisition to fit the feature of interest, such as the twisted crystals. It ranged from 50 µm x 50 µm to 100 µm x 100 µm. The pixel width was between 0.15 and 0.2 µm for all the resulting images. Images were acquired in positive ion polarity, with a final PIDD of approximately 1.0 x 10^{12} primary ions/cm^2. The mass spectral information was recorded in the mass range of 0–900 Da and calibrated as recommended by Green et al. (Green et al., 2006) using $C_2H_5^+$, $C_3H_7^+$, $C_4H_9^+$, $C_{14}H_{12}^+$ and $C_{15}H_{13}N_2O_2^+$ ($[M+H]^+$) ions and including the Ag^+ and $^{109}Ag^+$ ions for the samples prepared on silver foil and on silver-coated glass, the Cu^+ and $^{65}Cu^+$ ions for the samples prepared on copper foil and on copper-coated glass, and the Al^+ ion for the samples prepared on aluminium foil. The obtained calibration deviations were below 100 ppm. The raw images were processed using *SurfaceLab 6.7* software (ION-TOF, Münster, Germany) to generate colour overlay images of selected peaks for OXCBZ and the metallic substrates.

3.2.7.9 High Performance Liquid Chromatography – Mass Spectrometry (HPLC-MS)

3.2.7.9.1 Theoretical Background

HPLC is a separation technique that has emerged over the years as a pivotal part of the pharmaceutical drug development process as it enables the purity of a sample to be identified by separating the pure component from any impurities that may be present within the sample and provide qualitative as well as quantitative information on the chemical composition of the specimen (Hansen, 2016). The technique has been extensively applied to the study of non-volatile samples (Ardrey, 2003) and involves chromatographic separation wherein a material of interest undergoes partition between two immiscible phases, a mobile phase and a stationary phase which move relative to one another. A schematic illustrating a typical HPLC experimental setup is presented in Figure 3.12. The stationary phase in a HPLC experiment usually takes the form of hydrophobic porous silica particles found within a solid column (the chromatographic column) whereas the mobile phase typically

comprises a binary solvent mixture comprising water and a miscible organic solvent (water/acetonitrile and water/methanol are the two most common combinations).

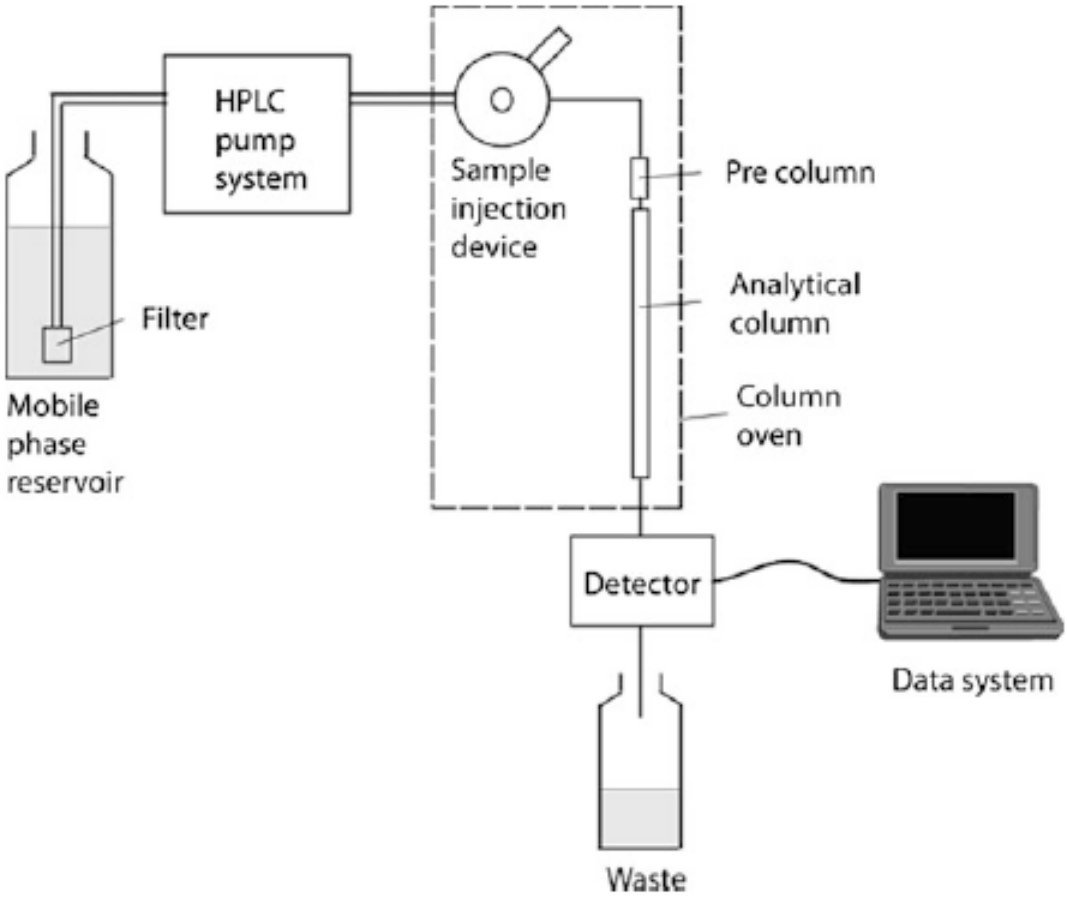

Figure 3.12: Schematic representation of a typical high performance liquid chromatography experimental setup (reproduced from Hansen, 2016).

Upon introducing a sample comprising a mixture of chemical compounds into a HPLC setup, the components of the mixture will be subjected to a variety of bond and/or intermolecular interactions such as hydrogen bonding, covalent bonding, ionic bonding, van der Waals' interactions and dipole-dipole interactions. The nature of interactions that the sample components will undergo in the setup will ultimately depend on their own physicochemical properties as well as the physicochemical properties of the mobile and stationary phases employed and these interactions will result in each component exhibiting a different partition profile from that of the other components.

The migration rates of sample components in HPLC measurements are largely dependent on the experimental conditions affecting the equilibrium distribution of each component between the mobile and the stationary phase, including the

composition of the two phases as well as the temperature of the experimental setup (Snyder et al., 2010). The equilibrium distribution of the sample components is defined using the distribution constant K_C which can be derived using Equation 3.10 (Hansen, 2016) and is dependent on the concentration C_S of each component in the stationary phase and the concentration C_m of each component in the mobile phase.

$$K_C = \frac{C_s}{C_m} \qquad \textbf{(Equation 3.10)}$$

The distribution constant plays a critical role in determining how much of a sample component will be retained by the chromatographic column. Generally, components exhibiting a large distribution constant will be more concentrated in the stationary phase and the column will retain them quite readily. On the contrary, components exhibiting small distribution constant values will be less concentrated in the stationary phase and the column will retain them less readily. The retention volume V_R of a component (Figure 3.13) is indicative of the volume of the mobile phase needed to extract the full amount of the component from the chromatographic column and is described by Equation 3.11 (Hansen, 2016) wherein t_R is the time of retention of the sample component and F corresponds to the flow rate (in mL/min) of the mobile phase. The volume V_M is commonly referred to as the hold-up volume and is indicative of the mobile phase volume found between the site of sample injection and the detector component of the HPLC setup.

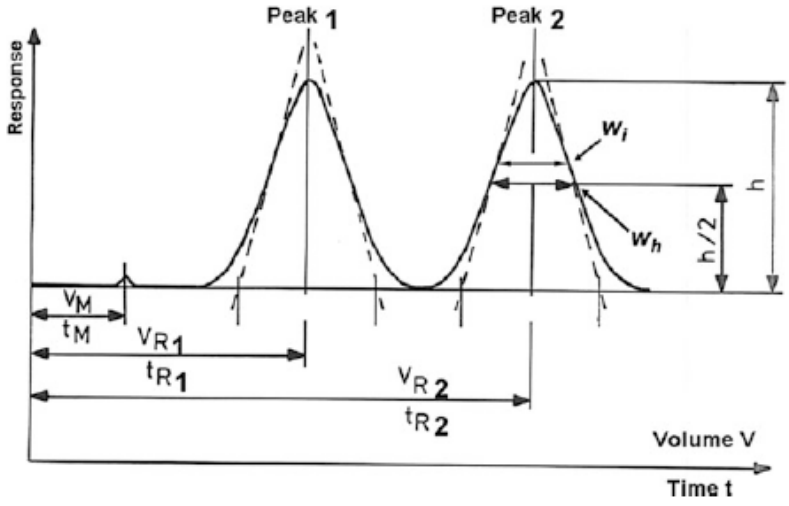

Figure 3.13: Schematic diagram representing a typical chromatogram with retention volumes V_R and retention times t_R depicted for two distinct sample components (adapted from Hansen, 2016).

$$V_R = t_R \, x \, F$$ (**Equation 3.11**)

In recent years, it has become a common occurrence for HPLC to be coupled with mass spectrometry analysis to maximise the amount of information that can be obtained with respect to the purity of a sample and has proven to be particularly useful with respect to identifying and quantifying degradation products arising during stability studies performed as part of the drug development process (Leurs et al., 2016). Water/acetonitrile is the most commonly employed combination of solvents for mobile phase preparation in HPLC-MS and both solvents are maintained at low pH values during measurements in order to facilitate the ionisation of polar sample components through the transfer of protons. In instances where the analysis needs to be conducted under high pH conditions, a volatile buffer is incorporated into the mobile phase. Ammonium acetate is one of the most prevalent buffers used in such cases.

3.2.7.9.2 Methodology

HPLC-MS analysis of OXCBZ samples was performed using a dual source LC-MS Agilent 6130 instrument (Agilent Technologies Inc., USA) with Agilent 1200 series LC component and UV detector set at 254 nm. An Agilent Poroshell 120 LC column (model EC C18, dimensions 4.6 mm x 75 mm, 2.7 µm total particle size) and mobile phase gradient from 95% water/5% acetonitrile (v/v, both containing 5 mM ammonium acetate) to 100% acetonitrile 5 mM ammonium acetate were utilised for chromatographic separation purposes. For preparation of the mobile phase gradient, acetonitrile (HPLC grade) and ammonium acetate (eluent additive for LC-MS, purity ≥ 99%) were sourced from VWR Chemicals and Sigma-Aldrich UK respectively, whereas ultrapure water was obtained from an in-house Direct-Q® UV water purification system (Merck Millipore).

Prior to analysis, a stock solution was prepared for each sample by dissolving an appropriate amount in pure acetonitrile. Working solutions were then prepared by performing 1:20 dilution of the stock solutions in acetonitrile/water (60:40 v/v). The mobile phase flow rate used for separation was 1 mL/min and the temperature of the column was maintained at 40°C. The injection volume employed was 10 µL and the experimental run time for each sample was 18 min. Mass spectra were recorded in MM-ES+APCI ionisation mode with both positive and negative polarity. The *Agilent*

OpenLab CDS ChemStation Edition software (Agilent Technologies Inc., USA) was utilised for data collection and processing. All HPLC-MS measurements were performed in triplicate.

3.2.7.10 Gastrointestinal (GI) Dissolution Studies

3.2.7.10.1 Theoretical Background

Over the last decade, an experimental approach that has gained significant prominence in the study of pharmaceuticals is the GI dissolution method (Gravestock et al., 2011). Upon administration of an API to a patient using a solid oral dosage form such as a tablet or capsule, the API will pass through the GI tract and undergo dissolution before reaching the liver and entering systemic circulation (Figure 3.14). The general purpose of GI dissolution studies is to develop an understanding of how much and how quickly APIs dissolve under experimental conditions that are meant to simulate the physiological conditions in the GI tract, thus ensuring optimal API effectiveness upon administration.

Unlike traditional dissolution testing approaches which utilise hundreds of mg for sample analysis (Mooney et al., 1981), the low volume, *in-vitro* GI dissolution method utilises small amounts of API (5 - 40 mg) to investigate sample dissolution under a dynamic pH environment wherein the pH can be altered to reflect the variations in the pH conditions encountered in the GI tract. A variety of dissolution media can be utilised in this method and experiments can be readily carried out in the presence of excipients so that their effect on the dissolution profile of the API of interest can be investigated under a variety of conditions. GI dissolution additionally enables the effect of a variety of experimental conditions (temperature, stirring rate, type of dissolution medium, presence of excipients, sample surface area, polymorphic form) on the dissolution properties of samples to be probed and the samples are typically compressed into tablets to ensure that their surface area is identical during measurements.

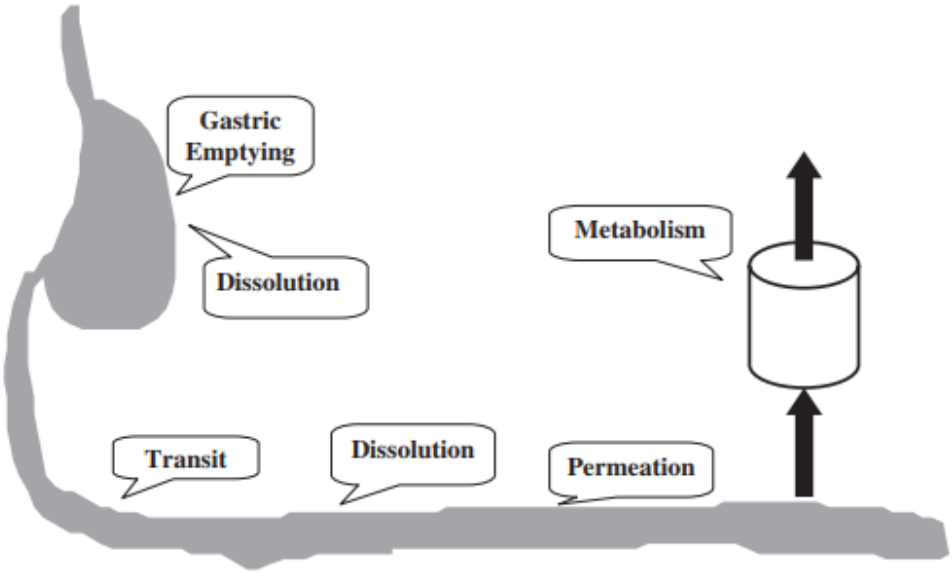

Figure 3.14: Schematic diagram providing a simplified overview of how APIs administered in solid oral dosage forms traverse the gastrointestinal tract and liver to enter systemic circulation (reproduced from Lee et al., 2008).

The experimental dissolution in the GI method is monitored in real time using UV-visible (UV-vis) spectrophotometry. UV-vis spectra reflect the ability of molecular compounds to absorb light as a function of wavelength (Østergaard, 2016). The absorption of UV-vis light can be mathematically derived using the Beer-Lambert law described in Equation 3.12 (Østergaard, 2016) which correlates the amount of monochromatic light absorption with the concentration (in solution) of the sample undergoing light absorption. In Equation 3.12, I_o is intensity of incident light, I the intensity of transmitted light, T the transmittance obtained by (I/I_o), A the sample absorbance, ε the molar absorption coefficient (in L mol^{-1} cm^{-1}), b the length (in cm) of the medium that the light travels through and c is concentration (in mol L^{-1}) of the absorbing sample. Adherence to Beer-Lambert's law is known to serve as the basis for quantitative studies of samples to be pursued using UV-vis spectrophotometry.

$$log_{10}\left(\frac{I_o}{I}\right) = log_{10}\left(\frac{1}{T}\right) = A = \varepsilon bc \qquad \textbf{(Equation 3.12)}$$

In the context of GI dissolution testing involving UV-vis measurements, determination of the molar absorption coefficient (MAC) through UV-metric titrations carried out prior to dissolution facilitates the process of calculating the dissolution profile of a

compound of interest through application of the Beer-Lambert law (Gravestock et al., 2011). During a GI dissolution experiment, UV-vis absorption spectra of the sample are captured at regular intervals through the use of a fibre optic dip probe equipped with a diode array detector. UV-vis spectra provide direct information on how the absorbance of the sample of interest is changing as a function of wavelength. If the MAC of the sample is known, it can then be used to derive the actual concentration of the sample at different absorbance profiles and convert the calculated concentrations into absolute concentrations that can be used to construct a plot depicting the change in concentration of the sample as a function of time. Appropriate software can then be utilised to fit the first order exponential Equation 3.13 (Gravestock et al., 2011) to the data and derive the corresponding dissolution rate profile and extrapolated solubility value. In Equation 3.13, $[X]_t$ corresponds to the weight (in g) of the compound X in solution at experimental time t (in min), S is extrapolated solubility (in g) of the compound, K_d is the dissolution rate constant (in min^{-1}) and t_0 is a term allowing for a temporal offset.

$$[\mathrm{X}]_t = S\left(1 = \ \mathrm{e}^{-k_d(t - t_\mathrm{o})}\right) \qquad \textbf{(Equation 3.13)}$$

3.2.7.10.2 Determination of Molar Absorption Coefficient (MAC)

A starting solution was obtained by dissolving OXCBZ form I sourced from Molekula in DMSO to achieve an initial solution concentration of 50 mM and latterly a 100 mM concentration. A Sirius Inform instrument (Sirius PAT2000i from Sirius Analytical, now Pion Inc., East Sussex) was utilised to obtain the MAC value by performing a p*K*a assay. 25 µL of solution were added to a vial and the Inform p*K*a assay was carried out using the *Inform Control* software as follows: 1) Initially, a blank reading was taken titrating from pH 2 to pH 12 in 40 mL of sodium chloride solution using hydrochloric acid and sodium hydroxide. 2) 33 mL of potassium chloride and 2 mL of acetate phosphate buffer were added in an automated fashion. 3) A total of 3 titrations were performed by the instrument going initially from low pH to high pH, then high pH to low pH and then ultimately low pH to high pH using hydrochloric acid and sodium hydroxide. Data were analysed using the *Inform Refine* software, importing the blank aqueous reading to give a mean MAC value based on the molecular weight of OXCBZ which could be imported into the dissolution data set.

3.2.7.10.3 Gastrointestinal (GI) Dissolution Measurements

Powder samples (17 - 21 mg) of OXCBZ I sourced from Molekula and OXCBZ III prepared from 67:33 v/v ethanol/toluene were compressed into tablets with a diameter of 6 mm to obtain a uniform surface area, using a manual hydraulic tablet press. The duration of compression for each tablet was 5 minutes and a compression weight of 0.5 tonnes was employed. The tablets were added to Inform vials manually in advance of the measurements. Samples were exposed to a pH range from 2 to 7.4 to simulate the effect of GI transit as follows: 1) 36 mL of potassium chloride and 4 mL of acetate phosphate buffer were added in an automated fashion. 2) The pH was adjusted in an automated fashion to pH 2 using hydrochloric acid. 3) The pH was maintained for approximately 20 minutes before gradually increasing to pH 5.5 by addition of sodium hydroxide. 4) The pH was maintained for approximately 20 minutes before gradually increasing to pH 6.5 by addition of sodium hydroxide. 5) The pH was maintained for approximately 20 minutes before gradually increasing to pH 7.4 by addition of sodium hydroxide. All measurements for OXCBZ I and III were carried out in triplicate using a temperature of 25°C and stirring speed of 100 rpm. Data analysis was performed using *Inform Refine*, importing the blank aqueous reading and the mean MAC value based on the molecular weight of OXCBZ. All results were plotted and compared using *Microsoft Excel*.

3.2.7.11 Dynamic Vapour Sorption (DVS)

DVS analysis of EVC and TAEVC1/TAEVC2/TAEVC3 samples was performed with a DVS Advantage instrument by Surface Measurement Systems using deionised water as the solvent of choice. Powder samples weighing 1 - 45 mg were placed in a steel pan and 2 cycles of sorption-desorption were carried out at 25°C in steps of 5% RH. An overall experimental range of 0 - 95% RH was investigated and a dm/dt criterion of 0.001% in 15 minutes was used as the equilibrium parameter for each RH step.

Chapter 4: Solid-State Screening Studies of Oxcarbazepine and Characterisation of Form III

4.1 Introduction

Crystals structure underpins the physical, chemical and mechanical properties of materials used in pharmaceutical manufacture. Hence, selecting the most suitable crystal form (polymorph, solvate, salt, co-crystal) is an important step during preclinical development. Solid-form screening therefore plays a pivotal role in modern pharmaceutical development as it aims to allow different solid forms of an API to be identified and characterised efficiently in the early stages of the drug development process and avoid unwanted surprises in later stages. Screening and solid-form selection is critical to informing the most suitable solid form in terms of physicochemical properties to be selected for production and use in clinical studies, formulation design and eventually commercial application (Aaltonen et al., 2009; Yamano, 2011; Thakuria and Thakur, 2017).

Screening approaches typically comprise solution-based crystallisation experiments for sample preparation and various methodologies have been employed over the years in both academic and industrial settings (Morissette et al., 2004; Newman, 2013). The goal of these approaches is to assess the effect of different crystallisation conditions on the thermodynamic and kinetic outcomes of crystallisation and identify all relevant solid forms that are possible for a given pharmaceutical compound. The interplay between thermodynamic (e.g. solubility, temperature, pressure) and kinetic (e.g. rate of cooling, stirring) conditions needs to be explored thoroughly in terms of establishing a comprehensive solid-form landscape for a pharmaceutical and the relationships between form and crystallisation conditions. Screening experiments conducted under slow timescales, wherein solid-form formation is often driven by thermodynamics, are expected to yield thermodynamically stable forms. More aggressive kinetic conditions such as rapid cooling can promote the nucleation of metastable forms (Anderton, 2007; Aaltonen et al., 2009).

Crystallisation methods such as solution evaporation, cooling and anti-solvent addition have been amongst the most common approaches utilised to perform solid-form screening (Guillory, 1999; Morissette et al., 2004; Anderton, 2007; Aaltonen et al., 2009; Newman, 2013). Whilst solution-based methods typically dominate the polymorph screening landscape in both academia and industry, solvent-free approaches such as physical vapour deposition and crystallisation from the melt have gained greater traction in recent years as a potent tool for the successful isolation of anhydrous polymorphs for a variety of systems of pharmaceutical relevance (Arlin et

al., 2011; Karpinska et al., 2011; Karpinska et al., 2013; Kamali et al., 2016; Srirambhatla et al., 2016; Zhang et al., 2016; Case et al., 2018; Kamali et al., 2018).

As discussed in section 1.6, the crystallisation process typically commences through the occurrence of heterogeneous nucleation on a surface (Artusio and Pisano, 2018) and over the years different types of surfaces such as emulsion droplets, polymers, electrochemically tunable metals, single-crystal ensembles, glass capillaries and surface-induced metal-organic frameworks have successfully been employed to control nucleation and polymorphism in crystallisation processes (Ueno et al., 2003; López-Mejías et al., 2011; Kwokal et al., 2014; Srirambhatla et al., 2016; Yang et al., 2017; Bolla and Myerson, 2018a).

This chapter describes polymorph screening investigations, using both solvent-based and solvent-free methods, of the pharmaceutical OXCBZ. A motivation for the study was to explore, in addition to previously reported studies from the literature, whether the incorporation of metallic surfaces as templates may result in the selective crystallisation of specific solid-state forms of OXCBZ. A key target was to obtain samples of form III to enable structural characterisation and identify any novel forms produced under the conditions tested. A range of characterisation techniques including X-ray powder diffraction (XRPD), Raman spectroscopy, simultaneous differential scanning calorimetry/thermogravimetric analysis (DSC/TGA), optical microscopy, scanning electron microscopy (SEM) and gastrointestinal (GI) dissolution are utilised to obtain insight into the solid-state properties of the samples obtained.

4.2 Oxcarbazepine (OXCBZ)

OXCBZ (IUPAC name: 10,11-dihydro-10-oxo-5H-dibenz(b,f)azepine-5-carboxamide), marketed by Novartis Pharmaceuticals under the brand name Trileptal®, is a commercially available anticonvulsant drug, primarily employed for the treatment of partial epileptic seizures and generalised tonic-clonic seizures. It is a carbonylated analogue of the fellow, and widely studied, anticonvulsant agent carbamazepine (CBZ) (Walker and Patsalos, 1995; Rabasseda, 2001; Hempel et al., 2005; Geng and Wang, 2017). OXCBZ's molecular structure is presented in Figure 4.1.

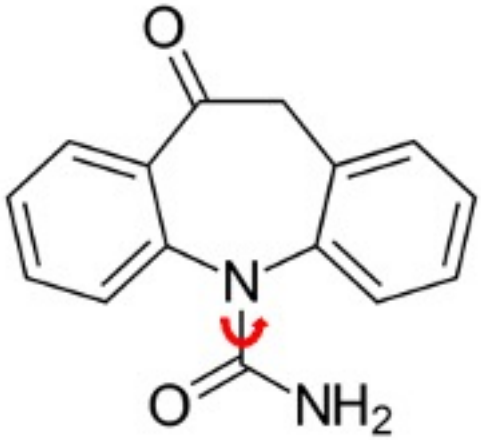

Figure 4.1: Molecular structure of OXCBZ ($C_{15}H_{12}N_2O_2$; molecular weight: 252.268 g/mol). The red arrow indicates the presence of a flexible torsion angle.

OXCBZ is a compound falling within Class II of the Biopharmaceutics Classification System (BCS), exhibiting poor solubility in water (8.4 mg/100 mL at 25°C) and high intestinal permeability (Amidon et al., 1995; Chadha et al., 2012b). Experimental work carried out by Lutker and Matzger (Lutker and Matzger, 2010) established that OXCBZ can crystallise in at least three anhydrous polymorphic forms out of which two were fully characterised, including crystal structure determination with single-crystal X-ray diffraction (SC-XRD). The thermodynamically stable, at ambient conditions, form I can be prepared by slow evaporation of OXCBZ from methanol solutions and crystallises in the monoclinic space group $P2_1/c$ with cell parameters a = 5.20194 (16) Å, b = 9.2638 (3) Å, c = 24.7989 (7) Å, β = 95.234° (2) and cell volume = 1190.07 Å^3 (SC-XRD data measured at -178°C, CSD Refcode: CANDUR01). OXCBZ form I is isostructural to form I of DHC (Cruz-Cabeza et al., 2007a). The metastable form II (Figure 4.2b) can be prepared through slow or rapid cooling of OXCBZ solutions in toluene and crystallises in the monoclinic group $P2_1$ with cell parameters a = 5.1606 (2) Å, b = 9.4057 (4) Å, c = 12.5984 (5) Å, β = 92.720° (3) and cell volume = 610.825 Å^3 (SC-XRD data measured at -178°C, CSD Refcode: CANDUR02). OXCBZ II is known to convert to OXCBZ I upon heating in the temperature range between 118 and 150°C (Lutker and Matzger, 2010). The crystal packing arrangements in form I and form II (Figure 4.2a and 4.2b) are stabilised by a hydrogen bond-based $C_1^1(4)$ catemeric packing motif involving intermolecular (O · · · N) hydrogen-bonding interactions between the carbonyl component of the carboxamide group on one OXCBZ molecule and the NH_2 component of the amide group on a second OXCBZ

molecule. The length of the hydrogen bond (O · · · N) is 2.771 Å for form I and 2.749 Å for form II. OXCBZ adopts similar molecular conformation in both forms (Figure 4.2c) with a root mean square deviation (RMSD) value of 0.0423 Å and packing analysis performed using *Mercury* yields a match of 11 molecules in a 15 molecule cluster and RMS value of 0.133 Å (Figure 4.2d).

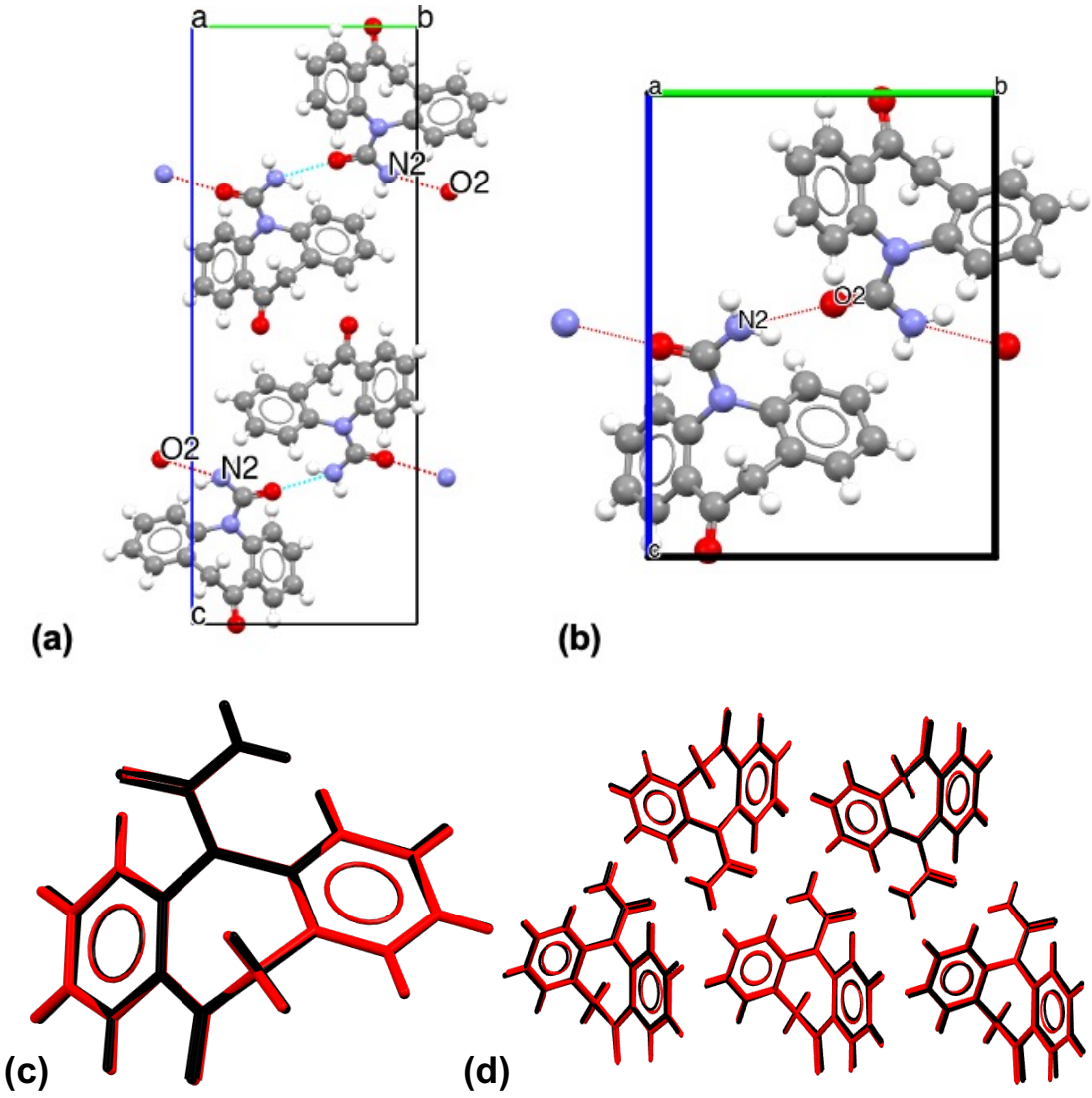

Figure 4.2: Unit cell packing arrangement in OXCBZ form I (a) and OXCBZ form II (b), viewed along the crystallographic *a* axis. Dashed red and cyan lines indicate the presence of intermolecular hydrogen-bonding interactions. An overlay highlighting the similar molecular conformation of the two forms is presented in (c) with the red structure corresponding to OXCBZ I and black structure representing OXCBZ II. An overlay of multiple molecular clusters of the two forms is presented in (d).

Form III of OXCBZ was originally obtained using a polymer-induced heteronucleation (PIHn) approach involving slow evaporation, at room temperature, from methanol solutions containing ethylene/vinyl acetate copolymer or high-density polyethylene substrates (Lutker and Matzger, 2010). Whilst the existence of this polymorph was verified using a number of characterisation techniques (XRPD data are presented in Figure 4.3), crystal structure determination was not possible due to the small size and poor quality of the crystals that were prepared.

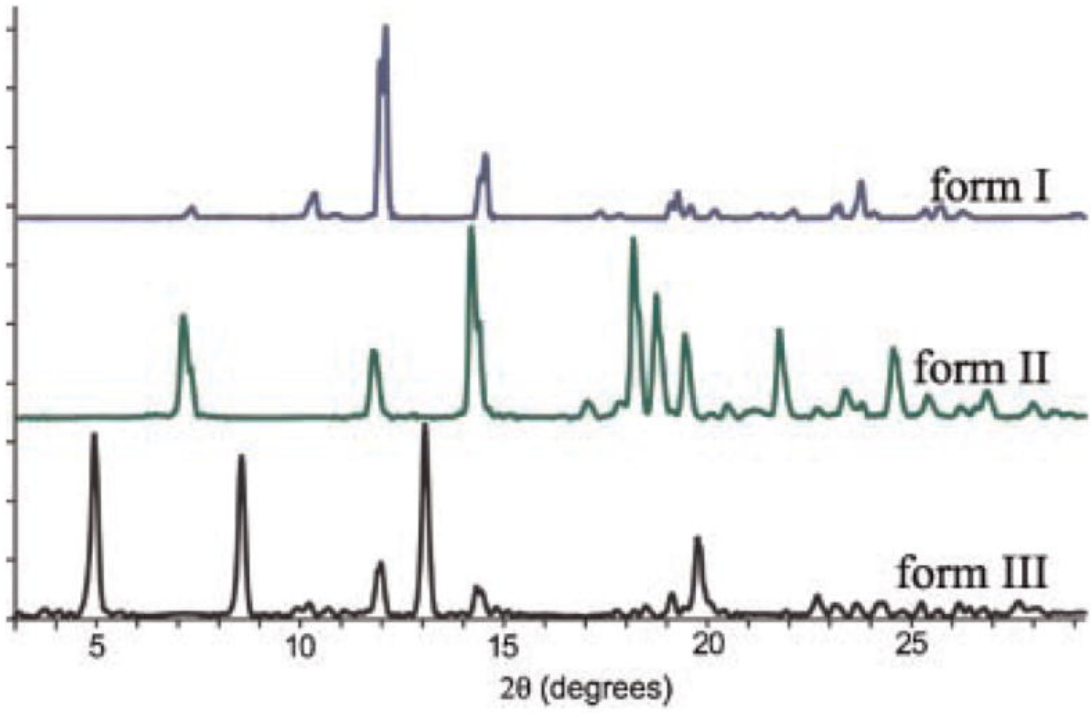

Figure 4.3: Experimental XRPD patterns of anhydrous OXCBZ polymorphs (reproduced from Lutker and Matzger, 2010).

In addition to crystallising in three non-solvated polymorphic forms, OXCBZ is reported to form a solvated structure with acetic acid and cocrystals with succinic acid/chloroform (solvated cocrystal system), saccharin, oxalic acid, 2,5-dihydroxybenzoic acid and salicylic acid (Chadha et al., 2012b; Li et al., 2019). Additional crystalline forms of OXCBZ have been claimed in the patent literature (Venkataraman et al., 2005; Aronhime et al., 2007), including an anhydrous form (termed ‘F’) and a solvated structure with chloroform. However, no crystal structures have been determined to verify any of these forms.

Extensive polymorph screening results for OXCBZ, covering a broad range of crystallisation methodologies and solvent systems, have not been reported in the literature. The lack of extensive screening data, coupled with the absence of a reported OXCBZ III structure, provided the motivation for this work to obtain and fully characterise form III and additional solid forms of OXCBZ which had not been isolated and/or been fully characterised before.

A crystal structure prediction (CSP) study of the OXCBZ crystal energy landscape was carried out to determine thermodynamically feasible crystal structures of OXCBZ. Given the published powder pattern for OXCBZ III (Lutker and Matzger, 2010; Figure 4.3) this may also provide a basis to assign or solve the crystal structure of form III and other anhydrous forms that have not been experimentally realised to date (Arlin et al., 2011; Srirambhatla et al., 2016; Case et al., 2018; Askin et al., 2019). Comparison of the experimental findings from a systematic experimental search with the calculated CSP landscape may also serve to validate the predictions or identify new structures that fall outwith the scope of the CSP (e.g. solvates, disordered structures).

The CSP landscape comprises two conformations of the OXCBZ molecule (Figure 4.4a) which are defined based on whether the NH_2 component of the amide group is on the same side (*syn*) or different sides *(anti*) of the kink on the azepine ring. Structurally characterised forms I and II of OXCBZ are circled in blue on the landscape (Figure 4.4b) and both exhibit the *anti* conformation. Predicted candidates for the experimental structure of form III are indicated by the dotted red circles and all of them are defined by the *anti* conformation as well. The CSP study that yielded the landscape accounted for the 60 most commonly occurring space groups and only considered crystal structures with $Z' = 1$.

The use of templates in exploring OXCBZ crystallisation has already been discussed, however the potential role of metallic substrates during solution-based and solvent-free crystallisations of OXCBZ is also of interest. A summary of conditions included in experimental search for crystal forms of OXCBZ is summarised in Table 4.1.

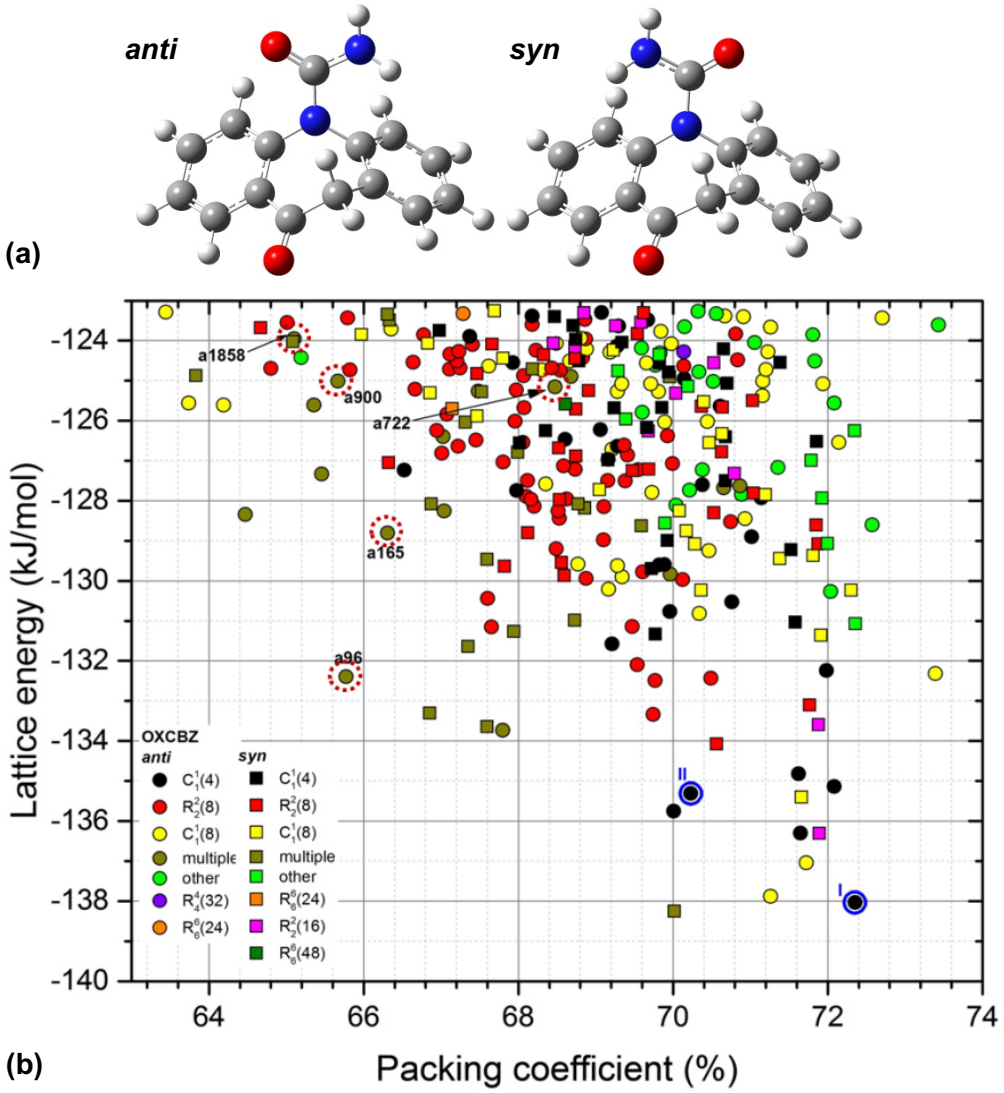

Figure 4.4: *Anti* and *syn* conformations in the molecular structure of OXCBZ (a), optimised in the gas phase by Gaussian09 software at PBE0/6-31G(d,p) level and (b) lattice energy landscape of OXCBZ, combining two separate CSP searches in the *anti* (circle) and *syn* (square) conformation regions.

Table 4.1: Overview of screening approaches utilised experimentally for obtaining various solid forms of OXCBZ.

Screening Approaches
Fast evaporation involving pure solvents
Fast evaporation involving pure solvents and the presence of a metallic substrate in solution
Fast evaporation involving binary solvent mixtures
Fast evaporation involving binary solvent mixtures and the presence of a metallic substrate in solution
Physical vapour deposition onto metallic substrates under atmospheric conditions
Physical vapour deposition onto metallic substrates under high-vacuum conditions

4.3 Materials and Methods

4.3.1 Materials

OXCBZ form I powders were used as starting materials for the preparation of samples investigated in the studies described herein. Details of the starting powders are provided in section 3.1. Details of substrates and solvents used are also provided in section 3.1.

4.3.2 Methods

Known polymorphs of OXCBZ and predicted candidates for the structure of OXCBZ form III were visualised and analysed using the methodology outlined in sections 3.2.1 and 3.2.2. The substrates utilised experimentally were characterised using the methods described in section 3.2.3. Preparation of vapour-grown OXCBZ samples was carried out using the physical vapour deposition protocols described in section 3.2.4. Solution-based screening experiments for OXCBZ were performed using the Crissy® platform (section 3.2.6.2). Vapour-grown and solution-grown crystalline samples of OXCBZ were characterised using XRPD methods (section 3.2.7.1), simultaneous DSC/TGA (section 3.2.7.3), Raman spectroscopy (section 3.2.7.4), optical microscopy (3.2.7.5) and SEM (3.2.7.7.1). The crystal structure of OXCBZ form III was determined using the methodology outlined in section 3.2.7.1.6.4. GI dissolution studies of form I and form III were performed with the methodology described in section 3.2.7.10.

4.4 Results and Discussion

4.4.1 Characterisation of Experimental Substrates

4.4.1.1 Nanoscale Roughness

Surface roughness is a property that can affect the nucleation rate of materials on different types of substrates, with rough surfaces favouring nucleation more significantly than smooth surfaces (Asanithi, 2014; Fu et al., 2015). AFM analysis is commonly utilised to measure the topography of surfaces and determine the roughness of materials at the nanoscale (De Chiffre et al., 1999; Jiang et al., 2016). AFM data were collected from all the materials used as prospective templates in this work (Figures 4.5 and 4.6). Experimental R_a values acquired for the substrates of interest are summarised in Table 4.2. The peak force error images that were obtained

(Figure 4.5) indicated that the copper-coated and silver-coated glass substrates had smooth surface structures with corresponding R_a values of 2.46 nm (± 2.02) and 6.5 nm (± 3.15). The silver-coated glass substrate was found to comprise some spherical features smaller than 6 µm in size which can be attributed to residual dirt. The aluminium, copper, and silver foil substrates exhibited significantly rougher surfaces with R_a values ranging from 19.4 nm (± 4.76) for copper to 135.7 nm (± 80.86) for aluminium. The high standard deviation values derived for the aluminium and silver foil substrates are indicative of the variability in the roughness of their surfaces across the areas that were scanned. Groove-like features were observed for both copper foil and silver foil, whilst the surface of aluminium foil was highly irregular and uneven.

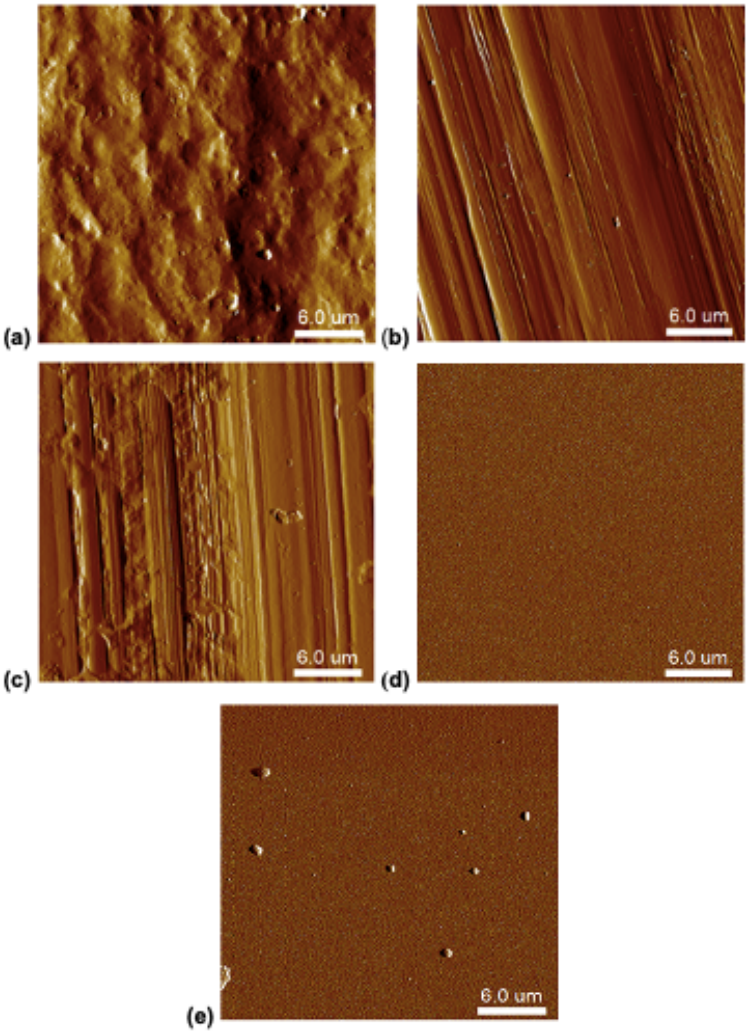

Figure 4.5: Representative peak force error AFM images of a) aluminium foil, R_a = 227 nm b) copper foil, R_a = 99 nm c) silver foil, R_a = 179 nm d) copper-coated glass, R_a = 1.04 nm e) silver-coated glass, R_a = 2.38 nm. The scan size for all images was 30 µm x 30 µm and the corresponding scale bars correspond to 6 µm.

Table 4.2: Overview of Ra values obtained for the experimental substrates. Standard deviation values are provided in parentheses (n = 3).

Substrate	R_a (nm)
Aluminium foil	135.7 (± 80.86)
Copper foil	19.4 (± 4.76)
Silver foil	128.7 (± 43.66)
Copper-coated glass	2.46 (± 2.02)
Silver-coated glass	6.5 (± 3.15)

The height sensor images presented in Figure 4.6 illustrate the height of protrusion of the surface features observed for each type of substrate. The foil substrates were all found to exhibit significantly higher heights of protrusion for their surface features compared to the coated glass substrates.

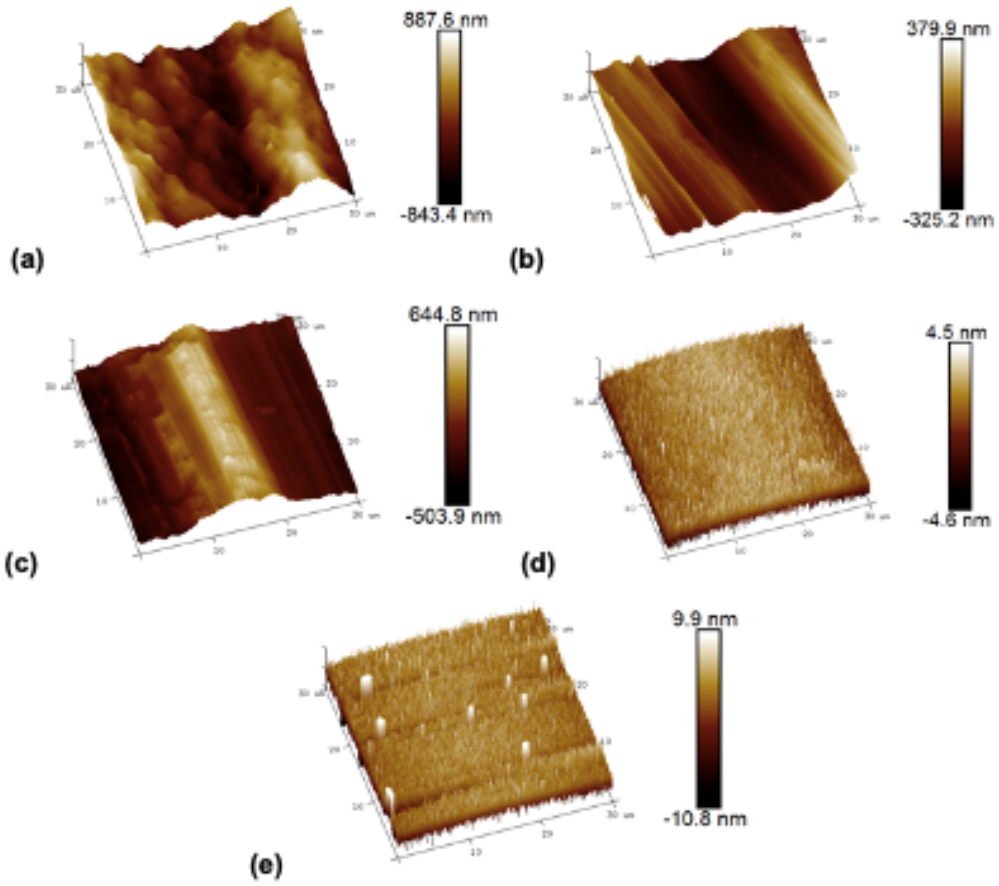

Figure 4.6: Representative height sensor AFM images of a) aluminium foil b) copper foil c) silver foil d) copper-coated glass e) silver-coated glass. The scan size for all images was 30 µm x 30 µm.

4.4.1.2 Wettability and Surface Free Energy Determination

Wettability and surface free energy can impact several properties of materials, including their molecular ordering, nucleation rate, crystallinity and morphology (Lee et al., 2012; Xiao et al., 2016; Zhang et al., 2018b). Contact angle goniometry can assist in assessing the wettability of materials and determining their corresponding surface free energies (Cwikel et al., 2010; Shaker and Salahinejad, 2018). Contact angle measurements and corresponding surface free energy values for each of the substrates were obtained as described in section 3.2.3.2 and results are shown in Table 4.3.

Table 4.3: Overview of contact angle measurements and corresponding surface free energy values for each of the substrates employed experimentally. Standard deviation values are provided in parentheses (n = 10).

Substrate	Average Contact Angle with Water (°)	Average Contact Angle with Diidomethane (°)	Average Contact Angle with Ethylene Glycol (°)	Surface Free Energy (mJ/m^2)
Aluminium foil	62.04 (± 2.11)	65.60 (± 3.31)	70.33 (± 4.50)	33.14
Copper foil	98.82 (± 2.26)	54.42 (± 3.88)	60.60 (± 3.50)	31.97
Silver foil	105.08 (± 2.70)	42.83 (± 1.59)	53.62 (± 2.72)	40.94
Copper-coated glass	98.55 (± 2.40)	43.83 (± 3.24)	70.68 (± 0.59)	25.85
Silver-coated glass	92.61 (± 3.24)	49.29 (± 1.25)	77.56 (± 2.59)	38.42

The contact angle measurements obtained using water as the probing liquid of choice indicate that 4 out of the 5 substrates assessed are hydrophobic. More specifically, copper foil, silver foil, copper-coated glass and silver-coated glass substrates were all found to have average contact angles greater than 90°. Hydrophobic copper and silver substrates have previously been reported in the literature (Valette, 1982). Aluminium foil was the only substrate found to exhibit hydrophilicity with an average contact angle of 62.04°, an observation in line with previous reporting (Yue et al., 2017). Average contact angles with diiodomethane and ethylene glycol assisted in determining the surface free energy of each substrate. The calculated surface free

energy values obtained for the substrates ranged from 31.97 to 40.94 mJ/m^2, with copper coated-glass being the only substrate exhibiting a lower value at 25.85 mJ/m^2.

4.4.2 Evaluation of Predicted Candidates for the Crystal Structure of OXCBZ Form III

In the lattice energy landscape of OXCBZ (Figure 4.4), five CSP structures, a96, a65, a722, a900 and a1858 were found to produce XRPD patterns similar to the one reported by Lutker and Matzger for OXCBZ III (Figures 4.3 & 4.9). All 5 structures contain void channels in their respective unit cells (Figure 4.7). Calculated BFDH morphologies for the structures show needle-like morphologies with a hexagonal cross section (Figure 4.8). As expected from the similar unit cell parameters and space groups (Table 4.4) these predicted structures share considerable similarities in the molecular packing (Table 4.5). All of them are additionally based on the $R_2^2(8)$ dimer-based hydrogen bonding motif that is prevalent in the polymorphic forms comprising the CBZ family of compounds (Grzesiak et al., 2003; Arlin et al., 2011).

Predicted structure a96 is 5.6 kJ/mol higher in the lattice energy landscape than the thermodynamically stable form I at PBE0/6-31G(d,p) level. This is the only candidate exhibiting a lattice energy difference (< 6 kJ/mol) that is characteristic of ≈ 90% of pairs of polymorphs (Burger and Ramberger, 1979b; Cruz-Cabeza et al., 2015), followed by structure a165 which is found 9.2 kJ/mol higher than OXCBZ I. Predicted structures a722, a900 and a1858 are all found considerably higher in the CSP landscape with corresponding lattice energy differences of 12.9, 13.0 and 14.1 kJ/mol relative to OXCBZ I. The void channels present in a165, a722 and a900 are sizeable enough to accommodate solvent molecules as guests, similar to the well described channels in CBZ form II, in which inclusion of chloroform, tetrahydrofuran (THF), toluene and *n*-tridecane has been reported (Cruz-Cabeza et al., 2007b; Fabbiani et al., 2007), and the isostructural cytenamide (CYT) form I for which solvent inclusion has also been observed (Florence et al., 2008a).

Among the five OXCBZ III CSP candidates, three structures (a96, a165 and a900) crystallise in the trigonal *R*-3 space group, similar to CBZ II (CSD Refcode: CBMZPN03) and CYT I (CSD Refcode: SOGLEG). Structure a1858 is also trigonal and can be found in the *P*-3 group with a unit cell equal to one third of those of the three *R*-3 structures, while a722 is hexagonal and crystallises in the $P6_1$ group. By comparing the candidate structures using a 30-molecule cluster generated with a 20% distance tolerance and 20° angle tolerance, a good structural match (>18 molecules

in common) can be achieved among a96, a900 and a1858, or between a165 and a1858, as shown in Table 4.5. Whilst structures a96/a1858 and a165/a1858 were found to have the highest number of molecules in common, structures a96 and a900 exhibited the lowest RMS value, indicative of highest packing similarity, as well as the highest XRPD similarity.

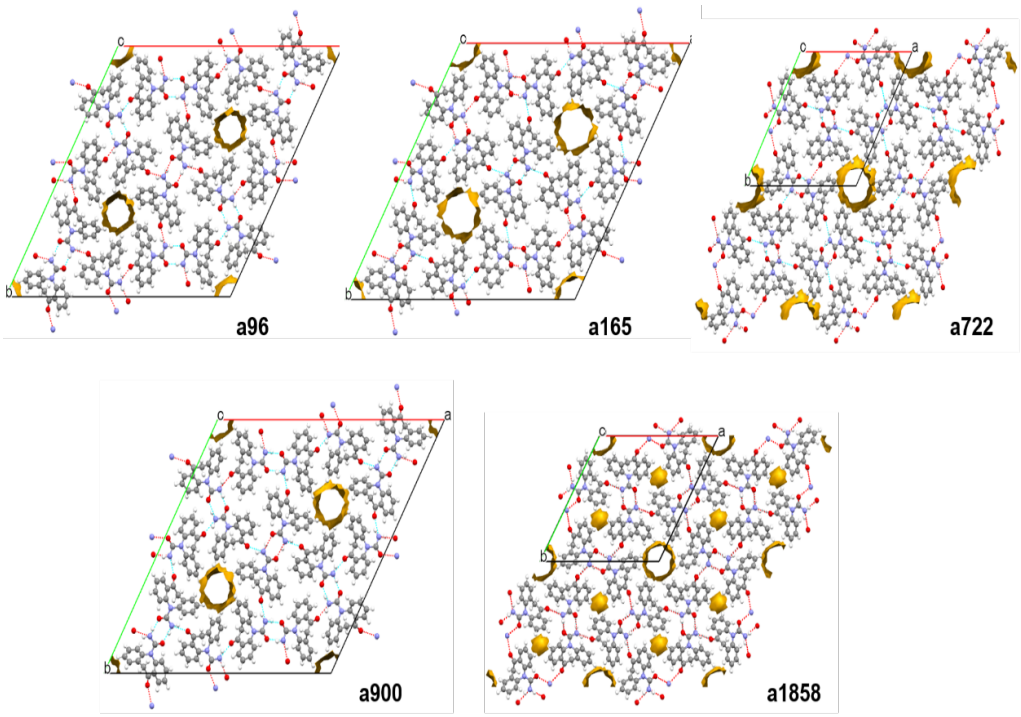

Figure 4.7: Unit cell packing arrangement and void channel presence in the form III candidates derived from the CSP landscape of OXCBZ. All structures are viewed down the crystallographic *c* axis and void channels are indicated by the contact yellow surfaces.

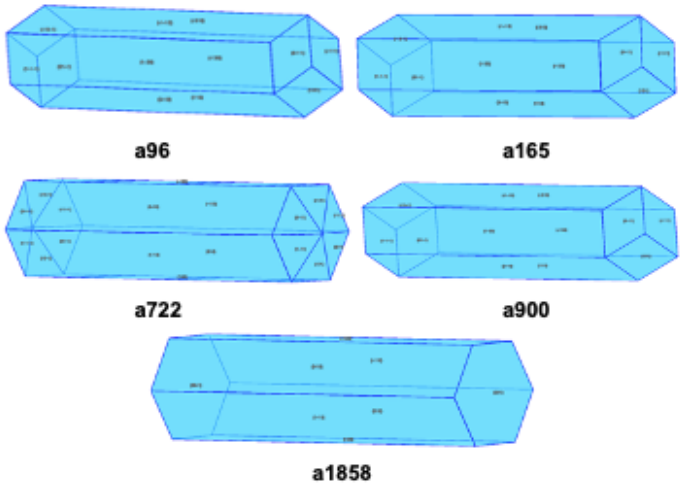

Figure 4.8: Calculated BFDH morphologies for the CSP-generated OXCBZ III candidate structures.

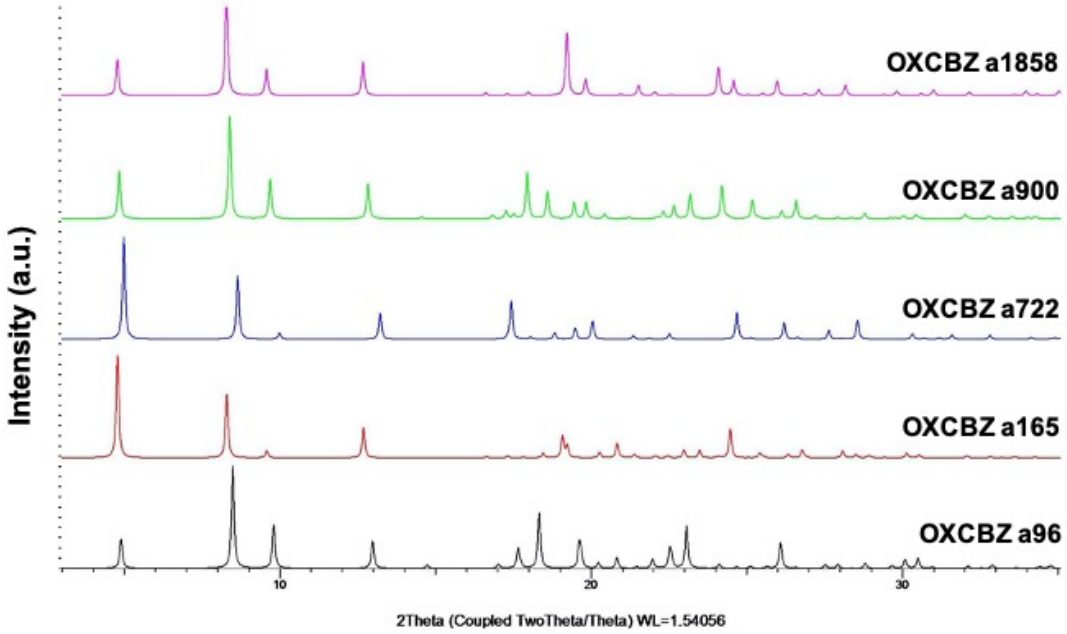

Figure 4.9: Simulated XRPD patterns of the form III candidate structures identified in the CSP landscape of OXCBZ. A wavelength of 1.54060 Å and step size of 0.017° *2θ* was used to calculate the patterns in *Mercury*.

Table 4.4: Crystallographic data of predicted OXCBZ III candidate structures.

CSP Structure	Space Group	*Z*	*a, b* (Å)	*c* (Å)	α, β (°)	γ (°)	Cell Volume (Å^3)	Void Volume (Å^3)	Void Volume (% of Unit Cell)
OXCBZ a96	*R*-3	18	36.0565	5.3017	90	120	5969.16	226.82	3.8
OXCBZ a165	*R*-3	18	36.8890	5.0353	90	120	5934.03	387.64	6.5
OXCBZ a722	$P6_1$	6	20.4388	5.3061	90	120	1919.63	146.10	7.6
OXCBZ a900	*R*-3	18	36.4698	5.1989	90	120	5988.37	268.08	4.5
OXCBZ a1858	*P*-3	6	21.3178	5.1156	90	120	2013.32	138.27	6.9

Table 4.5: Overview of results from a packing similarity study of the OXCBZ III candidates conducted using *Mercury*. A comparison of the OXCBZ III candidates with CBZ form II and CYT form I is additionally provided.

Reference Structure	Comparison Structure	Molecules in Common	RMS	XRPD Similarity
a722	**a1858**	11/30	1.846	0.919
a96	**a165**	12/30	1.321	0.937
a722	**a900**	16/30	1.086	0.931
a165	**a722**	17/30	0.982	0.925
a96	**a1858**	21/30	0.96	0.925
a96	**a722**	7/30	0.937	0.917
a165	**a900**	14/30	0.748	0.952
a165	**a1858**	21/30	0.652	0.968
a900	**a1858**	20/30	0.422	0.947
a96	**a900**	19/30	0.198	0.969
a1858	**CBZ II (CBMZPN03)**	16/30	0.577	0.917
a165	**CBZ II (CBMZPN03)**	19/30	0.659	0.950
a722	**CBZ II (CBMZPN03)**	16/30	0.896	0.955
a900	**CBZ II (CBMZPN03)**	13/30	0.783	0.934
a96	**CBZ II (CBMZPN03)**	11/30	1.161	0.916
a1858	**CYT I (SOGLEG)**	14/30	0.776	0.830
a165	**CYT I (SOGLEG)**	7/30	0.957	0.879
a722	**CYT I (SOGLEG)**	16/30	1.092	0.930
a900	**CYT I (SOGLEG)**	10/30	1.016	0.869
a96	**CYT I (SOGLEG)**	7/30	0.741	0.873

4.4.3 Solution-Based Screening Studies of OXCBZ

4.4.3.1 Solvent Selection and Solubility Determination

Solvents selected for screening studies with selected physicochemical descriptors based on the Strathclyde24 model described in section 3.2.6.1 are outlined in Table 4.6. Dielectric constant values for the selected solvents were derived from the literature (Marcus, 1998; Lide, 2005). Hydrogen bond donor and acceptor numbers for each solvent were obtained from the PubChem database (National Institutes of Health, US). The experimental solubility of OXCBZ form I sourced from Molekula in the solvents employed experimentally (both pure and binary) was determined as described in section 3.2.6.1 and the corresponding results are presented in Tables 4.6 and 4.7.

Form I was found to be most soluble in pure acetic acid, *N,N*-dimethylacetamide (DMA) and *N,N*-dimethylformamide (DMF) with a solubility ≥ 50 mg/mL in each solvent and readily soluble in dimethyl sulfoxide (DMSO) and 2,2,2-trifluoroethanol (TFE) with corresponding solubilities of 42.86 and 37.5 mg/mL. Poor solubility (< 5 mg/mL) was noted for the vast majority of solvents selected (21 out of the 30) with form I being practically insoluble in 1-bromobutane, 1-pentanol, toluene and trichloroethylene (solubility < 0.75 mg/mL). In the context of the binary solvent mixtures utilised for screening, which were selected based on the miscibility profiles of the individual components, poor OXCBZ solubility was also the predominant outcome with 30 out of the 35 mixtures selected yielding values < 5 mg/mL. Form I was most soluble in the pyridine/water 50:50 (v/v) mixture with a solubility value of 13 mg/mL, followed by chloroform/ethanol 50:50 (9.09 mg/mL) and ethanol/nitromethane 50:50 (9.01 mg/mL).

Table 4.6: Solvents utilised in OXCBZ solid-state screening studies. Select physicochemical properties and the solubility of OXCBZ form I at room temperature (RT) in each solvent are additionally presented.

Solvent	Molecular Weight (g/mol)	Boiling Point (°C)	Dielectric Constant	H-Bond Donor Count	H-Bond Acceptor Count	Solubility of OXCBZ I at RT (mg/mL)
Acetic Acid	60.05	118	6.15	1	2	60
Acetone	58.08	56.05	20.56	0	1	3.45
Acetonitrile	41.05	81.65	35.94	0	1	3.16
Anisole	108.14	153.8	4.33	0	1	1.10 – 1.23
1-Bromobutane	137.02	101.4	7.10	0	0	< 0.75
1-Butanol	74.12	117.7	17.8	1	1	0.96 – 1.10
2-Butanone	72.11	79.6	18.11	0	1	3.03
Chloroform	119.38	61.2	4.89	0	0	8.82
1,2-Dichloroethane	98.96	83.5	10.36	0	0	1.41
DMA	87.12	165	37.78	0	1	50
DMF	73.09	153	36.71	0	1	50
DMSO	78.13	189	46.45	0	2	42.86
1,4-Dioxane	88.11	101.1	2.21	0	2	4.48
Ethanol	46.07	78.5	24.55	1	1	0.87 – 0.90
2-Ethoxyethanol	90.12	135.6	29.60	1	2	4.35
Ethyl Acetate	88.11	77	6.02	0	2	1.20 – 1.21
Methanol	32.04	64.6	32.66	1	1	3.16
2-Methoxyethanol	76.09	124	16.93	1	2	9.86
Methyl Acetate	74.08	57.1	5.01	0	2	2.19
4-Methyl-2-Pentanone	100.16	117-118	13.11	0	1	0.90
Nitrobenzene	123.11	210.9	34.78	0	2	2.48
Nitromethane	61.04	101.2	35.87	0	2	3.21
1-Pentanol	88.15	138	13.90	1	1	< 0.75
1-Propanol	60.10	97	20.45	1	1	1.60
2-Propanol	60.10	82.4	19.92	1	1	0.80
Pyridine	79.10	115.2	12.91	0	1	13
THF	72.11	65	7.58	0	1	5.45
Toluene	92.14	110.6	2.38	0	0	< 0.75
Trichloroethylene	131.4	87.2	3.42	0	0	< 0.75
TFE	100.04	78	26.27	1	4	37.5
Water	18.02	100	78.36	1	1	< 0.75

Table 4.7: RT solubility of OXCBZ form I in binary solvents utilised in solid-state screening studies.

Solvent (Volume/Volume %)	Solubility of OXCBZ I at RT (mg/mL)
Acetic Acid/Water (50:50)	5.88
Acetone/Water (50:50)	2.86
Acetonitrile/Water (50:50)	4.62 – 4.76
1-Butanol/Toluene (50:50)	1.37
2-Butanol/Toluene (50:50)	1.10
2-Butanone/Toluene (50:50)	1.64
Chloroform/Ethanol (50:50)	9.09
Chloroform/Toluene (50:50)	0.87
1,2-Dichloroethane/Toluene (50:50)	0.87
DMA/Water (50:50)	1.31
DMF/Water (50:50)	1.91
1,4-Dioxane/Water (50:50)	2.56
Ethanol/1-Bromobutane (50:50)	1.60
Ethanol/Methanol (50:50)	2.10
Ethanol/Nitromethane (50:50)	9.01
Ethanol/1-Pentanol (50:50)	1.27
Ethanol/Toluene (50:50)	4.11
Ethanol/Toluene (50:50)	4.11
Ethanol/Toluene (67:33)	2.56
Ethanol/Toluene (33:67)	2.29
Ethanol/Toluene (20:80)	2.00
Ethanol/Toluene (80:20)	2.00
Ethanol/Toluene (10:90)	1.37
Ethanol/Toluene (90:10)	1.91
Ethanol/Water (50:50)	1.27
2-Ethoxyethanol/Water (50:50)	1.60
Ethyl Acetate/Toluene (50:50)	0.75
Methanol/Water (50:50)	1.27 – 1.37
2-Methoxyethanol/Water (50:50)	1.60 – 1.75
1-Propanol/Water (50:50)	2.10
2-Propanol/Water (50:50)	1.27 – 2.10
Pyridine/Water (50:50)	13
THF/Water (50:50)	7.69
Toluene/4-Methyl-2-Pentanone (50:50)	0.90
TFE/Water (50:50)	4.76

4.4.3.2 Screening Studies & Sample Characterisation

Solution-based screening studies of OXCBZ were performed using a Zinsser Crissy® platform (refer to section 3.2.6.2). The experimental workflow presented in Figure 3.8 was implemented using the solvents presented in Tables 4.6 and 4.7 and all samples prepared were characterised with XRPD (refer to section 3.2.7.1.2). Further analysis of samples found to comprise form III and/or previously unidentified forms of OXCBZ

was also pursued. Over 400 evaporative crystallisations were conducted in total and the crystallisation outcomes emerging from the screening experiments are summarised in Tables 4.8 and 4.9. XRPD patterns representative of different outcomes are shown in Appendix Figure A4.1.

Table 4.8: Summary of results for evaporative crystallisation screening studies of OXCBZ utilising pure solvents. At least 3 replicates were performed for each set of experimental conditions.

Solvent	Evaporation Conditions	Outcome without Substrate	Outcome with Aluminium Substrate
Acetic Acid	70°C & 150 rpm	Form I	Form I
Acetone	25°C & 150 rpm	Form I	Form I
Acetonitrile	45°C & 150 rpm	Mixture of forms I & III	Mixture of forms I & III
Anisole	70°C & 150 rpm	Mixture of forms I & III	Mixture of forms I & III
1-Bromobutane	50°C & 150 rpm	Mixture of forms I & II	Mixture of forms I & II
1-Butanol	50°C & 150 rpm	Form I	Form I
2-Butanone	45°C & 150 rpm	Mixture of forms I & III	Mixture of forms I & III
Chloroform	25°C & 0 rpm	Mixture of forms I & III	Mixture of forms I & III
Chloroform	25°C & 150 rpm	Mixture of form III & unidentified form	Mixture of form I & unidentified form
1,2-Dichloroethane	50°C & 150 rpm	Mixture of forms I & III	Mixture of forms I & III
DMA	80°C & 150 rpm	Form I	Form I
DMF	70°C & 150 rpm	Form I	Form I
DMSO	90°C & 150 rpm	Form I	Form I
1,4-Dioxane	50°C & 150 rpm	Form I	Form I
Ethanol	45°C & 150 rpm	Mixture of forms I & III	Form I
2-Ethoxyethanol	70°C & 150 rpm	Form I	Form I
Ethyl Acetate	45°C & 150 rpm	Mixture of forms I & III	Mixture of forms I & III
Methanol	25°C & 150 rpm	Form I	Form I
2-Methoxyethanol	70°C & 150 rpm	Mixture of forms I & III	Mixture of forms I & III
Methyl Acetate	32°C & 150 rpm	Mixture of forms I & III	Mixture of forms I & III
4-Methyl-2-Pentanone	70°C & 150 rpm	Mixture of forms I & III	Mixture of forms I & II
Nitrobenzene	90°C & 150 rpm	Form I	Form I
Nitromethane	50°C & 150 rpm	Mixture of forms I & III	Form I
1-Pentanol	70°C & 150 rpm	Mixture of forms I & III	Form I
1-Propanol	50°C & 150 rpm	Mixture of forms I & III	Mixture of forms I & III
2-Propanol	50°C & 150 rpm	Form I	Form I
Pyridine	50°C & 150 rpm	Mixture of forms I & III	Mixture of forms I & III
THF	25°C & 150 rpm	Mixture of forms I & III	Mixture of forms I & III
Toluene	50°C & 150 rpm	Mixture of forms I, II & III	Mixture of forms I & II
Trichloroethylene	50°C & 150 rpm	Form I	Mixture of forms I & II
TFE	32°C & 150 rpm	Mixture of form III & unidentified form	Mixture of form III & unidentified form
TFE	32°C & 0 rpm	Mixture of form III & unidentified form	Mixture of form III & unidentified form
TFE	25°C & 150 rpm	Mixture of forms I & III & unidentified form	Mixture of form III & unidentified form
TFE	25°C & 0 rpm	Mixture of form III & unidentified form	Mixture of form III & unidentified form

Table 4.9: Summary of results for evaporative crystallisation screening studies of OXCBZ utilising binary solvent mixtures. The "Form III" outcome indicates samples comprising form III and limited amounts of form I.

Solvent (Volume/Volume %)	Evaporation Conditions	Outcome without Substrate	Outcome with Aluminium Substrate
Acetic Acid/Water (50:50)	70°C & 300 rpm	Form I	Form I
Acetone/Water (50:50)	50°C & 300 rpm	Form I	Form I
Acetonitrile/Water (50:50)	50°C & 300 rpm	Form I	Form I
1-Butanol/Toluene (50:50)	50°C & 300 rpm	Form I	Form I
2-Butanol/Toluene (50:50)	50°C & 300 rpm	Mixture of forms I & III	Mixture of forms I & III
2-Butanone/Toluene (50:50)	50°C & 300 rpm	Mixture of forms I, II & III	Mixture of forms I, II & III
Chloroform/Ethanol (50:50)	50°C & 300 rpm	Mixture of forms I, II & III	Mixture of forms I, II & III
Chloroform/Toluene (50:50)	50°C & 300 rpm	Mixture of forms I, II & III	Mixture of forms I & III
1,2-Dichloroethane/Toluene (50:50)	50°C & 300 rpm	Mixture of forms I, II & III	Mixture of forms I, II & III
DMA/Water (50:50)	70°C & 300 rpm	Form I	Mixture of forms I & III
DMF/Water (50:50)	50°C & 300 rpm	Mixture of forms I & III	Mixture of forms I & III
1,4-Dioxane/Water (50:50)	50°C & 300 rpm	Form I	Form I
Ethanol/1-Bromobutane (50:50)	50°C & 300 rpm	Mixture of forms I & III	Mixture of forms I & III
Ethanol/Methanol (50:50)	50°C & 300 rpm	Form I	Mixture of forms I & III
Ethanol/Nitromethane (50:50)	50°C & 300 rpm	Form I	Form I
Ethanol/1-Pentanol (50:50)	50°C & 300 rpm	Form I	Form I
Ethanol/Toluene (50:50)	50°C & 300 rpm	Mixture of forms I & III	Mixture of forms I & III
Ethanol/Toluene (50:50)	50°C & 150 rpm	Mixture of forms I & III	Mixture of forms I & III
Ethanol/Toluene (50:50)	50°C & 0 rpm	Form III	Mixture of forms I & III
Ethanol/Toluene (67:33)	50°C & 0 rpm	Form III	Mixture of forms I & III
Ethanol/Toluene (33:67)	50°C & 0 rpm	Mixture of forms I & III	Mixture of forms I & III
Ethanol/Toluene (20:80)	50°C & 0 rpm	Mixture of forms I & III	Mixture of forms I & III
Ethanol/Toluene (80:20)	50°C & 0 rpm	Mixture of forms I & III	Mixture of forms I & III
Ethanol/Toluene (10:90)	50°C & 0 rpm	Mixture of forms I & III	Mixture of forms I & III
Ethanol/Toluene (90:10)	50°C & 0 rpm	Mixture of forms I & III	Mixture of forms I & III
Ethanol/Water (50:50)	50°C & 300 rpm	Form I	Form I
2-Ethoxyethanol/Water (50:50)	70°C & 300 rpm	Form I	Form I
Ethyl Acetate/Toluene (50:50)	50°C & 300 rpm	Mixture of forms I & II	Mixture of forms I & II
Methanol/Water (50:50)	50°C & 300 rpm	Form I	Form I
2-Methoxyethanol/Water (50:50)	70°C & 300 rpm	Form I	Form I
1-Propanol/Water (50:50)	50°C & 300 rpm	Form I	Form I
2-Propanol/Water (50:50)	50°C & 300 rpm	Form I	Form I
Pyridine/Water (50:50)	50°C & 300 rpm	Mixture of forms I & II	Mixture of forms I & II
THF/Water (50:50)	50°C & 300 rpm	Form I	Form I
Toluene/4-Methyl-2-Pentanone (50:50)	50°C & 300 rpm	Mixture of forms I & II	Mixture of forms I & II
TFE/Water (50:50)	50°C & 300 rpm	Form I	Form I

In the evaporative crystallisation screen comprising 30 pure solvents (Table 4.8), 11 solvents were found to consistently yield mixtures of OXCBZ I and III with and without an aluminium foil substrate being present in solution during crystallisation. A further 11 solvents were found to produce form I in both the absence and presence of the aluminium substrate. The remanining solvents that were explored yielded different mixtures of forms and no samples comprising pure form II or form III were identified.

Samples recrystallised from chloroform and TFE exhibited XRPD patterns (Figures 4.10a and 4.11a) that comprised characteristic diffraction peaks which did not index with OXCBZ form I and II or any the predicted candidates for form III. In the case of the material obtained from chloroform characteristic low angle peaks were observed at 6.53, 10.99, 12.34 and 13.33° *2θ* whereas for TFE-derived material unique peaks were identified at 6.60, 9.25 and 13.33° *2θ*. DSC/TGA analysis (Figures 4.10b and 4.12b) of the polycrystalline material retrieved from crystallisation in chloroform and TFE revealed the occurrence of weight loss prior to sample melting, hinting towards the possibility of sample solvation. In the case of chloroform-derived material (Figure 4.10b), a weight loss of 1.41% was found to coincide with an exotherm exhibiting an onset of 110.6°C and peak of 124.6°C. Only a very limited amount of recrystallised OXCBZ was obtained from chloroform solution, precluding desolvation attempts and further characterisation attempts. However, the exotherm observed in the DSC trace of the chloroform samples (Figure 4.10b) is likely representative of a phase transformation to a non-solvated form. DSC/TGA measurements of the OXCBZ material recrystallised from TFE (Figure 4.12b) consistently yielded notable weight loss (11.42% ± 0.53) corresponding to 0.29 mole (± 0.01) of solvent per 1 mole of OXCBZ prior to sample melting, indicating potential desolvation. The weight loss observed following the melting endotherm in the DSC curves in Figures 4.10b and 4.12b can be attributed to sample decomposition. Optical microscopy examination (Figure 4.12a) of the OXCBZ material obtained from TFE indicated the presence of polycrystalline aggregates and suitable crystals could not be isolated for SC-XRD analysis. Because of limited diffraction quality of the OXCBZ material derived from TFE, It was not possible to obtain high-quality variable temperature XRPD (VT-XRPD) data and verify the observations noted through DSC/TGA measurements. However, attempted desolvation of the TFE-derived material in a drying oven maintained at 65°C over a period of one week resulted in a phase transformation to form I which was confirmed by Pawley refinement of XRPD data collected for the material (Figure 4.11b). The residual values obtained for the Pawley fit were R_{wp} = 8.24% and

R_p = 6.32% with refined cell parameters of *a* = 5.284 (14) Å, *b* = 9.310 (3) Å, *c* = 24.867 (6) Å and β = 95.635 (4)°.

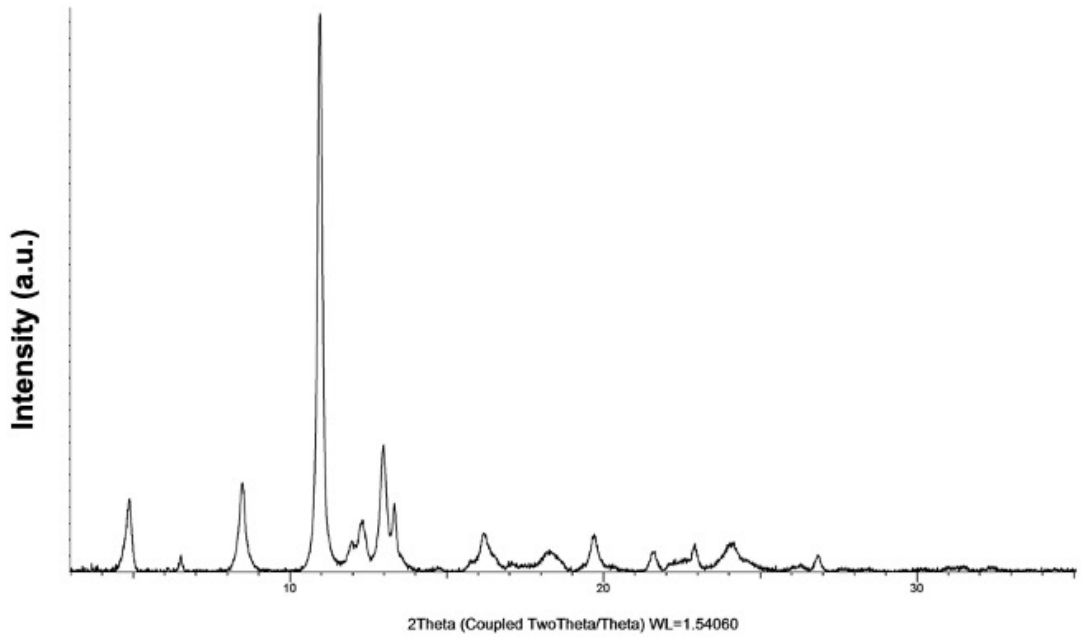

(a)

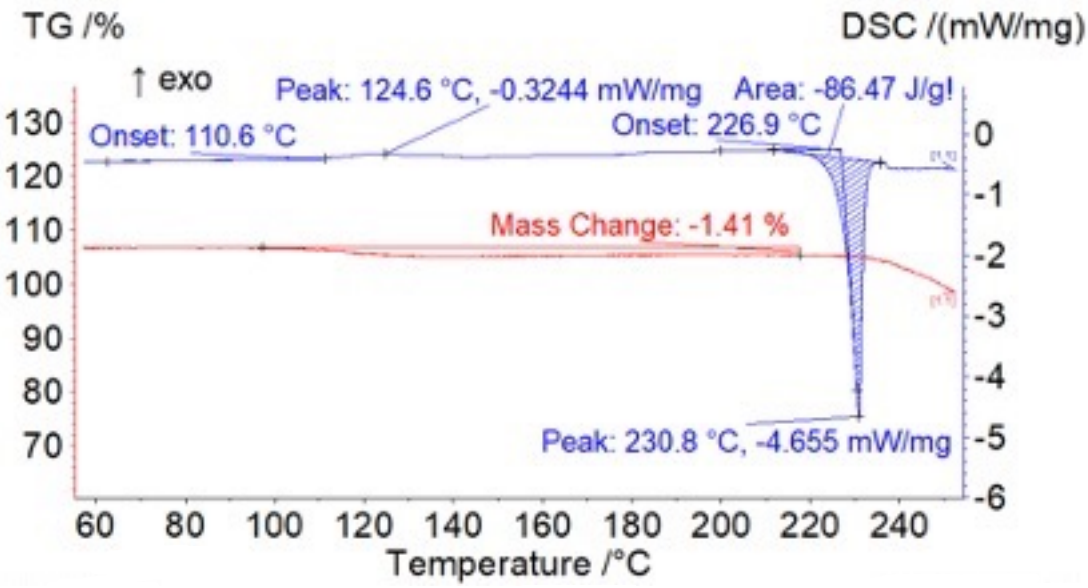

(b)

Figure 4.10: Representative XRPD pattern (a) and DSC/TGA traces (b) of OXCBZ material prepared via fast evaporation from chloroform.

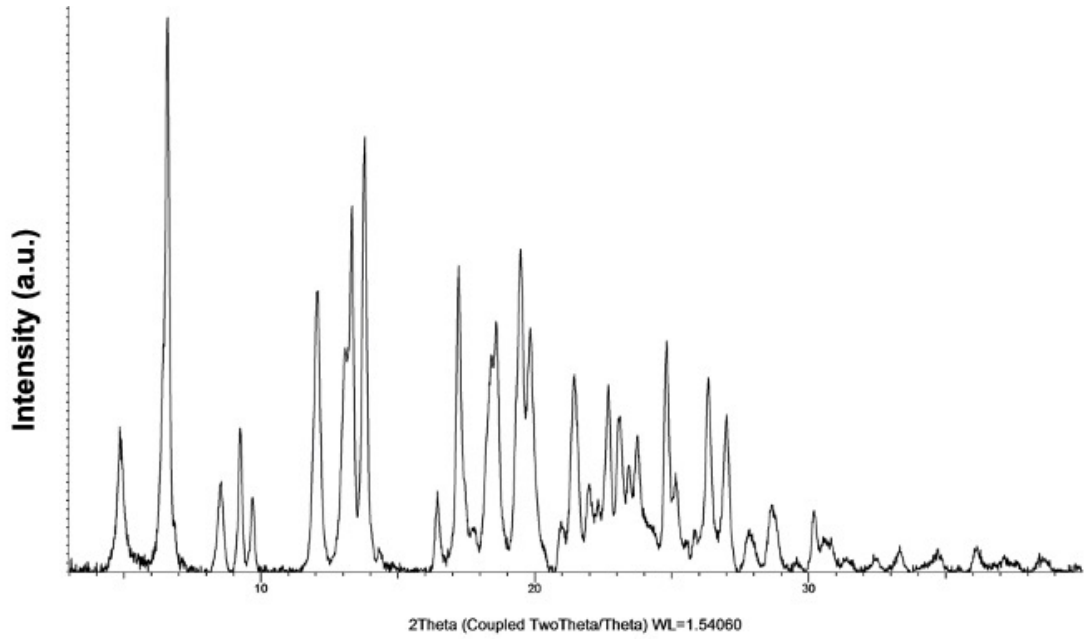

(a)

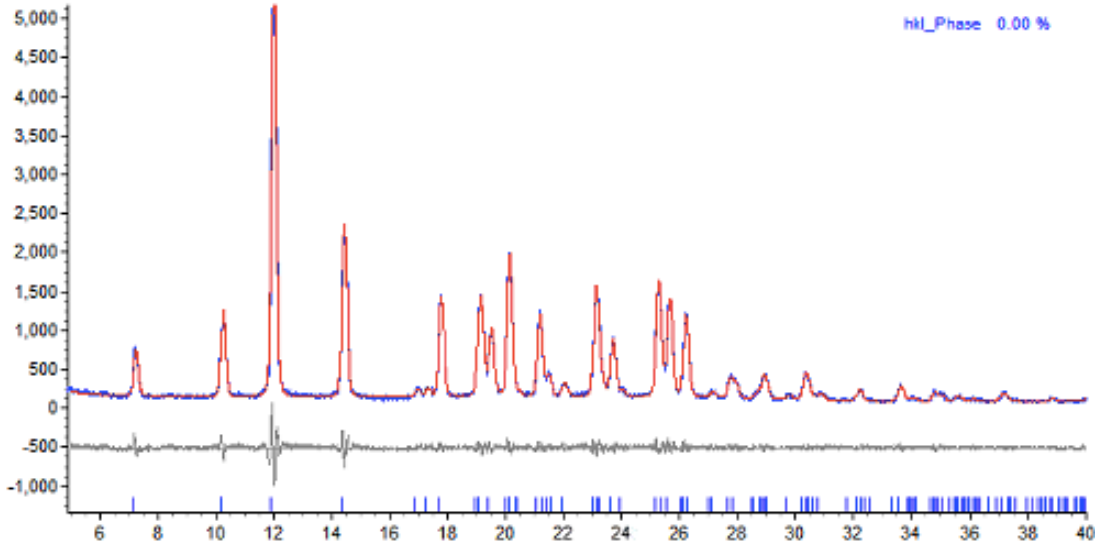

(b)

Figure 4.11: Representative XRPD pattern of OXCBZ material prepared by fast evaporation from TFE (a) and Pawley fit following desolvation at 65°C (b). In the Pawley fit, the blue pattern corresponds to experimentally observed data (y_{obs},) the red pattern represents calculated data (y_{calc}) based on the unit cell parameters of OXCBZ form I (CANDUR01) and the grey pattern indicates differences between the measured and calculated data [(y_{obs} - y_{calc})/$\sigma(y_{obs})$]. The blue tick marks represent calculated diffraction peaks based on the refined unit cell parameters of form I.

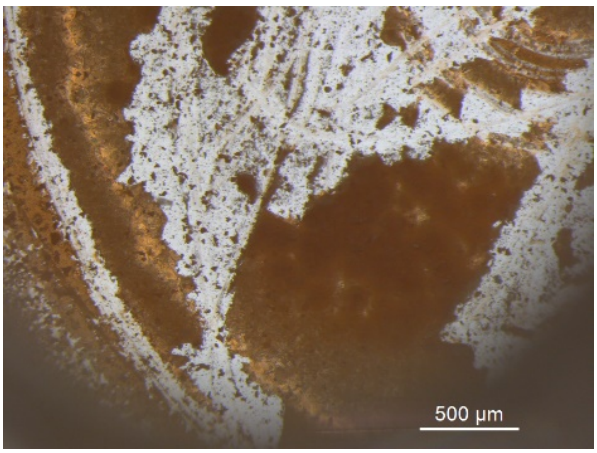

(a)

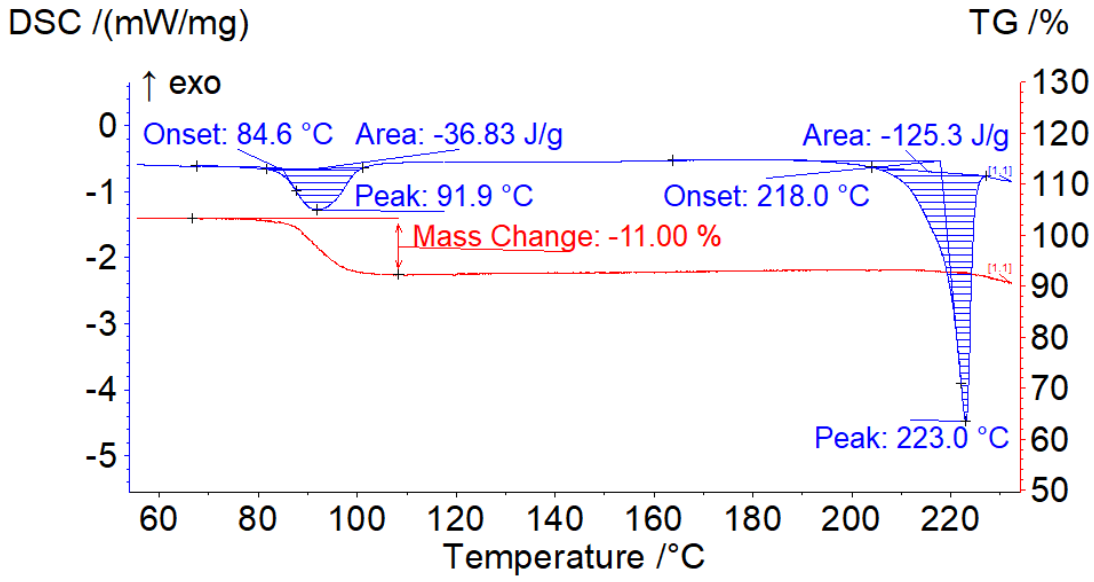

(b)

Figure 4.12: Representative optical micrograph (a) and DSC/TGA curves (b) of OXCBZ material prepared by fast evaporation from TFE. The micrograph scale bar corresponds to 500 µm.

In screening experiments involving the assessment of 30 binary solvent mixtures (Table 4.9), 15 solvent mixtures yielded OXCBZ I regardless of the presence of an aluminium substrate, indicating that the substrate has no effect on the outcome for the solution crystallisation of form I. The rest of the solvent mixtures investigated were found to yield different combinations of OXCBZ forms I – III. Similarly to the evaporative experiments involving the use of pure solvents, pure form II was not detected in the samples analysed although traces of the form were found to be present in samples obtained from 1-bromobutane, 4-methyl-2-pentanone (only with

with aluminium foil present), toluene and trichloroethylene (only with aluminium foil present), 2-butanone/toluene, chloroform/ethanol, chloroform/toluene, 1,2-dichloroethane/toluene, toluene/4-methyl-2-pentanone, ethyl acetate/toluene and pyridine/water.

Whilst 14 of the binary solvent systems employed experimentally gave rise to mixtures of OXCBZ form III and OXCBZ form I and no sample comprising solely form III could be isolated, samples of form III containing limited amounts of form I were successfully isolated from ethanol/toluene solutions (both 50:50 and 67:33 v/v proportions). The experiments resulting in form III samples that comprised limited form I are outlined in Table 4.10.

Table 4.10: Combinations of solvents and experimental conditions that crystallised OXCBZ form III samples comprising limited amounts of form I in evaporation screening experiments.

Solvent	Crystallisation Conditions
Ethanol/Toluene (50:50 v/v)	Fast evaporation at 50°C with no agitation applied and no substrate present in solution
Ethanol/Toluene (67:33 v/v)	Fast evaporation at 50°C with no agitation applied and no substrate present in solution

Out of the two crystallisation conditions highlighted in Table 4.10 that yielded samples of OXCBZ III with limited form I, 67:33 v/v ethanol/toluene was most reproducible, with over a dozen recrystallisations consistently yielding the same outcome. When an aluminium foil substrate was incorporated into the experiments outlined in Table 4.10, mixtures of form and III and I were consistently obtained, with form I as the major component based on relative peak intensities in the XRPD pattern. Whilst this observation indicates that the presence of the aluminium surface does not result in samples comprising solely form III, the nature of the mechanism directing the crystallisation outcome upon incorporation of the aluminium foil substrate into solution remains speculative. Because of the layout of the Crissy® screening platform, it was not possible to monitor the crystallisation process *in situ* using, for example, a non-invasive analytical probe (Pallipurath et al., 2020) to identify the growth of OXCBZ polymorphs at different time points and check for solution-mediated phase transformations (Greco and Bogner, 2012) before complete evaporation was noted.

Suitable crystals for single-crystal structure determination of OXCBZ III could not be isolated through fast evaporation from ethanol/toluene which yielded needle-like

structures, commonly arranged in bundles (Figure 4.13), with a cross-section size of ≈ 160 – 540 nm. The cross section of the crystals was measured using *ImageJ* (refer to section 3.2.7.7.2 for software details). Evidence of twisting was observed for some of the solution-grown crystals of form III and the twisted morphology is explored further in Chapter 5 of this work. In the absence of suitable crystals for SC-XRD, phase identification was attempted by fitting the CSP-derived candidate structures to capillary XRPD data collected from a sample of form III prepared using the 50:50 v/v ethanol/toluene combination and comprising limited amounts of form I (Figure 4.14a). Each of the unit cell and space groups for the candidate structures were utilised as the basis of an initial Pawley refinement against the OXCBZ III capillary data (Figure 4.15, Table 4.11, Appendix Figure A4.2) to identify the most suitable candidate to be used as an initial structural model for structure solution by simulated annealing in *DASH* (David et al., 2006) and subsequent Rietveld refinement (Rietveld, 1967 & 1969). The OXCBZ III data were also subjected to a two-phase Pawley refinement to confirm the inclusion of minor amounts of form I in the sample (Figure 4.14b). The corresponding Pawley fit indicated the presence of characteristic OXCBZ I peaks at 11.9 and 14.3° *2θ*; the residual values obtained were R_{wp} = 1.92% and R_p = 1.46% with refined cell parameters of $a = b$ = 35.988 (15) Å, c = 5.297 (5) Å for form III and a = 5.109 (3) Å, b = 9.066 (10), c = 25.29 (6), β = 93.67 (5)° for form I.

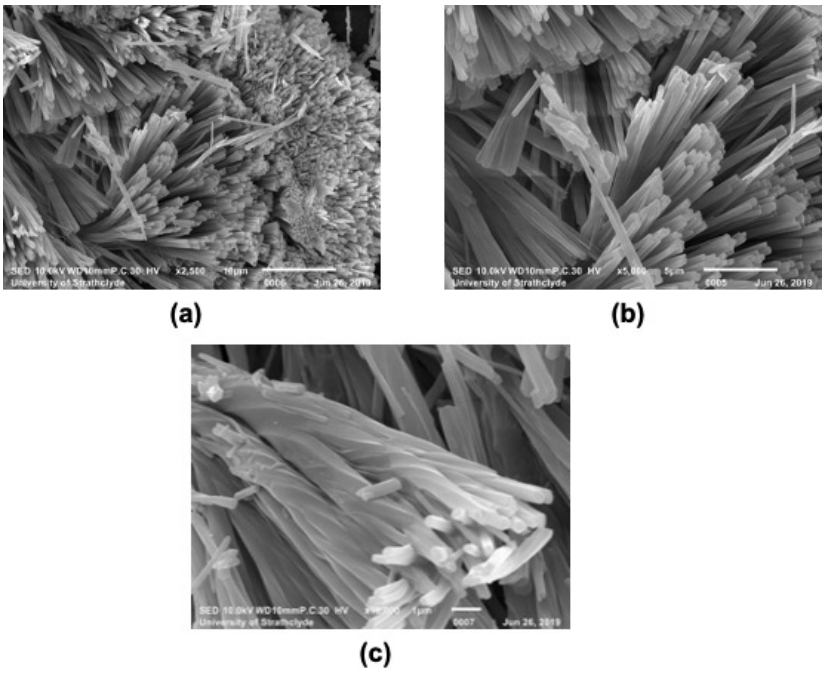

Figure 4.13: Representative SEM micrographs of OXCBZ III crystals grown from 67:33 ethanol/toluene mixture via fast evaporation. The scale bar is 100 μm for (a) and 5 μm for (b) and (c).

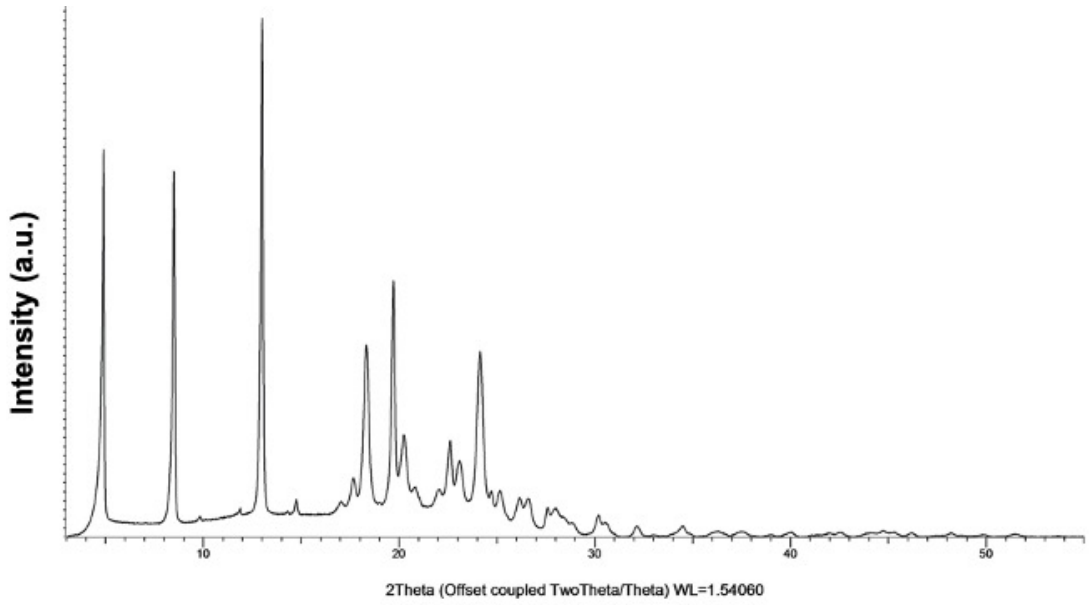

(a)

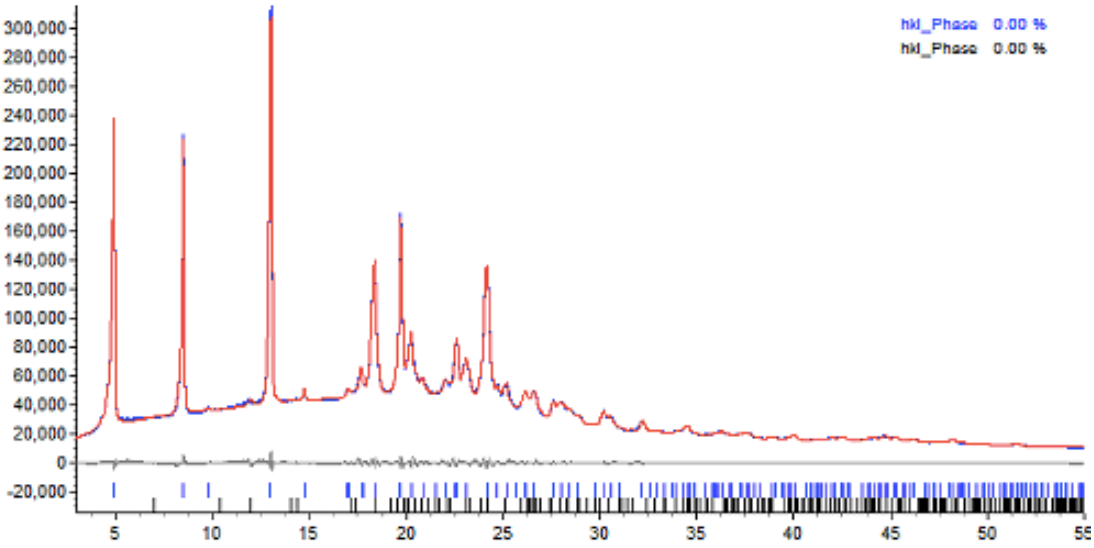

(b)

Figure 4.14: Representative XRPD pattern (a) of OXCBZ material prepared via fast evaporation from 50:50 (v/v) ethanol/toluene and two-phase Pawley fit obtained using CSP candidate structure a96 and OXCBZ form I (CANDUR01). Blue and black tick marks represent calculated diffraction peaks based on the refined unit cell parameters of a96 and form I respectively.

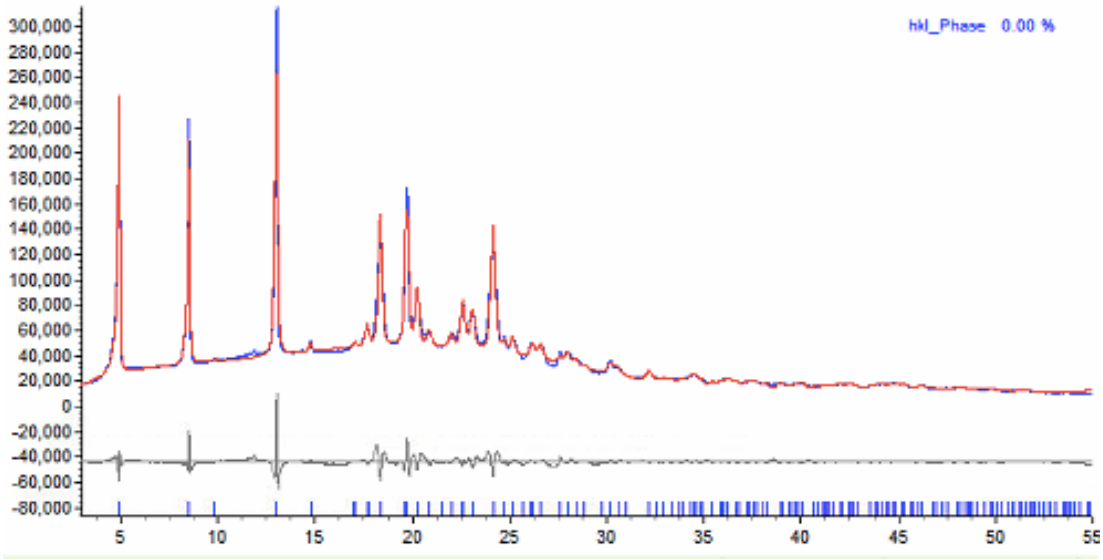

(a)

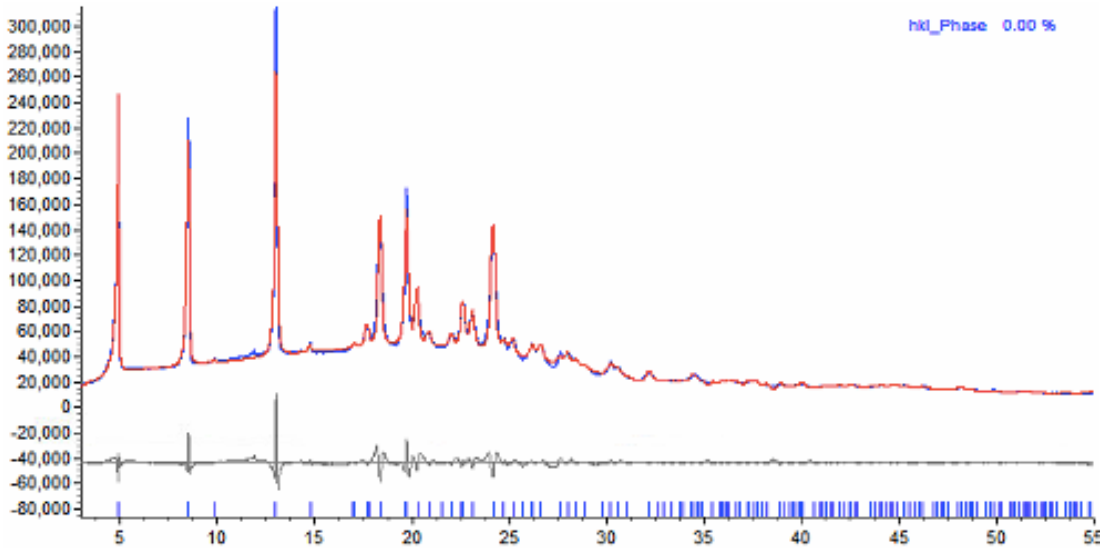

(b)

Figure 4.15: Pawley fits of OXCBZ material obtained via fast evaporation from 50:50 (v/v) ethanol/toluene mixture. The Pawley refinements were performed using the predicted CSP candidates a96 (a) and a900 (b) as starting models.

Table 4.11: Refined cell parameters and residual values (R_{wp} and R_p) for OXCBZ III, obtained by performing Pawley fitting (Figure 4.15 and Appendix Figure A4.2) of experimental data using each of the candidate structures as a starting model for refinement purposes.

CSP Structure Used in Refinement	Space Group	*a, b* (Å)	*c* (Å)	α, β (°)	γ (°)	Cell Volume (Å^3)	R_{wp} (%)	R_p (%)
a96	*R*-3	35.992 (4)	5.298 (4)	90	120	5943.0 (13)	4.98	3.53
a165	*R*-3	35.995 (10)	5.085 (12)	90	120	5706 (3)	12.43	6.39
a722	$P6_1$	20.778 (5)	5.225 (17)	90	120	1953.4 (12)	12.15	7.45
a900	*R*-3	35.993 (4)	5.298 (5)	90	120	5943.5 (16)	4.90	3.50
a1858	*P*-3	20.783 (2)	5.017 (6)	90	120	1876.6 (5)	11.45	6.27

The results of the Pawley fits show structures a96 and a900 fit the experimental data for OXCBZ III almost equally well and significantly better than the rest of the candidate structures, an observation that raises the possibility of OXCBZ III being a physical mixture of closely related polymorphic forms that crystallise concomitantly (Bernstein et al., 1999).

Simultaneous DSC/TGA analysis conducted for solution-grown, polycrystalline OXCBZ III material (Figure 4.16) suggests that solvent molecules are present in the crystal structure of form III and release themselves upon subjection to elevated temperature conditions. TGA traces obtained for OXCBZ III samples revealed that minor weight loss (3.52% ± 1.64) occurs within the temperature range of 110 - 190°C prior to melting taking place. In the TGA trace specifically presented in Figure 4.16, the mass change of 1.63% that was observed corresponds to 0.045 mole of toluene or 0.089 mole of ethanol per 1 mole of OXCBZ. This observation indicates that solvent molecules originally occupied the void channels present in the structure of form III in non-stoichiometric amounts and heating facilitated their release. DSC measurements obtained for OXCBZ III show the occurrence of a broad exotherm coinciding with the weight loss observed. Endothermic peaks corresponding to melting of OXCBZ I and OXCBZ III were observed at 232.5°C (± 0.32) and 230.7°C respectively with corresponding onsets of 229.5°C (± 0.49) and 228.0°C. The heat of fusion of OXCBZ I measured 149.5 J/g (± 29.96) which is higher than the heat of fusion corresponding to OXCBZ III (134.6 J/g). The TGA curves obtained for form I and form III material

generally depicted continuous weight loss following the onset of melting, indicating the occurrence of concomitant melting and decomposition. This observation is in good agreement with previously reported data for OXCBZ polymorphs (Lutker and Matzger, 2010).

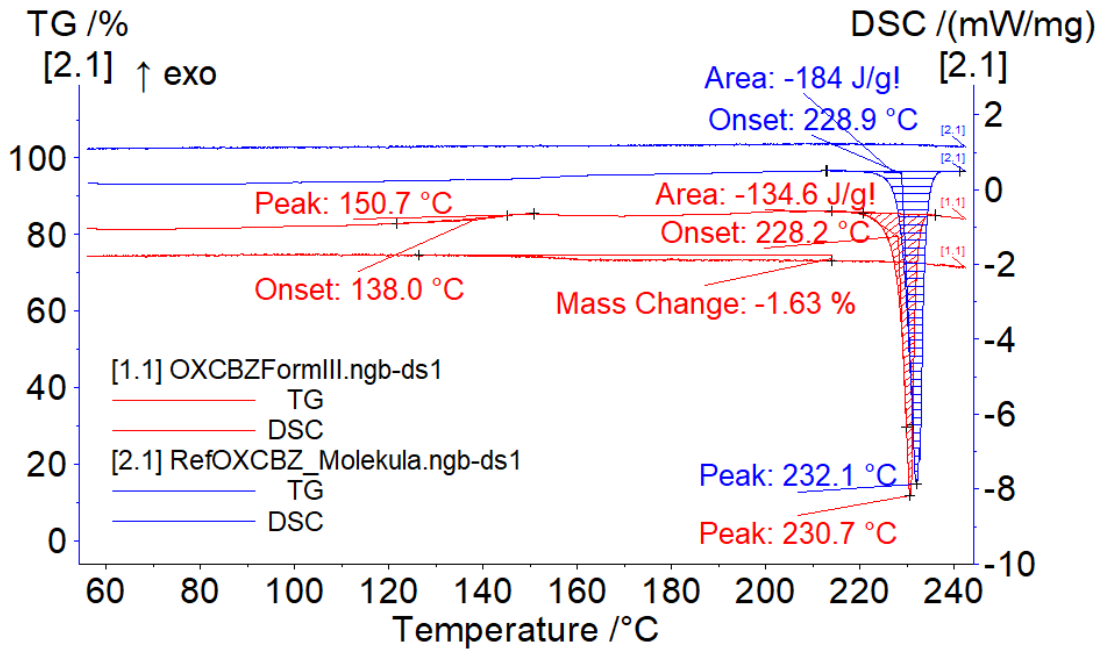

Figure 4.16: Representative DSC/TGA analysis of pure OXCBZ form I sourced from Molekula (blue curves) and OXCBZ form III material obtained from 50:50 v/v ethanol/toluene mixture via fast evaporation (red curves).

VT- and VH-XRPD studies of solution-grown OXCBZ III material (Figures 4.17a and 4.17b) were conducted to obtain further insight into the behaviour of form III under non-ambient atmospheric conditions. Upon being subjected to temperatures in the region of 100 - 120°C, the form III material began to undergo a transformation to the thermodynamically stable form I, as evidenced by an increase in the intensity of the diffraction peaks present at 12° and 14.4° *2θ* which are both characteristic of form I. The transformation of the material to OXCBZ I at high temperature was completed by the time the sample was measured at 190°C, with all of the characteristic form III peaks disappearing completely from the diffraction pattern and the sample comprising peaks which were all found to be in agreement with reference data for form I. When compared to reference powder patterns for form I and simulated powder patterns for candidate structures a96 and a900, a shift in the position of the experimental peaks in Figure 4.17a was observed. The peaks corresponding to form

III were found to have shifted by ≈ +0.2° *2θ,* whereas the shift for the ones corresponding to OXCBZ I was ≈ 0.1° *2θ*. The behaviour of the peaks can most likely be attributed to the loss of residual solvent from the channels of form III coming into effect during the variable temperature scan, leading to contraction of the unit cell in a manner similar to that expected for CBZ form II upon solvent removal (Cruz-Cabeza et al., 2007b).

The variable temperature analysis of the form III material (Figure 4.17a) can be correlated with the combined DSC/TGA measurements presented in Figure 4.16. The transformation of OXCBZ III to OXCBZ I was found to occur in the temperature range of 110 - 190°C, the same range in which weight loss was observed for the sample. By combining the observations from the variable temperature and TGA analyses, it becomes reasonable to suggest that the transformation of OXCBZ III to OXCBZ I facilitates the process of solvent release from the crystal structure of the sample upon heating. Moreover, the occurrence of this polymorphic transformation can be used to explain the observation of the broad exothermic event depicted in the DSC curve of the OXCBZ III sample. Based on the occurrence of an exothermic polymorph transformation and the heat of transition rule proposed by Burger and Ramberger (Burger and Ramberger, 1979a), OXCBZ I and OXCBZ III appear to be a pair of monotropically related polymorphs. The transformation of form III to form I at high temperature additionally suggests that the melting endotherm of 230.7°C noted for the OXCBZ III sample is indicative of form I rather than form III because the melting of the sample occurs after the full transformation of the metastable form to its stable counterpart has been completed.

The results obtained for the variable humidity study (Figure 4.17b) performed for the OXCBZ III material revealed no significant differences between the diffraction patterns collected at different relative humidity profiles, suggesting that form III remains stable and does not convert to the thermodynamically stable form I or the metastable form II when subjected to high moisture uptake.

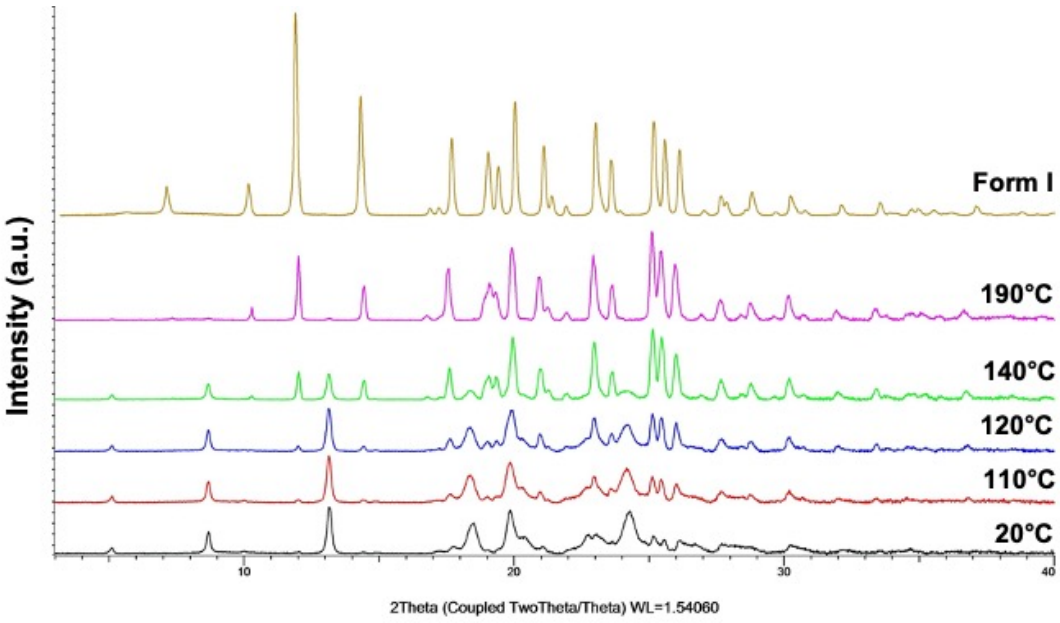

(a)

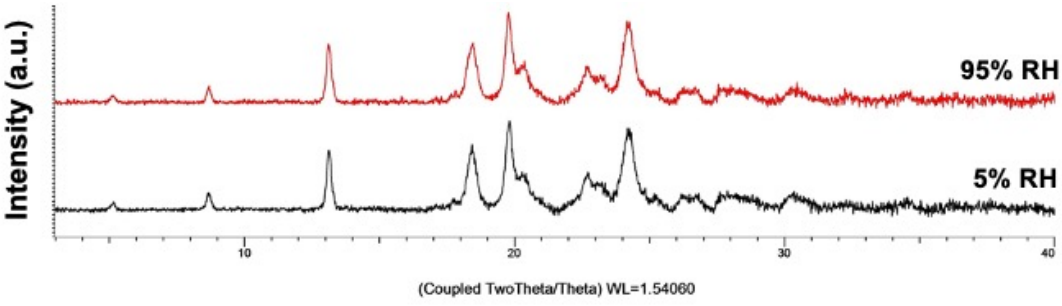

(b)

Figure 4.17: VT-XRPD (a) and VH-XRPD (b) analyses of OXCBZ form III material obtained from 67:33 (v/v) ethanol/toluene mixture by fast evaporation.

.

The Raman spectra of OXCBZ form I and solution-grown form III material are presented in Figure 4.18. Pure form I exhibits characteristic peaks at 415.87, 610.16, 1235.36, 1260.33, 1300.49 and 1650.00 cm^{-1}. The form III material can be distinguished from form I through the presence of characteristic peaks at 425.63, 598.22, 619.93, 765.37, 810.96, 870.66, 1000.91, 1241.88, 1254.90, 1273.35, 1284.4, and 1412.29 cm^{-1}.

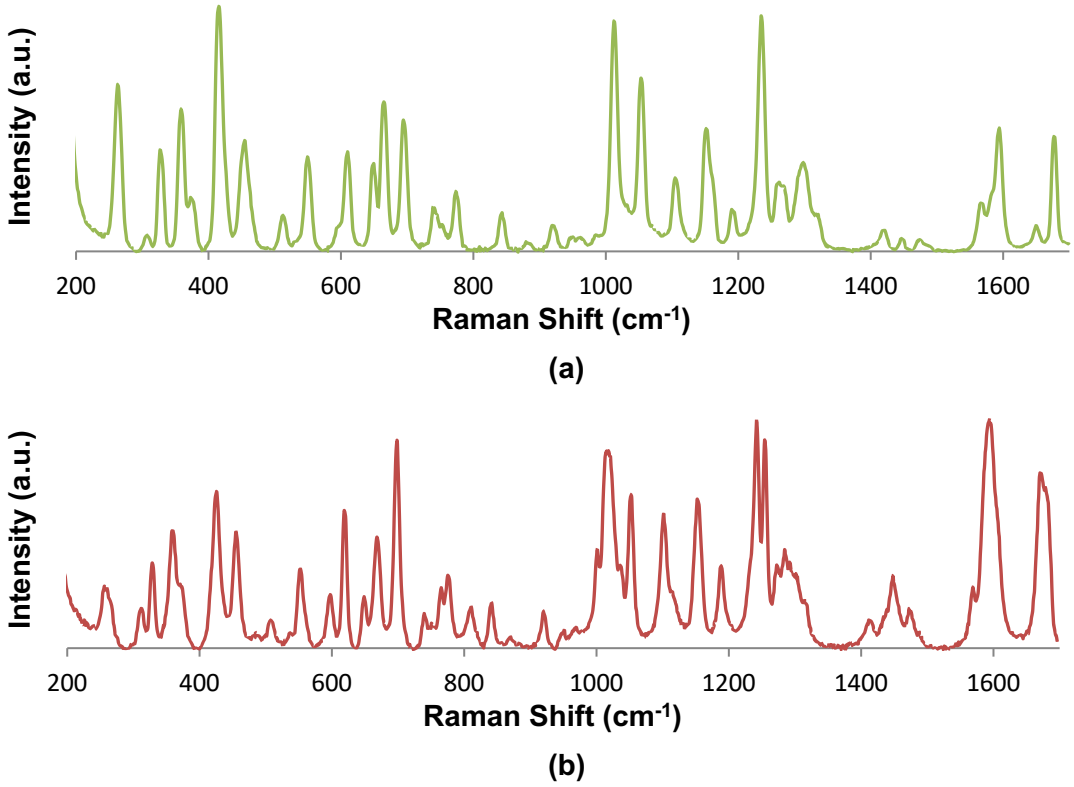

Figure 4.18: Raman spectra of pure OXCBZ form I sourced from Molekula (a) and OXCBZ form III obtained from 50:50 (v/v) ethanol/toluene mixture by fast evaporation (b).

The GI dissolution method has gained prominence over the last decade as a potent approach for assessing the behaviour of pharmaceuticals in the GI tract (Gravestock et al., 2011). Experimental data from GI dissolution studies comprising OXCBZ I and OXCBZ III compacts are presented in Figure 4.19. Across the pH range explored, the extrapolated dissolution rate was found to be higher for samples of form III when compared to pure form I material sourced from Molekula. Over the first ≈ 30 minutes of dissolution, the dissolution of compacts that included form III was found to be ≈ 2.6 times greater than those containing form I. The use of compacts with identical diameters in these studies ensured that differences in the particle size of forms I and III would not affect the dissolution outcome. OXCBZ III dissolving more readily than OXCBZ I is in line with past observations of metastable pharmaceutical polymorphs exhibiting improved dissolution compared to their more stable counterparts (Censi and Di Martino, 2015). OXCBZ is a BCS Class II drug likely to exhibit dissolution rate-limited bioavailability (Amidon et al., 1995) and, whilst the oral bioavailability profile of OXCBZ III was not investigated herein, it is anticipated that the superior dissolution of

form III relative to form I will result in more favourable bioavailability properties and, potentially, more effective pharmaceutical formulations of OXCBZ (Censi and Di Martino, 2015).

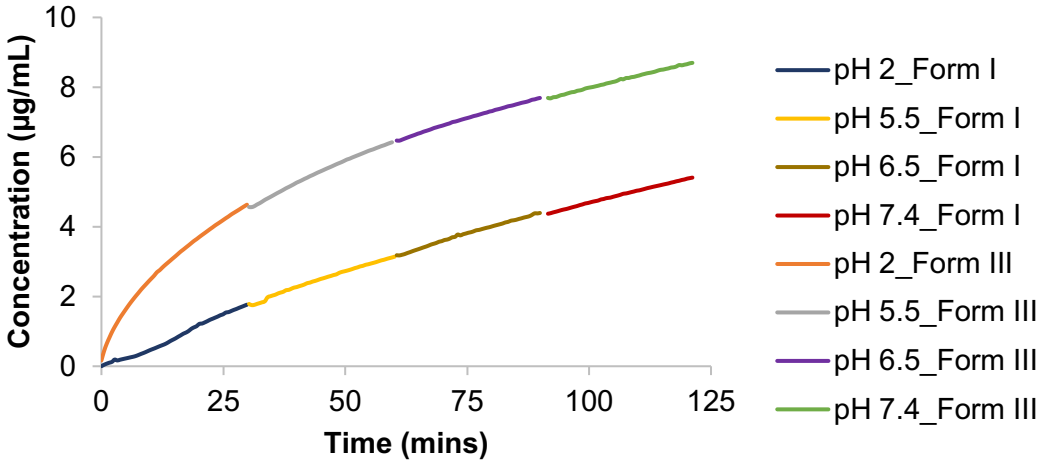

Figure 4.19: GI dissolution profiles of OXCBZ form I sourced from Molekula and OXCBZ form III material prepared via fast evaporation from ethanol/toluene (67:33 v/v). Dissolution data were collected in the pH range of 2 - 7.4 and the profiles depicted represent average measurements corresponding to 3 samples.

4.4.4 Physical Vapour Deposition Studies of OXCBZ under Atmospheric Conditions

The physical vapour deposition experiments that were conducted typically led to the formation of needle-like and fibre-like crystals for OXCBZ III, with optical microscopy analysis revealing a tendency of the crystals to form tangled clusters on each experimental substrate (Figure 4.20). Some evidence for dendritic crystal growth (Glicksman and Lupulescu, 2004) was additionally obtained (Figure 4.21). The observation of needle-like crystals for OXCBZ III is consistent with the morphology originally reported for the polymorph (Lutker and Matzger, 2010) and the predicted BFDH morphologies (Figure 4.8) for the OXCBZ III candidate structures in the CSP. When the OXCBZ III crystals grown on metallic substrates were examined using SEM, needle-like and fibre-like crystals exhibiting a highly unusual twisted morphology were observed (Figure 4.22). The emergence and evolution of the twisted OXCBZ III crystals during the vapour deposition process is discussed in Chapter 5.

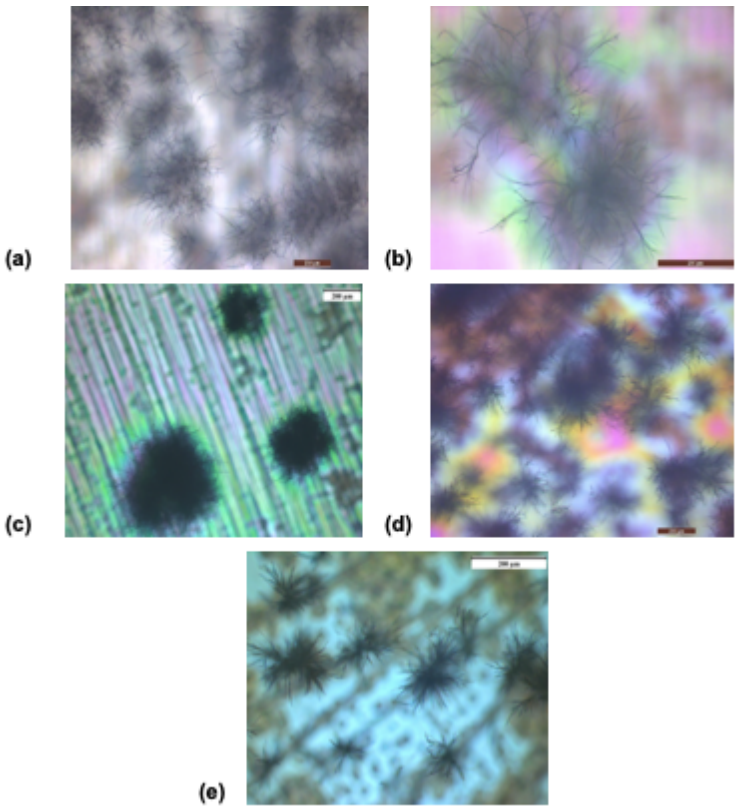

Figure 4.20: Optical micrographs depicting tangled clusters comprising fibrous OXCBZ III crystals obtained from physical vapour deposition onto a) aluminium foil, b) copper foil, c) silver foil, d) copper-coated glass, e) silver-coated glass. The scale bar is 200 μm for all micrographs.

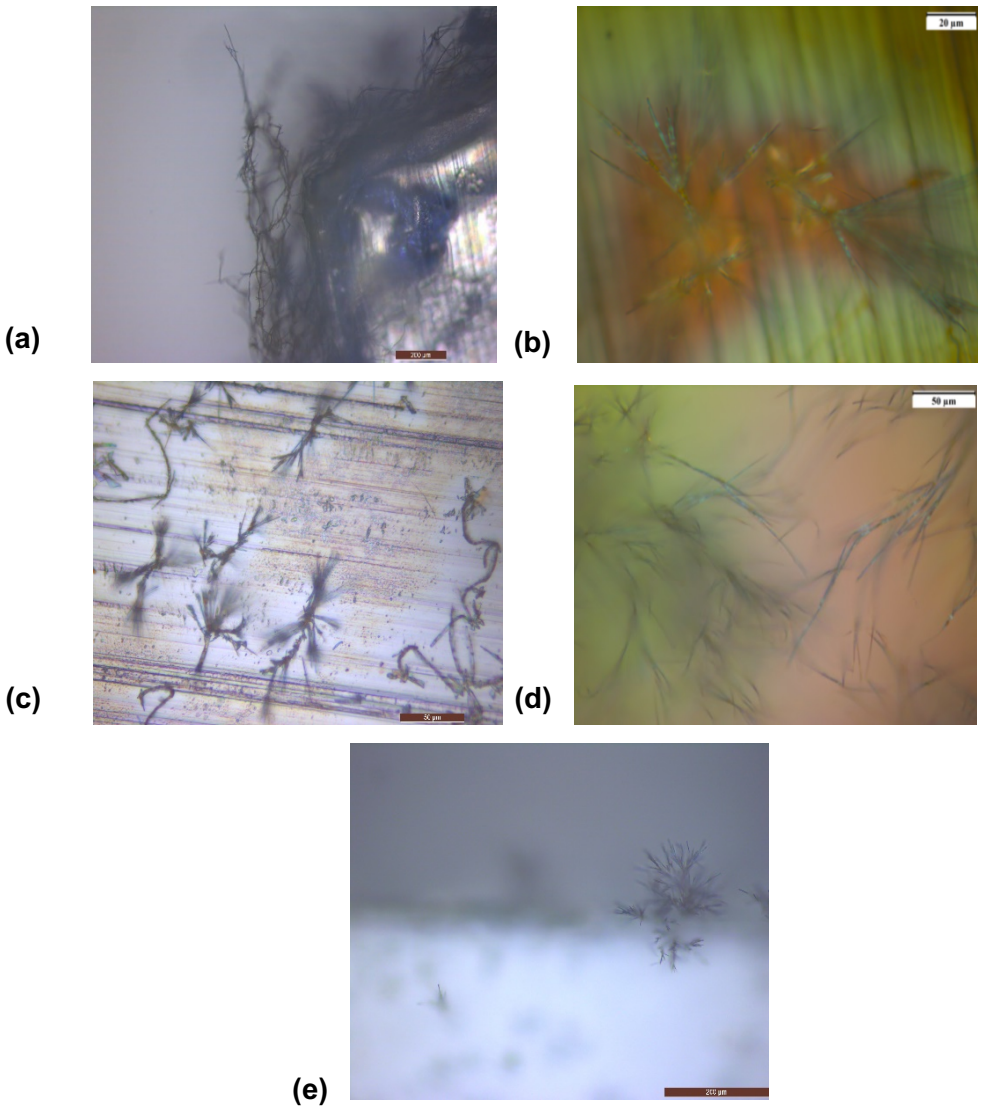

Figure 4.21: Optical micrographs depicting dendritic OXCBZ III crystals obtained from physical vapour deposition onto a) aluminium foil (scale bar = 200 μm), b) copper foil (scale bar = 20 μm), c) silver foil (scale bar = 50 μm), d) copper-coated glass (scale bar = 50 μm), e) silver-coated glass (scale bar = 200 μm).

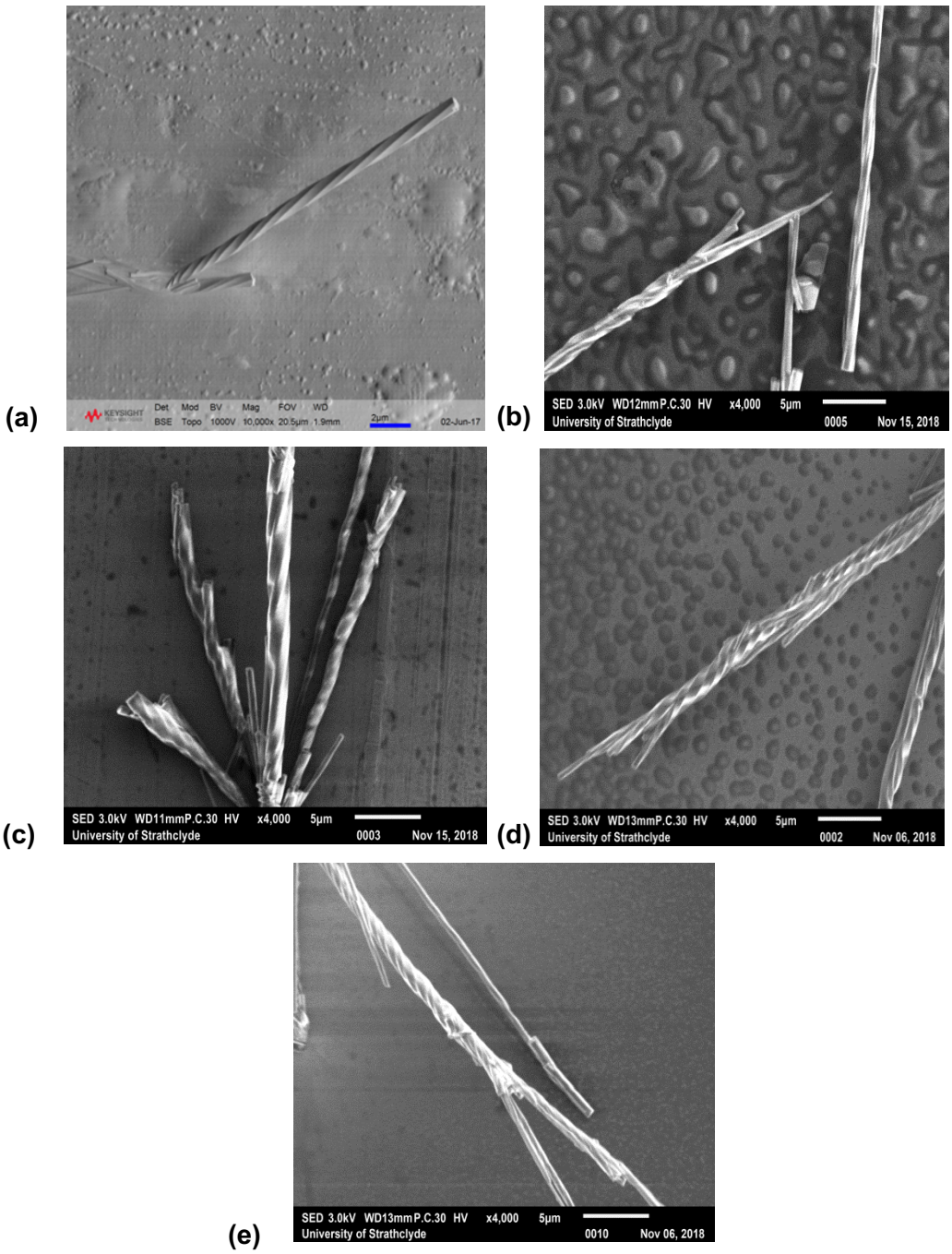

Figure 4.22: SEM micrographs of twisted OXCBZ III crystals grown via physical vapour deposition of OXCBZ onto a) silver foil, scale bar = 2 µm b) aluminium foil, scale bar = 5 µm c) copper foil, scale bar = 5 µm d) copper-coated glass, scale bar = 5 µm e) silver-coated glass, scale bar = 5 µm.

The complete summary of outcomes for the physical vapour deposition experiments performed for OXCBZ are summarised in Table 4.12.

Table 4.12: Overview of physical vapour deposition experiments conducted for OXCBZ. The duration of the vapour deposition process was 48 hours for all experiments.

Substrate	Deposition Temperature (°C)	Polymorphic Outcome
Aluminium foil	125	Mixture of form I & impurity peaks
Aluminium foil	130	Poorly crystalline material
Aluminium foil	135	Mixture of forms I & II
Aluminium foil	140	Mixture of forms I & III
Aluminium foil	145	Mixture of forms I & III
Copper foil	125	Form I
Copper foil	130	Poorly crystalline material
Copper foil	135	Form I
Copper foil	140	Form III
Copper foil	145	Form III
Silver foil	125	Form I
Silver foil	130	Mixture of form I & unidentified form
Silver foil	135	Mixture of forms I & III with impurity peaks present
Silver foil	140	Mixture of form III & unidentified form
Silver foil	145	Mixture of forms I & III with impurity peaks present
Copper-coated glass	125	Form I
Copper-coated glass	130	Mixture of forms I & III
Copper-coated glass	135	Mixture of forms I & III
Copper-coated glass	140	Mixture of forms I & III
Copper-coated glass	145	Mixture of forms I & III
Silver-coated glass	125	Mixture of forms I & III
Silver-coated glass	130	Mixture of forms I & III
Silver-coated glass	135	Mixture of forms I & III
Silver-coated glass	140	Mixture of forms I & III
Silver-coated glass	145	Mixture of forms I, II & III

XRPD analysis of OXCBZ III samples prepared via vapour deposition typically yielded diffraction patterns with less than 20 peaks, which is the number typically required for successful indexing and subsequent structure determination using global optimisation methods (Werner, 2002; Florence et al., 2005; Florence, 2009). The experimental patterns were compared with simulated diffraction data for each predicted candidate for OXCBZ III from the CSP study (Figure 4.4) and found to match best with structure a96. Representative patterns corresponding to samples comprising form III are shown in Figure 4.23. CSP structure a96 exhibits four characteristic diffraction peaks in the

3 - 15° *2θ* range that help differentiate it from the two fully characterised polymorphic forms of the compound; these peaks can be found at 4.89, 8.48, 9.80, and 12.98° *2θ* respectively and are readily present in the patterns shown in Figure 4.23, with the exception of the peak at 9.80°. As Table 4.12 shows, the formation of OXCBZ III on metallic substrates is largely independent of the type of substrate used (metallic foil or metal-coated glass) and the specific properties that each substrate exhibits (i.e. nanoscale roughness and wettability/surface energy profile; refer to section 4.4.1). However, the results obtained suggest that OXCBZ III is not the only form of the compound crystallising on the experimental substrates. Samples in which peaks matching form I were observed (e.g. aluminium foil sample shown in Figure 4.23a), as well as samples were unidentified peaks were present which did not correspond to any of the reported OXCBZ forms or form III candidates (e.g. silver foil sample in Figure 4.23c). These observations suggest that aluminium foil and silver foil substrates may have induced the concomitant crystallisation of multiple forms of OXCBZ, although the possibility of metastable forms following Ostwald's rule of stages (Ostwald, 1897) by crystallising first and undergoing partial transformations to more stable phases by the time of analysis cannot be ruled out. Furthermore, the presence of broad 'humps' was noted for some of the experimental patterns (e.g. Figures 4.23b and 4.23c), which suggests that amorphous OXCBZ could additionally be present in the samples as these humps are typically indicative of the presence of amorphous material in a specimen (Bates et al., 2006) and were not found to be present in reference patterns collected for the experimental substrates prior to deposition studies commencing.

In the case of OXCBZ deposition onto silver foil, nucleation of an unknown crystalline phase with characteristic XRPD peaks at 9.0, 11.1 and 16.2° *2θ* appeared to be induced in the temperature range between 130 and 140°C (Table 4.12) and sample purity with respect to this phase appeared to be most prevalent in samples obtained via vapour deposition at 130°C over a period of 48 hours; representative XRPD, Raman spectroscopy and optical microscopy data corresponding to samples of OXCBZ prepared via deposition under these experimental conditions are presented in Figure 4.24. The XRPD pattern of the proposed new form of OXCBZ (Figure 4.24a) exhibits close similarity with the simulated pattern of a predicted structure from the compound's CSP landscape. The aforementioned CSP structure, denoted s68 (Figure 4.25a), is found 4.7 kJ/mol higher than form I and crystallises in the triclinic *P*-1 space group with unit cell parameters *a* = 10.7814 Å, *b* = 8.7534 Å, *c* = 7.6886 Å,

α = 99.5249°, β = 84.6557°, γ = 67.6409° and cell volume = 652.036 Å^3. Predicted structure s68 adopts the *syn* conformation of the OXCBZ molecule, unlike forms I and II and all predicted candidates for form III, and its unit cell packing arrangement, hydrogen bonding pattern and predicted BFDH morphology are presented in Figures 4.25b and 4.25c. The Raman spectrum (Figure 4.24b) of the OXCBZ material isolated from vapour deposition onto silver foil at 130°C was found to differ from those of OXCBZ forms I and III (Table 4.13). Further examination of the vapour-grown material on silver substrate using optical microscopy (Figure 4.24c) revealed the presence of crystalline particles with block-like morphology. This observation is in line with the BFDH morphology of structure s68 which was also found to be block-like. However, the small size (< 50 μm in all dimensions) of the vapour-grown crystals on silver foil prevented SC-XRD analysis from being pursued. Unfortunately, crystal structure determination by means of XRPD was not possible either due to the limited quality of the diffraction data that were obtained, making it impossible to confirm whether the unknown OXCBZ phase observed on silver foil truly corresponds to predicted structure s68.

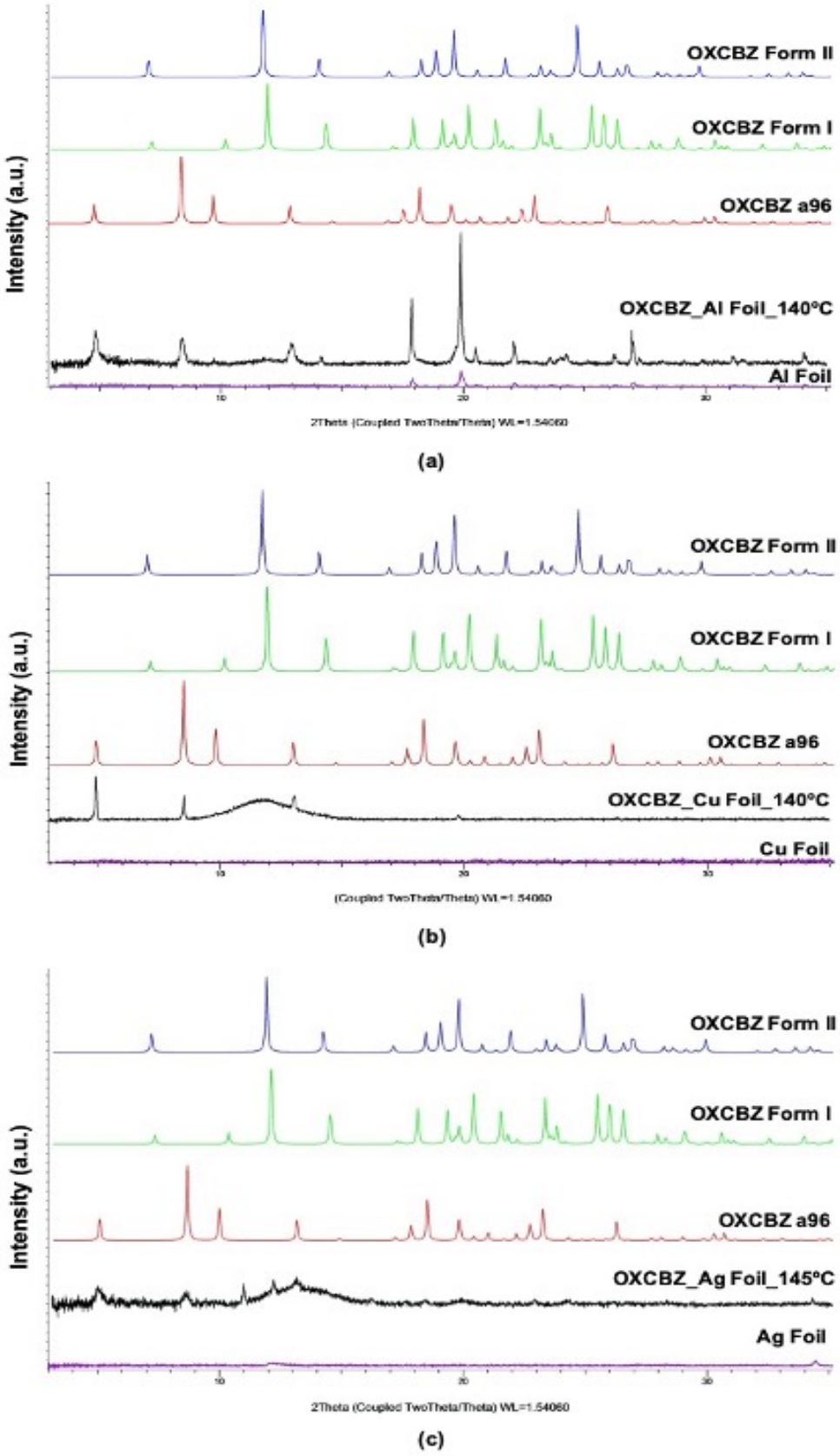

Figure 4.23: XRPD patterns of OXCBZ material obtained from vapour deposition onto aluminium foil at 140°C (a), copper foil at 140°C (b) and silver foil at 145°C (c).

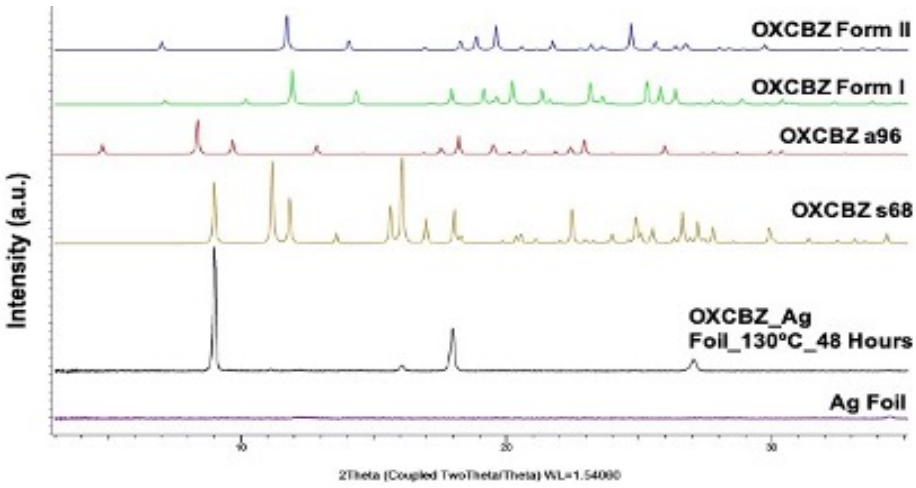

(a)

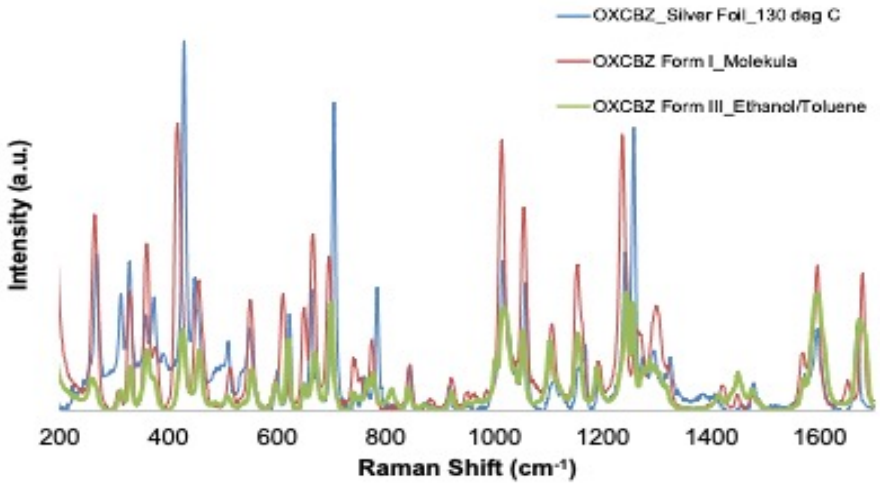

(b)

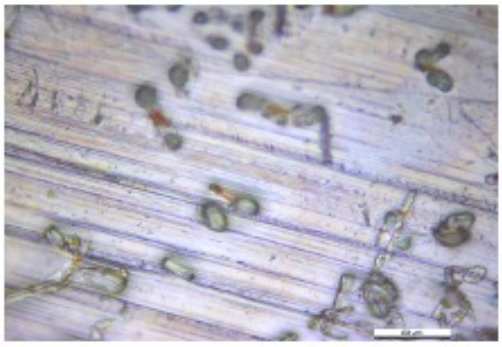

(c)

Figure 4.24: Representative XRPD pattern (a), Raman spectrum (b) and optical micrograph (c) of unidentified OXCBZ phase emerging via physical vapour deposition of OXCBZ onto silver foil at 130°C. The XRPD pattern and Raman spectrum of the unidentified phase are compared with reference data for other forms of OXCBZ. The scale bar for the optical micrograph is 50 μm.

Table 4.13: Overview of characteristic Raman peak positions (in cm^{-1}) for OXCBZ form I material sourced from Molekula, OXCBZ form III material obtained via fast evaporation from ethanol/toluene mixture and unidentified OXCBZ phase crystallised from physical vapour deposition onto silver foil at 130°C.

Form I	Form III	Unidentified Phase
415.87	425.63	266.93
610.16	598.22	311.71
1235.36	619.93	326.98
1260.33	765.37	358.53
1300.49	810.96	371.76
1650.00	870.66	391.09
	1000.91	427.73
	1241.88	447.07
	1254.90	509.15
	1273.35	548.84
	1284.4	598.71
	1412.29	621.10
		647.57
		661.81
		703.54
		744.25
		757.48
		782.93
		843.99
		916.25
		1014.97
		1037.36
		1056.70
		1108.60
		1121.83
		1154.40
		1166.61
		1192.06
		1240.91
		1256.18
		1274.50
		1293.83
		1323.35
		1476.01
		1571.68
		1593.05

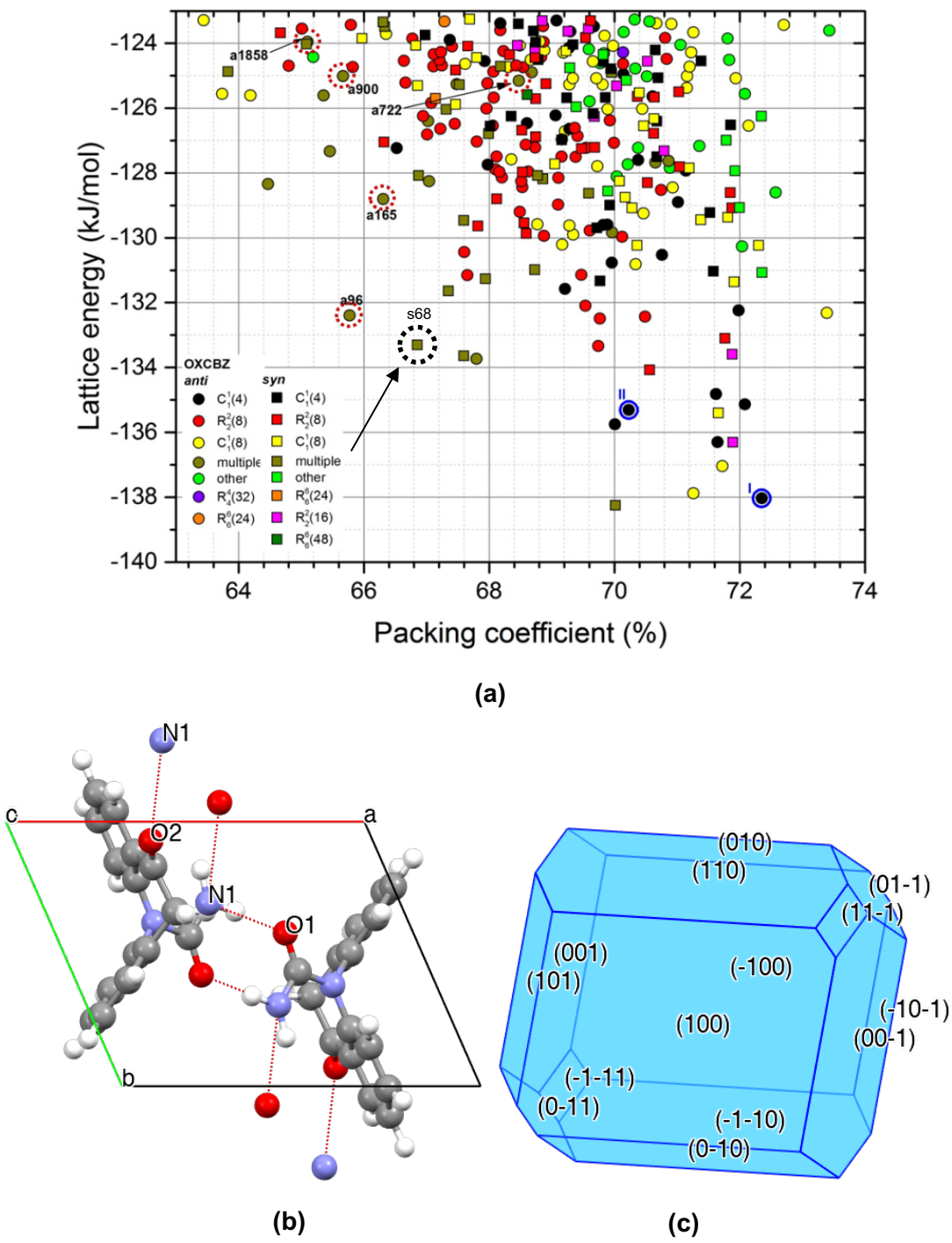

Figure 4.25: CSP landscape of OXCBZ (a), wherein predicted structure s68 is indicated by the dotted black circle, unit cell packing arrangement of s68 viewed down the crystallographic *c* axis (b), and BFDH morphology of s68 generated using *Mercury* (c). Dashed red and cyan lines in (b) indicate the presence of intermolecular (O · · · N) hydrogen-bonding interactions.

The outcomes of the physical vapour deposition screening studies discussed herein were found to be reproducible with respect to the preparation of form III, as triplicate experiments consistently yielded similar results. This suggests that the substrates explored can promote the formation of OXCBZ III under the conditions explored. At temperatures ≥ 125°C form III was found to crystallise in all of the substrates investigated, typically as part of mixtures which were also found to comprise form I at the time of analysis. The most phase-pure samples of OXCBZ III isolated via crystallisation from the vapour phase were derived when copper foil was utilised as the substrate of choice, with deposition time of 48 hours and temperature of 140 or 145°C used respectively. The fact that OXCBZ III was found to crystallise under all of the temperature profiles investigated indicates that temperature is not the driving force governing the crystallisation of form III from the vapour. Experiments yielding different forms when identical deposition temperatures and durations were utilised suggests that the substrates utilised may potentially be playing some part in influencing the crystallisation outcomes although the exact role that these surfaces play is unclear. The observation of copper foil being the only substrate to yield samples of form III with high phase purity can likely be attributed to the interplay between the copper foil and the rest of the conditions (temperature, duration of vapour deposition) utilised in the respective experiments.

Whilst OXCBZ III could be grown on all experimental substrates, eliminating the possibility of a templating effect (Arlin et al., 2011; Srirambhatla et al., 2016; Case et al., 2018) unique to a specific substrate, and no correlation was identified between the nanoscale roughness/wettability/surface free energy properties of the substrates and the crystallisation outcomes observed in the screen, the vapour deposition experiments provided the first known evidence of form III crystallising using a solvent-free methodology.

4.4.5 Physical Vapour Deposition Studies of OXCBZ under High Vacuum

The QBox platform provides opportunities for greater control to be obtained over the vapour deposition process when compared to utilising the heating plate setup described in section 3.2.4.1. It allows parameters such as pressure, deposition rate and thickness of a deposited material to be monitored in real time (section 3.2.4.3) enabling investigation of the impact of these factors on the resultant form. Physical vapour deposition of OXCBZ under high-vacuum conditions was carried out using

silver foil substrates with slow, medium and fast deposition rates described in Table 4.14 in an attempt to check for the formation of OXCBZ III and the unidentified phase presented in Figure 4.24 under high-vacuum deposition conditions and assess the effect on different deposition rate profiles on the polymorphic outcome of the deposition process. The rate of physical vapour depositon has been found to direct polymorphism in the crystallisation of organic materials (Benvenuti et al., 2018), hence the interest in exploring its potential impact on the formation of different polymorphs of OXCBZ from the vapour phase.

All of the experiments using the QBox platform resulted in polycrystalline films identified as OXCBZ form I by Raman analysis (Figure 4.26). The morphology of the experimental samples prepared with the QBox was assessed with SEM and the micrographs obtained revealed the presence of dendritic form I crystals (Figures 4.27 - 4.29).

Table 4.14: Overview of physical vapour deposition studies of OXCBZ conducted using the QBox 450 system.

Average Deposition Rate (Å/s)	Estimated Film Thickness Derived from QCM (µm)	Average Deposition Temperature (°C)	Distance between Ag Substrate & Starting Material (cm)	Polymorphic Outcome
2 (slow)	1.2	140	14	Form I
2.8 (medium)	1.2	137	14	Form I
5.4 (fast)	1.2	154	14	Form I

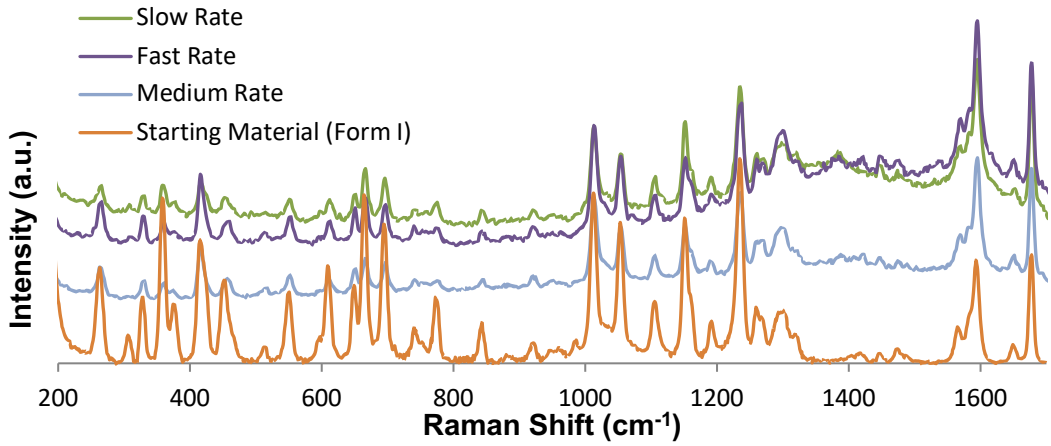

Figure 4.26: Overlay of Raman spectra of OXCBZ films grown on silver foil substrates using different deposition rates with a reference spectrum for form I OXCBZ powder sourced from Sigma-Aldrich UK.

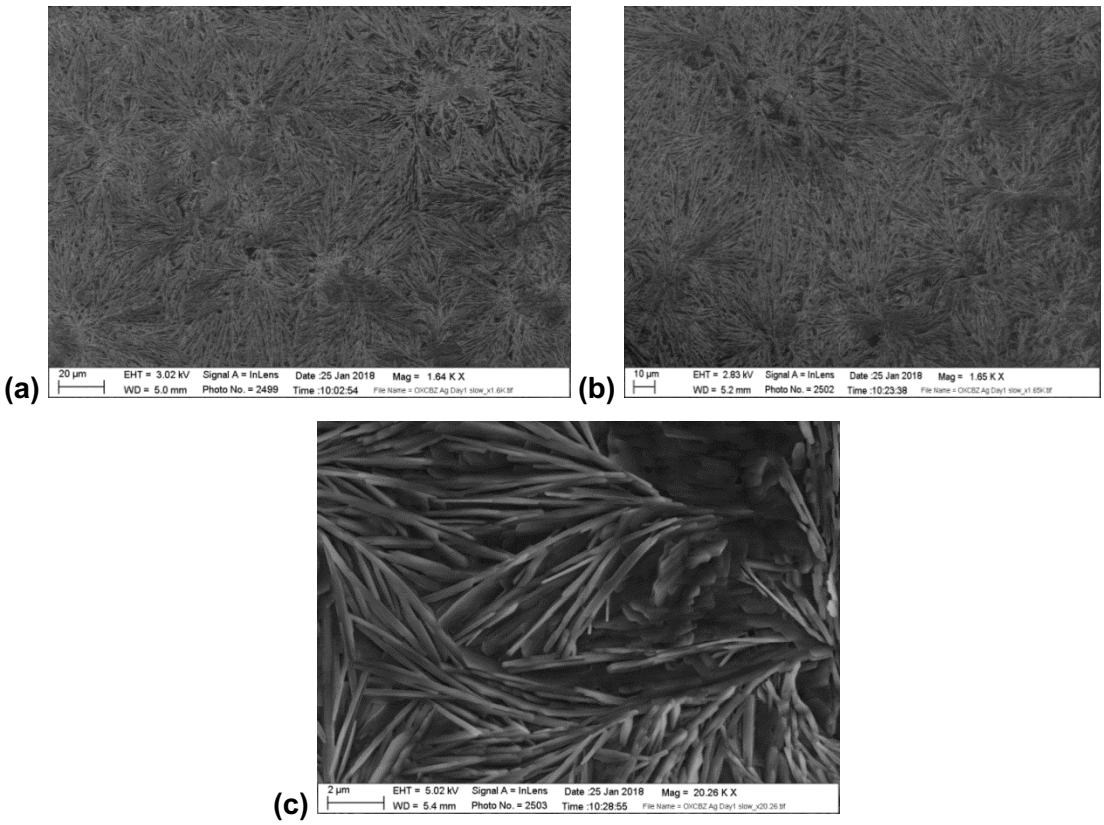

Figure 4.27: SEM micrographs of OXCBZ I crystals grown on silver foil using a slow deposition rate of 2 Å/s. The scale bar is 20 µm for (a), 10 µm for (b) and 2 µm for (c).

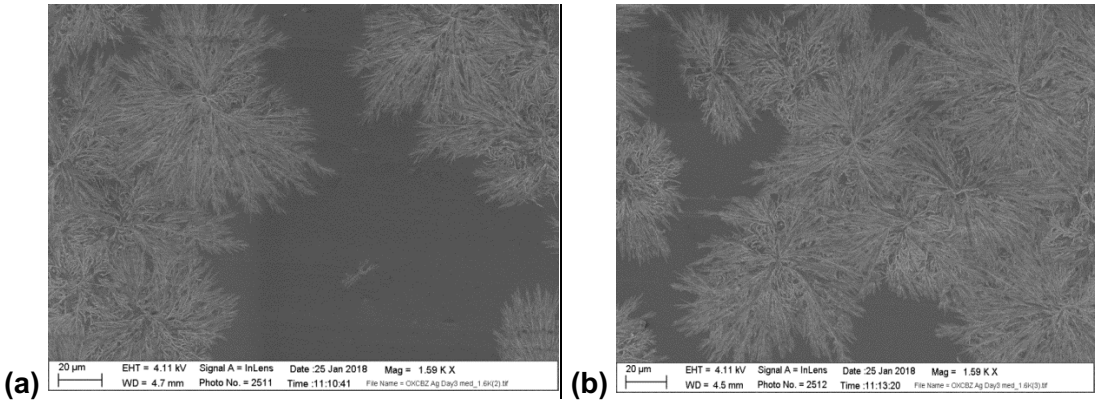

Figure 4.28: SEM micrographs of OXCBZ I crystals grown on silver foil using a medium deposition rate of 2.8 Å/s. The scale bar is 20 µm for both images.

(a) 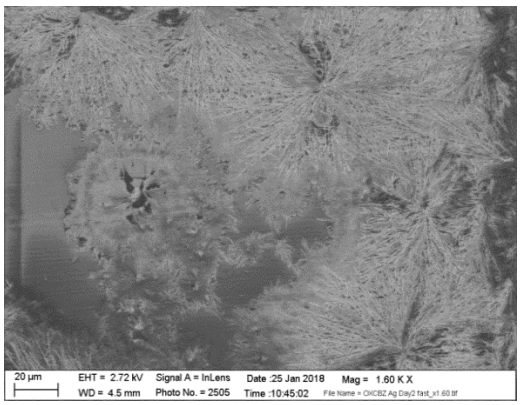

(b) 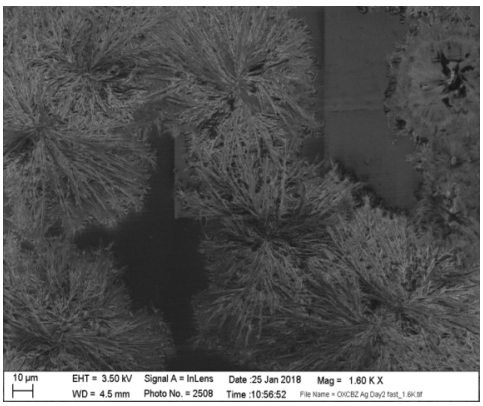

Figure 4.29: SEM micrographs of OXCBZ I crystals grown on silver foil using a fast deposition rate of 5.4 Å/s. The scale bar is 20 µm for (a) and 10 µm for (b).

The results obtained for the vapour deposition of OXCBZ onto silver foil under high vacuum clearly suggest that deposition rate does not affects polymorphic outcome, as all of the rates explored ended up crystallising the thermodynamically stable form I. Because of the inability to monitor deposition rate profiles using the heating plate method used for vapour deposition under atmospheric conditions, a direct comparison between the influence of rate on the polymorphic outcome induced by the two distinct experimental setups used for deposition purposes is unfortunately not possible. Whilst starting powder heating profiles similar to the ones employed in heating plate experiments were used for the QBox studies, OXCBZ III was not found to crystallise on the experimental substrates investigated and form I was consistently present in all of the samples prepared regardless of the deposition rate and temperature profiles employed.

The absence of OXCBZ III in the polycrystalline samples prepared using the QBox could possibly be attributed to the difference in temperature of the experimental substrates during the deposition process (Firsich, 1984; Karpinska et al., 2013; Lin et al., 2016), which was ambient for the QBox experiments but non-ambient for the studies conducted using the heating plate. The distance between the starting material and the experimental surfaces in the QBox experiments could also have played a role in facilitating the nucleation of form I over other forms of OXCBZ (Solomos et al., 2018).

4.4.6 Structure Determination from Powder Diffraction (SDPD) of OXCBZ Form III

For SDPD purposes, capillary XRPD data corresponding to a highly phase-pure sample of OXCBZ III, obtained via evaporative crystallisation from 50:50 ethanol/ toluene, were best indexed to a hexagonal unit cell (Table 4.15) using *DICVOL04* in *DASH*. After performing a Pawley refinement of the data in the *R*-3 space group which was selected on the basis of corresponding to CSP structure a96, the predicted candidate anticipated to be the most thermodynamically feasible, a z-matrix was constructed using a96 to provide an ideal geometry. This was used in subsequent simulated annealing runs in the programme *DASH* (David et al., 2006). The positions and spatial orientations of the OXCBZ molecules in the unit cell as well as the flexible torsion angle previously shown in Figure 4.1 were varied using the Mogul Distribution Bias (Kabova et al., 2017b). Several trial structure solutions from different DASH runs exhibited very similar packing arrangement. A representative structure from trial solutions was refined by the Rietveld method (Rietveld, 1967 & 1969) using *TOPAS* (Coelho, 2018) and the residual values obtained from the refinement were R_{wp} = 6.75%, R_p = 5.52% with refined unit cell parameters a = 35.974 (2) Å and c = 5.291 (5) Å. To ensure sensible molecular geometries, standard restraints recommended by *DASH* were applied to bond lengths, bond angles, and for planar groups in the final Rietveld cycle. A closer inspection of the final refined structure revealed the structure was chemically sensible and exhibited plausible hydrogen bond patterns and sensible intermolecular interactions.The unit cell packing arrangement in the Rietveld-refined crystal structure of OXCBZ III (Figure 4.30) and corresponding set of crystallographic data are presented in Figure 4.31 and Table 4.16. The packing arrangement of form III consists of a ring motif of the $R_6^6(72)$ type hydrogen-bonded arrangement formed by the carbonyl oxygen of the 7-membered ring and one of the N-H donors of the amide groups. This comprises alternating $R_2^2(8)$ and $C_1^1(4)$ hydrogen bonding arrangements along the 3_1 screw axis which extend the structure infinitely along the crystallographic *c* axis. A comparison of the unit cell parameters of OXCBZ III, predicted structure a96, CBZ II and CYT I is presented in Table 4.17 and indicates that all four structures exhibit an isostructural relationship. Overlays of the molecular conformations in OXCBZ forms I – III are presented in Figure 4.32.

Table 4.15: Best indexing solution of OXCBZ form III XRPD pattern as derived from *DICVOL04* in *DASH*.

Crystal System	*a* (Å)	*b* (Å)	*c* (Å)	α (°)	β (°)	γ (°)	Volume (Å^3)	M (16)	F (16)
Hexagonal	35.9554	35.9554	5.2915	90	90	120	5924.28	12.9	23.5

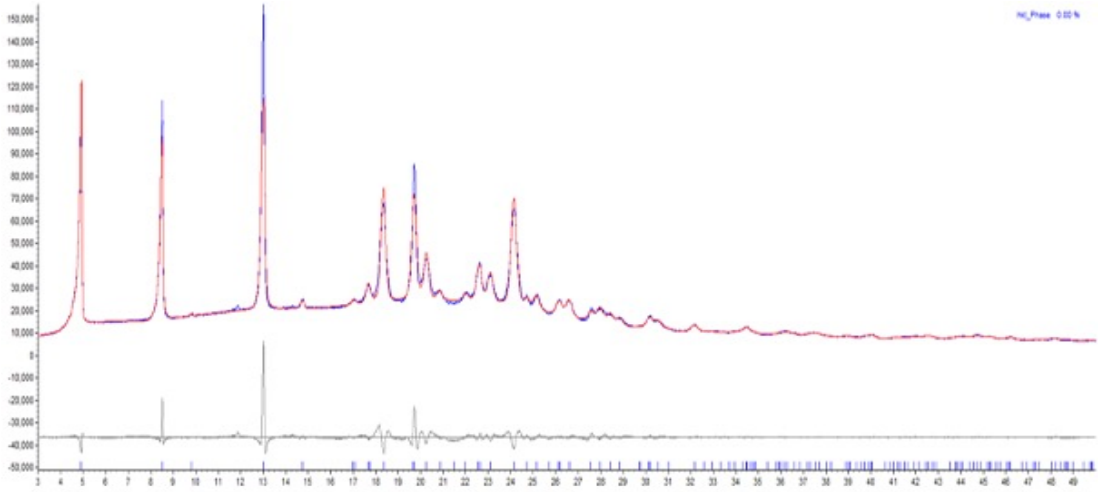

Figure 4.30 Plot from Rietveld refinement of the final fit achieved for the structure returned by DASH simulated annealing against the capillary transmission XRPD data for OXCBZ form III. the blue pattern corresponds to experimentally observed data (y_{obs},) the red pattern represents calculated data (y_{calc}) and the grey pattern indicates differences between the measured and calculated data [(y_{obs} - y_{calc})/σ(y_{obs})]. The blue tick marks correspond to peak positions indicative of the OXCBZ III structure.

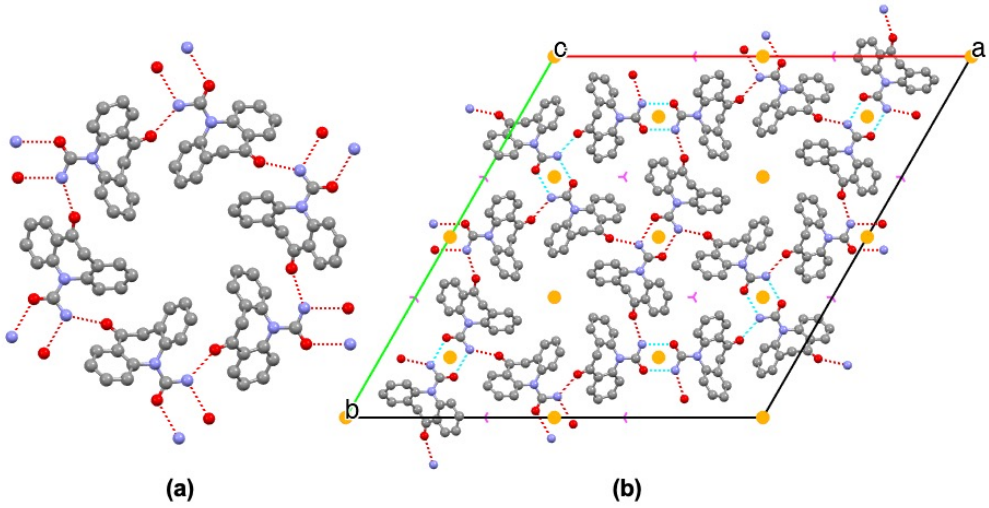

Figure 4.31: Hydrogen bonding motif (a) and crystal packing arrangement viewed down the crystallographic *c* axis (b) of OXCBZ form III. Yellow features in the packing diagram indicate the presence of inversion centres whilst pink features are indicative of 3_1 screw axes. Hydrogen atoms are omitted for clarity.

Table 4.16: Overview of crystallographic data for OXCBZ form III, generated at room temperature conditions.

OXCBZ Form III	
Chemical formula	$C_{15}H_{12}N_2O_2$
Crystal system	Hexagonal
***a* (Å)**	35.974 (2)
***b* (Å)**	35.974 (2)
***c* (Å)**	5.2917 (5)
α (°)	90
β (°)	90
γ (°)	120
Space group	*R*-3
Volume (Å^3)	5930.66
Z	18
Radiation type	Monochromated Cu $K\alpha_1$ (λ = 1.54060 Å)

Table 4.17: Comparison of the unit cell parameters of OXCBZ form III, predicted OXCBZ structure a96, CBZ form II and CYT form I.

Structure	Space Group	*a* (Å)	*b* (Å)	*c* (Å)	α (°)	β (°)	γ (°)	Volume (Å^3)
OXCBZ Form III (Experimental)	*R*-3	35.974 (2)	35.974 (2)	5.2917 (5)	90	90	120	5930.66
OXCBZ CSP a96	*R*-3	36.0565	36.0565	5.3017	90	90	120	5969.16
CBZ Form II (CBMZPN03)	*R*-3	35.454 (3)	35.454(3)	5.253 (1)	90	90	120	5718.32
CYT Form I (SOGLEG)	*R*-3	33.9078 (10)	33.9078 (10)	5.6754 (2)	90	90	120	5651.01

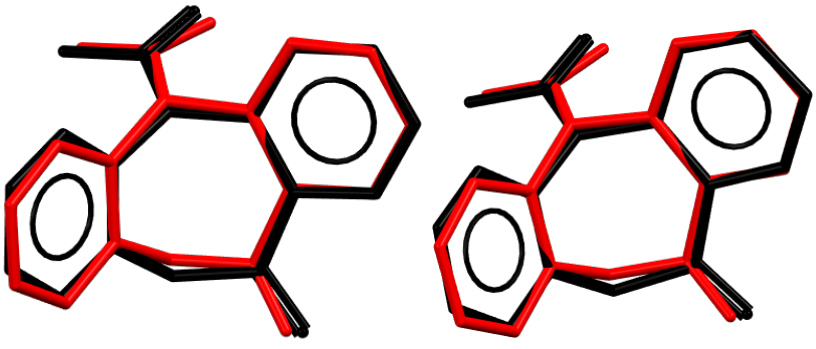

(a) RMSD = 0.2402 Å (b) RMSD = 0.2501 Å

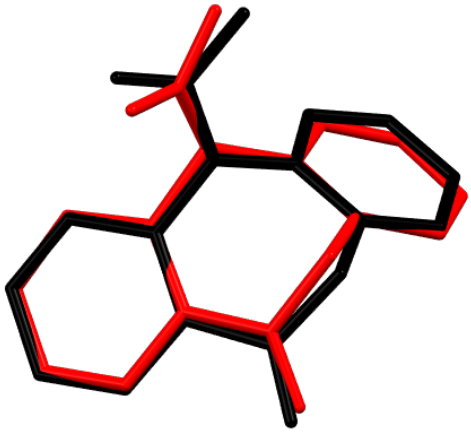

(c) RMSD = 0.3090 Å

Figure 4.32: Overlay of molecular conformation of Rietveld-refined OXCBZ form III (red structure) with OXCBZ form I (a), OXCBZ form II (b) and predicted CSP structure a96 (c).

4.5 Summary

A number of solvent-based and solvent-free screening approaches with and without substrates were explored for investigating the solid-state landscape of OXCBZ. A CSP study assisted in identifying suitable models for the crystal structure of the metastable form III by comparing the predicted models with reference XRPD data for this polymorph which were obtained from the literature. Using the predicted CSP structures as a guide for experimental screening, robust methodologies enabled the metastable OXCBZ III to be reliably crystallised by fast evaporation from solution and physical vapour deposition onto metallic substrates of various topographies under atmospheric conditions. In solution-crystallisation experiments, the most phase-pure samples of form III were isolated from evaporation of ethanol/toluene binary mixtures.

Whilst OXCBZ III was reliably prepared using both solvent evaporation and physical vapour deposition under atmospheric conditions and no substrate-induced templating effect was found to direct its crystallisation, isolating high quality crystals of size suitable for structural characterisation with SC-XRD was not possible. Moreover, the overwhelming majority of solvents that yielded form III in the experimental screen additionally crystallised the thermodynamically stable form I under the conditions employed, further complicating the process of structure determination. Physical vapour deposition studies of OXCBZ pursued under high vacuum and controlled conditions only produced the thermodynamically stable form I of the compound with no experimental evidence for the formation of metastable form III. The inability of the controlled experiments under high vacuum to crystallise OXCBZ III can likely be attributed to a number of experimental factors, including the ambient temperature of the experimental substrates during OXCBZ deposition and the distance between the substrates and the starting material that was used for deposition purposes. These experimental factors differed significantly from those employed in vapour deposition experiments performed under atmospheric conditions and further studies are required to understand how the deposition temperature and distance affect polymorphism in vapour-grown OXCBZ crystals.

Following extensive screening efforts, polycrystalline samples of OXCBZ III comprising only limited amounts of form I were obtained from ethanol/toluene mixtures. DSC/TGA analysis conducted for these samples provided the first piece of experimental evidence for solvent inclusion in the crystal structure of form III. The polycrystalline samples were further utilised to collect transmission capillary XRPD data for SDPD. The structure of form III was successfully solved using simulated annealing and refined with the Rietveld method. The final structure emerging from the refinement was found to be in good agreement with predicted structure a96 from the CSP landscape of OXCBZ. OXCBZ III exhibits an isostructural relationship to CBZ form II and CYT form I, providing another example wherein polymorphic forms within the CBZ family of compounds share close structural similarity (Figure 4.33). OXCBZ III, CBZ II and CYT I all crystallise in the *R*-3 space group and comprise void channels capable of accommodating solvent molecules of suitable size. However, the fact that OXCBZ III was successfully isolated in this work by means of physical vapour deposition, a solvent-free crystallisation approach, indicates that the presence of a solvent in the void channels of form III is not a requirement for its nucleation and subsequent growth.

GI dissolution studies showed that, as expected, OXCBZ III dissolves more readily compared to the commercially available OXCBZ I, with an increase in the order of ≈ 2.6 noted during the early stages of the dissolution process. This suggests that the metastable form III could potentially be used to improve the oral bioavailability of OXCBZ formulations during the pharmaceutical manufacturing process.

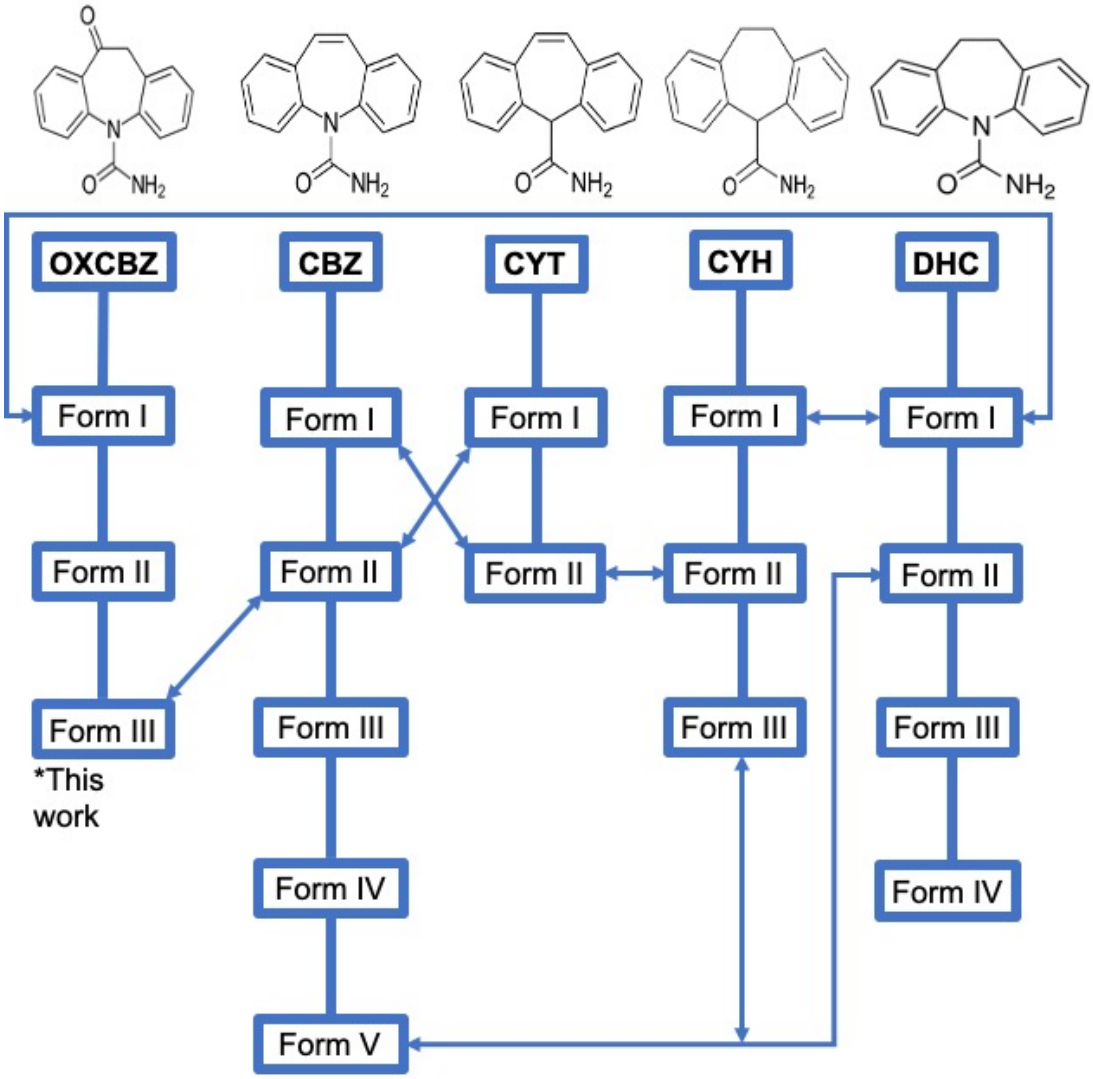

Figure 4.33: Overview of polymorphism in the CBZ family of compounds, based on the schematic diagram by Arlin et al., 2011. Double arrows indicate isostructurality between different polymorphs.

Chapter 5: Investigation of the Emergence of Twisted Crystals in Oxcarbazepine

5.1 Introduction

Polymorphism is the ability of a compound to exist in different crystal packing arrangements (Bernstein, 2002; Brittain, 2012). Polymorphism is ubiquitous in nature and has been reported in biological systems, food products, pigments, agrochemical product as well as pharmaceuticals (Cruz-Cabeza and Bernstein, 2014; Cruz-Cabeza et al., 2015; Price et al., 2016). The polymorphic form, crystal shape and size of crystals are critically depended on the kinetic pathway and the phase transformations that occur during crystallisation. However, understanding of the crystal nucleation and growth mechanisms in small organic compounds is very limited. Whilst the monomer-by-monomer, addition-based classical nucleation theory (CNT) is still one of the most commonly used models and gives reasonable prediction of the nucleation rates of thermodynamic phases (Volmer and Weber, 1926; Becker and Döring, 1935; Giuffre et al., 2013; Petsev et al., 2003), it fails to provide a quantitative/qualitative interpretation of some of the experimentally observed phenomena occurring during the crystallisation process (Habraken et al., 2013). For instance, CNT does not take into consideration the fact that some polymorphic systems do not necessarily nucleate to form the most stable phase but pass through a path where the free energy barrier is minimum, implying the existence of multiple metastable polymorphic forms during crystallisation as described by Ostwald's rule of stages (Ostwald, 1897). Another example is that of the crystallisation process observed in several biominerals, where it was experimentally demonstrated that these systems crystallise via amorphous precursors (Jin et al., 2018). These characteristics have been attributed to non-classical crystal growth processes (De Yoreo et al., 2015) which are distinct from those predicted by the traditional (classical) models. These non-classical models mostly introduce an additional step or steps that precede the nucleation event (Oxtoby, 1998; Vekilov, 2004; De Yoreo et al., 2015). In recent years, several researchers have attempted to shed light on possible intermediate stages during the early stages of crystallisation while studying proteins (Vekilov, 2004) colloids (Auer and Frenkel, 2001; Anderson and Lekkerkerker, 2002), inorganic compounds (Wallace et al., 2013; Nielsen et al., 2014) and small organic compounds (Warzecha et al., 2017). The identification of intermediate states would provide new insights into the transformation kinetics during crystallisation and ultimately lead to better overall control of the crystallisation process.

In the present chapter, it is demonstrated that oxcarbazepine (OXCBZ) form III follows an unconventional crystallisation process resulting in the formation of twisted crystals.

Molecular materials are occasionally known to crystallise in the form of structures exhibiting unusual morphologies (Figure 5.1), including, but not limited to, bent, scrolled and twisted architectures (Lehmann, 1888; Xiong et al., 2011; Shtukenberg et al., 2014c; Commins et al., 2019).

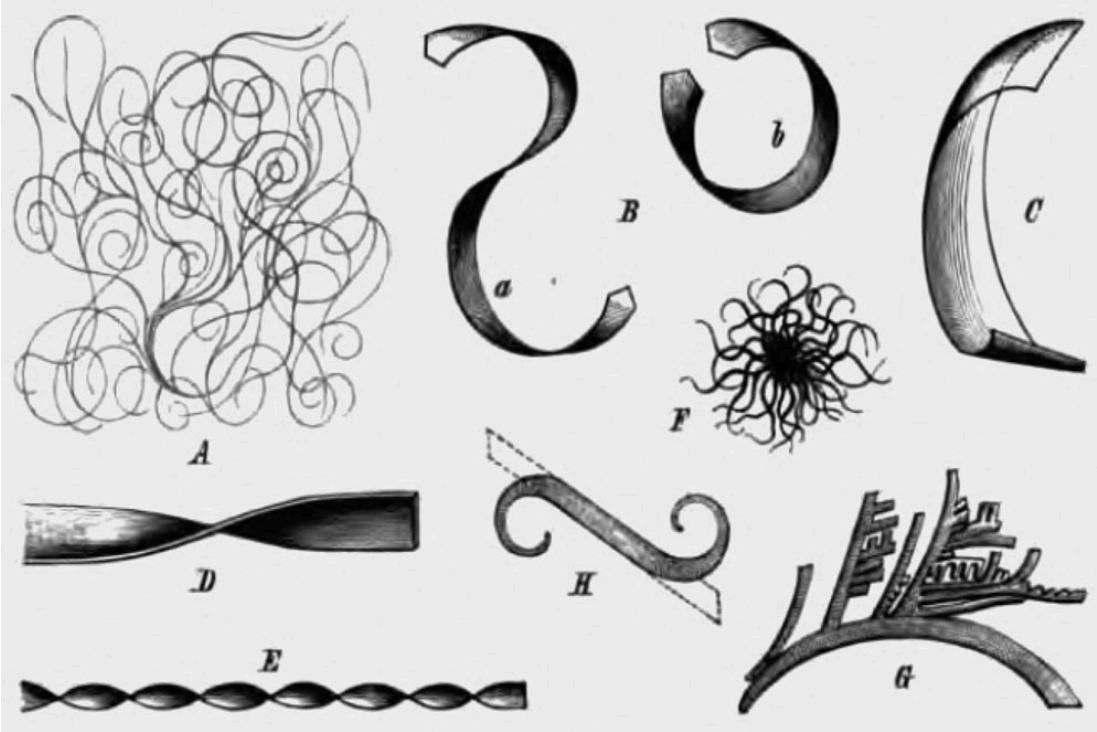

Figure 5.1: Examples of experimentally observed bent, scrolled and twisted crystals (reproduced from Lehmann, 1888).

The existence of molecular materials with twisted morphologies is well-documented and dates back to the early 19th century (Sowerby, 1811). Bernauer claimed through his studies that over 25% of all organic compounds are capable of crystallising in the form of twisted architectures (Bernauer, 1929), a claim that has been verified in recent years (Shtukenberg at al., 2011 & 2014c). Molecular crystals of any space group symmetry can exhibit twisted morphology (Shtukenberg and Kahr, 2014a) and twisting is one of the most commonly occurring growth-based deformation mechanisms (Shtukenberg et al., 2015). Several examples of pharmaceutical compounds exhibiting twisted crystal morphologies have been reported. These include aspirin, paracetamol, ibuprofen and naproxen, four of the most readily available over-the-counter analgesics, all of which have been found to yield twisted crystals under appropriate experimental conditions (Cui et al., 2013; Kahr et al., 2019;

Shtukenberg et al., 2019). Previously proposed mechanisms of twisting in molecular crystals are generally divided into three categories (Shtukenberg at al., 2014c): (1) defects forming through various crystal growth mechanisms and mediating deformation; (2) concentration, electrical, mechanical, and/or temperature fields creating a mechanical force that can act on a growing crystal; (3) internal compositional and structural inhomogeneities resulting in lattice mismatch and the generation of a mechanical moment at the growth front. Despite the fact that all of the aforementioned mechanisms may be applicable under certain conditions, the third has been identified as the most common.

The growth mechanism of twisted crystals of OXCBZ III is detailed in the work presented in this chapter. As discussed in Chapter 4, the twisted crystals of OXCBZ III can be obtained by both solution-based crystallisation and physical vapour deposition methods. The crystal structure of OXCBZ III determined from experimental X-ray powder diffraction (XRPD) data is presented in Section 4.4.6. Whilst the hydrogen-bonding arrangement in OXCBZ III is unique to this form, form III exhibits isostructurality to carbamazepine (CBZ) form II (Cruz-Cabeza et al., 2007b; Fabbiani et al., 2007; Zhong et al., 2019) and cytenamide (CYT) form I (Florence et al., 2008a). These isostructural polymorphs of CBZ and CYT were also crystallised in the work described herein to compare their morphology against the twisted crystal morphology of OXCBZ III. By monitoring the vapour deposition experiments at different time points using off-line scanning electron microscopy (SEM) analysis, it is demonstrated experimentally that the crystallisation of vapour-grown OXCBZ III follows an unconventional vapour-condensate-solid growth mechanism (Ye et al., 2018). Direct experimental evidence for the origin of twisting in vapour-grown OXCBZ III crystals is presented. The SEM analysis indicated the presence of adjacent nanocrystals, nucleating within amorphous condensate aggregates and twisting spontaneously as they grew to form twisted fibres. Additionally, in the absence of suitable experimental data, theoretical models are proposed herein which suggest that lattice mismatch could be the possible reason for twisting in solution-grown crystals of OXCBZ III.

5.2 Oxcarbazepine (OXCBZ)

The molecular structure of OXCBZ is shown in Figure 5.2 Full details of OXCBZ and its polymorphic properties are provided in section 4.2. Information on the experimental structure of form III is provided in section 4.4.6.

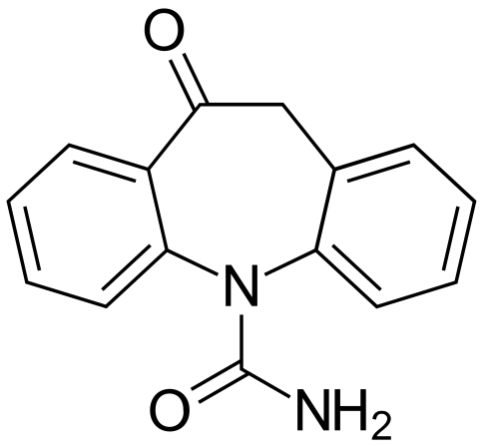

Figure 5.2: Molecular structure of OXCBZ ($C_{15}H_{12}N_2O_2$; molecular weight: 252.268 g/mol).

5.3 Carbamazepine (CBZ)

CBZ (IUPAC name: 5H-dibenzo[b,f]azepine-5-carboxamide), marketed by Novartis Pharmaceuticals under the brand name Tegretol®, is a prominent anticonvulsant and antiepileptic drug (Brewster et al., 1991; Elqidra et al., 2004; Martins et al., 2012) that is practically insoluble in water (solubility of 120 µg/mL) and falls under Class II of the BCS (Nair et al., 2002; Hemenway et al., 2010). The molecular structure of CBZ is shown in Figure 5.3.

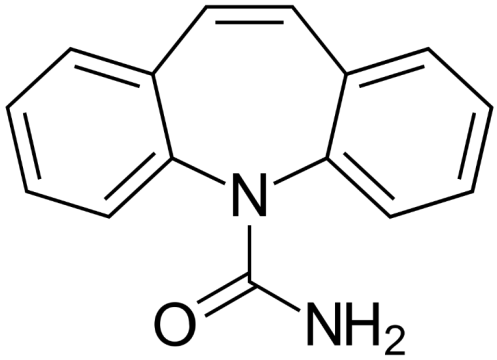

Figure 5.3: Molecular structure of CBZ ($C_{15}H_{12}N_2O$, molecular weight: 236.269 g/mol).

The polymorphism of CBZ has been studied extensively over the years to discover new forms and understand the structural properties that underpin the solid-state landscape of CBZ (Lang et al., 2002b; Grzesiak et al., 2003; Elqidra et al., 2004;

Lui et al., 2009; Arlin et al., 2011). There are five known anhydrous polymorphic forms of CBZ reported in the literature and their structural information is summarised in Table 5.1. The unit cell packing arrangement in CBZ form II, which is isostructural to OXCBZ III and CYT I (Table 5.2), is shown in Figure 5.4. In addition to the five reported anhydrous polymorphs, several solvates, hydrates, and cocrystals of CBZ have been reported (Murphy et al., 2002; Fleischman et al., 2003; Harris et al., 2005; Florence et al., 2006; Childs et al., 2008; Johnston et al., 2008; Porter III et al., 2008; Musumeci et al., 2011; Arora et al., 2013). Out of the known anhydrous polymorphs of CBZ, the monoclinic form III, which crystallises in $P2_1/n$, is known to be the thermodynamically stable form at ambient conditions (El Hassan et al., 2013). Whilst forms I-IV all comprise amide-amide hydrogen-bonding interactions (Grzesiak et al., 2003), CBZ V crystallises via catemeric N-H…O = C hydrogen boding interactions (Arlin et al., 2011).

Table 5.1: Overview of crystallographic data for the five known polymorphs of CBZ.

CBZ Polymorph	Space Group	Z/Z'	*a* (Å)	*b* (Å)	*c* (Å)	α (°)	β (°)	γ (°)	Volume (Å^3)
Form I (CBMZPN13)	*P*-1	8/4	5.186 (1)	20.576 (2)	22.241 (3)	84.194 (8)	87.976 (7)	85.105 (8)	2351.44
Form II (CBMZPN03)	*R*-3	18/1	35.454 (3)	35.454 (3)	5.253 (1)	90	90	120	5718.32
Form III (CBMZPN27)	$P2_1/n$	4/1	7.494 (10)	11.064 (14)	13.804 (15)	90	92.914 (11)	90	1143.12
Form IV (CBMZPN12)	*C*2/*c*	8/1	26.609 (4)	6.927 (10)	13.957 (2)	90	109.702 (2)	90	2421.93
Form V (CBMZPN16)	*Pbca*	8/1	9.125 (5)	10.452 (5)	24.822 (11)	90	90	90	2367.25

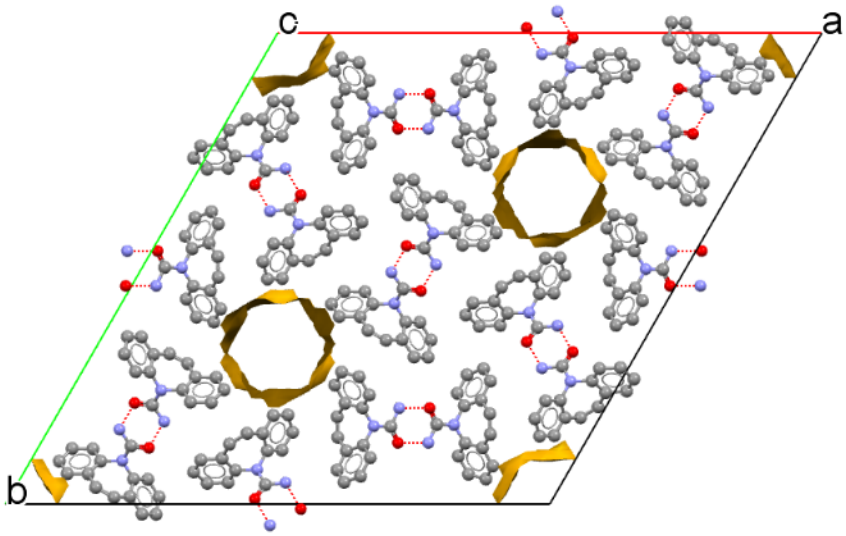

Figure 5.4: Unit cell packing arrangement in CBZ form II, viewed down the crystallographic *c* axis. Dashed red lines indicate the presence of hydrogen-bonding interactions. Yellow surfaces indicate the presence of void channels which occupy 9.1% of the total cell volume.

5.4 Cytenamide (CYT)

CYT (IUPAC name: 5H-dibenzo[a,d]cyclo-hepta-triene-5-carboxamide) is a structural analogue of CBZ and OXCBZ and its molecular structure is depicted in Figure 5.5. CYT is known to crystallise in two anhydrous polymorphs (Florence et al., 2008a) and form solvates readily with acetic acid (Johnston et al., 2008a), butyric acid (Johnston et al., 2008b), trifluoroacetic acid (Johnston et al., 2008d), formic acid (Johnston et al., 2008e) and 1,4-dioxane (Johnston et al., 2008c).

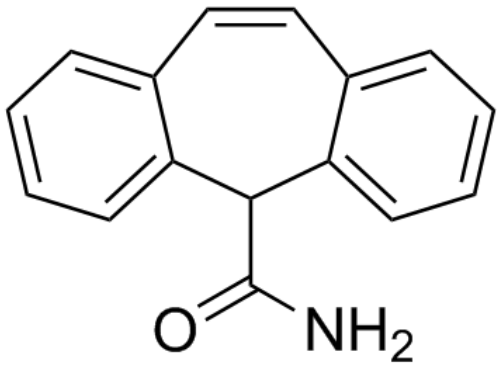

Figure 5.5: Molecular structure of CYT ($C_{16}H_{13}NO$, molecular weight: 235.28 g/mol).

The anhydrous form I of CYT (Figure 5.6, CSD Refcode: SOGLEG) crystallises in the trigonal space group *R*-3 with cell parameters *a* = *b* = 33.9078 (10) Å, *c* = 5.6754 (2) Å, α = β = 90° and γ = 120° and is isostructural to OXCBZ III and CBZ II (Table 5.2). Anhydrous form II of CYT (CSD Refcode: SODNOP) crystallises in triclinic space group *P*-1 with cell parameters *a* = 5.8100 (2) Å, *b* = 19.6315 (5) Å, *c* = 21.7087 (6) Å, α = 85.918° (2), β = 86.164° (2), γ = 84.482° (2) and is isostructural to CBZ form I and cyheptamide form II (Florence et al., 2008b).

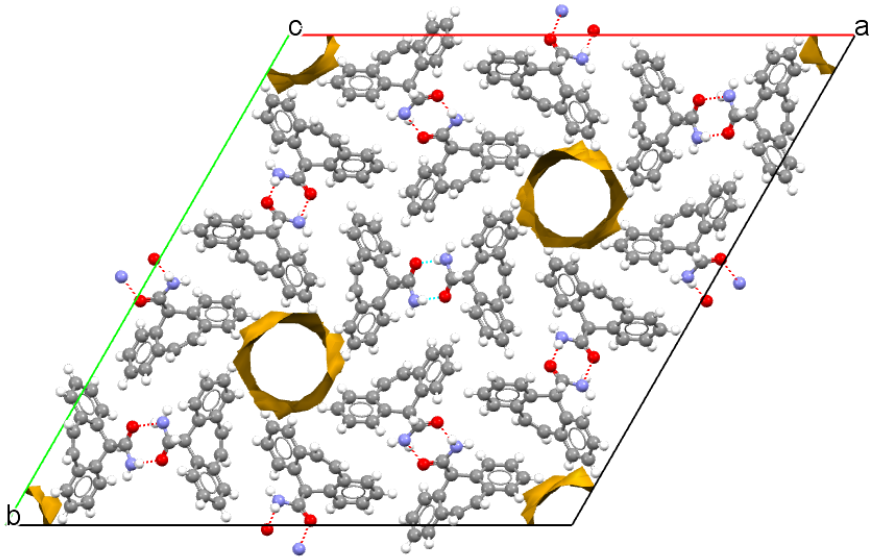

Figure 5.6: Unit cell packing arrangement in CYT form I, viewed down the crystallographic *c* axis. Dashed red and cyan lines indicate the presence of hydrogen-bonding interactions. Yellow surfaces indicate the presence of void channels which occupy 6.6% of the total cell volume.

Table 5.2: Overview of crystallographic data for OXCBZ form III, CBZ II and CYT I.

Structure	Space Group	*Z*/*Z*'	*a*, *b* (Å)	*c* (Å)	α, β (°)	γ (°)	Cell Volume (Å^3)	Void Volume (Å^3)	Void Volume (%)
OXCBZ III (Experimental)	*R*-3	18/1	35.974(2)	5.292(5)	90	120	5930.66	270.32	4.6
CBZ II (CBMZPN03)	*R*-3	18/1	35.454(3)	5.253(1)	90	120	5718.32	522.70	9.1
CYT I (SOGLEG)	*R*-3	18/1	33.907(9)	5.675(2)	90	120	5651.01	375.53	6.6

5.5 Materials and Methods

5.5.1 Materials

OXCBZ, CBZ and CYT powders were used as starting materials for the preparation of samples investigated in the studies described herein. Details of the starting powders for all three compounds are provided in section 3.1. Details of the substrates employed experimentally are also provided in section 3.1.

5.5.2 Methods

The substrates utilised experimentally were characterised using the methods described in section 3.2.3. Visualisation of known polymorphs of OXCBZ, CBZ and CYT was performed using the methodology outlined in sections 3.2.1 and 3.2.2. Preparation of vapour-grown OXCBZ, CBZ and CYT crystals was carried out using the physical vapour deposition protocol described in section 3.2.4.1. Solution-grown crystals of OXCBZ, CBZ and CYT were prepared using the Crissy® platform (section 3.2.6.2) by fast evaporation of 50:50 v/v ethanol/toluene mixtures at a temperature of 50°C and with no agitation applied. For OXCBZ crystal preparation, a 67:33 v/v ethanol/toluene proportion was additionally used. Sample characterisation was performed using XRPD methods (section 3.2.7.1), differential scanning calorimetry (DSC; section 3.2.7.3), Raman spectroscopy (section 3.2.7.4), atomic force microscopy (AFM; section 3.2.7.6) SEM (section 3.2.7.7), time-of-flight secondary ion mass spectrometry (ToF-SIMS; section 3.2.7.8) and high performance liquid chromatography-mass spectrometry (HPLC-MS; section 3.2.7.9)

5.6 Results and Discussion

5.6.1 Scanning Electron Microscopy (SEM) Analysis

5.6.1.1 Solution-Grown Crystals of OXCBZ Form III

Representative SEM micrographs of twisted OXCBZ III crystals grown via solution crystallisation are shown in Figure 5.7. Whilst several structures exhibiting twisted morphology were identified through SEM analysis (refer to section 3.2.7.7.1), straight crystals of form III were found to be readily present as well and generally outnumbered the twisted crystals. Further analysis of the SEM micrographs using *ImageJ* (refer to section 3.2.7.7.2) additionally indicated that the cross-section size and length of the solution-grown crystals were in the range ≈ 160 – 540 nm and ≈ 1.6 – 9.5 μm

respectively. Figure 5.8a shows an annotated diagram indicating the measured cross-section size for a number of crystals. Whilst the cross-section size and length were found to change considerably between the measured crystals, uniform cross sections along the length were consistently observed. It is shown in Figure 5.7a that multiple twisted crystals appear to emerge from the same central bundle, suggesting that the solution-grown OXCBZ III crystals are likely not single crystals but structures that can best be described as either helical polycrystalline aggregates or polycrystalline fibres, wherein crystals are wrapped around each other to form periodic multihelical architectures. Interestingly, the SEM images also indicated that some of the twisted crystals of form III were bent along their respective lengths. Measuring the angle of twist at different positions along several crystals showed that the solution-grown crystals are uniformly twisted over their respective lengths, suggesting that they exhibit a pitch. The pitch of the crystals, defined as the length corresponding to a rotation of 180°, was calculated using Equation 5.1 and a schematic depiction is presented in Figure 5.8b. In Equation 5.1, *P* is indicative of the pitch, *h* is the cross-section size, α is the angle of twist and *cot* corresponds to the cotangent of the angle of twist.

$$P = \pi h \; x \; cot \; \alpha \qquad \textbf{(Equation 5.1)}$$

A plot of *h* against *P* of solution-grown OXCBZ III crystals is shown in Figure 5.9 and *P* was found to to vary between 3 - 7 μm and increase in linear fashion as *h* increased. This behaviour of solution-grown OXCBZ III is intuitive and in alignment with that of other twisted crystals reported in the literature (Shtukenberg et al., 2014c & 2015). It can be envisaged that increased thickness of these crystals leads to increased rigidity capable of resisting the twist moment applied to the crystals (Shtukenberg et al., 2014c).

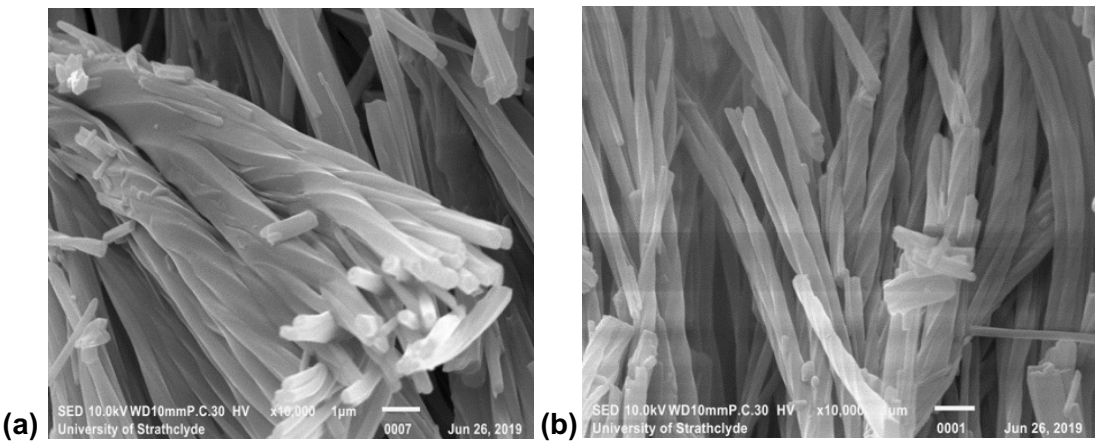

Figure 5.7: Representative SEM micrographs of solution-grown OXCBZ III crystals prepared via fast evaporation from 67:33 v/v ethanol/toluene mixture. The scale bar is 1 μm for both micrographs.

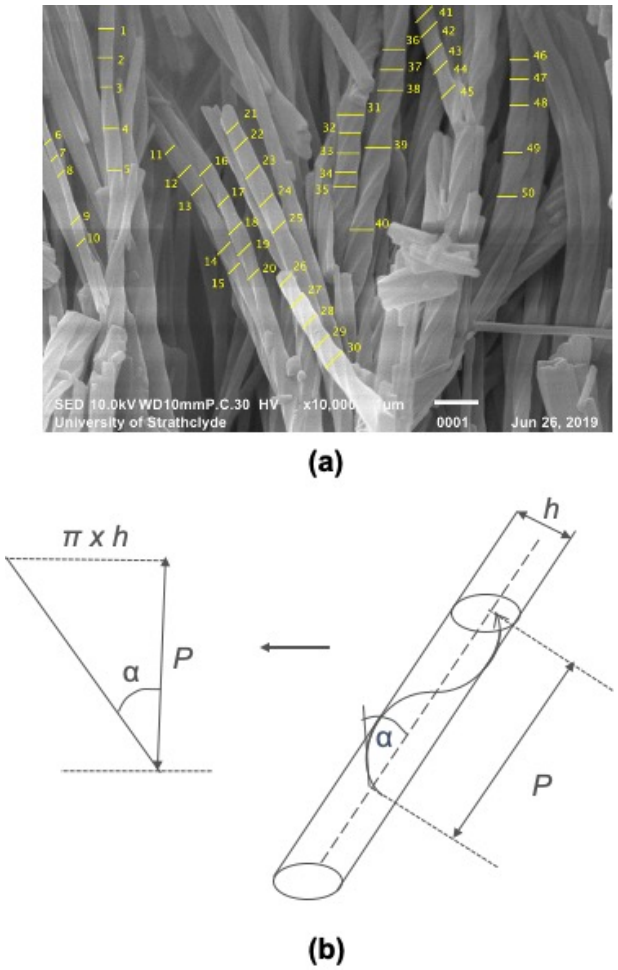

Figure 5.8: (a) Annotated SEM micrograph showing measured cross section *h* for solution-grown OXCBZ III crystals and (b) schematic diagram based on Fang et al. (Fang et al., 2015) indicating how the pitch *P* of the crystals was measured. In (b), α is the angle of twist.

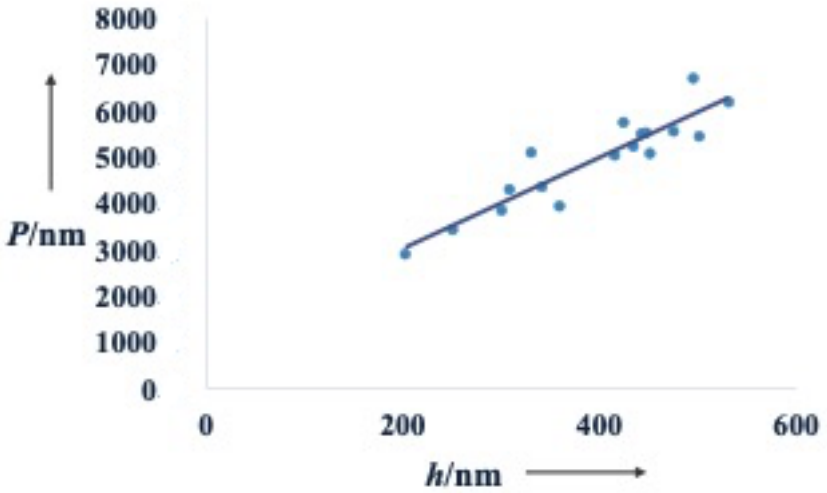

Figure 5.9: Correlation between pitch (*P*) and cross-section size (*h)* in solution-grown crystals of OXCBZ III.

5.6.1.2 Twisted Crystals of OXCBZ Form III from Physical Vapour Deposition

SEM micrographs of vapour-grown OXCBZ III crystals prepared on silver foil (refer to section 3.2.7.7.1) are presented in Figure 5.10. Analysis of several crystals obtained from the physical vapour deposition experiments showed that the crystals exhibited a cross-section size in the range of ≈ 60 – 650 nm, generally similar to that observed for the solution-grown OXCBZ III crystals. Moreover, the cross-section size of the vapour-grown crystals was found to be nearly constant along their respective lengths, indicating further similarity with the twisted crystals prepared via solution crystallisation. In samples prepared from the vapour phase, twisted crystals of OXCBZ III significantly outnumbered the non-twisted crystals found to be present on silver foil, suggesting that solvent-solute interactions influenced the emergence of twisted crystals from solution. SEM analysis following prolonged vapour deposition (refer to Figure 5.17a, section 5.6.2) revealed the occurrence of twisted strands splitting into multiple crystals in all directions, suggesting that, similarly to the solution-grown crystals, vapour-grown OXCBZ III crystals are likely not single crystals but can also be described as helical polycrystalline aggregates or polycrystalline fibres comprising multiple strands. Whilst the solution- and vapour-grown crystals were found to be similar with regards to cross-section size, the observed twist in vapour-grown crystals of OXCBZ III was found to be different relative to that noted for the solution-grown crystals. The solution-grown crystals showed uniform twisting along their respective lengths while the form III crystals grown from the vapour phase consistently exhibited

irregular twists, suggesting a lack of long-range periodicity. A representative plot of crystal length (*l*) against pitch *P* for a vapour-grown OXCBZ III crystal is presented in Figure 5.11 and shows that *P* increases linearly with increasing *l*. Examination of the vapour-grown OXCBZ material on silver foil also indicated the presence of both left- and right-handed twisted crystals (Figure 5.10b).

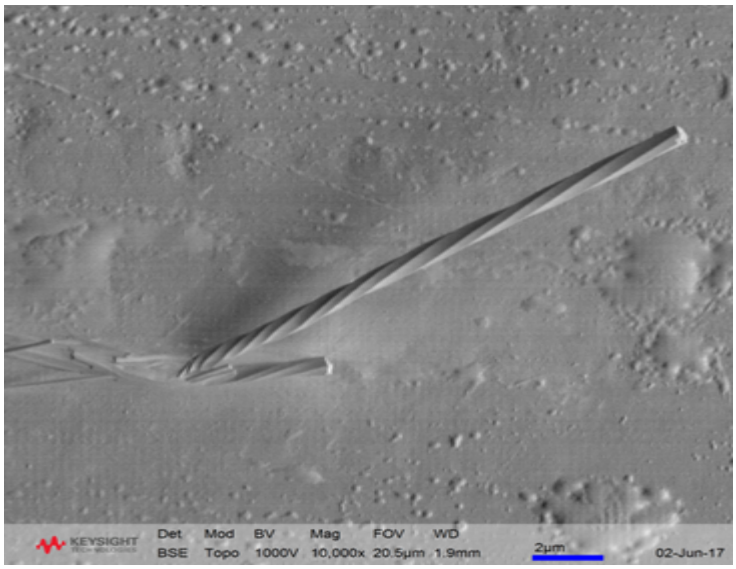

(a)

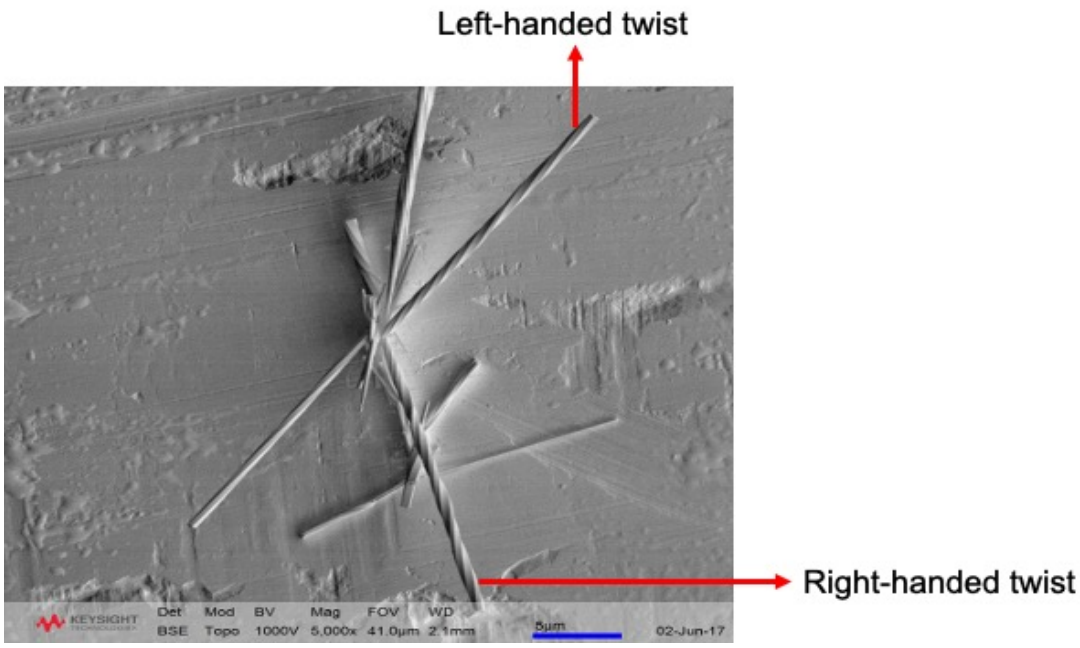

(b)

Figure 5.10: Representative SEM micrographs of twisted OXCBZ III crystals prepared via physical vapour deposition onto silver foil. The scale bar is 2 µm for (a) and 5 µm for (b).

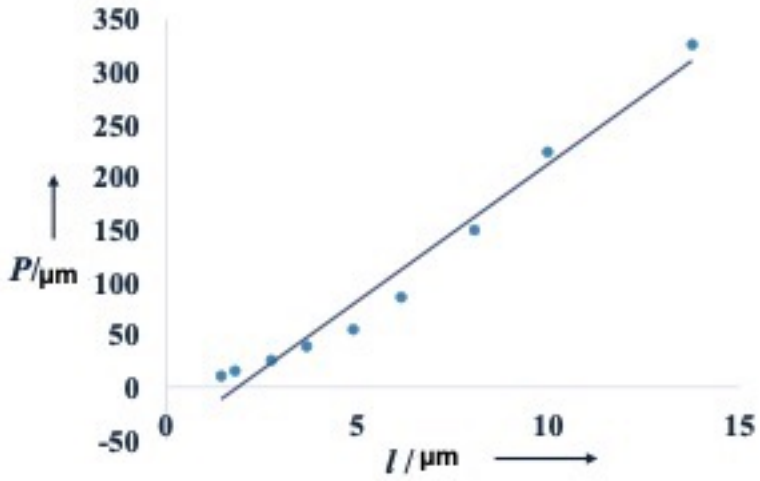

Figure 5.11: Correlation between pitch (*P*) and length (*l)* in a vapour-grown crystal of OXCBZ III.

Enantiomorphic crystals (Figure 5.12) are chiral crystals which are mirror-related, non-superimposable on each other (Hahn, 2002b) and can exhibit twisting in both right- and left-handed screw directions (Shtukenberg et al., 2014c).

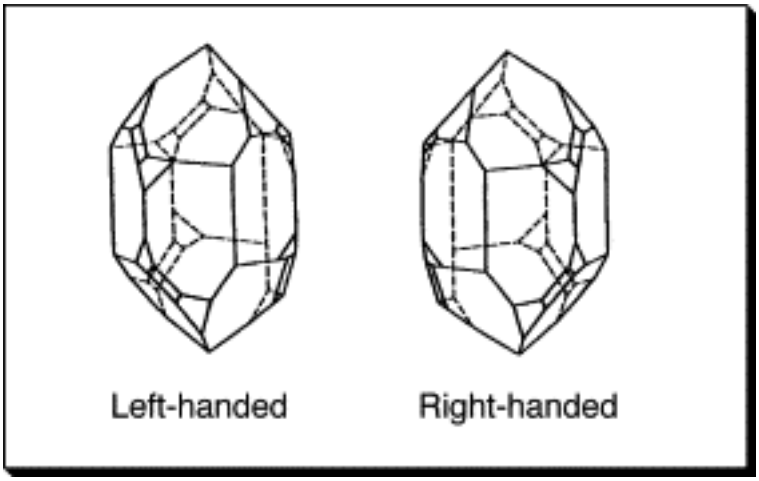

Figure 5.12: Enantiomorphic crystals of quartz (reproduced from Matsuura and Koshima, 2005).

Helices and helicoids are generally chiral and several researchers have tried, mostly in vain, to establish the correlation between macroscopic chiral morphologies and crystallographic symmetry. Whilst a few examples have been noted for polymers (Singfield and Brown., 1995; Saracovan et al., 1999), where molecular chirality is translated to supramolecular helicity, establishing an enantiomorphic relationship in small molecular twisted crystals is challenging (Shtukenberg et al., 2010). The

literature indicates that quartz is the only experimentally verified substance for which enantiomorphic crystals are known to twist in opposite directions (Punin and Shtukenberg, 2008). However, it has been suggested by Bernauer (Bernauer, 1929) that enantiomorphism is not a precondition for twisting. In the case of twisted OXCBZ III, it was not possible to establish the absolute structure of single crystals. The crystal structure of bulk OXCBZ III material prepared via solution crystallisation could only be solved from XRPD data and form III was found to crystallise in the centrosymmetric *R*-3 space group. Moreover, the evidence from SEM analysis suggested that the OXCBZ III crystals resulting from vapour deposition experiments are unlikely to be single crystals.

In addition to the fact that vapour-grown OXCBZ III crystals showed irregular twisting behaviour along their lengths, the angle of twist was found to be different for various crystals resulting from the same experiment, i.e. individual crystals exhibited their own characteristic angle of twist. These observations suggested that the experimental factors governing the twisting mechanism for OXCBZ III at the nanoscale are likely to vary for different crystals arising from the same experiment and prompted further investigations into the growth process of twisted form III during the vapour deposition process.

5.6.2 Evolution of Twisted OXCBZ Form III Crystals during Physical Vapour Deposition

Whilst physical vapour deposition onto surfaces has been used previously to isolate single crystals of suitable quality for X-ray diffraction measurements (Arlin et al., 2011; Srirambhatla et al., 2016; Case et al., 2018), monitoring the growth of OXCBZ III onto silver foil at different time points during the deposition process with off-line SEM indicated the emergence of crystals with cross-section sizes that were typically in the order of hundreds of nanometers. The crystals grew up to ≈ 23 μm in length and consistently displayed the twisted morphology highlighted in section 5.6.1.2. The section below describes the evolution of the sample presentation based on these experiments and points to non-classical crystallisation mechanisms (De Yoreo et al., 2015).

Within the first hour of vapour deposition of OXCBZ, spherical droplets were observed on silver foil substrates (Figure 5.13). Liquid-like precursors, similar to the droplets observed for OXCBZ, have been reported in crystallisation studies of both organic and inorganic materials and are associated with the occurrence of non-classical

crystal growth (Lee and Maa,1991; Vekilov, 2004; Zhang and Liu, 2007; Vekilov, 2010a & 2010b; Gebauer et al., 2014; Sleutel and Van Driessche, 2014; Vorontsova et al., 2015; Shahar et al., 2016; Jiang et al., 2017; Warzecha et al., 2017; Wolf et al., 2017; Li et al., 2018; Tsarfati et al., 2018). The droplets arising on silver foil during vapour deposition of OXCBZ were imaged using AFM (Figure 5.14) and found to exhibit a diameter of 70.18 ± 8.78 nm (n = 30 droplets). The height of protrusion of the droplets from silver foil was found to be less than 15 nm. For the purposes of obtaining greater insight into the nature of these droplets, Raman spectra were collected from a number of them in the low frequency region of 10 - 400 cm^{-1} and the corresponding results are presented in Figure 5.15a. Raman analysis in low frequency regions is a reliable approach for probing the solid-state structure of pharmaceutical materials and readily distinguishing between amorphous and crystalline sample states as it enables crystal lattice vibrations to be identified (Nanubolu and Burley, 2012; Roy et al., 2013; Walker et al., 2017). The analysis of droplets emerging on silver foil consistently yielded spectra that exhibited a single peak at ≈ 43 cm^{-1}, a broad peak at ≈ 200 - 300 cm^{-1} and a complete absence of periodic sharp peaks in the low-frequency region, all of which are traits typically characteristic of amorphous materials.

In order to obtain further confirmation with respect to the amorphous nature of the droplets, amorphous OXCBZ was generated via fast evaporation from a saturated solution of 2-methoxyethanol at 70°C and 150 rpm using the Crissy® platform. Low-frequency Raman spectra (Figure 5.15c) were collected from this material, which was confirmed to be amorphous via XRPD analysis (Appendix Figure A5.1), and compared directly with spectra generated from the droplets on silver foil (Figure 5.15a) and reference spectra obtained from the starting, fully crystalline form I material (Figure 5.15b). Similarities were observed between the spectra obtained from OXCBZ droplets on silver foil and solution-generated, amorphous OXCBZ in terms of the presence of a single peak below 50 cm^{-1} and the absence of numerous, well-defined peaks indicative of periodic arrangement in crystalline materials which were observed in Raman spectra of OXCBZ I. Spectra obtained from amorphous OXCBZ prepared from 2-methoxyethanol exhibited an additional broad feature in the 300 – 400 cm^{-1} compared to those collected from the droplets on silver foil. This observation may be attributed to the fact that using distinct preparation methods for generating amorphous samples can result in structural variations in the short-range order of the molecules (Karmwar et al., 2011 & 2012).

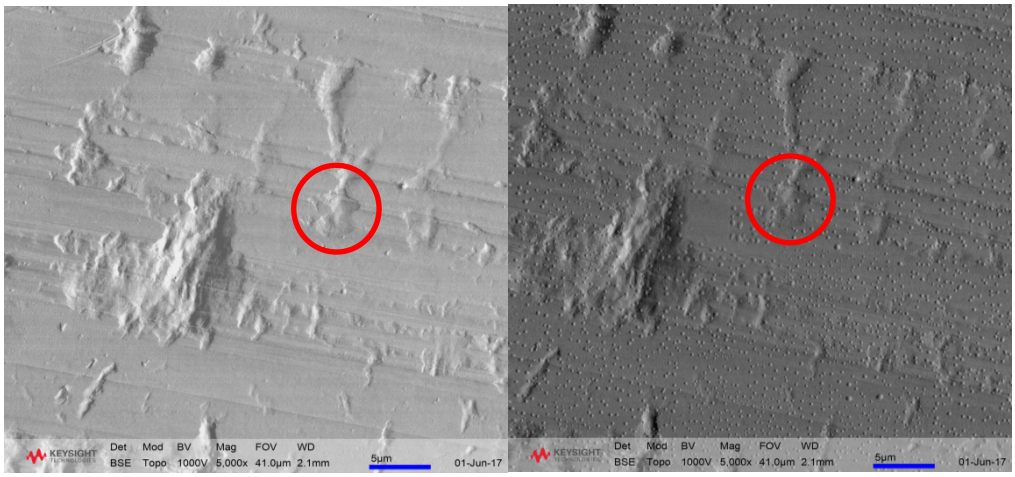

Before vapour deposition **1 hour of vapour deposition**

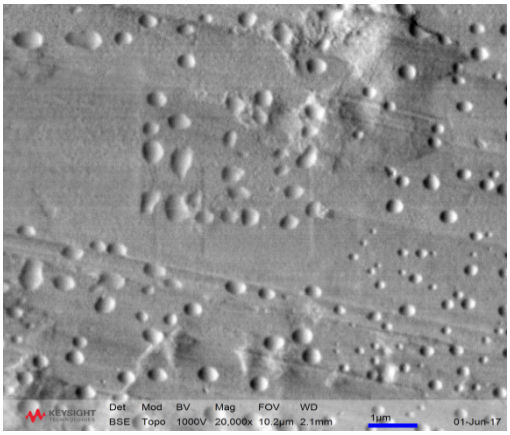

1 hour of vapour deposition (higher magnification)

Figure 5.13: SEM micrographs showing the emergence of droplets on silver foil within 1 hour of OXCBZ vapour deposition. For collection of the micrograph shown at the bottom (scale bar = 1 µm), higher magnification was used to zoom in on the region circled in red (top micrographs, scale bar = 5 µm).

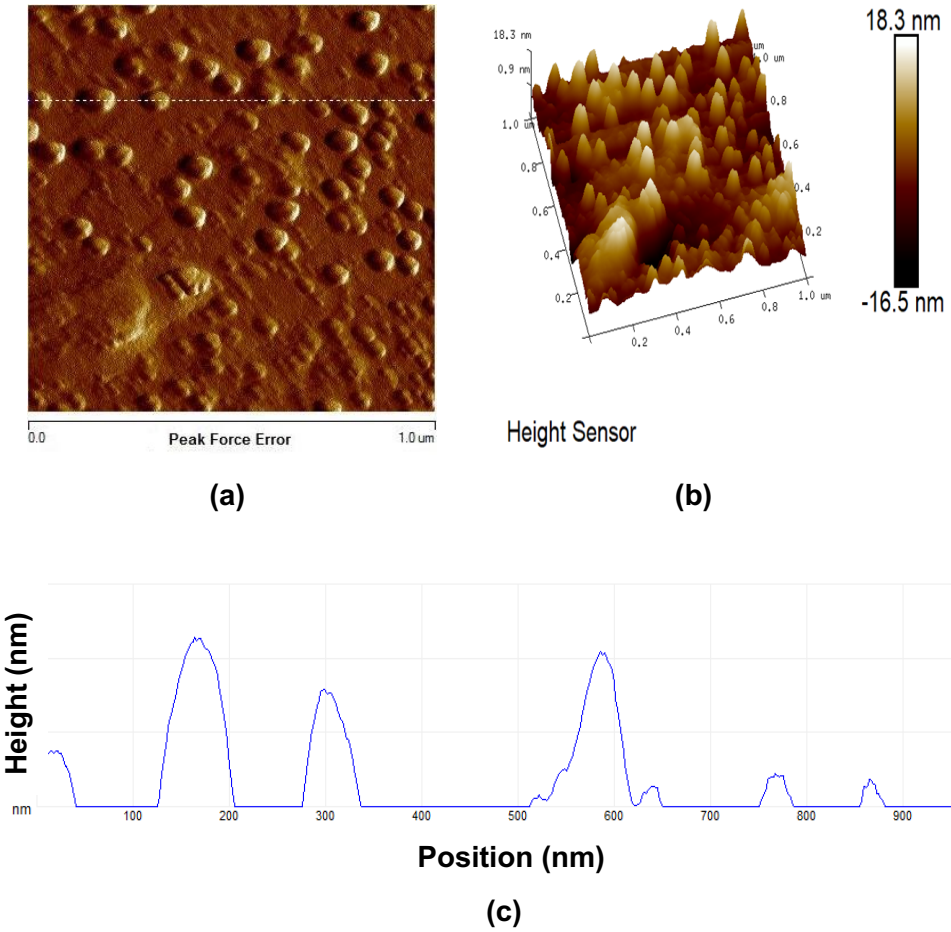

Figure 5.14: AFM images depicting the emergence of droplets on silver foil from the vapour deposition of OXCBZ (a & b) and corresponding cross section of height (c) indicated by the dashed white line in (a). Image collection occurred using a scan size of 1 µm x 1 µm after 2 hours of OXCBZ deposition.

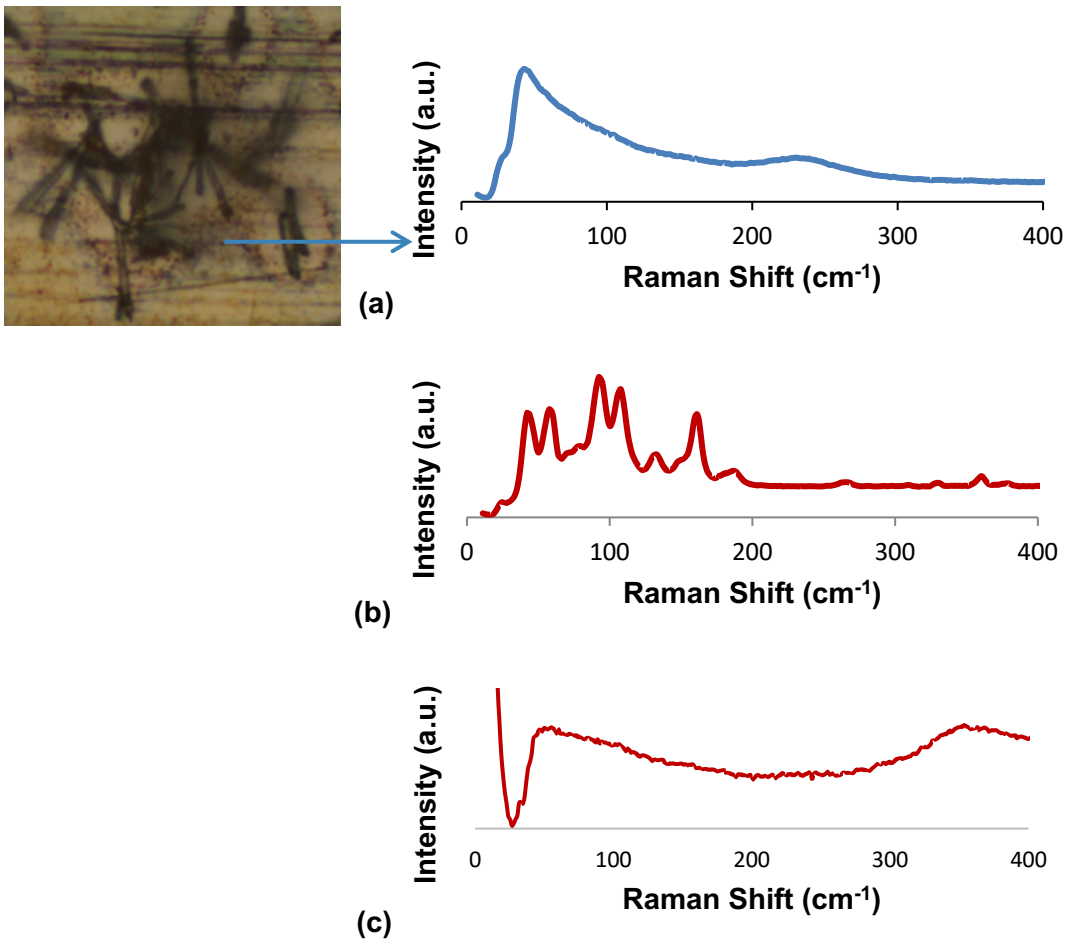

Figure 5.15: Representative low-frequency Raman spectra of (a) OXCBZ droplet on silver foil, (b) OXCBZ form I sourced from Sigma-Aldrich and (c) amorphous OXCBZ generated via fast evaporation from 2-methoxyethanol.

After 16 hours of vapour deposition (Figure 5.16a), the observed droplets were seen to have grown in size or coalesced to produce amorphous aggregates of average diameter 808 ± 243 nm (n = 30 aggregates). SEM micrographs collected following 40 hours of vapor deposition presented striking evidence for the emergence of needle-like nanocrystals within the amorphous matrix of droplet aggregates (Figure 5.16b). At 40 hours of vapour deposition, twisted crystals similar to those shown in Figure 5.17 were additionally observed. Examination of the SEM micrographs of the vapour-grown material prepared after 40 hours of deposition indicated that the cross-section size and length of the observed crystals were in the size range 60 – 450 nm and 1.5 – 6 μm respectively. The plot of crystal length *vs* pitch previously shown in Figure 5.11 is representative of the twisted crystals observed following 40 hours of deposition. The fact that the pitch of these crystals increased with increasing length

indicated renormalisation of the pitch (Haddad et al., 2019), i.e. untwisting of the twisted crystals. Splitting of individual strands was also noted for some of the crystals observed at 40 hours of deposition, with SEM indicating the presence of multiple strands growing from the original crystal ends in multiple directions.

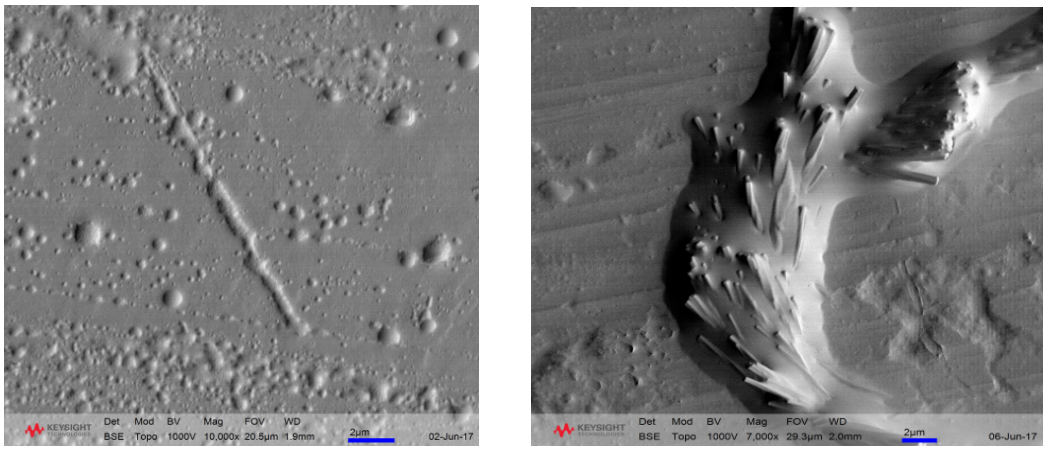

(a) **(b)**

Figure 5.16: SEM micrographs depicting the aggregation of amorphous droplets following 16 hours of OXCBZ vapour deposition (a) and the emergence of needle-like nanocrystals from the amorphous matrix at 40 hours of deposition (b). The scale bar is 2 μm for both micrographs.

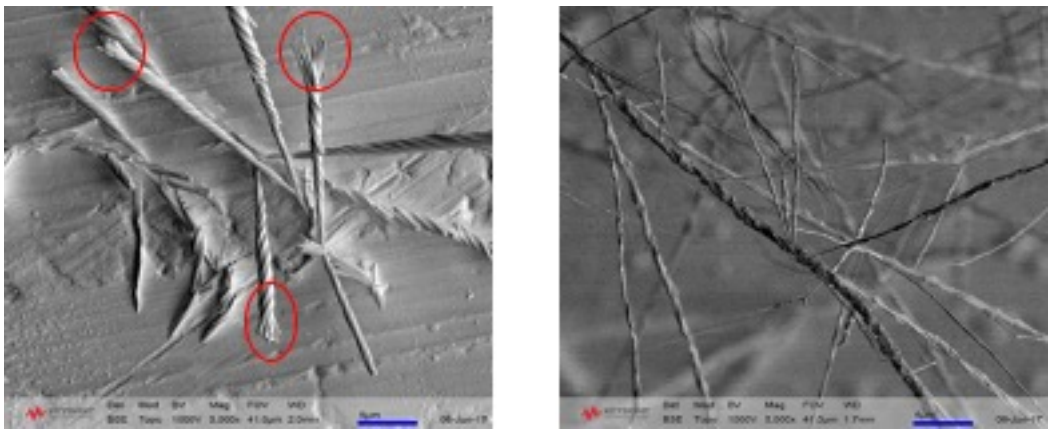

(a) **(b)**

Figure 5.17: SEM micrographs of twisted OXCBZ III crystals grown on silver foil following 40 hours of vapour deposition. The scale bar is 5 μm for both micrographs. Red circles in (a) indicate strand splitting.

5.6.3 Investigating the Presence of Impurities in Twisted OXCBZ Form III Crystals

The OXCBZ III crystals resulting from physical vapour deposition experiments showed increasing pitch along their length, indicating untwisting of the crystals as growth continued. Untwisting in mannitol (Shtukenberg et al., 2012) and hippuric acid (Shtukenberg et al., 2015) crystals has been linked to an increase in the thickness of crystals as they grow. The density of structural defects and the presence of impurities have also been proposed as possible mechanisms for the untwisting of oxalic acid dihydrate and gypsum crystals (Punin and Shtukenberg, 2008). The vapour-grown crystals of OXCBZ III were found to show irregular pitch. This prompted an extensive investigation into the presence of impurities in vapour-grown OXCBZ III crystals and the starting OXCBZ material. For this purpose, OXCBZ samples were subjected to ToF-SIMS, XRPD, DSC, and HPLC-MS analyses. With ToF-SIMS, studying the distribution of deposited OXCBZ on the experimental substrates and the twisted crystals themselves was additionally of interest. Due to the limited amounts of vapour-grown material available on the experimental substrates employed, XRPD, DSC and HPLC-MS could only be performed on the starting OXCBZ powders that were used to prepare the crystals. The starting powders were all analysed at different time points along the vapour deposition process to identify potential correlations between the presence of impurities and the duration of OXCBZ deposition.

In the case of ToF-SIMS analysis, it was possible to analyse some of the twisted OXCBZ III crystals obtained by deposition onto silver foil directly. Reference mass spectra were collected for OXCBZ starting material sourced from Sigma-Aldrich, silver foil and OXCBZ III crystals obtained after vapour deposition between 16 and 48 hours. The mass spectra from ToF-SIMS analysis are shown in Figure 5.18. The OXCBZ starting material is identified by the presence of secondary ions $C_{15}H_{13}N_2O_2^+$ ($[M+H]^+$, *m/z* 253.1) and $C_{14}H_{12}$ (*m/z* 180.1) as shown by the top most spectra in Figure 5.14. The mass spectra of crystals obtained after 16 and 48 hours of deposition are consistent with the mass spectra of the starting OXCBZ material. ToF-SIMS is highly sensitive towards the detection of chemical impurities and previous work has established that the technique can detect impurity concentrations as low as 0.5% (w/w) in pharmaceutical tablets (Pajander et al., 2013). Moreover, ToF-SIMS can readily distinguish between active pharmaceutical ingredients and their closely related impurities (Ottoboni et al., 2018). Whilst the analysis described herein confirmed the

purity of twisted crystals with respect to OXCBZ, the mass spectra that were collected provided no definitive evidence for the inclusion of impurities.

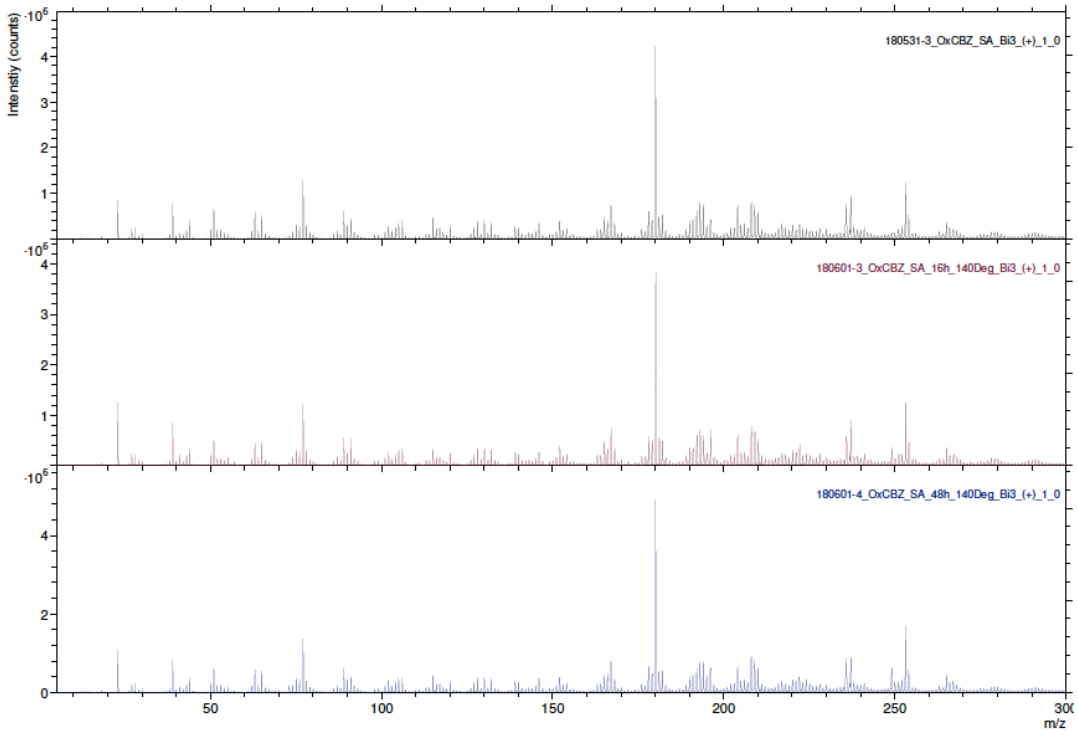

Figure 5.18: Mass spectra of OXCBZ starting material from Sigma-Aldrich (top) and OXCBZ material after 16 hours (middle) and 48 hours of vapour deposition (bottom).

Figure 5.19 shows ToF-SIMS images of OXCBZ crystals grown on silver foil after 24 hours of vapour deposition. The analysed area depicted in the figure is 100 µm × 100 µm. Additional data from further areas analysed on other substrates (aluminium foil, copper foil, copper coated and silver coated glass) are available in Appendix Figures A5.2 – A5.5. The total ion image is presented in Figure 5.19a to aid visualisation of the main topographic features of the analysed area, namely the twisted structure of the twisted form III crystals in the centre of the image and the inhomogeneous surface distribution of OXCBZ in the surrounding area. The colour overlay included in Figure 5.19b shows that the silver substrate is covered by a layer of deposited OXCBZ (red) which is depleted around the base of the OXCBZ crystals, exposing the silver foil beneath (green); this type of layer depletion has previously been reported as an example of crystallisation-induced dewetting in thin films of indomethacin (Sun et al., 2011) and suggests that amorphous droplets observed on silver foil are likely diffusing across the surface of the growing crystals. Single ion

images of OXCBZ and silver are included in Figures 5.19c and 5.19d respectively and further highlight the distinct surface distribution of the two components.

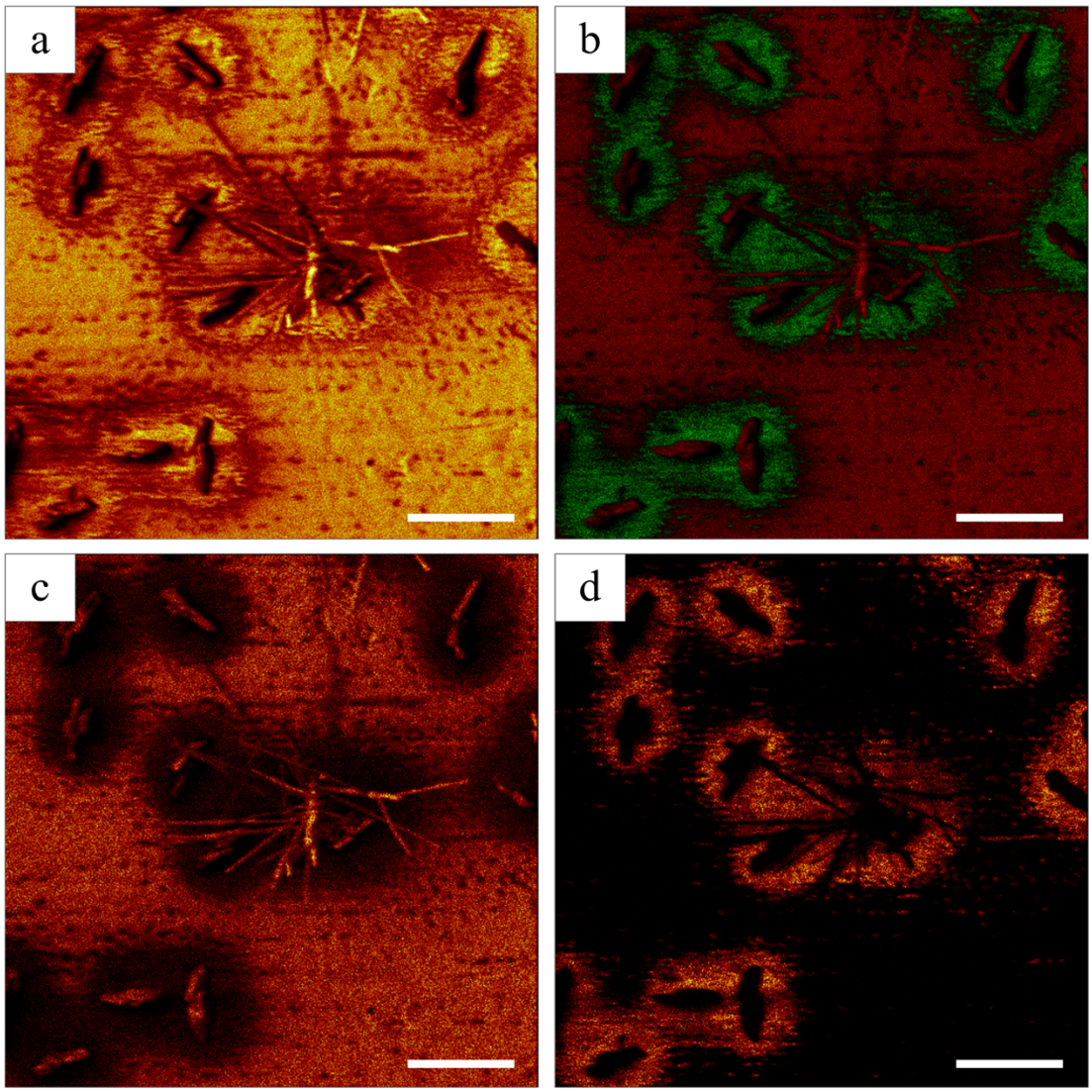

Figure 5.19: ToF-SIMS total ion image (a), colour overlay image (b) and single ion images representing the OXCBZ (c) and silver (d) distribution on the surface of a silver foil substrate following 24 hours of vapour deposition. In (b), red represents OXCBZ secondary ions $C_{15}H_{13}N_2O_2^+$ ($[M+H]^+$, *m/z* 253.1) and $C_{14}H_{12}$ (*m/z* 180.1), and green represents silver secondary ions Ag^+ (*m/z* 106.9) and $^{109}Ag^+$ (*m/z* 108.9). The scale bar is 20 μm for all images.

XRPD analysis of starting powders used in vapour deposition studies of OXCBZ at different time scales during the deposition process is presented in Figure 5.20 and indicates the presence of an impurity following prolonged experimentation. At 48 hours of vapour deposition, unidentified peaks were observed at ≈ 11 and 12.1° 2θ (highlighted in blue arrows) which were not present in the starting material and cannot be attributed to any other known forms of OXCBZ. Traces of the unidentified impurity appeared to be present in the samples analysed following 16 hours of deposition as the peak at 12.1° 2θ is observed in the corresponding patterns as well, albeit with decreased intensity.

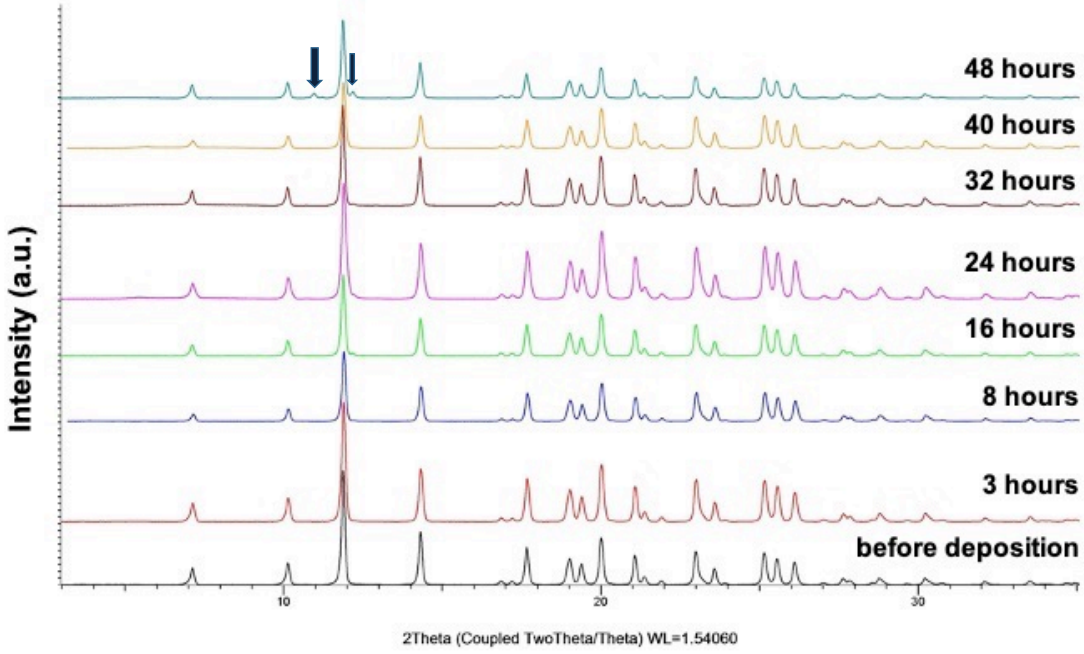

Figure 5.20: XRPD analysis, at various timescales, of starting OXCBZ powder samples used in physical vapour deposition experiments. Blue arrows indicate the presence of impurity peaks.

DSC analysis was further performed to cross-correlate the presence of impurity peaks observed in the XRPD patterns. At physical vapour deposition times > 16 hours, the melting point of OXCBZ starting powder used to grow the twisted crystals was found to decrease by at least 1°C when compared to the reference material from Sigma-Aldrich (Figure 5.21). At 48 hours of vapour deposition, the decrease in melting point was ≈ 3.7°C compared to the reference, indicating that the purity of the sample had changed considerably. These observations align well with the general expectation that impurity presence in a sample will result in its melting point decreasing (Brown, 2001).

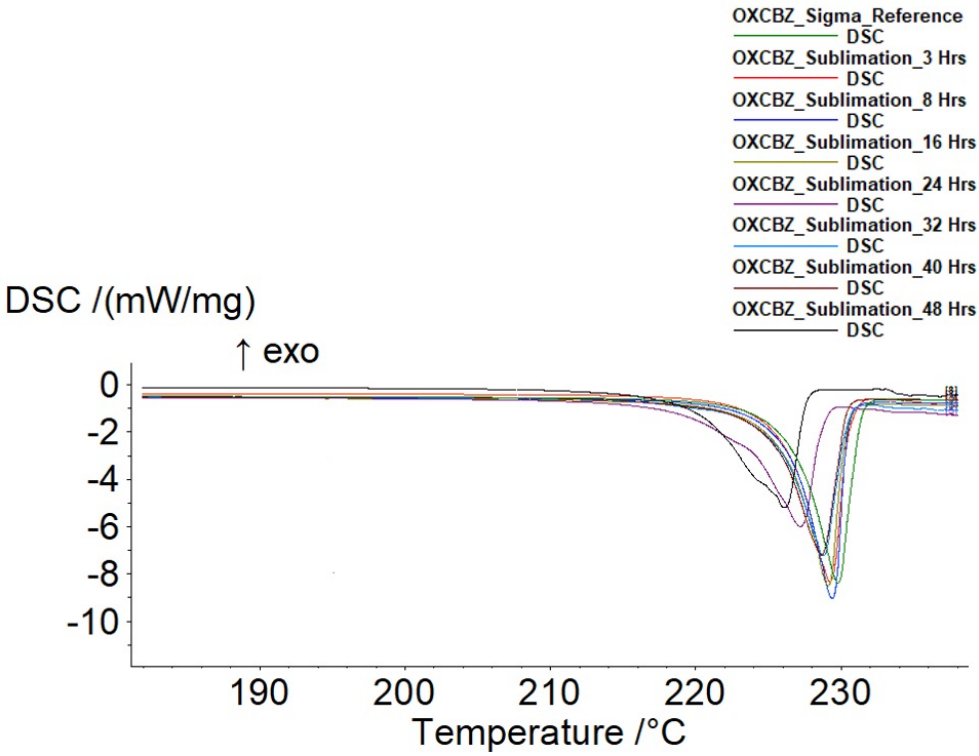

Figure 5.21: DSC analysis, at various timescales, of starting OXCBZ powder samples used in physical vapour deposition experiments and overlay with data for the reference OXCBZ material sourced from Sigma-Aldrich.

The OXCBZ starting powders subjected to vapour deposition for 16, 24, and 48 hours were additionally analysed with HPLC-MS analysis. Prior to analysis commencing, blank samples were ran to establish reference data for subsequent comparisons. A representative chromatogram obtained from a blank run is shown in Figure 5.22a. Comparison of the chromatogram of the OXCBZ reference material from Sigma-Aldrich with those of the powders used in vapour deposition experiments confirmed the presence of a chemical impurity (Table 5.3 and Figures 5.22b – 5.22e). The impurity had a retention time of ≈ 6.52 min in the liquid chromatograms with a corresponding *m/z* of 222.2 (Figure 5.23) and was found to be present in all of the samples analysed, including the reference material from Sigma-Aldrich. The impurity was subsequently identified as dibenzazepinodione (DBZ), a pharmacopeial impurity of OXCBZ which has recently been the subject of comprehensive solid-state characterisation (Faudone et al., 2019). The molecular structure of DBZ is shown in Figure 5.24. HPLC-MS indicated that the amount of DBZ was greater in powder samples of OXCBZ subjected to longer vapour deposition experiments, suggesting that prolonged exposure of OXCBZ to high temperature induces thermal degradation

and a subsequent increase in the amount of DBZ. Whilst the presence of DBZ was not apparent when ToF-SIMS was used to characterise OXCBZ and the twisted crystals derived from it, the combination of mass spectrometry with chromatographic analysis through HPLC-MS provided unambiguous evidence for its inclusion in both the reference material sourced from Sigma-Aldrich and the experimental samples from vapour deposition experiments. This highlighted the strong complementarity between the two techniques and allowed compositional information to be obtained for the starting OXCBZ powders and the twisted crystals on the experimental substrates, which was not possible using XRPD and DSC.

As the presence of impurities is often a prerequisite for the emergence of twisted morphology in crystals (Shtukenberg et al., 2014c), HPLC-MS was additionally used to examine solution-grown material of OXCBZ form III and the starting OXCBZ material from Molekula that was used to derive it (Table 5.3 and Appendix Figure A5.6.) The analysis confirmed the presence of DBZ in both types of material, with the concentration of the impurity found to be less in the solution-grown material than in OXCBZ samples subjected to vapour deposition. Whilst the presence of DBZ in the solution-grown material was verified, its significance on the emergence of twisting for both the solution- and vapour-grown crystals of OXCBZ III remained unclear.

Table 5.3: Overview of HPLC analysis of OXCBZ starting material from Sigma-Aldrich and Molekula, OXCBZ starting powders subjected to physical vapour deposition, and solution-grown OXCBZ III material. Retention times and peak areas corresponding to OXCBZ and DBZ are shown (n = 3). The actual concentration for each sample was 1 mg/mL.

Sample	Retention time of OXCBZ (min)	Peak area of OXCBZ (%)	Retention time of DBZ (min)	Peak area of DBZ (%)
OXCBZ (Sigma-Aldrich)	5.932 ± 0.002	81.18 ± 2.59	6.526 ± 0.002	1.811 ± 0.04
OXCBZ – 16 hrs of vapour deposition	5.932 ± 0.005	79.53 ± 2.25	6.524 ± 0.005	3.047 ± 0.4
OXCBZ – 24 hrs of vapour deposition	5.935 ± 0.001	78.68 ± 1.36	6.524 ± 0.001	4.323 ± 0.1
OXCBZ – 48 hrs of vapour deposition	5.934 ± 0.002	81.11 ± 0.99	6.522 ± 0.003	6.601 ± 0.1
OXCBZ (Molekula)	5.935 ± 0.003	81.07 ± 0.64	6.524 ± 0.003	1.969 ± 0.04
OXCBZ III (50:50 v/v Ethanol/Toluene)	5.935 ± 0.001	75.86 ± 1.77	6.527 ± 0.0006	2.199 ± 0.02

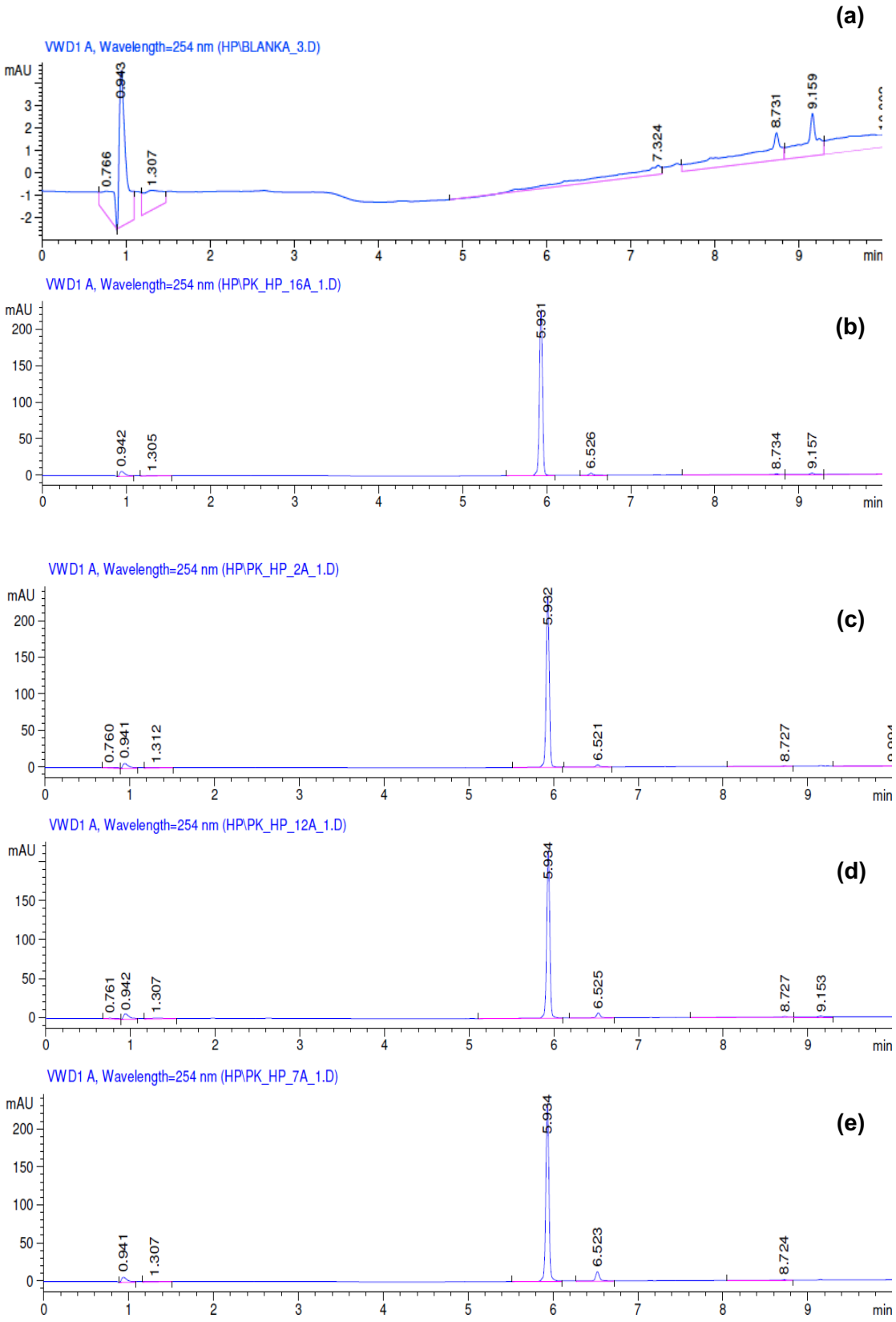

Figure 5.22: Representative UV chromatograms of blank sample (a) and OXCBZ starting material (b) as obtained from Sigma-Aldrich, (c) following 16 hours of vapour deposition, (d) following 24 hours of vapour deposition and (e) following 48 hours of vapour deposition.

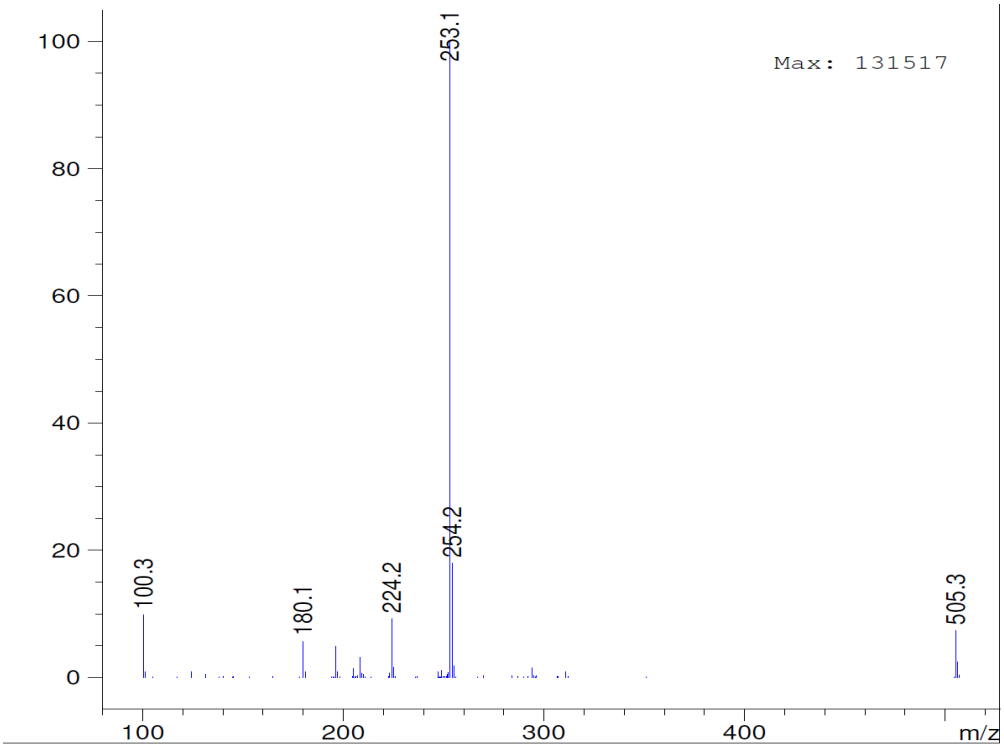

(a)

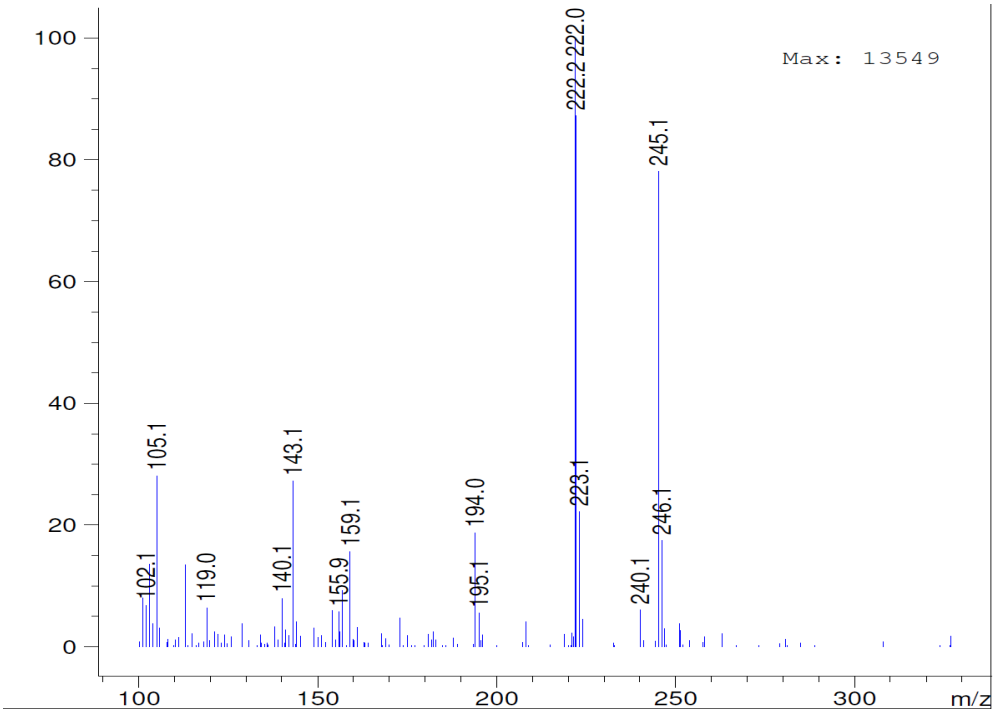

(b)

Figure 5.23: Representative mass spectra (a & b) corresponding to UV chromatogram peaks characteristic of OXCBZ and DBZ. Spectrum (a) corresponds to OXCBZ and spectrum (b) is representative of DBZ.

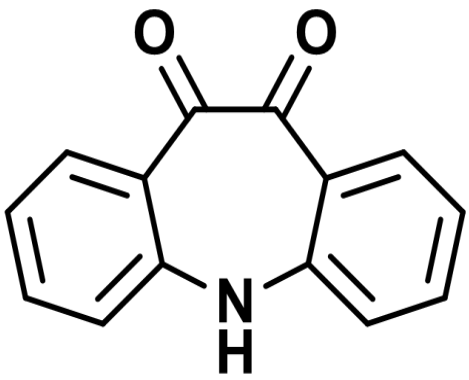

Figure 5.24: Molecular structure of DBZ (IUPAC name: 5*H*-dibenzo[*b,f*]azepine-10,11-dione, $C_{14}H_9NO_2$, molecular weight: 223.23).

5.6.4 Discussion

The observation of unusual twisted crystals of OXCBZ form III obtained from solution and physical vapour deposition experiments raised several important research questions: (i) why do OXCBZ III crystals exhibit twisted morphologies? (ii) what is the reason behind the twist renormalisation observed in the vapour-grown twisted crystals? (iii) what is the significance of impurity presence in the context of crystal twisting of OXCBZ III? (iv) finally, do other isostructural polymorphs (CBZ II and CYT I) within the CBZ family of compounds also exhibit similar twisted morphologies?

5.6.4.1 Rationalising Twisting in Crystals of OXCBZ Form III

5.6.4.1.1 Role of Compositional and Structural Inhomogeneities in the Twisted Crystal Lattice

The presence of compositional and structural inhomogeneities in the crystal structure, leading to the occurrence of lattice mismatch, has been identified as the most universal cause of twisting and operates through generation of a mechanical moment at the growth front (Shtukenberg at al., 2014c). In order to account for the possibility of lattice mismatch occurring in the vapour- and solution-grown twisted crystals of OXCBZ III and rationalise their twisting, the “growth error” arising due to competition from other closely related structures of form III identified in the CSP landscape of OXCBZ (refer to section 4.4.2) can be considered. OXCBZ III and its related CSP-generated structures all comprise void channels parallel to the crystallographic *c* axis (Figure 5.25) and these channels are sizeable enough to accommodate non-stoichiometric amounts of solvent molecules. The thermogravimetric analysis

previously presented for the experimentally determined form III structure supports the presence of non-stoichiometric amounts of residual solvents in the void channels (Figure 4.16, section 4.4.3.2).

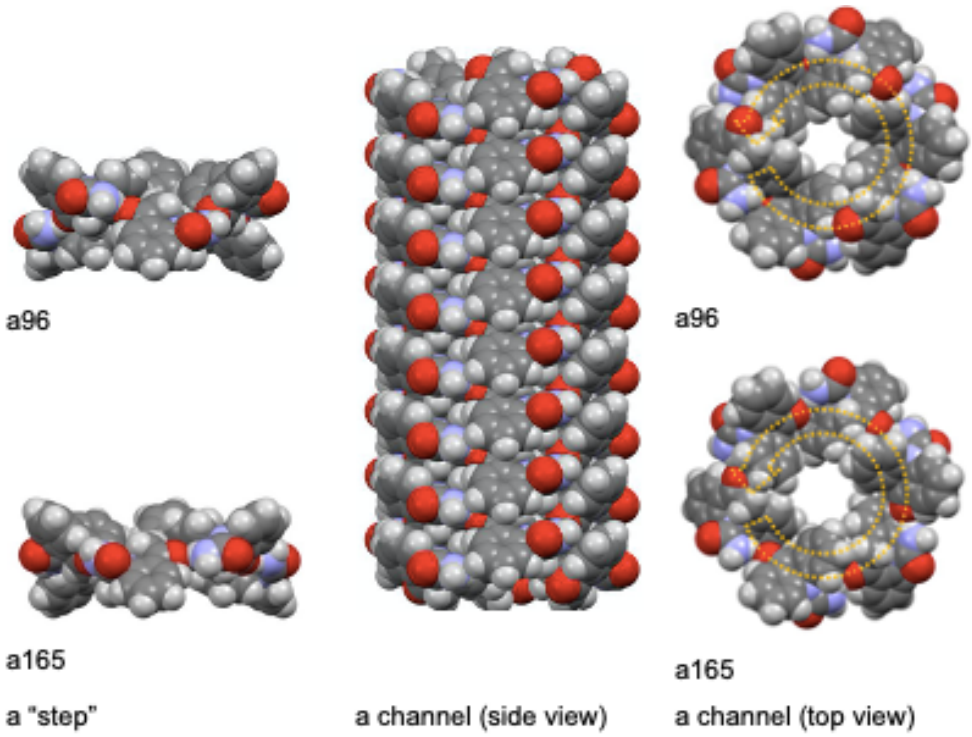

Figure 5.25: A single "step" and a channel from side and top views, similarly constructed in the 4 trigonal candidates of OXCBZ form III and displayed here using a96 and a165 as examples. The dashed circular arrows indicate the propeller direction built in each channel.

The channels in form III and its related structures have a propeller-like directionality and comprise stacked steps, shown in Figure 5.25 using a96 and a165 as examples. Each step is built as an $R_6^6(48)$ hydrogen-bonded ring using the carbonyl groups on the 7-membered ring and one of the NH of the amide groups. There is no hydrogen bond between the steps as they interact entirely through dispersion interactions and stack by translation (Childs et al., 2009) along the *c* axis (5.0 - 5.3 Å). Six amide groups are exposed on the outside wall of each step, which connects the channel to its six neighbouring channels by $R_2^2(8)$ amide hydrogen bonding of varying geometries. Although the stacking of structure a96 steps leading to the formation of columns is energetically favourable, the presence of other predicted structures (a165,

a1858, and a900) with similar channel constructs can be used to rationalise the twisted morphology in both the vapour- and solution-grown crystals of form III.

Slight changes in $R_2^2(8)$ amide-amide hydrogen bonds can lead to the emergence of four different trigonal structures of OXCBZ that were originally identified as form III candidates. These structures are summarised in Figure 5.26, in which the top row shows the top view of the inter-channel hydrogen bonds whilst the bottom row shows the top view of the arrangement of screw directions. Short red/blue/green lines indicate $R_2^2(8)$ dimeric hydrogen bonds between the channels. Each long cylinder in the middle row of Figure 5.26 is a channel, as packed in Figure 5.25, with a void through its centre. The steps within the channels are presented as single "building blocks" shown on the right hand-side of the channels. Structure a165 is coloured differently to highlight its larger variance from the other three.

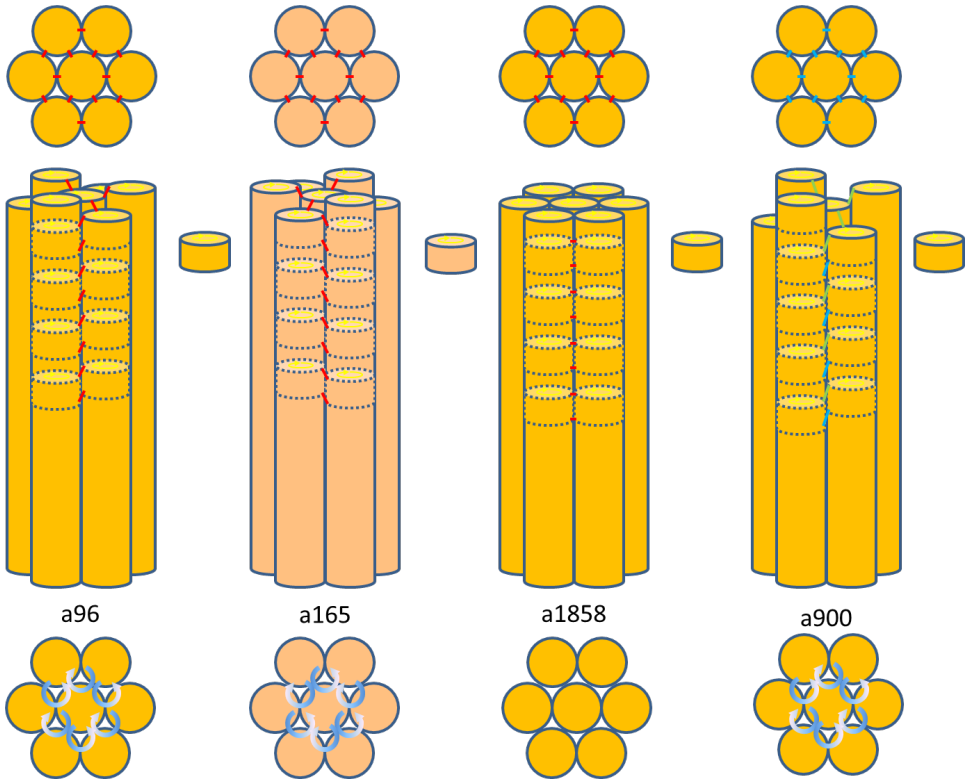

Figure 5.26: Packing comparison of the 4 trigonal CSP structures as OXCBZ form III candidates: a96, a165, a1858, a900.

Considering a1858 as an example: the six $R_2^2(8)$ interactions of the central channel with its six neighbours lie in the same plane normal to the axis of the central channel, leading to a flat growth front at the end of the bundle. However, in structures a96,

a165 and a900 the inter-channel hydrogen bonds do not lie in the same plane. Instead, three amide-amide interactions are pointing up whilst the other three interactions are pointing down. This leads to a sense of screw as in Figure 5.26 the front two channels of a96 form a right-handed screw with the central channel through three $R_2^2(8)$ hydrogen bonds, which link one step in a channel to the immediate step on top of it. In the case of a165, the same three channels form a left-handed screw. In a900, a right-handed screw is also formed between the central and front two channels, as shown in Figure 5.26, but with a doubled pitch as the $R_2^2(8)$ hydrogen bonds link one step to the second step on top of it. This screw dictates how three phenyl rings, those not used to line the inner walls of the void channels, from three OXCBZ molecules in three adjacent channels, stack with each other. The close similarity between the packings in the CSP candidate structures raises the possibility of disorder during the stacking of steps.

One of the proposed mechanisms ("growth error/incommensurate") for rationalising the formation of observed twisted morphology of vapour- and solution-grown OXCBZ III crystals would be the formation of growth errors during crystallisation of OXCBZ. In ideal growth cases, once one type of channel shown in Figure 5.26 begins to grow (e.g. a96), it will continue to grow along the direction of the other channels. However, the stacking of other competing growth steps would lead to a stacking error in the channels, resulting in the dangling amide groups being slightly distorted and the growth of one of the other structures depicted in Figure 5.26. A modulation of this type of growth error would potentially lead to the emergence of an incommensurate crystal structure (van Smaalen, 1995; Janssen and Janner, 2014) exhibiting twisted morphology. Incommensurate modulated structures are defined by a notable lack of long-range periodicity in three dimensions and consequently cannot be described using any of the 230 space groups describing three-dimensional crystals (Hahn, 2002a). However, these structures do exhibit long-range periodicity in four dimensions or more and originate from crystals having three-dimensional space group symmetry, with a modulation (e.g. stacking error described herein for OXCBZ III) disrupting the periodicity of the three-dimensional lattice.

Another possible explanation ("attached channel") of the twisted morphology of vapour- and solution-grown OXCBZ III arises from the fact that all channels, as constructed in Figure 5.26, pack with each other through dimeric hydrogen bonds along their outer walls, and the observation that the channels themselves are relatively rigid with little capability of twisting. Given the observation of twisted crystals,

it is possible for an a96 channel to become attached to an a165 channel through hydrogen bonding with the dangling amide groups, as shown in Figure 5.27.

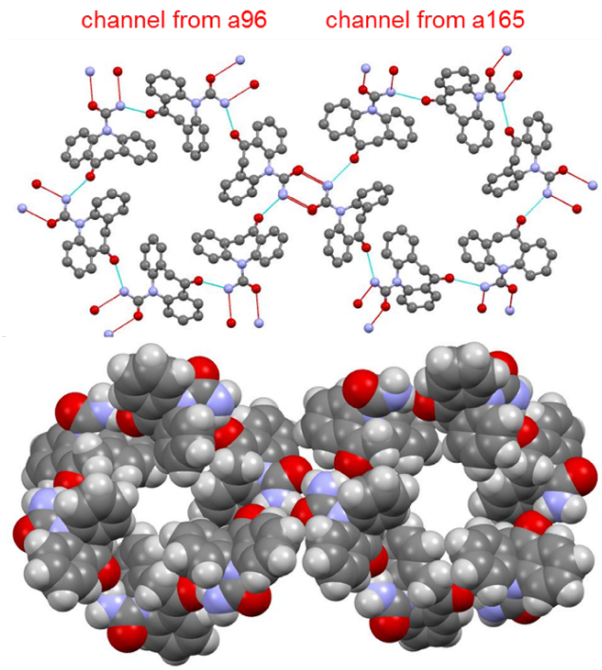

Figure 5.27: Illustration showing one step of a channel in OXCBZ a96 connected to another step of a channel in OXCBZ a165.

The small variance in the construct of the a96 and a165 channels means that their packing won't be as neat as those in Figure 5.26, as there would be a small angle between the axes of the two channels. This could also happen to an established bundle of several a96 or a165 channels. In such a circumstance, channels of one structure would become attached to the external walls of a central bundle of another structure, tilting at a small angle. Then, under appropriate experimental conditions, similar channels would continue to attach to the same bundle. This continuation of tilted attachment of channels to the external walls of a central bundle would maintain hydrogen bond contacts with other tilted channels, as well as the central bundle. A modulation of different type of structural inhomogeneities formed through the proposed "attached channel" mechanism could lead to the formation of lattice mismatch at the nanoscale, resulting in the mechanical movement of the growth front and subsequent formation of twisted crystal morphology. However, in the absence of detailed experimental evidence at the atomic scale, comprehensive mechanistic understanding of the formation of twisted crystals in both the vapour- and solution-grown OXCBZ III crystals remains elusive. Moreover, XRPD analysis of OXCBZ III

samples cannot be used to conclusively eliminate the possibility of multiple CSP structures being present as the limit of detection of the technique, typically within the range of 1 – 2 % by mass for laboratory diffractometers (Surana and Suryanarayanan, 2000; Crowley and Zografi, 2002), may prevent their identification.

5.6.4.1.2 Role of Elastic Deformation and Attractive Forces from Crystal Aggregation

Experimental evidence for the origin of twisting in vapour-grown OXCBZ III crystals appears in a series of micrographs derived from SEM analysis. The micrograph collected after 16 hours of physical vapour deposition (Figure 5.28) indicated the emergence of columnar nanocrystals within the amorphous matrix and can be described as a continuum of the crystal growth process of OXCBZ III, i.e. different regions within the micrograph can be considered as different time points during the crystallisation of OXCBZ III. Figure 5.28 comprises (i) amorphous droplets, (ii) nanocrystals which are not twisted (coloured by yellow boundaries), (iii) nanocrystals emerging from the droplets, which are not randomly oriented but possess orientational order, and (iv) the presence of twisted crystals (coloured by red boundaries).

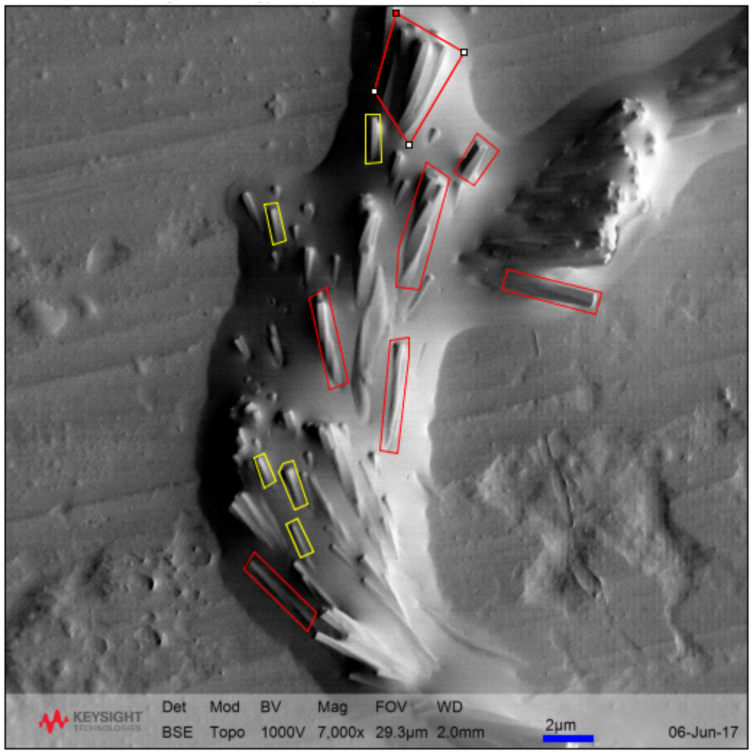

Figure 5.28: Annotated SEM micrograph of OXCBZ material obtained after 16 hours of physical vapour deposition. Yellow boundaries represent crystals that are not twisted whilst red boundaries indicate crystals that are twisted. The scale bar is 2 µm.

It is notable from Figure 5.28 that columnar crystals nucleating within the amorphous droplets aggregate and twist spontaneously along the longest crystal length to form bundles of twisted fibres. It is also apparent that polycrystalline fibres comprising multiple single crystals wrapped around each other are formed spontaneously, depending on the proximity of crystals nucleating within the droplets. These observations indicate that OXCBZ III crystals aggregate and twist spontaneously. The tendency of the columnar crystals to form twisted fibres is dependent on the interplay between the elastic energy associated with twisting and the attractive forces resulting from the aggregation of crystals (Turner et al., 2003). Whilst the decrease in surface area and free energy of the crystals due to aggregation provides the driving force, shear forces due to twisting are energetically unfavourable and their competition with the surface free energy may hinder the formation of twisted morphology (Yang et al., 2006). In order to gain greater insight into the elastic deformation of twisted OXCBZ crystals, the diagonal compression and shear components of calculated elastic constants (Day et al., 2001) of OXCBZ III were determined with DMACRYS (Price et al., 2010) using FIT potential and distributed multipoles derived from PBE/6-31G(d,p) wavefunctions. The corresponding values are given in Table 5.4, alongside values corresponding to CBZ II and CYT I which were calculated for comparison purposes. A schematic representation of the planar stress state of a crystal structure is presented in Figure 5.29 and indicates how stress forces are applied to different directions, including those in the OXCBZ III structure.

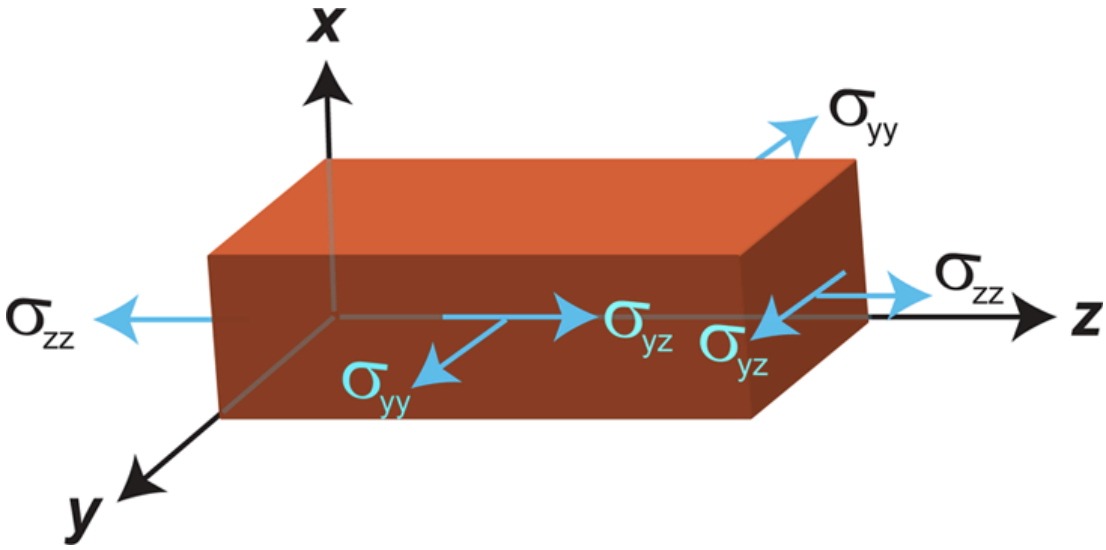

Figure 5.29: Schematic diagram depicting the planar stress state in a crystal structure, wherein σ_{yy} and σ_{zz} represent compression stress whilst σ_{yz} is indicative of shear stress (reproduced from Naumov et al., 2015).

Table 5.4: Diagonal compression (C_{11}-C_{33}) and shear (C_{44}-C_{55}) components (in GPa) of calculated elastic constants of OXCBZ III (based on CSP structure a96), CBZ II and CYT I. C_{33} is the compression along *z* direction (crystallographic *c* axis) whilst C_{11} and C_{22} represent compression in *x* (crystallographic *a* axis) and *y* (crystallographic *b* axis) directions.

	C_{11} = C_{xxxx}	C_{22} = C_{yyyy}	C_{33} = C_{zzzz}	C_{44} = C_{yzyz}	C_{55} = C_{xzxz}	C_{66} = C_{xyxy}
OXCBZ III	24.8	24.8	13.1	7.6	7.6	11.0
CBZ II	15.6	15.6	19.5	5.7	5.7	4.9
CYT I	14.8	14.8	21.1	5.5	5.5	5.0

The values of the diagonal compression and shear components derived for OXCBZ III indicate that the form III structure is easier to compress along the crystallographic *c* axis (*z* direction in Figure 5.29) compared to the other two axes (C_{33}<<C_{11}=C_{22}), in contrast to CBZ II and CYT I. This is likely due to the presence of additional N-H···O=C hydrogen-bonding interactions in OXCBZ III, which prevents distortion of the steps that give rise to the void channels in the form III structure (refer to Figure 5.25 for depiction of a representative step and channel). However, the OXCBZ III structure is more prone to shear towards the *x*-or *y*-direction on *z* than to shear towards the *x*- (or *y*-) direction on *y* (or *x*) in Figure 5.29, as indicated by the values of C_{44}, C_{55}, and C_{66} (C_{44}=C_{55}<C_{66}). In other words, OXCBZ III is more prone to slippage between steps than between channels. This is in accordance with the fact that in OXCBZ III the steps are stacked along the crystallographic *c* axis through dispersion interactions which are more compliant to pressure along *c* and slippage in the *a*-*b* plane, unlike CBZ II and CYT I. Further evidence can be derived from SEM analysis showing that twisting occurs along the longest length of OXCBZ III crystals (Figure 5.28). Therefore, based on the experimental observations and calculations of diagonal compression and shear components, it is proposed that a suitable mechanism of twisting for vapour-grown OXCBZ III involves spontaneous twisting following aggregation of non-twisted form III crystals.

5.6.4.2 Rationalising Twist Renormalisation and the Significance of Impurity Presence in OXCBZ III

The twist renormalisation observed for vapour-grown OXCBZ III crystals can be qualitatively explained by considering the fact that these crystals may have comprised a chemical impurity in the form of DBZ, which was found to be present in the starting powders that were used in the preparation of the crystals from the vapour phase (refer to Section 5.6.3). As indicated previously, impurity presence has been identified as a possible mechanism for rationalising untwisting in twisted crystals of oxalic acid dihydrate and gypsum (Punin and Shtukenberg, 2008). Impurities are capable of affecting the pitch in twisted crystals by limiting their size, modifying their morphology and packing arrangement, or causing their growth to be suppressed under certain supersaturations (Shtukenberg et al., 2014c). In the case of twisted OXCBZ III, direct confirmation of the presence of DBZ within the structure of the polycrystalline fibres comprising the form III material crystallised from the vapour could not be obtained. Therefore, the exact mechanism of untwisting in vapour-grown OXCBZ III remains speculative. Whilst impurities have been known to facilitate untwisting, their presence in increasing amounts has also been associated with decreasing pitch values and more significant twisting in a number of systems, including aspirin (Cui et al., 2013). Establishing understanding of any effect that DBZ may have on the twisting behaviour of vapour- and solution-grown OXCBZ III would entail detailed structural analysis of the polycrystalline fibres and identification of differences in their respective lattice metrics at different positions along the long axis of each fibre. This type of analysis was not possible herein using conventional XRD and precluded definitive answers to be obtained with regards to DBZ's significance in the twisting of form III. It was noted that twisting was less prevalent in solution-grown material of form III than it was in the material grown from the vapour phase. Whilst the presence of smaller amounts of DBZ could have potentially played a role in the lower prevalence of twisting for solution-grown OXCBZ III, it is anticipated that the growth of twisted form III crystals from solution is influenced, at least in part, by solvent – solute interactions affecting the interfacial free energy (Spaepen, 1975; Spaepen and Meyer, 1976) between form III crystals and the ethanol/toluene mixture nucleating them and subsequently the growth of different facets on the surface of the crystals (Hartman and Bennema, 1980).

5.6.4.3 Twisting in the CBZ Family

To investigate the possible emergence of twisted morphology for the structurally related analogue molecules CBZ and CYT, vapour deposition at 140°C was performed separately onto silver foil substrates. The SEM micrographs of vapour-grown CBZ and CYT crystals are shown in Figures 5.30 and 5.31. The crystals were obtained after 18.5 hours of vapour deposition. XRPD was used to confirm the polymorphic form of the materials resulting from vapour deposition and the analysis indicated that they corresponded to CBZ form I (Appendix Figure A5.7) and a mixture of CYT forms I and II (Appendix Figure A5.8). Whilst several of the CBZ I crystals exhibited twisted ribbon-like morphology (Figure 5.30b), the CYT I and II crystals were not twisted but many were observed to be bent along the long axis (Figure 5.31). Droplets were clearly observed in the CBZ samples prepared by vapour deposition (Figure 5.30a), typically following two hours of depositing CBZ onto silver foil. However, experimental evidence confirming the direct growth of twisted CBZ I crystals from the droplets was never obtained, suggesting that these crystals may follow a different growth mechanism compared to OXCBZ III. The vapour-grown CBZ I ribbons are fundamentally different to the twisted fibres observed in OXCBZ III. The OXCBZ III crystals obtained from both solution and vapour deposition experiments are best described as aggregates of single crystals whereas the CBZ I crystals are twisted single crystals. Despite the differences noted between twisted CBZ I and OXCBZ III, the observation of twisted crystals for at least two out of five, i.e. 40% of compounds comprising the CBZ family (refer to Figure 4.33, section 4.5) reinforces the notion originally proposed by Bernauer that a significant number of molecular compounds are susceptible to crystal twisting (Bernauer, 1929). Fast evaporation experiments performed in attempts to crystallise twisted CBZ and CYT crystals from solution did not yield any evidence of twisting. More specifically, the solution-grown crystals obtained for CBZ (Figure 5.32a) corresponded to form II (Appendix Figure A5.9) and had block-like morphology whilst the CYT crystals (Figure 5.32b) comprised clusters of straight needles corresponding to a mixture of forms I and II (Appendix Figure A5.10). Overall, the observations derived from both the vapour deposition and solution crystallisation studies of OXCBZ, CBZ and CYT indicated that the occurrence of twisted morphology for OXCBZ III is unique amongst the isostructural *R*-3 structures in the CBZ family, with CBZ II and CYT I never found to exhibit twisting. This is in line with the diagonal compression and shear components previously described in Table 5.4 which suggest that CBZ II and CYT I crystals are

less susceptible to spontaneous twisting along their longest lengths than OXCBZ III crystals.

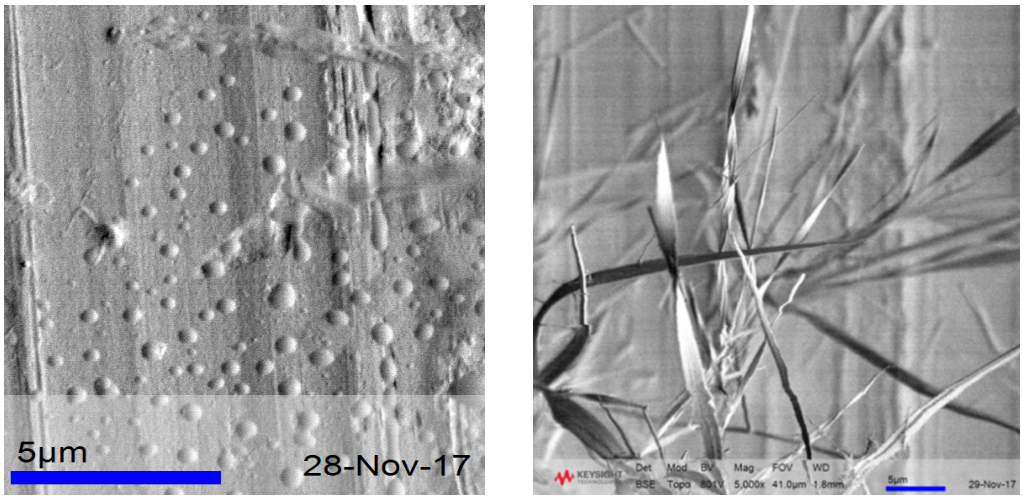

(a) (b)

Figure 5.30: SEM Micrographs depicting droplets (a) and twisted CBZ I crystals grown on silver foil following 18.5 hours of vapour deposition. The scale bar is 5 µm for both micrographs.

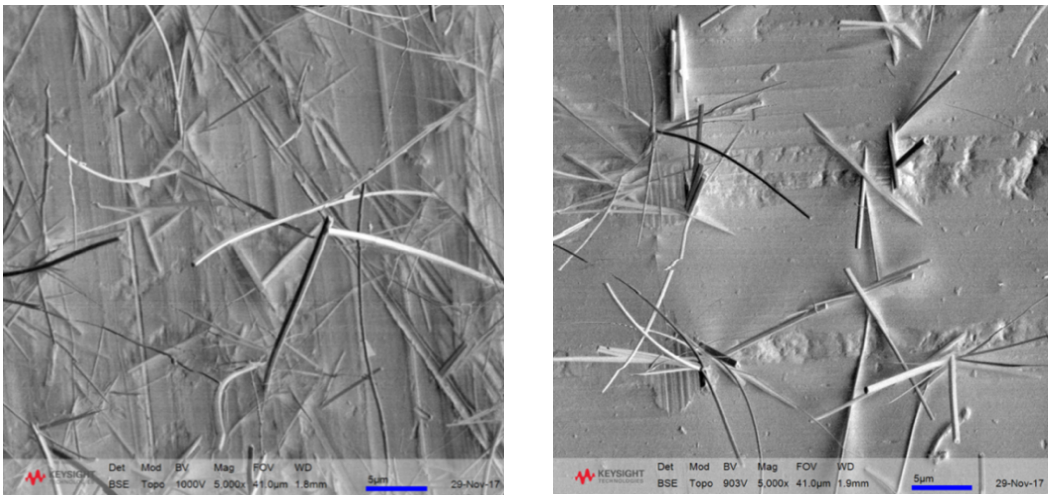

(a) (b)

Figure 5.31: SEM Micrographs depicting bent and straight CYT crystals grown on silver foil following 18.5 hours of CYT vapour deposition. The scale bar is 5 µm for both micrographs.

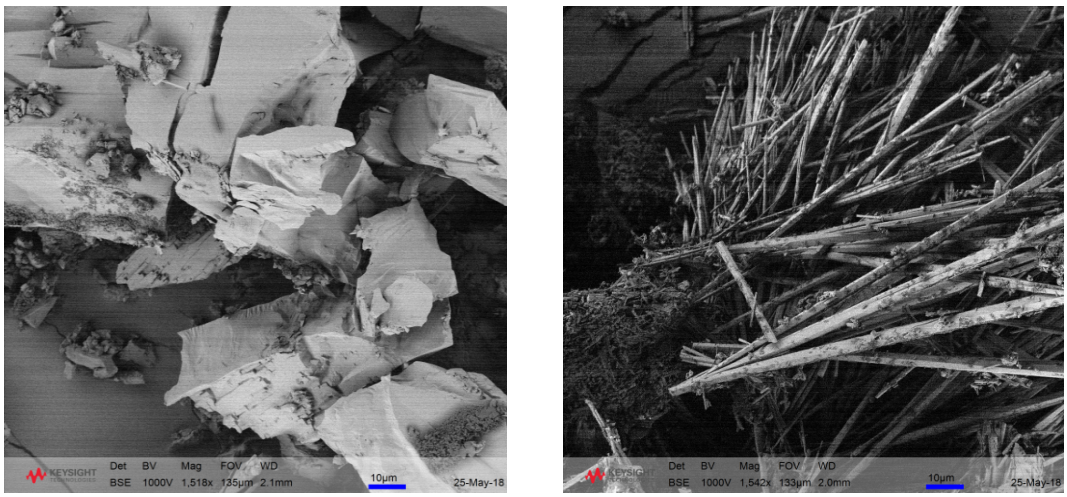

(a) **(b)**

Figure 5.32: SEM micrographs depicting CBZ (a) and CYT (b) crystals grown from 50:50 v/v ethanol/toluene mixture via fast evaporation at 50°C. The scale bar is 10 µm for both micrographs.

5.7 Summary

Twisted morphologies were unexpectedly observed under specific crystallisation conditions for OXCBZ form III, namely via physical vapour deposition and also from solution recrystallisation using ethanol/toluene mixtures. Vapour-grown twisted crystals of OXCBZ III were found to exhibit variable pitch along their respective lengths whereas solution-grown crystals exhibited regular pitch. SEM studies of the vapour-grown OXCBZ III material indicated that columnar twisted crystals emerge directly from amorphous droplets arising on the experimental substrates. Adjacent nanocrystals were found to nucleate within aggregates of the amorphous droplets and twisted spontaneously as they underwent growth. The aggregation of columnar crystals, resulting in a decrease in their surface area and free energy, was identified as the driving force for the emergence of twisted morphology and examination of the diagonal compression and shear components of calculated elastic constants indicated that form III is prone to spontaneous twisting. Figure 5.33 depicts the schematic representation of the crystal growth process observed during the crystallisation of OXCBZ III from vapour deposition. HPLC-MS analysis confirmed the presence of DBZ, a pharmacopeial impurity of OXCBZ, in the powder samples that yielded the twisted form III crystals, which can be used to explain the observed twist renormalisation. The experimental observations made suggest that the OXCBZ III crystals materialising from the vapour phase follow a non-classical, multi-step

nucleation model, analogous to protein crystallisation and biomineral studies as well as solution crystallisation investigations of organic and inorganic materials.

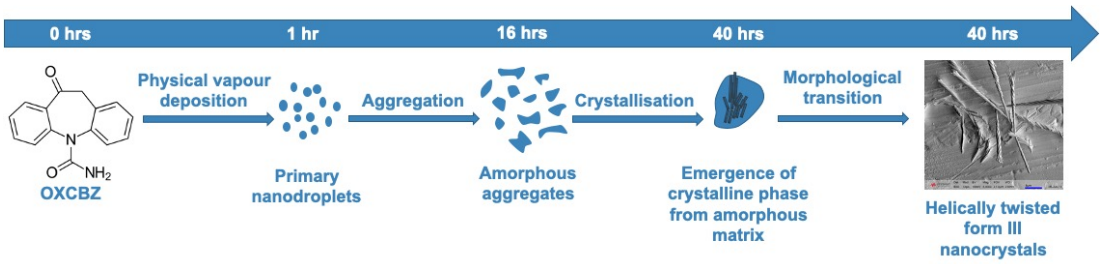

Figure 5.33: Schematic representation of the crystal growth mechanism observed in this work for twisted OXCBZ form III crystals grown from the vapour phase.

In the absence of direct experimental evidence and detailed mechanistic understanding for the formation of twisted crystals in solution-based crystallisation, "growth error/incommensurate" and "attached channel" theoretical models are proposed to explain the twisted morphology of OXCBZ III. These theoretical models are also applicable to the growth of the vapour-grown form III crystals and suggest that lattice mismatch between competing isostructural forms of OXCBZ III, predicted using CSP, can be used to rationalise the observation of twisting. The twisted morphology described herein for OXCBZ III is unique to this polymorph and was not observed in the isostructural CBZ II and CYT I forms. However, evidence of twisting was observed for crystals of CBZ form I grown from the vapour, indicating that multiple compounds in the CBZ family can crystallise with twisted morphology. The spontaneous twisting of OXCBZ III crystals limits their radial crystal growth and leads to the formation of bundles of polycrystalline fibres, thus explaining the difficulty in obtaining suitable single crystals for XRD measurements and comprehensive structural characterisation.

Chapter 6: Solid-State Screening Investigations of Evacetrapib and a Tetrazole Analogue

6.1 Introduction

The processing steps involved in the development of pharmaceutical drugs may result in unforeseen changes to their crystalline form (Grant et. al., 1986). One such change is solvent incorporation into a drug's crystal structure, resulting in hydrate or solvate formation. It has been estimated that 33% of organic compounds are susceptible to hydrate formation whilst ≈ 10% are capable of forming solvates robustly with organic solvents (Clarke et. al., 2010). The phenomenon of solvate formation has significant implications in pharmaceutical manufacturing as it can affect the physicochemical properties of drugs and the unexpected formation of solvates in the later stages of drug development can have notable impact on the manufacturability and pharmacokinetic properties of drug candidates (Vippagunta et. al., 2001). Therefore, a complete knowledge of the solid-form landscape, encompassing all possible polymorphs, hydrates and solvates is pivotal for designing robust manufacturing processes and avoiding the late appearance of unknown solid forms. A literature survey of solvates indicates that some compounds indiscriminately form solvates across a range of solvents (Bingham et al., 2001; Price et al., 2006; Campeta et al., 2010; Bhardwaj et al., 2013; Bhardwaj et al., 2019) while others are considerably more selective (Morissette et al., 2004; Braun et al., 2011; Braun et al., 2014a). Although progress has been made to understand the structural features that lead to solvate formation (Vippagunta et al., 2001; Price et al., 2006; Tessler and Goldberg, 2006), a comprehensive understanding of why some molecules form solvates more readily than others remains elusive. Hence, empirical approaches are required for the discovery of solvates.

Salts and cocrystals represent multi-component solids whose formation, similar to hydrates and solvates, can significantly affect the physicochemical properties of drugs, including optimising their aqueous solubility and dissolution rate (Serajuddin, 2007; Elder et al., 2013; Dai et al., 2018). Under appropriate conditions, solid-state screening investigations comprising solvates/hydrates, salts and/or cocrystals may result in the formation of more complex multi-component solids: solvated/hydrated salts, solvated/hydrated cocrystals and solvated/hydrated salt cocrystals (Aitipamula et al., 2012; Grothe et al., 2016). Solvated/hydrated salt cocrystals represent the most complex of these structures and can be defined as multi-component crystals that comprise one or more liquid solvents, two or more ions, and one or more coformers that are unionised and not liquid solvents (Grothe et al., 2016). The occurrence of solvated/hydrated salt cocrystals is rare (Grothe et al., 2016), accounting for 1.1% of

over 54500 multi-component organic crystal structures previously surveyed in the Cambridge Structural Database (CSD).

Solid-state screening studies typically comprise multiple crystallisation methods, both solvent-based and solvent-free, in order to maximise the likelihood of obtaining all practically relevant forms for a given compound. The resultant forms are characterised using a broad range of analytical tools to establish a thorough understanding of their structure, properties and relative thermodynamic stabilities. Cooling crystallisation, solvent evaporation, anti-solvent addition, vapour diffusion and slurry equilibration are solution-based protocols that have been utilised regularly in both industrial and academic screening studies (Morissette et al., 2004; Newman, 2013). In order to enhance the likelihood of solid-form discovery through solution-based crystallisation methods, an extensive library of solvents exhibiting a diverse range of physicochemical properties is usually employed (Carlson et al., 2003; Allesø et al., 2008; Mangin et al., 2009; Johnston et al., 2017). Manipulating process conditions such as temperature, supersaturation, agitation speed and cooling profile can improve the likelihood of sampling the true extent of solid-form diversity (Florence et al., 2006; Newman, 2013). Approaches targeting the formation of solvent-free products provide additional mechanisms for screening and, whilst not an exhaustive list, include physical vapour deposition (Srirambhatla et al., 2016; Case et al., 2018), crystallisation from the melt (Zhu et al., 2016), supercritical fluid (SCF) extraction (Akao et al., 2002; Chakravarty et al., 2019) and subjection to variable temperature or variable humidity conditions (Bhardwaj et al., 2019).

Chiral compounds are commonly encountered in pharmaceuticals and have been investigated with regards to solid-form diversity, with examples of polymorphic enantiomers (Burger et al., 1997; Stephenson et al., 2012) and racemates (Reutzel-Edens et al., 2000; Zhang et al., 2003; Dudognon et al., 2008; Kaemmerer et al., 2009; Isakov et al., 2013) reported. Moreover, chiral materials exhibiting multiple polymorphs in both pure enantiomer and racemic form have additionally been noted (Matell, 1952), including the active pharmaceutical ingredients (APIs) felodipine (Rollinger and Burger, 2001), modafinil (Linol et al., 2007) and diprophylline (Brandel et al., 2013).

In recent years, with the advancement in crystal structure prediction (CSP) studies, CSP has complemented experimental screening investigations and successfully contributed towards better informing the extent of solid-form diversity for a variety of pharmaceuticals and understanding their crystallisation behaviour (Price, 2004;

Neumann and Perrin, 2009; Bhardwaj et al., 2013; Kendrick et al., 2013; Braun et al., 2014a; Price et al., 2016; Price and Reutzel-Edens, 2016; Case et al., 2018; Askin et al., 2019; Bhardwaj et al., 2019). Figure 6.1 depicts some examples of select pharmaceuticals that have been subjected to a combination of CSP studies and experimental screening, illustrating the molecular complexity in terms of functionality and flexibility that can be tackled using contemporary CSP methods.

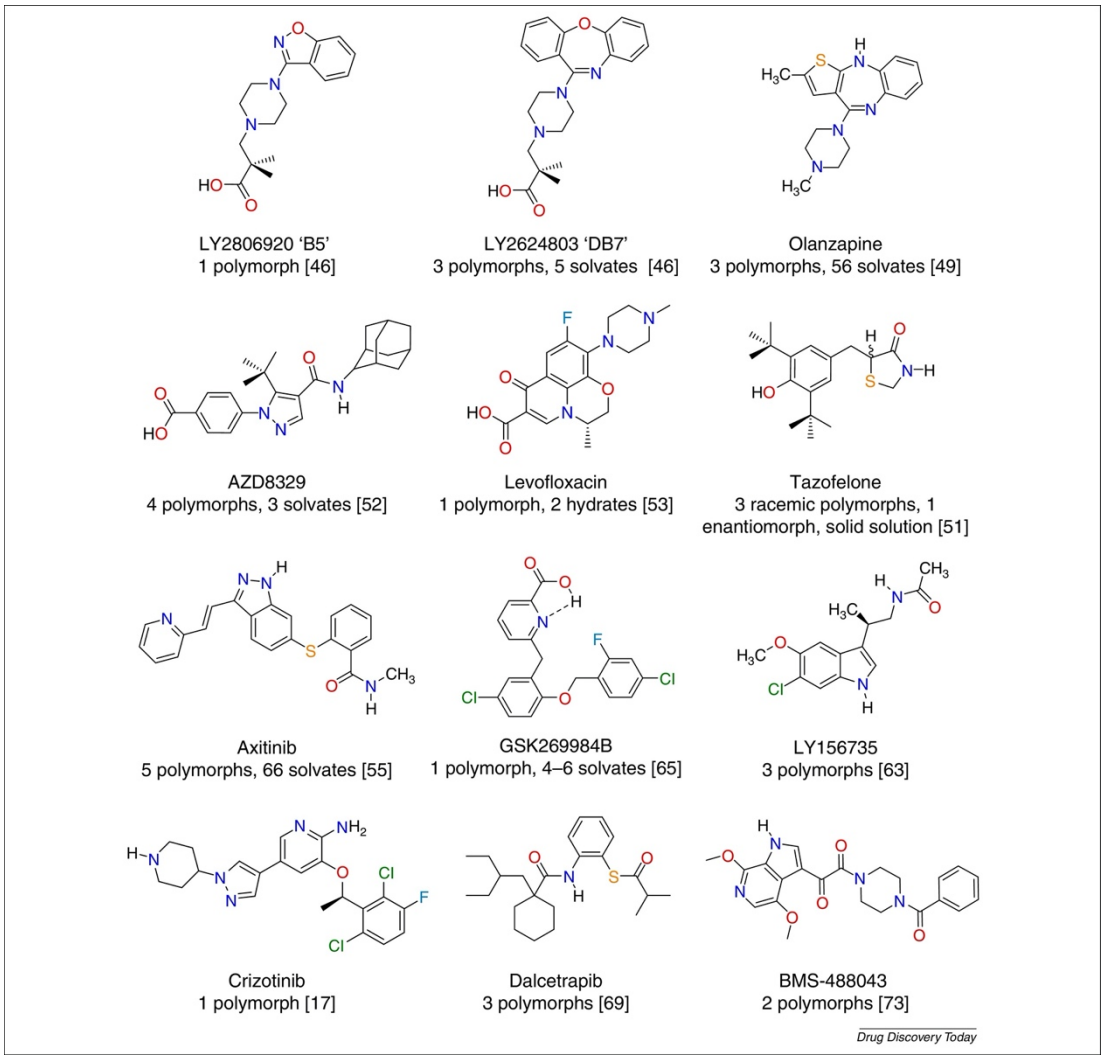

Figure 6.1: Examples of pharmaceutical compounds for which a combination of CSP investigations and experimental screening studies have been reported (reproduced from Price and Reutzel-Edens, 2016).

A particularly interesting case is that of crizotinib (Abramov, 2013), wherein CSP was used to rationalise the compound's lack of polymorphism by identifying a large energy gap (≥ 7.6 kJ/mol) between the most thermodynamically stable anhydrous form

observed experimentally and the rest of the computationally predicted structures identified in the CSP search. In the case of 5-HT_{2a} agonist 'DB7' (Braun et al., 2014a), the combination of CSP structures with experimental X-ray powder diffraction (XRPD) and solid-state ^{13}C nuclear magnetic resonance (NMR) data identified the presence of disorder in the dimethylpropanoic acid side-chain of the metastable form III, enabling a suitable structural model to be proposed for this polymorph. The combined use of XRPD, solid-state NMR and CSP has additionally been used to propose a suitable model for the crystal structure of form IV of AZD8329 in the absence of suitable single crystals for successful structure determination (Baias et al., 2013). Olanzapine form III represents an example of CSP rationalising the inability of a metastable form to yield phase-pure crystalline samples as form III was proposed to have a different stacking of the same molecular layers as metastable form II, consistently resulting in concomitant crystallisation of both forms in the experimental screen (Bhardwaj et al., 2013). The CSP landscape of olanzapine additionally highlighted the propensity of the compound to form solvated crystal structures with a diverse range of solvents. This was attributed to the inability of olanzapine to pack well with itself and form dense crystal structures. In the case of dalcetrapib, CSP studies inspired crystallisation experiments at high pressure which successfully induced nucleation of a novel, more stable dalcetrapib polymorph at non-ambient conditions (Neumann et al., 2015).

Whilst CSP offers several advantages with regards to understanding the solid-state behaviour of APIs when used as a complementary tool to experimental screening, covering the crystallographic space required to obtain structural information on all feasible forms of a compound is time-consuming and computationally demanding, particularly for multi-component structures comprising multiple molecules in the asymmetric unit (Price, 2014).

Even though many experimental studies have been able to produce novel forms, there have been relatively few studies that have successfully targeted the formation of previously unobserved but novel predicted polymorphs. CSP-informed templating experiments involving the use of isostructural crystal seeds to target the nucleation of predicted structures have been effectively used for a small number of chemically distinct APIs, yielding novel metastable polymorphs that had not been accessible using conventional screening methods (Arlin et al., 2011; Srirambhatla et al., 2016; Case et al., 2018). Carbamazepine (CBZ) form V was crystallised by physical vapour deposition onto crystals of 10,11-dihydrocarbamazepine (DHC) form II (Arlin et al.,

2011; Srirambhatla et al., 2016) and tolfenamic acid forms VI and VII were similarly prepared using crystals of mefenamic acid form I and a solid solution of tolfenamic and flufenamic acid respectively as templates (Case et al., 2018).

At the outset of the experimental work described herein, it was envisaged that utilising CSP as a guiding tool towards synthesising a structural analogue of evacetrapib (EVC) with a suitable stereochemistry would enable an isostructural template for a novel, predicted polymorph of EVC to be obtained. Whilst it was not possible to synthesise the analogue molecule with the required stereochemistry to be an exact molecular template, a tetrazole analogue bearing significant chemical similarity with EVC was derived instead. In light of the similarity between the two compounds, the potential structural similarities in experimentally produced forms are of interest.

The research described in this chapter aimed at implementing solid-state screening and characterisation studies of EVC and its closely-related tetrazole analogue (TAEVC) for the purpose of 1) exploring solid-state diversity in these structurally related compounds, 2) obtaining an understanding of the structures, stabilities and similarities between the solid forms observed experimentally and 3) assessing the possibility of utilising CSP-inspired, isostructural templating to crystallise novel solid forms for both compounds. Overall, 15 novel solvated/hydrated salt cocrystals are reported for EVC, including a hemi *tert*-butylamine (TBA) – hemihydrate structure successfully elucidated using single-crystal X-ray diffraction (SC-XRD). For TAEVC, a solid-form landscape is established for the first time, encompassing 28 solvated forms and 2 anhydrous forms. The crystal structures of 8 solvated TAEVC forms were derived using SC-XRD and the structure of an anhydrous racemic form was determined using XRPD.

6.1.1 Evacetrapib (EVC) and its Tetrazole Analogue (TAEVC)

EVC (IUPAC name: trans-4-({(5S)-5-[{[3,5-bis(trifluoromethyl)phenyl]methyl}(2-methyl-2H-tetrazol-5-yl)amino]-7,9-dimethyl-2,3,4,5-tetrahydro-1H-benzazepin-1-yl}methyl) cyclohexanecarboxylic acid) is a cholesterylester transfer protein inhibitor originally developed under the investigational name LY2484595 by Eli Lilly & Company for reducing the risk of cardiovascular disease (Cao et al., 2011; Eyvazian and Frishman, 2017). The molecular structures of EVC ($C_{31}H_{36}F_6N_6O_2$, molecular weight: 638.66 g/mol) and its recently-synthesised tetrazole analogue, TAEVC, ($C_{31}H_{36}F_6N_6O_3$, molecular weight: 654.66 g/mol) are shown in Figures 6.2a and 6.2b respectively. Both compounds were provided for experimental use by Lilly Research

Laboratories (Indianapolis, USA). EVC was supplied as a solvated salt cocrystal comprising one unionised EVC molecule, one EVC – TBA ion pair and residual solvents from the synthetic process of the material; the molecular structure of the as-received EVC material, excluding the residual solvents, is presented in Figure 6.2c. TAEVC was sourced as a racemic compound and two pure enantiomers with absolute configurations *R*,*R* and *S*,*S* which were confirmed using SC-XRD (refer to section 6.3.6.4). The details of the starting EVC and TAEVC materials provided by Eli Lilly and Company are shown in Table 6.4. Physical characterisation of the as-received materials is described in sections 6.3.1 and 6.3.5.

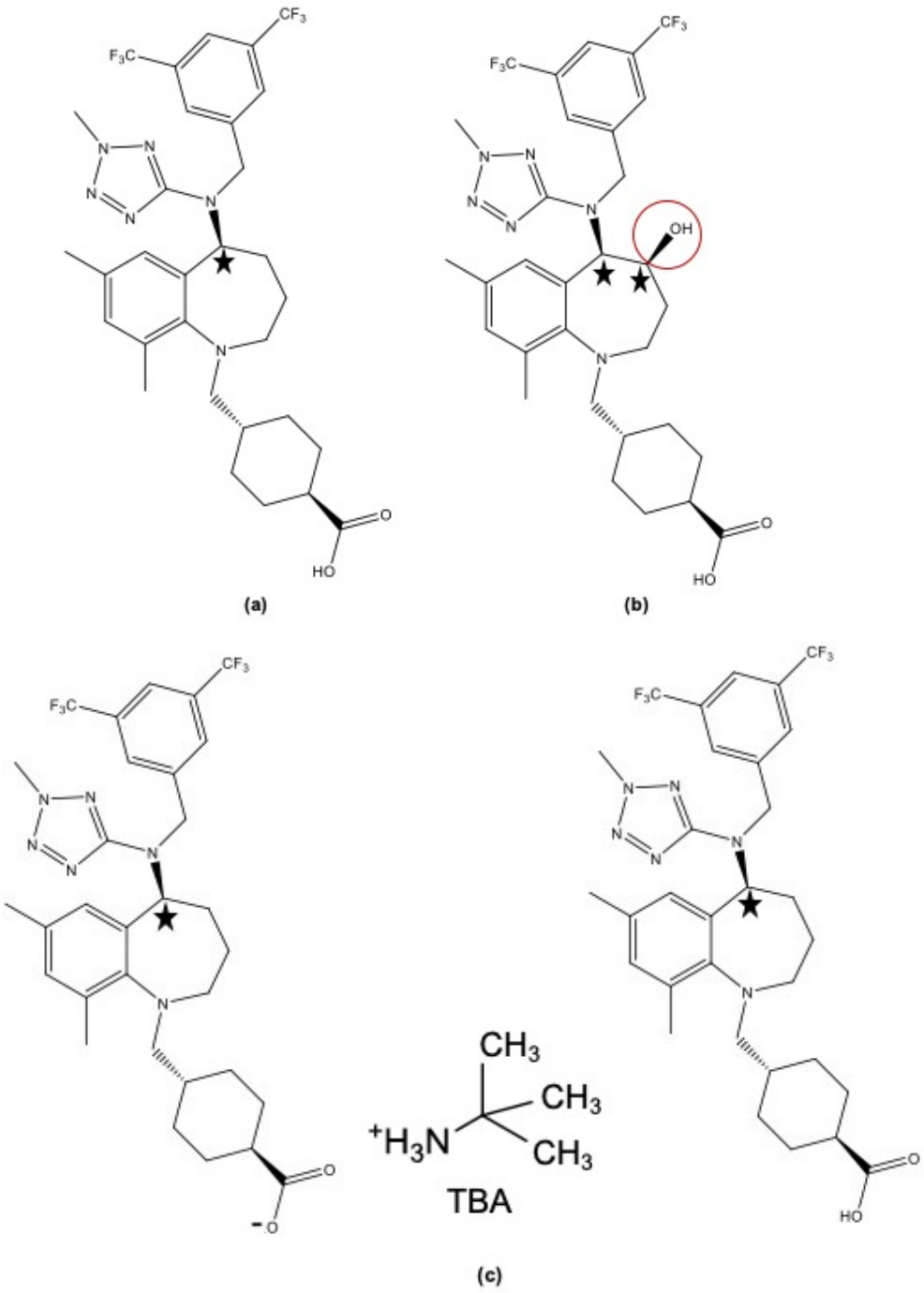

Figure 6.2: Molecular structures of EVC (a), TAEVC (b) and EVC – TBA solvated salt cocrystal supplied by Eli Lilly and Company (c). The red circle in TAEVC indicates the presence of an additional hydroxy group relative to EVC. Asterisks denote the presence of chiral centres. Residual solvents in (c) have been omitted.

EVC is an amphoteric API, exhibiting both acidic (OH in -COOH) and basic (N atom in benzazepine moiety) functionalities with known p*K*a values of 5.01 ± 0.02 (acid) and 3.77 ± 0.02 (base), making it prone to ionisation in solution under most pH profiles (Eli Lilly and Company, 2018-2020). The Δp*K*a value for EVC is less than zero, suggesting that the molecule can readily form cocrystals when interacting with suitable counterions (Bhogala et al., 2005). An anhydrous form of EVC, form I, has been reported in the CSD (Refcode: GIXHUS). Form I is known to crystallise in the monoclinic $P2_1$ space group with cell parameters a = 13.606(3) Å, b = 8.480(2) Å, c = 13.986(3) Å and β = 104.21(9)°. Experimental screening studies conducted previously revealed that EVC form I can be readily crystallised upon cooling solutions of EVC in 3:2 (v/v) 2-propanol/water, 3:1 acetonitrile/water and 1:3 butyl acetate/heptane (Eli Lilly and Company, 2018-2020). The unit cell packing arrangement of EVC form I is shown in Figure 6.3a. The tetrazole nitrogen (N1) (see Figure 6.3b for numbering) is hydrogen bonded to the carboxylic acid component via O-H···N interactions which extend infinitely along the crystallographic c axis (Figure 6.3a).

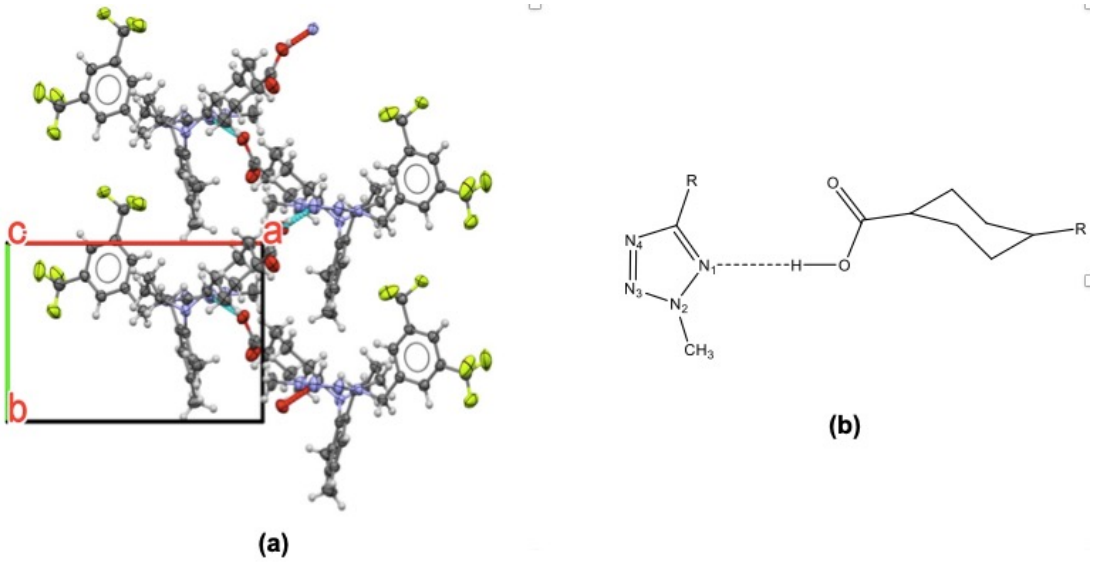

Figure 6.3: (a) Unit cell packing arrangement in EVC form I, viewed along the crystallographic c axis. (b) ChemDraw representation of hydrogen bonding observed in EVC form I. R in (b) denotes the rest of the molecule which has been omitted for clarity.

The crystallographic data of all known solid forms of EVC that have been fully characterised by SC-XRD, including a monohydrate, 3 solvates, a solvated salt and 3 solvated salt cocrystals, are presented in Tables 6.1 and 6.2.

Table 6.1: SC-XRD data of form I, known solvates and the monohydrate structure of EVC (Eli Lilly and Company, 2018-2020).

	Form I	Monohydrate	Methanol Solvate	Ethanol Solvate	Formic Acid Solvate
Crystal System	Monoclinic	Orthorhombic	Orthorhombic	Orthorhombic	Orthorhombic
Space Group	$P2_1$	$P2_12_12_1$	$P2_12_12_1$	$P2_12_12_1$	$P2_12_12_1$
***a* (Å)**	13.6083 (7)	8.5754 (5)	8.3881 (7)	8.4276 (10)	8.3660 (3)
***b* (Å)**	8.4771 (4)	16.3728 (9)	16.9057 (13)	17.004 (3)	17.7905 (5)
***c* (Å)**	13.9852 (7)	22.9830 (13)	23.4346 (16)	23.726 (3)	22.0059 (7)
β (°)	104.054 (4)	90	90	90	90
Volume (Å³)	1565.04 (1)	3226.9 (3)	3323.2 (4)	3400.1 (8)	3275.26 (18)
Z	2	4	4	4	4
Density (g/cm³)	1.355	1.315	1.341	1.338	1.389
Temperature (°C)	-173 (2)	-173 (2)	-173 (2)	-173 (2)	-173 (2)
Wavelength (Å)	1.54178	1.54178	1.54178	0.71073	1.54178

Table 6.2: SC-XRD data of known solvated salt and solvated salt cocrystal forms of EVC (Eli Lilly and Company, 2018-2020).

	TBA – 2-Propanol Solvated Salt	Hemi TBA – Hemi Ethanol Solvated Salt Cocrystal	Hemi TBA – Hemi 2-Propanol Solvated Salt Cocrystal	Hemi TBA – Hemi 1-Butanol Solvated Salt Cocrystal
Crystal System	Orthorhombic	Monoclinic	Monoclinic	Monoclinic
Space Group	$P2_12_12_1$	$P2_1$	$P2_1$	$P2_1$
***a* (Å)**	8.7856 (10)	19.9450 (4)	20.1022 (17)	19.8537 (4)
***b* (Å)**	20.7656 (4)	9.1976 (2)	9.1860 (8)	9.1309 (2)
***c* (Å)**	21.8088 (4)	20.1807 (5)	20.2168 (17)	20.1650 (4)
β (°)	90	103.503 (10)	103.710 (7)	104.896 (10)
Volume (Å³)	3978.76 (12)	3599.92 (13)	3626.8 (5)	3532.71 (13)
Z	4	4	4	4
Density (g/cm³)	1.289	1.288	1.292	1.339
Temperature (°C)	-173 (2)	23 (2)	23 (2)	-173 (2)
Wavelength (Å)	1.54178	0.71073	1.54178	1.54178

Solvates of EVC with methanol, ethanol, and formic acid and the known monohydrate form are all isostructural with one another (Table 6.1). Solvated forms with acetic acid, acetone, dimethyl sulphoxide (DMSO) and pyridine have also been identified, although their crystal structures have not been determined (Eli Lilly and Company, 2018-2020). EVC has been found to form a 1:1 solvated salt with TBA and 2-propanol, as well as solvated salt cocrystals comprising TBA, ethanol, 2-propanol and 1-butanol (Table 6.1). All of the aforementioned solvated salt cocrystals are isostructural and comprise one unionised EVC molecule, one EVC - TBA ion pair (identical to that shown in Figure 6.2c), and one unionised molecule of ethanol/2-propanol/1-butanol in the respective crystal structures, yielding a stoichiometry characteristic of that of hemisolvates. An additional 8 isostructural solvated salt cocrystals of EVC with TBA have been found in prior screening efforts, including structures comprising acetone and tetrahydrofuran (THF) as unionised solvent components, but the complete structures could not be elucidated (Eli Lilly and Company, 2018-2020).

This work aims to extend prior screening studies by investigating experimental approaches, process conditions and solvents that had not been previously explored in an effort to isolate and characterise additional solid forms of EVC and further study its structural diversity in the solid state. Contrary to EVC, no reported structural data of TAEVC have been reported to date, presenting a need to screen the analogue molecule and establish a solid-form landscape for the first time.

6.1.2 Crystal Structure Prediction (CSP) Investigations of EVC and TAEVC

CSP studies of EVC and TAEVC were performed using GRACE V 2.4 software (Avant-garde Materials Simulation, Germany) and the corresponding lattice energy landscapes are presented in Figures 6.4a and 6.4b respectively. The CSP-derived structures indicated isostructural templating as a potential route towards crystallising a novel EVC polymorph, predicted to be thermodynamically more stable than the known anhydrous form I. In the lattice energy landscape of EVC, the predicted global minimum is found 4.4 kJ/mol lower than the experimentally observed form I. In the landscape of TAEVC, the predicted structure circled in orange is isostructural to the lowest ranked EVC structure and is found 10.1 kJ/mol higher than the predicted global minimum, a region wherein ≈ 90% of polymorphic pairs are unlikely to be realised experimentally (Burger and Ramberger, 1979; Cruz-Cabeza et al., 2015). The unit cell parameters of the target EVC and TAEVC predicted structures are given in

Table 6.3. The target structures have similar lattice metrics and also exhibit similar hydrogen bonding arrangements (Figure 6.5a), hinting towards the possibility of utilising the predicted TAEVC form as a template to nucleate the low energy EVC structure in a manner similar to how CBZ form V and tolfenamic acid forms VI and VII were originally prepared (Arlin et al., 2011; Srirambhatla et al., 2016; Case et al., 2018). However, the synthesised TAEVC molecule was found to exhibit a different stereochemistry compared to the predicted molecule. The stereochemistry of the synthesised molecule was assigned as C9 (*R*) and C8 (*R*) based on SC-XRD studies (refer to section 6.3.6.4), whilst the predicted TAEVC molecule (Figure 6.5b) exhibited conformation of C9 (*R)* and C8 (*S)*. Therefore, the isostructural templating methodology was no longer a feasible option for pursuing targeted crystallisation of the low-energy EVC structure.

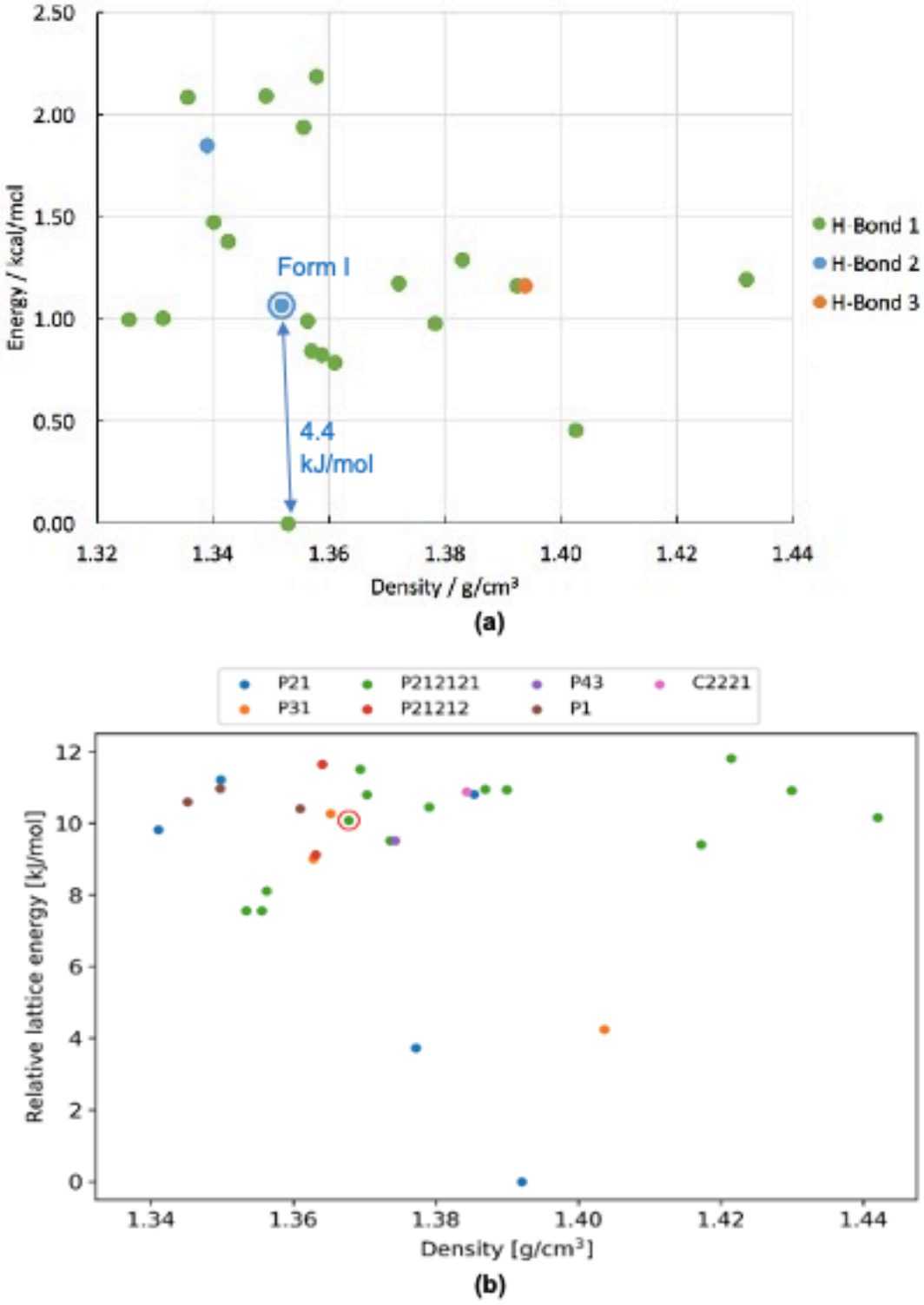

Figure 6.4: CSP lattice energy landscape of (a) EVC and (b) TAEVC (Eli Lilly and Company, 2018-2020). All predicted structures depicted are DFT-D optimised, comprise Z' = 1 and correspond to chiral space groups only.

Table 6.3: Crystallographic data of the target EVC form and the isostructural TAEVC template (Eli Lilly and Company, 2018-2020).

Crystal Structure	Space Group	*a* (Å)	*b* (Å)	*c* (Å)	α/β/γ (°)	Volume (Å^3)
Target EVC Form	$P2_12_12_1$	9.641	11.461	28.376	90	3135.36
TAEVC Template	$P2_12_12_1$	9.424	11.712	28.802	90	3179.09

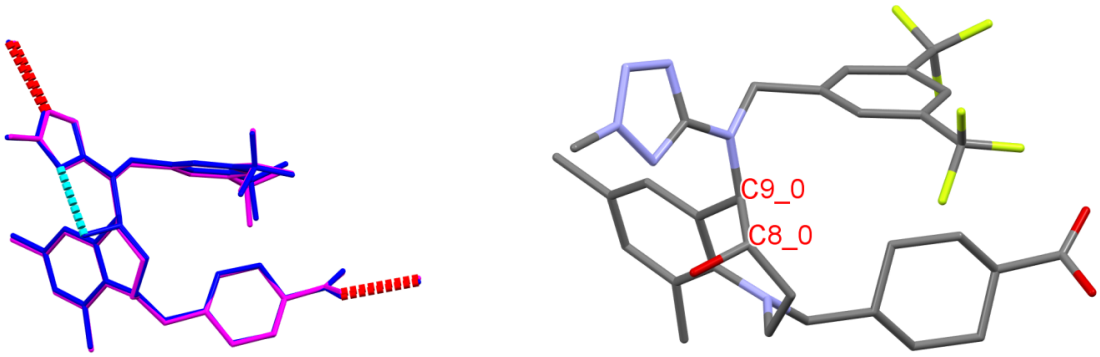

(a) (b)

Figure 6.5: (a) overlay of molecular conformations of predicted forms of EVC and TAEVC. Blue – molecular conformation of EVC; purple – molecular conformation of TAEVC. (b) The absolute configuration of atoms C9 and C8 atoms in the predicted TAEVC structure was assigned as C9 (*R*), C8 (*S*).

6.2 Materials and Methods

6.2.1 Materials

The details of the starting EVC and TAEVC materials provided by Eli Lilly for physical characterisation and experimental solid-form screening are provided in Table 6.4.

Table 6.4: Overview of starting materials obtained from Eli Lilly and Company for physical characterisation and solid-state screening investigations of EVC and TAEVC.

Material	Eli Lilly and Company Identifier	Experimental Notation	Amount
EVC (Solvated Salt Cocrystal with TBA)	LY2484595	EVC – TBA	10 g
TAEVC - 1 (Amorphous Enantiomer)	LSN-3516604	TAEVC1	6.5 g
TAEVC - 2 (Crystalline Enantiomer)	LSN-3516605	TAEVC2	7 g
TAEVC - 3 (Racemic Compound)	LSN-3516606	TAEVC3	450 mg

6.2.2 Methods

The experimental approach utilised herein followed the workflow depicted in Figure 6.6. Details on the individual methods comprising this workflow are presented in sections 3.2.1, 3.2.4.1, 3.2.5, 3.2.6.3, 3.2.7.1.2, 3.2.7.1.3, 3.2.7.1.4, 3.2.7.1.5, 3.2.7.1.6, 3.2.7.2 – 3.2.7.5, 3.2.7.7.1 and 3.2.7.11.

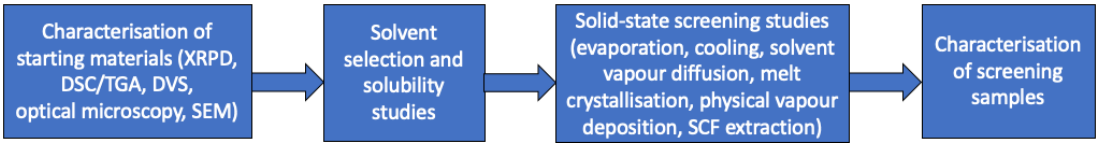

Figure 6.6: Workflow of experimental approach implemented for physical characterisation and solid-state screening of the EVC and TAEVC starting materials.

6.3 Results and Discussion

6.3.1 Characterisation of EVC Starting Material (EVC – TBA)

6.3.1.1 Optical Microscopy and Scanning Electron Microscopy (SEM)

Representative optical and SEM micrographs of EVC – TBA were collected using the methods described in sections 3.2.7.5 and 3.2.7.7.1 and are presented in Figure 6.7. Crystals were found to be agglomerated with an average size below 10 μm in all dimensions, which precluded characterisation using SC-XRD.

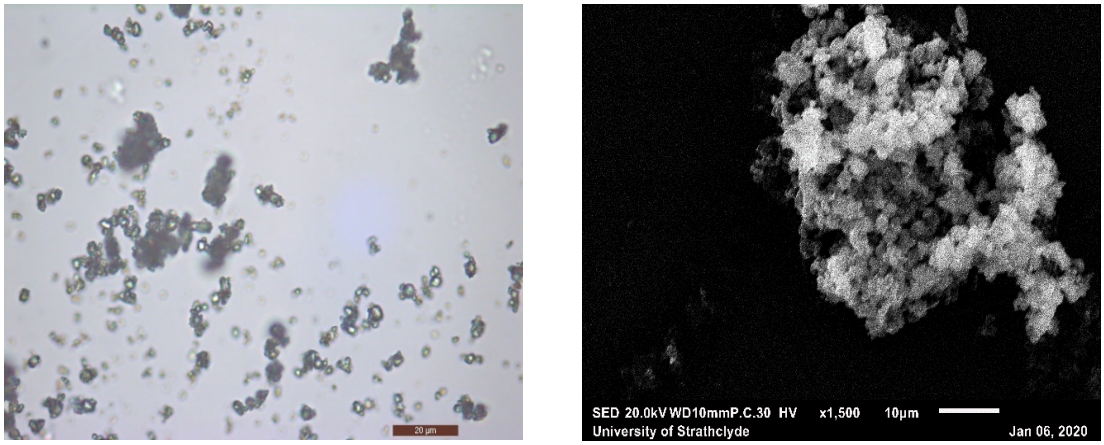

Figure 6.7: Optical microscopy (left) and SEM (right) micrographs of EVC – TBA. The scale bar is 20 μm for the optical micrograph and 10 μm for the SEM micrograph.

6.3.1.2 X-ray Powder Diffraction (XRPD)

A representative XRPD pattern (Figure 6.8) of EVC – TBA was collected using the method described in section 3.2.7.1.6.4. It was noted that the powder diffraction pattern of this material matched closely with those of the isostructural solvated salt cocrystals of EVC outlined in Table 6.2 (Eli Lilly and Company, 2018-2020). The pattern was indexed with *DICVOL91 (*Boultif and Louër, 1991) as implemented in *DASH* software (David et al., 2006). The solutions from the indexing routine are shown in Table 6.5. The monoclinic-*b* solution with the highest figures of merit, M (20) = 13.1 and F (20) = 44.9, was assigned to the $P2_1$ space group through assessment of systematic absences aided by *ExtSym* (Markvardsen et al., 2008) in *DASH*. Pawley refinement (Pawley, 1981) was performed in *TOPAS* (Coelho, 2018) to confirm the indexing and space group assignments (Figure 6.8). The residual values obtained for the Pawley fit were R_{wp} = 4.14% and R_p = 3.06% and suggested that the best indexing solution returned by *DICVOL91* was representative of the XRPD pattern of EVC – TBA. The refined unit cell parameters derived from Pawley fitting were *a* = 20.179 (9) Å, *b* = 9.210 (5) Å, *c* = 19.914 (11) Å and β = 103.519 (3)°. No further structure determination attempts were made for EVC – TBA following Pawley refinement.

Table 6.5: Indexing solutions, derived from *DICVOL91* in *DASH*, corresponding to the XRPD pattern of EVC – TBA.

Crystal System	*a* (Å)	*b* (Å)	*c* (Å)	α (°)	β (°)	γ (°)	Volume (Å^3)	M (20)	F (20)
Monoclinic	20.147	9.182	19.873	90.0	103.44	90.0	3575.89	13.1	44.9
Monoclinic	20.130	9.187	19.874	90.0	76.56	90.0	3574.94	11.9	41.8

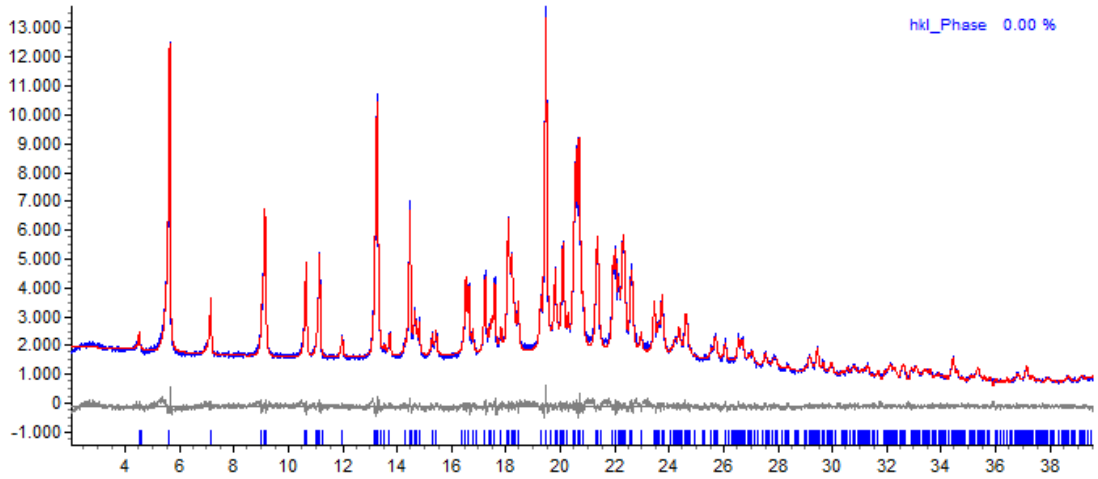

Figure 6.8: Pawley fit of EVC – TBA. the blue pattern corresponds to experimentally observed data (y_{obs},) the red pattern represents calculated data (y_{calc}) based on the indexing solution with the highest figures of merit in Table 6.5 and the grey pattern indicates differences between the measured and calculated data [(y_{obs} - y_{calc})/$\sigma(y_{obs})$]. The blue tick marks represent calculated diffraction peaks based on the refined unit cell parameters of EVC – TBA.

6.3.1.3 Differential Scanning Calorimetry/Thermogravimetric Analysis (DSC/TGA) and Variable Temperature XRPD (VT-XRPD)

Representative DSC/TGA traces (Figure 6.9) and VT-XRPD scans (Figure 6.10) of EVC – TBA were collected using the methods described in sections 3.2.7.3 and 3.2.7.1.3 and illustrate changes in the material as a function of temperature. DSC/TGA analysis indicates that sample weight loss (1.60% ± 0.07%) occurs which coincides with two endothermic peaks at 126.6°C (± 1.29°C) and 142.1°C (± 0.31°C); an onset temperature of 116.8°C (± 1.57°C) was noted for the first endothermic peak. The endotherms observed can be attributed to sample desolvation followed by a melting event occurring in succession.

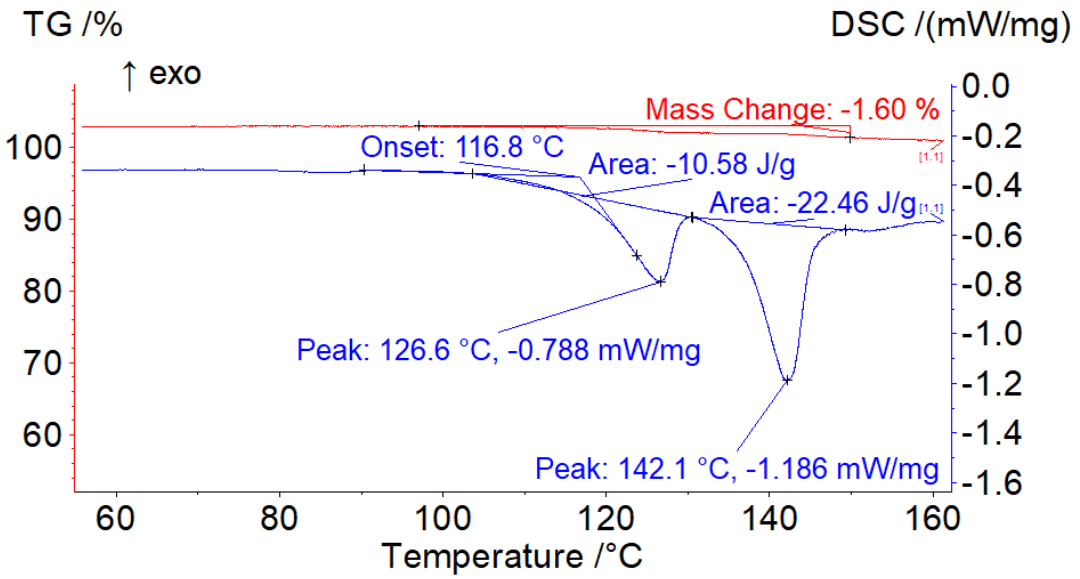

Figure 6.9: Representative DSC/TGA traces of EVC – TBA.

VT-XRPD analysis indicates significant decrease in the intensity of the reflections at ≈ 122°C. This is followed by gradual melting of the material with complete melting occurring at above 147°C, consistent with the thermal analysis (Figure 6.9). The Pawley profile fitting of the pattern at 132°C (Figure 6.11) indicates no significant change in the unit cell parameters, confirming that the phase composition of the material does not change upon heating. The refined cell parameters obtained at 132°C were a = 20.394 (5) Å, b = 9.259 (2) Å, c = 19.989 (5) Å and β = 103.814 (11)° with residual values of R_{wp} = 4.32% and R_p = 2.36%.

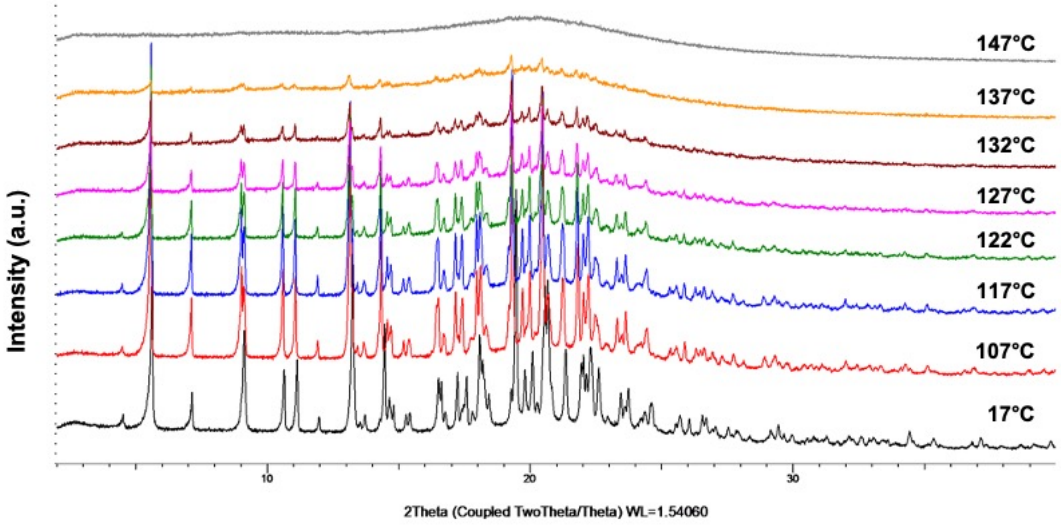

Figure 6.10: VT-XRPD analysis of EVC – TBA.

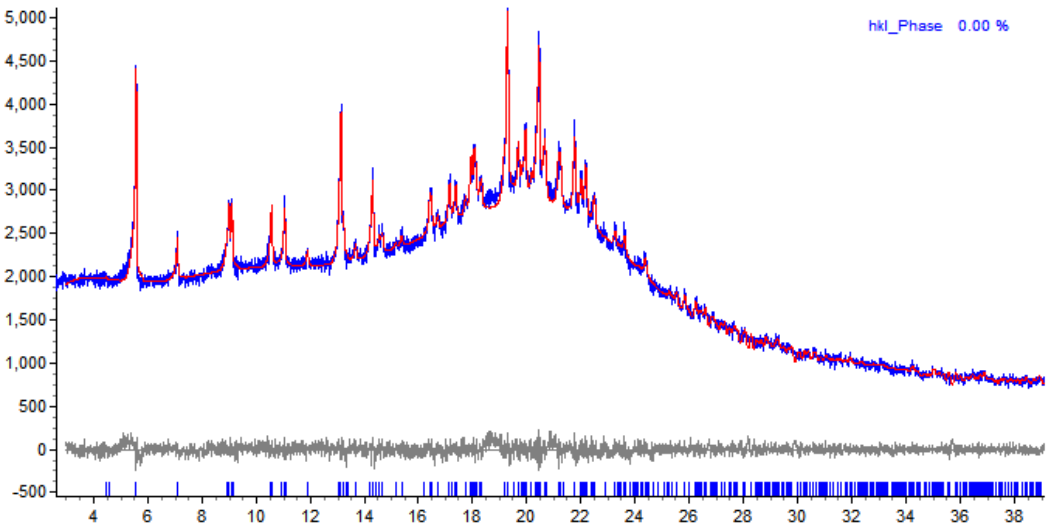

Figure 6.11: Pawley fit of EVC – TBA at 132°C.

6.3.1.4 Dynamic Vapour Sorption (DVS)

DVS analysis (refer to section 3.2.7.11 for method details) was employed to investigate the hydration and dehydration profiles of EVC – TBA. The isotherm plot of the material is given in Figure 6.12. A change in mass ≈ 0.9% was observed in the 0 to 95% RH range during both sorption and desorption cycles, which is likely due to surface adsorption of water molecules. The mass change occurred gradually for both sorption and desorption cycles and the largest amount of moisture uptake during the sorption cycles was observed between 70 – 80% RH and corresponded to 0.22%, hinting towards non-stoichiometric hydrate formation (Griesser, 2006). Whilst the mechanism of moisture uptake remains speculative, a small difference (hysteresis) between both sorption and desorption isotherms was observed, suggesting that trace amounts of solvent molecules in the crystal structure may have been replaced by water molecules.

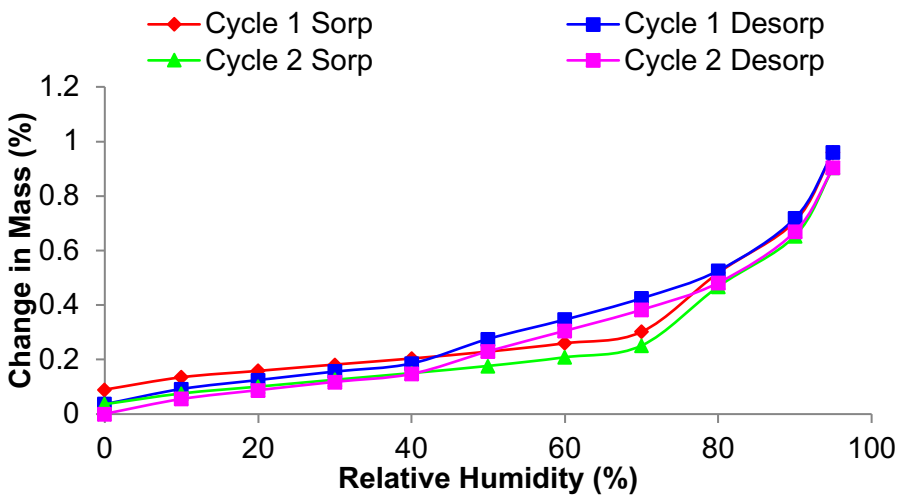

Figure 6.12: DVS isotherm plot of EVC – TBA.

6.3.2 Solubility of Starting Materials

The experimental solubility of the starting materials in the solvents used for solid-state screening was determined by solvent addition method (refer to section 3.2.6.1) and the corresponding values are provided in Table 6.6. A list of select physicochemical properties for the chosen solvents is provided in Appendix Table A6.1. It should be noted that three of the solvents utilised in screening experiments (cyclohexane, hexane and water) are not shown in Table 6.6 as they were solely employed as anti-solvents due to their inability to dissolve any of the starting materials at room temperature. In the case of EVC – TBA, the experimental solubility in a range of solvents had previously been established by Eli Lilly and Company (Eli Lilly and Company, 2018-2020) and those solvents were generally excluded from the solubility determination protocol and subsequent solid-state screen in order to cover novel experimental space. For TAEVC3, only 10 solvents could be investigated due to the limited amount of material that was received.

The solubility data obtained indicate that EVC – TBA has solubility > 40 mg/mL in 15 out of the 16 solvents investigated and for 10 of those solvents high solubility ≥ 150 mg/mL was noted. The lowest solubility (17.6 mg/mL) for EVC – TBA was observed in 2-butanol. TAEVC1 was found to be more soluble than TAEVC2 in up to 12 of the 22 solvents selected, an expected outcome given the amorphous nature of the TAEVC1 material (Murdande et al., 2010). The solubility data further indicate that TAEVC3 is less soluble than TAEVC1 and TAEVC2 in up to 9 of the 10 solvents studied with significant solubility differences noted in acetonitrile, 1,4-dioxane,

ethyl acetate, methanol, and THF. Racemic compounds are generally known to exhibit lower solubility than the respective enantiomers (Repta et al., 1976; El-Arini et al., 1998; Gu and Grant, 2003) so the observation of enhanced solubility properties for TAEVC1 and TAEVC2 relative to TAEVC3 is not surprising. Toluene was the only solvent in which TAEVC3 was found to be more soluble than TAEVC1 and TAEVC2, albeit with minor differences in the experimentally derived values.

Table 6.6: Experimental solubility at room temperature of EVC – TBA and TAEVC starting materials in various solvents. N/A indicates that the corresponding solvent was not used in the screening experiments of the respective material.

Solvent	Experimental Solubility of EVC – TBA (mg/mL)	Experimental Solubility of TAEVC1 (mg/mL)	Experimental Solubility of TAEVC2 (mg/mL)	Experimental Solubility of TAEVC3 (mg/mL)
Acetic Acid	300	150 – 300	150	N/A
Acetone	42.9	106.7	106.7	N/A
Acetonitrile	N/A	80	64	7.69
1-Butanol	60	80	42.9 – 60	40
2-Butanol	17.6	150	20 – 23.1	11.1
2-Butanone	150	150	140	N/A
Butyl Acetate	300	21.4	18.8	N/A
Chloroform	N/A	106.7	60	N/A
1,2-Dichloroethane	150	10	7.69	3.61 – 4.11
1,4-Dioxane	N/A	32	45.7	11.1
Diethyl Ether	42.9	30	29.1 – 35.6	N/A
Ethanol	60	30	37.5	34
2-Ethoxyethanol	300	150	130	N/A
Ethyl Acetate	N/A	150	150	33.3
Furfural	300	160	100	N/A
Methanol	300	150	150	60
2-Methoxyethanol	150	150	150	N/A
Methyl Acetate	60	106.7	60	N/A
2-Propanol	N/A	8.89	13.9 – 15.2	N/A
THF	150	150	150	60
Toluene	N/A	6.15	6.81	7.69
TFE	300	14.3	11 – 11.9	N/A

6.3.3 Solid-State Screening Studies of EVC

6.3.3.1 Summary of Solution-Based Screening Studies

The results of screening studies of EVC are summarised in Table 6.7. These outcomes are based on sample analysis using XRPD (an overview of the distinct powder pattern types is provided in Appendix Figure A6.5) and SC-XRD (refer to section 6.3.3.3) where sufficient sample was obtained or single crystals were of appropriate quality to allow analysis.

Table 6.7: Summary of solution-based screening studies of EVC.

Solvent	Evaporation at Room Temperature	Evaporation at 50°C	Cooling Crystallisation
Acetic Acid	Amorphous material	Amorphous material	Insufficient material/no solid product available for analysis
Acetone	Solvated material isostructural to EVC – TBA	Solvated material isostructural to EVC – TBA	Solvated material isostructural to EVC – TBA
1-Butanol	Solvated material isostructural to EVC – TBA	Solvated material isostructural to EVC – TBA	Solvated material isostructural to EVC – TBA
2-Butanol	Solvated material isostructural to EVC – TBA	Amorphous material	Solvated material isostructural to EVC – TBA
2-Butanone	Solvated material isostructural to EVC – TBA	Poorly crystalline material	Solvated material isostructural to EVC – TBA
Butyl Acetate	Amorphous material	Amorphous material	Solvated material isostructural to EVC – TBA
1,2-Dichloroethane	Solvated material isostructural to EVC – TBA	Solvated material isostructural to EVC – TBA	Solvated material isostructural to EVC – TBA
Diethyl Ether	Poorly crystalline material	Amorphous material	Solvated material isostructural to EVC – TBA
Ethanol	hemi TBA, hemihydrate salt cocrystal	Amorphous material	hemi TBA, hemihydrate salt cocrystal
2-Ethoxyethanol	Poorly crystalline material	Amorphous material	Solvated material isostructural to EVC – TBA
Furfural	Amorphous material	Amorphous material	Solvated material isostructural to EVC – TBA
Methanol	Mixture of methanol solvate & monohydrate	Mixture of methanol solvate & monohydrate	Mixture of methanol solvate & monohydrate

2-Methoxyethanol	Solvated material isostructural to EVC – TBA	Solvated material isostructural to EVC – TBA	Solvated material isostructural to EVC – TBA
Methyl Acetate	Solvated material isostructural to EVC – TBA	Solvated material isostructural to EVC – TBA	Solvated material isostructural to EVC – TBA
THF	Solvated material isostructural to EVC – TBA	Amorphous material	Insufficient material/no solid product available for analysis
TFE	Solvated material isostructural to EVC – TBA	Amorphous material	Insufficient material/no solid product available for analysis
Vapour Diffusion Experiments			
Solvent	**Anti-Solvent**	**Experimental Outcome**	
Butyl Acetate	2-Butanol	Solvated material isostructural to EVC – TBA	
Butyl Acetate	1,2-Dichloroethane	Solvated material isostructural to EVC – TBA	
2-Butanone	Cyclohexane	Solvated material isostructural to EVC – TBA	
Acetone	Cyclohexane	Solvated material isostructural to EVC – TBA	
1,2-Dichloroethane	Cyclohexane	Solvated material isostructural to EVC – TBA	
Ethanol	2-Butanol	hemi TBA, hemihydrate salt cocrystal	
Methanol	2-Butanol	Solvated material isostructural to EVC – TBA	
2-Methoxyethanol	Water	Solvated material isostructural to EVC – TBA	
THF	Water	Solvated material isostructural to EVC – TBA	
TFE	Butyl Acetate	Insufficient material/no solid product available for analysis	
2-Ethoxyethanol	Water	Amorphous material	
Acetic Acid	Cyclohexane	Amorphous material	

Evaporative crystallisation of EVC – TBA in ethanol under room temperature conditions resulted in the formation of a novel hemi TBA, hemihydrate salt cocrystal and yielded suitable single crystals for the full structure to be determined (refer to section 6.3.3.3 for complete crystallographic analysis). Pawley fitting of crystalline material derived from 1-butanol against the unit cell parameters of the known hemi TBA, hemi 1-butanol solvated salt cocrystal of EVC described in Table 6.2 indicated isostructurality (see Appendix Figure A6.6); however, the lack of high-quality single crystals for the material recrystallised from 1-butanol by evaporation did not allow confirmation to be obtained as to whether the two structures are identical. Evaporation at room temperature in 9 out of the 16 solvents employed experimentally resulted in polycrystalline powders that exhibited diffraction patterns which were highly similar to the pattern of EVC – TBA, confirming the existence of more structures that are isostructural to EVC – TBA and the previously known solvated salt cocrystals of EVC. Samples obtained via evaporation of acetic acid, butyl acetate and furfural

solutions yielded powder or gel-like materials which were found to be amorphous whereas materials derived via crystallisation from diethyl ether and 2-ethoxyethanol showed poor crystallinity and could not be indexed. Unlike the evaporation studies performed at ambient temperature, screening experiments involving solvent evaporation at 50°C predominantly resulted in amorphous products (9 out of 16 solvents). In the case of acetone, 1-butanol, 1,2-dichloroethane, 2-methoxyethanol and methyl acetate solutions, evaporation at elevated temperature yielded samples for which poor crystallinity was noted and for 2-butanone solutions poorly crystalline products were obtained.

In the cooling crystallisation and vapour diffusion screens the majority of solvent systems (11 out of 16 in cooling and 9 out of 12 in vapour diffusion) were found to yield samples isostructural to EVC – TBA. Cooling crystallisation from ethanol yielded the novel hemi TBA, hemihydrate structure whereas cooling of acetic acid, furfural, THF and 2,2,2-trifluoroethanol (TFE) solutions yielded insufficient sample for characterisation. Two of the solvent/anti-solvent combinations explored in the vapour diffusion experiments (2-ethoxyethanol/water and acetic acid/cyclohexane) resulted in amorphous materials and TFE/butyl acetate yielded no solid product for subsequent characterisation. All crystallisation experiments performed in methanol, with the exception of those comprising vapour diffusion, resulted in disproportionation (Stephenson et al., 2011) of EVC – TBA and yielded mixtures of the known methanol solvate and monohydrate structures of unionised EVC presented in Table 6.1. The composition of the bulk materials retrieved from the methanol-based crystallisations was verified using Pawley fitting (Appendix Figure A6.7).

Whilst several amorphous products were derived from the screening experiments conducted for EVC, insufficient sample amounts precluded efforts to crystallise these products and characterise them further.

6.3.3.2 DSC/TGA Analysis of Screening Samples

Simultaneous DSC/TGA studies (refer to section 3.2.7.3 for method) were performed for the solvated EVC samples to obtain information on their stoichiometry and attempt to correlate that information with data extracted from SC-XRD analysis where applicable. A complete overview of generated DSC/TGA data is presented in Table 6.8.

The TGA measurements obtained for the various solvated samples indicated a predominantly non-stoichiometric nature as they were found to comprise significantly

less than 1 mole of solvent in the unit cell per 1 mole of EVC, with the exception of samples obtained from ethanol where an average of 0.50 mole (± 0.04) was observed, indicating the formation of a hemisolvate/hemihydrate which was confirmed by SC-XRD. Representative DSC/TGA traces (Figure 6.13) of the hemihydrate salt cocrystal material obtained by recrystallisation of EVC – TBA from ethanol revealed a broad endothermic peak at 149.1°C with corresponding onset of 134.9°C, coinciding with a weight loss of 3.43%. The occurrence of the broad endotherm can be attributed to simultaneous desolvation and melting of the material.

It should be noted that the DSC/TGA measurements obtained solely comprised materials that were derived following complete solvent evaporation and therefore a notable loss in the amount of solvent included in the crystal structures of these materials was to be expected. DSC/TGA data for solvated samples obtained by crystallisation from butyl acetate, 2-ethoxyethanol and furfural could not be obtained.

Table 6.8: Overview of DSC/TGA measurements performed for solvated EVC samples. Standard deviation values are provided in parentheses (n = 3 except for methyl acetate samples where n = 2).

Solvent of Crystallisation	Peak of Melting (°C)	Weight Loss Observed (%)	Corresponding Amount of Solvent (mole) per 1 mole of EVC
Acetone	137.8 (± 7.60)	3.18 (± 1.55)	0.35 (± 0.17)
1-Butanol	134.3 (± 2.94)	2.99 (± 1.17)	0.28 (± 0.13)
2-Butanol	140.0 (± 0.95)	4.41 (± 0.45)	0.38 (± 0.04)
2-Butanone	130.4 (± 4.01)	2.48 (± 0.47)	0.21 (± 0.04)
1,2-Dichloroethane	136.1 (± 0.31)	3.11 (± 0.36)	0.20 (± 0.02)
Diethyl Ether	130.6 (± 0.64)	1.93 (± 1.72)	0.17 (± 0.16)
Ethanol	147.4 (± 1.92)	3.69 (± 0.36)	0.50 (± 0.04)
Methanol	100.6 (± 5.21)	1.50 (± 0.32)	0.30 (± 0.06)
2-Methoxyethanol	128.5 (± 5.51)	3.53 (± 2.02)	0.30 (± 0.17)
Methyl Acetate	137.1 (± 3.61)	4.26 (± 0.40)	0.37 (± 0.04)
THF	143.8 (± 3.35)	4.81 (± 0.73)	0.44 (± 0.04)
TFE	134.7 (± 1.70)	5.47 (± 3.24)	0.35 (± 0.21)

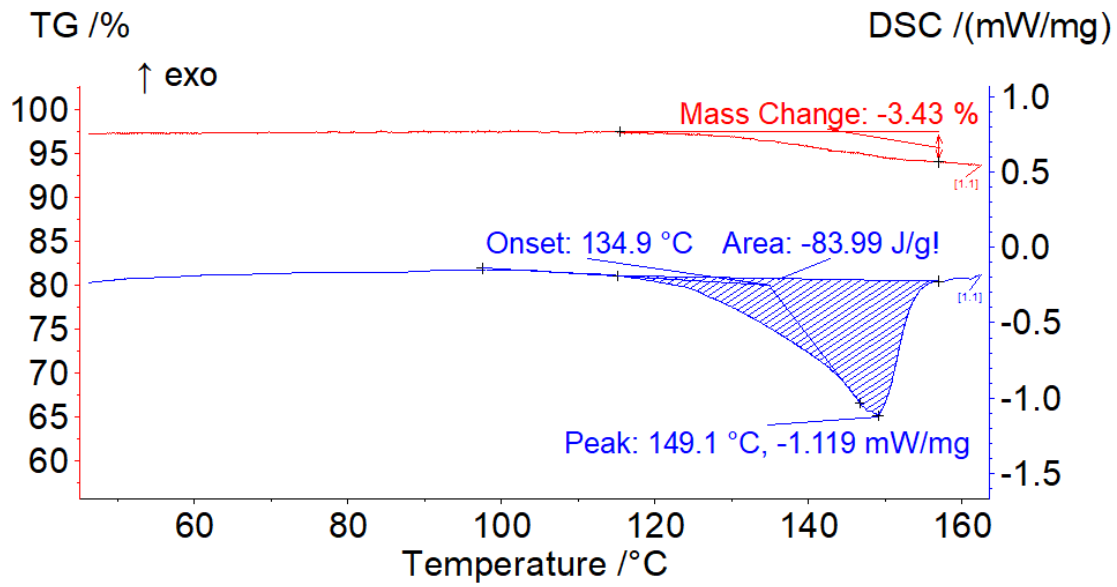

Figure 6.13: Representative DSC/TGA traces of hemi TBA – hemihydrate salt cocrystal obtained by recrystallisation of EVC – TBA from ethanol.

6.3.3.3 Single-Crystal X-ray Diffraction (SC-XRD) Analysis of Screening Samples

The optical microscopy (refer to section 3.2.7.5 for method) images of select crystalline samples resulting from screening experiments of EVC are presented in Appendix Figures A6.8 and A6.9. EVC crystals were predominantly found to comprise needle-like morphology and were often arranged in polycrystalline aggregates. A number of those crystals were subsequently indexed by SC-XRD (refer to section 3.2.7.2). Unit cell parameters derived through indexing with SC-XRD are presented in Table 6.9 and indicate that all of the solvated EVC samples analysed, with the exception of those obtained via crystallisation from methanol, are isostructural to one another as well as EVC – TBA. The parameters presented in Table 6.9 correspond to single crystals which diffracted to a poor resolution (typically less than 1 Å) for structure determination and subsequent refinement to be pursued. The differences in the cell volume of the isostructural EVC samples suggests that the solvent of inclusion is likely not the same for each of these solvated materials. Representative cell parameters for solvated samples derived from crystallisations in 2-butanone, butyl acetate, methyl acetate and THF could not be obtained.

Table 6.9: Representative unit cell parameters of solvated EVC samples.

Solvent of Crystallisation	Preparation Method	Bravais Lattice	*a* (Å)	*b* (Å)	*c* (Å)	α, γ (°)	β (°)	Volume (Å^3)
Acetone	Evaporation at RT	Monoclinic *P*	20.09	9.19	20.19	90	104.49	3609
1-Butanol	Evaporation at RT	Monoclinic *P*	20.25	9.19	20.30	90	104.42	3658
2-Butanol	Evaporation at RT	Monoclinic *P*	20.22	9.17	20.35	90	103.86	3663
1,2-Dichloroethane	Cooling	Monoclinic *P*	20.08	9.18	20.23	90	103.50	3627
Diethyl Ether	Cooling	Monoclinic *P*	20.29	9.15	20.42	90	104.97	3660
2-Ethoxyethanol	Cooling	Monoclinic *P*	20.13	9.19	20.29	90	103.95	3643
Furfural	Cooling	Monoclinic *P*	20.30	9.19	20.34	90	104.49	3673
Methanol	Evaporation at RT	Orthorhombic *P*	8.50	16.81	23.95	90	90	3422
2-Methoxyethanol	Evaporation at RT	Monoclinic *P*	20.20	9.19	20.26	90	104.33	3643
TFE	Evaporation at RT	Monoclinic *P*	20.12	9.20	20.16	90	104.65	3612

Analysis of single crystals prepared via evaporation of EVC – TBA from ethanol at room temperature enabled the structure of the novel EVC hemihydrate salt cocrystal, isostructural to the known solvated salt cocrystals of EVC (Table 6.2), to be elucidated. The asymmetric unit of the hemihydrate salt cocrystal (thermal ellipsoid model shown in Appendix Figure A6.30) was confirmed to comprise one unionised molecule of EVC, one EVC – TBA ion pair and one disordered water molecule. Disorder was observed in the -CF_3 groups of both EVC molecules and the carboxylic acid component of the unionised EVC molecule. The TBA cation was also found to be disordered and represents an example of substitutional disorder (Habgood et al., 2011). Full crystallographic data for the structure of EVC hemi TBA - hemihydrate are provided in Table 6.10 and complete details of the disorder observed are given in Appendix Table A6.2.

In the crystal structure of EVC hemi TBA – hemihydrate salt cocrystal, the carboxyl groups of EVC are hydrogen bonded to other EVC molecules via O-H···O interactions (Figure 6.14a) to form the unit cell packing arrangement shown in Figure 6.14b. Water molecules, disordered over two positions with regards to the oxygen atom (Appendix Figure A6.30), were not found to be involved in hydrogen-bonding interactions and are omitted from Figures 6.14a and 6.14b. An overlay presented in Figure 6.15 indicates that EVC adopts a different molecular conformation in the hemihydrate salt cocrystal when compared to the anhydrous form I. EVC hemi TBA – hemihydrate exhibits a packing coefficient of 0.648 which is lower than that of form I (0.659), suggesting that the packing of molecules in the anhydrous form is more efficient.

Disordered water occupies isolated-site void space (Figure 6.16) corresponding to 6.5% (234.57 $Å^3$) of the unit cell volume in the EVC hemi TBA - hemihydrate structure.

Table 6.10: Crystallographic data of EVC hemi TBA – hemihydrate salt cocrystal.

EVC Hemi TBA – Hemihydrate Salt Cocrystal	
Crystal System	Monoclinic
***a* (Å)**	19.961 (2)
***b* (Å)**	9.188 (11)
***c* (Å)**	20.154 (2)
β (°)	103.553 (6)
Space Group	$P2_1$
Volume ($Å^3$)	3593.3 (7)
Z	4
$N_{reflection}/N_{parameter}$	9492/956
Density (g/cm^3)	1.247
X-ray Radiation Source	Mo $K\alpha_1$ (λ = 0.71073 Å)
Temperature (°C)	23 (2)
θ range (°)	1.039 – 22.601
range of *h*	$-21 \leqslant h \leqslant 21$
range of *k*	$-9 \leqslant k \leqslant 9$
Range of *l*	$-21 \leqslant l \leqslant 21$
R_1 (%)	6.04
WR_2 (%)	17.79
goodness of fit	1.286
Flack parameter	-0.5 (4)

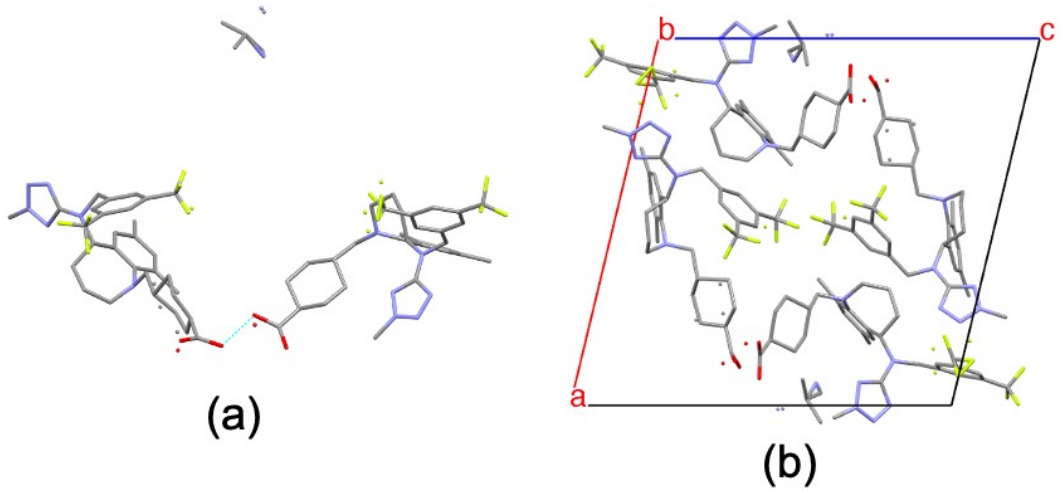

Figure 6.14: Hydrogen bonding motif (a) and unit cell packing arrangement, viewed along the crystallographic *b* axis (b), in the hemi TBA - hemihydrate salt cocrystal of EVC. Hydrogen atoms and disordered water molecules have been omitted.

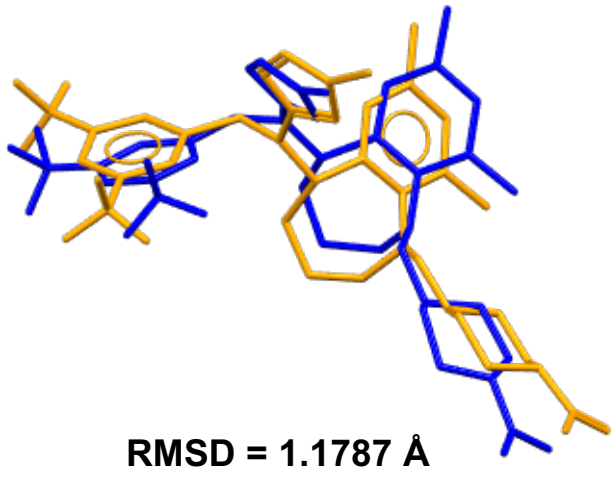

Figure 6.15: Conformational overlay of EVC molecule in form I (orange) with unionised EVC molecule in EVC hemi TBA – hemihydrate salt cocrystal (blue). Hydrogen atoms have been omitted for clarity.

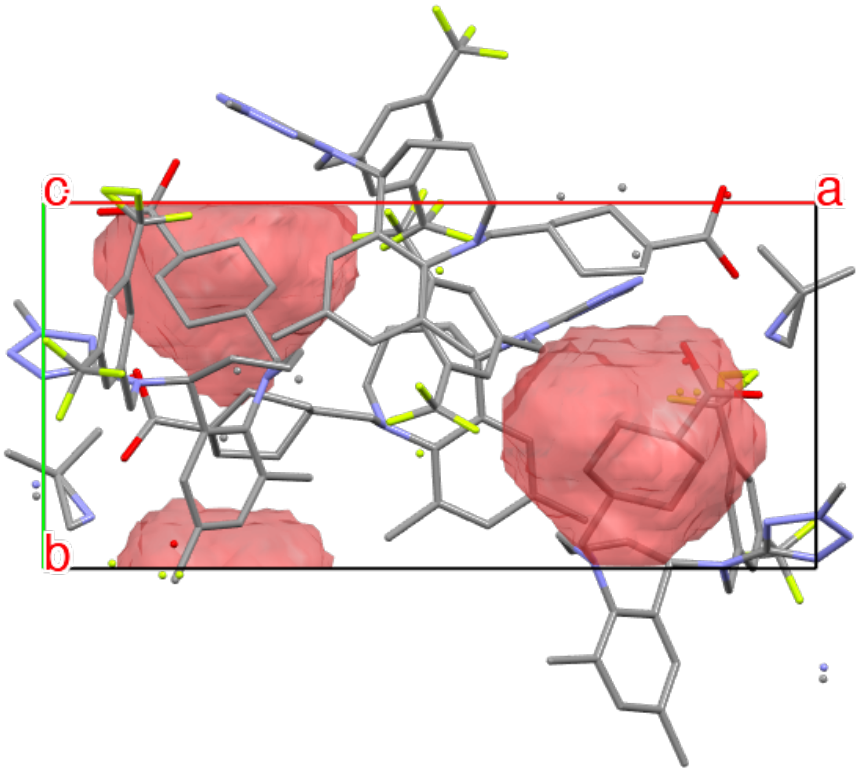

Figure 6.16: Presence of isolated-site void space, indicated by red contact surfaces, in the crystal structure of the hemi TBA - hemihydrate salt cocrystal of EVC. Hydrogen atoms and disordered water molecules have been omitted.

6.3.3.4 Desolvation Studies

Evaporation, vapour diffusion and cooling crystallisation screening experiments readily resulted in the preparation of solvated forms of EVC (Table 6.7). In order to investigate the possibility of these samples undergoing desolvation into anhydrous polymorphic forms in a manner similar to the pharmaceutically relevant solvates of *R*-cinacalcet hydrochloride (Braun et al., 2008), β-resorcylic acid (Braun, et al., 2011), orotic acid (Braun et al., 2016a), 4-aminoquinaldine (Braun et al., 2016b) and galunisertib (Bhardwaj et al., 2019), a desolvation screen was pursued which involved storing solvated samples in a drying oven at non-ambient temperature (65°C) or subjecting them to VT-XRPD experiments. The desolvation experiments attempted (Table 6.11) did not result in any apparent change in solid form for 10 out of the 12 solvated materials that were investigated using XRPD. Solvated samples derived from 2-methoxyethanol and TFE solutions were found to completely convert into an amorphous state. The hemi TBA – hemihydrate salt cocrystal of EVC was amongst the solvated materials for which XRPD analysis indicated no change in solid form.

Table 6.11: Overview of desolvation experiments performed for solvated EVC samples.

Starting Material	Desolvation Conditions	Desolvation Outcome
Hemi TBA – Hemihydrate Salt Cocrystal	Stored in drying oven at 65°C for 6 days	No change in solid form evident
Solvated material – 1,2-Dichloroethane	Stored in drying oven at 65°C for 1 day	No change in solid form evident
Solvated material – THF	Stored in drying oven at 65°C for 6 days	No change in solid form evident
Solvated material – 2-Butanol	Stored in drying oven at 65°C for 6 days	No change in solid form evident
Solvated material – 2-Butanone	Stored in drying oven at 65°C for 6 days	No change in solid form evident
Solvated material – Diethyl Ether	Stored in drying oven at 65°C for 6 days	No change in solid form evident
Solvated material – Methyl Acetate	Stored in drying oven at 65°C for 6 days	No change in solid form evident
Solvated material – Acetone	Stored in drying oven at 65°C for 6 day	No change in solid form evident
Solvated material – TFE	Stored in drying oven at 65°C for 6 days	Amorphous material
Methanol solvate/Monohydrate mixture	VT-XRPD	No change in solid form evident
Solvated material - Ethanol	Stored in drying oven at 65°C for 6 days	No change in solid form evident
Solvated material – 2-Methoxyethanol	Stored in drying oven at 65°C for 6 days	Amorphous material

6.3.3.5 Physical Vapour Deposition and Supercritical Fluid (SCF) Extraction

Physical vapour deposition and SCF extraction were investigated for the purpose of targeting the isolation of anhydrous forms of EVC. Physical vapour deposition studies pursued using sublimation temperatures in the 50 - 100°C did not result in the

formation of any crystals. Attempted SCF extraction resulted in an EVC product (Appendix Figure A6.10) that was found to be isostructural to EVC – TBA, the EVC hemi TBA - hemihydrate salt cocrystal and the known solvated salt crystals of EVC.

6.3.4 Summary of EVC Characterisation and Screening

EVC – TBA, a solvated salt cocrystal, was sourced from Eli Lilly and Company, subjected to physical characterisation studies and utilised as a starting material in solid-state screening investigations. Whilst single-crystal structure determination was not possible because of the small crystal size characteristic of this material, a comparison of the unit cell parameters obtained by indexing XRPD data suggested that EVC – TBA is isostructural to the known hemi TBA solvated salt cocrystals of EVC comprising unionised ethanol, 1-butanol and 2-propanol as solvents of inclusion. Whilst DSC/TGA analysis indicated slight weight loss over two endothermic events at higher temperature, VT-XRPD did not indicate any change in the solid form of EVC – TBA at higher temperatures. Characterisation of EVC – TBA using DVS indicated gradual uptake of moisture and possible non-stoichiometric hydrate formation at higher relative humidities. As a general rule, channel hydrates exhibit largely continuous and non-stoichiometric sorption and desorption behaviour, whilst isolated-site hydrates tend to follow a stepwise (stoichiometric) sorption and desorption mechanism (Griesser, 2006). In the absence of a definitive crystal structure for EVC – TBA, it is anticipated that this material does not exhibit the characteristics of a channel solvate but likely contains isolated sites of solvent-accessible void space in its crystal structure.

A total of 120 solution-based crystallisation experiments were performed using the EVC – TBA as the starting material. Whilst some of the materials resulting from screening studies were found to be amorphous or poorly crystalline, a common outcome in instances where faster solvent evaporation was pursued under 50°C, the crystalline materials obtained experimentally yielded two distinct types of powder patterns. These distinct patterns are representative of the monoclinic structure type of a novel hemi TBA – hemihydrate salt cocrystal that was isolated in the experimental screen, crystallising in $P2_1$ space group, and the unionised, orthorhombic methanol solvate and monohydrate structures of EVC which crystallise in $P2_12_12_1$. Crystal structure determination of the hemi TBA – hemihydrate salt cocrystal confirmed the presence of disordered water that occupies isolated-site void space in the unit cell and does not participate in hydrogen-bonding interactions directly with

EVC molecules. Moreover, the EVC molecules in the hemi TBA - hemihydrate structure were found to be less densely packed than those present in the anhydrous form I.

The powder patterns and unit cell parameters derived from XRPD and SC-XRD analyses of materials obtained from solution-based screening experiments indicated that EVC is a highly potent isostructural solvate former. Whilst it was not possible to carry out complete structural determination for samples obtained from each solvent explored in the experimental screen due to limitations in the size and quality of the corresponding crystals, as many as 15 out of the 16 solvents that were investigated yielded samples showing common structural features under the conditions explored. Given the fact that several isostructural solvated salt cocrystals comprising EVC and TBA had been identified prior to commencement of this work (Eli Lilly and Company, 2018-2020), it is anticipated that the samples that could not be fully characterised structurally herein are also isostructural solvated salt cocrystals comprising an unionised EVC molecule, an EVC – TBA ion pair and different types of unionised solvent molecules in their respective crystal structures.

6.3.5 Characterisation of TAEVC Starting Materials

In the following sections, the physical characterisation of the TAEVC1, TAEVC2 and TAEVC3 starting materials is discussed.

6.3.5.1 XRPD

Representative XRPD patterns corresponding to the starting materials are presented in Figure 6.17. XRPD analysis shows that TAEVC1 is amorphous with no observable Bragg diffraction peaks. On the contrary, TAEVC2 and TAEVC3 are shown to be strongly diffracting polycrystalline samples.

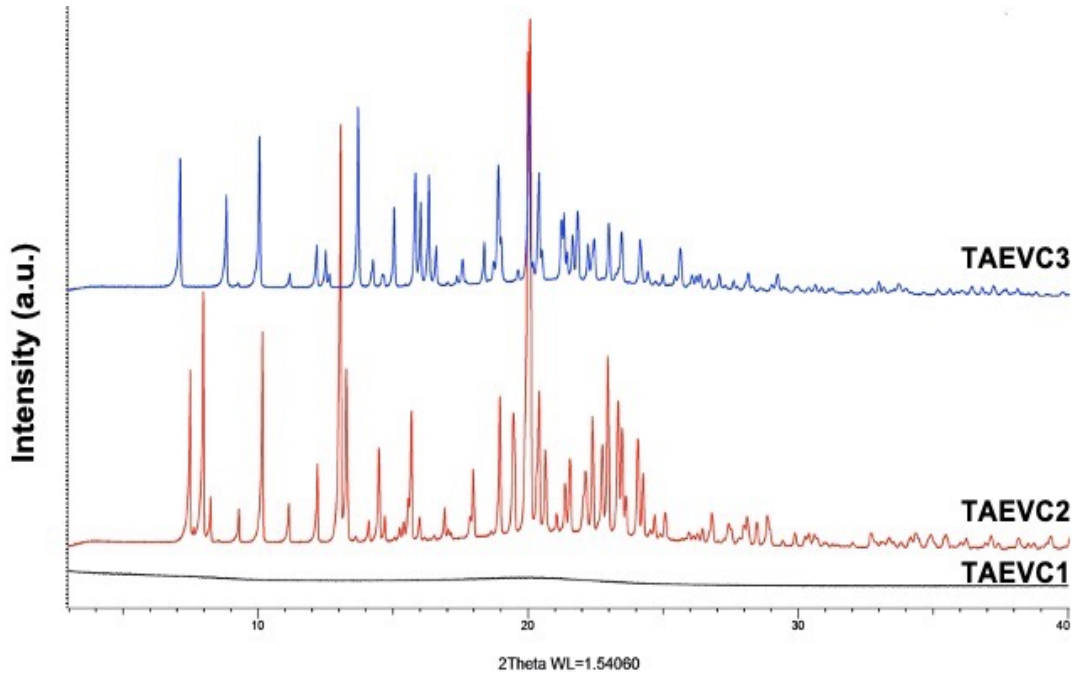

Figure 6.17: Representative XRPD patterns of TAEVC1, TAEVC2 and TAEVC3 starting materials.

Preliminary attempts to index the XRPD pattern of TAEVC2 using *TOPAS* (Coelho, 2003) always yielded indexing solutions corresponding to the hexagonal $P6_1$ space group as the best possible fits to the diffraction data. When the pattern of TAEVC2 was indexed using *DICVOL91* in *DASH*, only a single solution was identified in the hexagonal crystal system (Table 6.12) and subsequently used for Pawley refinement (Figure 6.18). Residual values obtained from Pawley fitting were R_{wp} = 6.04% and R_p = 4.13% and suggested that the hexagonal indexing solution derived from *DICVOL91* in *DASH* is representative of the XRPD pattern of the starting TAEVC2 material. The refined unit cell parameters were $a = b$ = 13.630 (9) Å and c = 64.30 (2) Å. Hofmann's volume increments (Hofmann, 2002) suggest that two molecules of TAEVC are present in the asymmetric unit.

Crystal structure determination from XRPD data by global optimisation methods becomes challenging when the total number of degrees of freedom accounting for molecular position, orientation and conformation exceeds 20 (Fernandes et al., 2007). This limit was exceeded for the structure of TAEVC2 wherein each asymmetric unit seemingly comprises two TAEVC molecules with each molecule having 15 degrees of freedom, resulting in a total of 30. All attempts to solve the structure in hexagonal $P6_1$ did not produce any sensible structural parameters.

Table 6.12: Indexing details of the starting TAEVC2 material. The best solution corresponding to a hexagonal crystal system is presented as derived from *DICVOL91* in *DASH*.

Crystal System	*a* (Å)	*b* (Å)	*c* (Å)	α, β (°)	γ (°)	Volume (Å^3)	M (20)	F (20)
Hexagonal	13.609	13.609	61.241	90.0	120.0	10304.83	28.4	85.5

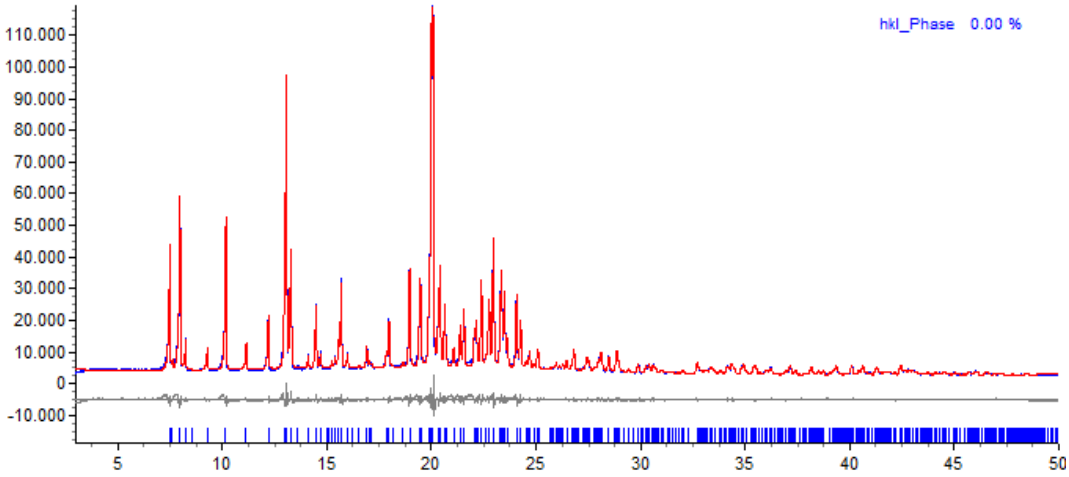

Figure 6.18: Pawley fit of the TAEVC2 starting material. XRPD data were refined against the unit cell parameters of the indexing solution presented in Table 6.12 and $P6_1$ was the space group of choice.

The powder pattern of the starting TAEVC3 material was indexed with *DICVOL91* as implemented in *DASH* and the corresponding indexing details are presented in Table 6.13. The space group ($P2_1/n$) was assigned by analysing the systematic absences using *ExtSym*. Hofmann's volume increment assessment suggested one molecule of TAEVC3 in the asymmetric unit. The indexing and space group assignments were confirmed by Pawley fitting. The structure of TAEVC3 was solved using simulated annealing in *DASH*. Lattice parameters, the space group and the molecular geometry of TAEVC were used as input; the positions and spatial orientations of the molecules in the unit cell as well as the intramolecular degrees of freedom (rotations around the single bonds) were varied. The Mogul Distribution Bias (MDB) was applied to the torsion angles of the TAEVC molecule prior to annealing in order to reduce the conformational search space and enhance the likelihood of successful structure elucidation. Several trial structure solutions from different *DASH* runs exhibited very

similar molecular geometry. A representative structure from trial solutions was refined by the Rietveld method (Rietveld, 1967 & 1969) with *TOPAS* (Figure 6.19). To ensure sensible molecular geometries, standard restraints were applied to bond length, bond angles, and for planar groups in the Rietveld refinement cycle. A closer inspection of the final refined structure revealed the structure was chemically sensible and exhibited plausible hydrogen bond patterns and sensible intermolecular interactions. The unit cell parameters derived from the final refinement were a = 17.645 (3) Å, b = 13.119 (2) Å, c = 14.344 (3) Å, and β = 104.980 (18)°, the residual R values were R_{wp} = 4.92 (3)% and R_p = 3.69 (3)% and GoF = 1.72 (3). Full crystallographic details for the structure of the TAEVC3 starting material are provided in Table 6.14 and the corresponding packing arrangement is shown in Figure 6.20. The OH group of the benzazepine moiety is involved in O-H···N interactions with the tetrazole nitrogen to form a one-dimensional (1D) network which extends infinitely along the crystallographic b axis (Figure 6.20a). In addition, the OH groups of carboxylic acid and benzazepine form hydrogen bonds via O-H···O interactions to form a ring motif as shown in Figure 6.20b. The two hydrogen bonds extend the crystal packing arrangement infinitely to form a two-dimensional (2D) network as shown in Figure 6.20c.

Table 6.13: Indexing details of the starting TAEVC3 material. The 5 most likely unit cells parameters are presented as derived from *DICVOL91* in *DASH*.

Crystal System	*a* (Å)	*b* (Å)	*c* (Å)	α (°)	β (°)	γ (°)	Volume (Å^3)	M (20)	F (20)
Monoclinic	18.000	12.901	14.479	90.0	77.43	90.0	3281.84	17.0	51.9
Monoclinic	18.000	12.901	14.479	90.0	102.56	90.0	3281.84	17.0	51.9
Monoclinic	20.500	12.901	14.479	90.0	121.02	90.0	3281.84	17.0	51.9
Triclinic	14.357	12.381	16.786	55.71	117.85	114.78	2130.25	6.9	22.5
Triclinic	15.145	11.271	16.882	115.3	122.67	86.47	2138.16	5.5	17.7

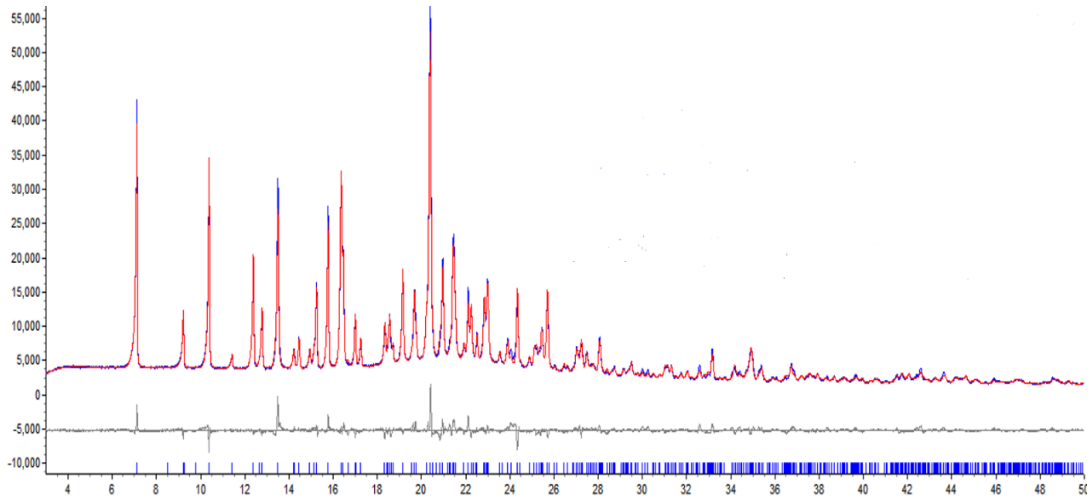

Figure 6.19: Rietveld refinement plot of XRPD data corresponding to the crystal structure of the starting TAEVC3 material, showing the observed (blue), calculated (red) and difference (grey) profiles.

Table 6.14: Crystallographic data of the starting TAEVC3 material.

TAEVC3 Starting Material	
Crystal System	Monoclinic
Space Group	$P2_1/n$
***a* (Å)**	17.645 (3)
***b* (Å)**	13.119 (2)
***c* (Å)**	14.344 (3)
β (°)	104.980 (18)
Volume (Å^3)	3207.65 (12)
Z	4
X-ray Radiation Source	Cu Kα_1 (λ = 1.54060 Å)
Temperature (°C)	-123 (2)

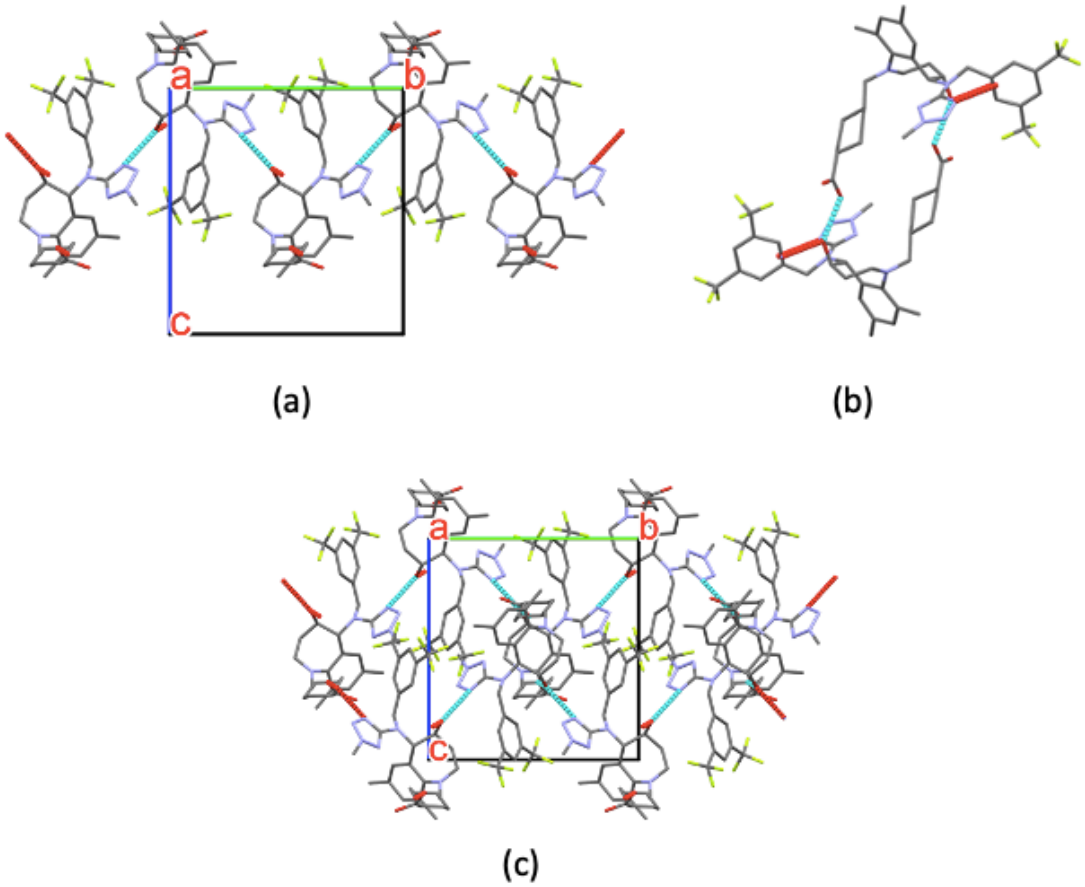

Figure 6.20: Unit cell packing arrangement and hydrogen bonding motifs in the crystal structure of the starting TAEVC3 material.

6.3.5.2 Optical Microscopy and SEM

Representative optical and SEM micrographs of the starting TAEVC materials are provided in Figure 6.21. The presence of irregular morphology was noted for particles of TAEVC1, an expected outcome given the amorphous nature of the material. TAEVC2 crystals were agglomerated and TAEVC3 comprised crystalline particles with needle-like morphologies which also exhibited agglomeration. Crystals of TAEVC2 and TAEVC3 were not suitable enough to pursue characterisation with SC-XRD as their size was generally found to be less than 50 μm in all dimensions.

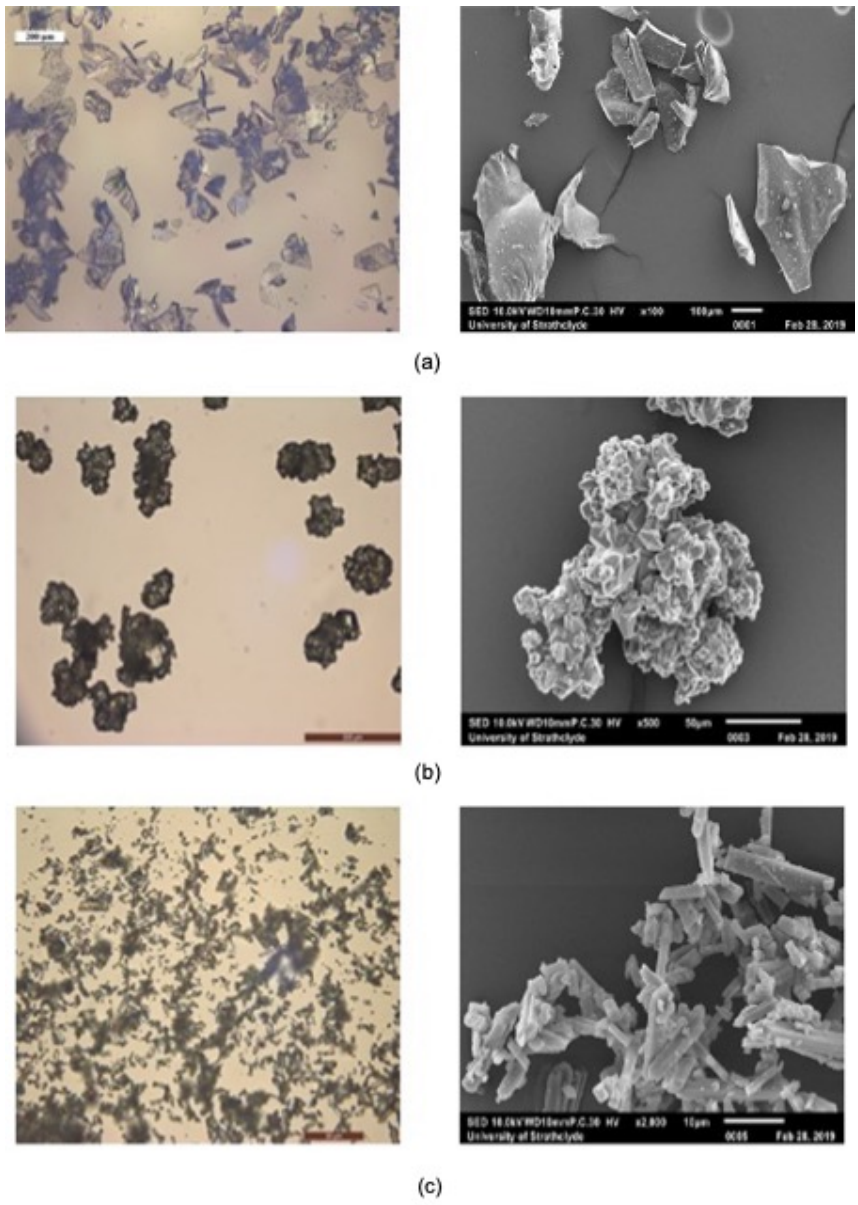

Figure 6.21: Optical and SEM micrographs of TAEVC1 (a), TAEVC2 (b) and TAEVC3 (c) starting materials.

6.3.5.3 DSC/TGA and VT-XRPD

Representative DSC/TGA traces and VT-XRPD scans of the starting materials are provided in Figures 6.22 and 6.23. Analysis of TAEVC1 (Figure 6.22a) revealed the presence of an endothermic peak with an onset temperature of 77.3°C (± 1.91) which can be attributed to structural relaxations occurring in the amorphous material (Málek and Shánělová, 2001). The DSC traces obtained from triplicate analysis of TAEVC1 consistently yielded no evidence of any exothermic events that could possibly be attributed to crystallisation being induced. Based on the absence of crystallisation

taking place with increasing temperature, the endothermic peak noted at ≈ 77°C is unlikely to correspond to a melting event.

In the TGA trace of TAEVC2 (Figure 6.22b), weight loss (2.54% ± 0.47) was observed and found to coincide with the occurrence of two endothermic peaks at 166.5°C (± 2.89) and 174.7°C (± 3.21) with an onset temperature of 156.4°C (± 3.76) for the first endotherm. Whilst there is no definitive evidence, the presence of these peaks in the DSC traces is probably due to desolvation and melting events occurring in succession, similar to the behaviour exhibited by the starting EVC material (refer to section 6.3.1.3). The observed desolvation temperature of the TAEVC2 starting material is unusually high for compounds of pharmaceutical relevance although the ethanol solvate of nevirapine has been found to desolvate at a temperature of ≈ 151.5°C (Chadha et al., 2010). The melting of TAEVC2 within the temperature range indicated by DSC was corroborated using VT-XRPD (Figure 6.23a). However, no evidence of transformation to a different crystal structure was observed prior to melting with Pawley profile fitting of the TAEVC2 material at 162°C (Figure 6.24a) returning unit cell parameters a = b = 13.77 (4) Å and c = 64.80 (5) Å, with R_{wp} = 4.55% and R_p = 2.46%, which were found to exhibit no significant difference to those derived when the sample was measured at room temperature conditions (Table 6.11).

The thermal behaviour of TAEVC3 is presented in Figure 6.22c and shown to be different compared to that of TAEVC1 and TAEVC2. The DSC thermogram displays a single, sharp endothermic peak at 196.3°C (± 0.11) with an onset of 193.3°C (± 0.1) which corresponds to melting of the compound. The observation of a higher melting point for TAEVC3 relative to TAEVC1 and TAEVC2 was to be expected as racemic compounds commonly melt at higher temperatures than the respective enantiomers (Repta et al., 1976; El-Arini et al., 1998; Faigl et al., 2010). The TGA curve of TAEVC3 does not show any weight loss in the material suggesting that TAEVC3 is not a solvated or hydrated form. The VT-XRPD analysis of TAEVC3 (Figure 6.23b) indicates that the sample melts at ≈ 197°C, consistent with the thermal analysis. The Pawley profile fitting of the TAEVC3 material at 187°C (Figure 6.24b) yielded unit cell parameters a = 18.162 (17) Å, b = 13.033 (10) Å, c = 14.627 (14) Å and β = 101.818 (6)° with profile residual values of R_{wp} = 3.50% and R_p = 2.47%. This indicates isotropic thermal expansion of the material and no change in the phase composition compared to the room temperature structure.

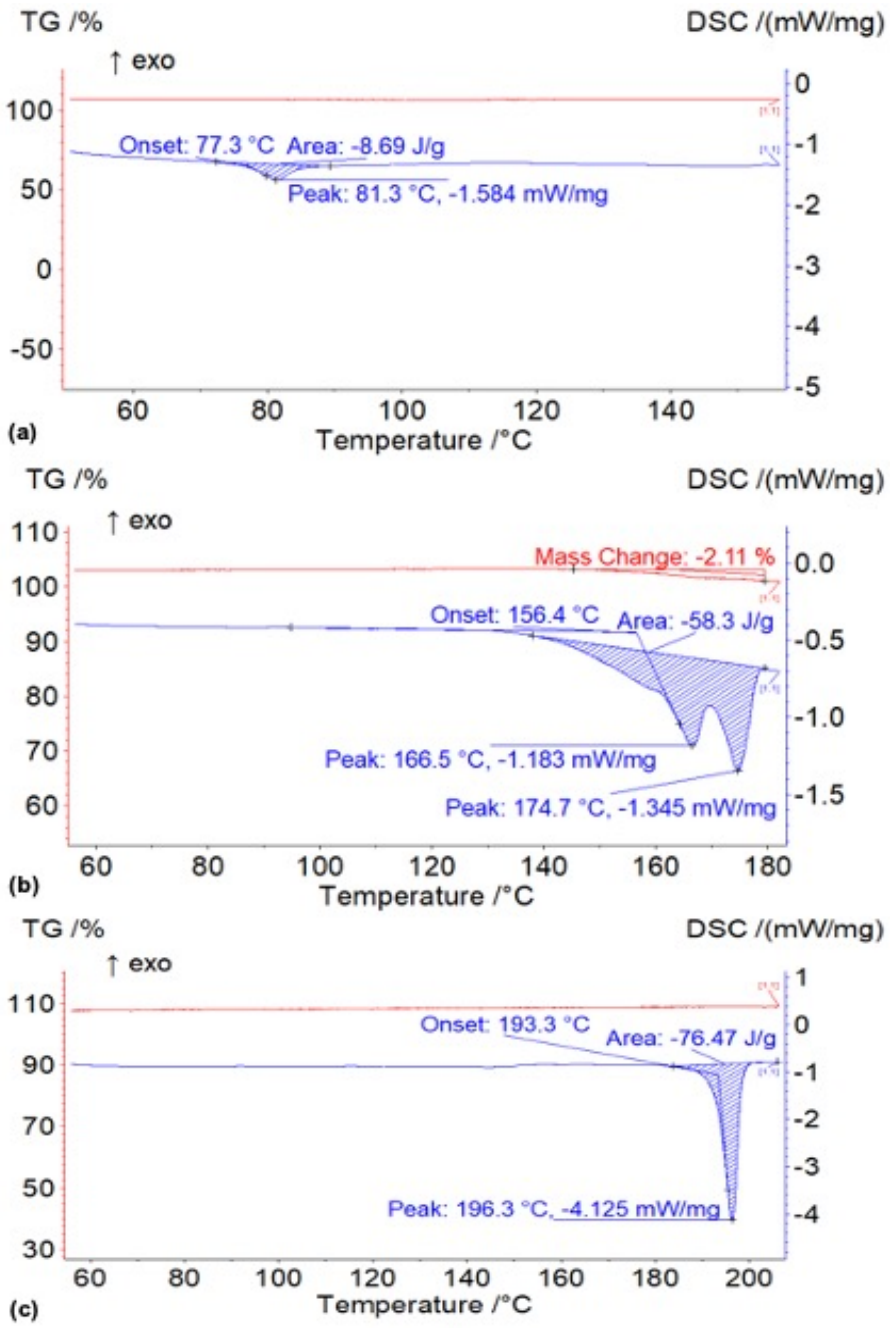

Figure 6.22: Representative DSC and TGA traces of TAEVC1 (a), TAEVC2 (b) and TAEVC3 (c) starting materials.

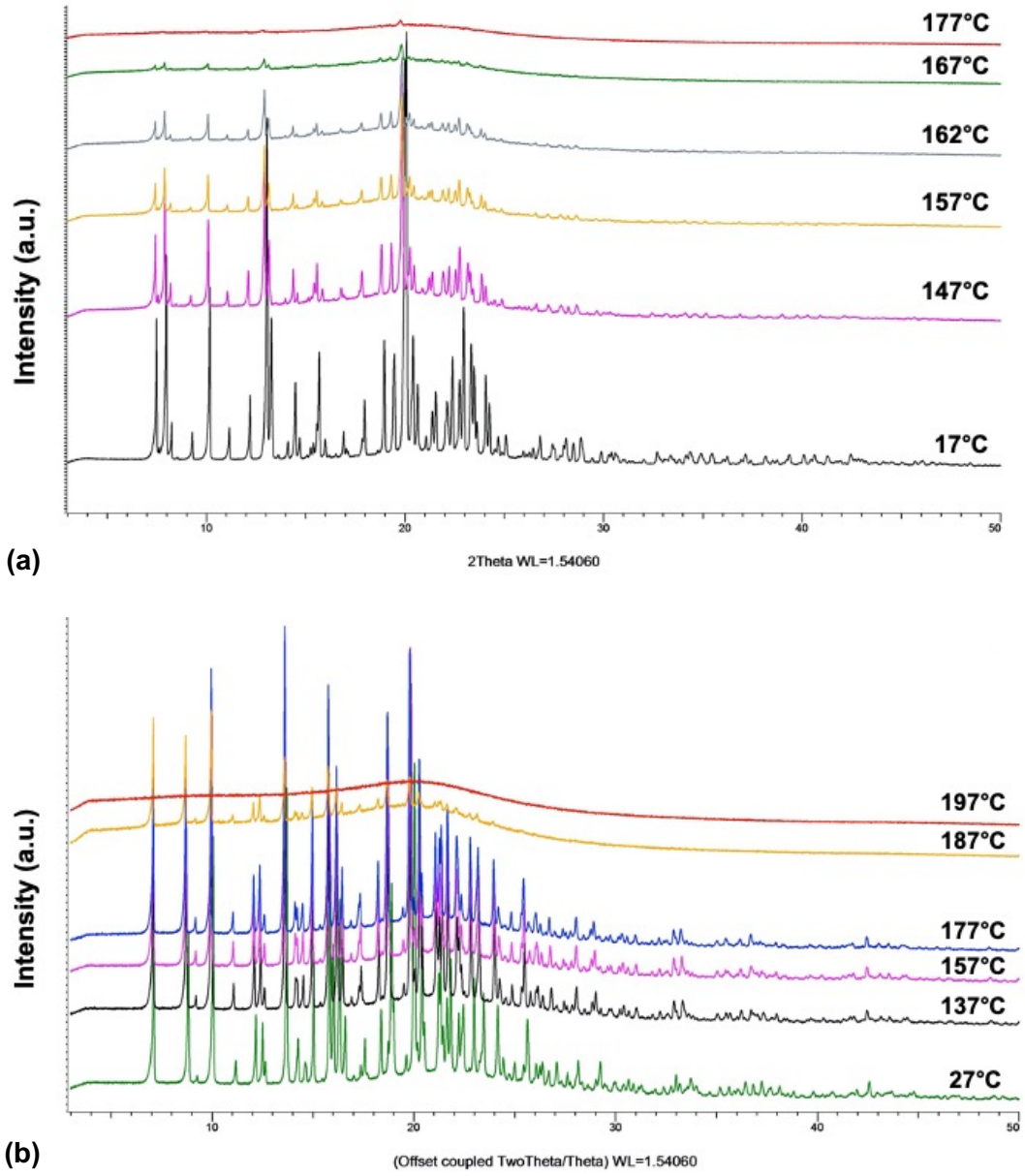

Figure 6.23: VT-XRPD analysis of TAEVC2 (a) and TAEVC3 (b) starting materials.

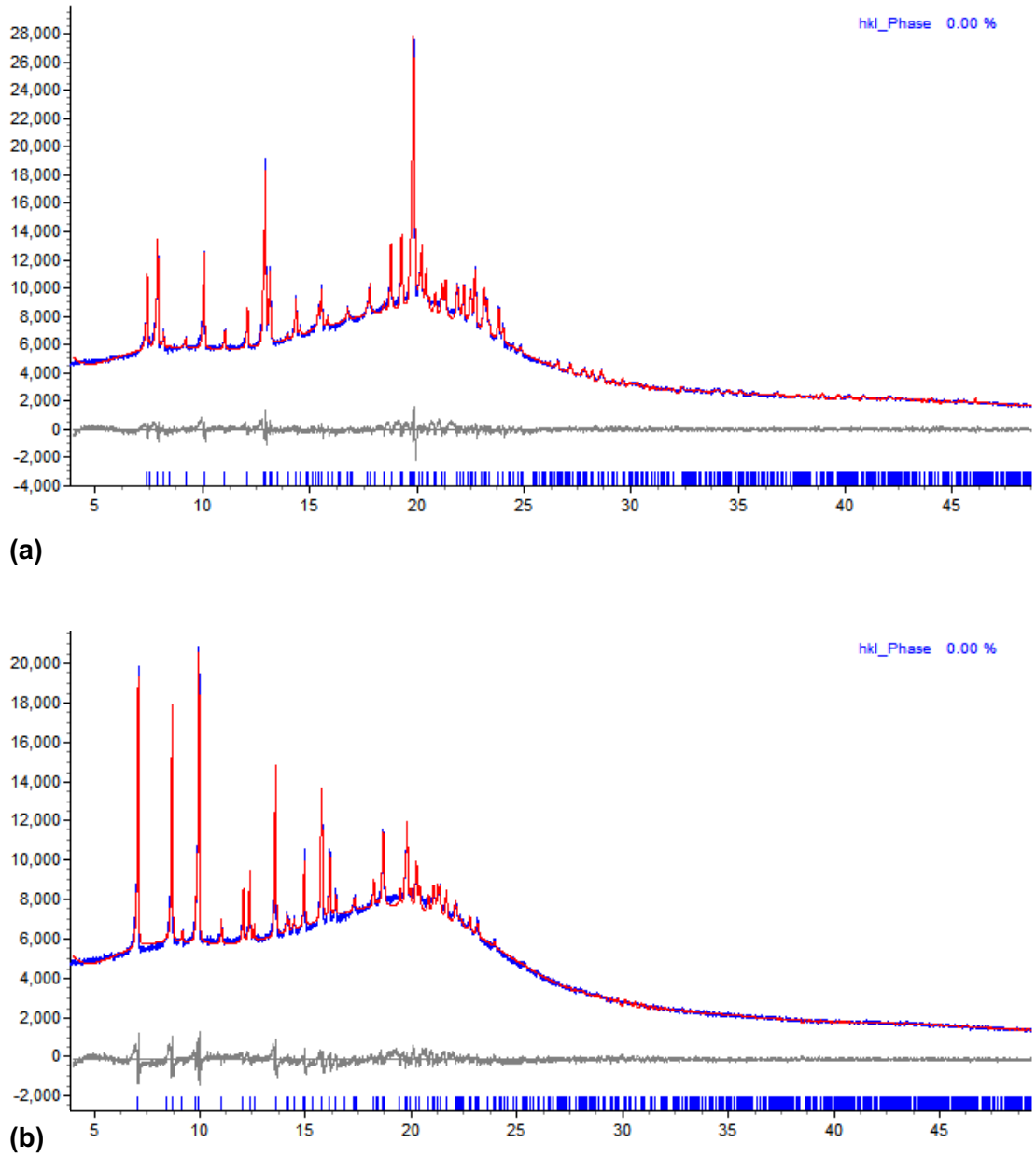

Figure 6.24: Pawley fits of (a) starting TAEVC2 material at 162°C and (b) starting TAEVC3 material at 187°C.

6.3.5.4 DVS and VH-XRPD

DVS isotherm plots for TAEVC1, TAEVC2 and TAEVC3 are shown in Figure 6.25. In the cases of TAEVC1 (Figure 6.25a) and TAEVC3 (Figure 6.25c), continuous weight gain was noted with a maximum of 1.6% for TAEVC 1 and 1.29% for TAEVC3 during the respective sorption cycles in the 0 – 95% RH range. A minor hysteresis was observed for TAEVC1 and no observable hysteresis was noted for TAEVC3 during the sorption and desorption cycles. Whilst the exact reasons for the occurrence of

minor hysteresis in TAEVC1 are not clear, the gradual moisture uptake is likely due to surface adsorption of water, a behaviour characteristic of non-stoichiometric hydrates (Griesser, 2006). TAEVC2 (Figure 6.25b) exhibited continuous weight gain and the lowest overall moisture uptake (0.40%) relative to all the other starting materials analysed and is characterised by a notable hysteresis in the 60 – 90% RH range. The desorption cycles of TAEVC2 revealed a maximum weight loss of 0.16% occurring between 70 – 60% RH, the largest one observed across the RH region explored. This behaviour matches with that typically exhibited by non-stoichiometric hydrates. VH-XRPD analysis and Pawley fitting performed in the 5 – 95 % RH range under temperatures of 20 and 50°C indicated no change in the patterns of TAEVC1 (Appendix Figure A6.1) and TAEVC2 (Appendix Figures A6.2 - A6.4) respectively, suggesting that their internal structure remains intact under different RH conditions.

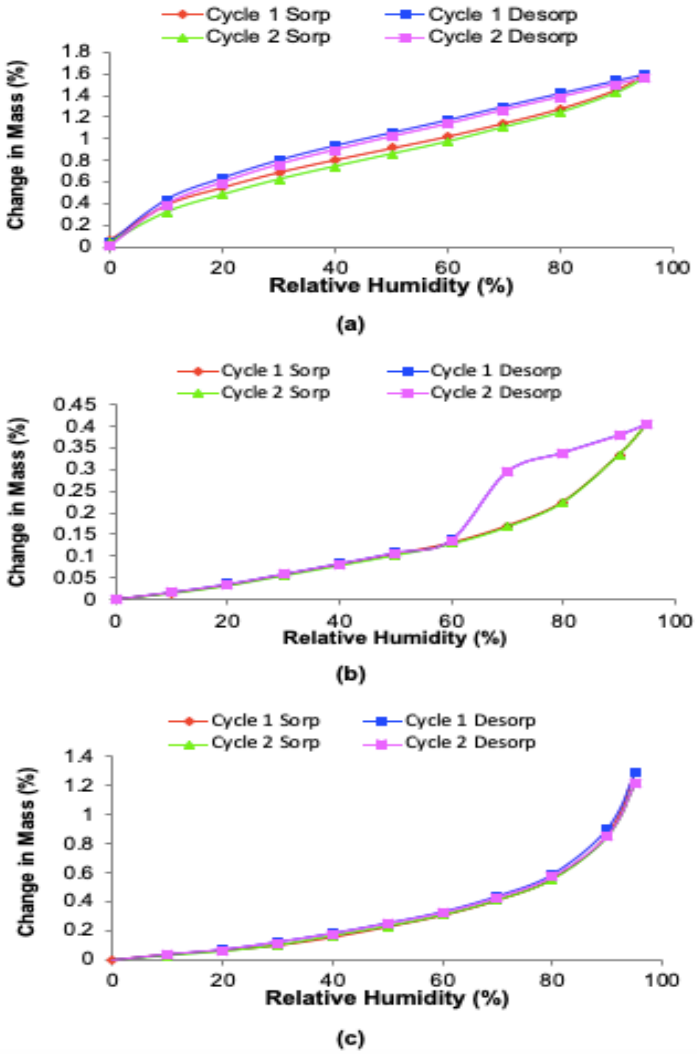

Figure 6.25: DVS isotherm plots of (a) TAEVC1, (b) TAEVC2, and (c) TAEVC3 starting materials.

6.3.6 Solid-State Screening Studies of TAEVC

6.3.6.1 Summary of Solution-Based Screening Studies

The experimental solubility data of TAEVC starting materials is presented in Table 6.6 (refer to section 6.3.2). The experimental outcomes of solution-based screening studies of TAEVC1, TAEVC2 and TAEVC3 are summarised in Tables 6.15 – 6.17 and are based on sample analysis using XRPD and, where appropriate, SC-XRD (refer to section 6.3.6.4).

Table 6.15: Summary of solution-based screening studies of TAEVC1.

Solvent	Evaporation at Room Temperature	Cooling Crystallisation
Acetic Acid	Solvated material isostructural to the starting TAEVC2 material	Solvated material isostructural to the starting TAEVC2 material
Acetone	Solvated material isostructural to the starting TAEVC2 material	Solvated material isostructural to the starting TAEVC2 material
Acetonitrile	Solvated material isostructural to the starting TAEVC2 material	Solvated material isostructural to the starting TAEVC2 material
1-Butanol	Solvated material isostructural to the starting TAEVC2 material	Solvated material isostructural to the starting TAEVC2 material
2-Butanol	Solvated material isostructural to the starting TAEVC2 material	Solvated material isostructural to the starting TAEVC2 material
2-Butanone	Solvated material isostructural to the starting TAEVC2 material	Solvated material isostructural to the starting TAEVC2 material
Butyl Acetate	Solvated material crystallising in *C*2	Insufficient material/no solid product available for analysis
Chloroform	Solvated material isostructural to the starting TAEVC2 material	Insufficient material/no solid product available for analysis
1,2-Dichloroethane	Solvated material crystallised from 1,2-dichloroethane	Amorphous material
Diethyl Ether	Poorly crystalline solvated material crystallised from diethyl ether	Insufficient material/no solid product available for analysis
1,4-Dioxane	Solvated material isostructural to the starting TAEVC2 material	Solvated material isostructural to the starting TAEVC2 material
Ethanol	Solvated material isostructural to the starting TAEVC2 material	Solvated material isostructural to the starting TAEVC2 material

2-Ethoxyethanol	Amorphous material	Solvated material isostructural to the starting TAEVC2 material
Ethyl Acetate	Solvated material crystallising in *C*2	Solvated material crystallising in *C*2
Furfural	Solvated material crystallised from furfural	Insufficient material/no solid product available for analysis
Methanol	Amorphous material	Solvated material isostructural to the starting TAEVC2 material
2-Methoxyethanol	Solvated material isostructural to the starting TAEVC2 material	Insufficient material/no solid product available for analysis
Methyl Acetate	Solvated material isostructural to the starting TAEVC2 material	Solvated material isostructural to the starting TAEVC2 material
2-Propanol	Solvated material isostructural to the starting TAEVC2 material	Solvated material isostructural to the starting TAEVC2 material
THF	Solvated material isostructural to the starting TAEVC2 material	Solvated material isostructural to the starting TAEVC2 material
Toluene	Poorly crystalline solvated material crystallised from toluene	Poorly crystalline solvated material crystallised from toluene
TFE	Solvated material isostructural to the starting TAEVC2 material	Insufficient material/no solid product available for analysis
Vapour Diffusion Experiments		
Solvent	**Anti-Solvent**	**Experimental Outcome**
Acetonitrile	Cyclohexane	Solvated material crystallising in *C*2
Acetone	Butyl Acetate	Solvated material crystallising in *C*2

Table 6.16: Summary of solution-based screening studies of TAEVC2.

Solvent	Evaporation at Room Temperature	Evaporation at 50°C	Cooling Crystallisation
Acetic Acid	Solvated material isostructural to the starting TAEVC2 material	Solvated material isostructural to the starting TAEVC2 material	Experiment could not be performed due to limitations in starting material quantity
Acetone	Solvated material isostructural to the starting TAEVC2 material	Solvated material isostructural to the starting TAEVC2 material	Experiment could not be performed due to limitations in starting material quantity
Acetonitrile	Solvated material isostructural to the starting TAEVC2 material	Solvated material isostructural to the starting TAEVC2 material	Insufficient material/no solid product available for analysis
1-Butanol	Solvated material isostructural to the starting TAEVC2 material	Amorphous material	Experiment could not be performed due to limitations in starting material quantity
2-Butanol	Solvated material isostructural to the starting TAEVC2 material	Solvated material isostructural to the starting TAEVC2 material	Experiment could not be performed due to limitations in starting material quantity
2-Butanone	Solvated material isostructural to the starting TAEVC2 material	Solvated material isostructural to the starting TAEVC2 material	Experiment could not be performed due to limitations in starting material quantity
Butyl Acetate	Solvated material crystallising in *C*2	Amorphous material	Experiment could not be performed due to limitations in starting material quantity
Chloroform	Solvated material isostructural to the starting TAEVC2 material with impurity peaks present	Solvated material isostructural to the starting TAEVC2 material	Experiment could not be performed due to limitations in starting material quantity
1,2-Dichloroethane	Solvated material crystallising in *C*2	Solvated material isostructural to the starting TAEVC2 material with impurity peaks present	Experiment could not be performed due to limitations in starting material quantity
Diethyl Ether	Solvated material crystallising in *C*2	N/A	Experiment could not be performed due to limitations in starting material quantity
1,4-Dioxane	Solvated material isostructural to the starting TAEVC2 material	Amorphous material	Experiment could not be performed due to limitations in starting material quantity
Ethanol	Solvated material isostructural to the starting TAEVC2 material	Amorphous material	Experiment could not be performed due to limitations in starting material quantity
2-Ethoxyethanol	Solvated material crystallising in *C*2	Amorphous material	Experiment could not be performed due to limitations in starting material quantity

Ethyl Acetate	Solvated material crystallising in $P2_1$	Solvated material crystallising in $P2_1$	Experiment could not be performed due to limitations in starting material quantity
Furfural	Solvated material isostructural to the starting TAEVC2 material	N/A	Experiment could not be performed due to limitations in starting material quantity
Methanol	Solvated material isostructural to the starting TAEVC2 material	Solvated material isostructural to the starting TAEVC2 material	Experiment could not be performed due to limitations in starting material quantity
2-Methoxyethanol	Solvated material isostructural to the starting TAEVC2 material	Amorphous material	Solvated material isostructural to the starting TAEVC2 material
Methyl Acetate	Solvated material isostructural to the starting TAEVC2 material	Solvated material isostructural to the starting TAEVC2 material	Experiment could not be performed due to limitations in starting material quantity
2-Propanol	Solvated material isostructural to the starting TAEVC2 material	Solvated material isostructural to the starting TAEVC2 material	Experiment could not be performed due to limitations in starting material quantity
THF	Solvated material isostructural to the starting TAEVC2 material	Solvated material isostructural to the starting TAEVC2 material	Experiment could not be performed due to limitations in starting material quantity
Toluene	Poorly crystalline solvated material crystallised from toluene	Poorly crystalline solvated material crystallised from toluene	Experiment could not be performed due to limitations in starting material quantity
TFE	Solvated material isostructural to the starting TAEVC2 material	Amorphous material	Experiment could not be performed due to limitations in starting material quantity
Vapour Diffusion Experiments			
Solvent	**Anti-Solvent**	**Experimental Outcome**	
Toluene	Hexane	Solvated material isostructural to the starting TAEVC2 material	
1,4-Dioxane	Hexane	Solvated material isostructural to the starting TAEVC2 material	
Toluene	Cyclohexane	Solvated material crystallising in $P2_1$	
Ethyl Acetate	Toluene	Solvated material crystallising in $P2_1$	
1,4-Dioxane	Cyclohexane	Insufficient material/no solid product available for analysis	
Acetonitrile	Cyclohexane	Solvated material crystallising in $C2$	
Ethyl Acetate	Cyclohexane	Solvated material crystallising in $P2_1$	
Ethyl Acetate	TFE	Insufficient material/no solid product available for analysis	
Ethyl Acetate	1,2-Dichloroethane	Insufficient material/no solid product available for analysis	
Butyl Acetate	TFE	Insufficient material/no solid product available for analysis	
Butyl Acetate	1,2-Dichloroethane	Insufficient material/no solid product available for analysis	
Butyl Acetate	Toluene	Insufficient material/no solid product available for analysis	

Table 6.17: Summary of solution-based screening studies of TAEVC3.

Solvent	Evaporation at Room Temperature	
Acetonitrile	Solvated material obtained from acetonitrile and crystallising in $P2_1/c$	
1-Butanol	Starting TAEVC3 material (anhydrous form)	
2-Butanol	Solvated material recrystallised from 2-butanol	
1,2-Dichloroethane	Solvated material obtained from 1,2-dichloroethane and crystallising in $P2_1/n$	
1,4-Dioxane	Unidentified material different than the starting TAEVC3 material. Possible solvation could not be confirmed.	
Ethanol	Starting TAEVC3 material (anhydrous form)	
Ethyl Acetate	Starting TAEVC3 material (anhydrous form)	
Methanol	Solvated material obtained from methanol and crystallising in $P2_1/n$	
THF	Solvated material recrystallised from tetrahydrofuran	
Toluene	Starting TAEVC3 material (anhydrous form)	
Vapour Diffusion Experiments		
Solvent	**Anti-Solvent**	**Experimental Outcome**
Toluene	Cyclohexane	Solvated material obtained from toluene and crystallising in $P2_1/c$
1,2-Dichloroethane	Cyclohexane	Solvated material obtained from 1,2-dichloroethane and crystallising in $P2_1/n$
Acetonitrile	Cyclohexane	Solvated material obtained from acetonitrile and crystallising in $P2_1/c$

Solution-based screening experiments conducted for the TAEVC materials revealed that all of them are highly potent solvate formers as evidence for solvent inclusion was readily obtained through DSC/TGA analysis for the crystalline products which showed some weight loss upon heating (refer to section 6.3.6.2). Representative XRPD

patterns corresponding to samples derived from solution crystallisation experiments of TAEVC1, TAEVC2 and TAEVC3 are presented in Appendix Figures A6.11 – A6.23. The patterns were grouped based on their similarity to the corresponding TAEVC2 and TAEVC3 starting materials with close similarity indicating isostructurality.

In the experimental screen of TAEVC1, 16 out of the 22 solvents that were explored yielded samples which were found to be isostructural to the starting material of TAEVC2 depending on the crystallisation method that was employed. Screening of TAEVC2 revealed a similar outcome with 17 solvents out of the 22 used resulting in the crystallisation of samples bearing close similarity to the starting TAEVC2 material under given conditions. The type of starting material utilised for evaporation experiments at room temperature predominantly did not affect experimental outcomes as crystallisation of TAEVC1 and TAEVC2 from 14 solvents always resulted in the same product. Different crystalline outcomes were observed when the two enantiomers where crystallised from chloroform, 1,2-dichloroethane, diethyl ether, ethyl acetate and furfural. Attempted evaporation of TAEVC1 from 2-ethoxyethanol and methanol solutions failed to induce crystallisation and amorphous products resembling gels and powders respectively were retrieved from these solvents. However, the occurrence of amorphous products in the experimental screen was more prevalent when evaporation of TAEVC2 was pursued at 50°C with 7 out of 22 solvents yielding such products. Because of the limited amount of TAEVC3 starting material available at the onset of this work, a solvent-based screen as extensive as those implemented for TAEVC1 and TAEVC2 could not be pursued. Out of the 10 solvents investigated in the screen of TAEVC3, 4 of them crystallised with powder patterns similar to the starting material, i.e. the anhydrous form of TAEVC3. Solvated forms of TAEVC3 were produced when crystallised from acetonitrile, 2-butanol, 1,2-dichloroethane, methanol, THF and toluene (vapour diffusion only). Crystal structures for 4 solvated samples of TAEVC3 where successfully elucidated using SC-XRD (refer to section 6.3.6.4).

6.3.6.2 DSC/TGA

An overview of measurements from simultaneous DSC/TGA studies performed for the solvated TAEVC products isolated from solution-based screening experiments are presented in Tables 6.18 and 6.19. The data obtained for the various solvated samples of TAEVC materials indicate that the samples are predominantly non-stoichiometric. Variability in the peak of melting, the weight loss observed and the

corresponding stoichiometries suggests that not all of the materials for which isostructurality was noted through XRPD and SC-XRD analyses likely correspond to the same solvated form. For TAEVC1 material derived from ethyl acetate and samples obtained from 2-propanol and THF the possibility of hemisolvate formation was noted and for solvated material of TAEVC3 recrystallised from THF a 1.5:1 mole ratio of solvent to TAEVC3 was noted.

Table 6.18: Overview of DSC/TGA measurements performed for solvated samples of TAEVC1 and TAEVC2. Standard deviation values are provided in parentheses (n = 3 except for chloroform, 1,4-dioxane, furfural, 2-propanol and toluene samples where n = 2). For each solvent of crystallisation, data were collected from samples derived using both TAEVC1 and TAEVC2 as starting materials unless indicated otherwise.

Solvent of Crystallisation	Peak of Melting (°C)	Weight Loss Observed (%)	Corresponding Amount of Solvent (mole) per 1 mole of TAEVC
Acetic Acid	174.4 (± 4.31)	2.23 (± 0.22)	0.24 (± 0.03)
Acetone	168.5 (± 1.60)	3.73 (± 0.64)	0.42 (± 0.07)
Acetonitrile	158.8 (± 0.85)	0.23 (± 0.22)	0.004 (± 0.004)
1-Butanol	149.3 (± 1.82)	3.44 (± 0.35)	0.30 (± 0.04)
2-Butanol	144.9 (± 10.9)	4.70 (± 0.65)	0.38 (± 0.11)
2-Butanone	158.8 (± 3.49)	3.00 (± 0.49)	0.27 (± 0.04)
Butyl Acetate	104.0 (± 1.11)	4.21 (± 1.72)	0.24 (± 0.10)
Chloroform	160.5 (± 0.35)	6.81 (± 0.84)	0.38 (± 0.05)
1,2-Dichloroethane	149.7 (± 4.14)	4.74 (± 2.06)	0.31 (± 0.14)
Diethyl Ether (TAEVC1)	90.7	2.77	0.25
Diethyl Ether (TAEVC2)	154.2	1.22	0.11
1,4-Dioxane	-	8.55 (± 1.64)	0.06 (± 0.01)
Ethanol	175.5 (± 7.00)	2.80 (± 0.58)	0.40 (± 0.08)
2-Ethoxyethanol	103.2 (± 3.53)	4.41 (± 0.32)	0.32 (± 0.02)
Ethyl Acetate (TAEVC1)	96.3	6.67	0.50
Ethyl Acetate (TAEVC2)	140.1 (± 0.21)	10.59 (± 1.96)	0.79 (± 0.15)
Furfural (TAEVC1)	150.2 (± 5.23)	5.67 (± 0.36)	0.39 (± 0.02)
Methanol	159.5 (± 2.00)	0.46 (± 0.14)	0.01 (± 0.001)
2-Methoxyethanol	145.4 (± 5.89)	3.05 (± 0.39)	0.26 (± 0.04)
Methyl Acetate	162.4 (± 2.84)	3.51 (± 0.52)	0.31 (± 0.05)
2-Propanol	175.4 (± 0.64)	5.36 (± 1.34)	0.59 (± 0.15)
THF	177.3 (± 4.95)	5.77 (± 0.83)	0.52 (± 0.08)
Toluene	132.5 (± 2.12)	6.72 (± 0.30)	0.48 (± 0.02)
TFE	167.6	7.23	0.47

Table 6.19: Overview of DSC/TGA measurements performed for solvated samples of TAEVC3.

Solvent of Crystallisation	Peak of Melting (°C)	Weight Loss Observed (%)	Corresponding Amount of Solvent (mole) per 1 mole of TAEVC
Acetonitrile	197.5	3.16	0.50
2-Butanol	181.8	2.12	0.19
Methanol	196.9	1.09	0.22
THF	196.3	16.62	1.51

6.3.6.3 Optical Microscopy

Complete sets of optical micrographs corresponding to TAEVC samples derived from solution-based screening are given in Appendix Figures A6.24 – A6.26 and reveal a broad range of experimental morphologies upon crystallisation from each solvent. Crystals with hexagonal, prismatic, dendritic (Figure 6.26a), spherulitic, star-shaped (Figure 6.26b), block-like, plate-like and needle-like morphologies were all noted for solvated TAEVC samples. The fact that several of the solvated TAEVC materials which were found to exhibit isostructurality (Tables 6.20 and 6.21) crystallised with distinct morphologies can be attributed to variability in the solvent - solute interactions occurring during crystal growth (Lahav and Leiserowitz, 2001; Bhat and Dharmaprakash, 2002; Chen et al., 2008). Suitable single crystals were analysed further using SC-XRD.

(a)

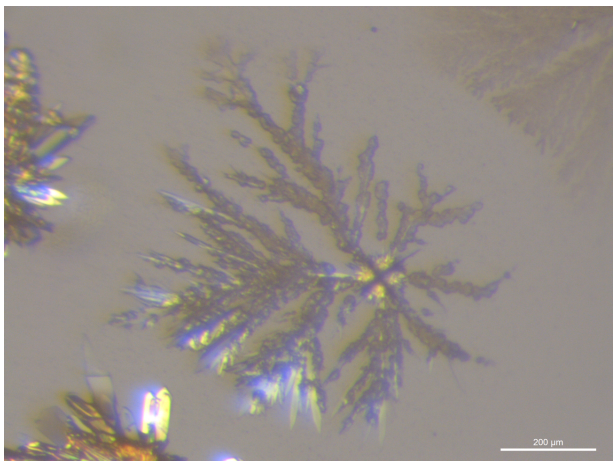

(b)

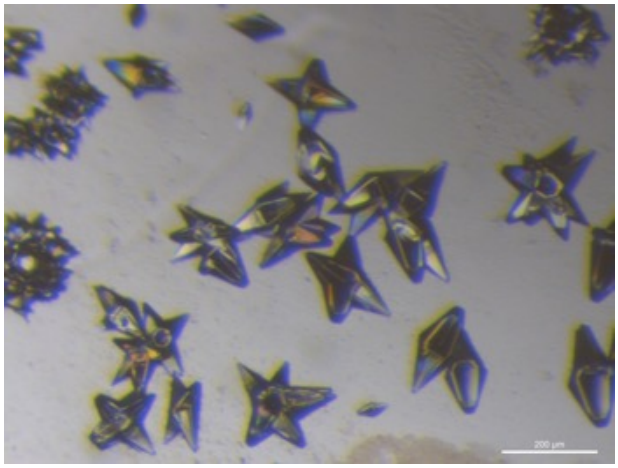

Figure 6.26: Optical micrographs showing dendritic (a) and star-shaped (b) crystals of TAEVC2 prepared via evaporation from 1,2-dichloroethane and acetone solutions respectively. The scale bar in both micrographs corresponds to 200 µm.

6.3.6.4 Indexing and Single-Crystal Structure Analysis

Unit cell parameters of TAEVC solvates derived through indexing of single crystals are shown in Table 6.20. Similar to EVC, the majority of solvated crystals of TAEVC analysed via SC-XRD typically diffracted to a resolution lower than 1 Å, rendering them unsuitable for structure solution and refinement. The unit cell parameters for samples derived from crystallisation of TAEVC1 and TAEVC2 in chloroform, methanol, 2-methoxyethanol, toluene and TAEVC3 in 2-butanol, 1,2-dichloroethane and THF could not be obtained. A total of 8 single-crystal structures were solved and refined and the corresponding crystallographic data, including thermal ellipsoid models of the structures and atomic disorder parameters are presented in Tables 6.21 – 6.22, Appendix Figure A6.30 and Appendix Table 6.3.

Table 6.20: Representative unit cell parameters of solvated TAEVC samples. All single crystals measured were prepared via evaporation at room temperature.

Solvent of Crystallisation	Starting Material	Bravais Lattice	*a* (Å)	*b* (Å)	*c* (Å)	α (°)	β (°)	γ (°)	Volume (Å^3)
Acetic Acid	TAEVC2	Hexagonal *P*	13.60	13.60	64.05	90	90	120	10267
Acetone	TAEVC2	Hexagonal *P*	13.63	13.63	64.06	90	90	120	10313
Acetonitrile	TAEVC2	Hexagonal *P*	13.59	13.59	64.11	90	90	120	10259
1-Butanol	TAEVC2	Hexagonal *P*	13.68	13.68	65.14	90	90	120	10553
2-Butanol	TAEVC2	Hexagonal *P*	13.70	13.70	64.84	90	90	120	10542
2-Butanone	TAEVC2	Hexagonal *P*	13.68	13.68	64.59	90	90	120	10472
Butyl Acetate	TAEVC2	Monoclinic *C*	24.42	13.24	13.70	90	93.66	90	4421
1,2-Dichloroethane	TAEVC2	Monoclinic *C*	24.66	12.92	13.91	90	94.22	90	4413
Diethyl Ether	TAEVC2	Monoclinic *C*	24.13	12.87	13.50	90	94.02	90	4183
1,4-Dioxane	TAEVC2	Hexagonal *P*	13.71	13.71	63.86	90	90	120	10397
Ethanol	TAEVC2	Hexagonal *P*	13.55	13.55	64.16	90	90	120	10202
Ethyl Acetate	TAEVC1	Monoclinic *C*	24.17	12.78	13.60	90	93.88	90	4191
2-Ethoxyethanol	TAEVC2	Monoclinic *C*	24.12	12.75	13.58	90	93.89	90	4166
Furfural	TAEVC2	Hexagonal *P*	13.77	13.77	64.09	90	90	120	10528
Methyl Acetate	TAEVC2	Hexagonal *P*	13.76	13.76	63.46	90	90	120	10411
2-Propanol	TAEVC2	Hexagonal *P*	13.61	13.61	64.27	90	90	120	10311
THF	TAEVC2	Hexagonal *P*	13.66	13.66	64.05	90	90	120	10349
TFE	TAEVC2	Hexagonal *P*	13.61	13.61	64.33	90	90	120	10321

SC-XRD analysis of the crystal structures of TAEVC1 material crystallised from butyl acetate (TAEVC1 – butyl acetate), TAEVC1 material crystallised from acetonitrile (TAEVC1 – acetonitrile) and TAEVC2 material recrystallised from acetonitrile (TAEVC2 – acetonitrile) indicated that these structures all crystallise in the monoclinic *C*2 space group and have closely related unit cell parameters (Table 6.21). The packing arrangement of TAEVC1 butyl – acetate is shown in Figure 6.27. The OH group of the benzazepine moiety is involved in O-H···N interactions with the tetrazole nitrogen to form a 1D network which extends infinitely along the crystallographic *b* axis (Figure 6.27a). The OH groups of carboxylic acid and benzazepine connect these 1D chains via O-H···O interactions to form a honeycomb type 2D network as shown in Figure 6.27b. Whilst the solvent molecules occupy the isolated sites of empty space within the 2D network, these are not involved in hydrogen bonding with the TAEVC molecules and are therefore not presented in the packing diagrams.

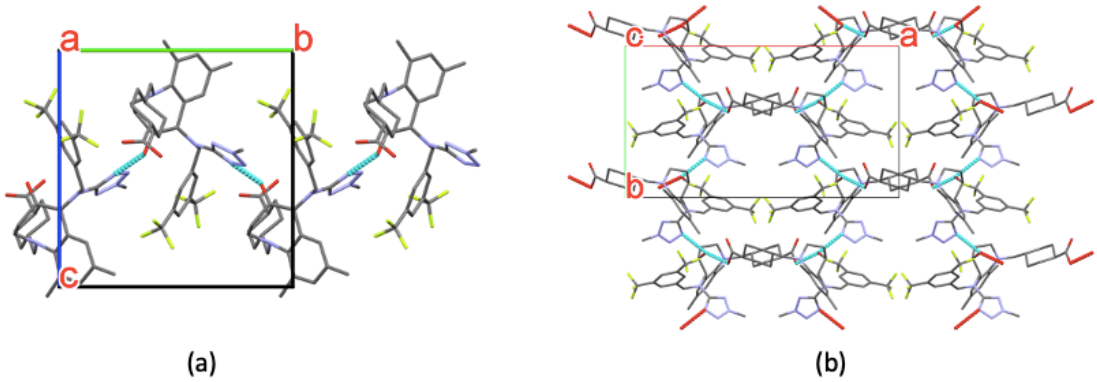

Figure 6.27: Unit cell packing arrangement in TAEVC1 material crystallised from butyl acetate, viewed along (a) crystallographic *a* axis and (b) crystallographic *c* axis. The solvent molecules and hydrogen atoms have been omitted for clarity.

The packing arrangement of the TAEVC1 – acetonitrile structure is presented in Figure 6.28. The structure exhibits a similar packing arrangement compared to TAEVC1 – butyl acetate, with the TAEVC molecules arranging to form a 2D hydrogen-bonded network as shown in Figure 6.28b. The TAEVC2 – acetonitrile crystal structure was found to have a packing arrangement identical to that of TAEVC1 – acetonitrile and is not shown herein. The TAEVC molecules in TAEVC1 – acetonitrile and TAEVC2 – acetonitrile were confirmed to have opposite handedness (Table 6.21).

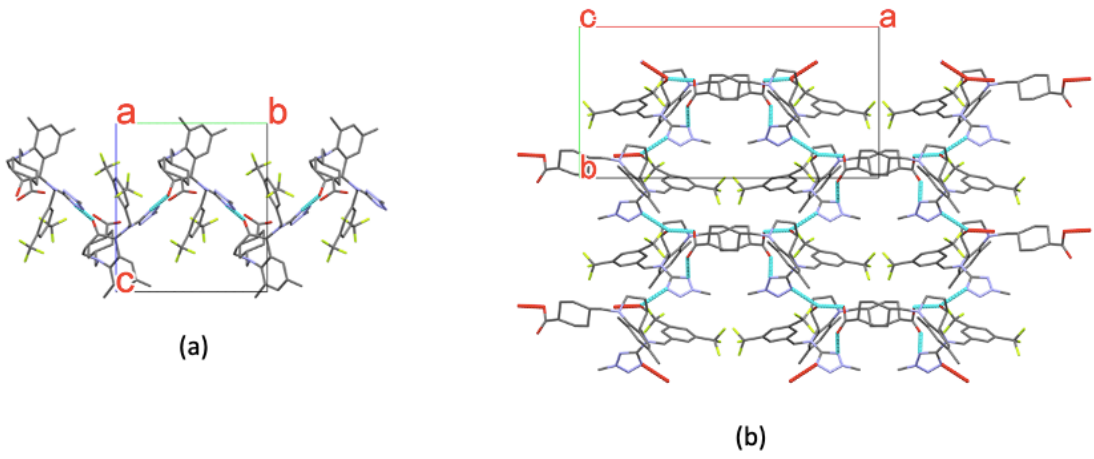

Figure 6.28: Unit cell packing arrangement in TAEVC1 material crystallised from acetonitrile, viewed along (a) crystallographic *a* axis and (b) crystallographic *c* axis. The solvent molecules and hydrogen atoms have been omitted for clarity.

The packing arrangement in the crystal structure of TAEVC2 material recrystallised from ethyl acetate (TAEVC2 – ethyl acetate) is shown in Figure 6.29. This structure was found to crystallise in monoclinic $P2_1$ space group with two molecules of TAEVC and two molecules of ethyl acetate present in the asymmetric unit. The two TAEVC molecules are hydrogen bonded via O-H···O interactions involving the hydroxy groups of carboxylic acid and the benzazepine moiety to form a dimeric $R_2^2(24)$ motif as shown in Figure 6.29a. These dimeric motifs are bridged via O-H···N interactions between the hydroxy group of benzazepine and the nitrogen of the tetrazole ring to form a 2D network which extends infinitely in the (011) plane as shown in Figure 6.29b. Whilst the orientation of the TAEVC molecules in the TAEVC2 – ethyl acetate structure is different compared to the acetonitrile and butyl acetate structures, the molecules do exhibit similar 2D packing arrangements. An overlay of the molecular conformations of TAEVC1 in the acetonitrile, butyl acetate and ethyl acetate structures is presented in Figure 6.30.

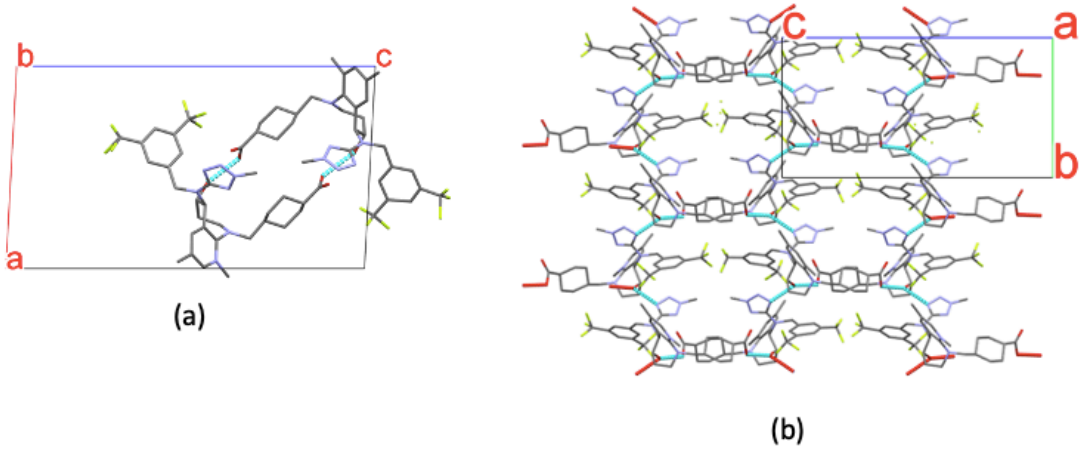

Figure 6.29: Unit cell packing arrangement in TAEVC2 material recrystallised from ethyl acetate, viewed along (a) crystallographic *b* axis and (b) the [011] direction. The solvent molecules and hydrogen atoms have been omitted for clarity.

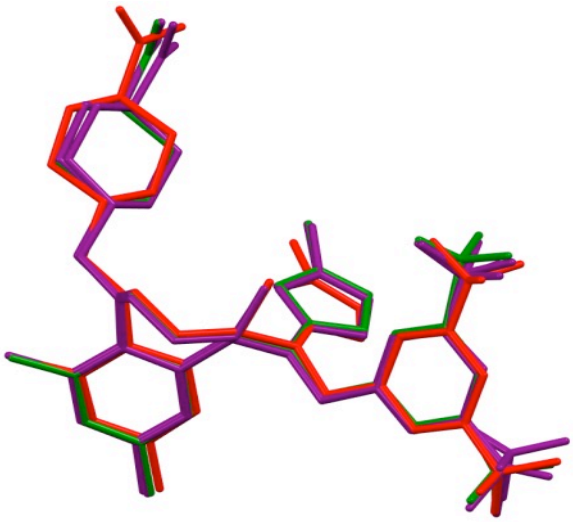

Figure 6.30: Overlay of the molecular conformations of TAEVC1 crystallised from butyl acetate (red), TAEVC1 crystallised from acetonitrile (green) and TAEVC2 (purple) recrystallised from ethyl acetate.

In the case of TAEVC3, crystal structures were solved for materials that were obtained from crystallisation in acetonitrile (TAEVC3 – acetonitrile), 1,2-dichloroethane (TAEVC3 – 1,2-dichloroethane), methanol (TAEVC3 – methanol) and toluene (TAEVC3 – toluene). Examination of the hydrogen bonding motifs present in the crystal structures of TAEVC3 – acetonitrile, TAEVC3 – 1,2-dichloroethane, and TAEVC3 – methanol indicated close structural similarity for these structures. The packing arrangements of TAEVC3 - acetonitrile, TAEVC3 - 1,2-dichloroethane, and TAEVC3 - methanol are shown in Figures 6.31 – 6.33.

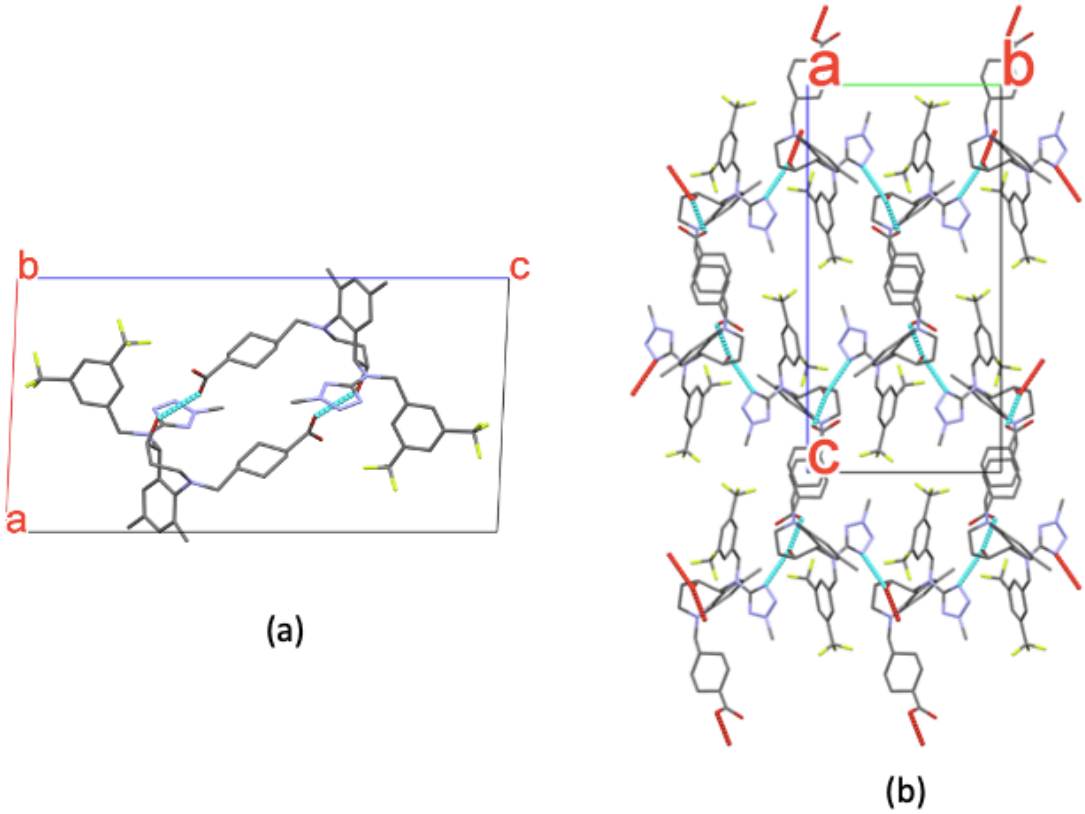

Figure 6.31: Unit cell packing arrangement in TAEVC3 material recrystallised from acetonitrile, viewed along (a) crystallographic *b* axis and (b) crystallographic *a* axis. The solvent molecules and hydrogen atoms have been omitted for clarity.

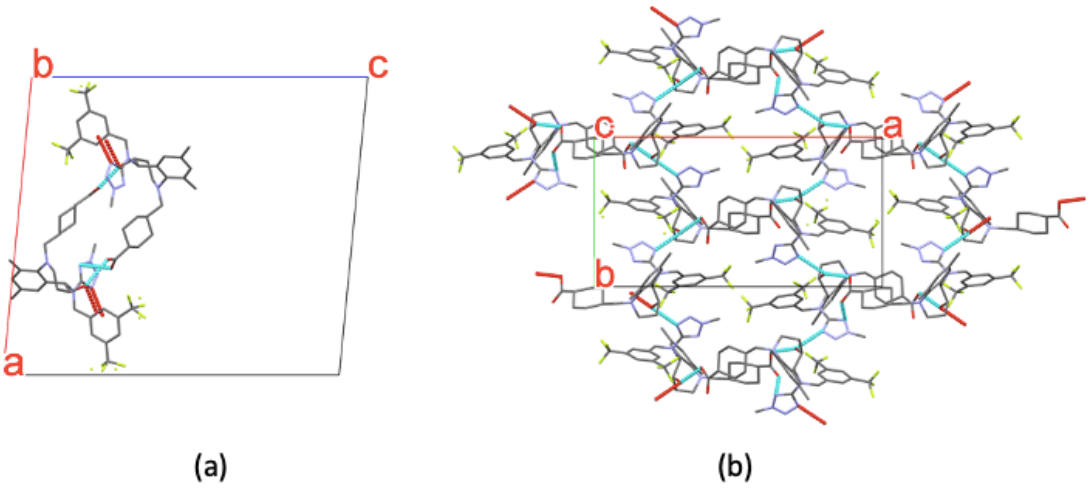

Figure 6.32: Unit cell packing arrangement in TAEVC3 material recrystallised from 1,2-dichloroethane viewed along (a) crystallographic *b* axis and (b) crystallographic *c* axis. The solvent molecules and hydrogen atoms have been omitted for clarity.

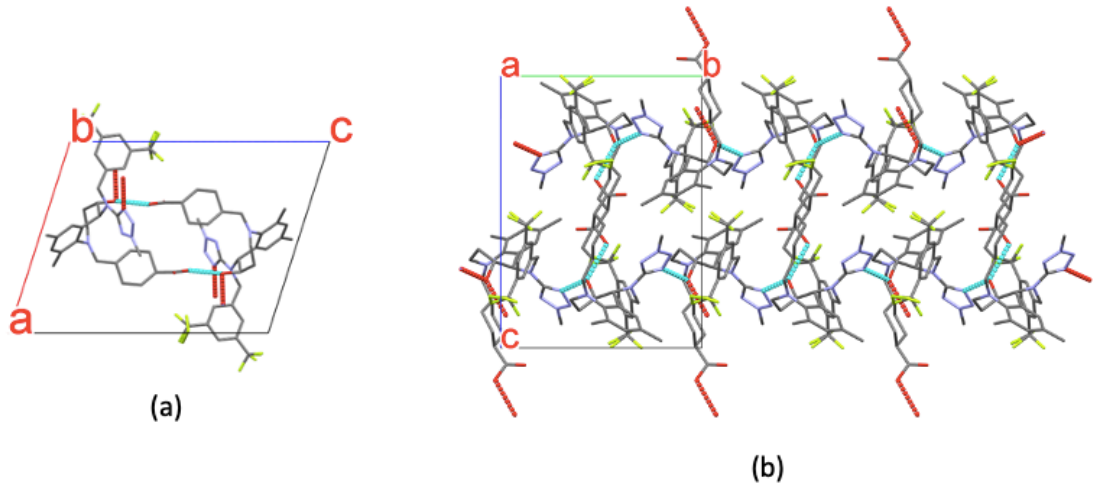

Figure 6.33: Unit cell packing arrangement in TAEVC3 material recrystallised from methanol viewed along (a) crystallographic *b* axis and (b) crystallographic *a* axis. The solvent molecules and hydrogen atoms have been omitted for clarity.

In the abovementioned TAEVC3 structures (acetonitrile, 1,2-dichloroethane, and methanol), the OH group of benzazepine moiety is involved in O-H···N interactions with the tetrazole nitrogen while the OH groups of carboxylic acid and benzazepine hydrogen bond to form a 2D network similar to those observed in TAEVC1 and TAEVC2. However, the hydrogen bonding motif observed in TAEVC3 material recrystallised from (TAEVC3 – toluene) is significantly different compared to the rest of the crystal structures of TAEVC described in this section (including TAEVC2 and TAEVC1). The packing arrangement in TAEVC3 – toluene is depicted in Figure 6.34. This structure is unique amongst all of the TAEVC structures as the carboxyl groups in TAEVC3 form a dimeric $R_2^2(8)$ motif. These TAEVC3 molecules are bridged via hydrogen bonds between the OH of benzazepine and nitrogen of the tetrazole ring to form O-H···N interactions. Whilst the molecules arrange to form a 2D hydrogen-bonded network, the network observed in TAEVC3 recrystallised from toluene is different compared to the rest of the crystal structures of TAEVC. An overlay of the molecular conformations of TAEVC3 in the experimentally determined single-crystal structures and the starting material is presented in Figure 6.35. The crystal structure of TAEVC3 – 1,2-dichloroethane contains two molecules in the asymmetric unit and was not included in the overlay. Overviews of the unit cell void space occupied by solvent molecules and packing coefficients of the various TAEVC crystal structures characterised by SC-XRD are presented in Appendix Tables A6.4 and A6.5.

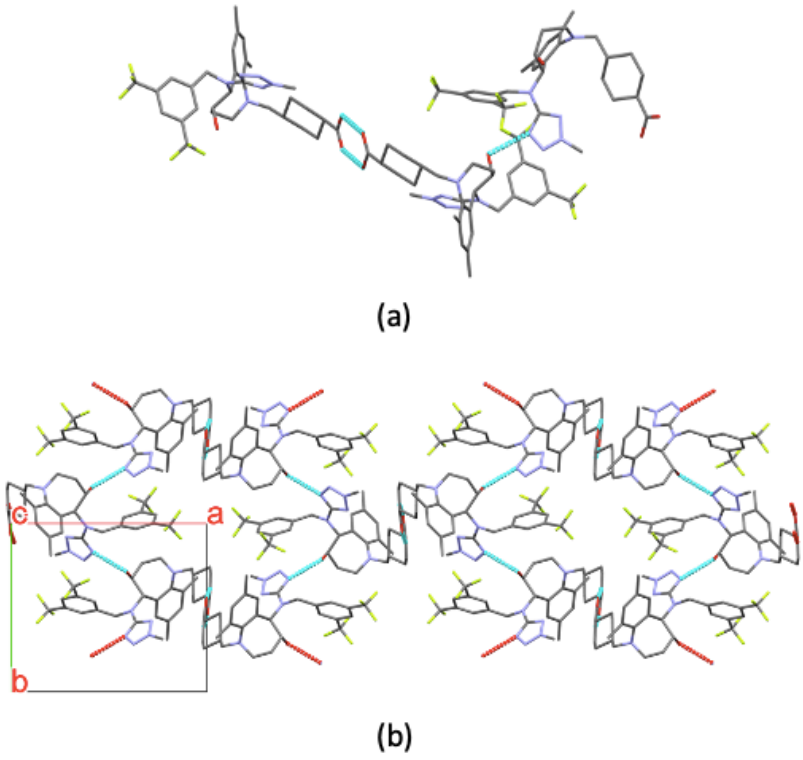

Figure 6.34: Hydrogen-bonding interactions (a) and unit cell packing arrangement, viewed along the crystallographic *c* axis (b) of TAEVC3 material recrystallised from toluene. The solvent molecules and hydrogen atoms have been omitted for clarity.

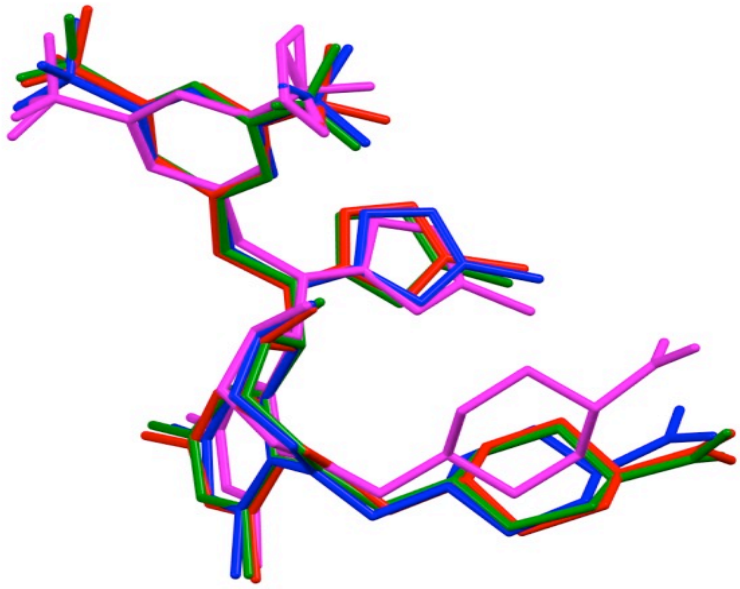

Figure 6.35: Overlay of conformations of TAEVC molecules in TAEVC3 - toluene (blue), TAEVC3 - acetonitrile (red), TAEVC3 - methanol (magenta) and the TAEVC3 starting material (green).

Table 6.21: Overview of crystallographic data for solvated structures of TAEVC1 and TAEVC2 derived via SC-XRD analysis.

	TAEVC1 – Acetonitrile	TAEVC1 – Butyl Acetate	TAEVC2 – Acetonitrile	TAEVC2 – Ethyl Acetate
Crystal System	Monoclinic	Monoclinic	Monoclinic	Monoclinic
Space Group	*C*2	*C*2	*C*2	$P2_1$
***a* (Å)**	24.328 (2)	24.002 (13)	24.378 (14)	13.545 (4)
***b* (Å)**	12.254 (12)	13.241 (8)	12.263 (7)	12.286 (4)
***c* (Å)**	13.637 (13)	13.403 (7)	13.619 (8)	23.923 (7)
β (°)	92.458 (4)	93.561 (3)	92.350 (2)	93.086 (10)
Voume (Å^3)	4061.5 (7)	4251.4 (4)	4068.1 (4)	3975.4 (2)
Z	4	4	4	4
Density (g/cm^3)	1.814	1.733	1.811	1.390
X-ray Radiation Source	Mo $K\alpha_1$ (λ = 0.71073 Å)	Cu $K\alpha_1$ (λ = 1.54060 Å)	Mo $K\alpha_1$ (λ = 0.71073 Å)	Cu $K\alpha_1$ (λ = 1.54060 Å)
Temperature (°C)	-183 (2)	-173 (2)	-173 (2)	-173 (2)
R_1 (%)	7.76	9.26	8.68	11.13
WR_2 (%)	21.49	25.23	25.16	30.77
Flack Parameter	0.048 (3)	0.12 (8)	0.08 (14)	0.88 (4)
Absolute Configuration	*S*,*S*	*S*,*S*	*R*,*R*	*S*,*S*,*S*,*S*

Table 6.22: Overview of crystallographic data for solvated structures of TAEVC3 derived via SC-XRD analysis.

	TAEVC3 – Acetonitrile	TAEVC3 – 1,2-Dichloroethane	TAEVC3 – Methanol	TAEVC3 – Toluene
Crystal System	Monoclinic	Monoclinic	Monoclinic	Monoclinic
Space Group	$P2_1/c$	$P2_1/n$	$P2_1/n$	$P2_1/c$
***a* (Å)**	13.154 (3)	24.004 (2)	14.225 (19)	14.277 (3)
***b* (Å)**	12.655 (3)	12.407 (13)	13.007 (7)	12.272 (2)
***c* (Å)**	25.351 (7)	27.057 (3)	18.484 (4)	22.416 (5)
β (°)	92.679 (8)	95.524 (3)	107.900 (11)	92.296 (10)
Voume (Å^3)	4215.4 (19)	8020.6 (14)	3254.3 (8)	3924.12 (14)
Z	4	8	4	4
Density (g/cm^3)	1.748	2.082	1.361	1.408
X-ray Radiation Source	Mo $K\alpha_1$ (λ = 0.71073 Å)	Mo $K\alpha_1$ (λ = 0.71073 Å)	Mo $K\alpha_1$ (λ = 0.71073 Å)	Cu $K\alpha_1$ (λ = 1.54060 Å)
Temperature (°C)	26 (2)	-173 (2)	-173 (2)	-171 (2)
R_1 (%)	13.75	8.06	7.4	9.45
WR_2 (%)	38.72	23.00	25.11	31.23
Flack Parameter	N/A	N/A	N/A	N/A
Absolute Configuration	*S*,*S*	*S*,*S*,*R*,*R*	*S*,*S*	*S*,*S*

6.3.6.5 Desolvation Studies

The complete overview of desolvation studies carried out for solvated TAEVC materials is presented in Table 6.23 and the outcomes shown are based on XRPD analysis. 16 out of the 23 solvated materials investigated were found to undergo no apparent change in solid form under the conditions investigated. Solvated TAEVC2 material derived from diethyl ether was found to comprise additional peaks that were not present upon commencement of attempted desolvation, however indexing was not successful because the subjection to elevated temperature likely caused the original material to convert into a mixture of forms. Solvated material obtained from TFE was the only one that was found to undergo a complete loss of crystallinity and transform into an amorphous state whereas partial loss of crystallinity, resulting in material that could not be indexed, was noted for solvated TAEVC3 crystallised from acetonitrile. A number of desolvation experiments yielded evidence of an anhydrous form which was found to be isostructural to the starting material of TAEVC2. More specifically, the anhydrous form was isolated through *in-situ* desolvation by means of VT-XRPD experiments of solvated materials derived from crystallisation in acetonitrile, 1,2-dichloroethane, ethyl acetate and toluene. Representative VT-XRPD scans and DSC/TGA traces of the TAEVC2 – ethyl acetate solvate are presented in Figures 6.36a and 6.36b and a Pawley fit of the corresponding desolvation product is shown in Figure 6.36c. The residual values obtained for the Pawley fit were R_{wp} = 3.39% and R_p = 2.51% and the refined unit cell parameters derived were $a = b$ = 13.714 (3) Å and c = 64.053 (9) Å.

Table 6.23: Overview of desolvation experiments performed for solvated TAEVC materials.

Starting Material	Desolvation Conditions	Desolvation Outcome
TAEVC2 - Ethanol	Stored in drying oven at 65°C for 6 days	No change in solid form evident
TAEVC2 – 1,4-Dioxane	Stored in drying oven at 65°C for 6 days	No change in solid form evident
TAEVC2 – 2-Propanol	Stored in drying oven at 65°C for 6 days	No change in solid form evident
TAEVC2 - THF	Stored in drying oven at 65°C for 6 days	No change in solid form evident
TAEVC1 – 2-Butanol	Stored in drying oven at 65°C for 1 day	No change in solid form evident
TAEVC2 – 2-Butanone	Stored in drying oven at 65°C for 6 days	No change in solid form evident
TAEVC2 – Diethyl Ether	Stored in drying oven at 65°C for 3 days	New diffraction peaks emerged but pattern could not be indexed
TAEVC2 – 1-Butanol	Stored in drying oven at 65°C for 6 days	No change in solid form evident
TAEVC2 – Ethyl Acetate	VT-XRPD	Anhydrous form isostructural to the starting TAEVC2 material
TAEVC2 - Toluene	VT-XRPD	Anhydrous form isostructural to the starting TAEVC2 material
TAEVC2l - Acetone	Stored in drying oven at 65°C for 6 days	No change in solid form evident
TAEVC2 – Methyl Acetate	Stored in drying oven at 65°C for 6 days	No change in solid form evident
TAEVC2 – 2-Ethoxyethanol	Stored in drying oven at 65°C for 6 days	Amorphous material
TAEVC2 - TFE	Stored in drying oven at 65°C for 6 days	No change in solid form evident
TAEVC2 - Furfural	Stored in drying oven at 65°C for 6 days	No change in solid form evident
TAEVC2 - Chloroform	Stored in drying oven at 65°C for 6 days	No change in solid form evident
TAEVC1 – 1,2-Dichloroethane	VT-XRPD	Anhydrous form isostructural to the starting TAEVC2 material
TAEVC2 – Butyl Acetate	Stored in drying oven at 65°C for 6 days	No change in solid form evident
TAEVC2 - Methanol	Stored in drying oven at 65°C for 6 days	No change in solid form evident
TAEVC3 - Methanol	Stored in drying oven at 65°C for 1 day	No change in solid form evident
TAEVC2 – 2-Methoxyethanol	Stored in drying oven at 65°C for 3 days	No change in solid form evident
TAEVC1 - Acetonitrile	VT-XRPD	Anhydrous form isostructural to the starting TAEVC2 material
TAEVC3 - Acetonitrile	Stored in drying oven at 65°C for 1 day	Poorly crystalline material

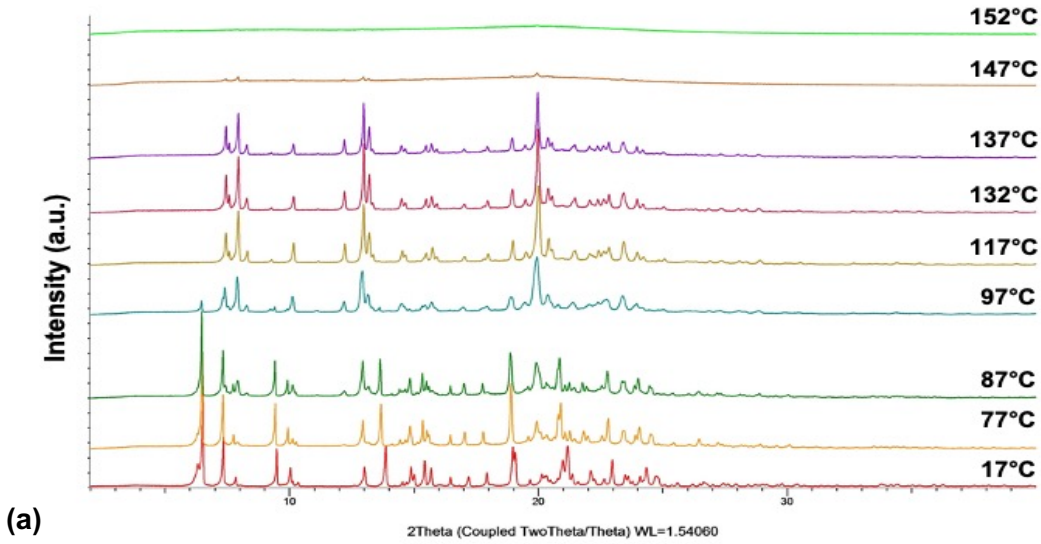

(a)

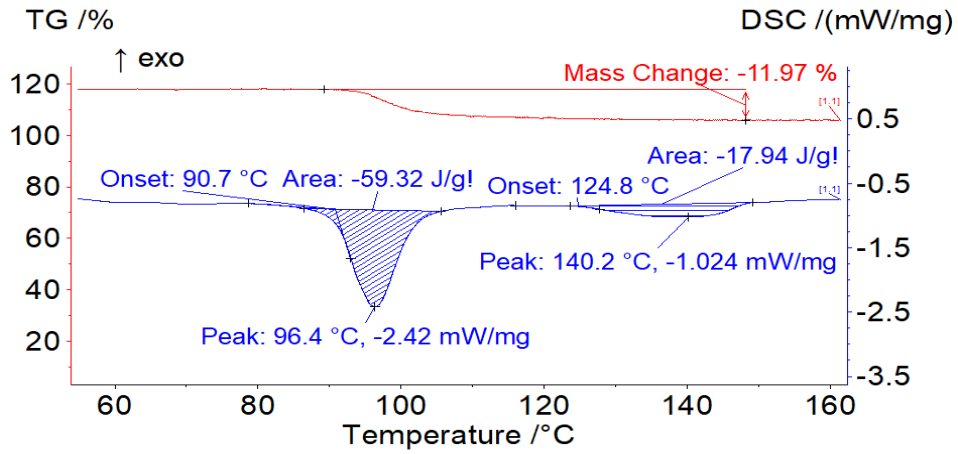

(b)

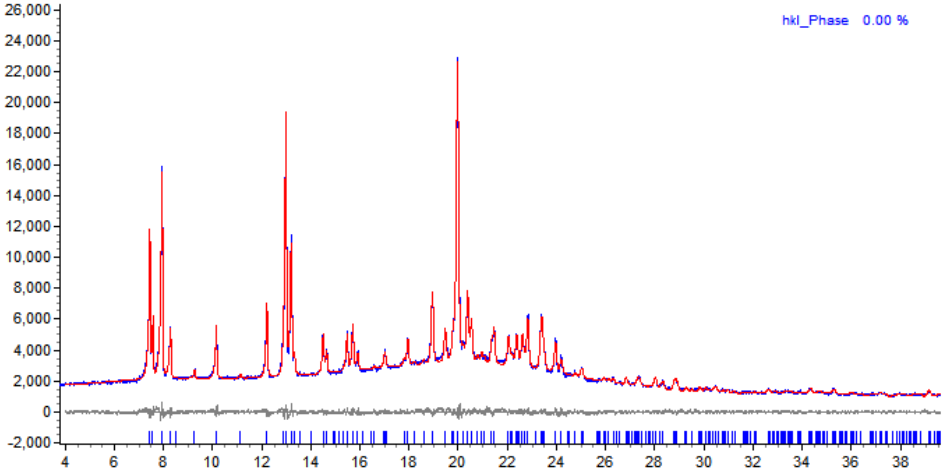

(c)

Figure 6.36: VT-XRPD scans (a), representative DSC/TGA traces (b) of the ethyl acetate solvate of TAEVC2 and Pawley fit of its desolvation product at 137°C (c).

6.3.6.6 Physical Vapour Deposition, Crystallisation from the Melt and SCF Extraction

Physical vapour deposition studies of the TAEVC materials using sublimation temperatures in the 50 - 100°C did not result in the formation of any crystals. Crystallisation of TAEVC2 following melting at 175°C resulted in the formation of an anhydrous form isostructural to the starting material of TAEVC2 (Appendix Figure A6.27). Attempted crystallisation of TAEVC3 melted at 200°C solely yielded an amorphous product (Appendix Figure A6.28). SCF extraction of TAEVC2 yielded polycrystalline material which was found to be isostructural to the starting TAEVC2 material (Appendix Figure A6.29).

6.3.7 Cocrystallisation Screen for Solid-Solution Formation

Results from the cocrystallisation screen of EVC and TAEVC are presented in Tables 6.24 and 6.25. The experiments that were conducted provided no evidence for solid solution formation. More specifically, attempted cocrystallisation involving EVC – TBA and TAEVC1 as the starting materials resulted in non-crystalline outcomes being most prevalent, with 12 out of the 16 solvents investigated yielding amorphous products. Crystallisation in acetic acid and 1,2-dichloroethane resulted in poorly crystalline materials for which indexing was not possible whilst the material derived from 2-butanol was found to be a mixture of materials isostructural to EVC – TBA and the starting TAEVC2 form. Crystallisation in furfural provided insufficient material for characterisation. Similar to experiments involving TAEVC1 as one of the starting materials, the formation of amorphous products was the most common outcome in the attempted cocrystallisation studies featuring EVC and TAEVC2, with 6 out of 16 solvents found to yield such products. The attempted cocrystallisation of EVC – TBA and TAEVC1/TAEVC2 in 1,2-dichloroethane only resulted in the formation of poorly crystalline material that could not be indexed. Samples obtained from experiments carried out in 2-butanol, diethyl ether, methanol, THF and TFE were all found to correspond to mixtures of materials isostructural to EVC – TBA and the starting TAEVC2 form whilst ethanol, furfural and methyl acetate solutions solely yielded products isostructural to the starting TAEVC2 form. Due to the absence of sufficient material and suitable single crystals for further characterisation, confirmation on whether the products isostructural to TAEVC2 solely comprised TAEVC molecules or

a solid solution with EVC could not be obtained. Attempted cocrystallisation in butyl acetate exclusively resulted in the formation of material crystallising in *C*2, isostructural to the solvate obtained from crystallisation in butyl acetate when pure TAEVC1 was used as the starting material (Table 6.21). Due to the limited amounts of sample available, it was not possible to characterise this product further and confirm whether it corresponded to the exact same solvated structure obtained from butyl acetate which is described in Table 6.21.

The inability of chiral compounds to readily form solid solutions upon crystallisation is well established (Jacques et al., 1981) and is further illustrated herein with EVC and TAEVC. The fact that the two compounds failed to co-crystallise in a solid solution can be attributed to enantiopure EVC and TAEVC not being able to form quasi-centrosymmetric crystal structures wherein molecules that exhibit identical configuration adopt different conformations which are approximate mirror images to one another (Brandel et al., 2016; Rekis et al., 2017).

Table 6.24: Overview of cocrystallisation experiments performed for EVC and TAEVC1.

Solvent	Experimental Outcome
Acetic Acid	Poorly crystalline material
Acetone	Amorphous material
1-Butanol	Amorphous material
2-Butanol	Mixture of materials isostructural to EVC – TBA and the starting TAEVC2 material
2-Butanone	Amorphous material
Butyl Acetate	Amorphous material
1,2-Dichloroethane	Poorly crystalline material
Diethyl Ether	Amorphous material
Ethanol	Amorphous material
2-Ethoxyethanol	Amorphous material
Furfural	Insufficient material available for analysis
Methanol	Amorphous material
2-Methoxyethanol	Amorphous material
Methyl Acetate	Amorphous material
THF	Amorphous material
TFE	Amorphous material

Table 6.25: Overview of cocrystallisation experiments performed for EVC and TAEVC2.

Solvent	Experimental Outcome
Acetic Acid	Amorphous material
Acetone	Amorphous material
1-Butanol	Amorphous material
2-Butanol	Mixture of materials isostructural to EVC – TBA and the starting TAEVC2 material
2-Butanone	Amorphous material
Butyl Acetate	Material obtained from butyl acetate and crystallising in *C*2
1,2-Dichloroethane	Poorly crystalline material
Diethyl Ether	Mixture of materials isostructural to EVC – TBA and the starting TAEVC2 material
Ethanol	Material isostructural to starting TAEVC2 material
2-Ethoxyethanol	Amorphous material
Furfural	Material isostructural to starting TAEVC2 material
Methanol	Mixture of materials isostructural to EVC – TBA and the starting TAEVC2 material
2-Methoxyethanol	Amorphous material
Methyl Acetate	Material isostructural to starting TAEVC2 material
THF	Mixture of materials isostructural to EVC – TBA and the starting TAEVC2 material
TFE	Mixture of materials isostructural to EVC – TBA and the starting TAEVC2 material

6.4 Summary

Extensive solid-state screening and characterisation investigations were pursued in an attempt to investigate solid-form diversity in EVC and a closely related tetrazole analogue (TAEVC) that had never been characterised and subjected to solid-form screening studies previously. Both solvent-based and solvent-free crystallisation approaches were explored in an effort to maximise the likelihood of isolating all possible solid forms of the two compounds. The solution-based screening experiments that were performed helped establish an initial solid-form landscape for the novel TAEVC molecule and expanded the solid-form landscape of EVC that had previously been established by Eli Lilly and Company. An overview of the screening outcomes derived from solution-based studies of EVC and TAEVC is provided in Figure 6.37. The EVC screening work was previously summarised in section 6.3.4. In screening experiments carried out using the enantiopure TAEVC1 and TAEVC2 materials, the majority of solvated structures exhibited isostructurality to the TAEVC2

starting form based on XRPD and SC-XRD analyses. However, a number of solvated structures distinct from the starting material were also obtained when crystallisation was performed in solvents such as butyl acetate, 1,2-dichloroethane, diethyl ether, 2-ethoxyethanol, ethyl acetate, furfural and toluene. Screening studies of racemic TAEVC3 frequently resulted in crystallisation of the anhydrous form corresponding to the starting material and solvated forms were isolated via crystallisation in acetonitrile, 2-butanol, 1,2-dichloroethane, methanol, THF and toluene.

The solid-state screen conducted for EVC and TAEVC revealed the propensity of both compounds to readily crystallise in the form of solvated materials, a behaviour that has previously been exhibited by several compounds of pharmaceutical relevance, including sulfathiazole (Bingham et al., 2001), axitinib (Campeta et al., 2010), olanzapine (Bhardwaj et al., 2013) and galunisertib (Bhardwaj et al., 2019). It has been well documented that the formation of isostructural crystals, crystallising in the same structure type but potentially exhibiting minor deviations with respect to their corresponding unit cell parameters, is more likely to occur in multi-component solid forms such as solvates and salts rather than single component forms comprising one particular type of molecule (Cruz-Cabeza et al., 2006; Galcera et al., 2013; Sridhar et al., 2017). Isostructural solvate formation was readily noted for EVC and TAEVC in this work and is a particularly prevalent phenomenon in pharmaceutically relevant compounds (Schultheiss et al., 2009; Chadha et al., 2012a; Thakuria and Nangia, 2013). The formation of isostructural solvates involves the ability of one host crystal structure to accommodate different types of solvent molecules in its structural voids (Griesser, 2006; Zhang et al., 2014). In general, the formation of solvates is predominantly dependent on two factors (Price et al., 2006): 1) unsatisfied intermolecular interactions between molecules in the unit cell (Tessler and Goldberg, 2006), most typically caused due to a misbalance in the number of hydrogen bond donors and acceptors present in each molecule and compensated through the incorporation of solvent molecules in the unit cell, and 2) inclusion of solvent molecules in the unit cell causing a decrease in the void space within and/or leading to more efficient molecular packing (Vippagunta et al., 2001). The majority of experimentally reported solvates in the literature have been found to form through contributions of both factors which cause a decrease in lattice free energy (Price et al., 2006); this is particularly prevalent in isostructural solvates whose formation can be attributed to the molecular shape of molecules that become incorporated into the

host crystal structure (Hosokawa et al., 2004) and specific interactions occurring between the guest molecules and the host structure (Braun et al., 2009; Stieger et al., 2010).

The crystal packing efficiency is reported to be one of the driving forces for solvate formation (Price et al., 2006). However, in the absence of a fully characterised anhydrous form of TAEVC1 & TAEVC2 the propensity of these materials to form solvates cannot be rationalised based on their calculated packing efficiency. In the case of TAEVC3, whilst some crystals exhibit larger packing coefficients than the non-solvated form this is not true across all the experimentally observed structures. This highlights that the packing efficiency is not the only indicator for the stability of a solvated phase, suggesting that the solvate formation is rather an interplay of packing efficiency and the strength of intermolecular interactions, which drives the crystallisation of solvates.

Examination of the hydrogen-bonded networks indicates that TAEVC readily forms a similar hydrogen bonding framework in most of the crystal structures that were successfully solved and refined. Most current efforts in molecular crystal engineering focus mainly on targeting and reproducing a particular supramolecular synthon. Whilst this approach has been extremely successful, it offers little or no control over the crystal-packing characteristics of ancillary functional groups in the molecules. It is therefore desirable to discover novel crystalline solids that preferentially crystallise with predefined solid-state architectures. The 2D network of guanidinium cations and sulfonate anions offers a very elaborate and advanced example of crystal engineering (Russell, 1994 & 1997). Additional examples of two-dimensional networks have been reported in the literature (Chang, 1993; Hollingsworth, 1994). A novel, robust 2D hydrogen-bonded network has been observed in most of the crystal structures of TAEVC, except for that of the TAEVC3 material recrystallised from toluene. This robust network makes use of the carboxyl, hydroxy and tetrazole functional groups in TAEVC. From the unit cell packing arrangements presented in Figure 6.27 – 6.29 and 6.31 – 6.34 it can also be noted that the hydroxy groups of benzazepine moiety act as donors and acceptors simultaneously by forming hydrogen bonds with the carboxylic acid and tetrazole donors. The TAEVC molecules do not follow the hierarchical rule of hydrogen bonding where a best donor preferentially hydrogen bonds with the best acceptor (Etter, 1990). Instead, the molecules form hydrogen bonds wherein all the best donors and acceptors within the molecule are involved in

hydrogen bonding. It is interesting to note that the two enantiomers and the racemic form of TAEVC exhibit similar hydrogen-bonded networks whilst exhibiting different symmetry between the molecules. The fact that the crystal structures comprise similar supramolecular networks can be interpreted as an indication of the molecules' preference to self-associate during the nucleation and growth process. The robust hydrogen-bonded network in TAEVC incorporates solvent molecules where possible to produce solvated forms and the observation that most of these molecules are highly disordered and do not participate in hydrogen-bonding interactions suggests that they are merely occupying the void space within the crystal lattice.

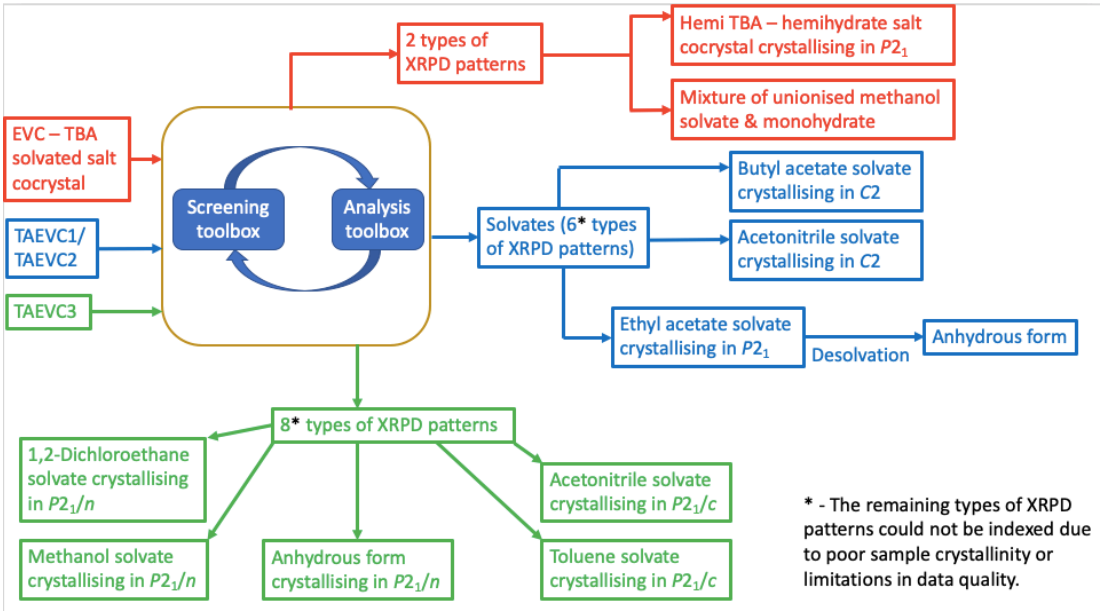

Figure 6.37: Overview of EVC and TAEVC screening outcomes presented in this work.

Chapter 7: Conclusions and Future Work

The research described in this thesis explores the diversity of several pharmaceutically relevant compounds in the solid state and includes characterisation of solid forms isolated through experimental screening protocols using a variety of crystallisation methods. All of the compounds investigated were subjected to both solvent-based and solvent-free crystallisation methods in an attempt to maximise the experimental space covered and increase the likelihood of obtaining all possible solid forms. The main outcomes observed for the pharmaceutical ingredients investigated are summarised in the following sub-sections and recommendations for further experimental work are additionally provided.

7.1 Solid-State Screening Studies of Oxcarbazepine and Characterisation of Form III

7.1.1 Conclusions

Screening of oxcarbazepine (OXCBZ) using fast evaporation and physical vapour deposition onto different types of metallic substrates enabled polycrystalline samples of metastable form III to be obtained for structure determination and characterisation. Polycrystalline material of form III obtained via evaporation from a 50:50 v/v ethanol/toluene mixture was characterised using X-ray powder diffraction (XRPD), enabling crystal structure determination using simulated annealing and subsequent Rietveld refinement. The structure of form III was experimentally determined for the first time, 10 years after OXCBZ III was initially reported in the literature, and differential scanning calorimetry/thermogravimetric analysis (DSC/TGA) provided novel evidence for solvent inclusion in the void channels occupying space within the unit cell of form III. The structure of form III was in good agreement with one of the predicted structures identified in the crystal structure prediction (CSP) landscape of OXCBZ, crystallising in the *R*-3 space group. Furthermore, form III was found to be isostructural to carbamazepine (CBZ) form II and cytenamide (CYT) form I, a finding that builds upon the significant structural similarities already known to exist between different polymorphs in the CBZ family of compounds. Gastrointestinal (GI) dissolution studies of form III indicated that, as expected, this metastable form dissolves ≈ 2.6 times more quickly than the commercially available OXCBZ I within the first ≈ 30 minutes of dissolution, an observation that makes form III a potential candidate

for improving the oral bioavailability of OXCBZ formulations and enhancing their efficacy upon administration.

7.1.2 Future Work

The screening investigations pursued for OXCBZ in this work were limited to fast evaporation and physical vapour deposition onto metallic substrates, with the CSP landscape of OXCBZ indicating that there are still several predicted structures in close proximity to form I that have not been observed experimentally. Consequently, a broader range of solid-state screening approaches could be pursued in future studies to investigate the possibility of isolating additional solid forms of OXCBZ, including, but not limited to, cooling crystallisation/anti-solvent addition /solvent vapour diffusion (Morissette et al., 2004; Newman, 2013), crystallisation from supercritical fluids (Chakravarty et al., 2019), subjection to high pressure (Neumann et al., 2015), and vapour deposition (Arlin et al., 2011; Srirambhatla et al., 2016; Case et al., 2018) onto non-metallic substrates such as organic crystals, glass and polymers.

In the vapour deposition studies that were pursued for OXCBZ under atmospheric conditions using a heating plate setup, preliminary experimental evidence for a novel anhydrous form was obtained when form I was sublimed onto silver foil substrates using a temperature of 130°C. XRPD analysis indicated close similarity between the deposited material isolated from the silver substrates and a predicted, triclinic structure from the CSP landscape of OXCBZ. Unfortunately, the small size of the crystals observed for this proposed new form and limited quality of the XRPD measurements derived experimentally precluded full structural characterisation. Three-dimensional electron diffraction (3D-ED) has emerged in recent years as a promising complementary tool to XRD for elucidating the structure of powder samples comprising multiple crystalline phases and organic micron-sized crystals that are unsuitable for single-crystal X-ray diffraction (Yu et al., 2012; Yun et al., 2015; Li et al., 2017). Employing 3D-ED as an analytical tool for structure determination purposes has been explored in the context of pharmaceuticals (van Genderen et al., 2016; Das et al., 2018) and could assist in overcoming the characterisation limitations encountered in this work by determining the definitive crystal structure of the blocky OXCBZ crystals grown by deposition onto silver foil and confirming whether they truly correspond to a novel anhydrous form.

Vapour deposition studies performed for OXCBZ under high-vacuum conditions failed to crystallise form III. This observation was attributed to the significant differences observed between the experimental parameters used for deposition of OXCBZ under atmospheric conditions and the parameters used in the high vacuum experiments, namely the substrate temperature and distance between the substrates and the starting material that was deposited onto them. The effect of substrate temperature (Firsich, 1984; Karpinska et al., 2013; Lin et al., 2016) and deposition distance (Solomos et al., 2018) can be investigated further by utilising an experimental setup capable of accommodating substrates at elevated temperature, similar to the heating plate used in atmospheric vapour deposition studies in this work, and varying the height separating the substrate and starting material more readily to allow for a range of distances to be studied, including the 1 cm distance on the heating plate setup.

The fast evaporation experiments performed for OXCBZ yielded solvated samples with chloroform and 2,2,2-trifluoroethanol (TFE) which appeared to correspond to previously unreported crystal structures of OXCBZ. However, the size and quality of the crystals obtained experimentally prevented full structural characterisation for these solvated phases. Experimental work should be pursued in the future to target further characterisation of the chloroform and TFE solvates and gain additional insight into their physicochemical properties, including crystallisation experiments under slower experimental conditions to target the growth of more suitable single crystals for structure determination.

Whilst OXCBZ form III was found to exhibit enhanced dissolution rate over the commercially available form I, the oral biovailability profile of form III was not investigated. In the future, the bioavailability properties of OXCBZ III should be explored to estabilish whether this metastable form can enhance the effectiveness of pharmaceutical formulations comprising OXCBZ (Censi and Di Martino, 2015).

7.2 Investigation of the Emergence of Twisted Crystals in Oxcarbazepine

7.2.1 Conclusions

OXCBZ form III crystals exhibiting twisted morphologies were observed in both physical vapour deposition and solution-based crystallisation experiments. Scanning electron microscopy (SEM) and atomic force microscopy (AFM) were utilised to obtain insight into the formation of the vapour-grown crystals of OXCBZ III, which could best be described as polycrystalline fibres rather than single crystals. SEM analysis showed that the vapour-grown crystals arose following aggregation of nano-sized, amorphous droplets emerging on the experimental substrates employed. Twisted crystals emerging from the droplets were noted and found to arrange in columns, in addition to a number of nanocrystals which did not exhibit twisting. Twisted polycrystalline fibres comprising multiple single crystals wrapped around one another were formed spontaneously. The formation of these fibres was attributed to the interplay between the elastic energy associated with twisting and the attractive forces resulting from aggregation of columns of crystals (Turner et al., 2003), with a decrease in surface area and free energy due to aggregation providing the driving force for twisting. Calculation of the diagonal compression and shear components of elastic constants confirmed that the crystal structure of OXCBZ form III is susceptible to spontaneous twisting.

Further analysis of the twisted OXCBZ III crystals prepared from the vapour using time-of-flight secondary ion mass spectrometry (ToF-SIMS) indicated that the layer of OXCBZ material around the crystals was depleted, presumably due to diffusion of the deposited material across the surface of the growing crystals. All of the experimental evidence obtained suggested that twisted form III crystallises through a non-classical, multi-step nucleation mechanism bearing similarity to examples noted in protein crystallisation studies (Vekilov, 2004), crystallisation of biominerals (Jin et al., 2018), and solution crystallisation investigations of organic (Warzecha et al., 2017) and inorganic materials (Wallace et al., 2013; Nielsen et al., 2014). The vapour-grown crystals were found to exhibit variable pitch along their respective lengths and an increase in pitch was correlated with an increase in length, indicating renormalisation (Haddad et al., 2019) of twisted OXCBZ III. No correlation was identified between the

pitch and the cross-section size of the crystals, which was generally uniform along their respective lengths. DSC and HPLC-MS analysis provided evidence for the presence of an impurity in OXCBZ starting powders that were used to yield twisted OXCBZ III crystals from the vapour phase. HPLC-MS data allowed the impurity to be identified as dibenzazepinodione (DBZ), a pharmacopeial impurity of OXCBZ (Faudone et al., 2019). The amount of DBZ present in the OXCBZ powders was found to increase upon prolonged vapour deposition experiments, hinting towards thermal degradation of OXCBZ. The incorporation of DBZ molecules into the crystal structure of OXCBZ III can be used to rationalise (Punin and Shtukenberg, 2008) the renormalisation observed for the twisted form III crystals grown from the vapour although direct experimental evidence to confirm this remains elusive.

The CSP landscape of OXCBZ was utilised in an effort to rationalise the formation of twisted crystals for OXCBZ III grown from solution, based on the observation of multiple closely related predicted structures which were originally treated as candidates for the experimental structure of this form. The abundance of closely similar crystal packings in these structures, constructed with virtually identical channels, can be used to rationalise the difficulty in obtaining suitable crystals of form III for subsequent characterisation with single-crystal XRD. There is likely to be disorder in the packing of the channels, leading to problems in radial crystal growth which ultimately limit the thickness of the OXCBZ III crystals. In appropriate experimental conditions, this could lead to the emergence of twisted morphology. A simple “attached channel” mechanism for the growth of crystals exhibiting this type of morphology was proposed and compared with another possible mechanism (“growth error/incommensurate”). Whilst these mechanisms can account for the occurrence of solution-grown OXCBZ III crystals exhibiting twisting, and are also applicable to the vapour-grown crystals of form III studied in this work, it is anticipated that the emergence of twisted morphology is likely influenced at least in part due to solvent-solute interactions affecting interfacial free energy and subsequently the growth of different facets on the surface of the OXCBZ III crystals (Hartman and Bennema, 1980).

The investigations described in this chapter additionally provided evidence for the emergence of crystals with twisted morphology for CBZ form I and bent morphology for CYT I and II crystals, prepared by performing physical vapour deposition experiments using experimental conditions similar to the ones that gave rise to the

twisted OXCBZ III crystals. No crystal twisting was observed for solution-grown CBZ form II and CYT form I which are both isostructural to OXCBZ III and crystallise in . This observation, coupled with the outcomes of the vapour deposition experiments carried out using CBZ and CYT, suggests tha the twisted morphology and growth mechanism observed for OXCBZ III is unique amongst these isostructural structures in the CBZ family of compounds. Calculation of the diagonal compression and shear components of OXCBZ III, CBZ II and CYT I confirmed that OXCBZ III is more prone to exhibiting spontaneous twisting than CBZ II and CYT I.

7.2.2 Future Work

With regards to future work pertaining to twisted OXCBZ III crystals, characterisation techniques such as microfocus XRD (Shtukenberg et al., 2011) and microbeam small-angle X-ray scattering (Nozue et al., 2003) could be employed experimentally for accurately quantifying the twists observed in the twisted crystals that were derived experimentally and correlating that information with the impact of impurity presence on the emergence of twisted morphology. Whilst the presence of DBZ was identified in OXCBZ powders giving rise to vapour-grown twisted OXCBZ III, the exact role that this impurity plays in the emergence of the vapour-grown crystals remains poorly understood. Incorporating DBZ willingly into the crystallisation of form III from the vapour phase by varying its concentration and characterising the resulting crystals to identify differences in their twisting behaviours could provide greater clarity with regards to how impurities influence the twisted morphology of OXCBZ III. Characterisation using 3D-ED (Yu et al., 2012; Yun et al., 2015; van Genderen et al., 2016; Li et al., 2017; Das et al., 2018) could potentially assist in determining the structure and configuration of the twisted OXCBZ III crystals grown from solution and the vapour phase at different points along the length of each crystal, identifying potential disorder within the crystals and/or confirming the presence of chemical or physical impurities. The use of 3D-ED may allow differences in the cell parameters of the twisted crystals to be identified and confirm whether the crystals comprise more than one of the predicted CSP structures sharing structural similarity with the experimental structure of form III. This would provide experimental data that would allow the theoretical models presented in this work for rationalising the growth of solution-grown form III to be verified or disproved. Analysis using 3D-ED could

additionally shed greater insight into the nature of the amorphous droplets giving rise to twisted OXCBZ III and help identify traces of nanocrystallinity within the droplets, further informing the growth mechanism and structural evolution of the twisted structures over the course of the vapour deposition process.

Pharmaceutical crystals capable of twisting have been found to exhibit remarkable plasticity and tabletability properties, making them potential candidates for overcoming compression problems associated with the manufacturing process of pharmaceutical formulations (Hu et al., 2019). The twisted OXCBZ III crystals could be investigated further in an effort to examine whether they have preferable compression properties for formulation purposes compared to non-deformed crystals of the thermodynamically stable form I.

7.3 Solid-State Screening Investigations of Evacetrapib and a Tetrazole Analogue

7.3.1 Conclusions

Extensive solid-state screening and characterisation investigations were pursued in an attempt to investigate solid-form diversity in EVC and a closely related tetrazole analogue (TAEVC) that had never been characterised and subjected to solid-form screening studies previously. Both solvent-based and solvent-free crystallisation approaches were explored in an effort to maximise the likelihood of crystallising all possible solid forms of the two compounds.

Characterisation of EVC and TAEVC samples derived from experimental screening revealed the high propensity of both compounds to form solvated materials and the majority of solvents explored in the screen yielded samples that appeared to be linked isostructurally. The solid-form landscape of EVC was expanded through the identification of several novel solvated/hydrated salt cocrystals which all exhibited isostructurality, including a hemi TBA – hemihydrate structure that was fully characterised and found to comprise a different packing arrangement and molecular conformation relative to the anhydrous form I. The screening studies pursued for TAEVC enabled an initial landscape of solid forms to be identified for this novel compound, comprising solvated and anhydrous forms for both the racemic and the enantiomerically pure forms of TAEVC that were utilised as starting materials. Crystal

structure analysis revealed that TAEVC is capable of forming a highly robust network of two-dimensional (2D) hydrogen bonds in the solid state. The aforementioned 2D network was found to be present in 8 out 9 structures that could be fully characterised for TAEVC, including both enantiomeric and racemic ones.

7.3.2 Future Work

Limitations pertaining to the size and overall quality of the single crystals that were prepared prevented comprehensive structural characterisation from being pursued for all solid forms of EVC and TAEVC that were identified in this work. Characterising these forms further in the future, particularly with regards to their crystal structure, could provide further insight into the propensity of both EVC and TAEVC to readily form multi-component solids. The CSP landscape of EVC indicates that there are thermodynamically feasible anhydrous forms that have not been realised experimentally. Whilst a broad range of crystallisation methodologies were unsuccessfully employed in screening studies to try and isolate some of those forms, approaches such as compression under high pressure were not pursued. Subjecting the solvated forms of EVC and TAEVC isolated in this work to high pressure could potentially result in structural transformations and the emergence of novel solid forms for both compounds (Neumann et al., 2015). Templating experiments utilising the various solvated forms of TAEVC that were successfully characterised as seeds could be pursued as a route towards more novel forms of EVC. Spectroscopic investigations involving techniques such as Raman, Fourier-transform infrared and proton nuclear magnetic resonance spectroscopy (Spitaleri et al., 2004; Kulkarni et al., 2012) may be utilised in the future to investigate the molecular association process for TAEVC in solution and rationalise its ability to form a robust 2D hydrogen-bonding network in the solid state.

References

1. Aaltonen, J., Allesø, M., Mirza, S., Koradia, V., Gordon, K.C. and Rantanen, J. (2009). Solid form screening – A review. *Eur. J. Pharm. Biopharm.*, **71**, 23-37.
2. Abràmoff, M.D., Magalhães, P. J. and Ram, S.J. (2004). Image Processing with ImageJ. *Biophotonics Int.*, **11**, 36-42.
3. Abramov, Y.A. (2013). Current Computational Approaches to Support Pharmaceutical Solid Form Selection. *Org. Process Res. Dev.*, **17**, 472-485.
4. Agranat, I., Wainschtein, S.R. and Zusman, E.Z. (2012). The predicated demise of racemic new molecular entities is an exaggeration. *Nat. Rev. Drug Discov.*, **11**, 972-973.
5. Agrawal, S.G. and Paterson, A.H.J. (2015). Secondary Nucleation: Mechanisms and Models. *Chem. Eng. Commun.*, **202**, 698-706.
6. Aguiar, A.J. and Zelmer, J.E. (1969). Dissolution behavior of polymorphs of chloramphenicol palmitate and mefenamic acid. *J. Pharm. Sci.*, **58**, 983-987.
7. Aitipamula, S., Banerjee, R., Bansal, A. K., Biradha, K., Cheney, M. L., Choudhury, A. R., Desiraju, G. R., Dikundwar, A. G., Dubey, R., Duggirala, N.; Ghogale, P. P., Ghosh, S., Goswami, P. K., Goud, N. R., Jetti, R. R. K. R., Karpinski, P., Kaushik, P., Kumar, D., Kumar, V., Moulton, B., Mukherjee, A., Mukherjee, G., Myerson, A. S., Puri, V., Ramanan, A., Rajamannar, T., Reddy, C. M., Rodríguez-Hornedo, N., Rogers, R. D., Row, T. N. G., Sanphui, P., Shan, N., Shete, G., Singh, A., Sun, C. C., Swift, J. A., Thaimattam, R., Thakur, T. S., Kumar Thaper, R., Thomas, S. P., Tothadi, S., Vangala, V. R., Variankaval, N., Vishweshwar, P., Weyna, D. R. and Zaworotko, M. J. (2012). Polymorphs, Salts, and Cocrystals: What's in a Name? *Cryst. Growth Des.*, **12**, 2147-2152.
8. Aitipamula, S., Chow, P.S. and Tan, R.B.H. (2011). Conformational Polymorphs of a Muscle Relaxant, Metaxalone. *Cryst. Growth Des.*, **11**, 4101-4109.
9. Akao, K., Okubo, Y., Inoue, Y. and Sakurai, M. (2002). Supercritical CO_2 fluid extraction of crystal water from trehalose dihydrate. Efficient production of form II (T_α) phase. *Carbohydr. Res.*, **337**, 1729-1735.
10. Alander, E.M. and Rasmuson, A.C. (2007). Agglomeration and adhesion free energy of paracetamol crystals in organic solvents. *AIChE J.*, **53**, 2590-2605.

11. Alatalo, H.M., Hatakka, H., Louhi-Kultanen, M., Kohonen, J. and Reinikainen, S.P. (2010). Closed-Loop Control of Reactive Crystallization. Part I: Supersaturation-Controlled Crystallization of L-Glutamic Acid. *Chem. Eng. Technol.*, **33**, 743-750.
12. Allesø, M., van den Berg, F., Cornett, C., Jørgensen, F. S., Halling-Sørensen, B., de Diego, H. L. and Rantanen, J. (2008). Solvent diversity in polymorph screening. *J. Pharm. Sci.*, **97**, 2145-2159.
13. Altomare, A., Cascarano, G., Giacovazzo, C., Guargliardi, A., Burla, M., Polidori, G. and Camalli, M. (1994). *SIR*92 – a program for automatic solution of crystal structures by direct methods. *J. Appl. Cryst.*, **27**, 435.
14. Alvarez, A.J. and Myerson, A.S. (2010). Continuous Plug Flow Crystallization of Pharmaceutical Compounds. *Cryst. Growth Des.*, **10**, 2219-2228.
15. Amidon, G.L., Lennernäs, H., Shah, V.P. and Crison, J.R. (1995). A Theoretical Basis for a Biopharmaceutic Drug Classification: The Correlation of in Vitro Drug Product Dissolution and in Vivo Bioavailability. *Pharm. Res.*, **12**, 413-420.
16. Andereck, C.D., Liu, S.S. and Swinney, H.L. (1986). Flow regimes in a circular Couette system with independently rotating cylinders. *J. Fluid Mech.,* **164**, 155-183.
17. Anderson, V. J. and Lekkerkerker., H. N. W. (2002). Insight into phase transition kinetics from colloid science. *Nature*, **416**, 811-815.
18. Anderton, C. (2007). A valuable technique for polymorph screening. *Am. Pharmaceut. Rev.*, **10**, 34-40.
19. Ardrey, R.E. (2003). Liquid chromatography-mass spectrometry: an introduction. Wiley, New York.
20. Arlin, J. B., Price, L. S., Price, S. L. and Florence, A. J. (2011). A strategy for producing predicted polymorphs: catemeric carbamazepine form V. *Chem. Commun.*, **47**, 7074-7076.
21. Aronhime J, Dolitzky B-H, Berkovich Y, Garth N. US7183272. Crystal forms of oxcarbazepine and processes for their preparation. (published on February 27, 2007).
22. Arora, K. K., Thakral, S. and Suryanarayanan, R. (2013). Instability in Theophylline and Carbamazepine Hydrate Tablets: Cocrystal Formation Due to Release of Lattice Water. *Pharm. Res.*, **7**, 1779-1789.

23. Artusio, F. and Pisano, R. (2018). Surface-induced crystallization of pharmaceuticals and biopharmaceuticals: A review. *Int. J. Pharm.*, **547**, 190-208.
24. Asanithi, P. (2014). Surface Porosity and Roughness of Micrographite Film for Nucleation of Hydroxyapatite. *J. Biomed. Mater. Res. Part A*, **102**, 2590-2599.
25. Askin, A., Cockcroft, J.K., Price, L.S., Goncalves, A., Zhao, M., Tocher, D.A., Williams, G.R., Gaisford, S. and Craig, D.Q.M. (2019). Olanzapine form IV: discovery of a new polymorphic form enabled by computed crystal energy landscapes. *Cryst. Growth Des.*, **19**, 2751-2757.
26. Auer, S. F. and Frenkel, D. (2001). Prediction of absolute crystal-nucleation rate in hard-sphere colloids. *Nature***, 409***,* 1020-1023.
27. Ayciriex, S., Touboul, D., Brunelle, A. and Laprévote, O. (2011). Time-of-flight secondary ion mass spectrometer: a novel tool for lipid imaging. *Clin. Lipidol*., **6**, 437-445.
28. Baias, M., Dumez, J.-N., Svensson, P.H., Schantz, S., Day, G.M. and Emsley, L. (2013). *De Novo* Determination of the Crystal Structure of a Large Drug Molecule by Crystal Structure Prediction-Based Powder NMR Crystallography. *J. Am. Chem. Soc.*, **135**, 17501-17507.
29. Balz, M., Therese, H.A., Li, J., Gutmann, J.S., Kappl, M., Nasdala, L., Hofmeister, W., Butt, H.-J. and Tremel, W. (2005). Crystallization of Vaterite Nanowires by the Cooperative Interaction of Tailor-Made Nucleation Surfaces and Polyelectrolytes. *Adv. Funct. Mater.*, **15**, 683-688.
30. Barrett, P. and Glennon, B. (2002). Characterizing the Metastable Zone Width and Solubility Curve Using Lasentec FBRM and PVM. *Chem. Eng. Res. Des.*, **80**, 799-805.
31. Bates, S., Zografi, G., Engers, D., Morris, K., Crowley, K. and Newman, A. (2006). Analysis of Amorphous and Nanocrystalline Solids from Their X-Ray Diffraction Patterns. *Pharm. Res.*, **23**, 2333-2349.
32. Bauer, J., Spanton, S., Henry R., Quick, J., Dziki, W., Porter, W. and Morris, J. (2001). Ritonavir: An Extraordinary Example of Conformational Polymorphism. *Pharm. Res.*, **18**, 859-866.

33. Baxendale, I.R., Braatz, R.D., Hodnett, B.K., Jensen, K.F., Johnson, M.D., Sharratt, P., Sherlock, J.-P. and Florence, A.J. (2015). Achieving Continuous Manufacturing: Technologies and Approaches for Synthesis, Workup, and Isolation of Drug Substance May 20–21, 2014 Continuous Manufacturing Symposium. *J. Pharm. Sci.*, **104**, 781-791.
34. Beck, R., Häkkinen, A., Malthe-Sørenssen, D. and Andreassen, J.P. (2009). The effect of crystallization conditions, crystal morphology and size on pressure filtration of L-glutamic acid and an aromatic amine. *Sep. Purif. Technol.*, **66**, 549-558.
35. Becker, R. and Döring, W. (1935). Kinetische Behandlung der Keimbildung in übersättigten Dämpfen. *Ann. Phys.***, 416**, 719-752.
36. Beckmann, W. (2013). Mechanisms of Crystallization. In: *Crystallization Basic Concepts and Industrial Applications*. *ed. W. Beckmann*. pp. 7-34. Wiley-VCH, Weinheim.
37. Beckmann, W., Otto, W. and Budde, U. (2001). Crystallisation of the Stable Polymorph of Hydroxytriendione: Seeding Process and Effects of Purity. *Org. Proc. Res. Dev.*, **5**, 387-392.
38. Beiner, M., Rengarajan, G.T., Pankaj, S., Enke, D. and Steinhart, M. (2007). Manipulating the Crystalline State of Pharmaceuticals by Nanoconfinement. *Nano Lett.*, **7**, 1381-1385.
39. Beloborodova, A.A., Minkov, V.S., Rychkov, D.A., Rybalova, T.V. and Boldyreva, E.V. (2017). First Evidence of Polymorphism in Furosemide Solvates. *Cryst. Growth Des.*, **17**, 2333-2341.
40. Benvenuti, E., Gentili, D., Chiarella, F., Portone, A., Barra, M., Cecchini, M., Cappuccino, C., Zambianchi, M., Lopez, S.G., Salzillo, T., Venuti, E., Cassinese, A., Pisignano, D., Persano, L., Cavallini, M., Maini, L., Melucci, M., Muccini, M. and Toffanin, S. (2018). Tuning polymorphism in 2,3-thienoimide capped oligothiophene based field-effect transistors by implementing vacuum and solution deposition methods. *J. Mater. Chem. C*, **6**, 5601-5608.
41. Berge, S.M., Bighley, L.D. and Monkhouse, D.C. (1977). Pharmaceutical Salts. *J. Pharm. Sci.*, **66**, 1-19.
42. Bernardo, A. and Giulietti, M. (2010). Modeling of crystal growth and nucleation rates for pentaerythritol batch crystallization. *Chem. Eng. Res. Des.*, **88**, 1356-1364.

43. Bernauer, F. (1929). “Gedrillte” Kristalle. Gebrüder Borntraeger, Berlin.
44. Bernstein, J. (2002). Fundamentals. In: *Polymorphism in Molecular Crystals.* pp 28-64. Oxford University Press, Oxford.
45. Bernstein, J., Davey, R.J. and Henck, J.-O. (1999). Concomitant Polymorphs. *Angew. Chem. Int. Ed*., **38**, 3440-3461.
46. Bhardwaj, R. M., McMahon, J.A., Nyman, J., Price, L.S., Konar, S., Oswald, I.D.H, Pulham, C.R., Price, S.L. and Reutzel-Edens, S.M. (2019). A Prolific Solvate Former, Galunisertib, under the Pressure of Crystal Structure Prediction, Produces Ten Diverse Polymorphs. *J. Am. Chem. Soc.*, **141**, 13887-13897.
47. Bhardwaj, R.M., Price, L.S., Price, S.L., Reutzel-Edens, S.M., Miller, G.J., Oswald, I.D.H., Johnston, B.F. and Florence, A.J. (2013). Exploring the Experimental and Computed Crystal Energy Landscape of Olanzapine. *Cryst. Growth Des.*, **13**, 1602-1617.
48. Bhat, M.N. and Dharmaprakash, S.M. (2002). Effect of solvents on the growth morphology and physical characteristics of nonlinear optical γ-glycine crystals. *J. Cryst. Growth.*, **242**, 245-252.
49. Bhogala, B.R., Basavoju, S. and Nangia, A. (2005). Tape and layer structures in cocrystals of some di- and tricarboxylic acids with 4,4′-bipyridines and isonicotinamide. From binary to ternary cocrystals. *CrystEngComm*, **7**, 551-562.
50. Bingham, A.L., Hughes, D.S., Hursthouse, M.B., Lancaster, R.W., Tavener, S. and Threlfall, T.L. (2001). Over one hundred solvates of sulfathiazole. *Chem. Commun.*, **2001**, 603-604.
51. Black, J.F.B., Cruz-Cabeza, A.J., Davey, R.J., Willacy, R.D. and Yeoh, A. (2018). The kinetic story of tailor-made additives in polymorphic systems: new data and molecular insights for p-aminobenzoic acid. *Cryst. Growth Des.*, **18**, 7518-7525.
52. Black, S. and Muller, F. (2010). On the Effect of Temperature on Aqueous Solubility of Organic Solids. *Org. Process Res. Dev.*, **14**, 661-665.
53. Blagden, N. and Davey, R.J. (2003). Polymorph Selection: Challenges for the Future? *Cryst. Growth Des.*, **3**, 873-885.
54. Blaser, H.-U. (2013). Chirality and its implications for the pharmaceutical industry. *Rend. Fis. Acc. Lincei*, **24**, 213-216.

55. Bolla, G. and Myerson, A.S. (2018a). SURMOF induced polymorphism and crystal morphological engineering of acetaminophen polymorphs: advantage of heterogeneous nucleation. *CrystEngComm*, **20**, 2084-2088.
56. Bolla, G. and Myerson, A.S. (2018b). SURMOF induced morphological crystal engineering of the substituted bezamides. *Cryst. Growth Des.*, **18**, 7048-7058.
57. Bonafede, S.J. and Ward, M.D. (1995). Selective Nucleation and Growth of an Organic Polymorph by Ledge-Directed Epitaxy on a Molecular Crystal Substrate. *J. Am. Chem. Soc.*, **117**, 7853-7861.
58. Bond, A.D. (2016). Single-Crystal X-ray Diffraction. In: *Analytical Techniques in the Pharmaceutical Sciences. eds. A. Müllertz, Y. Perrie, T. Rades.* pp. 315-338. Springer-Verlag, New York.
59. Bosetti, L. and Mazzotti, M. (2020). Population Balance Modeling of Growth and Secondary Nucleation by Attrition and Ripening. *Cryst. Growth Des.*, **20**, 307–319.
60. Botsaris, G.D. (1976). Secondary Nucleation – A Review. In: *Industrial Crystallization.* pp. 3-22. Springer, New York.
61. Boultif, A. and Louër, D. (1991) Indexing of powder diffraction patterns for low-symmetry lattices by the successive dichotomy method. *J. Appl. Cryst.*, **24**, 987-993.
62. Boultif, A. and Louër, D. (2004). Powder pattern indexing with the dichotomy method. *J. Appl. Cryst.*, **37**, 724-731.
63. Braga, D., Grepioni, F., Chelazzi, L., Nanna, S., Rubini, K., Curzi, M., Giaffreda, S.L., Saxell, H.E., Bratz, M. and Chiodo, T. (2014). Bentazon: Effect of Additives on the Crystallization of Pure and Mixed Polymorphic Forms of a Commercial Herbicide. *Cryst. Growth Des.*, **14**, 5729-5736.
64. Bragg, W.L. (1934). The Crystalline State: Volume I. The Macmillan Company, New York.
65. Brandel, C., Amharar, Y., Rollinger, J.M., Griesser, U.J., Cartigny, Y., Petit, S. and Coquerel, G. (2013). Impact of Molecular Flexibility on Double Polymorphism, Solid Solutions and Chiral Discrimination during Crystallization of Diprophylline Enantiomers. *Mol. Pharmaceutics*, **10**, 3850-3861.
66. Brandel, C., Petit, S., Cartigny, Y. and Coquerel, G. (2016). Structural Aspects of Solid Solutions of Enantiomers. *Curr. Pharm. Des.*, **22**, 4929-4941.

67. Braun, D.E., Gelbrich, T. and Griesser, U.J. (2019). Experimental and computational approaches to produce and characterise isostructural solvates. *CrystEngComm*, **21**, 5533-5545.
68. Braun, D.E., Gelbrich, T., Kahlenberg, V. and Griesser, U.J. (2015). Solid state forms of 4-aminoquinaldine – from void structures with and without solvent inclusion to close packing. *CrystEngComm*, **17**, 2504-2516.
69. Braun, D.E., Gelbrich, T., Kahlenberg, V., Tessadri, R., Wieser, J. and Griesser, U.J. (2009). Stability of Solvates and Packing Systematics of Nine Crystal Forms of the Antipsychotic Drug Aripiprazole. *Cryst. Growth Des.*, **9**, 1054-1065.
70. Braun, D.E., Gelbrich, T., Wurst, K. and Griesser, U.J. (2016b). Computational and Experimental Characterization of Five Crystal Forms of Thymine: Packing Polymorphism, Polytypism/Disorder, and Stoichiometric 0.8-Hydrate. *Cryst. Growth Des.*, **16**, 3480-3496.
71. Braun, D.E. and Griesser, U.J. (2018). Supramolecular Organization of Nonstoichiometric Drug Hydrates: Dapsone. *Front Chem.*, **6**, 31.
72. Braun, D.E., Kahlenberg, V., Gelbrich, T., Ludescher, J. and Griesser, U.J. (2008). Solid state characterisation of four solvates of R-cinacalcet hydrochloride. *CrystEngComm*, **10**, 1617-1625.
73. Braun, D.E., Karamertzanis, P.G., Arlin, J.-B., Florence, A.J., Kahlenberg, V., Tocher, D.A., Griesser, U.J. and Price, S.L. (2011). Solid-State Forms of β-Resorcylic Acid: How Exhaustive Should a Polymorph Screen Be? *Cryst. Growth Des.*, **11**, 210-220.
74. Braun, D.E., Koztecki, L.H., McMahon, J.A., Price, S.L. and Reutzel-Edens, S.-M. (2015). Navigating the Waters of Unconventional Crystalline Hydrates. *Mol. Pharmaceutics*, **12**, 3069-3088.
75. Braun, D.E., Lingireddy, S.R., Beidelschies, M.D., Guo, R., Müller, P., Price, S.L. and Reutzel-Edens, S.M. (2017). Unraveling Complexity in the Solid Form Screening of a Pharmaceutical Salt: Why so Many Forms? Why so Few? *Cryst. Growth Des.*, **17**, 5349-5365.
76. Braun, D.E., McMahon, J.A., Koztecki, L.H., Price, S.L. and Reutzel-Edens, S.M. (2014a). Contrasting Polymorphism of Related Small Molecule Drugs Correlated and Guided by the Computed Crystal Energy Landscape. *Cryst. Growth Des.*, **14**, 2056-2072.

77. Braun, D.E., Nartowski, K.P., Khimyak, Y.Z., Morris, K.R., Byrn, S.R. and Griesser, U.J. (2016c). Structural Properties, Order–Disorder Phenomena, and Phase Stability of Orotic Acid Crystal Forms. *Mol. Pharmaceutics*, **13**, 1012-1029.
78. Braun, D.E., Oberacher, H., Arnhard, K., Orlova, M. and Griesser, U.J. (2016a). 4-Aminoquinaldine monohydrate polymorphism: prediction and impurity aided discovery of a difficult to access stable form. *CrystEngComm*, **18**, 4053-4067.
79. Braun, D.E., Orlova, M. and Griesser, U.J. (2014b). Creatine: Polymorphs Predicted and Found. *Cryst. Growth Des.*, **14**, 4895-4900.
80. Braun, D.E., Tocher, D.A., Price, S.L. and Griesser, U.J. (2012). The Complexity of Hydration of Phloroglucinol: A Comprehensive Structural and Thermodynamic Characterization. *J. Phys. Chem. B*, **116**, 3961-3972.
81. Bredikhin, A.A., Bredikhina, Z.A., Kurenkov, A.V. and Gubaidullin, A.T. (2017). Synthesis, crystal structure, and absolute configuration of the enantiomers of chiral drug xibenolol hydrochloride. *Tetrahedron: Asymmetry*, **28**, 1359-1366.
82. Breuer, M., Ditrich, K., Habicher, T., Hauer, B., Keßeler, M., Stürmer, R. and Zelinski, T. (2004). Industrial Methods for the Production of Optically Active Intermediates. *Angew. Chem. Int. Ed.*, **43**, 788-824.
83. Brewster, M.E., Anderson, W.R., Estes, K.S. and Bodor, N. (1991). Development of Aqueous Parenteral Formulations for Carbamazepine through the Use of Modified Cyclodextrins. *J. Pharm. Sci.*, **80**, 380-383.
84. Brittain, H.G. (2012). Polymorphism and Solvatomorphism 2010. *J. Pharm. Sci.*, **101**, 464-484.
85. Brooks, W.H., Guida, W.C. and Daniel, K.G. (2011). The Significance of Chirality in Drug Design and Development. *Curr. Top. Med. Chem.*, **11**, 760-770.
86. Brown, M.E. (2001). Purity Determination Using DSC. In: *Introduction to Thermal Analysis, Techniques and Applications, Second Edition*. pp 215-227. Kluwer Academic Publishers, Dordrecht.

87. Brown, C.J., McGlone, T., Yerdelen, S., Srirambhatla, V., Mabbott, F., Gurung, R., Briuglia, M.L., Ahmed, B., Polyzois, H., McGinty, J., Perciballi, F., Fysikopoulos, D., MacFhionnghaile, P., Siddique, H., Raval, V., Harrington, T.S., Vassileiou, A.D., Robertson, M., Prasad, E., Johnston, A., Johnston, B., Nordon, A., Srai, J.S., Halbert, G., ter Horst, J.H., Price, C.J., Rielly, C.D., Sefcik, J. and Florence, A.J. (2018). Enabling precision manufacturing of active pharmaceutical ingredients: workflow for seeded cooling continuous crystallisations. *Mol. Syst. Des. Eng.*, **3**, 518-549.
88. Brun, G.W., Martín, Á., Cassel, A., Vargas, R.M.F. and Cocero, M.J. (2012). Crystallization of Caffeine by Supercritical Antisolvent (SAS) Process: Analysis of Process Parameters and Control of Polymorphism. *Cryst. Growth Des.*, **12**, 1943-1951.
89. Brunsteiner, M., Jones, A.G., Pratola, F., Price, S.L. and Simons, S.J.R. (2005). Toward a Molecular Understanding of Crystal Agglomeration. *Cryst. Growth Des.*, **5**, 3-16.
90. Bučar, D.-K., Day, G.M., Halasz, I., Zhang, G.G.Z., Sander, J.R.G., Reid, D.G., MacGillivray, L.R., Duer, M.J. and Jones, W. (2013). The curious case of (caffeine)·(benzoic acid): how heteronuclear seeding allowed the formation of an elusive cocrystal. *Chem. Sci.*, **4**, 4417-4425.
91. Bunjes, H. and Kuntsche, J. (2016). Light and Electron Microscopy. In: *Analytical Techniques in the Pharmaceutical Sciences. eds. A. Müllertz, Y. Perrie, T. Rades.* pp. 363-388. Springer-Verlag, New York.
92. Burcham, C.L., Florence, A.J. and Johnson, M.D. (2018). Continuous Manufacturing in Pharmaceutical Process Development and Manufacturing. *Annu. Rev. Chem. Biomol. Eng.*, **9**, 253-281.
93. Burger, A. and Ramberger, R. (1979a). On the polymorphism of pharmaceuticals and other molecular crystals, I. *Microchim. Acta*, **72**, 259-271.
94. Burger, A. and Ramberger, R. (1979b). On the polymorphism of pharmaceuticals and other molecular crystals, II. *Microchim. Acta*, **72**, 273-316.
95. Burger, A., Rollinger, J. M. and Brüggeller, P. (1997). Binary System of (R)- and (S)-Nitrendipine-Polymorphism and Structure. *J. Pharm. Sci.*, **86**, 674-679.

96. Burnett, D.J., Thielmann, F. and Sokoloski, T.D. (2007). Investigating Carbamazepine-Acetone Solvate Formation via Dynamic Gravimetric Vapor Sorption. *J. Therm. Anal. Calorim.*, **89**, 693-698.
97. Burton, W. K., Cabrera, N. and Frank, F. C. (1951). The Growth of Crystals and the Equilibrium Structure of Their Surfaces. *Philos. Trans. R. Soc. A Math. Phys. Eng. Sci.*, **243**, 299-358.
98. Byrn, S., Futran, M., Thomas, H., Jayjock, E., Maron, N., Meyer, R.F., Myerson, A.S., Thien, M.P. and Trout, B.L. (2015). Achieving Continuous Manufacturing for Final Dosage Formation: Challenges and How to Meet Them May 20–21 2014 Continuous Manufacturing Symposium. *J. Pharm. Sci.*, **104**, 792-802.
99. Byrn, S., Pfeiffer, R., Ganey, M., Hoiberg, C. and Poochikian, G. (1995). Pharmaceutical Solids: A Strategic Approach to Regulatory Considerations. *Pharm. Res.*, **12**, 945-954.
100. Cahn, R.S., Ingold C.K. and Prelog V. (1956). The specification of asymmetric configuration in organic chemistry. *Experientia*, **12**, 81-124.
101. Campeta, A.M., Chekal, B.P., Abramov, Y.A., Meenan, P.A., Henson, M.J., Shi, B., Singer, R.A. and Horspool, K.R. (2010). Development of a Targeted Polymorph Screening Approach for a Complex Polymorphic and Highly Solvating API. *J. Pharm. Sci.*, **99**, 3874-3886.
102. Cao, G., Beyer, T.P., Zhang, Y., Schmidt, R.J., Chen, Y. Q., Cockerham, S.L., Zimmerman, K.M., Karathanasis, S.K., Cannady, E.A., Fields, T. and Mantlo, N.B. (2011). Evacetrapib is a novel, potent, and selective inhibitor of cholesteryl ester transfer protein that elevates HDL cholesterol without inducing aldosterone or increasing blood pressure. *J. Lipid Res.*, **52**, 2169-2176.
103. Capacci-Daniel, C., Gaskell, K.J. and Swift, J.A. (2010). Nucleation and Growth of Metastable Polymorphs on Siloxane Monolayer Templates. *Cryst. Growth Des.*, **10**, 952-962.
104. Carlson, E.D., Cong, P., Chandler Jr., W.H., Chau, H.K., Crevier, T., Desrosiers, P.J., Doolen, R.D., Freitag, C., Hall, L.A., Kudla, T., Luo, R., Masui, C., Rogers, J., Song, L., Tangkilisan, A., Ung, K.Q. and Wu, L. (2003). An integrated high throughput workflow for pre-formulations: polymorph and salt selection studies. *PharmaChem.*, **2**, 10-15.

105. Case, D.H., Srirambhatla, V.K., Guo, R., Watson, R.E., Price, L.S, Polyzois, H., Cockcroft, J.K., Florence, A.J., Tocher, D.A. and Price, S.L. (2018). Successful Computationally Directed Templating of Metastable Pharmaceutical Polymorphs. *Cryst. Growth Des.*, **18**, 5322-5331.
106. Censi, R. and di Martino, P. (2015). Polymorph Impact on the Bioavailability and Stability of Poorly Soluble Drugs. *Molecules*, **20**, 18759-18776.
107. Censi, R., Rascioni, R. and di Martino, P. (2015). Changes in the solid state of anhydrous and hydrated forms of sodium naproxen under different grinding and environmental conditions: Evidence of the formation of new hydrated forms. *Eur. J. Pharm. Biopharm.*, **92**, 192-203.
108. Chadha, R., Arora, P., Saini, A. and Jain, D.S. (2010). Solvated Crystalline Forms of Nevirapine: Thermoanalytical and Spectroscopic Studies. *AAPS PharmSciTech*, **11**, 1328-1339.
109. Chadha, R., Kuhad, A., Arora, P. and Kishor, S. (2012a). Characterisation and evaluation of pharmaceutical solvates of Atorvastatin calcium by thermoanalytical and spectroscopic studies. *Chem. Cent. J.*, **6**, 114.
110. Chadha, R., Saini, A., Jain, D.S. and Venugopalan, P. (2012b). Preparation and Solid-State Characterization of Three Novel Multicomponent Solid Forms of Oxcarbazepine: Improvement in Solubility through Saccharin Cocrystal. *Cryst. Growth Des.*, **12**, 4211-4224.
111. Chadwick, K., Myerson, A. and Trout, B. (2011). Polymorphic control by heterogeneous nucleation - A new method for selecting crystalline substrates. *CrystEngComm*, **13**, 6625-6627.
112. Chakravarty, P., Famili, A., Nagapudi, K. and Al-Sayah, M.A. (2019). Using Supercritical Fluid Technology as a Green Alternative During the Preparation of Drug Delivery Systems. *Pharmaceutics*, **11**, 629.
113. Chang, Y.L., West, M.A., Fowler, F.W. and Lauher, J.W. (1993). An approach to the design of molecular solids. Strategies for controlling the assembly of molecules into two-dimensional layered structures. *J. Am. Chem. Soc.*, **115**, 5991-6000.
114. Chen, J., Sarma, B., Evans, J.M.B. and Myerson, A.S. (2011). Pharmaceutical Crystallization. *Cryst. Growth. Des.*, **11**, 887-895.

115. Chen, J., Wang. J., Ulrich, J., Yin, Q. and Xue, L. (2008). Effect of Solvent on the Crystal Structure and Habit of Hydrocortisone**.** *Cryst. Growth Des.*, **8**, 1490-1494.

116. Chew, J.W., Black, S.N., Chow, P.S. and Tan, R.B.H. (2007). Comparison between Open-Loop Temperature Control and Closed-Loop Supersaturation Control for Cooling Crystallization of Glycine. *Ind. Eng. Chem. Res.*, **46**, 830-838.

117. Chianese, A., Di Berardino, F. and Jones, A.G. (1993). On the effect of secondary nucleation on the crystal size distribution from a seeded batch crystallizer. *Chem. Eng. Sci.*, **48**, 551-560.

118. Childs, S.L., Rodríguez-Hornedo, N., Reddy, L.S., Jayasankar, A., Maheshwari, C., McCausland, L., Shipplett, R. and Stahly, B.C. (2008). Screening strategies based on solubility and solution composition generate pharmaceutically acceptable cocrystals of carbamazepine. *CrystEngComm*, **10**, 856-864.

119. Childs, S.L., Wood, P.A., Rodríguez-Hornedo, N., Reddy, L.S. and Hardcastle, K.I. (2009). Analysis of 50 Crystal Structures Containing Carbamazepine Using the Materials Module of Mercury CSD. *Cryst. Growth Des.*, **9**, 1869-1888.

120. Choi, H., Choi, H., Inoue, M. and Sengoku, R. (2017). Control of the Polymorphism of Calcium Carbonate Produced by Self-Healing in the Cracked Part of Cementitious Materials. *Appl. Sci.*, **7**, 546.

121. Chow, E. H. H., Bučar, D.-K. and Jones, W. (2012). New opportunities in crystal engineering - the role of atomic force microscopy in studies of molecular crystals. *Chem. Commun.*, **48**, 9210-9226.

122. Chow, K., Tong, H.H.Y., Lum, S. and Chow, A.H.I. (2008). Engineering of pharmaceutical materials: an industrial perspective. *J. Pharm. Sci.*, **97**, 2855-2877.

123. Clarke, H. D., Arora, K. K., Bass, H., Kavuru, P., Ong, T. T., Pujari, T.; Wojtas, L. and Zaworotko, M. J. (2010). Structure−Stability Relationships in Cocrystal Hydrates: Does the Promiscuity of Water Make Crystalline Hydrates the Nemesis of Crystal Engineering? *Cryst. Growth Des.*, **10**, 2152-2167.

124. Clegg, W. (1998). Crystal Structure Determination. Oxford University Press Inc., New York.

125. Coelho, A.A. (2003). Indexing of powder diffraction patterns by iterative use of singular value decomposition. *J. Appl. Cryst.*, **36**, 86-95.
126. Coelho, A.A. (2018). *TOPAS* and *TOPAS-Academic*: an optimization program integrating computer algebra and crystallographic objects written in C++. *J. Appl. Cryst.*, **51**, 210-218.
127. Commins, P., Karothu, D.P. and Naumov, P. (2019). Is a Bent Crystal Still a Single Crystal? *Angew. Chem. Int. Ed.*, **58**, 10052-10060.
128. Connelly, J.C., Hasegawa, R., McArdle, J.V. and Tucker, M.L. (1997). ICH Guideline Residual Solvents. *Pharmeuropa*, **Suppl 9**, 57.
129. Craig, D.Q.M. (2006). Characterization of Polymorphic Systems Using Thermal Analysis. In: *Polymorphism in the Pharmaceutical Industry. ed. R. Hilfiker*. pp. 43-79. Wiley-VCH Verlag GmbH & Co. KGaA, Weinheim.
130. Cross, W.I., Blagden, N., Davey, R.J., Pritchard, R.G., Neumann, M.A., Roberts, R.J. and Rowe, R.C. (2002). A Whole Output Strategy for Polymorph Screening: Combining Crystal Structure Prediction, Graph Set Analysis, and Targeted Crystallization Experiments in the Case of Diflunisal. *Cryst. Growth Des.*, **3**, 151-158.
131. Crowley, K.J. and Zografi, G. (2002). Cryogenic grinding of indomethacin polymorphs and solvates: assessment of amorphous phase formation and amorphous phase physical stability. *J. Pharm. Sci.*, **91**, 492-507.
132. Cruz-Cabeza, A. J. and Bernstein, J. (2014). Conformational polymorphism. *Chem. Rev.***, 114**, 2170-2191.
133. Cruz-Cabeza, A.J., Day, G.M., Motherwell, W.D.S. and Jones, W. (2006). Prediction and Observation of Isostructurality Induced by Solvent Incorporation in Multicomponent Crystals. *J. Am. Chem. Soc.*, **128**, 14466-14467.
134. Cruz-Cabeza, A.J., Day, G.M., Motherwell, W.D.S. and Jones, W. (2007a). Importance of Molecular Shape for the Overall Stability of Hydrogen Bond Motifs in the Crystal Structures of Various Carbamazepine-Type Drug Molecules. *Cryst. Growth. Des.*, **7**, 100-107.
135. Cruz-Cabeza, A.J., Day, G.M., Motherwell, W.D.S. and Jones, W. (2007b). Solvent inclusion in form II carbamazepine. *Chem. Commun.*, **0**, 1600-1602.
136. Cruz-Cabeza, A.J., Reutzel-Edens, S.M. and Bernstein, J. (2015). Facts and fictions about polymorphism. *Chem. Soc. Rev.*, **44**, 8619-8635.

137. Cui, X., Rohl, A.L., Shtukenberg, A. and Kahr, B. (2013). Twisted Aspirin Crystals. *J. Am. Chem. Soc.*, **135**, 3395-3398

138. Cwikel, D., Zhao, Q., Liu, C., Su, X. and Marmur, A. (2010). Comparing Contact Angle Measurements and Surface Tension Assessments of Solid Surfaces. *Langmuir*, **26**, 15289-15294.

139. Dai, X.-L., Chen, J.-M. and Lu, T.-B. (2018). Pharmaceutical cocrystallization: an effective approach to modulate the physicochemical properties of solid-state drugs. *CrystEngComm*, **20**, 5292-5316.

140. Danesh, A., Davies, M.C., Roberts, C.J., Sanders, G.H.W., Tendler, S.J.B., Williams, P.M. and Wilkins, M.J. (2000). Polymorphic Discrimination Using Atomic Force Microscopy: Distinguishing between Two Polymorphs of the Drug Cimetidine. *Langmuir*, **16**, 866-870.

141. David, W.I.F. and Shankland, K. (2008). Structure determination from powder diffraction data. *Acta Cryst. A*, **64**, 52-64.

142. David, W.I.F., Shankland, K., van de Streek, J., Pidcock, E., Motherwell, W.D.S. and Cole, J.C. (2006). *DASH*: a program for crystal structure determination from powder diffraction data. *J. Appl. Cryst.*, **39**, 910-915.

143. Davis, M.A., Winthrop, S.O., Thomas, R.A., Herr, F., Charest, M.-P. and Gaudry, R. (1964). Anticonvulsants. I. Dibenzo[a,d]cycloheptadiene-5-carboxamide and Related Compounds. *J. Med. Chem.*, **7**, 88-94.

144. Das, P.P., Mugnaioli, E., Nicolopoulos, S., Tossi, C., Gemmi, M., Galanis, A., Borodi, G. and Pop, M.M. (2018). Crystal Structures of Two Important Pharmaceuticals Solved by 3D Precession Electron Diffraction Tomography. *Org. Process Res. Dev.*, **22**, 1365-1372.

145. Davey, R.J., Schroeder, S.L.M. and ter Horst, J.H. (2013). Nucleation of Organic Crystals—A Molecular Perspective. *Angew. Chem. Int. Ed.*, **52**, 2166-2179.

146. Day, G. M. (2011). Current Approaches to Predicting Molecular Organic Crystal Structures. *Crystallogr. Rev.*, **17**, 3-52.

147. Day, G.M., Price, S.L. and Leslie, M. (2001). Elastic Constant Calculations for Molecular Organic Crystals. *Cryst. Growth Des.*, **1**, 13-27.

148. De Chiffre, L., Hansen, H.N. and Kofod, N. (1999). Surface Topography Characterization Using an Atomic Force Microscope Mounted on a Coordinate Measuring Machine. *CIRP Ann. Manuf. Technol.*, **48**, 463-466.

149. de Gennes, P.G. (1985). Wetting: statics and dynamics. *Rev. Mod. Phys.*, **57**, 827.

150. De Villiers, M. M., van der Watt, J. G. and Lötter, A. P. (1992). Kinetic study of the solid-state photolytic degradation of two polymorphic forms of furosemide. *Int. J. Pharm.*, **88**, 275-283.

151. De Yoreo, J.J., Gilbert, P.U.P.A., Sommerdijk, N.A.J.M., Penn, R.L., Whitelam, S., Joester, D., Zhang, H., Rimer, J.D., Navrotsky, A., Banfield, J.F., Wallace, A.F., Michel, F.M., Meldrum, F.C., Cölfen, H. and Dove, P.M. (2015). Crystallization by particle attachment in synthetic, biogenic, and geologic environments. *Science*, **349**, 498.

152. Deem, M.W. and Newsam, J.M. (1989). Determination of 4-connected framework crystal structures by simulated annealing. *Nature*, **342**, 260-262.

153. Delmas, T., Shah, U.V., Roberts, M.M., Williams, D.R. and Heng, J.Y.Y. (2013). Crystallisation of the orthorhombic form of acetaminophen: Combined effect of surface topography and chemistry. *Powder Technol.*, **236**, 24-29.

154. Di Profio, G., Fontananova, E., Curcio, E. and Drioli, E. (2012). From Tailored Supports to Controlled Nucleation: Exploring Material Chemistry, Surface Nanostructure, and Wetting Regime Effects in Heterogeneous Nucleation of Organic Molecules. *Cryst. Growth Des*., **12**, 3749-3757.

155. Diao, Y., Harada, T., Myerson, A.S., Hatton, T.A., and Trout, B.L. (2011a). The role of nanopore shape in surface-induced crystallization. *Nat. Mater.*, **10**, 867-871.

156. Diao, Y., Myerson, A.S., Hatton, T.A. and Trout, B.L. (2011b). Surface Design for Controlled Crystallization: The Role of Surface Chemistry and Nanoscale Pores in Heterogeneous Nucleation*. Langmuir*, **27**, 5324-5334.

157. Diao, Y., Whaley, K.E., Helgeson, M.E., Woldeyes, M.A., Doyle, P.S., Myerson, A.S., Hatton, T.A. and Trout, B.L. (2012). Gel-Induced Selective Crystallization of Polymorphs. *J. Am. Chem. Soc.*, **134**, 673-684.

158. Docherty, R., Clydesdale, G., Roberts, K.J. and Bennema, P. (1991). Application of Bravais-Friedel-Donnay-Harker, attachment energy and Ising models to predicting and understanding the morphology of molecular crystals. *J. Phys. D: Appl. Phys.*, **24**, 89-99.

159. Dressler, D. H. and Mastai, Y. (2007). Controlling Polymorphism by Crystallization on Self-Assembled Multilayers. *Cryst. Growth Des.*, **7**, 847-850.

160. Dudognon, E., Danède, F., Descamps, M. and Correia, N. T. (2008). Evidence for a New Crystalline Phase of Racemic Ibuprofen. *Pharm. Res.*, **25**, 2853-2858.
161. Dupouey, J., Doudka, N., Belo, S., Blin, O. and Guilhaumou, R. (2016). Simultaneous determination of four antiepileptic drugs in human plasma samples using an ultra-high-performance liquid chromatography tandem mass spectrometry method and its application in therapeutic drug monitoring. *Biomed Chromatogr.*, **30**, 2053-2060.
162. Ehmann, H.M.A. and Werzer, O. (2014). Surface Mediated Structures: Stabilization of Metastable Polymorphs on the Example of Paracetamol. *Cryst. Growth Des.*, **14**, 3680-3684.
163. El-Arini, S.K., Giron, D. and Leuenberger, H. (1998). Solubility Properties of Racemic Praziquantel and Its Enantiomers. *Pharma. Dev. Technol.*, **3**, 557-564.
164. El Hassan, N., Ikni, A., Gillet, J.-M., Spasojevic-de Biré, A. and Ghermani, N.E. (2013). Electron Properties of Carbamazepine Drug in Form III. *Cryst. Growth Des.*, **13**, 2887-2896.
165. Elder, D.P., Holm, R. and de Diego, H.L. (2013). Use of pharmaceutical salts and cocrystals to address the issue of poor solubility. *Int. J. Pharm.*, **453**, 88-100.
166. Eli Lilly and Company. (2018 – 2020). Personal Communications.
167. Eliel, E.L., Wilen, S.H. and Mander, L.N. (1994). Glossary. In: *Stereochemistry of Organic Compounds.* pp 1191. John Wiley & Sons, New York.
168. Elliott, S.R. (2001). The Structure of Amorphous Materials. In: *Properties and Applications of Amorphous Materials. eds. M.F. Thorpe, L. Tichý.* pp. 1-11. Springer, Dordrecht.
169. Elqidra, R., Ünlü, N., Çapan, Y., Sahin, G., Dalkara, T. and Hincal, A.A. (2004). Effect of polymorphism on *in vitro-in vivo* properties of carbamazepine conventional tablets. *J. Drug Del. Sci. Tech.*, **14**, 147-153.
170. Erdemir, D., Lee, A.Y. and Myerson, A.S. (2009). Nucleation of Crystals from Solution: Classical and Two-Step Models. *Acc. Chem. Res.*, **42**, 621-629.
171. Etter M. C. (1990). Encoding and decoding hydrogen-bond patterns of organic compounds. *Acc. Chem. Res.*, **23**, 120-126.

172. Eyvazian, V.A. and Frishman, W.H. (2017). Evacetrapib: Another CETP Inhibitor for Dyslipidemia With No Clinical Benefit. *Cardiol Rev.*, **25**, 43-52.

173. Fabbiani, F.P.A., Byrne, L.T., McKinnon, J.J. and Spackman, M.A. (2007). Solvent inclusion in the structural voids of form II carbamazepine: single-crystal X-ray diffraction, NMR spectroscopy and Hirshfeld surface analysis. *CrystEngComm*, **9**, 728-731.

174. Faigl, F., Fogassy, E., Nógrádi, M, Pálovics, E. and Schindler, J. (2010). Separation of non-racemic mixtures of enantiomers: an essential part of optical resolution. *Org. Biomol. Chem.*, **8**, 947-959.

175. Fang, L., Feng, L., Huixian, G., Chao, C., Bo, L., Yu, W. and Huajun, L. (2015). Comparison and Analysis of Twist Pitch Length Test Methods for ITER Nb_3Sn and NbTi Strands. *Rare Metal Mat. Eng.*, **44**, 2095-2099.

176. Faudone, S.N., Paschoal, A.R., Carvalho Jr., P.S., Ellena, J., Terra Martins, F., Cuffini, S.L., Ayala, A.P. and Sperandeo, N.R. (2019). X-ray diffraction, vibrational and thermal study of dibenzazepinodione, a pharmacopeial impurity of oxcarbazepine. *J. Mol. Struct.*, **1182**, 204-212.

177. Ferguson, S., Ortner, F., Quon, J., Peeva, L., Livingston, A., Trout, B.L. and Myerson, A.S. (2014). Use of Continuous MSMPR Crystallization with Integrated Nanofiltration Membrane Recycle for Enhanced Yield and Purity in API Crystallization. *Cryst. Growth Des.*, **14**, 617-627.

178. Fernandes, P., Shankland, K., Florence, A.J., Shankland, N. and Johnston, A. (2007). Solving molecular crystal structures from X-ray powder diffraction data: The challenges posed by γ-carbamazepine and chlorothiazide *N*,*N*,-dimethylformamide (1/2) solvate. *J. Pharm. Sci.*, **96**, 1192-1202.

179. Firsich, D.W. (1984). Energetic materials separations and specific polymorph preparations via thermal gradient sublimation. *J. Hazard. Mater.*, **9**, 133-137.

180. Flack, H.D. (1983). On enantiomorph-polarity estimation. *Acta Cryst. A*, **39**, 876-881.

181. Flack, H. D. (2003). Chiral and Achiral Crystal Structures. *Helv. Chim. Acta*, **86**, 905-921.

182. Flack, H.D. and Bernardinelli, G. (1999). Absolute structure and absolute configuration. *Acta Cryst. A*, **55**, 908-915.

183. Flack, H.D. and Bernardinelli, G. (2000). Reporting and evaluating absolute-structure and absolute-configuration determinations. *J. Appl. Cryst.*, **33**, 1143-1148.

184. Flack, H.D. and Bernardinelli, G. (2008). The use of X-ray crystallography to determine absolute configuration. *Chirality*, **20**, 681-690.

185. Fleischman, S.G., Kuduva, S.S., McMahon, J.A., Moulton, B., Bailey Walsh, R.D., Rodríguez-Hornedo, N. and Zaworotko, M.J. (2003). Crystal Engineering of the Composition of Pharmaceutical Phases: Multiple-Component Crystalline Solids Involving Carbamazepine. *Cryst. Growth Des.*, **3**, 909-919.

186. Florence, A.J. (2009). The Solid State. In: *Modern Pharmaceutics Volume 1 Basic Principles and Systems. eds. A.T. Florence, A.T, J. Siepmann.* pp 253-310. CRC Press, Boca Raton.

187. Florence, A.J., Bedford, C.T., Fabbiani, F.P.A., Shankland, K., Gelbrich, T., Hursthouse, M.B., Shankland, N., Johnston, A. and Fernandes, P. (2008a). Two-dimensional similarity between forms I and II of cytenamide, a carbamazepine analogue. *CrystEngComm*, **10**, 811-813.

188. Florence, A.J., Johnston, A., Price, S.L., Nowell, H., Kennedy, A.R. and Shankland, N. (2006). An Automated Parallel Crystallisation Search for Predicted Crystal Structures and Packing Motifs of Carbamazepine. *J. Pharm. Sci.*, **95**, 1918-1930.

189. Florence, A.J., Shankland, K., Gelbrich, T., Hursthouse, M.B., Shankland, N., Johnston, A., Fernandes, P. and Leech, C.K. (2008b). A catemer-to-dimer structural transformation in cyheptamide. *CrystEngComm*, **10**, 26-28.

190. Florence, A.J., Shankland, N., Shankland, K., David, W.I.F., Pidcock, E., Xu, X., Johnston, A., Kennedy, A.R., Cox, P.J., Evans, J.S.O., Steele, G., Cosgrove, S.D. and Frampton, C.S. (2005). Solving molecular crystal structures from laboratory X-ray powder diffraction data with DASH: the state of the art and challenges. *J. Appl. Cryst.*, **38**, 249-259.

191. Foster, J.A., Damodaran, K.K., Maurin, A., Day, G.M., Thompson, H.P.G., Cameron, G.J., Bernal, J.C. and Steed, J.W. (2017). Pharmaceutical polymorph control in a drug-mimetic supramolecular gel. *Chem. Sci.*, **8**, 78-84.

192. Fours, B., Cartigny, Y., Petit, S. and Coquerel, G. (2015). Formation of new polymorphs without any nucleation step. Desolvation of the rimonabant monohydrate: directional crystallisation concomitant to smooth dehydration. *Faraday Discuss.*, **179**, 475-488.
193. Frank, D.S. and Matzger, A.J. (2017). Influence of Chemical Functionality on the Rate of Polymer-Induced Heteronucleation. *Cryst. Growth Des.*, **17**, 4056-4059.
194. Fu, Q.T., Liu, E.J., Wilson, P. and Chen, Z. (2015). Ice Nucleation Behaviour on Sol-gel Coatings with Different Surface Energy and Roughness. *Phys. Chem. Chem. Phys.*, **17**, 21492-21500.
195. Galcera, J., Friščić, T., Molins, E. and Jones, W. (2013). Isostructurality in three-component crystals achieved by the combination of persistent hydrogen bonding motifs and solvent inclusion. *CrystEngComm*, **15**, 1332-1338.
196. Garabedian, H. and Strickland-Constable, R.F. (1972). Collision breeding of crystal nuclei: Sodium chlorate. I. *J. Cryst. Growth*, **13-14**, 506-509.
197. Gavezzotti, A. (2005). Quantitative Ranking of Crystal Packing Modes by Systematic Calculations on Potential Energies and Vibrational Amplitudes of Molecular Dimers. *J. Chem. Theory Comput.*, **1**, 834-840.
198. Gebauer, D., Kellermeier, M., Gale, J.D., Bergström, L. and Cölfen, H. (2014). Pre-nucleation clusters as solute precursors in crystallisation. *Chem. Soc. Rev.*, **43**, 2348-2371.
199. Geng, H. and Wang, C. (2017). Efficacy and safety of oxcarbazepine in the treatment of children with epilepsy: a meta-analysis of randomized controlled trials. *Neuropsychiatr. Dis. Treat.*, **13**, 685-695.
200. Giron, D., Goldbronn, C., Mutz, M., Pfeffer, S. and Piechon, P. (2002). Solid State Characterizations of Pharmaceutical Hydrates. *J. Therm. Anal. Calorim.*, **68**, 453-465.
201. Giuffre, A. J., Hamm, L. M., Han, N., De Yoreo, J. J. and Dove, P. M. (2013). Polysaccharide chemistry regulates kinetics of calcite nucleation through competition of interfacial energies. *Proc. Natl. Acad. Sci.*, **110**, 9261-9266.
202. Glicksman, M.E. and Lupulescu, A.O. (2004). Dendritic crystal growth in pure materials. *J. Cryst. Growth*, **264**, 541-549.

203. Glusker, J.P., Lewis, M. and Rossi, M. (1994). Symmetry in Crystals and Their Diffraction Patterns. In: *Crystal Structure Analysis for Chemists and Biologists*. pp 105-142. Wiley-VCH, New York.

204. Gong, Y. U. T., Killian, C. E., Olson, I. C., Appathurai, N. P., Amasino, A. L., Martin, M. C., Holt, L. J., Wilt, F. H. and Gilbert, P. U. P. A. (2012). Phase Transitions in Biogenic Amorphous Calcium Carbonate. *Proc. Natl. Acad. Sci.* **109**, 6088-6093.

205. Good, R. J. and van Oss, C. J. (1992). The modern theory of contact angles and the hydrogen bond components of surface energies. In: *Modern approaches to wettability: Theory and applications*. pp 1-27. Springer, Boston.

206. Gordon, K.C. and Fraser-Miller, S.J. (2016). Raman Spectroscopy. In: *Analytical Techniques in the Pharmaceutical Sciences. eds. A. Müllertz, Y. Perrie, T. Rades.* pp. 139-170. Springer-Verlag, New York.

207. Grant, D.J.W. and York, P. (1986). Entropy of processing: a new quantity for comparing the solid state disorder of pharmaceutical materials. *Int. J. Pharm.*, **30**, 161-180.

208. Gratz, A. J., Hillner, P. E. and Hansma, P. K. (1993). Step Dynamics and Spiral Growth on 180 Calcite. *Geochim. Cosmochim. Acta*, **57**, 491-495.

209. Graubner, G., Rengarajan, G. T., Anders, N., Sonnenberger, N., Enke, D., Beiner, M. and Steinhart, M. (2013). Morphology of Porous Hosts Directs Preferred Polymorph Formation and Influences Kinetics of Solid/Solid Transitions of Confined Pharmaceuticals. *Cryst. Growth Des.*, **14**, 78-86.

210. Gravestock, T., Box, K., Comer, J., Frake, E., Judge, S. and Ruiz, R. (2011). The “GI dissolution” method: a low volume, *in vitro* apparatus for assessing the dissolution/precipitation behaviour of an active pharmaceutical ingredient under biorelevant conditions. *Anal. Methods*, **3**, 560-567.

211. Greco, K. and Bogner, R. (2012). Solution-mediated phase transformation: Significance during dissolution and implications for bioavailability. *J. Pharm. Sci.*, **101**, 2996-3018.

212. Green, F. M., Gilmore, I. S. and Seah, M. P. (2006). TOF-SIMS: accurate mass scale calibration. *J. Am. Soc. Mass Spectrom.*, **17**, 514-523.

213. Griesser, U.J. (2006). The Importance of Solvates. In: *Polymorphism in the Pharmaceutical Industry. ed. R. Hilfiker*. pp. 211-233. Wiley-VCH, Weinheim.

214. Grooff, D., De Villiers, M.M. and Liebenberg, W. (2007). Thermal methods for evaluating polymorphic transitions in nifedipine. *Thermochim. Acta*, **454**, 33-42.

215. Grothe, E., Meekes, H., Vlieg, E., ter Horst, J.H. and de Gelder, R., (2016). Solvates, Salts, and Cocrystals: A Proposal for a Feasible Classification System. *Cryst. Growth Des*, **16**, 3237-3243.

216. Grzesiak, A.L., Lang, M., Kim, K. and Matzger, A.J. (2003). Comparison of the Four Anhydrous Polymorphs of Carbamazepine and the Crystal Structure of Form I. *J. Pharm. Sci.*, **92**, 2260-2271.

217. Gu, C.-H., Li, H., Gandhi, R. B. and Raghavan, K. (2004). Grouping solvents by statistical analysis of solvent property parameters: implication to polymorph screening. *Int. J. Pharm.*, **283**, 117-125.

218. Gu, C.-H and Grant., D.J.W. (2003). Physical Properties and Crystal Structures of Chiral Drugs. In: *Stereochemical Aspects of Drug Action and Disposition. eds. M. Eichelbaum, B. Testa, A. Somogyi.* pp. 113-139. Springer-Verlag, Berlin.

219. Guillory, K. (1999). Generation of polymorphs, hydrates, solvates and amorphous solids. In: *Polymorphism in Pharmaceutical Solids. ed. H.G Brittain*. pp. 183-226. Marcel Dekker, New York.

220. Guo, Q. (2016). X-ray Diffraction from Polymers. In: *Polymer Morphology - Principles, Characterization, and Processing.* pp. 14-33. John Wiley and Sons Inc., Hoboken.

221. Ha, J.-M., Wolf, J.H., Hillmyer, M.A. and Ward, M.D. (2004). Polymorph Selectivity under Nanoscopic Confinement. *J. Am. Chem. Soc.*, **126**, 3382-3383.

222. Habermehl, S., Mörschel, P., Eisenbrandt, P., Hammer, S.M. and Schmidt, M.U. (2014). Structure determination from powder data without prior indexing, using a similarity measure based on cross-correlation functions. *Acta Cryst. B*, **70**, 347-359.

223. Habgood, M., Grau-Crespo, R. and Price, S.L. (2011). Substitutional and orientational disorder in organic crystals: a symmetry-adapted ensemble model. *Phys. Chem. Chem. Phys.*,**13**, 9590-9600.

224. Habraken, W.J.E,M, Tao, J., Brylka, L. J., Friedrich, H., Bertinetti, L., Schenk, A. S., Verch, A., Dmitrovic, V., Bomans, P.H.H., Frederik, P. M., Laven, J., van der Schoot, P., Aichmayer, B., de With, G., DeYoreo, J. J., and Sommerdijk, N.A.J.M (2013). Ion-association complexes unite classical and non-classical theories for the biomimetic nucleation of calcium phosphate. *Nat Commun,* **4**, 1507.

225. Haddad, A., Aharoni, H., Sharon, E., Shtukenberg, A.G., Kahr, B. and Efrati, E. (2019). Twist renormalization in molecular crystals driven by geometric frustration. *Soft Matter*, **15**, 116-126.

226. Hahn, T. (2002a). The 230 Space Groups. In: *International Tables for Crystallography, Volume A: Space Group Symmetry (5th ed.)*. *ed. T. Hahn*. pp. 111-719. Springer, Dordrecht.

227. Hahn, T. (2002b). Point Groups and Crystal Classes. In: *International Tables for Crystallography, Volume A: Space Group Symmetry (5th ed.)*. *ed. T. Hahn*. pp. 761-808. Springer, Dordrecht.

228. Haleblian, J. and McCrone, W. (1969). Pharmaceutical applications of polymorphism. *J. Pharm. Sci.*, **58**, 911-929.

229. Hamilton, B.D., Ha, J.-M., Hillmyer, M.A. and Ward, M.D. (2012). Manipulating Crystal Growth and Polymorphism by Confinement in Nanoscale Crystallization Chambers. *Acc. Chem. Res.*, **45**, 414-423.

230. Hamilton, B.D., Hillmyer, M.A. and Ward, M.D. (2008). Glycine Polymorphism in Nanoscale Crystallization Chambers. *Cryst. Growth Des.*, **8**, 3368-3375.

231. Hansen, S.H. (2016). HPLC/UHPLC. In: *Analytical Techniques in the Pharmaceutical Sciences. eds. A. Müllertz, Y. Perrie, T. Rades.* pp. 413-438. Springer-Verlag, New York.

232. Harris, R.K., Ghi, P.Y., Puschmann, H., Apperley, D.C., Griesser, U.J., Hammond, R.B., Ma, C., Roberts, K.J., Pearce, G.J., Yates, J.R. and Pickard, C.J. (2005). Structural Studies of the Polymorphs of Carbamazepine, Its Dihydrate, and Two Solvates. *Org. Process Res. Dev.*, **9**, 902-910.

233. Hartman, P. and Bennema, P. (1980). The attachment energy as a habit controlling factor: I. Theoretical considerations. *J. Cryst. Growth*, **49**, 145-156.

234. He, Y., Wang, B., Dukor, R.K. and Nafie, L.A. (2011). Determination of absolute configuration of chiral molecules using vibrational optical activity: a review. *Appl. Spectrosc.*, **65**, 699-723.

235. He, G., Wong, A.B.H., Chow, P.S. and Tan, R.B.H. (2011). Effects of the rate of supersaturation generation on polymorphic crystallization of *m*-hydroxybenzoic acid and *o*-aminobenzoic acid. *J. Cryst. Growth,* **314**, 220-226.

236. Healy, A.M., Worku, Z.A., Kumar, D. and Madi, A.M. (2017). Pharmaceutical solvates, hydrates and amorphous forms: A special emphasis on cocrystals. *Adv. Drug. Deliv. Rev.*, **117**, 25-46.

237. Hemenway, J.N., Jarho, P., Henri, J.T., Nair, S.K., VanderVelde, D., Georg, G.I. and Stella, V.J. (2010). Preparation and physicochemical characterization of a novel water-soluble prodrug of carbamazepine. *J. Pharm. Sci.*, **99**, 1810-1825.

238. Hempel, A., Camerman, N., Camerman, A. and Mastropaolo, D. (2005). Oxcarbazepine: Structure and anticonvulsant activity. *Acta Cryst*. *E*, **61**, 1313-1315.

239. Henry, D. Eby, E., Goodge, G. and Mogk, D. (2016). X-ray reflection in accordance with Bragg's Law. From https://serc.carleton.edu/research_education/geochemsheets/BraggsLaw.html.

240. Hermes, S., Schröder, F., Chelmowski, R., Wöll, C. and Fischer, R.A. (2005). Selective Nucleation and Growth of Metal−Organic Open Framework Thin Films on Patterned COOH/CF_3-Terminated Self-Assembled Monolayers on Au (111). *J. Am. Chem. Soc.*, **127**, 13744-13745.

241. Hiendrawan, S., Widjojokusumo, E., Veriansyah, B. and Tjandrawinata, R.R. (2017). Pharmaceutical Salts of Carvedilol: Polymorphism and Physicochemical Properties. *AAPS PharmSciTech*, **18**, 1417-1425.

242. Hilfiker, R. (2013a). Polymorphism of Crystalline Systems. In: *Crystallization: Basic Concepts and Industrial Applications*. *ed. W. Beckmann*. pp 85-103. Wiley-VCH Verlag GmbH & Co., Weinheim.

243. Hilfiker, R. (2013b). Characterisation of Crystalline Products. In: *Crystallization Basic Concepts and Industrial Applications. ed. W. Beckmann.* pp. 149-171. Wiley-VCHVerlag GmbH & Co., Weinheim.

244. Hilfiker, R., Blatter, F. and von Raumer, M. (2006). Relevance of solid-state properties for pharmaceutical products. In: *Polymorphism in the Pharmaceutical Industry*. pp 1-18. Wiley-VCH Verlag GmbH & Co., Weinheim.

245. Hiller, H. (1986). Crystallography and cohomology of groups. *Amer. Math. Monthly*, **93**, 765-779.
246. Hiremath, R., Basile, J. A., Varney, S. W. and Swift, J. A. (2005). Controlling molecular crystal polymorphism with self-assembled monolayer templates. *J. Am. Chem. Soc.*, **127**, 18321-18327.
247. Hiremath, R., Varney, S. W. and Swift, J. A. (2004). Oriented Crystal Growth of 4-Iodo-4'-nitrobiphenyl on Polar Self-Assembled Monolayer Templates: A Case for "Chemical Epitaxy". *Chem. Mater.*, **16**, 4948-4954.
248. Hofmann, D.W.M. (2002). Fast estimation of crystal densities. *Acta Cryst. B*, **58**, 489-493.
249. Hogan, S.E. and Buckton, G. (2001). The Application of Near Infrared Spectroscopy and Dynamic Vapor Sorption to Quantify Low Amorphous Contents of Crystalline Lactose. *Pharm. Res.*, **18**, 112-116.
250. Hollingsworth, M.D., Brown, M.E., Santarsiero, B. D., Huffman, J. C. and Goss, C.R. (1994). *Chem. Mater.*, **6**, 1227-1244.
251. Hook, J.R. and Hall, H.E. (1991). Crystal Structure. In: *Solid State Physics (2nd ed.)*. pp 1-32. John Wiley & Sons, Chichester.
252. Hosokawa, T., Datta, S., Sheth, A.R., Brooks, N.R., Young, V.G. and Grant, D.J.W. (2004). Isostructurality among Five Solvates of Phenylbutazone. *Cryst. Growth Des.*, **4**, 1195-1201.
253. Hu, S., Mishra, M.K. and Sun, C.C. (2019). Twistable Pharmaceutical Crystal Exhibiting Exceptional Plasticity and Tabletability. *Chem. Mater.*, **31**, 3818-3822.
254. Hu, Y.-B., Wolthers, M., Wolf-Gladrow, D.A. and Nehrke, G. (2015). Effect of pH and Phosphate on Calcium Carbonate Polymorphs Precipitated at near-Freezing Temperature. *Cryst. Growth Des.*, **15**, 1596-1601.
255. Hunter, C.A., McCabe, J.F. and Spitaleri, A. (2012). Solvent effects of the structures of prenucleation aggregates of carbamazepine. *CrystEngComm*, **14**, 7115.
256. Isakov, A.I., Kotelnikova, E.N., Kryuchkova, L.Y. and Lorenz, H. (2013). Effect of crystallization conditions on polymorphic diversity of malic acid *RS* — Racemate. *Trans. Tianjin Univ.*, **19**, 86-91.

257. Iski, E.V., Johnston, B.F., Florence, A.J., Urquhart, A.J. and Sykes, E.C.H. (2010). Surface-Mediated Two-Dimensional Growth of the Pharmaceutical Carbamazepine. *ACS Nano*, **4**, 5061-5068.
258. IUCr Online Dictionary of Crystallography, “Isostructural crystals”.
259. Iuraş, A., Scurr, D.J., Boissier, C., Nicholas, M.L., Roberts, C. J. and Alexander, M.R. (2016). Imaging of Crystalline and Amorphous Surface Regions Using Time-of-Flight Secondary-Ion Mass Spectrometry (ToF-SIMS): Application to Pharmaceutical Materials. *Anal. Chem.*, **88**, 3481-3487.
260. Jacques, J., Collet, A. and Wilen, S.H. (1981). Enantiomers, Racemates, and Resolutions. Wiley, New York.
261. Janssen, T. and Janner, A. (2014). Aperiodic crystals and superspace concepts. *Acta Cryst. B*, **70**, 617-651.
262. Jiang, Y., Kellermeier, M., Gebauer, D., Lu, Z., Rosenberg, R., Moise, A., Przybylski, M. and Cölfen, H. (2017). Growth of organic crystals via attachment and transformation of nanoscopic precursors. *Nat. Commun.*, **8**, 15933.
263. Jiang, Y. and Turner, K.T. (2016). Measurement of the strength and range of adhesion using atomic force microscopy. *Extreme Mech. Lett.*, **9**, 119-126.
264. Jin, W., Jiang, S., Pan, H. and Tang, R. (2018). Amorphous Phase Mediated Crystallization: Fundamentals of Biomineralization. *Crystal*s, **8**, 48.
265. Johnston, A., Bhardwaj-Miglani, R., Gurung, R., Vassileiou, A.D., Florence, A.J. and Johnston, B.F. (2017). Combined Chemoinformatics Approach to Solvent Library Design Using clusterSim and Multidimensional Scaling. *J. Chem. Inf. Model.*, **57**, 1807-1815.
266. Johnston, A., Florence, A.J., Fabbiani, F.J.A., Shankland, K. and Bedford, C.T. (2008a). Cytenamide acetic acid solvate. *Acta Cryst. E*, **64**, o1175-o1176.
267. Johnston, A., Florence, A.J., Fabbiani, F.J.A., Shankland, K. and Bedford, C.T. (2008b). Cytenamide–butyric acid (1/1). *Acta Cryst. E*, **64**, o1295-o1296.
268. Johnston, A., Florence, A.J., Fabbiani, F.J.A., Shankland, K. and Bedford, C.T. (2008c). Cytenamide–1,4-dioxane (2/1). *Acta Cryst. E*, **64**, o1345-o1346.
269. Johnston, A., Florence, A.J., Fabbiani, F.J.A., Shankland, K., Bedford, C.T. and Bardin, J. (2008d). Cytenamide trifluoroacetic acid solvate. *Acta Cryst. E*, **64**, o1215-o1216.

270. Johnston, A., Florence, A.J., Miller, G.J., Kennedy, A.R. and Bedford, C.T. (2008e). Cytenamide–formic acid (1/1). *Acta Cryst. E*, **64**, o1379-o1380.
271. Johnston, A., Johnston, B.F., Kennedy, A.R. and Florence, A.J. (2008f). Targeted crystallisation of novel carbamazepine solvates based on a retrospective Random Forest classification. *CrystEngComm*, **10**, 23-25.
272. Jones, A.O.F., Chattopadhyay, B., Geerts, Y.H. and Resel, R. (2016). Substrate-Induced and Thin-Film Phases: Polymorphism of Organic Materials on Surfaces. *Adv. Funct. Mater.*, **26**, 2233-2255.
273. Jones, H.P., Davey, R.J. and Cox, B.G. (2005). Crystallization of a Salt of a Weak Organic Acid and Base: Solubility Relations, Supersaturation Control and Polymorphic Behavior. *J. Phys. Chem. B*, **109**, 5273-5278.
274. Kabova, E.A., Cole, J.C., Korb, O., López-Ibáñez, M., Williams, A.C. and Shankland, K. (2017a). Improved performance of crystal structure solution from powder diffraction data through parameter tuning of a simulated annealing algorithm. *J. Appl. Cryst.*, **50**, 1411-1420.
275. Kabova, E.A., Cole, J.C., Korb, O., Williams, A.C. and Shankland, K. (2017b). Improved crystal structure solution from powder diffraction data by the use of conformational information. *J. Appl. Cryst.*, **50**, 1421-1427.
276. Kadam, S.S., Kulkarni, S.A., Ribera, R.C., Stankiewicz, A.I., ter Horst, J.H. and Kramer, H.J.M. (2012). A new view on the metastable zone width during cooling crystallization. *Chem. Eng. Sci.*, **72**, 10-19.
277. Kaemmerer, H., Lorenz, H., Black, S. N. and Seidel-Morgenstern, A. (2009). Study of System Thermodynamics and the Feasibility of Chiral Resolution of the Polymorphic System of Malic Acid Enantiomers and Its Partial Solid Solutions. *Cryst. Growth Des.*, **9**, 1851-1862.
278. Kahr, B., Tan, M., Ye, H.-M. and Shtukenberg, A.G. (2019). Polymorphism and Morphology Folklore. *Cryst. Growth Des.*, **19**, 5999-6003.
279. Kamali, N., Erxleben, A. and McArdle, P. (2016). Unexpected Effects of Catalytic Amounts of Additives on Crystallization from the Gas Phase: Depression of the Sublimation Temperature and Polymorph Control. *Cryst. Growth Des.*, **16**, 2492-2495.

280. Kamali, N., O'Malley, C., Mahon, M.F., Erxleben, A. and McArdle, P. (2018). Use of Sublimation Catalysis and Polycrystalline Powder Templates for Polymorph Control of Gas Phase Crystallization. *Cryst. Growth Des.*, **18**, 3510-3516.

281. Kaneniwa, N. and Otsuka, M. (1985). Effect of grinding on the transformation of polymorphs of chloramphenicol palmitate. *Chem. Pharm. Bull.*, **33**, 1660-1668.

282. Karimi-Jafari, M., Padrela, L., Walker, G.M. and Croker, D.M. (2018). Creating Cocrystals: A Review of Pharmaceutical Cocrystal Preparation Routes and Applications. *Cryst. Growth Des.*, **18**, 6370-6387.

283. Karmwar, P., Graeser, K., Gordon, K.C., Strachan, C.J. and Rades, T. (2011). Investigation of properties and recrystallisation behaviour of amorphous indomethacin samples prepared by different methods. *Int. J. Pharm.*, **417**, 94-100.

284. Karmwar, P., Graeser, K., Gordon, K.C., Strachan, C.J. and Rades, T. (2012). Effect of different preparation methods on the dissolution behaviour of amorphous indomethacin. *Eur. J. Pharm. Biopharm.*, **80**, 459-464.

285. Karpinska, J., Erxleben, A. and McArdle, P. (2011). 17β-Hydroxy-17α-methylandrostano[3,2-c]pyrazole, Stanozolol: The Crystal Structures of Polymorphs 1 and 2 and 10 Solvates. *Cryst. Growth Des.*, **11**, 2829-2838.

286. Karpinska, J., Erxleben, A. and McArdle, P. (2013). Applications of Low Temperature Gradient Sublimation in Vacuo: Rapid Production of High Quality Crystals. The First Solvent-Free Crystals of Ethinyl Estradiol. *Cryst. Growth Des.*, **13**, 1122-1130.

287. Karthika, S., Radhakrishnan, T,K. and Kalaichelvi, P. (2016). A Review of Classical and Nonclassical Nucleation Theories. *Cryst. Growth Des.*, **16**, 6663-6681.

288. Kempson, I.M. and Prestidge, C.A. (2016). Mass Spectrometry Imaging of Pharmaceuticals: From Tablets to Tissues. In: *Analytical Techniques in the Pharmaceutical Sciences. eds. A. Müllertz, Y. Perrie, T. Rades.* pp. 629-648. Springer-Verlag, New York.

289. Kendrick, J., Stephenson, G.A., Neumann, M.A. and Leusen, F.J.J. (2013). Crystal Structure Prediction of a Flexible Molecule of Pharmaceutical Interest with Unusual Polymorphic Behavior. *Cryst. Growth Des.*, **13**, 581-589.

290. Khoshkhoo, S. and Anwar, J. (1993). Crystallization of polymorphs: the effect of solvent. *J. Phys. D: Appl. Phys.*, **26**, B90.
291. Kirkpatrick, S., Gelatt, Jr., C.D. and Vecchi, M.P. (1983). Optimization by Simulated Annealing. *Science*, **220**, 671-680.
292. Kishi, Y. and Matsuoka, M. (2010). Phenomena and Kinetics of Solid-State Polymorphic Transition of Caffeine. *Cryst. Growth Des.*, **10**, 2916-2920.
293. Kitamura, M. (1989). Polymorphism in the crystallization of L-glutamic acid. *J. Cryst. Growth*, **96**, 541-546.
294. Kitamura, M. and Nakamura, K. (2002). Effects of solvent composition and temperature on polymorphism and crystallization behavior of thiazole-derivative. *J. Cryst. Growth*, **236**, 676-686.
295. Kitamura, M., Umeda, E. and Miki, K. (2012). Mechanism of Solvent Effect in Polymorphic Crystallization of BPT. *Ind. Eng. Chem. Res.*, **51**, 12814-12820.
296. Kobari, M., Kubota, N. and Hirasawa, I. (2010). Simulation of metastable zone width and induction time for a seeded aqueous solution of potassium sulfate. *J. Cryst. Growth*, **312**, 2734-2739.
297. Kubota, N. (2008). A new interpretation of metastable zone widths measured for unseeded solutions. *J. Cryst. Growth*, **310**, 629-634.
298. Kulkarni, S.A., Kadam, S.S., Meekes, H., Stankiewicz, A.I. and ter Horst, J.H. (2013). Crystal Nucleation Kinetics from Induction Times and Metastable Zone Widths. *Cryst. Growth. Des.*, **13**, 2435-2440.
299. Kulkarni, S.A., McGarrity, E.S., Meekes, H. and ter Horst, J.H. (2012). Isonicotinamide self-association: the link between solvent and polymorph nucleation. *Chem. Commun.*, **48**, 4983-4985.
300. Kuroda, R. (2008). Chirality in Crystals. In: *Engineering of Crystalline Materials Properties State of the Art in Modeling, Design and Applications. eds. J.J. Novoa*, *D. Braga, L. Addadi*. pp 251-270. Springer: New York.
301. Kwokal, A. and Roberts, K. J. (2014). Direction of the polymorphic form of entacapone using an electrochemical tuneable surface template. *CrystEngComm*, **16**, 3487-3493.
302. Lahav, M. and Leiserowitz, L. (2001). The effect of solvent on crystal growth and morphology. *Chem. Eng. Sci.*, **56**, 2245-2253.

303. Laibinis, P.E. and Whitesides, G. (1992). Self-Assembled Monolayers of n-Alkanethiolates on Copper Are Barrier Films That Protect the Metal against Oxidation by Air. *J. Am. Chem. Soc.*, **114**, 1990.

304. Lamprou, D. A., Smith, J. R., Nevell, T. G., Barbu, E., Willis, C. R. and Tsibouklis, J. (2010). Towards the Determination of Surface Energy at the Nanoscale: A Further Assessment of the AFM-Based Approach. *J. Adv. Microsc. Res.*, **5**, 137-142.

305. Lancaster, R.W., Harris, L.D. and Pearson, D. (2011). Fifty-year old samples of progesterone demonstrate the complex role of synthetic impurities in stabilizing a metastable polymorph. *CrystEngComm*, **13**, 1775-1777.

306. Landau, L.D., Akhiezer, A.I. and Lifshitz, E.M. (1967). CHAPTER VI - THE THEORY OF SYMMETRY. In: *General Physics – Mechanics and Molecular Physics*. pp 115-143. Pergamon Press, Oxford.

307. Lang, M., Grzesiak, A.L. and Matzger, A.J. (2002a). The Use of Polymer Heteronuclei for Crystalline Polymorph Selection. *J. Am. Chem. Soc.*, **124**, 14834-14835.

308. Lang, M., Kampf, J.W. and Matzger, A.J. (2002b). Form IV of Carbamazepine. *J. Pharm.Sci.*, **91**, 1186-1190.

309. Lawton, S., Steele, G., Shering, P., Laird, I., Zhao, L. and Ni, X. (2009). Continuous crystallisation of pharmaceuticals using a continuous oscillatory baffled crystalliser. *Org. Process Res. Dev.*, **13**, 1357-1363.

310. Lee, Y.L. and Maa, J.R. (1991). Nucleation and growth of condensate clusters on solid surfaces. *J. Mater. Sci.*, **26**, 6068-6072.

311. Lee, S.L., O'Connor, T.F., Yang, X., Cruz, C.N., Chatterjee, S., Madurawe, R.D., Moore, C.M.V., Yu, L.X. and Woodcock, J. (2015). Modernizing Pharmaceutical Manufacturing: from Batch to Continuous Production. *J. Pharm. Innov.*, **10**, 191-199.

312. Lee, S.L., Raw, A.S. and Yu, L. (2008). Dissolution Testing. In: *Biopharmaceutics Applications in Drug Development*. *eds. R. Krishna, L. Yu.* pp. 47-74. Springer-Verlag, Boston.

313. Lee, S.S., Tang, S.B., Smilgies, D.-M., Woll, A.R., Loth, M.A., Mativetsky, J.M., Anthony, J.E. and Loo, Y.-L. (2012). Guiding Crystallization around Bends and Sharp Corners. *Adv. Mater.*, **24**, 2692-2698.

314. Lehmann, O. (1888). Molecularphysik, Bd. 1, Verlag von Wilhelm Engelmann, Leipzig.
315. Leurs, U., Mistarz, U.H. and Rand, K.D. (2016). Applications of Mass Spectrometry in Drug Development Science. In: *Analytical Techniques in the Pharmaceutical Sciences. eds. A. Müllertz, Y. Perrie, T. Rades.* pp. 253-292. Springer-Verlag, New York.
316. Li, Y., Huang, M., Zang, L., Jacobs, D.L., Zhao, J., Zhu, Y. and Wang, C. (2018). Real-Time Atomic Scale Observation of Surface-Induced Crystallization of a Bismuth Nanodroplet by Stepwise Ordering Mechanism. *Cryst. Growth Des.*,**18**, 5808-5815.
317. Li, D., Nielsen, M. H., Lee, J. R. I., Frandsen, C., Banfield, J. F. and De Yoreo, J. J. (2012).Direction-Specific Interactions Control Crystal Growth by Oriented Attachment. *Science*, **336**, 1014-1018.
318. Li, J. and Sun, J. (2017). Application of X‑ray Diffraction and Electron Crystallography for Solving Complex Structure Problems. *Acc. Chem. Res.*, **50**, 2737-2745.
319. Li, X., Yu, G., Chen, X., He, L., Zhou, Z. and Ren, Z. (2019). Investigating solubilization effect of oxcarbazepine by forming cocrystals. *CrystEngComm*, **21**, 4718-4729.
320. Lide, D.R. (2005). RC Handbook of Chemistry and Physics 86th Edition 2005-2006. pp 6-138. CRC Press, Boca Raton.
321. Lin, K.-Y., Wang, Y.-J., Chen, K.-L., Yang, C.-C., Ho, C.-Y., Lee, K.-R., Shen, J.-L. and Chiu, K.-C. (2016). Rubrene polycrystalline films growth from vacuum deposition at various substrate temperatures. *J. Cryst. Growth*, **439**, 54-59.
322. Linol, J., Morelli, T., Petit, M.-N. and Coquerel, G. (2007). Inversion of the Relative Stability between Two Polymorphic Forms of (±) Modafinil under Dry High-Energy Milling: Comparisons with Results Obtained under Wet High-Energy Milling. *Cryst. Growth Des.*, **7**, 1608-1611.
323. Liu, J. and Rasmuson, Å. C. (2013). Influence of Agitation and Fluid Shear on Primary Nucleation in Solution. *Cryst. Growth Des.*, **13**, 4385-4394.

324. Liu, J., Svärd, M. and Rasmuson, Å. C. (2014). Influence of Agitation and Fluid Shear on Nucleation of *m*-Hydroxybenzoic Acid Polymorphs. *Cryst. Growth Des.*, **14**, 5521-5531.
325. Liu, J., Svärd, M. and Rasmuson, Å. C. (2015). Influence of Agitation on Primary Nucleation in Stirred Tank Crystallizers. *Cryst. Growth Des.*, **15**, 4177-4184.
326. Liu, W., Wei, H. and Black, S. (2009). An Investigation of the Transformation of Carbamazepine from Anhydrate to Hydrate Using in Situ FBRM and PVM. *Org. Process Res. Dev.*, **13**, 494-500.
327. Liu, J. and Wöll, C. (2017). Surface-supported metal–organic framework thin films: fabrication methods, applications, and challenges. *Chem. Soc. Rev.*, **46**, 5730-5770.
328. López-Mejías, V., Kampf, J.W. and Matzger, A.J. (2009). Polymer-induced heteronucleation of tolfenamic acid: structural investigation of a pentamorph. *J. Am. Chem. Soc.*, **131**, 4554-4555.
329. López-Mejías, V., Kampf, J.W. and Matzger, A.J. (2012). Nonamorphism in Flufenamic Acid and a New Record for a Polymorphic Compound with Solved Structures. *J. Am. Chem. Soc.*, **134**, 9872-9875.
330. López-Mejías, V., Knight, J.L., Brooks, C.L. and Matzger, A.J. (2011). On the Mechanism of Crystalline Polymorph Selection by Polymer Heteronuclei. *Langmuir*, **27**, 7575-7579.
331. López-Mejías, V., Myerson, A.S. and Trout, B.L. (2013). Geometric Design of Heterogeneous Nucleation Sites on Biocompatible Surfaces. *Cryst. Growth Des.*, **13**, 3835-3841.
332. Lorenz, H. and Seidel-Morgenstern, A. (2014). Processes To Separate Enantiomers. *Angew. Chem. Int. Ed.*, **53**, 1218-1250.
333. Love, C.J., Estroff, L.A., Kriebel., J.K., Nuzzo., R.G. and Whitesides, G.M. (2005). Self-Assembled Monolayers of Thiolates on Metals as a Form of Nanotechnology. *Chem. Rev.*, **105**, 1103-1169.
334. Lowry, M. (1964). Optical Rotatory Power. Dover Publications Inc., New York.
335. Lutker, K.M. and Matzger, A.J. (2010). Crystal Polymorphism in a Carbamazepine Derivative: Oxcarbazepine. *J. Pharm. Sci.*, **99**, 794-803.

336. Macielag, M.J. (2012). Chemical properties of antibacterials and their uniqueness. In: *Antibiotic Discovery and Development*. *eds. T.J. Dougherty, M.J. Pucci.* pp. 801-802. Springer, New York.

337. Macrae, C.F., Bruno, I.J., Chisholm, J.A., Edgington, P.R., McCabe, P., Pidcock, E., Rodriguez-Monge, L., Taylor, R., van de Streek, J. and Wood, P.A. (2008). *Mercury CSD 2.0* - new features for the visualization and investigation of crystal structures. *J. Appl. Cryst.*, **41**, 466-470.

338. Macrae, C.F., Edgington, P.R., McCabe, P., Pidcock, E., Shields, G.P., Taylor, R., Towler, M. and van de Streek, J. (2006). *Mercury*: visualization and analysis of crystal structures. *J. Appl. Cryst.*, **39**, 453-457.

339. Macrae, C.F., Sovago, I., Cottrell, S.J., Galek, P.T.A., McCabe, P. Pidcock, E., Platings, M., Shields, G.P., Stevens, J.S., Towler, M. and Wood, P.A. (2020). *Mercury 4.0*: from visualization to analysis, design and prediction. *J. Appl. Cryst.*, **53**, 226-235.

340. Madras, G. and McCoy, B.J. (2007). A fragmentation model for crystal attrition. *J. Cryst. Growth*, **305**, 211-217.

341. Málek, J. and Shánělová, J. (2001). Structural Relaxation in Amorphous Materials. In: *Properties and Applications of Amorphous Materials. eds. M.F. Thorpe, L. Tichy*. pp 35-44. Springer Netherlands, Dordrecht.

342. Mangin, D., Puel, F. and Veesler S. (2009). Polymorphism in Processes of Crystallization in Solution: A Practical Review. *Org. Process Res. Dev.*, **13**, 1241-1253.

343. Marcus, Y. (1998). Physical Properties of Solvents. In: *The Properties of Solvents*. pp 94-109. John Wiley & Sons Ltd, Chichester.

344. Markvardsen, A.J., Shankland, K., David, W.I.F., Johnston, J.C., Ibberson, R.M., Tucker, M., Nowell, H. and Griffin, T. (2008). *ExtSym*: a program to aid space-group determination from powder diffraction data. *J. Appl. Cryst.*, **41**, 1177-1181.

345. Martins, R.M., Siqueira, S., Tacon, L.A. and Freitas, L.A.P. (2012). Microstructured ternary solid dispersions to improve carbamazepine solubility. *Powder Technol.*, **215-216**, 156-165.

346. Mascia, S., Heider, P.L., Zhang, H., Lakerveld, R., Benyahia, B., Barton, P.I., Braatz, R.D., Cooney, C.L., Evans, J.M.B., Jamison, T.F., Jensen, K.F., Myerson, A.S. and Trout, B.L. (2013). End-to-End Continuous Manufacturing of Pharmaceuticals: Integrated Synthesis, Purification, and Final Dosage Formation. *Angew. Chem. Int. Ed.*, **52**, 2359-12363.

347. Massa, W. (2004). Crystal Structure Determination, 2nd edn. Springer-Verlag, Berlin.

348. Matell, M. (1952). On the Conditions for the Formation of Quasiracemic Compounds II Alkylsuccinic Acids and S-Alkylmercapto-3-succinic Acids. *Ark. Kemi*, **5**, 17-37.

349. Matsuura, T. and Koshima, H. (2005). Introduction to chiral crystallization of achiral organic compounds: Spontaneous generation of chirality. *J. Photochem. Photobiol. C*, **6**, 7-24.

350. Mazzarotta, B., Di Cave, S. and Bonifazi, G. (1996). Influence of time on crystal attrition in a stirred vessel. *AIChE J.*, **42**, 3554-3558.

351. McCusker, L.B., Von Dreele, R.B., Cox, D.E., Louër, D. and Scardi, P. (1999). Rietveld refinement guidelines. *J. Appl. Cryst.*, **32**, 36-50.

352. Miki, H., Terashima, T., Asakuma, Y., Maeda, K. and Fukui, K. (2005). Inclusion of mother liquor inside KDP crystals in a continuous MSMPR crystallizer. *Sep. Purif. Technol.*, **43**, 71-76.

353. Mimura, H., Kitamura, S., Kitagawa, T. and Kohda, S. (2002). Characterization of the non-stoichiometric and isomorphic hydration and solvation in FK041 clathrate. *Colloids Surf. B*, **26**, 397-406.

354. Mirmehrabi, M. and Rohani, S. (2005). An approach to solvent screening for crystallization of polymorphic pharmaceuticals and fine chemicals. *J. Pharm Sci.*, **94**, 1560-1576.

355. McKellar, S.C., Urquhart, A.J., Lamprou, D.A. and Florence, A.J. (2012). Polymer templating of supercooled indomethacin for polymorph selection. *ACS Comb. Sci.*, **14**, 155-159.

356. Montemurro, N., Postigo, C., Lonigro, A., Perez, S. and Barceló, D. (2017). Development and validation of an analytical method based on liquid chromatography-tandem mass spectrometry detection for the simultaneous determination of 13 relevant wastewater-derived contaminants in lettuce. *Anal. Bioanal. Chem.*, **409**, 5375-5387.

357. Mooney, K.G., Mintun, M.A., Himmelstein, K.J. and Stella, V.J. (1981). Dissolution kinetics of carboxylic acids I: effect of pH under unbuffered conditions. *J. Pharm. Sci.*, **70**,13-22.

358. Morissette, S.L., Almarsson, Ö., Peterson, M.L., Remenar, J.F., Read, M.J., Lemmo, A.V. and Gardner, C.R. (2004). High-throughput crystallization: polymorphs, salts, co-crystals and solvates of pharmaceutical solids. *Adv. Drug Deliv. Rev.*, **56**, 275-300.

359. Morris, K.R. and Rodríguez-Hornedo, N. (1993). Hydrates. In: *Encyclopedia of Pharmaceutical Technology*. *eds. J.Swarbrick, J. Boylan*. pp. 393-440. Marcel Dekker, New York.

360. Moss, G.P. (1996). Basic terminology of stereochemistry (IUPAC Recommendations 1996). *Pure Appl. Chem.*, **68**, 2193-2222.

361. Mukuta, T., Lee, A.Y., Kawakami, T. and Myerson, A.S. (2005). Influence of Impurities on the Solution-Mediated Phase Transformation of an Active Pharmaceutical Ingredient. *Cryst. Growth Des.*, **5**, 1429-1436.

362. Muller, G.W. (1997). Thalidomide: from tragedy to new drug discovery. *Chemtech*, **27**, 21-25.

363. Mullin, J.W. (2001). Metastable zone widths. In: *Crystallization*. pp. 201-204. Butterworth-Heinemann, Oxford.

364. Munroe, A., Croker, D., Hodnett, B. K. and Seaton, C. C. (2011). Epitaxial growth of polymorphic systems: The case of sulfathiazole. *CrystEngComm*, **13**, 5903-5907.

365. Murdande, S.B., Pikal, M.J., Shanker, R.M. and Bogner, R.H. (2010). Solubility advantage of amorphous pharmaceuticals: I. A thermodynamic analysis. *J. Pharm. Sci.*, **99**, 1254-1264.

366. Murdande, S.B., Pikal, M.J., Shanker, R.M. and Bogner, R.H. (2011). Aqueous solubility of crystalline and amorphous drugs: challenges in measurement. *Pharm. Dev. Technol.*, **16**, 187-200.

367. Murphy, D., Rodríguez-Cintrón, F., Langevin, B., Kelly, R.C. and Rodríguez-Hornedo, N. (2002). Solution-mediated phase transformation of anhydrous to dihydrate carbamazepine and the effect of lattice disorder. *Int. J. Pharm.*, **246**, 121-134.

368. Musumeci, D., Hunter, C.A. and McCabe, J.F. (2010). Solvent Effects on Acridine Polymorphism. *Cryst. Growth Des.*, **10**, 1661-1664.

369. Musumeci, D., Hunter, C.A., Prohens, R., Scuderi, S. and McCabe, J.F. (2011). Virtual cocrystal screening. *Chem. Sci.*, **2**, 883-890.

370. Myerson, A.S. and Ginde, R. (2002). Crystals, crystal growth and nucleation. In: *Handbook of Industrial Crystallization (2nd edn). ed. A. S. Myerson*. pp. 33-65. Butterworth-Heinemann, Boston.

371. Nair, R., Gonen, S. and Hoag, S.W. (2002). Influence of polyethylene glycol and povidone on the polymorphic transformation and solubility of carbamazepine. *Int. J. Pharm.*, **240**, 11-22.

372. Nanubolu, J.B. and Burley, J. C. (2012). Investigating the Recrystallization Behavior of Amorphous Paracetamol by Variable Temperature Raman Studies and Surface Raman Mapping. *Mol. Pharmaceutics*, **9**, 1544-1558.

373. Naumov, P., Chizhik, S., Panda, M.K., Nath, N.K. and Boldyreva, E. (2015). Mechanically Responsive Molecular Crystals. *Chem. Rev.*, **115**, 12440-12490.

374. Neumann, M. A. and Perrin, M.-A. (2005). Energy Ranking of Molecular Crystals Using Density Functional Theory Calculations and an Empirical van der Waals Correction. *J. Phys. Chem. B*, **109**, 15531-15541.

375. Neumann, M.A. and Perrin, M.-A. (2009). Can crystal structure prediction guide experimentalists to a new polymorph of paracetamol? *CrystEngComm*, **11**, 2475-2479.

376. Neumann, M.A., van de Streek, J., Fabbiani, F.P.A., Hidber, P. and Grassmann, O. (2015). Combined crystal structure prediction and high-pressure crystallization in rational pharmaceutical polymorph screening. *Nat. Commun.*, **6**, 7793.

377. Newman, A. (2011). X-ray Powder Diffraction in Solid Form Screening and Selection. *Am. Pharm. Rev.*, **14**, 44-51.

378. Newman, A. (2013). Specialized Solid Form Screening Techniques. *Org. Process Res. Dev.*, **17**, 457-471.

379. Nguyen, L.A. and He, H. and Pham-Huy, C. (2008). Chiral Drugs: An Overview. *Int. J. Biomed. Sci.*, **2**, 85-100.

380. Nielsen, M. H., Aloni, S. and De Yoreo, J. J. (2014). In situ TEM imaging of $CaCO_3$ nucleation reveals coexistence of direct and indirect pathways. *Science*, **345**, 1158-1162.

381. Nikolai, L.N., McClure, E.L., MacLeod, S.L. and Wong, C.S. (2006). Stereoisomer quantification of the -blocker drugs atenolol, metoprolol, and propranolol in wastewaters by chiral high-performance liquid chromatography–tandem mass spectrometry. *J. Chromatogr. A*, **1131**, 103-109.

382. Nordström, F.L., Svärd, M. and Rasmuson, A.C. (2013). Primary nucleation of salicylamide: the influence of process conditions and solvent on the metastable zone width. *CrystEngComm*, **15**, 7285-7297.

383. Nozue, Y., Kurita, R., Hirano, S., Kawasaki, N., Ueno, S., Iida, A., Nishi, T. and Amemiya, Y. (2003). Spatial distribution of lamella structure in PCL/PVB band spherulite investigated with microbeam small- and wide-angle X-ray scattering. *Polymer*, **44**, 6397-6405.

384. Nyman, J. and Day, G.M. (2015). Static and lattice vibrational energy differences between polymorphs. *CrystEngComm*, **17**, 5154-5165.

385. Nyman, J., Pundyke, O.S. and Day, G.M. (2016). Accurate Force Fields and Methods for Modelling Organic Molecular Crystals at Finite Temperatures. *Phys. Chem. Chem. Phys.*, **18**, 15828-15837.

386. Nyman, J., Yu, L. and Reutzel-Edens, S.M. (2019). Accuracy and reproducibility in crystal structure prediction: the curious case of ROY. *CrystEngComm*, **21**, 2080-2088.

387. Olafson, K.N., Ketchum, M.A., Rimer, J.D. and Vekilov, P.G. (2015). Molecular Mechanisms of Hematin Crystallization from Organic Solvent. *Cryst. Growth Des.*, **15**, 5535-5542.

388. Olmsted, B.K. and Ward, M.D. (2011). The role of chemical interactions and epitaxy during nucleation of organic crystals on crystalline substrates. *CrystEngComm*, **13**, 1070-1073.

389. Ooi, L.-I. (2010). Symmetry Elements. In: *Principles of X-ray Crystallography*. pp. 36-47, Oxford University Press Inc., New York.

390. Østergaard, J. (2016). UV/Vis Spectrophotometry and UV Imaging. In: *Analytical Techniques in the Pharmaceutical Sciences. eds. A. Müllertz, Y. Perrie, T. Rades.* pp. 3-28. Springer-Verlag, New York.

391. Ostwald, W.Z. (1897). Studien uber die Bildung und Umwandlung fester Korper. *Z. Phys. Chem.*, **22**, 289-330.

392. Ostwald, W. (1900). Über die vermeintliche Isomerie des roten und gelben Queck-silberoxyds und die Oberlfächenspannung fester Körper. *Z. Phys. Chem.*, **34**, 495-503.

393. Oszlányi, G., and Süto, A. (2004). *Ab initio* structure solution by charge flipping. *Acta Cryst. A*, **60**, 134-141.

394. Ottoboni, S., Chrubasik, M., Mir Bruce, L., Nguyen, T.T.H., Robertson, M., Johnston, B., Oswald, I.D.H., Florence, A. and Price, C., (2018). Impact of Paracetamol Impurities on Face Properties: Investigating the Surface of Single Crystals Using TOF-SIMS. *Cryst. Growth Des.*, **18**, 2750-2758.

395. Oxtoby, D. W. (1998). Nucleation of First-Order Phase Transitions. *Acc. Chem. Res.***, 31**, 91-97.

396. Pajander, J., Haugshøj, K.B., Bjørneboe, K., Wahlberg, P. and Rantanen, J. (2013). Foreign matter identification from solid dosage forms. *J. Pharm. Biomed. Anal.*, **80**, 116-125.

397. Pallipurath, A.R., Flandrin, P.-B., Wayment, L. E., Wilson, C.C. and Robertson, K. (2020). *In situ* non-invasive Raman spectroscopic characterisation of succinic acid polymorphism during segmented flow crystallisation. *Mol. Syst. Des. Eng.*, **5**, 294-303.

398. Parambil, J.V., Poornachary, S.L., Heng, J.Y.Y. and Tan, R.B.H. (2019). Template-induced nucleation for controlling crystal polymorphism: from molecular mechanisms to applications in pharmaceuticals processing. *CrystEngComm*, **21**, 4122-4135.

399. Parambil, J.V., Poornachary, S.K., Hinder, S.J., Tan, R.B.H. and Heng, J.Y.Y. (2015). Establishing template-induced polymorphic domains for API crystallisation: the case of carbamazepine. *CrystEngComm*, **17**, 6384-6392.

400. Parambil, J.V., Poornachary, S.K., Tan, R.B.H. and Heng, J.Y.Y. (2014). Template-induced polymorphic selectivity: the effects of surface chemistry and solute concentration on carbamazepine crystallisation. *CrystEngComm*, **16**, 4927-4930.

401. Park Y., Boerrigter, S.X.M., Yeon, J., Lee, S.H., Kang, S.K. and Lee, E.H. (2016). New Metastable Packing Polymorph of Donepezil Grown on Stable Polymorph Substrates. *Cryst. Growth Des.*, **16**, 2552-2560.

402. Parsons, S., Flack, H.D. and Wagner, T. (2013). Use of intensity quotients and differences in absolute structure refinement. *Acta Cryst. B*, **69**, 249-259.

403. Patel, M.A, Kaplan, K., Yuk, S.A., Saboo, S., Melkey, K. and Chadwick, K. (2016). Utilization of Surface Equilibria for Controlling Heterogeneous Nucleation: Making the “Disappeared” Polymorph of 3-Aminobenzensulfonic Acid “Reappear”. *Cryst. Growth Des.*, **16**, 6933-6940.

404. Patterson, A.L. (1934). A Fourier Series Method for the Determination of the Components of Interatomic Distances in Crystals. *Phys. Rev.*, **46**, 372-376.

405. Paulekuhn, G.S., Dressman, J.B. and Saal, C. (2007). Trends in Active Pharmaceutical Ingredient Salt Selection based on Analysis of the Orange Book Database. *J. Med. Chem.*, **50**, 6665-6672.

406. Pawley, G.S. (1981). Unit-cell refinement from powder diffraction scans. *J. Appl. Cryst.*, **14**, 357-361.

407. Payton, O., Champneys, A. R., Homer, M. E., Picco, L. and Miles, M. J. (2011). Feedback-induced instability in tapping mode atomic force microscopy: Theory and experiment. *Proc. R. Soc. A*, **467**, 1801-1822.

408. Perumalla, S.R., Shi, L. and Sun, C.C. (2012). Ionized form of acetaminophen with improved compaction properties. *CrystEngComm*, **14**, 2389-2390.

409. Petsev, D. N., Chen, K., Gliko, O. and Vekilov, P. G. (2003). Diffusion-limited kinetics of the solution-solid phase transition of molecular substances. *Proc. Natl. Acad. Sci.*, **100**, 792-796.

410. Pfund, L.Y. and Matzger, A.J. (2014). Towards Exhaustive and Automated High-Throughput Screening for Crystalline Polymorphs. *ACS Comb Sci.*, **16**, 309-313.

411. Pfund, L.Y., Price, C.P., Frick, J.J. and Matzger, A.J. (2015). Controlling Pharmaceutical Crystallization with Designed Polymeric Heteronuclei. *J. Am. Chem. Soc.*, **137**, 871-875.

412. Pindelska, E., Sokal, A. and Kolodziejski, W. (2017). Pharmaceutical cocrystals, salts and polymorphs: Advanced characterization techniques. *Adv. Drug. Deliv. Rev.*, **117**, 111-146.

413. Plumb, K. (2005). Continuous Processing in the Pharmaceutical Industry: Changing the Mind Set. *Chem. Eng. Res. Des.***83**, 730-738.

414. Pokroy, B., Chernow, V. F. and Aizenberg, J. (2009). Crystallization of malonic and succinic acids on SAMs: toward the general mechanism of oriented nucleation on organic monolayers. *Langmuir*, **25**, 14002-14006.

415. Pons Siepermann, C.A., Huang, S. and Myerson, A.S. (2017). Nucleation Inhibition of Benzoic Acid through Solution Complexation. *Cryst. Growth Des.*, **17**, 2646–2653.
416. Poornachary, S.K., Chow, P.S. and Tan, R.B.H. (2008). Influence of Solution Speciation of Impurities on Polymorphic Nucleation in Glycine. *Cryst. Growth Des.*, **8**, 179-185.
417. Poornachary, S.K., Lau, G., Chow, P.S., Tan, R.B.H. and George, N. (2011). The Effect and Counter-Effect of Impurities on Crystallization of an Agrochemical Active Ingredient: Stereochemical Rationalization and Nanoscale Crystal Growth Visualization. *Cryst. Growth Des.,* **11**, 492-500.
418. Porter III, W.W., Elie, S.C. and Matzger, A.J. (2008). Polymorphism in Carbamazepine Cocrystals. *Cryst. Growth Des.*, **8**, 14-16.
419. Price, S.L. (2004). The computational prediction of pharmaceutical crystal structures and polymorphism. *Adv. Drug. Deliv. Rev.*, **56**, 301-319.
420. Price, S. L. (2008). From crystal structure prediction to polymorph prediction: interpreting the crystal energy landscape. *Phys. Chem. Chem. Phys.*, **10**, 1996-2009.
421. Price, S.L. (2009). Computed Crystal Energy Landscapes for Understanding and Predicting Organic Crystal Structures and Polymorphism. *Acc. Chem. Res.*, **42**, 117-126.
422. Price, S.L. (2014). Predicting crystal structures of organic compounds. *Chem. Soc. Rev.*, **43**, 2098-2111.
423. Price, S.L., Braun, D.E. and Reutzel-Edens, S.M. (2016). Can computed crystal energy landscapes help understand pharmaceutical solids? *Chem. Commun.*, **52**, 7065-7077.
424. Price, C.P., Glick, G.D. and Matzger, A.J. (2006). Dissecting the Behavior of a Promiscuous Solvate Former. *Angew. Chem. Int. Ed.*, **45**, 2062-2066.
425. Price, C.P., Grzesiak, A.L. and Matzger, A.J. (2005). Crystalline Polymorph Selection and Discovery with Polymer Heteronuclei. *J. Am. Chem. Soc.*, **127**, 5512-5517.
426. Price, S.L., Leslie, M., Welch, G.W., Habgood, M., Price, L. S., Karamertzanis, P.G., and Day, G.M. (2010). Modelling organic crystal structures using distributed multipole and polarizability-based model intermolecular potentials. *Phys. Chem. Chem. Phys.*, **12**, 8478-8490.

427. Price, S.L. and Reutzel-Edens, S.M. (2016). The potential of computed crystal energy landscapes to aid solid-form development. *Drug Discov. Today*, **21**, 912-923.
428. Prohens, R., Barbas, R., Portell, A., Font-Bardia, M., Alcobé, X. and Puigjaner, C. (2016). Polymorphism of Cocrystals: The Promiscuous Behavior of Agomelatine. *Cryst. Growth Des.*, **16**, 1063-1070.
429. Prohotsky, D.L. and Zhao, F. (2012). A survey of Top 200 Drugs—Inconsistent Practice of Drug Strength Expression for Drugs Containing Salt Forms. *J. Pharm. Sci.*, **101**, 1-6.
430. Punin, Y.O. and Shtukenberg, A. G. (2008). Autodeformation Defects in Crystals. St. Petersburg Univ. Press: St. Petersburg. (in Russian).
431. Qi, S. (2016). Thermal Analysis of Pharmaceuticals. In: *Analytical Techniques in the Pharmaceutical Sciences. eds. A. Müllertz, Y. Perrie, T. Rades.* pp. 363-388. Springer-Verlag, New York.
432. Qi, S., Avalle, P., Saklatvala, R. and Craig, D.Q.M. (2008). An investigation into the effects of thermal history on the crystallisation behaviour of amorphous paracetamol. *Eur. J. Pharm. Biopharm.*, **69**, 364-371.
433. Rabasseda, X. (2001). Oxcarbazepine: anticonvulsant profile and safety. *Drugs Today*, **37**, 333-355.
434. Rahim, M.A., Hata, Y., Björnmalm, M., Ju, Y. and Caruso, F. (2018). Supramolecular Metal–Phenolic Gels for the Crystallization of Active Pharmaceutical Ingredients. *Small*, **14**, 1801202.
435. Reischl, D., Röthel, C., Christian, P., Roblegg, E., Ehmann, H.M.A., Salzmann, I. and Werzer, O. (2015). Surface-Induced Polymorphism as a Tool for Enhanced Dissolution: The Example of Phenytoin. *Cryst. Growth Des.*, **15**, 4687-4693.
436. Rengarajan, G.T., Enke, D. and Beiner, M. (2007). Crystallization Behavior of Acetaminophen in Nanopores. *Open Phys. Chem. J.*, **1**,18-24.
437. Rengarajan, G.T., Enke, D., Steinhart, M. and Beiner, M. (2008). Stabilization of the amorphous state of pharmaceuticals in nanopores. *J. Mater. Chem.*, **18**, 2537-2539.

438. Repta, A.J., Baltezor, M.J. and Bansal, P.C. (1976). Utilization of an enantiomer as a solution to a pharmaceutical problem: Application to solubilization of 1,2-di(4-piperazine-2,6-dione)propane. *J. Pharm. Sci.*, **65**, 238-242.

439. Reutzel-Edens, S.M., Russell, V.A. and Yu, L. (2000). Molecular basis for the stability relationships between homochiral and racemic crystals of tazofelone: a spectroscopic, crystallographic, and thermodynamic investigation. *J. Chem. Soc., Perkin Trans. 2*, **2000**, 913-924.

440. Ribeiro, A.R., Castro, P.M.L. and Tiritan, M.E. (2012). Chiral pharmaceuticals in the environment. *Environ. Chem. Lett.*, **10**, 239-253.

441. Rietveld, H.M. (1967). Line profiles of neutron powder-diffraction peaks for structure refinement. *Acta. Cryst.*, **22**, 151-152.

442. Rietveld, H.M. (1969). A profile refinement method for nuclear and magnetic structures. *J. Appl. Cryst.*, **2**, 65-71.

443. Rodríguez-Hornedo, N. and Murphy, D. (1999). Significance of controlling crystallization mechanisms and kinetics in pharmaceutical systems. *J. Pharm. Sci.*, **88**, 651-660.

444. Rodríguez-Spong, B., Price, C.P., Jayasankar, A., Matzger, A.J. and Rodríguez-Hornedo, N. (2004). General principles of pharmaceutical solid polymorphism: A supramolecular perspective. *Adv. Drug Deliv. Rev.*, **56**, 241-274.

445. Roelands, C.P.M., ter Horst, J.H., Kramer, H.J.M and Jansens, P.J. (2007). Precipitation mechanism of stable and metastable polymorphs of L-glutamic acid. *AIChE J.*, **53**, 354-362.

446. Rollinger, J.M. and Burger, A. (2001). Polymorphism of racemic felodipine and the unusual series of solid solutions in the binary system of its enantiomers. *J. Pharm. Sci.*, **90**, 949-959.

447. Roussel, C., Del Rio, A., Pierrot-Sanders, J., Piras, P. and Vanthuyne, N. (2004). Chiral liquid chromatography contribution to the determination of the absolute configuration of enantiomers. *J. Chromatogr. A*, **1037**, 311-328.

448. Roy, S., Chamberlin, B. and Matzger, A.J. (2013). Polymorph Discrimination Using Low Wavenumber Raman Spectroscopy. *Org. Process Res. Dev.*, **17**, 976-980.

449. Roy, S., Goud, N.R. and Matzger, A.J. (2016). Polymorphism in phenobarbital: discovery of a new polymorph and crystal structure of elusive form V. *Chem. Commun.*, **52**, 4389-4392.

450. Roy, S., Quiñones, R. and Matzger, A.J. (2012). Structural and Physicochemical Aspects of Dasatinib Hydrate and Anhydrate Phases. *Cryst. Growth Des.*, **12**, 2122-2126.

451. Rudawska, A. and Jacniacka, E. (2018). Evaluating uncertainty of surface free energy measurement by the van Oss-Chaudhury-Good method. *Int. J. Adhes. Adhes.*, **82**, 139-145.

452. Ruscica, R., Bianchi, M., Quintero, M., Martinez, A. and Vega, D.R. (2010). Solid-State Forms of Zoledronic Acid: Polymorphism in Hydrates. *J. Pharm. Sci.*, **99**, 4962-4972.

453. Russell, V. A., Etter, M. C. and Ward, M. D. (1994). Layered Materials by Molecular Design: Structural Enforcement by Hydrogen Bonding in Guanidinium Alkane- and Arenesulfonates. *J. Am. Chem. Soc.*, **116**, 1941-1952.

454. Russell, V. A., Evans, C. C., Li, W. and Ward, M. D. (1997). Nanoporous Molecular Sandwiches: Pillared Two-Dimensional Hydrogen-Bonded Networks With Adjustable Porosity. *Science*, **276**, 575-579.

455. Saal, C. and Becker, A. (2013). Pharmaceutical salts: A summary on doses of salt formers from the Orange Book. *Eur. J. Pharm. Sci.*, **49**, 614-623.

456. Sakamoto, M. (2004). Spontaneous chiral crystallization of achiral materials and absolute asymmetric transformation in the chiral crystalline environment. In: *Enantiomer Separation – Fundamentals and Practical Methods. ed. F. Toda.* pp. 103-134. Kluwer Academic Publishers, Dordrecht.

457. Saracovan, I., Keith, H.D., Manley, R.St.J. and Brown, G.R. (1999). Banding in Spherulites of Polymers Having Uncompensated Main-Chain Chirality. *Macromolecules*, **32**, 8918-8922.

458. Schlesinger, C., Tapmeyer, L., Gumbert, S.D., Prill, D., Bolte, M., Schmidt, M.U. and Saal, C. (2018). Absolute Configuration of Pharmaceutical Research Compounds Determined by X-ray Powder Diffraction. *Angew. Chem. Int. Ed.*, **57**, 9150-9153.

459. Schultheiss, N., Smit, J.P. and Hanko, J.A. (2009). Three isostructural solvates of finasteride and their solid-state characterization. *Eur. J. Pharm. Sci.*, **38**, 498-503.

460. Schuster, J.M., Schvezov, C.E. and Rosenberger, M.R. (2015). Influence of Experimental Variables on the Measure of Contact Angle in Metals Using the Sessile Drop Method. *Procedia Mater. Sci.*, **8**, 742-751.

461. SeethaLekshmi, S. and Guru Row, T.N. (2012). Conformational Polymorphism in a Non-steroidal Anti-inflammatory Drug, Mefenamic Acid. *Cryst. Growth Des.*, **12**, 4283-4289.

462. Selekman, J.A., Roberts, D., Rosso, V., Qiu, J., Nolfo, J., Gao, Q. and Janey, J. (2016). Development of a Highly Automated Workflow for Investigating Polymorphism and Assessing Risk of Forming Undesired Crystal Forms within a Crystallization Design Space. *Org. Process Res. Dev.*, **20**, 70-75.

463. Serajuddin, A.T.M. (2007). Salt formation to improve drug solubility. *Adv. Drug. Deliv. Rev.*, **59**, 603-616.

464. Shah, U.V., Amberg, C., Diao, Y., Yang, Z. and Heng, J.Y.Y. (2015). Heterogeneous nucleants for crystallogenesis and bioseparation. *Curr. Opin. Chem. Eng.*, **8**, 69-75.

465. Shahar, C., Dutta, S., Weissman, H., Shimon, L.J.W., Ott, H. and Rybtchinski, B. (2016). Precrystalline Aggregates Enable Control over Organic Crystallization in Solution. *Angew. Chem. Int. Ed.*, **55**, 179-182.

466. Shaker, M. and Salahinejad, E. (2018). A combined criterion of surface free energy and roughness to predict the wettability of non-ideal low-energy surfaces. *Prog. Org. Coat.*, **119**, 123-126.

467. Shankland, K. (2016). An Overview of X-ray powder diffraction and Its Relevance to Pharmaceutical Crystal Structures. In: *Analytical Techniques in the Pharmaceutical Sciences. eds. A. Müllertz, Y. Perrie, T. Rades.* pp. 363-388. Springer-Verlag, New York.

468. Shankland, K. and David, W. I. F. (2002). Global optimization strategies. In: *Structure Determination from Powder Diffraction Data*. *eds. W. I. F. David, K. Shankland, L. B. McCusker, C. Baerlocher.* pp. 252-285. IUCr/Oxford University Press, Oxford.

469. Shard, A.G., Havelund, R., Spencer, S. J., Gilmore, I. S., Alexander, M. R., Angerer, T. B., Aoyagi, S., Barnes, J.-P., Benayad, A., Bernasik, A., Ceccone, G., Counsell, J. D. P., Deeks, C., Fletcher, J. S., Graham, D. J., Heuser, C., Lee, T. G., Marie, C., Marzec, M. M., Mishra, G., Rading, D., Renault, O., Scurr, D. J., Shon, H. K., Spampinato, V., Tian, H., Wang, F., Winograd, N., Wu, K., Wucher, A., Zhou, Y. and Zhu, Z. (2015). Measuring Compositions in Organic Depth Profiling: Results from a VAMAS Interlaboratory Study. *J. Phys. Chem. B*, **119**, 10784-10797.

470. Shekhah, O., Wang, H., Kowarik, S., Schreiber, F., Paulus, M., Tolan, M., Sternemann, C., Evers, F., Zacher, D., Fischer, R.A. and Wöll, C. (2007). Step-by-Step Route for the Synthesis of Metal−Organic Frameworks. *J. Am. Chem. Soc.*, **129**, 15118-15119.

471. Sheldrick, G.M. (2015a). *SHELXT* - Integrated space-group and crystal-structure determination. *Acta Cryst. A*, **71**, 3-8.

472. Sheldrick, G.M. (2015b). Crystal structure refinement with *SHELXL*. *Acta Cryst. C*, **71**, 3-8.

473. Shtukenberg, A.G., Cui, X., Freudenthal, J., Gunn, E., Camp, E. and Kahr, B. (2012). Twisted Mannitol Crystals Establish Homologous Growth Mechanisms for High-Polymer and Small-Molecule Ring-Banded Spherulites. *J. Am. Chem. Soc.*, **134**, 6354-6364.

474. Shtukenberg, A.G., Freudenthal, J. and Kahr, B. (2010). Reversible Twisting during Helical Hippuric Acid Crystal Growth. *J. Am. Chem. Soc.*, **132**, 9341-9349.

475. Shtukenberg, A.G., Gujral, A., Rosseeva, E., Cui, X. and Kahr, B. (2015). Mechanics of twisted hippuric acid crystals untwisting as they grow. *CrystEngComm*, **17**, 8817-8824.

476. Shtukenberg, A., Gunn, E., Gazzano, M., Freudenthal, J., Camp, E., Sours, R., Rosseeva, E. and Kahr, B. (2011). Bernauer′s Bands. *ChemPhysChem*, **12**, 1558-1571.

477. Shtukenberg, A. and Kahr, B. (2014a). Twisted Crystals. *Acta Cryst. A*, **70**, C229.

478. Shtukenberg, A.G., Lee, S.S., Kahr, B. and Ward, M.D. (2014b). Manipulating Crystallization with Molecular Additives. *Annu. Rev. Chem. Biomol. Eng.*, **5**, 77-96.

479. Shtukenberg, A.G., Punin, Y.O., Gujral, A. and Kahr, B. (2014c). Growth Actuated Bending and Twisting of Single Crystals. *Angew. Chem. Int. Ed.*, **53**, 672-699.
480. Shtukenberg, A.G., Tan, M., Vogt-Maranto, L., Chan, E.J., Xu, W., Yang, J., Tuckerman, M.E., Hu, C.T. and Kahr, B. (2019). Melt Crystallization for Paracetamol Polymorphism. *Cryst. Growth Des.*, **19**, 4070-4080.
481. Shtukenberg, A.G., Zhu, Q., Carter, D.J., Vogt, L., Hoja, J., Schneider, E., Song, H., Pokroy, B., Polishchuk, I., Tkatchenko, A., Oganov, A.R., Rohl, A.L., Tuckerman, M.E. and Kahr, B. (2017). Powder diffraction and crystal structure prediction identify four new coumarin polymorphs. *Chem. Sci.*, **8**, 4926-4940.
482. Simões, R.G., Salzmann, I., Resel, R., Röthel, C. and Geerts, Y.H. (2018). Stabilization of the Metastable Form I of Piracetam by Crystallization on Silicon Oxide Surfaces. *Cryst. Growth Des.*, **18**, 4123-4129.
483. Singfield, K.L. and Brown, G.R. (1995). Optically Active Polyethers. 1. Studies of the Crystallization in Blends of the Enantiomers and the Stereoblock Form of Poly(epichlorohydrin). *Macromolecules*, 28, 1290-1297.
484. Singh, A., Lee, I. S., Kim, K. and Myerson, A. S. (2011). Crystal growth on self-assembled monolayers. *CrystEngComm*, **13**, 24.
485. Singhal, D. and Curatolo, W. (2004). Drug polymorphism and dosage form design: a practical perspective.*Adv. Drug Deliv. Rev.*, **56**, 335-347.
486. Šišak Jung, D., Baerlocher, C., McCusker, L.B., Yoshinari, T. and Seebach, D. (2014). Solving the structures of light-atom compounds with powder charge flipping. *J. Appl. Crystallogr.*, **47**, 1569-1576.
487. Sleutel, M. and Van Driessche, A.E.S. (2014). Role of clusters in nonclassical nucleation and growth of protein crystals. *Proc. Natl. Acad. Sci. U.S.A.*, **111**, E546-E553.
488. Smith, W.E., Barrett, H.H. and Paxman, R.G. (1983). Reconstruction of objects from coded images by simulated annealing. *Opt Lett.*, **8**, 199-201.
489. Snyder, L.R., Kirkland, J.J. and Dolan, J.W. (2010). Introduction to modern liquid chromatography, 3rd edn. Wiley, Hoboken.
490. Solomos, M.A., Capacci-Daniel, C., Rubinson, J.F. and Swift, J.A. (2018). Polymorph Selection via Sublimation onto Siloxane Templates. *Cryst. Growth Des.*, **18**, 6965-6972.

491. Sowerby, J. (1811). British Mineralogy: Or, Coloured Figure Intended to Elucidate the Mineralogy of Great Britain. A. R. Taylor and Company, London.
492. Spaepen, F.A. (1975). A structural model for the solid-liquid interface in monatomic systems. *Acta Metall.*, **23**, 729-743**.**
493. Spaepen, F. and Meyer, R.B. (1976). The surface tension in a structural model for the solid-liquid interface. *Scr. Metall.*, **10**, 257-263.
494. Spek, A.L. (2015). *PLATON* SQUEEZE: a tool for the calculation of the disordered solvent contribution to the calculated structure factors. *Acta Cryst. C*, **71**, 9-18.
495. Spitaleri, A., Hunter, C.A., McCabe, J.F., Packer, M.J. and Cockroft, S.L. (2004). A ^{1}H NMR study of crystal nucleation in solution. *CrystEngComm*, **6**, 490-493.
496. Sridhar, B., Nanubolu, J. B., Ravikumar, K., Karthik, G. and Reddy, B.V.S. (2017). Three isostructural solvates of a tetrahydrofurochromenone derivative. *Acta Cryst. C*, **73**, 407-413.
497. Srirambhatla, V.K, Guo, R., Price, S.L. and Florence, A.J. (2016). Isomorphous template induced crystallisation: a robust method for the targeted crystallisation of computationally predicted metastable polymorphs. *Chem. Commun.*, **52**, 7384-7386.
498. Stahly, G.P. (2007). Diversity in Single- and Multiple-Component Crystals. The Search for and Prevalence of Polymorphs and Cocrystals. *Crys. Growth. Des.*, **7**, 1007-1026.
499. Stahly, G.P., Bates, S., Andres, M.C. and Cowans, B.A. (2006). Discovery of a New Polymorph of Dehydroepiandrosterone (Prasterone) and Solution of Its Crystal Structure from X-ray Powder Diffraction Data. *Cryst. Growth Des.,* **6**, 925-932.
500. Steendam, R.R.E. and Frawley, P.J. (2019). Secondary Nucleation of Sodium Chlorate: The Role of Initial Breeding. *Cryst. Growth Des.*, **19**, 3453-3460.
501. Stephenson, G.A., Aburub, A. and Woods, T.A. (2011). Physical stability of salts of weak bases in the solid-state. *J. Pharm. Sci.*, **100**, 1607-1617.
502. Stephenson, G.A., Groleau, E.G., Kleemann, R.L., Xu, W. and Rigsbee, D.R. (1998). Formation of Isomorphic Desolvates: Creating a Molecular Vacuum. *J. Pharm. Sci.*, **87**, 536-542.

503. Stephenson, G.A., Kendrick, J., Wolfangel, C. and Leusen, F.J.J. (2012). Symmetry Breaking: Polymorphic Form Selection by Enantiomers of the Melatonin Agonist and Its Missing Polymorph. C*ryst. Growth Des.*, **12**, 3964-3976.

504. Stieger, N., Liebenberg, W., Wessels, J.C., Samsodien, H. and Caira, M.R. (2010). Crystal form conversion of nevirapine solvates subjected to elevated temperature and humidity: a qualitative study. *Struct. Chem.*, **21**, 771-777.

505. Stojaković, J., Baftizadeh, F., Bellucci, M.A., Myerson, A.S. and Trout, B.L. (2017). Angle-Directed Nucleation of Paracetamol on Biocompatible Nanoimprinted Polymers. *Cryst. Growth Des.*, **17**, 2955-2963.

506. Sugimoto, K., Dinnebier, R.E. and Zakrzewski, M. (2007). Structural characterization of anhydrous naloxone- and naltrexone hydrochloride by high resolution laboratory X-ray powder diffraction and thermal analysis. *J. Pharm. Sci.*, **96**, 3316-3323.

507. Sun, C.C. (2013). Cocrystallization for successful drug delivery. *Expert Opin. Drug Deliv.*, **10**, 201-213.

508. Sun, Y., Zhu, L., Kearns, K.L., Ediger, M.D. and Yu, L. (2011). Glasses crystallize rapidly at free surfaces by growing crystals upward. *Proc. Natl. Acad. Sci. U.S.A.*, **108**, 5990-5995.

509. Surana, R. and Suryanarayanan, R. (2000). Quantitation of crystallinity in substantially amorphous pharmaceuticals and study of crystallization kinetics by X-ray powder diffractometry. *Powder Diffr.*, **15**, 2-6.

510. Swichtenberg, B. (2008). Moving Beyond the Batch. *Pharm. Manuf.*, **7**, 24-26.

511. Sypek, K., Burns, I.S., Florence, A.J. and Sefcik, J. (2012). In Situ Monitoring of Stirring Effects on Polymorphic Transformations during Cooling Crystallization of Carbamazepine. *Cryst. Growth Des.*, **12**, 4821-4828.

512. Taden, A., Landfester, K. and Antonietti, M. (2004). Crystallization of Dyes by Directed Aggregation of Colloidal Intermediates: A Model Case. *Langmuir*, **20**, 957-961.

513. Tai, C.Y. and Chen, F.-B. (1998). Polymorphism of $CaCO_3$, precipitated in a constant-composition environment. *AIChE J.*, **44**, 1790-1798.

514. Tan, L., Davis, R.M., Myerson, A.S. and Trout, B.L. (2015). Control of Heterogeneous Nucleation via Rationally Designed Biocompatible Polymer Surfaces with Nanoscale Features. *Cryst. Growth Des.*, **15**, 2176-2186.

515. Tessler, L. and Goldberg, I. (2006). Crystal Structures of Aripiprazole, a New Anti-psychotic Drug, and of Its Inclusion Compounds with Methanol, Ethanol and Water. *J. Inclusion Phenom. Macrocycl. Chem.*, **55**, 255-261.

516. Thakuria, R. and Nangia, A. (2013). Olanzapinium Salts, Isostructural Solvates, and Their Physicochemical Properties. *Cryst. Growth Des.*, **13**, 3672-3680.

517. Thakuria, R. and Thakur, T.S. (2017). Crystal Polymorphism in Pharmaceutical Science. In: *Comprehensive Supramolecular Chemistry II, Second Edition*. *eds. J.L. Atwood, G.W. Gokel, L. Barbour, L.* pp. 283-309. Elsevier, Oxford

518. Thompson, A.L. and Watkin, D.J. (2009) X-ray crystallography and chirality: understanding the limitations. *Tetrahedron: Asymmetry*, **20**, 712-717.

519. Tilley, R.J.D. (2006). Symmetry in three dimensions. In: *Crystals and Crystal Structures.* pp. 67-92. John Wiley & Sons Ltd, Chichester.

520. Toschev, S., Milchev, A. and Stoyanov, S. (1972). On some probabilistic aspects of the nucleation process. *J. Cryst. Growth*, **13-14**, 123-127.

521. Tóth, G.I., Tegze, G., Pusztai, T., Tóth, G. and Gránásy, L. (2010). Polymorphism, crystal nucleation and growth in the phase-field crystal model in 2D and 3D. *J. Phys. Condens. Matter*, **22,** 364101.

522. Trabattoni, S., Moret, M., Campione, M., Raimondo, L. and Sassella, A. (2013). Epitaxial Growth of Organic Semiconductor Polymorphs on Natural Amino Acid Single Crystals. *Cryst. Growth Des*., **13**, 4268-4278.

523. Tsarfati, Y., Rosenne, S., Weissman, H., Shimon, L.J.W., Gur, D., Palmer, B.A. and Rybtchinski, B. (2018). Crystallization of Organic Molecules: Nonclassical Mechanism Revealed by Direct Imaging. *ACS Cent. Sci.*, **4**, 1031-1036.

524. Turner, M.S., Briehl., R.W., Ferrone, F. A. and Josephs, R. (2003). Twisted Protein Aggregates and Disease: The Stability of Sickle Hemoglobin Fibers. *Phys. Rev. Lett.* **90**, 128103.

525. Turner, T.D., Halfpenny, P.J. and Roberts, K.J. (2017). Pharmaceutical Solid-State Characterisation Techniques. In: *Engineering Crystallography – From Molecule to Crystal to Functional Form. eds. K.J. Roberts, R. Docherty, R. Tamura*. pp. 367-394. Springer, Dordrecht.

526. Uccello-Barretta, G. and Balzano, F. (2013). Chiral NMR solvating additives for differentiation of enantiomers. *Top. Curr. Chem.*, **341**, 69-131.
527. Ueno, S., Hamada, Y. and Sato, K. (2003). Controlling Polymorphic Crystallization of *n*-Alkane Crystals in Emulsion Droplets through Interfacial Heterogeneous Nucleation. *Cryst. Growth Des.*, **3**, 935-939.
528. van Genderen, E., Clabbers, M.T.B., Das, P.P., Stewart, A., Nederlof, I., Barentsen, K.C., Portillo, Q., Pannu, N.S., Nicolopoulos, S., Gruene, T. and Abrahams, J.P. (2016). Ab initio structure determination of nanocrystals of organic pharmaceutical compounds by electron diffraction at room temperature using a Timepix quantum area direct electron detector. *Acta Cryst. A*, **72**, 236-242.
529. van Smaalen, S. (1995). Incommensurate crystal structures. *Crystallogr. Rev.*, **4**, 79-202.
530. Valette, G. (1982). Hydrophilicity of metal surfaces: Silver, gold and copper electrodes. *J. Electroanal. Chem. Interf. Electrochem.*, **139**, 285-301.
531. Vartak, S. and Myerson, A.S. (2017). Continuous Crystallization with Impurity Complexation and Nanofiltration Recycle. *Org. Process Res. Dev.*, **21**, 253-261.
532. Veis, A. and Dorvee, J.R. (2013). Biomineralization Mechanisms: A new paradigm for crystal nucleation in organic matrices. *Calcif. Tissue Int.*, **93**, 307-315.
533. Vekilov, P. G. (2004). Dense Liquid Precursor for the Nucleation of Ordered Solid Phases from Solution. *Cryst. Growth Des.*, **4**, 671-685.
534. Vekilov, P. G. (2010a). Nucleation. *Cryst. Growth Des.*, **10**, 5007-5019.
535. Vekilov, P. G. (2010b). The two-step mechanism of nucleation of crystals in solution. *Nanoscale*, **2**, 2346-2357.
536. Venkataraman S, Raju NS, Purandhar K, Reddy LA, Kondaiah GCM. US20060166968. Crystalline form of oxcarbazepine. (published on July 15, 2005).
537. Vetter, T., Iggland, M., Ochsenbein, D.R., Hänseler, F.S. and Mazzotti, M. (2013). Modeling Nucleation, Growth, and Ostwald Ripening in Crystallization Processes: A Comparison between Population Balance and Kinetic Rate Equation. *Cryst. Growth. Des.*, **13**, 4890-4905.

538. Viedma, C., Coquerel, G. and Cintas, P. (2015). Crystallization of Chiral Molecules. In: *Handbook of Crystal Growth, 2nd Edition (Fundamentals: Thermodynamics and Kinetics). ed. T. Nishinaga.* pp. 951-1002. Elsevier, Amsterdam.

539. Vippagunta, S.R., Brittain, H.G. and Grant, D.J.W. (2001). Crystalline solids. *Adv. Drug Deliv. Rev.*, **48**, 3-26.

540. Viscomi, G.C., Campana, M., Barbanti, M., Grepioni, F., Polito, M., Confortini, D., Rosini, G., Righi, P., Cannata, V. and Braga, D. (2008). Crystal forms of rifaximin and their effect on pharmaceutical properties. *CrystEngComm*, **10**, 1074-1081.

541. Volmer, M. W. and Weber, A. Z. (1926). Nucleus Formation in Supersaturated Systems. *Z. Phys. Chem.*, **119**, 277-301.

542. Vorontsova, M.A., Maes, D. and Vekilov, P.G. (2015). Recent advances in the understanding of two-step nucleation of protein crystals. *Faraday Discuss.*, **179**, 27-40 .

543. Wainer, IV. and Marcotte, A.A. (1993). Stereochemical terms and concepts. An overview. In: *Drug stereochemistry. Analytical methods and pharmacology (2nd edn). ed. I.W. Wainer.* pp. 25-34. Marcel Dekker, New York.

544. Wallace, A. F., Hedges, L. O., Fernandez-Martinez, A., Raiteri, P., Gale, J. D., Waychunas, G. A., Whitelam, S., Banfield, J. F. and De Yoreo, J. J. (2013). Microscopic evidence for liquid-liquid separation in supersaturated CaCO3 solutions. *Science*, **341**, 885-889.

545. Walker, M.C. and Patsalos, P.N. (1995). Clinical pharmacokinetics of new antiepileptic drugs. *Pharmacol. Ther.*, **67**, 351-384.

546. Walker, G., Römann, P., Poller, B., Löbmann, K., Grohganz, H., Rooney, J.S., Huff, G.S., Smith, G.P.S., Rades, T., Gordon, K.C., Strachan, C.J. and Fraser-Miller, S.J. (2017). Probing Pharmaceutical Mixtures during Milling: The Potency of Low-Frequency Raman Spectroscopy in Identifying Disorder. *Mol. Pharmaceutics*, **14**, 4675-4684.

547. Wan, C.-Q., Li, A.-M., Al-Thabaiti, S.A., El-Mosslamy, E.-S.H. and Mak, T.C.W. (2014). Efficient solvent-controlled crystallization of pure polymorphs of 1-nitro-4-(4-nitrophenylmethylthio)benzene. *CrystEngComm*, **16**, 8960-8968.

548. Wang, J.-R., Wang, X., Lu, L. and Mei, X. (2013). Highly Crystalline Forms of Valsartan with Superior Physicochemical Stability. *Cryst. Growth Des.*, **13**, 3261-3269.

549. Ward, M. D. (2001). Bulk Crystals to Surfaces: Combining X-ray Diffraction and Atomic Force Microscopy to Probe the Structure and Formation of Crystal Interfaces. *Chem. Rev.*, **101**, 1697-1725.

550. Warzecha, M., Guo, R., Bhardwaj, R.M., Reutzel-Edens, S.M., Price, S.L., Lamprou, D.A. and Florence, A.J. (2017). Direct Observation of Templated Two-Step Nucleation Mechanism during Olanzapine Hydrate Formation. *Cryst Growth Des.*, **17**, 6382-6393.

551. Weissbuch, I., Lahav, M. and Leiserowitz, L. (2003). Toward Stereochemical Control, Monitoring, and Understanding of Crystal Nucleation. *Cryst. Growth Des.*, **3**, 125-150.

552. Werner, P.-E. (2002). Autoindexing. In: *Structure Determination from Powder Diffraction Data. eds. W.I.F. David, K. Shankland, L.B. McCusker, C. Baerlocher*. pp. 118-135. Oxford University Press, Oxford.

553. Werzer, O., Boucher, N., de Silva, J.P., Gbabode, G., Geerts, Y.H., Konovalov, O., Moser, A., Novak, J., Resel, R. and Sferrazza, M. (2012). Interface Induced Crystal Structures of Dioctyl-Terthiophene Thin Films. *Langmuir*, **28**, 8530-8536.

554. Wijethunga, T.K., Baftizadeh, F., Stojaković, J., Myerson, A.S. and Trout, B.L. (2017). Experimental and Mechanistic Study of the Heterogeneous Nucleation and Epitaxy of Acetaminophen with Biocompatible Crystalline Substrates. *Cryst. Growth Des.*, **17**, 3783-3795.

555. Wijethunga, T., Chen, X., Myerson, A.S. and Trout, B.L. (2019). The use of biocompatible crystalline substrates for heterogeneous nucleation and polymorphic selection of indomethacin. *CrystEngComm*, **21**, 2193-2202.

556. Withbroe, G.J., Seadeek, C., Girard, K.P., Guinness, S.M., Vanderplas, B.C. and Vaidyanathan, R. (2013). A Robust, Streamlined Approach to Bosutinib Monohydrate. *Org. Process Res. Dev.*, **17**, 500-504.

557. Wolf, S.L.P., Caballero, L., Melo, F. and Cölfen, H. (2017). Gel-Like Calcium Carbonate Precursors Observed by *in situ* AFM. *Langmuir*, **33**, 158-163.

558. Xiang, J.-H., Yu, S.-H. and Zu, X. (2004). Polymorph and Phase Discrimination of Lead Chromate Pigments by a Facile Room Temperature Precipitation Reaction. *Cryst. Growth Des.*, **4**, 1311-1315.

559. Xiao, M., Jasensky, J., Zhang, X., Li., Y., Pichan, C., Lu, X. and Chen, Z. (2016). Influence of the side chain and substrate on polythiophene thin film surface, bulk, and buried interfacial structures. *Phys. Chem. Chem. Phys.*, **18**, 22089-22099.

560. Xiong, H., Chen, C.-K, Lee, K., Van Horn, R.M., Liu, Z., Ren, B., Quirk, R.P., Thomas, E.L., Lotz, B., Ho, R.-M., Zhang, W.-B. and Cheng, S.Z.D. (2011). Scrolled Polymer Single Crystals Driven by Unbalanced Surface Stresses: Rational Design and Experimental Evidence. *Macromolecules*, **44**, 7758-7766.

561. Yamano, M. (2011). Development of new drug and crystal polymorphs. In: *Pharmaceutical Process Chemistry*. pp. 401-419. Wiley-VCH Verlag GmbH & Co. KGaA, Weinheim.

562. Yang, X., Sarma, B. and Myerson, A.S. (2012). Polymorph Control of Micro/Nano-Sized Mefenamic Acid Crystals on Patterned Self-Assembled Monolayer Islands. *Cryst. Growth Des.*, **12**, 5521-5528.

563. Yang. H., Song, C.L., Lim, Y.X.S., Chen, W. and Heng, J.Y.Y. (2017). Selective crystallisation of carbamazepine polymorphs on surfaces with differing properties. *CrystEngComm*, **19**, 6573-6578.

564. Yang., S., Zhao, L., Yu, C., Zhou, X., Tang, J., Yuan, P., Chen, D. and Zhao, D. (2006). On the Origin of Helical Mesostructures. *J. Am. Chem. Soc.*, **128**, 10460-10466.

565. Ye, X., Liu, Y., Han, Q., Ge, C., Cui, S., Zhang, L., Zheng, X., Liu, G., Liu, J., Liu, D., and Tao, X. (2018). Microspacing In-Air Sublimation Growth of Organic Crystals. *Chem. Mater.*, **30**, 412-420.

566. Young, P.M., Chiou, H., Tee T., Traini, D., Chan, H., Thielmann F. and Brunett, D. (2007). The Use of Organic Vapor Sorption to Determine Low Levels of Amorphous Content in Processed Pharmaceutical Powders. *Drug Dev. Ind. Pharm.*, **33**, 91-97.

567. Yousuf, M. and Frawley, P.J. (2018). Experimental Evaluation of Fluid Shear Stress Impact on Secondary Nucleation in a Solution Crystallization of Paracetamol. *Cryst. Growth Des.*, **18**, 6843-6852.

568. Yu, L. (1995). Inferring Thermodynamic Stability Relationship of Polymorphs from Melting Data. *J. Pharm. Sci.*, **84**, 966-974.

569. Yu, Z.-B., Han, Y., Zhao, L., Huang, S., Zheng, Q.-Y., Lin, S., Córdova, A., Zou, Z. and Sun. J. (2012). Intergrown New Zeolite Beta Polymorphs with Interconnected 12-Ring Channels Solved by Combining Electron Crystallography and Single-Crystal X-ray Diffraction. *Chem. Mater.*, **24**, 3701-3706.

570. Yu, L. and Ng., K. (2002). Glycine Crystallization during Spray Drying: The pH Effect on Salt and Polymorphic Forms. *J. Pharm. Sci.*, **91**, 2367-2375.

571. Yuan, Y. and Lee, T. R. (2013). Contact Angle and Wetting Properties. In: *Surface Science Techniques*. pp. 3-34. Springer-Verlag, Heidelberg.

572. Yue, Y., Wu, F., Choi, H., Shaver, C. Sanguino, M., Staffel, J. and Liang. H. (2017). Electrochemical synthesis and hydrophilicity of micro-pored aluminum foil. *Surf. Coat. Technol.*, **309**, 523-530.

573. Yun, Y., Zou, X., Hovmöller, S. and Wan, W. (2015). Three-dimensional electron diffraction as a complementary technique to X-ray powder diffraction for phase identification and structure solution of powders. *IUCrJ*, **2**, 267-282.

574. Zeng, D., Ren, M., Bao, S.-S., Feng, J.-S., Li, L. and Zheng, L.-M. (2015). pH-controlled polymorphism in a layered dysprosium phosphonate and its impact on the magnetization relaxation. *Chem. Commun.*, **51**, 2649-2652.

575. Zhang, C., Kersten, K.M., Kampf, J.W. and Matzger, A.J. (2018a). Solid-State Insight Into the Action of a Pharmaceutical Solvate: Structural, Thermal, and Dissolution Analysis of Indinavir Sulfate Ethanolate. *J. Pharm. Sci.*, **107**, 2731-2734.

576. Zhang, S., Lee, T.W.Y. and Chow, A.H.L. (2016). Crystallization of Itraconazole Polymorphs from Melt. *Cryst. Growth Des.*, **16**, 3791-3801.

577. Zhang, T.H. and Liu, X.Y. (2007). How Does a Transient Amorphous Precursor Template Crystallization. *J. Am. Chem. Soc.*, **129**, 13520-13526.

578. Zhang, J., Liu, A., Han, Y., Ren, Y., Gong, J., Li, W. and Wang, J. (2011). Effects of Self-Assembled Monolayers on Selective Crystallization of Tolbutamide. *Cryst. Growth Des.*, **11**, 5498-5506.

579. Zhang, Q., Lu, L., Dai, W. and Mei, X. (2013). New Polymorphs of Huperzine A: Preparation, Structures, and Physicochemical Properties of Anhydrous Crystal Forms. *Cryst. Growth Des.*, **13**, 2198-2207.

580. Zhang, F., Mohammadi, E., Luo, X., Strzalka, J., Mei, J. and Diao, Y. (2018b). Critical Role of Surface Energy in Guiding Crystallization of Solution-Coated Conjugated Polymer Thin Films. *Langmuir*, **34**, 1109-1122.

581. Zhang, G.G.Z., Paspal, S.Y.L., Suryanarayanan, R. and Grant, D.J.W. (2003). Racemic species of sodium ibuprofen: Characterization and polymorphic relationships. *J. Pharm. Sci.*, **92**, 1356-1366.

582. Zhang, Q., Lu, L., Dai, W. and Mei, X. (2014). Polymorphism and isomorphism of Huperzine A solvates: structure, properties and form transformation. *CrystEngComm*, **16**, 1919-1926.

583. Zhong, Z., Yang, X., Wang, B.-H., Yao, Y.-F., Guo, B. Yu, L., Huang, Y. and Xu, J. (2019). Solvent-polymer guest exchange in a carbamazepine inclusion complex: structure, kinetics and implication for guest selection. *CrystEngComm*, **21**, 2164-2173.

584. Zhu, M., Wang, Y., Li, F., Bao, Y., Huang, X., Shi, H. and Hao, H. (2019). Theoretical Model and Experimental Investigations on Solution-Mediated Polymorphic Transformation of Theophylline: From Polymorph I to Polymorph II. *Crystals*, **9**, 260.

585. Zhu, Q., Shtukenberg, A.G., Carter, D.J., Yu, T.-Q., Yang, J., Chen, M., Raiteri, P., Oganov, A.R., Pokroy, B., Polishchuk, I., Bygrave, P.J., Day, G.M., Rohl, A.L., Tuckerman, M.E. and Kahr, B. (2016). Resorcinol Crystallization from the Melt: A New Ambient Phase and New “Riddles”. *J. Am. Chem. Soc.*, **138**, 4881-4889.

586. Zink, F.E. (1997). X-ray Tubes. *RadioGraphics*, **17**, 1259-1268.

587. Zografi, G. and Kontny, M.J. (1995). Sorption of Water by Solids. In: *Physical Characterization of Pharmaceutical Solids. ed. H.G. Brittain*. pp. 385-418. Marcel Dekker Inc., New York.

Appendices

Appendix A4 (Chapter 4)

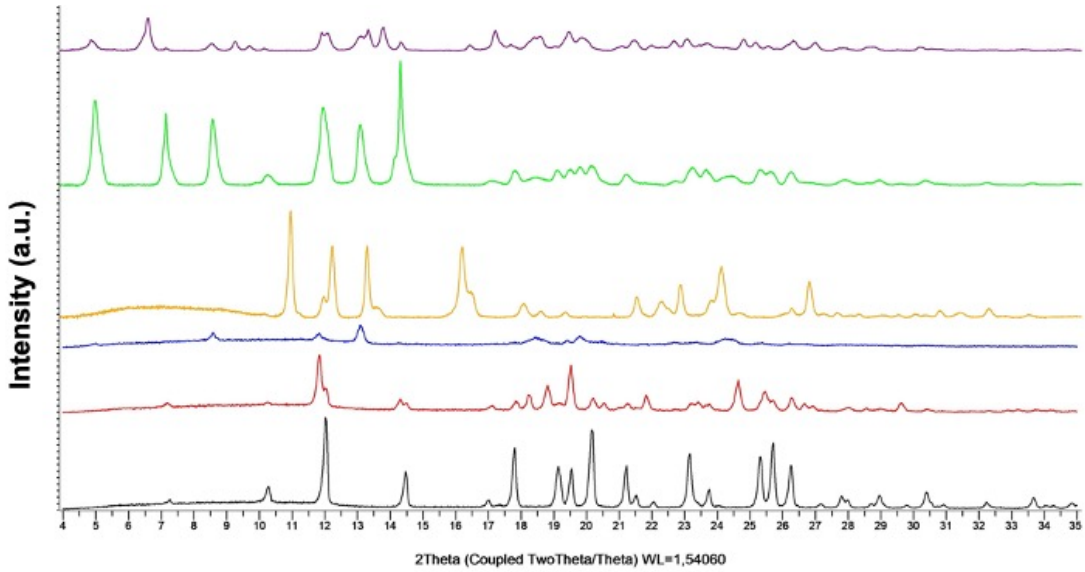

Figure A4.1: Distinct types of XRPD patterns observed in solid-state screening studies of OXCBZ. Black – form I; red – mixture of forms I and II; blue – mixture of forms I, II and II; orange – mixture of form I and unidentified form; green – mixture of forms I, II and III; purple – mixture of forms I, III and unidentified form.

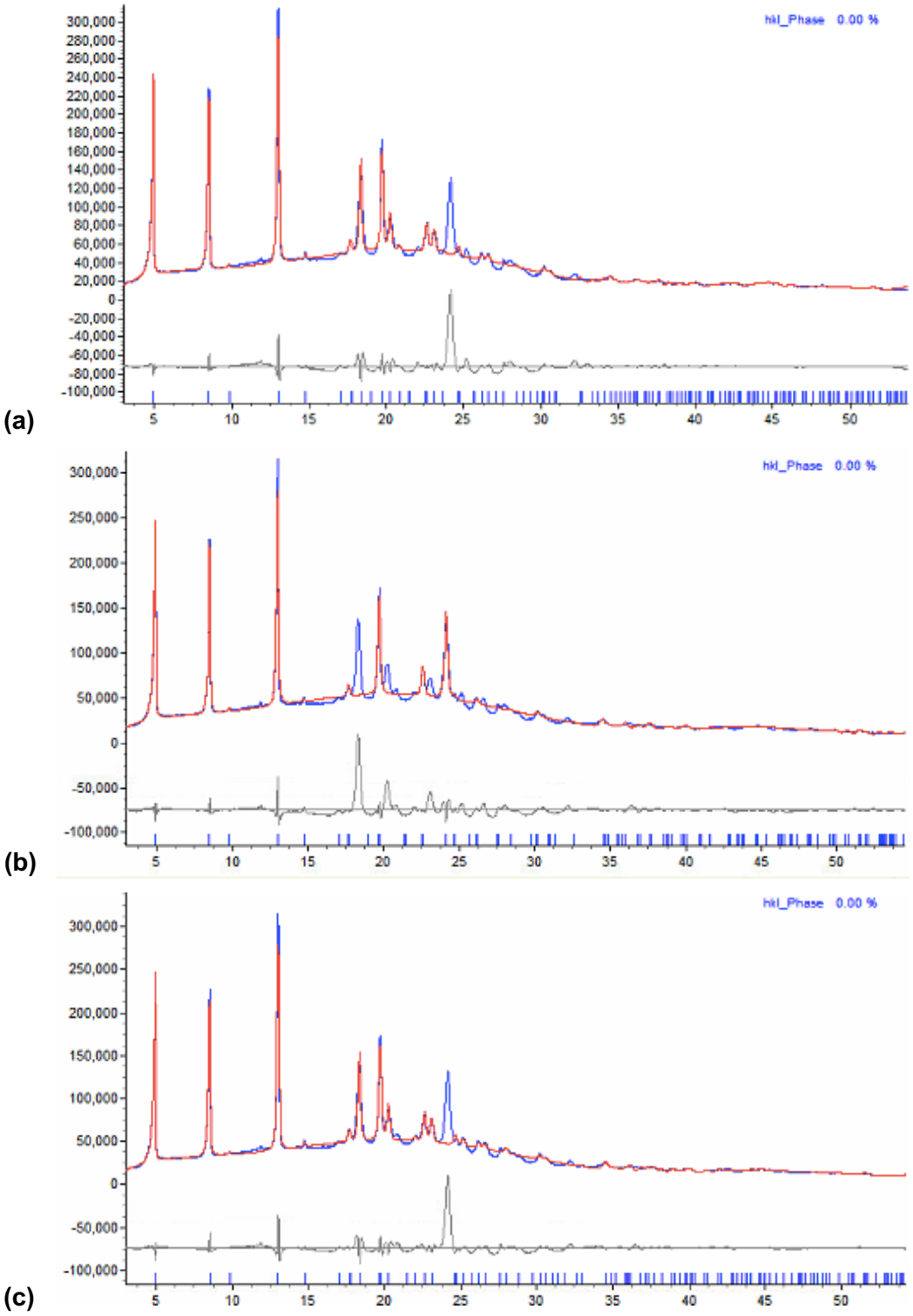

Figure A4.2: Pawley fits of OXCBZ material obtained via fast evaporation from 50:50 (v/v) ethanol/toluene mixture. Pawley refinements were performed using the predicted candidates for OXCBZ III as starting models in the following order: (a) a165, (b) a722 and (c) a1858.

Appendix A5 (Chapter 5)

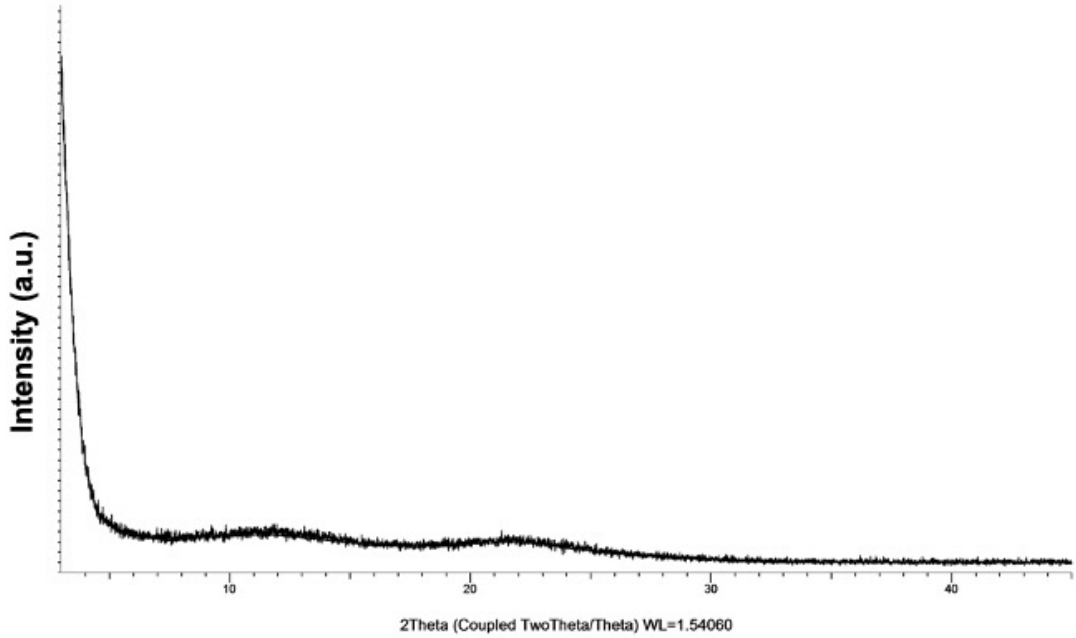

Figure A5.1: Representative XRPD pattern of amorphous OXCBZ material prepared via fast evaporation from 2-methoxyethanol at 70°C and 150 rpm using the Crissy platform.

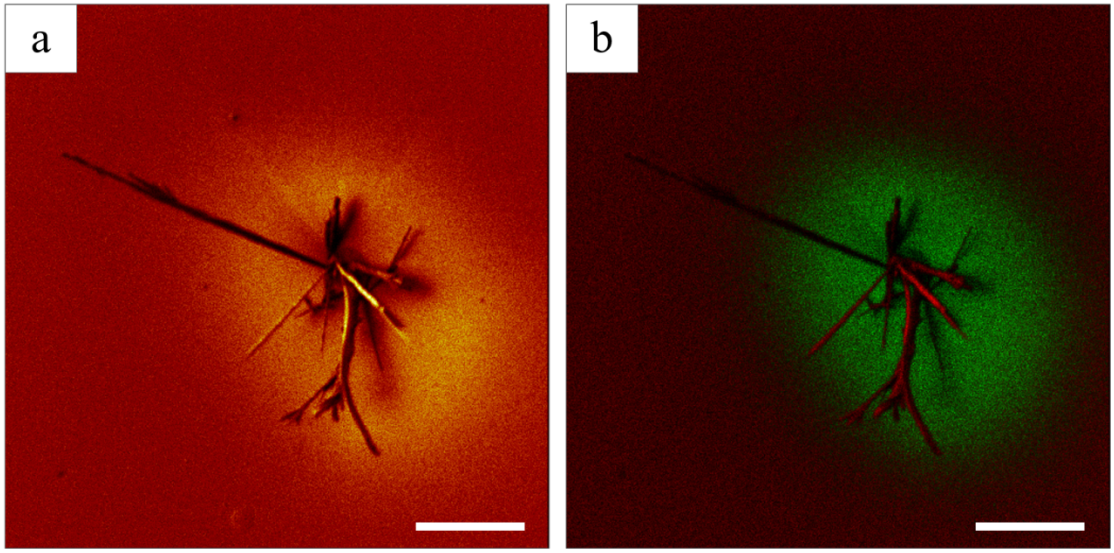

Figure A5.2: ToF-SIMS total ion image (a) and colour overlay image (b) of OXCBZ crystals grown on silver-coated glass. In (b), red represents OXCBZ secondary ions $C_{15}H_{13}N_2O_2^+$ ($[M+H]^+$, *m/z* 253.1) and $C_{14}H_{12}$ (*m/z* 180.1), and green represents silver secondary ions Ag^+ (*m/z* 106.9) and $^{109}Ag^+$ (*m/z* 108.9). The scale bar is 20 μm for both images.

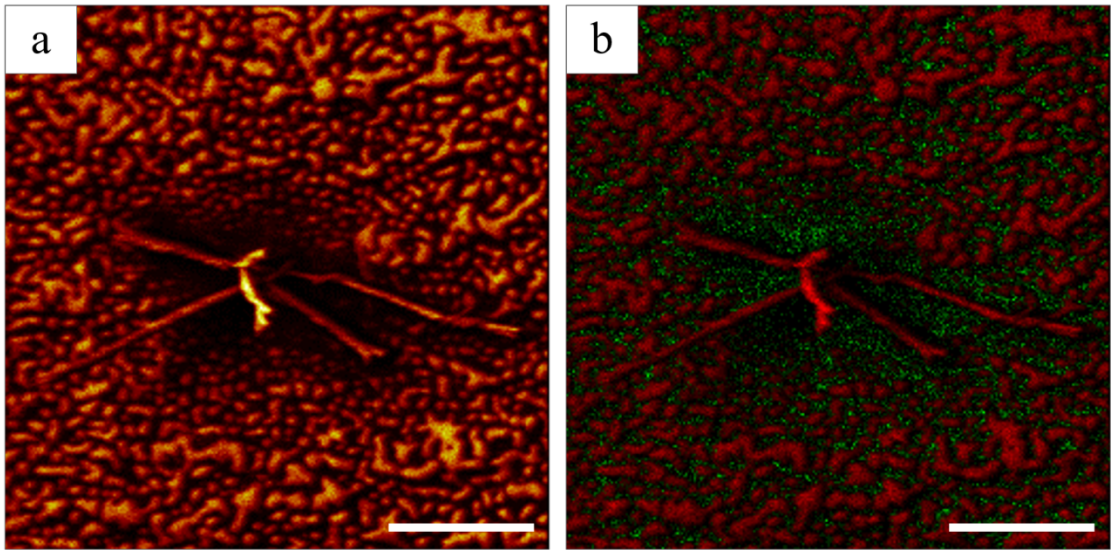

Figure A5.3: ToF-SIMS total ion image (a) and colour overlay image (b) of OXCBZ crystals grown on aluminium foil. In (b), red represents OXCBZ secondary ions $C_{15}H_{13}N_2O_2^+$ ($[M+H]^+$, *m/z* 253.1) and $C_{14}H_{12}$ (*m/z* 180.1), and green represents aluminium secondary ion Al^+ (*m/z* 26.98). The scale bar is 20 μm for both images.

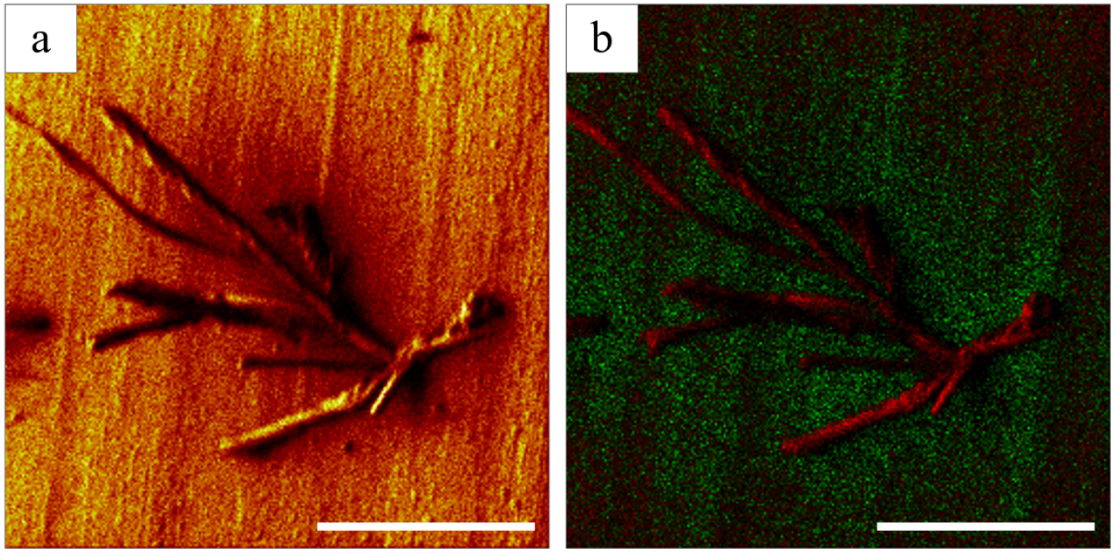

Figure A5.4: ToF-SIMS total ion image (a) and colour overlay image (b) of OXCBZ crystals grown on copper foil. In (b), red represents OXCBZ secondary ions $C_{15}H_{13}N_2O_2^+$ ($[M+H]^+$, *m/z* 253.1) and $C_{14}H_{12}$ (*m/z* 180.1), and green represents copper secondary ions Cu^+ (*m/z* 62.9) and $^{65}Cu^+$ (*m/z* 64.9). The scale bar is 20 μm for both images.

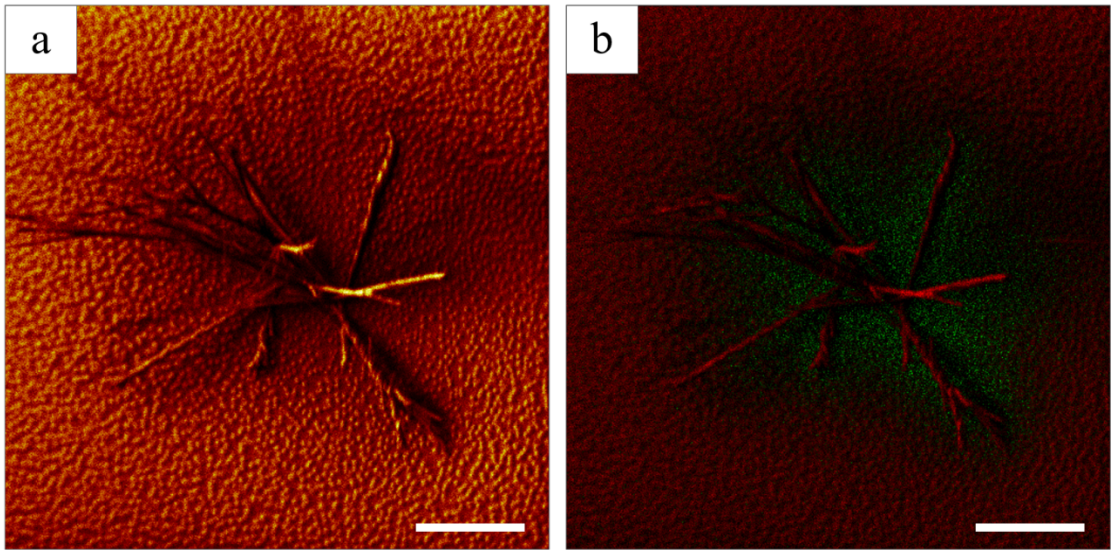

Figure A5.5: ToF-SIMS total ion image (a) and colour overlay image (b) of OXCBZ crystals grown on copper-coated glass. In (b), red represents OXCBZ secondary ions $C_{15}H_{13}N_2O_2^+$ ($[M+H]^+$, *m/z* 253.1) and $C_{14}H_{12}$ (*m/z* 180.1), and green represents copper secondary ions Cu^+ (*m/z* 62.9) and $^{65}Cu^+$ (*m/z* 64.9). The scale bar is 20 μm for both images.

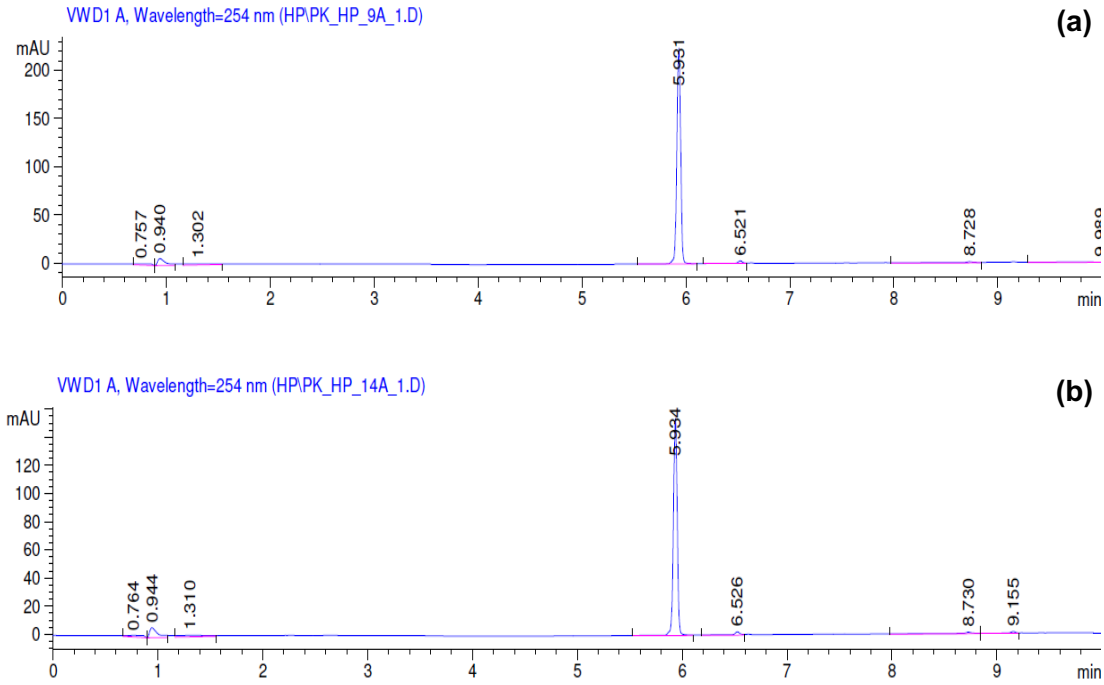

Figure A5.6: Representative UV chromatograms of (a) OXCBZ starting material obtained from Molekula and (b) OXCBZ form III material crystallised from 50:50 v/v ethanol/toluene (b).

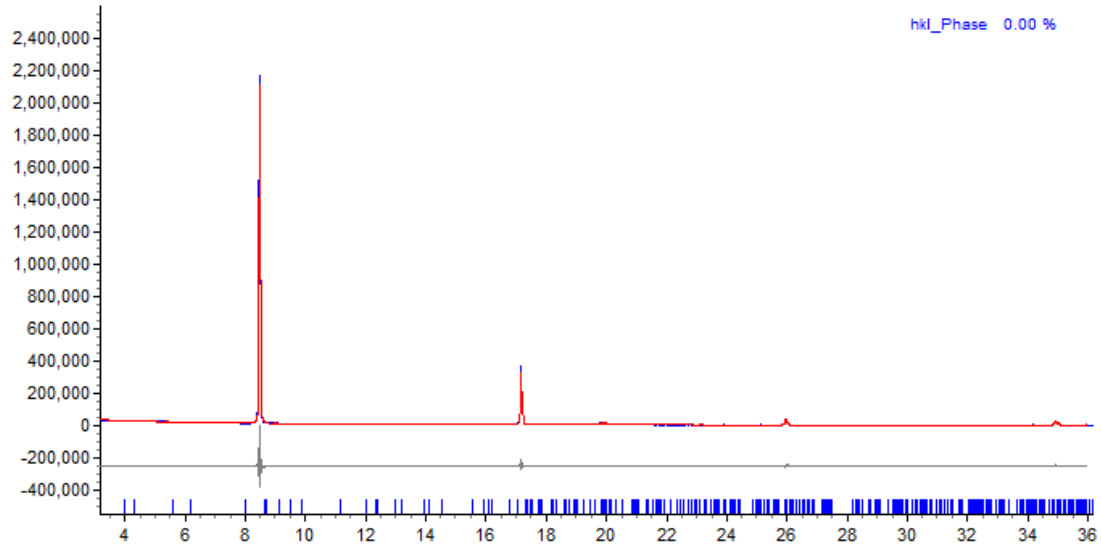

Figure A5.7: Pawley fit of XRPD data of CBZ material grown on silver foil by vapour deposition over 18.5 hours. The material obtained from the vapour phase was found to diffract poorly. The refinement was performed against the unit cell parameters of CBZ form I. The residual values obtained for the Pawley fit were R_{wp} = 6.98% and R_p = 5.07% with refined unit cell parameters of *a* = 5.133 (5) Å, *b* = 20.642 (17) Å, *c* = 22.185 (4) Å, α = 84.080 (15)°, β = 88.445 (14)° and γ = 85.243 (8)°.

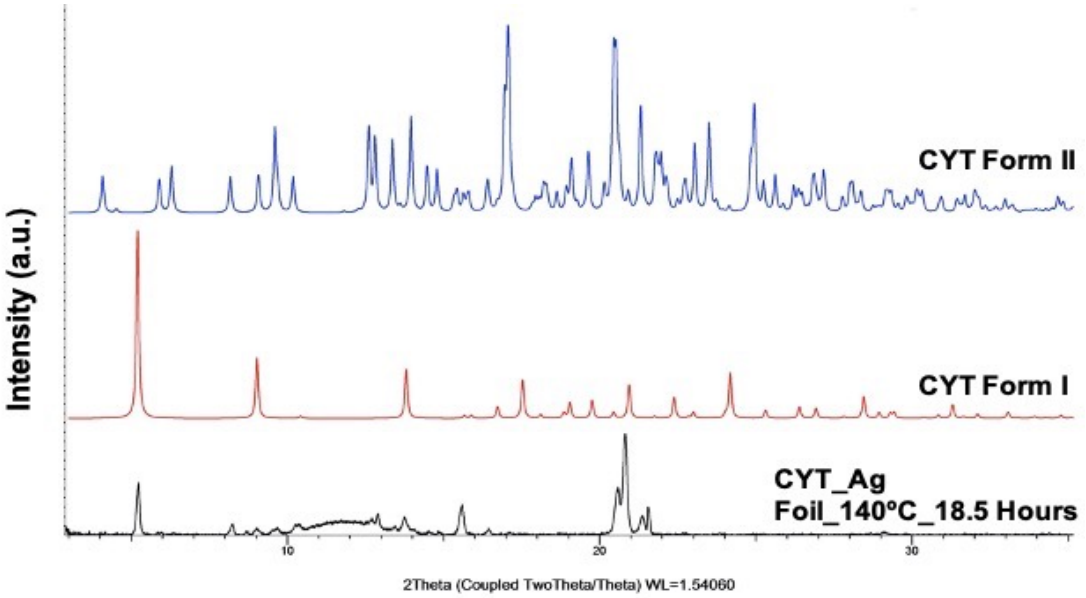

Figure A5.8: Comparison of XRPD pattern representative of the CYT material obtained via vapour deposition onto silver foil over 18.5 hours with simulated patterns of CYT form I and II. An unidentified impurity peak is present at 9.8° *2θ*.

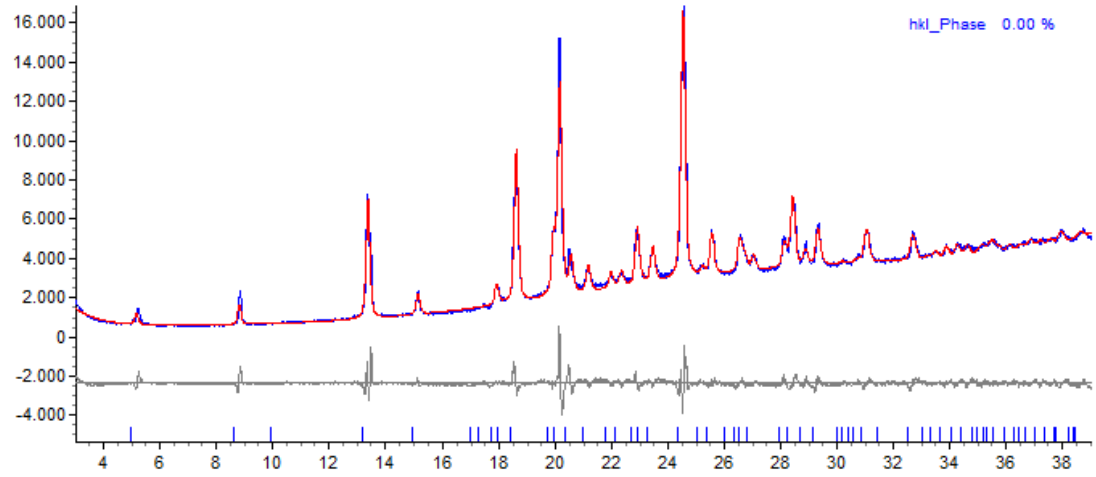

Figure A5.9: Pawley fit of XRPD data of CBZ material grown from 50:50 v/v ethanol/toluene mixture using fast evaporation. The refinement was performed against the cell parameters of CBZ form II. Residual values for the Pawley fit were R_{wp} = 5.55% and R_p = 3.57% with refined cell parameters are a = b = 35.541 (16) Å and c = 5.284 (2) Å.

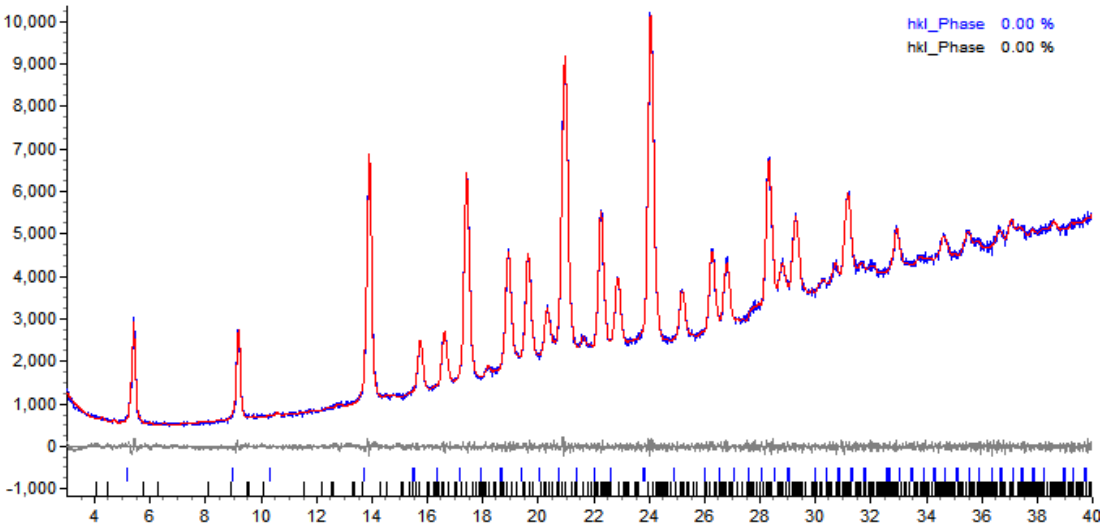

Figure A5.10: Pawley fit of XRPD data of CYT material grown from 50:50 v/v ethanol/toluene mixture using fast evaporation. The residual values for the Pawley fit were R_{wp} = 2.08% and R_p = 1.49% with refined cell parameters of a = b = 34.21 (5) Å, c = 5.825 (15) Å for form I crystals and a = 5.89 (3) Å, b = 19.98 (3) Å, c = 21.93 (5) Å, α = 85.05 (12)°, β = 85.1 (4)°, γ = 85.5 (3)° for form II crystals. The blue tick marks represent calculated diffraction peaks based on the refined unit cell parameters of CYT form I and the black tick marks correspond to calculated diffraction peaks based on the refined cell parameters of CYT form II.

Appendix A6 (Chapter 6)

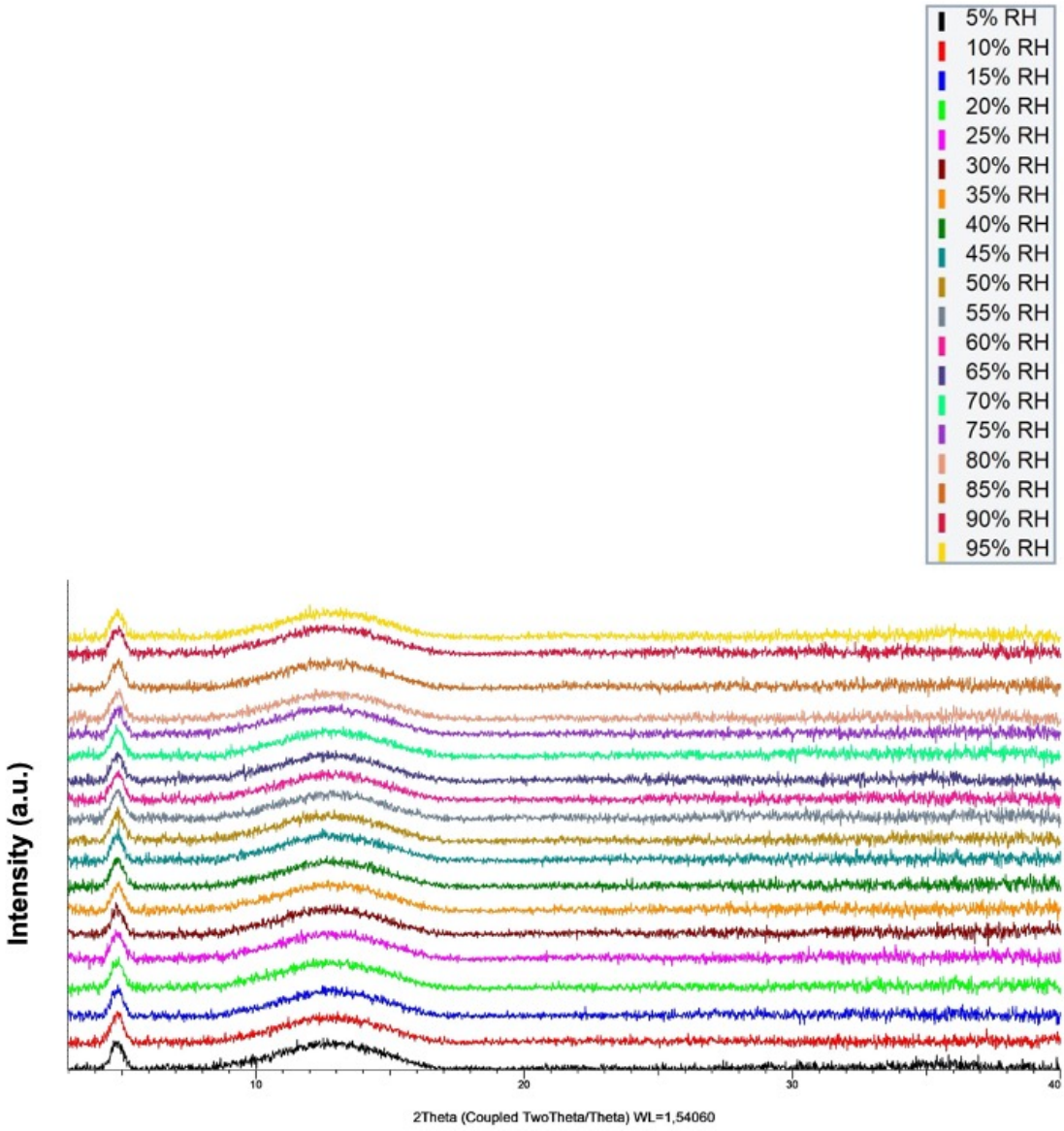

Figure A6.1: VH-XRPD analysis of TAEVC1 starting material. Background-subtracted patterns are presented in increasing % RH order from bottom to top. The broad diffraction peak observed at ≈ 4.9° *2θ* originates from the sample holder used for the analysis.

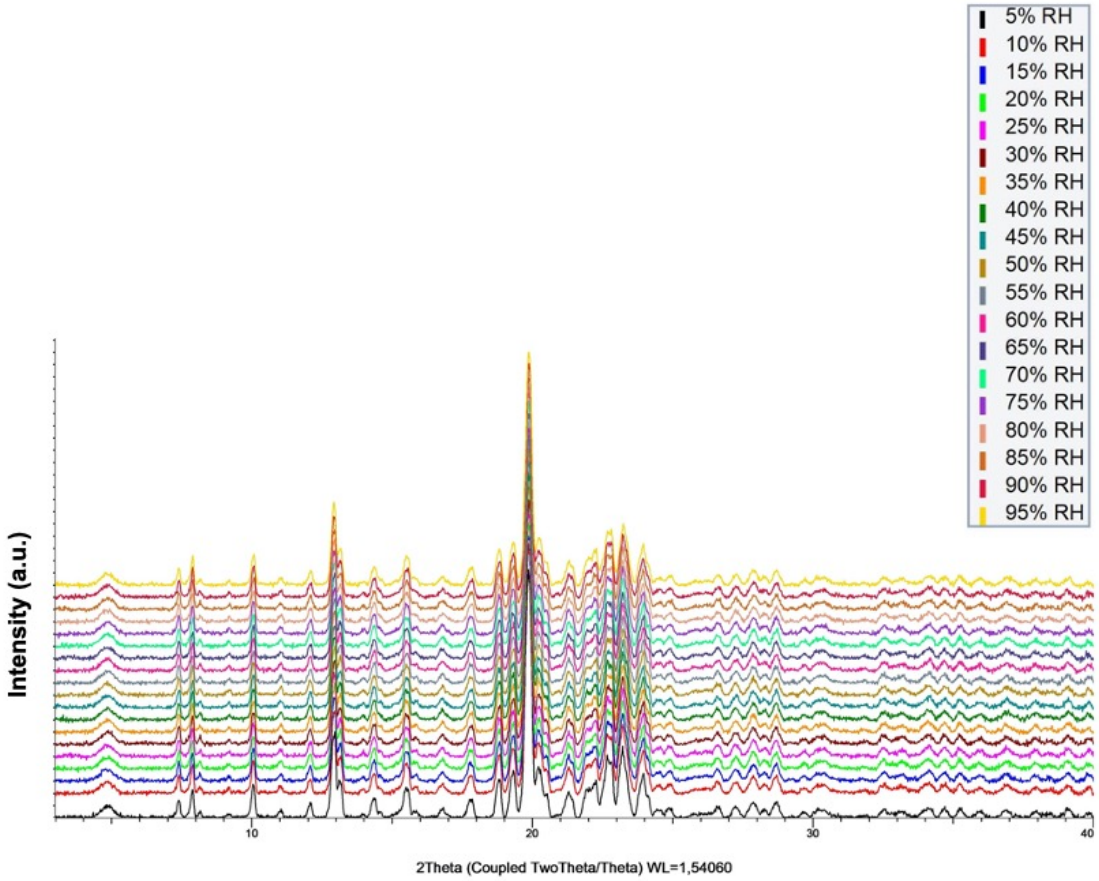

Figure A6.2: VH-XRPD analysis of TAEVC2 starting material. Background-subtracted patterns are presented in increasing order of % RH from bottom to top. The broad diffraction peak observed at ≈ 4.9° *2θ* originates from the sample holder used for the analysis.

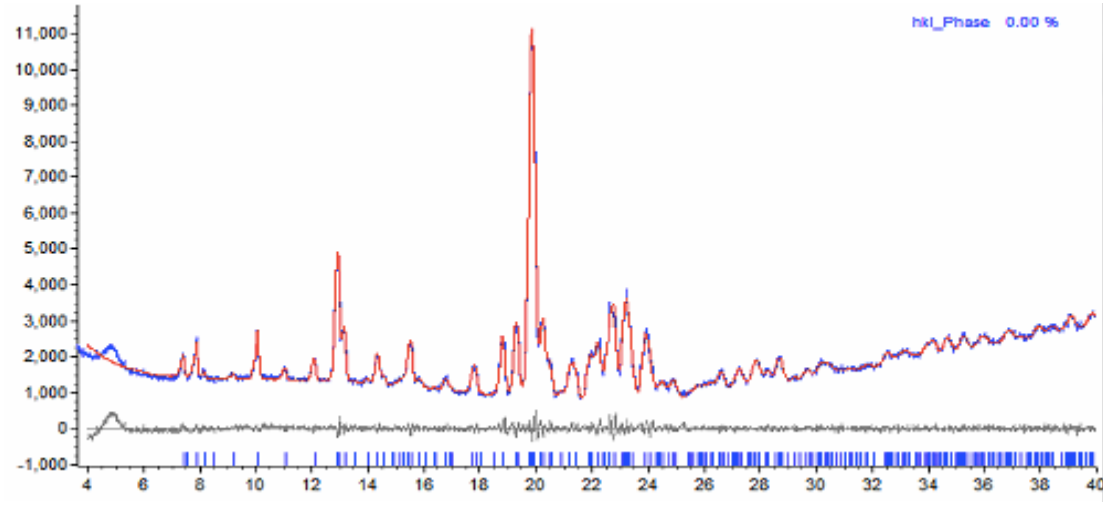

Figure A6.3: Pawley fit of TAEVC2 starting material at 5% RH. The residual values obtained for the Pawley fit were R_{wp} = 3.99% and R_p = 2.81% and the refined unit cell parameters were $a = b$ = 13.728 (6) Å and c = 64.78 (3) Å.

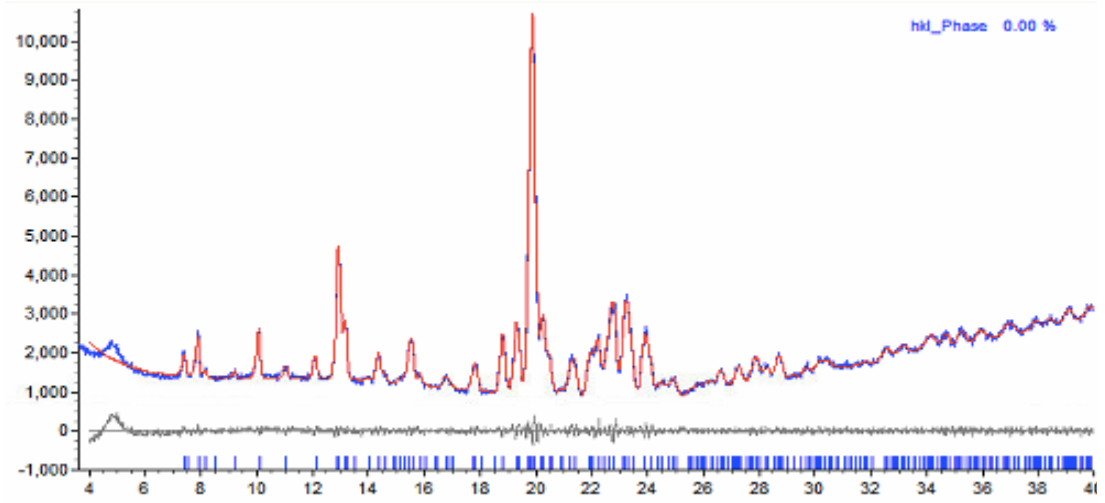

Figure A6.4: Pawley fit of TAEVC2 starting material at 95% RH. The residual values obtained for the Pawley fit were R_{wp} = 3.72% and R_p = 2.60% and the refined unit cell parameters were $a = b$ = 13.726 (8) Å and c = 64.71 (5) Å.

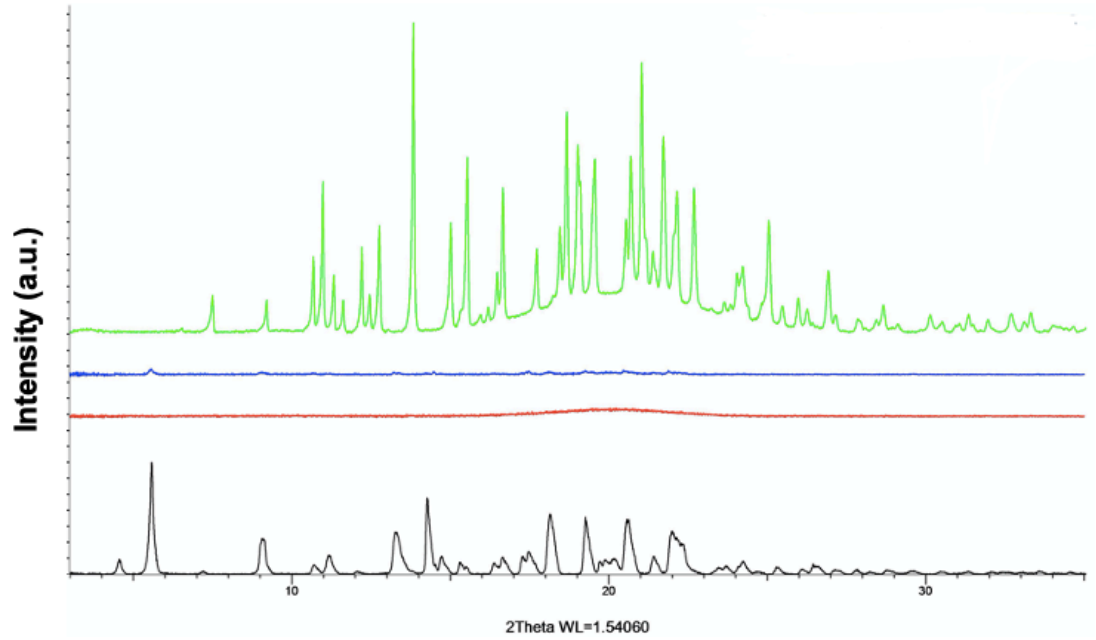

Figure A6.5: Representative XRPD patterns corresponding to different experimental outcomes observed in the solvent-based screen of EVC. Black - solvated material recrystallised from 1-butanol which was found to be isostructural to EVC – TBA; red - amorphous material sample obtained from furfural solution; blue - poorly crystalline material recrystallised from diethyl ether; green – unionised methanol solvate of EVC. All of the patterns depicted were derived from samples prepared by evaporation at room temperature.

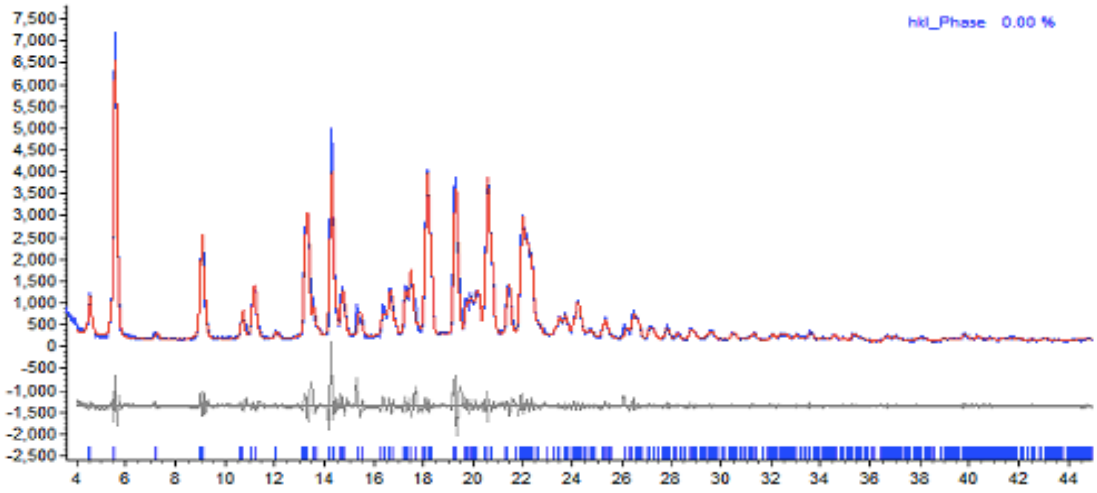

Figure A6.6: Pawley fit of EVC material recrystallised form 1-butanol. The residual values obtained for the Pawley fit were R_{wp} = 11.97% and R_p = 8.30% and the refined unit cell parameters were a = 20.044 (13) Å, b = 9.188 (7) Å and c = 20.325 (13) Å and β = 104.99 (2)°. The refinement was performed in the $P2_1$ space group.

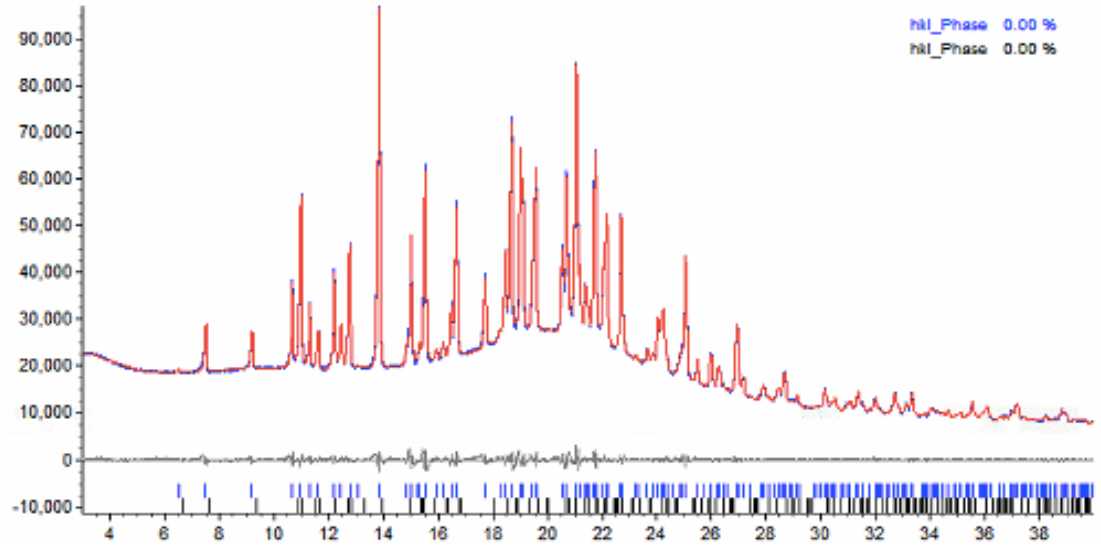

Figure A6.7: Pawley fit of EVC material obtained via cooling crystallisation and evaporation from methanol at room temperature and 50°C. The residual values obtained for the Pawley fit were R_{wp} = 1.74% and R_p = 1.24% and the refined unit cell parameters were *a* = 8.578 (3) Å, *b* = 16.572 (7) Å, *c* = 23.596 (9) Å for the methanol solvate of EVC and *a* = 8.63 (4) Å, *b* = 16.30 (10) Å, *c* = 23.05 (14) Å for the EVC monohydrate. The refinement was performed in the $P2_12_12_1$ space group. Blue tick marks indicate calculated peak positions for the methanol solvate and black tick marks represent calculated peak positions for the monohydrate.

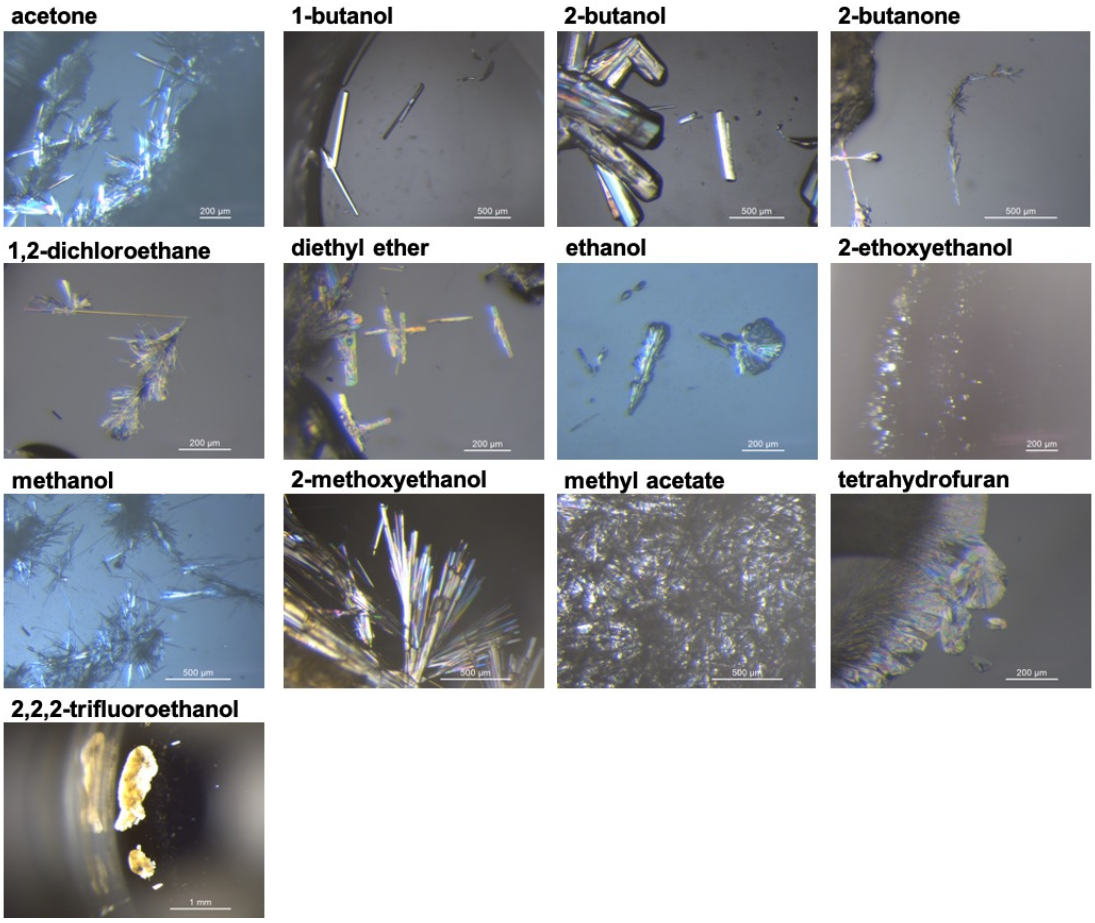

Figure A6.8: Representative optical micrographs of crystalline EVC samples prepared via evaporation experiments.

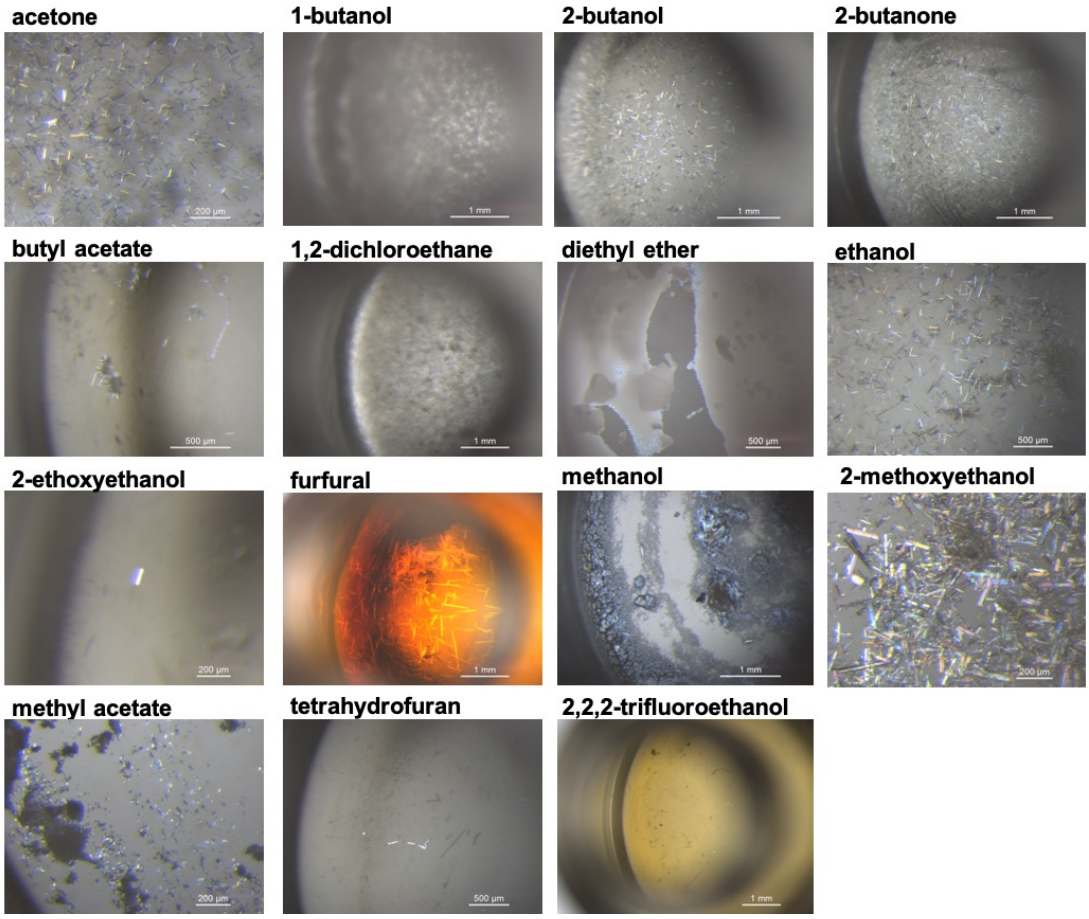

Figure A6.9: Representative optical micrographs of crystalline EVC samples prepared via cooling crystallisation experiments.

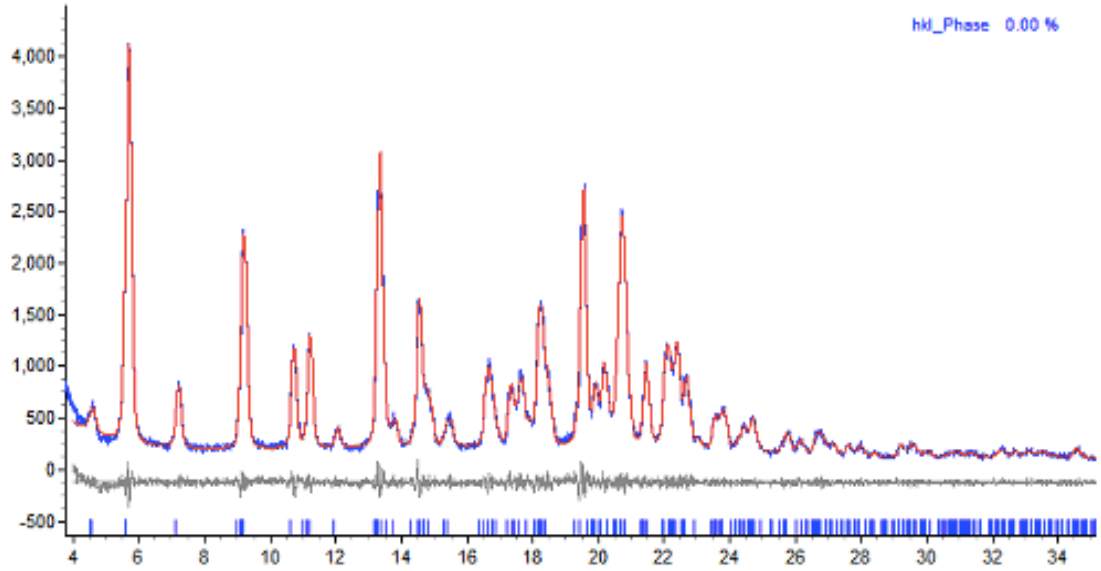

Figure A6.10: Pawley fit of EVC material obtained from attempted supercritical fluid extraction. Residual values for the Pawley fit were R_{wp} = 6.54% and R_p = 4.84%. The refined unit cell parameters were a = 20.195 (10) Å, b = 9.210 (4) Å, c = 19.934 (10) Å and β = 103.596 (12)°. The refinement was performed in the $P2_1$ space group.

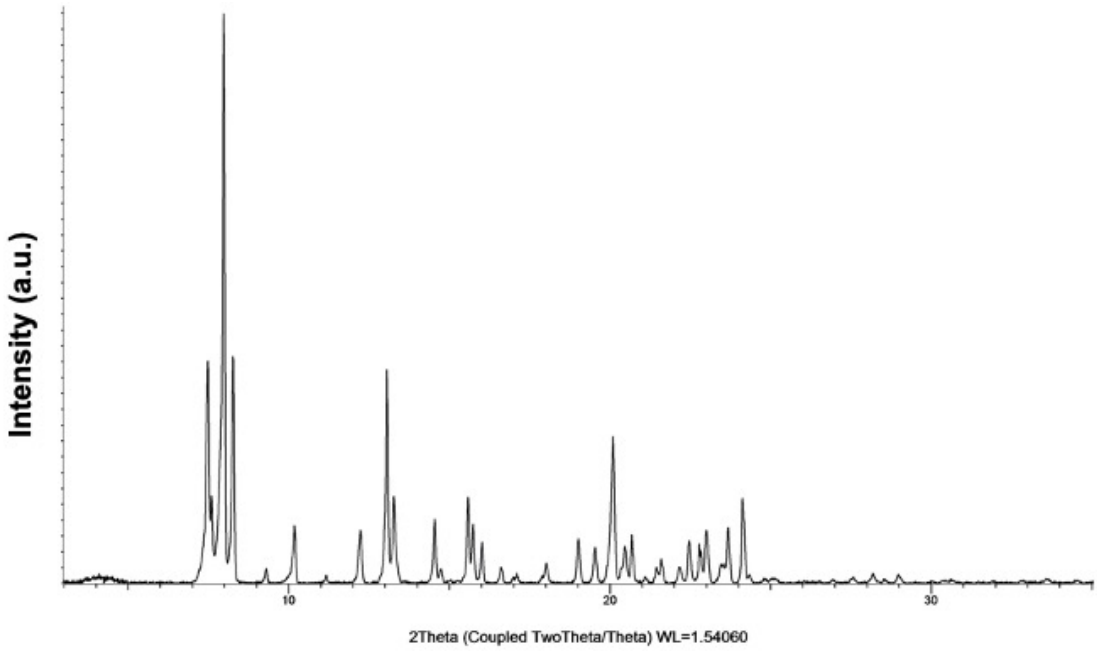

Figure A6.11: Representative XRPD pattern of solvated samples of TAEVC1 and TAEVC2 found to be isostructural to the TAEVC2 starting material. The pattern depicted corresponds to a solvated sample of TAEVC2 recrystallised from acetonitrile.

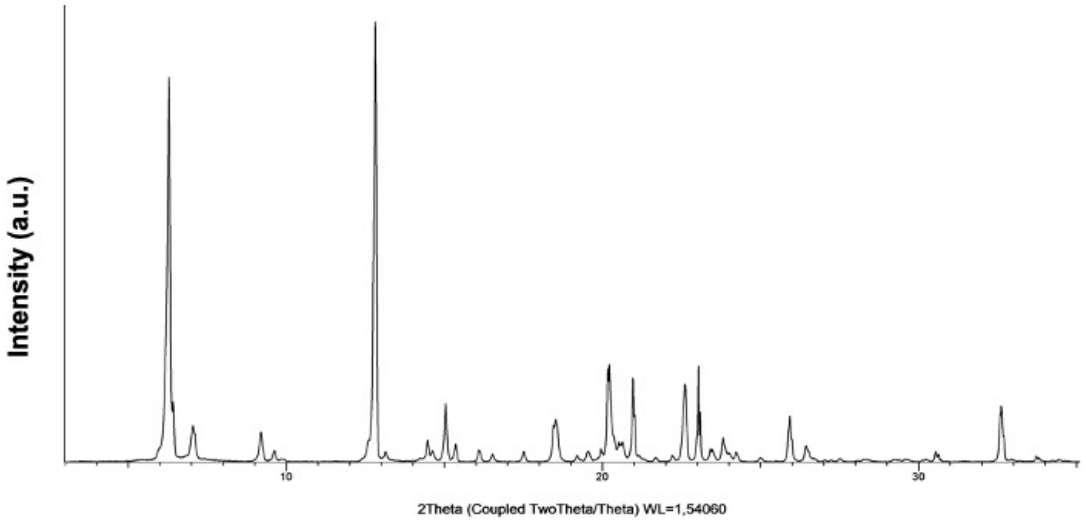

Figure A6.12: Representative XRPD pattern of solvated materials of TAEVC1 and TAEVC2 crystallising in the *C*2 space group. The pattern depicted corresponds to a sample prepared by recrystallising TAEVC1 from butyl acetate.

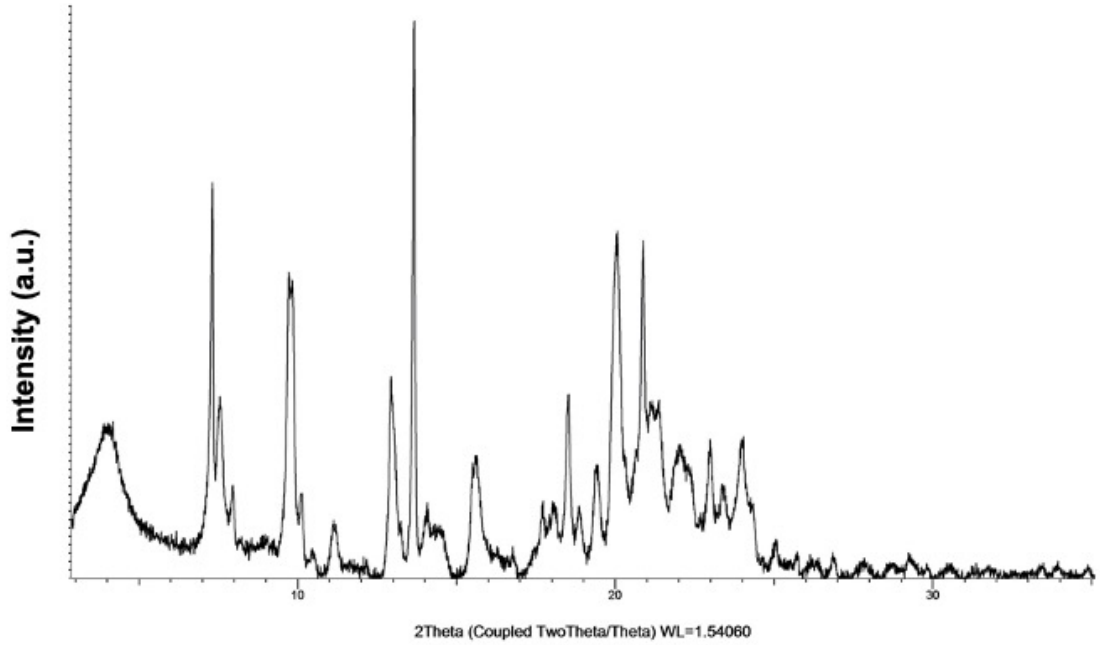

Figure A6.13: Representative XRPD pattern of solvated samples of TAEVC1 crystallised from 1,2-dichloroethane.

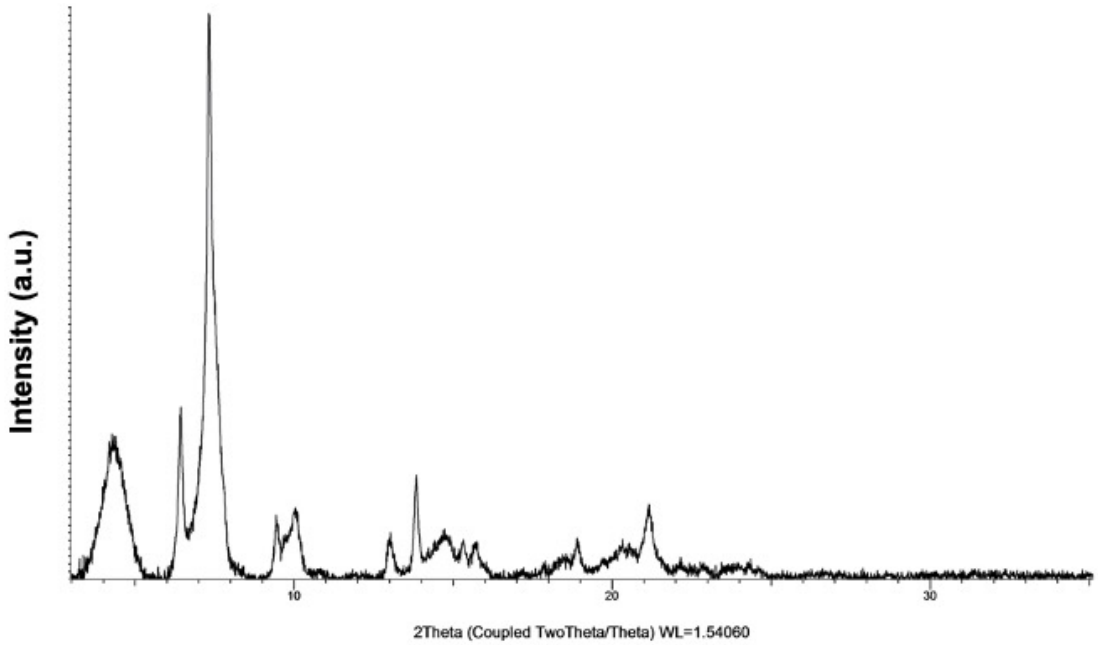

Figure A6.14: Representative XRPD pattern of solvated samples of TAEVC1 crystallised from diethyl ether.

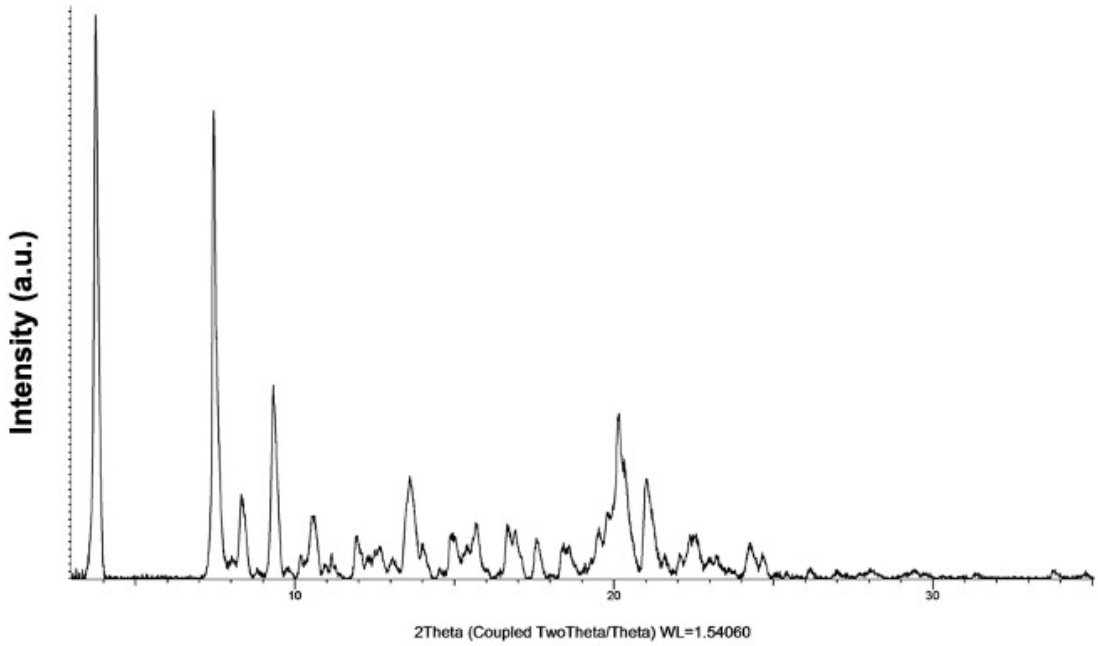

Figure A6.15: Representative XRPD pattern of solvated samples of TAEVC1 crystallised from furfural.

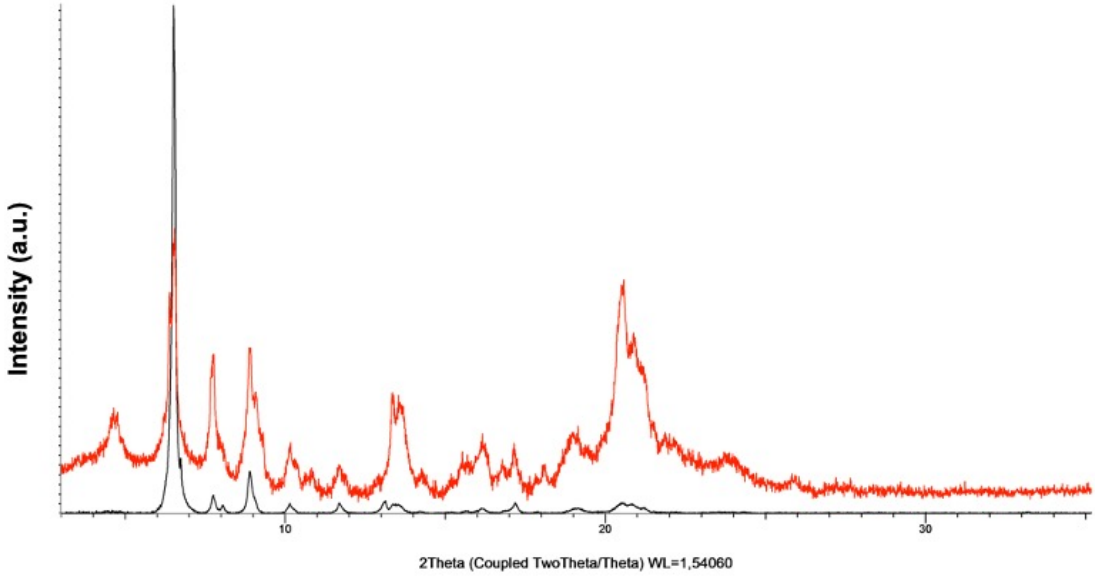

Figure A6.16: Representative XRPD patterns of solvated samples of TAEVC1 (black) and TAEVC2 (red) recrystallised from toluene.

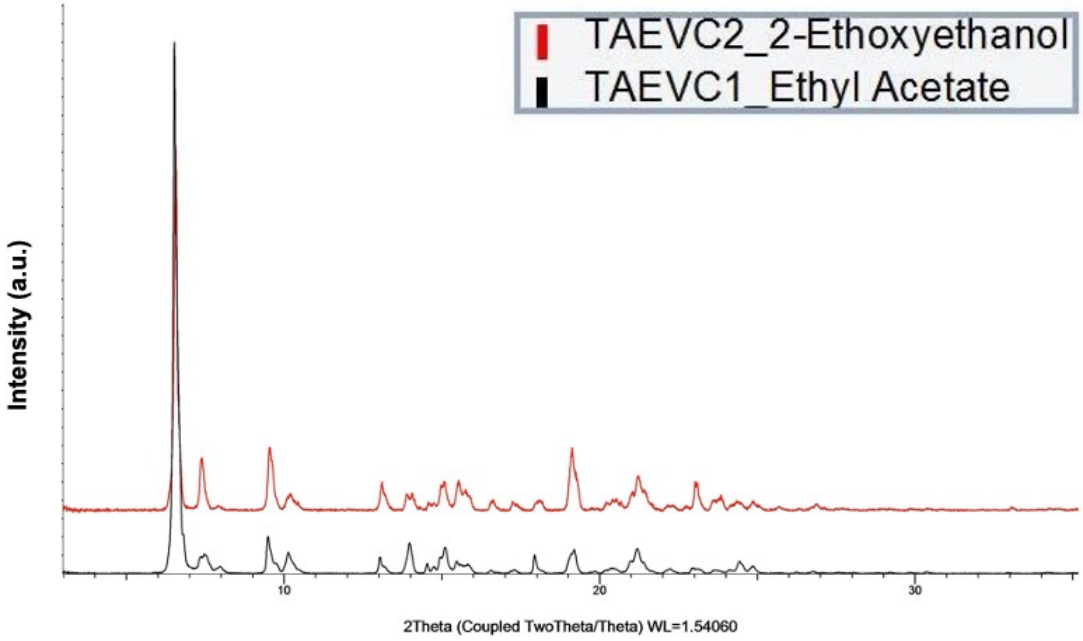

Figure A6.17: Representative XRPD patterns of solvated samples of TAEVC1 and TAEVC2 recrystallised from 2-ethoxyethanol and ethyl acetate.

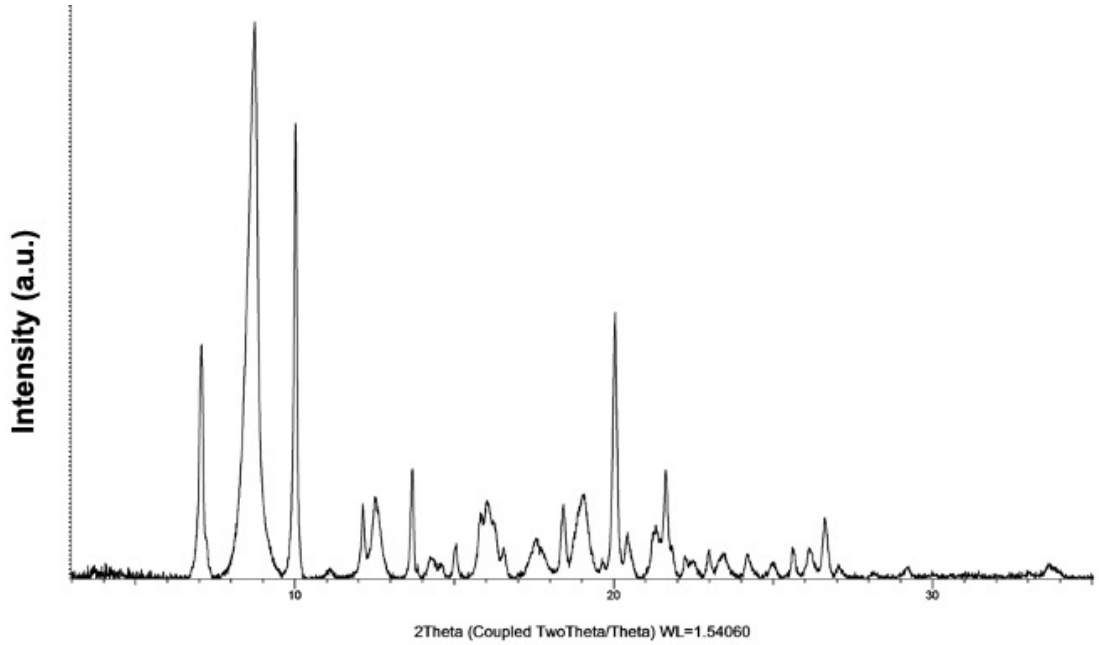

Figure A6.18: Representative XRPD pattern of anhydrous TAEVC3 samples recrystallised from ethyl acetate.

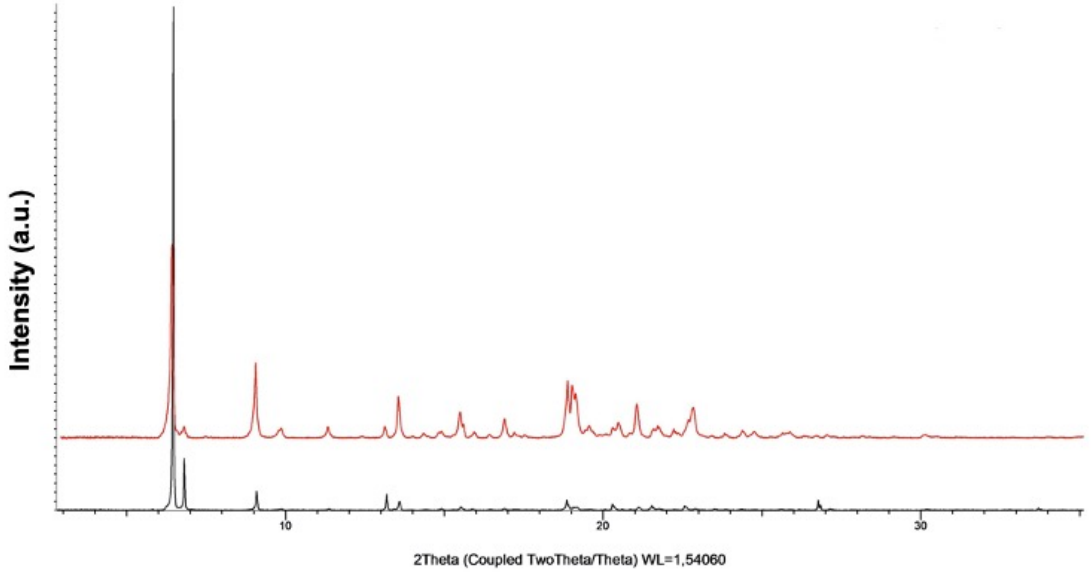

Figure A6.19: Representative XRPD patterns of solvated samples of TAEVC3 recrystallised from 1,4-dioxane (black) and tetrahydrofuran (red).

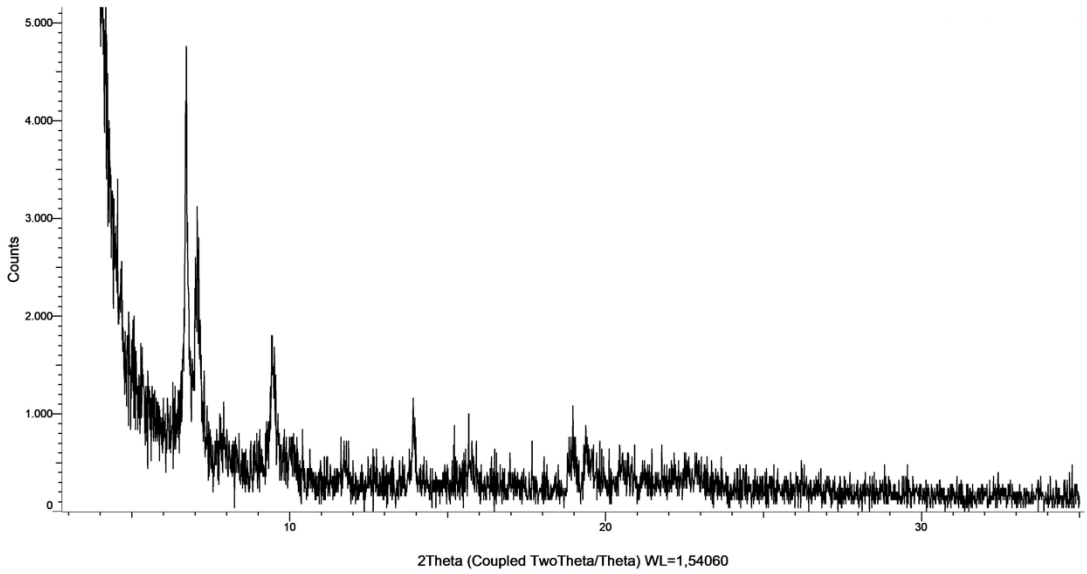

Figure A6.20: Representative XRPD pattern of solvated samples of TAEVC3 recrystallised from 1,2-dichloroethane.

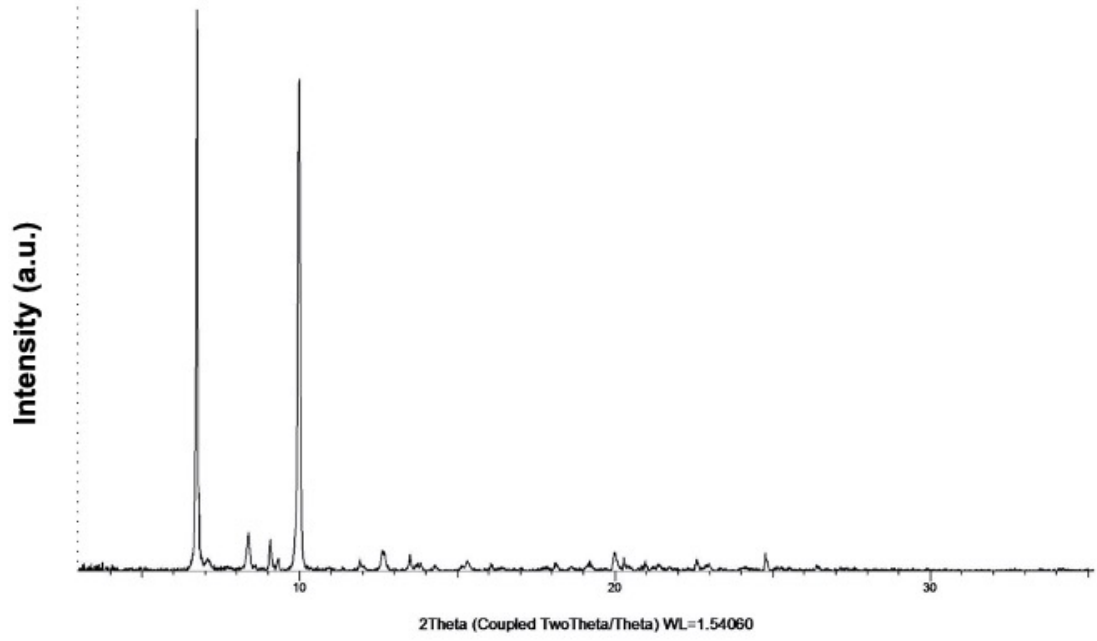

Figure A6.21: Representative XRPD pattern of solvated samples of TAEVC3 recrystallised from acetonitrile.

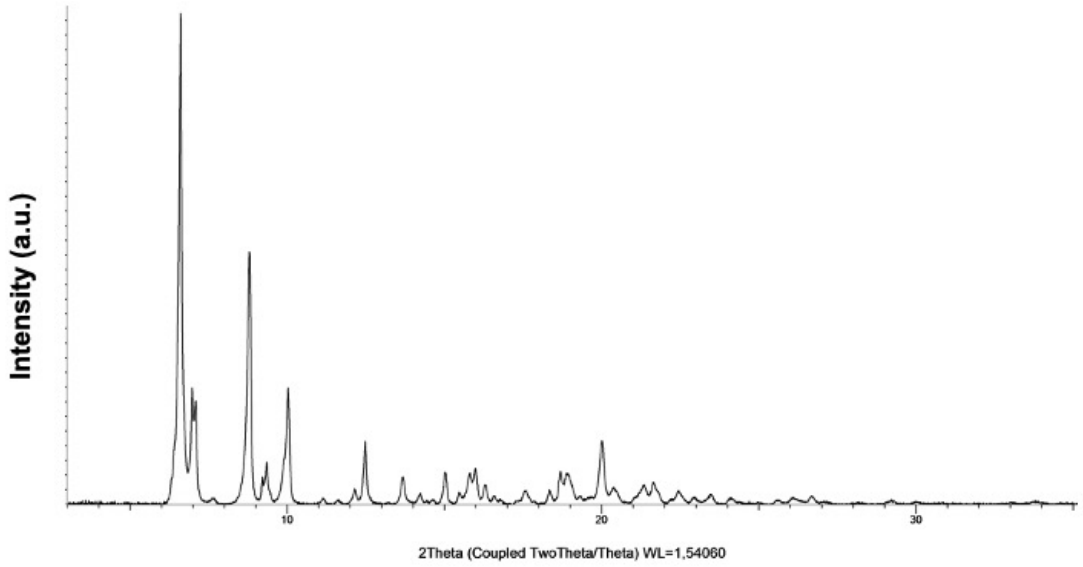

Figure A6.22: Representative XRPD pattern of solvated samples of TAEVC3 recrystallised from 2-butanol.

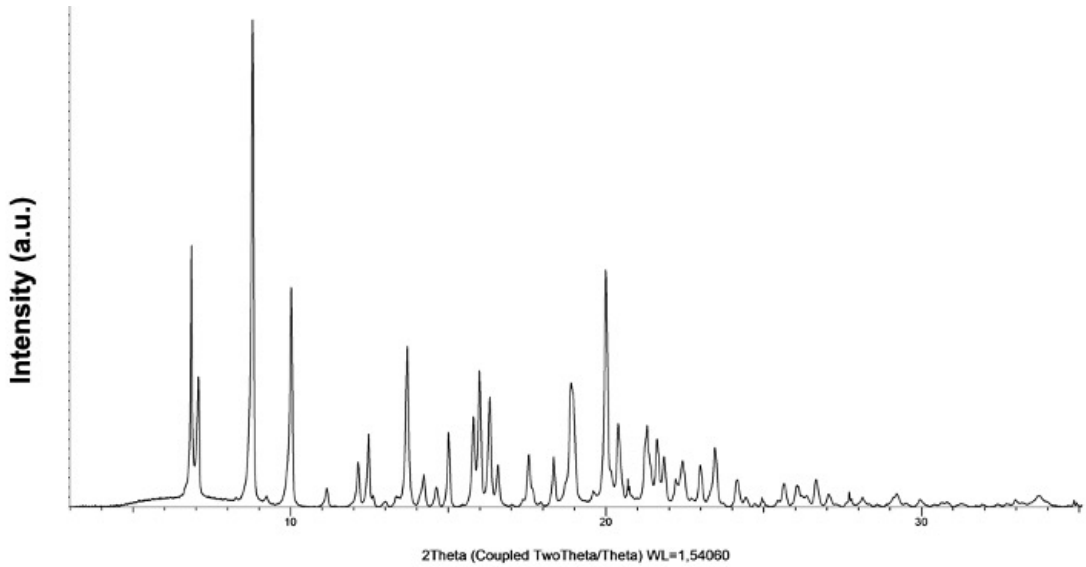

Figure A6.23: Representative XRPD pattern of solvated samples of TAEVC3 recrystallised from methanol.

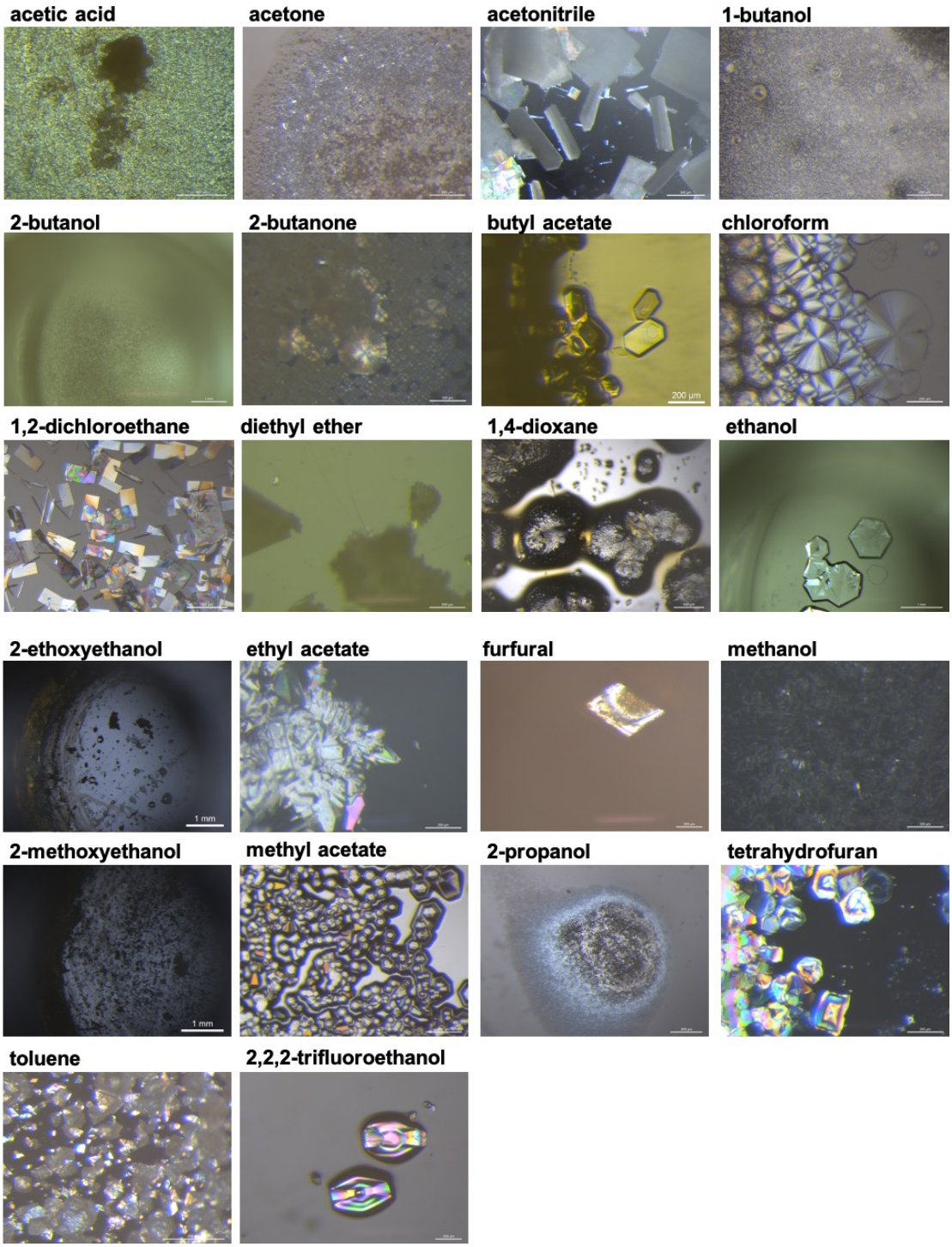

Figure A6.24: Representative optical micrographs of TAEVC1 samples crystallised from various solvents.

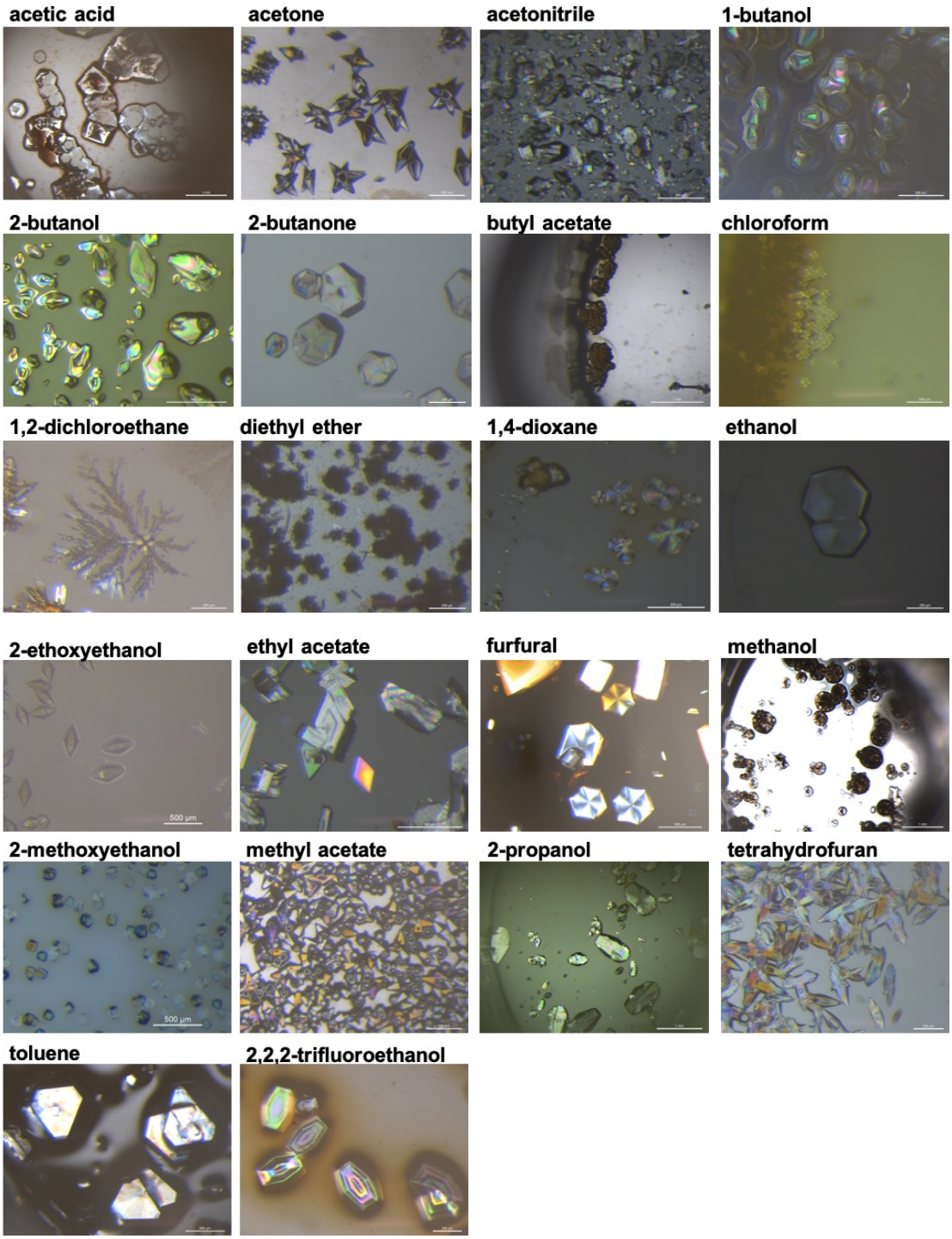

Figure A6.25: Representative optical micrographs of TAEVC2 samples recrystallised from various solvents.

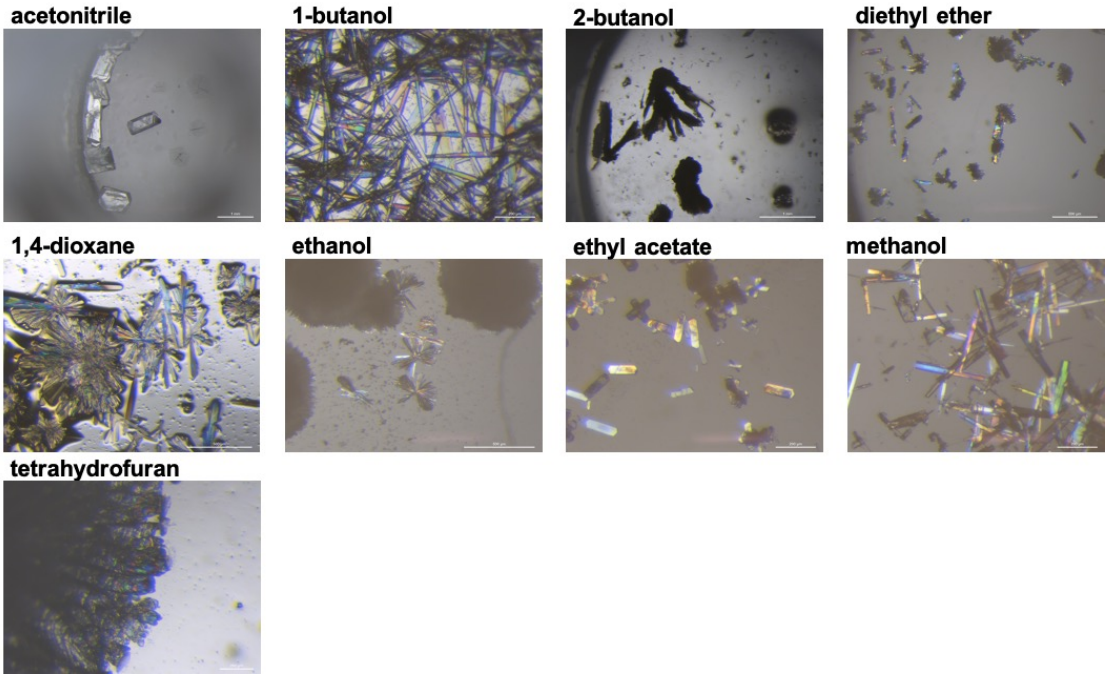

Figure A6.26: Representative optical micrographs of TAEVC3 samples recrystallised from various solvents.

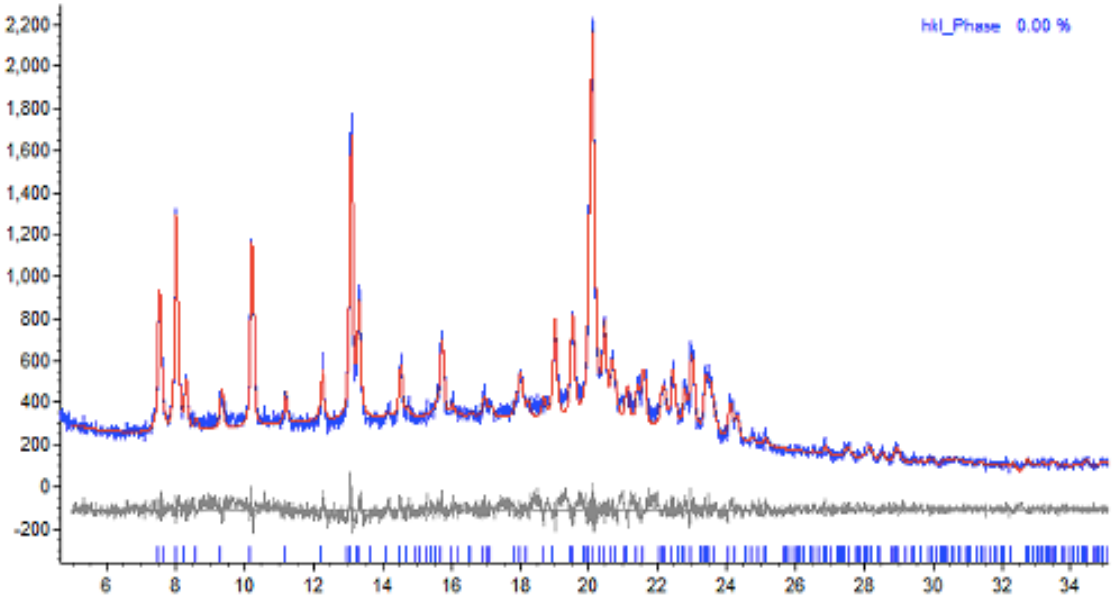

Figure A6.27: Pawley fit of TAEVC2 starting material melted at 175°C and allowed to recrystallise by slow cooling to room temperature. The residual values obtained for the Pawley fit were R_{wp} = 8.03% and R_p = 6.23% and the refined unit cell parameters were a = b = 13.65 (15) Å, and c = 64.3 (3) Å. The refinement was performed in the $P6_1$ space group.

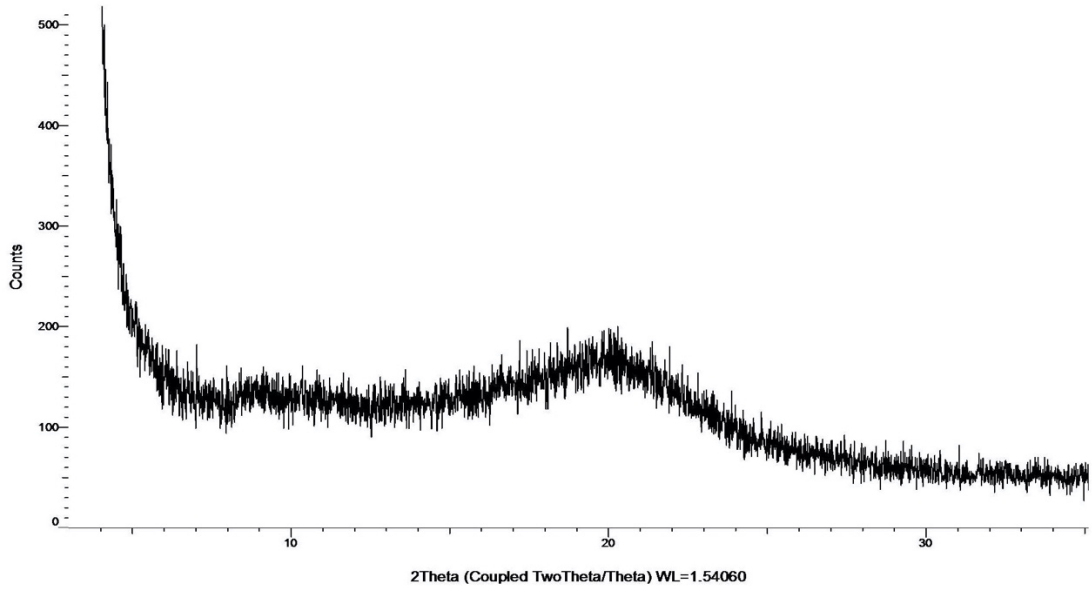

Figure A6.28: Representative XRPD pattern corresponding to TAEVC3 starting material melted at 200°C and allowed to recrystallise by slow cooling to room temperature.

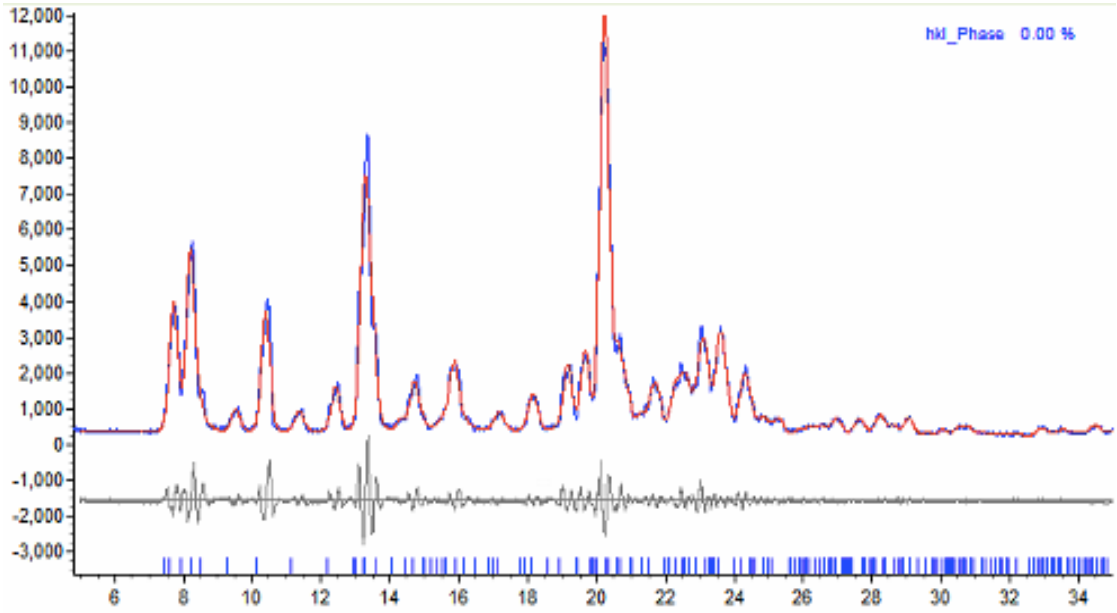

Figure A6.29: Pawley fit of TAEVC2 material obtained from supercritical fluid extraction. The residual values obtained for the Pawley fit were R_{wp} = 10.20% and R_p = 7.86% and the refined unit cell parameters were a = b = 13.682 (7) Å, and c = 64.518 (7) Å. The refinement was performed in the $P6_1$ space group.

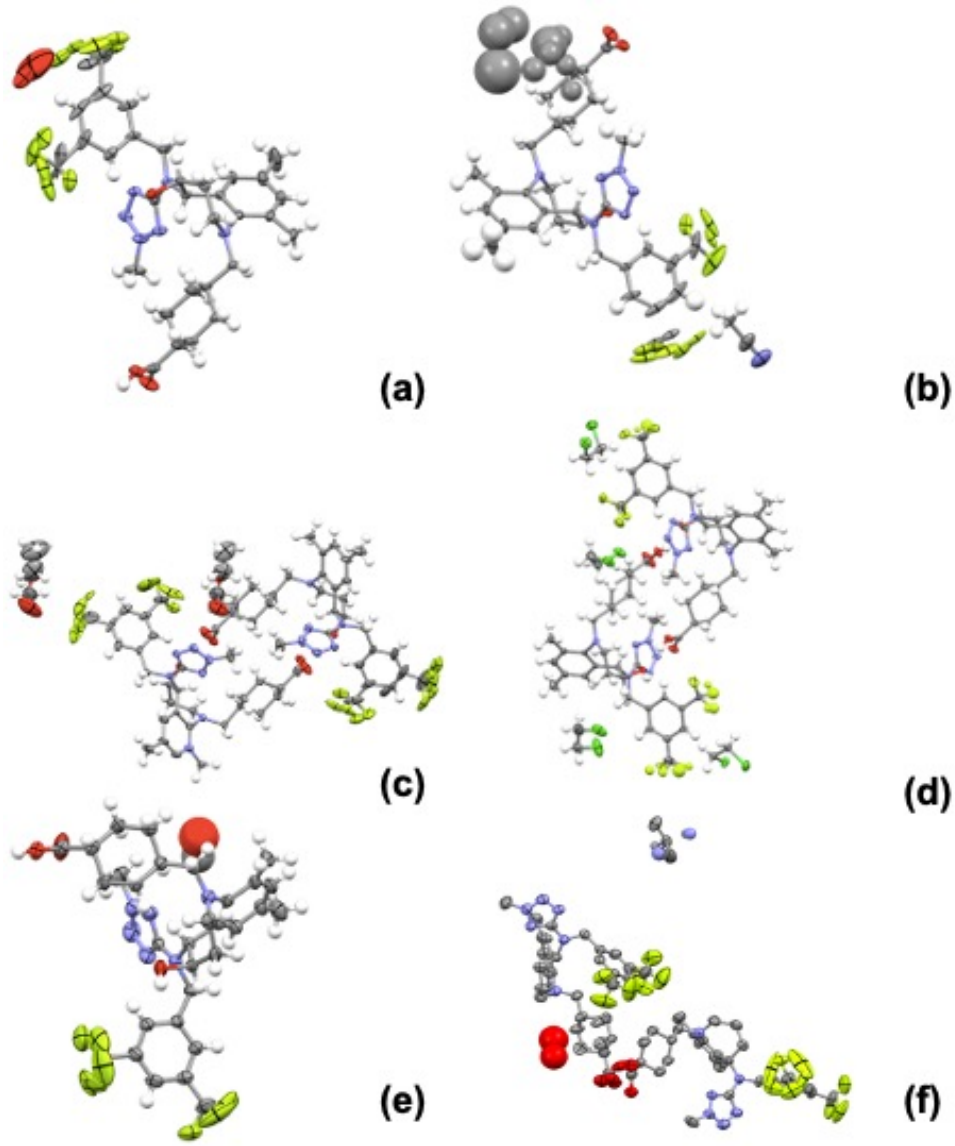

Figure A6.30: Thermal ellipsoid models, drawn at the 50% probability, depicting the asymmetric unit of TAEVC1 – acetonitrile (a), TAEVC2 – acetonitrile (b) TAEVC2 – ethyl acetate (c) TAEVC3 – 1,2-dichloroethane (d), TAEVC3 – methanol (e) solvates and EVC hemi TBA – hemihydrate salt cocrystal (f).

Table A6.1: Select physicochemical properties of solvents utilised in experimental screening of EVC and TAEVC. Dielectric constant values, indicative of solvent polarity, are derived from Marcus, 1998 and Lide, 2005. Hydrogen-bond donor and acceptor numbers were obtained from the PubChem database (National Institutes of Health, US).

Solvent	Molecular Weight (g/mol)	Boiling Point (°C)	Dielectric Constant	Hydrogen Bond Donor Count	Hydrogen Bond Acceptor Count
Acetic Acid	60.05	118	6.15	1	2
Acetone	58.08	56.05	20.56	0	1
Acetonitrile	41.05	81.65	35.94	0	1
1-Butanol	74.12	117.7	17.51	1	1
2-Butanol	74.12	98 – 100	16.56	1	1
2-Butanone	72.11	79.6	18.11	0	1
Butyl Acetate	116.16	126.1	5.01	0	2
Chloroform	119.38	61.2	4.89	0	0
Cyclohexane	84.16	80.74	2.02	0	0
1,2-Dichloroethane	98.96	83.5	10.36	0	0
Diethyl Ether	74.12	34.6	4.20	0	1
1,4-Dioxane	88.11	101.1	2.21	0	2
Ethanol	46.07	78.5	24.55	1	1
2-Ethoxyethanol	90.12	135.6	29.60	1	2
Ethyl Acetate	88.11	77	6.02	0	2
Furfural	96.09	162	42.1	0	2
Hexane	86.18	68.5 - 69.1	1.88	0	0
Methanol	32.04	64.6	32.66	1	1
2-Methoxyethanol	76.09	124	16.93	1	2
Methyl Acetate	74.08	57.1	5.01	0	2
2-Propanol	60.10	82.4	19.92	1	1
THF	72.11	65	7.58	0	1
Toluene	92.14	110.6	2.38	0	0
TFE	100.04	78	26.27	1	4

Table A6.2: Details of atomic disorder in the crystal structure of EVC hemi TBA – hemihydrate.

Crystal Structure	Disordered Atoms	Atomic Site Occupancy (%)
EVC Hemi TBA - Hemihydrate	F1A : F1B	48 : 52
	F2A : F2B	48 : 52
	F3A : F3B	48: 52
	F4A : F4B	48 : 52
	O13A : O13B	43 : 57
	C2A : C2B	51 : 49
	C3A : C3B	51 : 49
	C6A : C6B	51 : 49

Table A6.3: Details of atomic disorder in various crystal structures of TAEVC materials.

Crystal Structure	Disordered Atoms	Atomic Site Occupancy (%)
TAEVC1 - Acetonitrile	F1A : F1B	43 : 57
	F2A : F2B	43 : 57
	F3A : F3B	43 : 57
	F4A : F4B	43 : 57
	F6A : F6B	43 : 57
	C1A : C1B	43 : 57
	C5A : C5B	43 : 57
TAEVC2 - Acetonitrile	F1A : F1B	42 : 58
	F2A : F2B	42 : 58
	F3A : F3B	42 : 58
	F4A : F4B	42 : 58
	C5A : C5B	42 : 58
TAEVC2 – Ethyl Acetate	F1A : F1B	46.4 : 53.6
	F2A : F2B	46.4 : 53.6
	F3A : F3B	46.4 : 53.6
	F5A : F5B	46.4 : 53.6
	F6A : F6B	46.4 : 53.6
	F7A : F7B	46.4 : 53.6
	F9A : F9B	46.4 : 53.6
	F10A : F10B	46.4 : 53.6
	F11A : F11B	46.4 : 53.6
	F12A : F12B	46.4 : 53.6
	C40A : C40B	46.4 : 53.6
	C41A : C41B	46.4 : 53.6
TAEVC3 – 1,2-Dichloroethane	F1A : F1B	56.6 : 43.4
	F3A : F3B	56.6 : 43.4
	F4A : F4B	56.6 : 43.4
	F5A : F5B	56.6 : 43.4
	F8A : F8B	56.6 : 43.4
	F12A : F12B	56.6 : 43.4
TAEVC3 – Methanol	F1A : F1B	41.4 : 58.6
	F3A : F3B	41.4 : 58.6
	F5A : F5B	41.4 : 58.6

Table A6.4: Void volume occupied by solvent molecules in various TAEVC crystal structures.

Crystal Structure	Void Volume Occupied by Solvent (%)
TAEVC1 – Acetonitrile	26.3
TAEVC1 – Butyl Acetate	23.3
TAEVC2 – Acetonitrile	26.4
TAEVC2 – Ethyl Acetate	19.4
TAEVC3 – Acetonitrile	32.9
TAEVC3 – 1,2-Dichloroethane	15.8
TAEVC3 – Methanol	7.3
TAEVC3 – Toluene	28.4

Table A6.5: Packing coefficients of various TAEVC crystal structures.

Crystal Structure	Packing Coefficient
TAEVC1 – Acetonitrile	0.549
TAEVC1 – Butyl Acetate	0.559
TAEVC2 – Acetonitrile	0.678
TAEVC2 – Ethyl Acetate	0.624
TAEVC3 – Starting Material	0.650
TAEVC3 – Acetonitrile	0.564
TAEVC3 – 1,2-Dichloroethane	0.675
TAEVC3 – Methanol	0.677
TAEVC3 – Toluene	0.683